

The Minerals, Metals & Materials Series

Paul Follansbee

Fundamentals of Strength

Principles, Experiments, and
Applications of an Internal State
Variable Constitutive Formulation

Second Edition

TMS

 Springer

The Minerals, Metals & Materials Series

The Minerals, Metals & Materials Series publications connect the global minerals, metals, and materials communities. They provide an opportunity to learn about the latest developments in the field and engage researchers, professionals, and students in discussions leading to further discovery. The series covers a full range of topics from metals to photonics and from material properties and structures to potential applications.

More information about this series is available at <https://link.springer.com/bookseries/15240>

Paul Follansbee

Fundamentals of Strength

Principles, Experiments, and Applications
of an Internal State Variable Constitutive
Formulation

Second Edition

TMS

 Springer

Paul Follansbee
Greensburg, PA, USA

This book includes lecturer materials at [sn.pub/lecturer-material](https://doi.org/10.1007/978-3-031-04556-1)

ISSN 2367-1181

ISSN 2367-1696 (electronic)

The Minerals, Metals & Materials Series

ISBN 978-3-031-04555-4

ISBN 978-3-031-04556-1 (eBook)

<https://doi.org/10.1007/978-3-031-04556-1>

1st edition: © The Minerals, Metals & Materials Society 2014

2nd edition: © The Minerals, Metals & Materials Society 2022

This work is subject to copyright. All rights are solely and exclusively licensed by the Publisher, whether the whole or part of the material is concerned, specifically the rights of translation, reprinting, reuse of illustrations, recitation, broadcasting, reproduction on microfilms or in any other physical way, and transmission or information storage and retrieval, electronic adaptation, computer software, or by similar or dissimilar methodology now known or hereafter developed.

The use of general descriptive names, registered names, trademarks, service marks, etc. in this publication does not imply, even in the absence of a specific statement, that such names are exempt from the relevant protective laws and regulations and therefore free for general use.

The publisher, the authors and the editors are safe to assume that the advice and information in this book are believed to be true and accurate at the date of publication. Neither the publisher nor the authors or the editors give a warranty, expressed or implied, with respect to the material contained herein or for any errors or omissions that may have been made. The publisher remains neutral with regard to jurisdictional claims in published maps and institutional affiliations.

This Springer imprint is published by the registered company Springer Nature Switzerland AG
The registered company address is: Gewerbestrasse 11, 6330 Cham, Switzerland

Foreword to the Second Edition

This second edition monograph by Professor Paul S. Follansbee encompasses firstly an introduction to the elements controlling the mechanical behavior of metals, that is, crystal structure, thermodynamics, dislocations and twinning, defect-obstacle interactions, work hardening, deformation kinetics, and how the mechanical behavior of metals is quantified using mechanical testing. This book then provides an in-depth introduction as both a teaching aid to the faculty member and/or student to the mechanistic basis of an internal-state-variable-based constitutive model, specifically the Mechanical Threshold Strength (MTS) Model, as well as a seminal reference to the professional researching and modeling the mechanical behavior of FCC, BCC, and HCP metals and alloys. The thermodynamic and physical basis of the model's derivation is presented in detail as well as the evolution of the modeling approach to first treat pure metals, then alloys, and finally the complications imposed by multi-phase alloys, including a new chapter on nickel-base superalloys.

The methodology of data requirements, data analyses, and the derivation of the different terms of the MTS model are summarized for a fictitious metal to illustrate the step-by-step procedures for the model's construction. Thereafter, three chapters of the monograph present detailed reviews of the application of the MTS model to FCC pure metals and alloys, followed by BCC metals and alloys, and finally HCP metals and alloys where the complications of both deformation twinning and dynamic strain aging affects are discussed. Building upon the approaches set forth in the previous chapters, the author presents a chapter considering the deformation in austenitic stainless steels including both the effects of dynamic strain aging as well as the impact of irradiation damage on work hardening and deformation kinetics. A new chapter summarizes the observations of dynamic strain aging in several metals and introduces a model for the transport of solutes to the dislocation core, which gives insight to the kinetics. Application of the model to the strength and deformation response of heavily deformed metals, such as that encountered during ECAP (Equal Channel Angular Pressing) is described for a number of metals and alloys. Finally, a summary of the status of the MTS model and the challenges of additional

physics requirements for internal-state-variable models to complex loading and processing paths is discussed.

This is an exceptional monograph for the student, faculty researcher or professor, and the experimental or theoretical and modeling researcher tasked with understanding the use of physically based predictive constitutive models for metals and alloys written by the preeminent author of the Mechanical Threshold Strength Model.

Los Alamos National Laboratory,
Los Alamos, NM, USA

George T. (Rusty) Gray III

Preface to the First Edition

This monograph was compiled to accomplish several objectives. First, I have enjoyed the opportunity to work with undergraduate students at Saint Vincent College (SVC) in Latrobe, Pennsylvania, on projects related to deformation modeling in metals. While I teach an introductory materials course, I have found that each time I take on a student I have spent considerable time independently teaching the student about the basis of the Mechanical Threshold Stress (MTS) constitutive model—an internal state variable formulation. I have found it necessary to review topics related to mechanical testing, crystal structure, thermodynamics, dislocation motion, dislocation–obstacle interactions, hardening through dislocation accumulation, and deformation kinetics. Thus, I chose to write this monograph so that information they needed would be available in a single source. This monograph touches upon some topics that are covered in much more detail in available introductory materials textbooks. The chapter on structure and bonding, for instance, introduces the student to interatomic forces and dislocations, because these are essential to the understanding of strength. However, the material is incomplete and not intended to replace the level of coverage found in an introduction to materials engineering textbook.

A second objective has been to document as completely as possible the mechanistic basis of the MTS model. The model has been under development for 35 years and has experienced use and evolution by multiple investigators. I believed a monograph focused on the elements of the model would assist others in its application. To accomplish this, I have tried to be clear about parts of the model that are soundly based—and I attempt to describe this—and others that are based on less-sound assumptions. A chapter has also been included to instruct investigators how to develop MTS model constants. I created a fictitious metal—FoLLy alloy—to demonstrate the required experimental test matrix and how measurements are analyzed.

Finally, I have included numerous examples of model implementation. In most cases, data available in the open literature has been used. Often, data has been extracted from a published figure using a digitization protocol, followed by curve smoothing to remove digitization errors if the published curve is smooth. Experience

suggests that the digitized data agrees within 2% of the actual data. Analysis of published data is not intended to repeat work in the literature but to show how experience with the MTS model has evolved, how this experience has eased model implementation, and how the MTS model can be used to understand the effects of new strengthening mechanisms, e.g., fine grain processing or irradiation damage, when deformation in the base alloy is well understood.

Preface to the Second Edition

I was pleased with the first edition and with feedback from those who found it to be a useful reference. I did not think the treatment of dynamic strain aging was as clear as it could have been. The “signatures” of DSA were noted in niobium, vanadium, steels, titanium, and austenitic stainless steel. They were also found in analyses of the nickel-base superalloys added to the second edition. I reviewed existing models of DSA, and in Chap. 13 of this edition, I proposed a model based on the transport of solute to a dislocation core. Several simplifying assumptions were required to isolate the operative kinetics. The proposed model led to the conclusion that the kinetic equation proposed in the first edition was not accurate. Furthermore, the model enabled an estimate of the magnitude of strengthening introduced by DSA as well as an estimate of the strain-rate sensitivity. I am hoping that readers find this to be a useful addition to this monograph.

As mentioned above, a chapter was added on deformation in nickel-base superalloys. This was challenging due to the confounding contributions of the stress anomaly and DSA in these systems. However, analysis of deformation over a range of temperatures and strain rates using the MTS formalism allowed some deconvolution of these contributions. As in the analyses of irradiation damage and of shock-induced hardening that were included in the first edition, the superalloy chapter demonstrates how an internal state variable formulation, and the MTS model in particular, can be used to gain insight into some very complex deformation processes.

Finally, writing this second edition gave me the opportunity to correct numerous small and not-so-small errors that can creep into a textbook.

Greensburg, PA, USA

Paul Follansbee

Acknowledgment

Much of the work summarized in this monograph was performed at Los Alamos National Laboratory. Sig Hecker brought me there in 1981 to join the mechanical properties team and develop a research program in dynamic deformation mechanisms and experimentation. In the mid-1980s, Sig created and led the Center for Materials Science (CMS) at Los Alamos and hired Fred Kocks, Terry Mitchell, and Ricardo Schwartz as permanent CMS staff. Along with the opportunity to interact with these experienced materials scientists, the CMS supported a Summer Research Group, which included preeminent scientists such as Mike Ashby, David Embury, John Hirth, John Hutchinson, Ali Argon, Heinz Mecking, Frans Spaepen, and Tony Evans. The annual opportunity to present my evolving research and receive feedback was invaluable.

I particularly recall one seminar given by John Jonas, McGill University, in the early 1980s. The title of this seminar was, the perhaps blasphemous, “Metallurgy by MTS.” During this talk, John emphasized how much one can learn about a material and indeed its microstructure from a mechanical test. In a way, this monograph provides further support for this premise. Moreover, it is interesting to note how much impact a single seminar or professional interaction can have on an early career scientist.

The interactions with Fred Kocks over a 10-year period were intense and productive. Much of the theory that underpins the MTS model was developed by Fred and Heinz Mecking. My contribution was a thorough experimental program that endeavored to measure the state variables and their evolution in model (FCC) metals and then to expand the modeling to more complex materials systems and processing histories.

It is impossible to acknowledge enough my professional collaboration and friendship with Rusty Gray. Rusty was brought to Los Alamos to develop a research program studying shock deformation. He quickly rose to lead the dynamic deformation research team and is recognized as one of the world’s experts in this field. Members of his team, including Shuh-Rong Chen, Anna Zurek, John Bingert, Dick Hoagland, Ellen Ceretta, Carl Trujillo, Carl Cady, Bill Blumenthal, Mike Stout,

Manny Lovato, Mike Lopez, and, over the years, many post docs and graduate students, made up an incredibly strong research group.

I have had many productive interactions with scientists all around the world. Yuri Estrin and I share a strong interest in physically based constitutive laws. The work led by Sia Nemat-Nasser at the University of California, San Diego (UCSD), is of very high quality. I particularly enjoyed a chance to interact with this team during a 1987 sabbatical. I call attention to my discussions with Marc Meyers, Ron Armstrong, Paul Dawson, Rod Clifton, Amiya Mukerjee, Tony Rollett, Glenn Daehn, John Hack, K. T. Ramesh, Qiuming Wei, Yuntian Zhu, David Srolovitz, and many others.

I wish to thank Jim Williams who served as my mentor and thesis advisor at Carnegie Mellon University. He is a model for the melding of scientific depth with application in the materials discipline, which has been one objective of this monograph. Jim was an early supporter of this project and has offered much interest and encouragement.

I am grateful for the full support provided to me by Br. Norman Hipps, President of Saint Vincent College; Dr. John Smetanka, Vice President for Academic Affairs; and Steve Jodis, Dean of the Boyer School of Natural Sciences, Mathematics, and Computing. Saint Vincent College has provided me a wonderful environment for creating this monograph. I've also had the opportunity to work with several students on this project. Two of the chapters include work that comprised part of the undergraduate research projects of Frank McGrogan and Aaron Weiss. I acknowledge the work of Caitlin Sawyer, who reviewed chapters and searched for typographical errors; Marley Case, who created several diagrams using AutoCAD®; and Ashlee Zaffina and Loren Ostrosky, who helped compile the index.

My wife Carolyn has fully supported my efforts on this project and has even helped with scanning and digitization of literature data and other tasks. I could not have completed this monograph without her partnership. My three children, David, John, and Nicole, have followed my progress with interest and support. I hope the completion of this project has provided a lesson on the achievement of challenging goals.

How to Use This Textbook

Students and others who have not had an introductory materials engineering course and are unfamiliar with mechanical testing to measure strength will want to start with Chap. 1, since this introduces basic concepts of stress, strain, and strain rate. Then, they may wish to continue with Chap. 2, which provides basic information on crystal structure and interatomic forces. The concept of dislocations is also introduced. Basic knowledge of dislocations is required before the reader can continue with Chap. 3, which provides an overview of basic strengthening mechanisms.

Those readers who are equipped with a working knowledge of the concepts above and who are most interested in understanding the Mechanical Threshold Stress constitutive model may be able to begin with Chap. 4. This chapter discusses the dislocation–obstacle profile (variation of force versus distance moved) as the dislocation passes through a defected structure. It discusses features of this profile and the role played by thermal activation in deformation. Simple expressions for the temperature dependence of the yield stress are derived, and the importance of the yield stress at 0 K is emphasized. This chapter begins to compare model predictions with experimental data using simple kinetic analyses.

Chapter 5 introduces the basic MTS model—both the kinetic law and the hardening law. It discusses the path dependence that is observed in metal deformation and argues that a constitutive law needs to be able to follow path dependence.

Chapter 6 continues development of the MTS model by introducing various refinements that have been made to the basic development. Most important of these is the modification to the kinetic law to describe contributions from multiple strengthening mechanisms.

Chapter 7 demonstrates implementation of the MTS model through a fictitious metal—FoLLyalloy. With the desire to create a constitutive law for this alloy, the chapter leads the reader through the required experimental and analysis procedures.

Chapter 8 reviews work in copper, nickel, nickel-carbon alloys, and other alloys to illustrate application of the model in FCC systems. In fact, the model has been most rigorously applied to these systems. Questions related to the treatment of

multiple strengthening mechanisms are addressed. Also, the results demonstrate the temperature limit of the models developed to date.

The application of the model to BCC pure metals and alloys is discussed in Chap. 9. Deformation in AISI 1018 steel, pure vanadium, and pure niobium is analyzed according to the procedures described for another fictitious alloy—UfKone1. Contributions of the Peierls obstacle are included as a second state variable and complications introduced by deformation twinning and dynamic strain aging are discussed.

Chapter 10 addresses deformation in zinc, cadmium, magnesium, AZ31B (a magnesium alloy), zirconium, Zircaloy-2, titanium, and Ti6Al-4V. The confounding contributions of deformation twinning and dynamic strain aging are analyzed from the standpoint of an internal state variable formulation.

Chapter 11 considers deformation in austenitic stainless steels. It applies methods developed in earlier chapters. The unique effect of nitrogen on strengthening in these systems is analyzed. Dynamic strain aging is again observed under certain conditions, and the unique “signatures” of DSA when active are summarized. The effect of irradiation damage on hardening and deformation kinetics is also discussed.

Chapter 12 uses deformation in nickel-base superalloys to highlight the ability of the MTS formalism to de-convolute competing deformation mechanisms. In this case, anomalous hardening in these systems that has enabled their use at very high operating temperatures is not directly modeled using the operative equations. Rather, the differences between the measured stresses and the predicted stresses in absence of anomalous hardening are used to shed insight on the individual strength contributions.

The affect of dynamic strain aging documented in several of the metals analyzed in Chaps. 9 through 12 is analyzed in depth in Chap. 13. A model for transport of solutes to the dislocation core is used to better understand the resulting strength enhancements and the operating deformation kinetics.

Chapter 14 introduces complications introduced by large-strain processing of metals, including texture effects and the stress dependence of the activation energy. Predictions of the model for ECAP processed copper, nickel, stainless steel, and tungsten are compared to stress–strain measurements on the recovered, processed metals.

Chapter 15 offers a summary of the status of the MTS model formulation. Suggestions for further research are included. Included in this chapter is a discussion—based on all of the analyses presented in the monograph—of the applicable temperature limits of the models.

Chapters 1 through 14 include exercises to assist the reader with the model application. Hypothetical data as well as actual literature data are used. Analyses of these data sets serve as practice for the student. Solution sets for all of the

exercises are included in the supplementary material available at [https://doi.org/10.1007/978-3-031-04556-1_X¹]. The Microsoft Excel spreadsheets used for each of the exercises, where required, can also be found at this online resource. These spreadsheets offer templates for students and practitioners to use in their unique deformation analyses. Finally, Microsoft PowerPoint lecture charts for each of the chapters are available at this online resource.

¹Note that “X” is the chapter number. Replace “X” with the chapter number of interest, e.g., 1 through 15.

Contents

1	Measuring the Strength of Metals	1
1.1	How Is Strength Measured?	1
1.2	The Tensile Test	3
1.3	Stress in a Test Specimen	5
1.4	Strain in a Test Specimen	6
1.5	The Elastic Stress Versus Strain Curve	6
1.6	The Elastic Modulus	7
1.7	Lateral Strains and Poisson’s Ratio	9
1.8	Defining Strength	10
1.9	Stress–Strain Curve	11
1.10	The True Stress–True Strain Conversion	16
1.11	Example Tension Tests	18
1.12	Accounting for Strain Measurement Errors	22
1.13	Formation of a Neck in a Tensile Specimen	25
1.14	Strain Rate	27
1.15	Summary	29
	Exercises	29
	References	34
2	Structure and Bonding	35
2.1	Forces and Resultant Energies Associated with an Ionic Bond	35
2.2	Elastic Straining and the Force Versus Separation Diagram	38
2.3	Crystal Structure	39
2.4	Plastic Deformation	42
2.5	Dislocations	45
2.6	Summary	50
	Exercises	51
	References	53

- 3 Contributions to Strength 55**
 - 3.1 Strength of a Single Crystal 55
 - 3.2 The Peierls Stress 60
 - 3.3 The Importance of Available Slip Systems and Geometry of HCP Metals 62
 - 3.4 Contributions from Grain Boundaries 64
 - 3.5 Contributions from Impurity Atoms 67
 - 3.6 Contributions from Stored Dislocations 69
 - 3.7 Contributions from Precipitates 72
 - 3.8 Summary 72
 - Exercises 73
 - References 76

- 4 Dislocation–Obstacle Interactions 77**
 - 4.1 A Simple Dislocation/Obstacle Profile 77
 - 4.2 Thermal Energy—Boltzmann’s Equation 79
 - 4.3 The Implication of 0 K 80
 - 4.4 Addition of a Second Obstacle to a Slip Plane 80
 - 4.5 Kinetics 82
 - 4.6 Analysis of Experimental Data 84
 - 4.7 Multiple Obstacles 88
 - 4.8 Kinetics of Hardening 89
 - 4.9 Summary 90
 - Exercises 91
 - References 93

- 5 A Constitutive Law for Metal Deformation 95**
 - 5.1 Constitutive Laws in Engineering Design and Materials Processing 95
 - 5.2 Simple Hardening Models 100
 - 5.3 State Variables 103
 - 5.4 Defining a State Variable in Metal Deformation 104
 - 5.5 The Mechanical Threshold Stress Model 105
 - 5.6 Common Deviations from Model Behavior 110
 - 5.7 Summary 113
 - Exercises 114
 - References 116

- 6 Further MTS Model Developments 119**
 - 6.1 Removing the Temperature Dependence of the Shear Modulus 119
 - 6.2 Introducing a More Descriptive Obstacle Profile 123
 - 6.3 Dealing with Multiple Obstacles 125
 - 6.4 Defining the Activation Volume in the Presence of Multiple Obstacles Populations 132

- 6.5 The Evolution Equation 134
- 6.6 Adiabatic Deformation 135
- 6.7 Summary 138
- Exercises 139
- References 142
- 7 Data Analysis: Deriving MTS Model Parameters 143**
 - 7.1 A Hypothetical Alloy 143
 - 7.2 Pure Fosium 144
 - 7.3 Hardening in Pure Fosium 147
 - 7.4 Yield Stress Kinetics in Unstrained FoLLyalloy 147
 - 7.5 Hardening in FoLLyalloy 150
 - 7.6 Evaluating the Stored Dislocation Obstacle Population 152
 - 7.7 Deriving the Evolution Equation 160
 - 7.8 The Constitutive Law for FoLLyalloy 162
 - 7.9 Summary 164
 - Exercises 164
- 8 Application of MTS Model to Copper and Nickel 167**
 - 8.1 Pure Copper 168
 - 8.2 Follansbee and Kocks Experiments 169
 - 8.3 Temperature-Dependent Stress–Strain Curves 175
 - 8.4 Eleiche and Campbell Measurements in Torsion 179
 - 8.5 Analysis of Deformation in Nickel 185
 - 8.6 Predicted Stress–Strain Curves in Nickel
and Comparison with Experiment 190
 - 8.7 Application to Shock Deformed Nickel 192
 - 8.8 Deformation in Nickel Plus Carbon Alloys 194
 - 8.9 Monel 400—Analysis of Grain-Size Dependence 197
 - 8.10 Copper–Aluminum Alloys 201
 - 8.11 Summary 207
 - Exercises 208
 - References 209
- 9 Application of MTS Model to BCC Metals and Alloys 211**
 - 9.1 Pure BCC Metals 212
 - 9.2 Comparison with Campbell and Ferguson Measurements 220
 - 9.3 Trends in the Activation Volume for Pure BCC Metals 223
 - 9.4 Structure Evolution in BCC Pure Metals and Alloys 226
 - 9.5 Analysis of the Constitutive Behavior of a Fictitious
BCC Alloy—UfKonel 227
 - 9.6 Analysis of the Constitutive Behavior of AISI 1018 Steel 231
 - 9.7 Analysis of the Constitutive Behavior of Polycrystalline
Vanadium 241

9.8	Deformation Twinning in Vanadium	247
9.9	Signature of Dynamic Strain Aging in Vanadium	250
9.10	Analysis of Deformation Behavior of Polycrystalline Niobium	253
9.11	Summary	261
	Exercises	264
	References	269
10	Application of MTS Model to HCP Metals and Alloys	271
10.1	Pure Zinc	272
10.2	Kinetics of Yield in Pure Cadmium	277
10.3	Structure Evolution in Pure Cadmium	280
10.4	Pure Magnesium	284
10.5	Magnesium Alloy AZ31	287
10.6	Pure Zirconium	298
10.7	Structure Evolution in Zirconium	302
10.8	Analysis of Deformation in Irradiated Zircaloy-2	308
10.9	Analysis of Deformation Behavior of Polycrystalline Titanium	315
10.10	Analysis of Deformation Behavior of Titanium Alloy Ti6Al-4V	329
10.11	Summary	335
	Exercises	339
	References	342
11	Application of MTS Model to Austenitic Stainless Steels	345
11.1	Variation of Yield Stress with Temperature and Strain Rate in Annealed Materials	345
11.2	Nitrogen in Austenitic Stainless Steels	350
11.3	The Hammond and Sikka Study in 316	358
11.4	Modeling the Stress–Strain Curve	360
11.5	Dynamic Strain Aging in Austenitic Stainless Steels	363
11.6	Application of the Model to Irradiation-Damaged Material	367
11.7	Summary	370
	Exercises	371
	References	375
12	Application of MTS Model to Nickel-Base Superalloys	377
12.1	Deformation in Nickel-Based Superalloys	377
12.2	Yield Stress Kinetics	379
12.3	Strain Hardening in Several Nickel-Base Superalloys	383
12.4	Signatures of Dynamic Strain Aging	399
12.5	Summary	401
	Exercises	402
	References	405

13	A Model for Dynamic Strain Aging	409
13.1	Review of Signatures of DSA	409
13.2	Focusing on the Increased Stress Levels Accompanying DSA	414
13.3	Toward a Mechanistic Understanding	416
13.4	Model Predictions	420
13.5	Predicting the Stresses When DSA is Active	424
13.6	Summary	427
	Appendix 13.A1 The Effect of an Incorrect Assumption on the Analysis Using Eq. 13.15	428
	Appendix 13.A2 The Effect of DSA on the Stage II Hardening Rate	430
	Exercises	433
	References	433
14	Application of MTS Model to the Strength of Heavily Deformed Metals	435
14.1	Complications Introduced at Large Deformations	435
14.2	Stress Dependence of the Normalized Activation Energy g_{oe}	436
14.3	Addition of Stage IV Hardening to the Evolution Law	440
14.4	Grain Refinement	443
14.5	Application to Large-Strain ECAP Processing of Copper	449
14.6	Further Insight into the Strain Hardening at High Strains	457
14.7	A Large-Strain Constitutive Description of Nickel	462
14.8	Application to Large-Strain ECAP Processing of Nickel	466
14.9	Application to Large-Strain ECAP Processing of Austenitic Stainless Steel	470
14.10	Analysis of Fine-Grained Processed Tungsten	477
14.11	Summary	480
	Exercises	481
	References	484
15	Summary and Status of Model Development	487
15.1	Analyzing the Temperature-Dependent Yield Stress	488
15.2	Stress Dependence of the Normalized Activation Energy g_{oe}	491
15.3	Evolution	491
15.4	Temperature and Strain-Rate Dependence of Evolution (Strain Hardening)	493
15.5	The Effects of Deformation Twinning	497
15.6	The Signature of Dynamic Strain Aging	500
15.7	Adding Insight to Deformation in Nickel-Base Superalloys	505
15.8	Adding Insight to Complex Processing Routes	505

15.9	Temperature Limits	511
15.10	Summary	514
	References	516
Index	519

About the Author



Paul Follansbee is a materials scientist and engineer with 35 years combined experience at Los Alamos National Laboratory, Howmet Castings, General Electric Corporate Research and Development, and Pratt and Whitney Aircraft. He earned a PhD in materials science and engineering from Carnegie Mellon University in 1981. He has a strong interest in high temperature materials and materials processing and has published extensively in the area of low temperature and high strain rate deformation behavior. He proposed and developed an internal state variable constitutive model—termed the Mechanical Threshold Stress Model—and applied it to Cu, Ni, Ti6Al-4V, and several other metals. For the past 20 years, he has served at various levels of technology management and leadership, including positions as Vice President of Technology for Howmet Castings and Division Leader of the Materials Science and Technology Division at Los Alamos. He joined Saint Vincent College in 2008 as the James F. Will Professor of Engineering Sciences where he taught courses related to general physics, materials, mathematics, and energy technologies and proposed and developed a 4-year undergraduate degree program in engineering science. He now serves as professor emeritus at this institution.

Symbols

a	Length of a unit cell in a cubic crystal
A	Cross-section area (Eq. 1.2)
A_C	Parameter in temperature-dependent heat capacity equation (Eq. 6.B5) (units: J/g/K)
A_{CS}	Constant in Eq. 4.17 (units of T, K)
A_i	Initial cross-sectional area (e.g., of a tensile specimen)
A_o	Model parameter in Eq. 6.29 (units: MPa)
A_1	Model parameter in Eq. 6.29 (units: MPa when $\dot{\epsilon}$ in units of s^{-1})
A_2	Model parameter in Eq. 6.29 (units: MPa·s ^{-1/2})
b	Burgers vector
B	Parameter in temperature-dependent specific heat equation (Eq. 6.B5) (units: J/g/K ²)
c	Concentration (Eq. 3.10) (units: typically weight percent)
c_p	Heat capacity (Eq. 6.31)
C	Parameter in temperature-dependent specific heat equation (Eq. 6.B5) (units: J K/g) ²
C_0	Solute concentration (weight percent)
C'	Solute concentration (g/cm ³)
d_{gs}	Grain size (Eq. 3.9)
D	Diffusion coefficient (Eq. 13.16) (units: m ² /s)
D_i	Initial diameter of a test specimen
D_f	Final diameter of a test specimen
D_o	Constant in Eq. 6.8 for the temperature-dependent shear modulus (units: GPa)
D_o	Constant in the diffusion equation (Eq. 13.16) (units: m ² /s)
E	Young's modulus (Eq. 1.5; units GPa)

² C is also used as a proportionality constant in Equation 5.3 and a (different) proportionality constant in Equation 5.4.

E_{app}	Apparent Young's modulus (Eq. 1.15)
E_{act}	Actual Young's modulus (Eq. 1.15)
F	Force
F	Constant in Eq. 14.10
F_A	Attractive force between two ions (Eq. 2.1)
g_o	Normalized (and dimensionless) activation energy (Eq. 6.6)
g_{so}	Normalized (and dimensionless) value of A_{CS} (Eq. 6.7)
g_{oi}	Normalized activation energy representing a specific obstacle population "i" (Eq. 6.18)
g_{eso}	Model activation energy in Eq. 6.26 with subscript "e" to emphasize interactions of dislocations with the stored dislocation density.
g_{oe0}	Initial value of g_{oe} at low values of strain (Eq. 14.10)
G	Total activation energy in absence of stress assistance (Eq. 4.8) ³
ΔG	Activation energy (Eq. 4.3)
k	Boltzmann's constant ($1/38 \times 10^{-23}$ J / K) ⁴ (Eq. 4.1)
k_c	Proportionality constant in Eq. 3.10
k_d	Proportionality constant in the Hall-Petch equation (Eq. 3.9)
K	Constant in the power law hardening equation (units of stress) (Eq. 5.1)
K	Proportionality constant in equation relating threshold stress to a solute concentration (Eq. 13.5)
K_{DSA}	Slope of the plot of s_i (or σ_{DSA}) versus σ_e in Eq. 9.9
$K_{\text{DSA}0}$	Proportionality constant in Eq. 9.9
$K_{\rho m}$	Proportionality constant in Eq. 13.17
K_S	Spring constant (Eq. 1.1; units: N/m)
J_2	Second invariant of the stress deviator (see Box 1.2)
ℓ	distance moved by dislocations in Orowan Equation (Eq. 2.14) and in Eq. 13.12
L	Length of a test specimen
L_f	Final length of a test specimen
L_i	Initial length of a test specimen (Eq. 1.4)
ΔL	Change in length (Eq. 1.4)
n	Exponent in the power law hardening equation (Eq. 5.1)
m	Strain-rate sensitivity (exponent in Eq. 5.3)
M	Taylor factor (Eq. 6.B3)
p	Exponent in Eq. 6.9—a more rigorous form of $\sigma(\hat{\sigma}, T, \dot{\epsilon})$
p_i	Exponent p representing a specific obstacle population (Eq. 6.18)
r	Separation distance between two ions (Eq. 2.1)
q	Exponent in Eq. 6.9—a more rigorous form of $\sigma(\hat{\sigma}, T, \dot{\epsilon})$
q_i	Exponent q representing a specific obstacle population (Eq. 6.18)

³ G also is used to represent the shear modulus (see Exercise 2.11 and Table E.2.11) but the temperature T does not appear with G in these cases.

⁴ k also is used in several equations as a constant (e.g., Equation 2.1), but its use as Boltzmann's constant is most prevalent.

q_e	Electronic charge on an ion (1.602×10^{-19} C) (Eq. 2.1)
q_s	Amount of solute per unit dislocation line length transported to a dislocation core at time t (Eq. 13.8)
Q_D	Activation energy in diffusion equation (Eq. 13.16) (Units: J/mole)
R	Gas constant (8.31 J/mol/K) (Eq. 5.6) ⁵
R_a	Atomic radius
R_d	Radius of a dislocation loop (Eq. 6.2)
s	Proportionality between σ and $\hat{\sigma}$ (Eq. 5.9) ($0 \leq s \leq 1$)
s_{1a}	Apparent value of s for population “ i ” that is influenced by Dynamic Strain Aging (Eq. 13.1)
S	Stiffness (Eq. 2.6)
S_o	Stiffness at the equilibrium separation distance between two ions
S_p	Spacing between precipitates (Eq. 3.17)
T	Temperature
T_H	Homologous temperature
T_o	Constant in Eq. 6.8 for the temperature-dependent shear modulus
U	Net energy in an ionic pair (Eq. 2.4)
U_A	Energy gained as two ions approach (Eq. 2.2)
U_i	Energy required to form isolated ions (Eq. 2.3)
v	Average dislocation velocity (see discussion following Eq. 2.14)
V	Volume
V_{CH}	Cross head velocity of a testing machine (Eq. 1.18)
V_i	Initial volume of a test specimen
V_f	Final volume of a test specimen
w	Width of a dislocation (Eq. 3.6)
ΔX	Change in length (Eq. 1.1)
Z	Zener-Hollomon parameter (Eq. 5.B1)
α	Constant in Eq. 13.14
α_v	Thermal expansion coefficient (Eq. 2.8)
γ'	Gamma prime strengthening precipitate in nickel-base superalloys (see Sect. 12.2)
γ''	Gamma double prime—also strengthening precipitate in nickel-base superalloys (see Sect. 12.3)
β	Constant in Eq. 13.8
γ_{oct}	Octahedral shear strain (see Box 1.2)
$\dot{\gamma}_{so}$	Constant in Eq. 4.17 (units of s^{-1})
$\bar{\epsilon}$	Effective strain (see Box 1.2)
$\epsilon_{e\text{app}}$	Apparent strain (Eq. 1.15)
$\epsilon_{e\text{act}}$	Actual strain (Eq. 1.15)
ϵ	True strain (Eq. 1.11)
ϵ_e	Engineering strain (Eq. 1.4)

⁵Note that the gas constant, R , and Boltzmann's constant, k , are related by Avogadro's number (6.022×10^{23} mole⁻¹).

ϵ_{eD}	Diametrical strain (Eq. 1.7)
ϵ_{ep}	Plastic strain (see Sect. 1.9)
ϵ_v	von Mises strain (see Box 1.2)
ϵ_o	Permittivity of vacuum (8.854×10^{-12} F/m or 8.854×10^{-12} C ² /J m) (see Exercise 2.1)
$\dot{\epsilon}$	Strain rate (s ⁻¹) (see Sect. 1.14)
$\dot{\epsilon}_o$	Constant in Eq. 4.3 (units of s ⁻¹)
$\dot{\epsilon}_{so}$	Constant in Eq. 5.13 (units s ⁻¹)
$\dot{\epsilon}_{oi}$	Value of $\dot{\epsilon}_o$ representing a specific obstacle population (Eq. 6.18)
$\dot{\epsilon}_{eso}$	Constant in Eq. 6.26
θ_{II}	Stage II hardening rate in a single crystal
κ	Exponent in Eq. 6.28
λ	Angle between load axis and slip direction in a single crystal (Eq. 3.4)
μ	Shear modulus
μ_o	Shear modulus at 0 K (Eq. 6.3; also see Eq. 6.8)
ν	Poisson's ratio (Eq. 1.9)
ν_o	Attempt frequency (Eq. 4.5)
ν^*	Activation volume (Eq. 6.B2)
ρ	Material density
ρ_m	Mobile dislocation density (units: cm ⁻²) (Eq. 13.11)
ρ_t	Total dislocation density (Eq. 13.13)
ρ_D	Dislocation density (Eq. 2.14)
σ	True stress
σ_a	Athermal stress (Eq. 5.11)
σ_{DSA}	Stress contribution specifically from Dynamic Strain Aging (Eq. 13.1)
σ_e	Engineering stress (Eq. 1.2)
σ_x	Resolved normal stresses in an x, y, z coordinate system (see Box 1.1)
σ_y	“
σ_x	“
σ_v	von Mises stress
σ_1	Normal stresses mapped to a principal stress coordinate system (see Box 1.1)
σ_2	“
σ_3	“
$\bar{\sigma}$	Effective stress (see Box 1.2)
$\hat{\sigma}$	Mechanical threshold stress, which is the stress necessary at 0 K required to overcome an obstacle opposing dislocation motion (see Sect. 4.3)
$\hat{\sigma}_i$	Mechanical threshold stress characterizing interactions of dislocations with a specific obstacle population—defined by the subscript “ i ” (Eq. 6.17)
$\hat{\sigma}_N$	Threshold stress induced by interaction of dislocations with nitrogen solutes in austenitic stainless steels (Eq. 11.5a and Eq. 13.3)
$\hat{\sigma}_s$	Saturation threshold stress at a specific temperature and strain rate (Eq. 5.12)
$\hat{\sigma}_{so}$	Saturation threshold stress at 0 K (Eq. 5.13)

$\widehat{\sigma}_{es}$	Saturation value of the mechanical threshold stress characterizing interactions of dislocations with the stored dislocation density at a specific temperature and strain rate (Eq. 6.25) (a more rigorous definition of $\widehat{\sigma}_s$)
$\widehat{\sigma}_{eso}$	0 K value of $\widehat{\sigma}_{es}$ (Eq. 6.26)
τ_{CRSS}	Stress required to initiate slip on a specific crystallographic plane in a specific crystallographic direction (Eq. 3.4)
τ_p	Peierls stress (Eq. 3.6)
τ_{max}	Theoretical stress required to slide one plane of atoms over another (Eq. 2.13)
τ_{oct}	Octahedral shear stress
τ_s	Saturation shear stress (Eq. 3.15)
τ_{so}	Saturation shear stress at 0 K (Eq. 4.17)
τ_{xy}	Resolved shear stresses in an x, y, z coordinate system (see Box 1.1)
τ_{yz}	“
τ_{xz}	“
φ	Angle between load axis and the normal to the slip plane of a single crystal (Eq. 3.4)
ψ	Model parameter specifying the fraction of mechanical work converted to heat (Eq. 6.31)
Ω	Related to the ratio of the mobile to the forest (total) dislocation densities (Eq. 13.21)

Chapter 1

Measuring the Strength of Metals



Introduction

The strength of metals is a fascinating topic that carries engineering and scientific implications. You can't build a bridge, design a turbine blade, or construct a transmission line tower without understanding the strength of the materials of construction in balance with the requirements of the system.

1.1 How Is Strength Measured?

Let's take a piece of metal and machine a *test specimen* of either the geometry shown in Figs. 1.1 or 1.2. Note that two geometries are shown. At the center point of these specimens, one has a circular cross section, whereas the other has a rectangular cross section. Either geometry can be used according to the material stock available.

After machining, this sample is attached to the "grips" of a test machine. An example of a testing machine is shown in Fig. 1.3. This is an "electromechanical" machine in that the moving crosshead is attached to very large screws (in the columns) that move the crosshead up or down with great force. The test specimen is mounted between the two grips.

Figure 1.4 shows a test specimen mounted between two grips. It also shows a "deflection measurement device" attached to the specimen. As force is applied to the top grip and the specimen elongates, the deflection measurement device gives a precise measurement of how much the specimen has elongated.

Along with specimen elongation, another measurement is required in this test, which is the force applied to the top grip (and thus the top end of the specimen) required to elongate it. This measurement is supplied by a "load cell" usually

Supplementary Information The online version contains supplementary material available at [\[https://doi.org/10.1007/978-3-031-04556-1_1\]](https://doi.org/10.1007/978-3-031-04556-1_1)



Fig. 1.1 Test specimen machined from a plate thick enough to give a circular cross section. (Courtesy of Westmoreland Mechanical Testing and Research Inc.)



Fig. 1.2 Test specimen machined from a plate that is too thin to give a large enough circular cross section. (Courtesy of Westmoreland Mechanical Testing and Research Inc.)

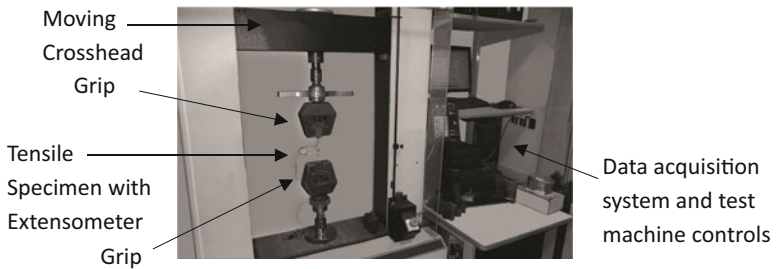


Fig. 1.3 Mechanical test frame with top and bottom grips. Courtesy of (Westmoreland Mechanical Testing and Research Inc.)

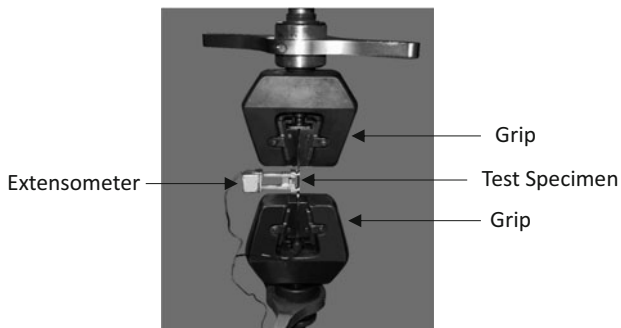


Fig. 1.4 Tensile specimen mounted in and ready for testing. Also shown is a deflection measurement device attached to two points on the specimen. (Courtesy of Westmoreland Mechanical Testing and Research Inc.)

mounted between the upper, moving crosshead and the top grip. Because the elongations in the specimen are so tiny, the measurement of elongation must be made on the actual test specimen. It is easier to measure the motion of the top crosshead, but this might be confounded by other deflections in the “load train” which is the ensemble of hardware between the moving crosshead and the stationary base; thus, the measurement movement of the top crosshead would likely be somewhat larger than the deflection in the test specimen. The measurement of force applied to the specimen, however, can be measured anywhere along the load train. In this sense, it is an easier measurement to make in materials testing.

1.2 The Tensile Test

After machining the test specimen, mounting it in a test machine, and setting up the load and displacement measurements, the test is ready to perform. This section describes what happens when a test specimen is mounted and a force is applied. Assume a cylindrical test specimen machined from mild steel with a machined cross-sectional diameter of 0.250 in. (6.35 mm) and a length of 1.0 in. (25.4 mm). Figure 1.5 illustrates the test configuration, including dimensions, for a mechanical test using a specimen such as shown in Fig. 1.1. For the test specimen indicated, the load F is applied to the end of the specimen, thereby stretching it. This is a “tensile” test in that the test specimen is placed into “tension.” If load were instead applied that led to shortening of the test specimen—and if the specimen could be kept from buckling—then the test is referred to as a “compression” test.

Table 1.1 shows the deflection in the specimen illustrated in Fig. 1.5 that would be measured as a function of the applied load. It is immediately evident that even with what appears to be very large forces on this test specimen, the deflections are quite small. With one ton of force (9897 N) pulling on the specimen, the specimen only elongates 0.00133 inches (33.7 μm).

Fig. 1.5 Schematic tensile test with dimensions

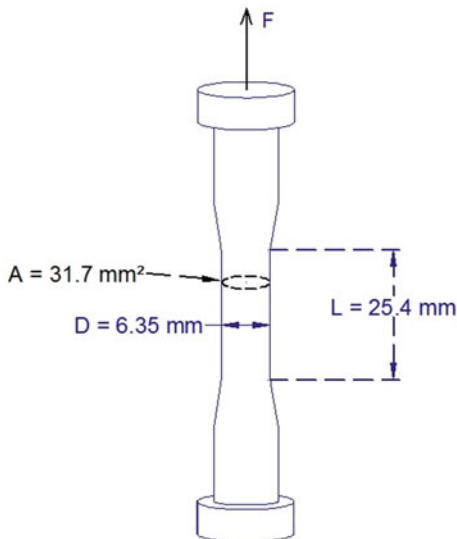


Table 1.1 Load and deflection measured for the specimen shown in Fig. 1.5

Load		Deflection	
Pounds	Newtons (N)	Inches	Meters
100	445	0.000066	0.00000169
200	890	0.000133	0.00000337
400	1179	0.000265	0.00000674
1000	4448	0.000664	0.0000169
1500	6672	0.000995	0.0000253
2000	8896	0.00133	0.0000337

Figure 1.6 plots the load versus the deflection—as if a deflection measurement was taken for every 100 pound increase in load. (Even though deflection has been defined as the dependent variable, which would normally be plotted on the y -axis, Fig. 1.6 plots deflection on the x -axis; this will be made clear later.)

It is evident in Fig. 1.6 that the force versus deflection measurements plot on a straight line. Recall from general physics that the behavior illustrated in Fig. 1.6 is analogous to the behavior of a spring, defined by the familiar equation:

$$F = K_S \Delta X \quad (1.1)$$

where F is the applied force and ΔX is the extension of the spring. In fact, the test specimen does behave like a spring. However, this test specimen is indeed a strong spring. Simple springs used in general physics laboratory experiments typically have spring constants on the order of ~ 10 N/m. As a comparison, the test specimen is a spring with a spring constant of:

$$K_S = \frac{F}{\Delta X} = \frac{8896 \text{ N}}{3.37 \times 10^{-5} \text{ m}} = 2.64 \times 10^8 \frac{\text{N}}{\text{m}}.$$

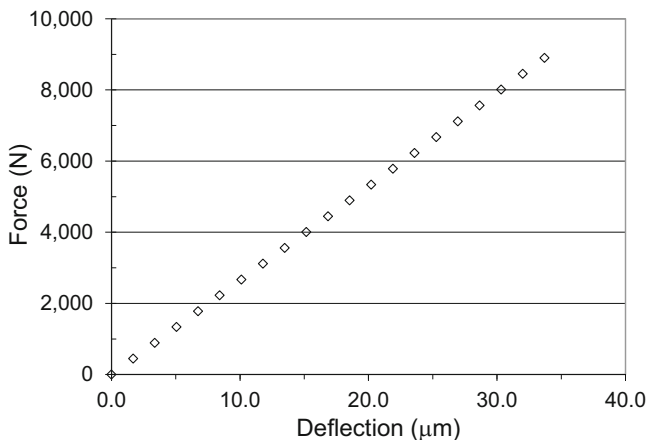


Fig. 1.6 Force (as MN or 10^6 N) plotted versus deflection (as μm or 10^{-6} m) for the specimen shown in Fig. 1.5

Thus, as a spring, the test specimen has a spring constant ~ 20 million times larger than the springs used in a common physics laboratory. When materials behave like this during a tensile test, they are said to be behaving as an “elastic” solid.

Just as with any spring, if the force on our tensile specimen is reduced, the elongation decreases until it reaches zero extension when the force goes to zero. That is, the elongation achieved due to the application of the load is “recovered” when the load is removed.

1.3 Stress in a Test Specimen

Imagine that the test specimen had a diameter of 0.500 in. (12.7 mm) instead of 0.250 in. (6.35 mm). One would expect that the spring constant of our test specimen would get even larger, and the same force would cause less elongation. To eliminate the effect of specimen size, the force, F , is divided by the cross-sectional area, A , to yield a “stress,” σ_e , where:

$$\sigma_e = \frac{F}{A} \quad (1.2)$$

Of course, stress in general is force divided by area. When deformation increases as shown in Fig. 1.6—which implies the specimen geometry changes—but stress is computed by dividing the force by the original area, then the stress is referred to as the *engineering stress*, which is why a subscript “e” is used in Eq. 1.2. Later (Sect. 1.10) the stress will be based on the current area. If F has the units of newtons and A has the units of m^2 , then the stress σ_e has the units N/m^2 , which is known as a pascal:

$$\text{Pa} = \frac{\text{N}}{\text{m}^2} \quad (1.2)$$

A pascal is a very small stress. Recall that the units of pressure are also force per unit area. Standard atmospheric air pressure is $\sim 10^5$ Pa. Thus, stresses in test specimens are more commonly stated in terms of 10^6 Pa or MPa. The engineering units for stress are pounds per square inch, or psi. Standard atmospheric air pressure is 14.7 psi. Accordingly, when using engineering units, stresses in test specimens are commonly stated in terms of 10^3 psi or ksi. (The “k” in ksi is often referred to as a “kip”—or 1000 lb.) The conversion between MPa and ksi is as follows:

$$\text{MPa} = \frac{\text{ksi}}{0.145} \quad (1.3)$$

1.4 Strain in a Test Specimen

Suppose the test specimen was machined with a length of 2.0 inches (50.8 mm) instead of 1.0 in. (25.4 mm). The same force would produce an extension in the 2.0-in.-long test specimen that is twice that in the 1.0-in.-long test specimen. To eliminate the effect of specimen length, L , on the test result, the extension, ΔL , is measured relative to the specimen’s initial length, L_i :

$$\varepsilon_e = \frac{\Delta L}{L_i} \quad (1.4)$$

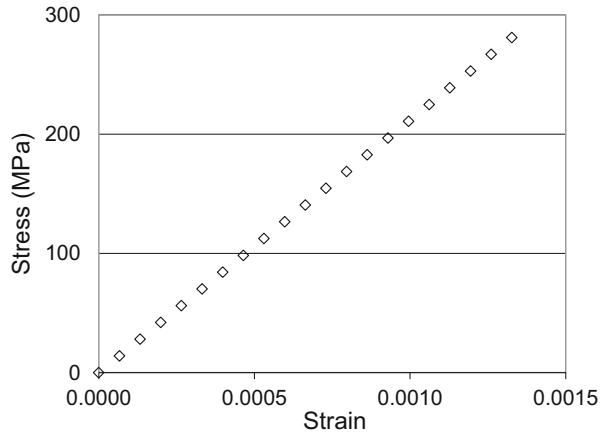
This relative extension is referred to as the “strain” ε_e . Note that since ΔL and L_i have the same units, the ratio ε_e is dimensionless. As in the calculation of stress, when strain is based on the initial specimen length, the value is referred to as the *engineering strain* denoted by the subscript “e.”

1.5 The Elastic Stress Versus Strain Curve

Since the cross-sectional area of the test specimen (with diameter 0.250 in. or 6.35 mm) and the length of the test specimen (1.0 in. or 25.4 mm) are known, the force versus extension curve can easily be converted to stress versus strain for the tensile test shown above. The resulting stress versus strain curve is shown as Fig. 1.7.

Note that there are no units shown for strain, which is a dimensionless quantity, and that the units for stress are MPa (or 10^6 Pa or 10^6 N/m²). Other than this, the curve appears identical to that shown in Fig. 1.6. The difference is that if a specimen with a diameter of 0.500 in. instead of 0.250 in. or a specimen with a length of 2.0 in.

Fig. 1.7 Stress versus strain for the specimen shown in Fig. 1.5



instead of 1.0 in. had been used, the resulting stress versus strain curves would have been identical. That is, converting from force to stress and extension to strain has eliminated specimen geometry effects.

1.6 The Elastic Modulus

Because of the normalizations of force by the cross-sectional area and of deflection by the length of the specimen, the curve shown in Fig. 1.7 is geometry invariant; the slope of this line takes on special meaning. This slope is defined as the “elastic modulus.” It is also referred to as Young’s modulus, named after a nineteenth-century British scientist. In fact, the equation for the line in Fig. 1.7 is as follows:

$$\sigma_e = E \varepsilon_e \quad (1.5)$$

$$\sigma_e = \frac{F}{A_i} = E \varepsilon_e = E \frac{\Delta L}{L_i} \quad (1.6)$$

where E is the elastic modulus and A_i is the initial cross-sectional area. Because ε_e in this equation is dimensionless, E has the units of σ_e , which as discussed above are N/m^2 or Pa. From the plot in Fig. 1.7, E for this steel is 30.7×10^6 psi (212×10^9 Pa).

It turns out E is a fundamental physical property of metals and ceramics. It is defined by interatomic forces (to be discussed in Chap. 2) and varies from material to material. Table 1.2 lists some values (at room temperature) of E for various materials.

Table 1.2 Elastic modulus of some common materials at room temperature

Material	E (10^6 psi)	E (10^9 Pa)
Aluminum	10.2	70.3
Copper	18.8	130
Beryllium	45.1	311
Molybdenum	47.1	325
Tantalum	26.9	186
Gold	11.5	79
Tungsten	59.6	411
Al_2O_3	50	345
Glass (Silica)	10	69

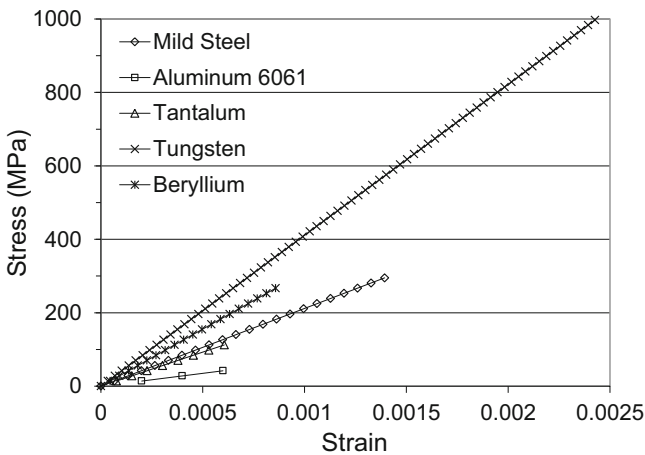


Fig. 1.8 Stress versus strain for five metals with differing values of the elastic modulus

The variation in the elastic modulus from material to material is evident. Note the stipulation that these measurements are at room temperature (RT). Indeed the elastic modulus is a function of temperature—generally E decreases with increasing T . This variation will become meaningful when the temperature dependence of strength is discussed.

Figure 1.8 shows results from the tensile test for a steel test specimen compared to what these results would have been for a beryllium, aluminum alloy, tungsten, and tantalum test specimen. Again, the test is run by incrementing the force in steps of 100 pounds for the same specimen (0.25 in. diameter). The slope of each of these lines is the elastic modulus for the material specified. Note that the slope of the plot for the tungsten specimen is much higher than the slope of the line for the aluminum alloy, which correlates with the values of the elastic modulus in the table above.

1.7 Lateral Strains and Poisson's Ratio

For the tensile tests described above, a deflection measuring device—also known as an *extensometer*—was attached to measure axial deflection, which was converted to strain. How about the strain in the radial direction (for the case of a cylindrical test specimen)? If volume is conserved during the test, then this can be estimated. Assume the initial and final diameters of the test specimen are D_i and D_f and that the initial and final lengths are L_i and L_f . Accordingly, when volume is conserved:

$$\begin{aligned}
 L_i \frac{\pi}{4} D_i^2 &= L_f \frac{\pi}{4} D_f^2 \\
 \frac{L_f}{L_i} &= \left(\frac{D_i}{D_f} \right)^2 \\
 \frac{L_f - L_i}{L_i} &= \frac{\Delta L}{L_i} = \varepsilon_e = \left(\frac{D_i}{D_f} \right)^2 - 1 \\
 \frac{D_i}{D_f} &= (1 + \varepsilon_e)^{1/2} \\
 \frac{D_f}{D_i} &= \frac{1}{(1 + \varepsilon_e)^{1/2}} \\
 \frac{D_f - D_i}{D_i} &= \varepsilon_{eD} = \frac{1}{(1 + \varepsilon_e)^{1/2}} - 1
 \end{aligned}$$

where ε_{eD} is defined as the strain in the direction of the diameter of the test specimen. The first term in the equation above can be estimated using a binomial series approximation:

$$\varepsilon_{eD} = \frac{1}{(1 + \varepsilon_e)^{1/2}} - 1 \cong \left(1 - \frac{\varepsilon_e}{2} \right) - 1 = -\frac{\varepsilon_e}{2} \quad (1.7)$$

When volume is conserved, the strain in the direction of the diameter—the *diametrical* strain—is one-half the axial strain, and it is of opposite sign. The ratio of diametrical strain to the axial strain is as follows:

$$\frac{\varepsilon_{eD}}{\varepsilon_e} = -\frac{1}{2} \quad (1.8)$$

The negative of this ratio is called *Poisson's ratio*, ν , named after the French mathematician Siméon Poisson.

$$\nu = -\frac{\varepsilon_{eD}}{\varepsilon_e} \quad (1.9)$$

Table 1.3 The Poisson’s ratio for metals, ceramics, and polymers differ and are in the ranges shown below

Material	Poisson’s ratio ν
Metals	~ 0.33
Ceramics	~ 0.25
Polymers	~ 0.40

The derivation above, however, assumed that the volume remains constant throughout the test. Materials that behave like this are referred to as “incompressible.” However, most materials are not incompressible but have a very small change in volume when elastically deformed. In fact, Table 1.3 summarizes typical values of Poisson’s ratio for metals, ceramics, and polymers; in each case Poisson’s ratio is less than the value of one-half expressed by Eq. 1.8.

How much does the volume and density change? Taking the example tensile test on a steel test specimen (which has a Poisson’s ratio of 0.33) shown in Fig. 1.7, the volume would be as follows:

$$\frac{V_f}{V_i} = \frac{\pi D_F^2 L_f}{\pi D_0^2 L_i} = \left(\frac{D_F}{D_i}\right)^2 \frac{L_f}{L_i} = (1 - \nu \varepsilon_{e_{\max}})^2 (1 + \varepsilon_{e_{\max}})$$

where V_i and V_f are the initial and final volumes, respectively, and $\varepsilon_{e_{\max}}$ is the maximum strain. Taking $\varepsilon_{e_{\max}} = 0.0013$ from Fig. 1.7:

$$\frac{V_f}{V_i} = (1 - 0.33 \times 0.0013)^2 (1 + 0.0013) = 1.00044$$

which shows the volume increases (thus, the density decreases) by 0.044%. Thus, the metal is compressible during elastic loading, but the change in volume is very small.

1.8 Defining Strength

One should wonder now whether a tensile specimen can be stretched elastically even further than shown in Figs. 1.6, 1.7, and 1.8. Intuitively, the answer of course is no; eventually the test specimen will break. Figure 1.9 shows a test sample before and after testing. Notice that the failed tensile specimen is longer than at start. This is one hint that something other than elastic strain occurred, since as described above elastic strain is reversible, meaning the specimen length would have returned to its initial length. Thus, the strain experienced by the test specimen was permanent—not recoverable. From inspection of Fig. 1.9, the sample elongates $\sim 50\%$ upon failure. Thus, the (permanent) strain experienced by this specimen is as follows:

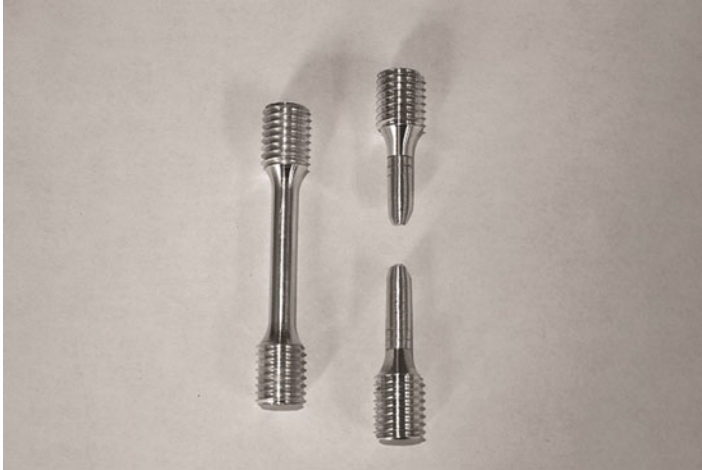


Fig. 1.9 Tensile test specimen before and after testing showing in the tested specimen the necked region and location of final fracture. (Courtesy of Westmoreland Mechanical Testing and Research Inc.)

$$\varepsilon_e = \frac{\Delta L}{L_i} = \frac{\approx \frac{L_i}{2}}{L_i} = 0.5$$

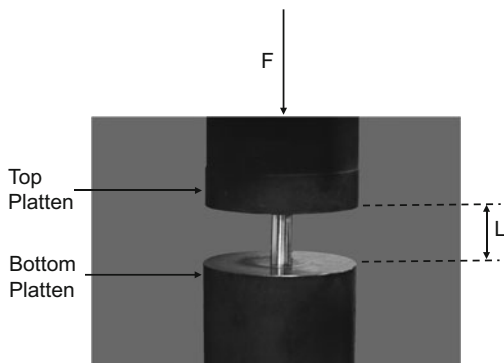
which is much larger than the elastic strains plotted in Figs. 1.7 and 1.8. Also evident in the photo is that the test specimen formed a “neck” (a location where the cross-sectional area decreased locally) and eventually broke. Thus, when a force is initially applied, the test specimen elongates elastically, but eventually the specimen experiences permanent strain. The transition between these two processes is one definition of strength.

There was actually a hint regarding this definition of strength in Fig. 1.8, when the lines were only plotted to a specific value of strain (or stress). The aluminum line was plotted only to a strain of only ~ 0.00065 , whereas the tungsten line was plotted all the way to a strain of ~ 0.0025 . The reason is that this maximum strain is the point on each curve where this transition occurs.

1.9 Stress–Strain Curve

To better understand the full stress–strain curve, it is useful to view an actual data set. First, since the example used is from a compression test rather than a tension test, it is necessary to describe how these tests differ. Figure 1.10 shows a schematic of a compression test. The test specimen is a solid cylinder with an aspect ratio (L_i/D_i) of ~ 1 to 1.5. It is sandwiched between two “platens” and usually a lubricant is coated

Fig. 1.10 Schematic of a compression test showing a solid cylinder between two platens. Note the direction of force is opposite that in the tensile shown in Fig. 1.5. (Courtesy of Westmoreland Mechanical Testing and Research Inc.)



on the mating surfaces. The crosshead in the testing machine is moved downward to compress the test specimen. An extension measurement system is used to measure ΔL .

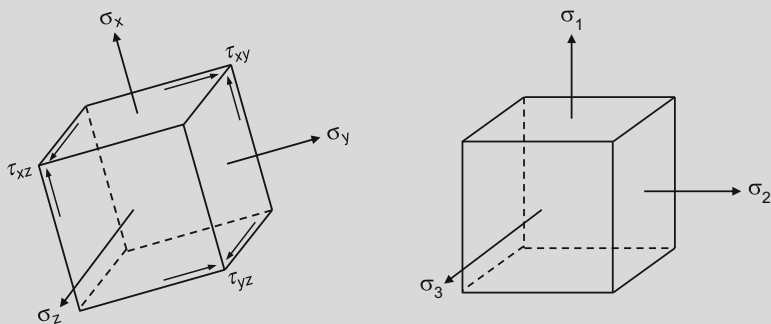
In this case, ΔL is a negative quantity. Thus:

$$\varepsilon_e = \frac{\Delta L}{L_i}$$

is also a negative quantity. Because the force is in an opposite direction than that in a tension test, the stress is also a negative quantity. In fact, the “stress state” which can be tension, compression, shear, or mixed mode is an important consideration in strength analysis (see Box 1.1).

Box 1.1 Stress State

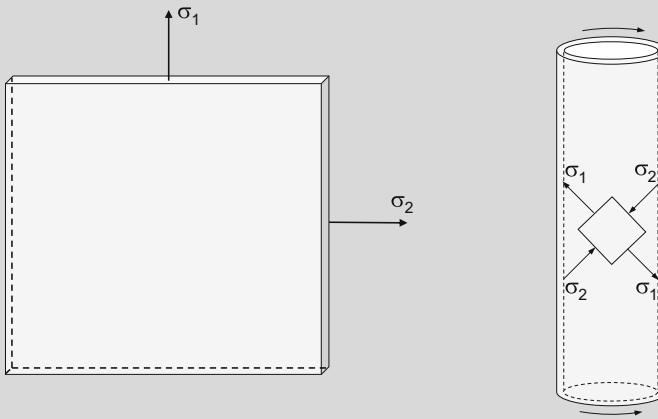
As illustrated in the figure on the left below, stress is a tensor quantity comprised in a general x, y, z coordinate system of three normal stresses— $\sigma_x, \sigma_y,$ and σ_z —and three shear stresses, $\tau_{xy}, \tau_{yz},$ and τ_{xz} .



(continued)

Box 1.1 (continued)

The principal coordinate system (on the right) is one where the *principal stresses* σ_1 , σ_2 , and σ_3 are normal to the three planes and the shear stress components on these planes are zero. Uniaxial tension and compression tests represent the case where the stress axis is a principal stress axis and σ_2 and σ_3 equal zero. Of course, in a tensile test, σ_1 is a positive quantity whereas in a compression test, it is a negative quantity. There is a myriad of stress states that are used in mechanical testing. The figure below shows the case on the left of a plane stress test on a thin sheet, where $\sigma_3 = 0$ and σ_1 and σ_2 can take on any (positive) values, and on the right a torsion test on a tube, where $\sigma_1 = -\sigma_2 = \tau$ and $\sigma_3 = 0$.



Uniaxial tension and compression tests are simple tests to perform—compared to the plane stress test, for instance. The question is how to correlate measurements from the uniaxial test with the behavior in a more general state of stress. This is addressed in the sidebar entitled “Scalar Stress Representations.”

The elastic loading behavior for our steel compression specimen is as shown in Fig. 1.11. Per convention, the stress and strain start at zero, but as the sample compresses, the stress and strain increase in a negative direction.

Figure 1.12 shows the measured stress–strain curve in an AISI 1018 steel compression test specimen [1]. The solid line is the measurement of force and extension converted to stress and strain as discussed above. The dashed line is the elastic loading line plotted in Fig. 1.11. Because the full-scale value of strain in Fig. 1.12 is -0.10 whereas that in Fig. 1.11 was -0.0015 , the elastic line in Fig. 1.12 seems to have a much higher slope. It actually is the same line.

How about the “bumps and wiggles” on the measured curve? More than likely in this case these represent “noise,” e.g., electronic noise, in the measurement system, although there are examples where features such as these may actually reflect a metallurgical process.

Fig. 1.11 Stress versus strain in the elastic regime for a compression test in AISI 1018 steel

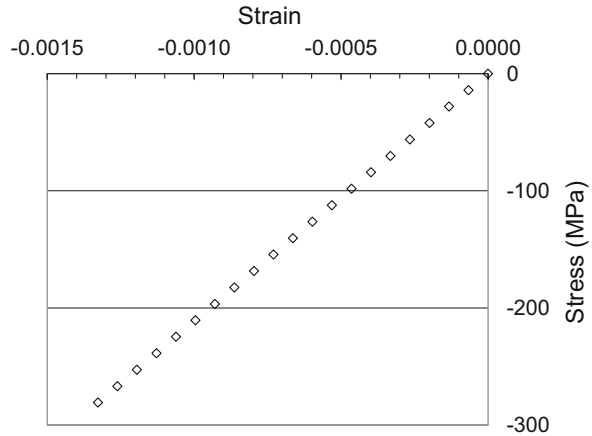
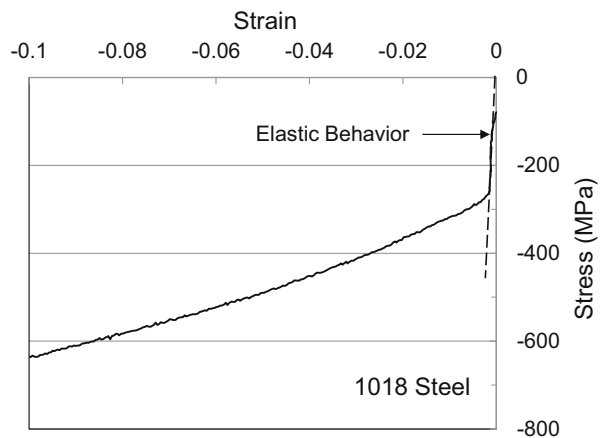


Fig. 1.12 Compression test in AISI 1018 steel showing stress versus strain up to a strain of -10%



The key point in Fig. 1.12 is that the measured behavior follows the elastic line to a stress of ~ -265 MPa, at which point a marked transition in behavior occurs and the strain begins to build rapidly while the stress increases slowly—opposite the trend during elastic loading. This point of transition is referred to as the “yield stress.” It is the point at which the strain becomes non-recoverable. As mentioned above, the yield stress is one definition of material strength.

The strain axis in Fig. 1.12 was limited to a value of -0.10 , but in fact this test was carried out to a much higher strain, as shown in Fig. 1.13. In this case, the elastic loading line is barely discernible from the ordinate. However, the blip at a strain of ~ -0.20 is very interesting. For this test, the load was momentarily released. Figure 1.14 shows the same data but with the x -axis adjusted to focus on the unloading/loading behavior. In Fig. 1.14, a line with the slope of the elastic loading line has been drawn to illustrate that the unloading/loading line follows the slope of the

Fig. 1.13 Compression test in AISI 1018 steel showing stress versus strain for the entire test. Included is a partial unload and reload step

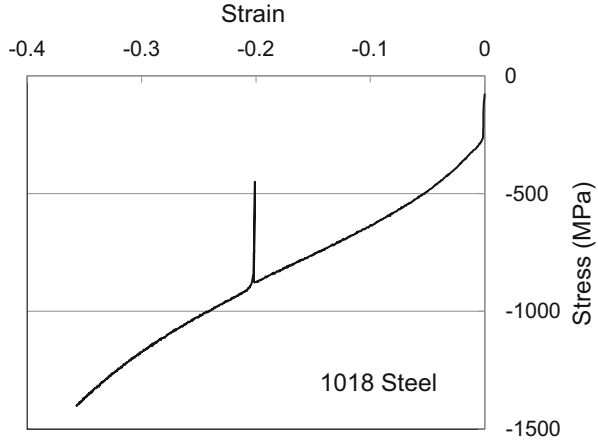
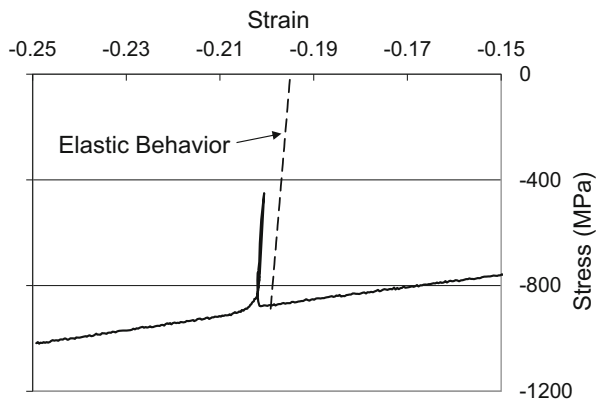


Fig. 1.14 The unload and reload step in the test shown in Fig. 1.13 plotted with a strain range that highlights the elastic behavior



elastic line. That is, when the load was decreased, the strain decreased along the elastic line rather than along the solid line. And when the load was once again increased, the strain increased along the elastic line until the previous maximum stress was reached. At this point the stress–strain curve followed the trend of the previous curve.

If the load had been decreased all the way to zero, then the strain would have relaxed elastically by:

$$\epsilon_e = \frac{\sim 875 \text{ MPa}}{212000 \text{ MPa}} = 0.004$$

which is the maximum (absolute value of the) stress reached before unloading divided by the elastic modulus, per Eq. 1.5. In the case of the compression test, the strain is negative; thus when the specimen is unloaded, it becomes less negative. The permanent strain in the test specimen would have been as follows:

$$\varepsilon_{ep} = -0.202 + 0.004 = -0.198$$

which is the maximum (negative) strain reached before unloading plus the elastic strain that is recovered. The compression test specimen would have been 19.8% shorter.

The strain past the yield stress has been referred to above as permanent and non-recoverable strain. The more traditional term is “plastic strain” as opposed to “elastic strain” during the initial elastic portion of the loading cycle.

1.10 The True Stress–True Strain Conversion

Recall that all of the calculations of stress and strain have been based on the initial cross-sectional area of the specimen (for the stress calculation) and the initial length of the specimen (for the strain calculation). The specimen, however, is deforming and the cross-sectional area changes. In a tension test, the cross-section area decreases, whereas in a compression test, the area increases. The stress–strain curves based on original dimension—as plotted in Fig. 1.13—are referred to as “engineering” stress–strain curves. When the stress during the test is based on the current (or actual) area and the strain is based on the current length, the resulting curve is referred to as a “true” stress–strain curve. That is, the incremental change in true strain, ε , is defined as follows:

$$d\varepsilon = \frac{dl}{l} \quad (1.10)$$

and the *true strain*, ε , in a test where the specimen’s length begins as L_i and ends as L_f is as follows:

$$\varepsilon = \int_{L_i}^{L_f} \frac{dl}{l} = \ln L_f - \ln L_i = \ln \left(\frac{L_f}{L_i} \right) = \ln (1 + \varepsilon_e) \quad (1.11)$$

The true strain is the logarithm of one plus the engineering strain. The *true stress*, σ , is defined as follows:

$$\sigma = \frac{F}{A}$$

where A is now taken as the current area.

$$\sigma = \frac{F}{A} \frac{A_i}{A_i} = \frac{F}{A_i} \frac{A_i}{A} = \sigma_e \frac{A_i}{A}$$

One distinction between elastic deformation and plastic deformation is that whereas (as discussed in Sect. 1.7) volume is not conserved in the former, it is conserved in the latter. Thus, plastic deformation is *incompressible*, and:

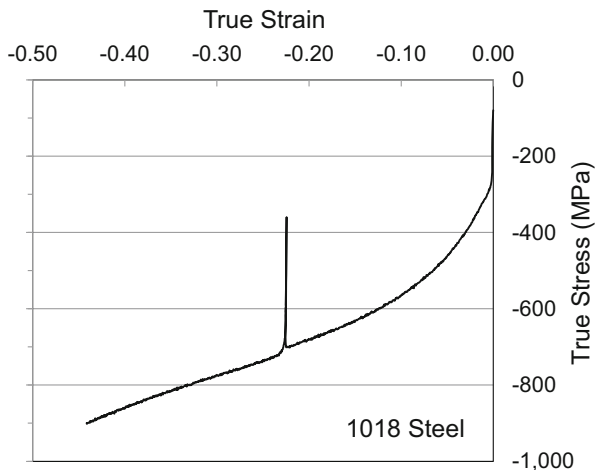
$$\sigma = \sigma_e \frac{A_i}{A} = \sigma_e \frac{L}{L_i} = \sigma_e (1 + \epsilon_e) \tag{1.12}$$

The true stress is simply the engineering stress multiplied by one plus the engineering strain. Here the distinction between a tension test where ϵ_e is positive and a compression test where ϵ_e is negative becomes critically important.

For the compression test shown in Fig. 1.13, the conversion from an engineering stress–strain curve to a true stress–strain curve yields the curve shown in Fig. 1.15. Compare this curve to that in Fig. 1.13. The absolute value of the maximum stress is lower in the true stress–strain curve because the diameter of the compression specimen increases during testing and the force divided by the current area gives a smaller stress. The peak strain has increased from ~ -0.35 on engineering coordinates to ~ -0.43 on true stress–strain coordinates which follow from $\epsilon = \ln(1 - 0.35)$.

In this monograph only true stress–strain properties will be considered. However, engineers need to check to verify whether it is engineering or true stress–strain curves that are being reported and be explicit themselves when reporting test results.

Fig. 1.15 The stress–strain curve in Fig. 1.13 (plotted as engineering stress versus engineering strain) converted to true stress versus true strain



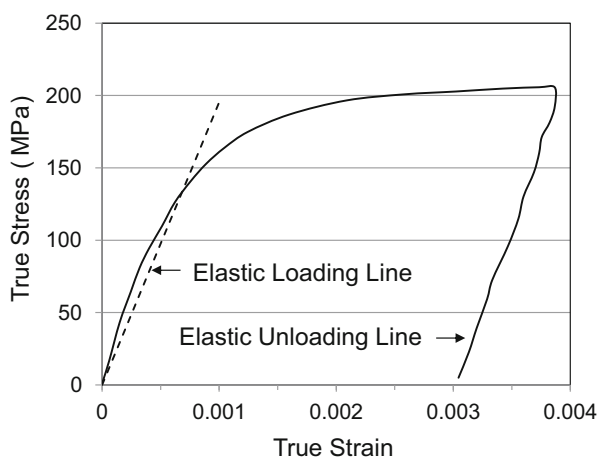
1.11 Example Tension Tests

Figure 1.15 showed a real compression test (in AISI 1018 steel) on true stress–true strain axes. Figure 1.16 shows such a tensile test in a 304 L stainless steel published by Krempl and Kallianpur [2]. This test specimen was only stretched to a strain of ~ 0.0038 —which is barely past the elastic loading region—then unloaded. Elastic loading and unloading curves (with $E = 195.2$ GPa) are included in the figure. Note that the measured curves do not follow exactly the elastic lines, although they do approximate them. This could be due to errors associated with measuring very small extensions, or it may be a real material effect, e.g., viscoelasticity (nonlinear elasticity)—commonly observed in polymeric materials.

If deviation from elastic loading is interpreted as a measure of strength, the curve in Fig. 1.16 illustrates the difficulty in precisely defining this point. One definition is called the “proportional limit” which is the point where the stress departs the elastic loading line. Although, as mentioned above, there is no ideally elastic behavior in the loading curve of Figs. 1.16 and 1.17 shows where one might identify the proportional limit.

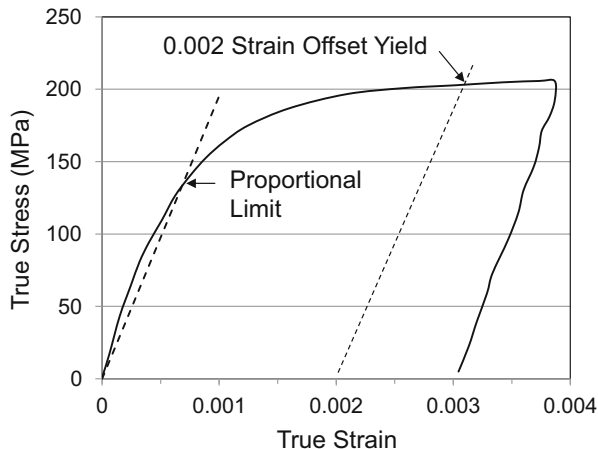
Engineers have adopted a convention for the yield stress as the stress at a strain of 0.002, referred to as the “0.002 offset.”¹ This also is shown in Fig. 1.17. While in this figure the 0.002 offset strain looks to be far from the elastic line, in fact this test specimen was tested to a very low strain. The 0.002 offset strain would be almost coincident with the elastic loading line in Fig. 1.13. Notice that the yield stress

Fig. 1.16 Stress versus strain curve in AISI 304 L stainless steel measured by Krempl [2] using very precise deflection measurements



¹It is not uncommon to specify a different—but still quite low value of—strain as the offset strain (e.g., 0.001).

Fig. 1.17 The curve of Fig. 1.16 shown with the 0.002 strain offset and a possible proportional limit to illustrate practicing definitions of the yield stress



defined by the proportional limit would be ~140 MPa whereas that defined by the 0.002 offset strain would be ~205 MPa, which is a big difference. When quoting yield stress, engineers need to verify how this is defined and measured.

Box 1.1 emphasized that stress is a tensor quantity. While the uniaxial tension and compression tests are often used to characterize strength, a scalar representation of stress that is independent of stress state has long been sought. Box 1.2 introduces some commonly used scalar stress and strain measures.

Box 1.2 Scalar Stress and Strain Representations

Figure 1.15 showed a compression stress–strain curve in AISI 1018 steel with a yield stress of ~−265 MPa, and Fig. 1.17 showed a tensile stress–strain curve in AISI 304LSS with a (0.002 offset) yield stress of ~205 MPa. The question arises what would be the yield stresses in these materials for a different stress state. That is, what would be the yield stress of the 1018 steel in tension or torsion? There are two ways to consider this. The second will be addressed in the Box 3.4 “crystal plasticity” in Chap. 3

The common model for stress-state dependence of the yield stress is based on the von Mises criterion. In the principal axes coordinate system, J_2 —the second invariant of the stress deviator—is as follows:

$$J_2 = \frac{1}{6} \left[(\sigma_1 - \sigma_2)^2 + (\sigma_2 - \sigma_3)^2 + (\sigma_3 - \sigma_1)^2 \right]$$

where J_2 is a scalar combination of the principal stresses. The von Mises yield criterion states that yield occurs when J_2 reaches the critical value of k^2 :

(continued)

Box 1.2 (continued)

If σ_o is the yield stress in uniaxial tension test, where $\sigma_1 = \sigma_o$ and $\sigma_2 = \sigma_3 = 0$, then:

$$k = \frac{\sigma_o}{\sqrt{3}}$$

which defines the value of k . Note that due to the squared terms, the yield stress in compression has the same absolute value as that in tension. In a torsion test where $\sigma_1 = -\sigma_2 = \tau$ and $\sigma_3 = 0$:

$$J_2 = k^2 = \frac{1}{6} [(\sigma_1 + \sigma_1)^2 + \sigma_1^2 + \sigma_1^2] = \sigma_1^2$$

$$\sigma_1 = \tau = k = \frac{\sigma_o}{\sqrt{3}}$$

$$\tau = \frac{\sigma_o}{\sqrt{3}}$$

Note that the yield stress in a torsion test is predicted to be 0.577 the yield stress in uniaxial tension. The yield stress in tension σ_o is also referred to as the von Mises stress σ_v . Rearranging the above equation defining J_2 gives (for principal stress coordinate system) the following:

$$\sigma_v = \left[\frac{1}{2} \{ (\sigma_1 - \sigma_2)^2 + (\sigma_2 - \sigma_3)^2 + (\sigma_3 - \sigma_1)^2 \} \right]^{1/2}$$

The von Mises strain (in principal axes) is defined as follows:

$$\varepsilon_v = \frac{2}{3} \left[\frac{1}{2} \{ (\varepsilon_1 - \varepsilon_2)^2 + (\varepsilon_2 - \varepsilon_3)^2 + (\varepsilon_3 - \varepsilon_1)^2 \} \right]^{1/2}$$

Recall in a tension test (with the tensile axis along the principal direction “1”) that:

$$\varepsilon_2 = \varepsilon_3 = -\frac{\varepsilon_1}{2}$$

In this case, it can be shown that $\varepsilon_v = \varepsilon_1$; von Mises strain is equal to the tensile strain.

For pure shear, $\varepsilon_1 = -\varepsilon_3 = \gamma/2$ and $\varepsilon_2 = 0$ where γ is the shear strain. It can be shown that:

(continued)

Box 1.2 (continued)

$$\varepsilon_v = \frac{2}{\sqrt{3}}\varepsilon_1 = \frac{\gamma}{\sqrt{3}}$$

The von Mises stress is one scalar stress definition. Another is the *octahedral shear stress* τ_{oct} , defined below. Note the relation between this scalar and the von Mises stress.

$$\tau_{\text{oct}} = \sqrt{\frac{2}{3}J_2} = \sqrt{\frac{2}{3} \frac{1}{3}\sigma_O^2} = \frac{\sqrt{2}}{3}\sigma_O = \frac{\sqrt{2}}{3}\sigma_v$$

The octahedral shear strain γ_{oct} is defined as follows:

$$\gamma_{\text{oct}} = \frac{2}{3} \left[(\varepsilon_1 - \varepsilon_2)^2 + (\varepsilon_2 - \varepsilon_3)^2 + (\varepsilon_3 - \varepsilon_1)^2 \right]^{1/2}$$

In a uniaxial tensile test, γ_{oct} relates to the tensile strain ε_1 through the following:

$$\begin{aligned} \gamma_{\text{oct}} &= \frac{2}{3} \left[\left(\varepsilon_1 + \frac{\varepsilon_1}{2} \right)^2 + \left(-\frac{\varepsilon_1}{2} - \varepsilon_1 \right)^2 \right]^{1/2} \\ \gamma_{\text{oct}} &= \frac{2}{3} \left[\left(\frac{3\varepsilon_1}{2} \right)^2 + \left(-\frac{3\varepsilon_1}{2} \right)^2 \right]^{1/2} = \frac{2}{3} \left[\frac{9}{2}\varepsilon_1^2 \right]^{1/2} = \sqrt{2}\varepsilon_1 \end{aligned}$$

Still another common scalar measure is the effective stress, $\bar{\sigma}$:

$$\bar{\sigma} = \frac{\sqrt{2}}{2} \left[(\sigma_1 - \sigma_2)^2 + (\sigma_2 - \sigma_3)^2 + (\sigma_3 - \sigma_1)^2 \right]^{1/2}$$

and the effective strain, $\bar{\varepsilon}$:

$$\bar{\varepsilon} = \frac{\sqrt{2}}{3} \left[(\varepsilon_1 - \varepsilon_2)^2 + (\varepsilon_2 - \varepsilon_3)^2 + (\varepsilon_3 - \varepsilon_1)^2 \right]^{1/2}$$

Both the effective stress and effective strain reduce to the uniaxial stress and strain, which is why the von Mises stress is often referred to as the von Mises effective stress and, similarly, the von Mises strain is often referred to as the von Mises effective strain.

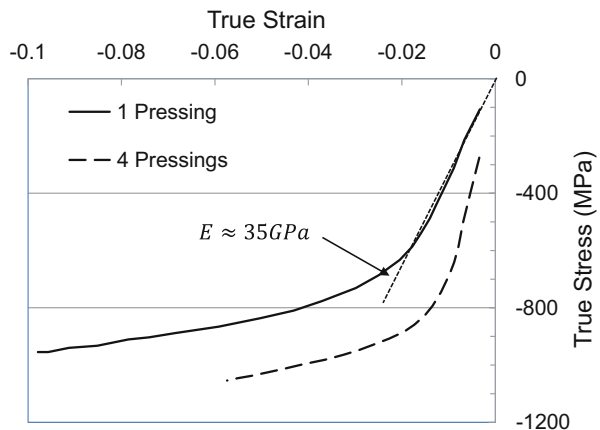
While the von Mises yield criterion explicitly refers to yield, stress–strain curves often plot the entire curve on von Mises stress and strain axes or octahedral shear stress and strain axes.

1.12 Accounting for Strain Measurement Errors

The measurement of strain in a tension or compression specimen can be challenging. A deflection measurement device such as shown in Fig. 1.4 is costly and can be difficult to install—particularly when experiments at cryogenic temperatures or elevated temperatures are desired. One common practice is to use the linear variable displacement transducer (LVDT) attached to the machine axis to record displacement in the test specimen, but as mentioned earlier, this measurement could represent displacements beyond those in the test specimen. Recent development of noncontact strain measurement devices based on laser interferometry offers an attractive alternative [3]. Even these new techniques, though, can introduce measurement artifacts. Thus, when viewing stress–strain measurements in the published literature, one must be cognizant of potential effects of errors in the strain measurement system.

An example of a published measurement that raises questions is shown in Fig. 1.18. The curves in this figure are compression stress–strain curves measured by Qu et al. on samples machined from a block of 304 L SS that had been equal channel angular pressing (ECAP) processed [4]. In this case, the material is extruded at 973 K (700 °C) through 90° dies such that the material is severely strained but without change in shape. (Chapter 14 includes a more detailed discussion of this processing method.) Whereas the (absolute value of the) yield strength in annealed 304 L SS is ~200 MPa, note that the yield strength in the ECAE processed material is on the order of 500 MPa. An elastic loading line for a sample subjected to a single pressing is drawn as a dotted line in Fig. 1.18. The slope of this line—the apparent elastic modulus—is ~35 MPa. The typical elastic modulus of stainless steels, however, is ~192 MPa. Since strain alone—even high levels of strain produced by ECAP processing—does not alter the interatomic forces, the apparent modulus must either be an artifact of the strain measurement or reflect unusual loading behavior.

Fig. 1.18 Compression stress versus strain curves measured by Qu et al. [4] on 304 L SS that had been equal channel angular extrusion processed 1 and 4 passes. The slopes of the elastic loading lines are unusually high



Although in this case Qu et al. are confident that the strain measurements reported by them are accurate and that the low initial slope is real² (perhaps indicating microplasticity in a few grains), this measurement serves as an example of the effect of a measurement system that indicates displacements beyond actual elastic displacements in the deforming specimen.

To illustrate the issue, Fig. 1.19 is a schematic two-spring system which is a model for the elastic displacements of a mechanical test specimen attached to a load frame. In this model the test specimen has a spring constant (equivalent to an elastic modulus) of E_1 , whereas the load frame has a spring constant of E_2 , which is assumed to be a constant. A force F is applied to the load axis and the total displacement ΔY is measured with an LVDT. In this case, the total displacement is as follows:

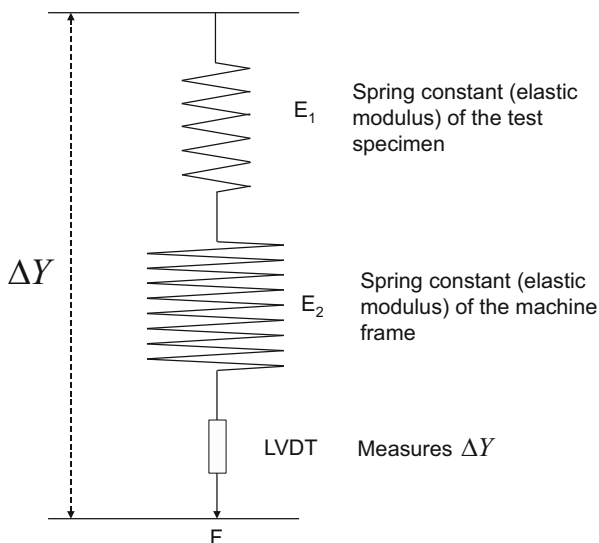
$$\Delta Y = \frac{F}{E_1} + \frac{F}{E_2} \tag{1.13}$$

and the displacement within the test specimen is as follows:

$$\Delta Y_1 = \Delta Y - \frac{F}{E_2} \tag{1.14}$$

If the displacements within the machine frame are not subtracted from the total displacements, the (absolute value of the) presumed displacements within the test specimen will be too large. Once the test specimen begins to plastically deform, the

Fig. 1.19 Schematic spring analogy illustrating how the stiffness (elastic modulus) of the machine can add to displacement measuring using an LVDT



²This was communicated in a private conversation with a member of the Qu et al. research group.

elastic displacements within the machine frame will continue to add to the measured displacements. Inaccurate measurement of displacements within the test specimen offers one source of error in the stress–strain curve.

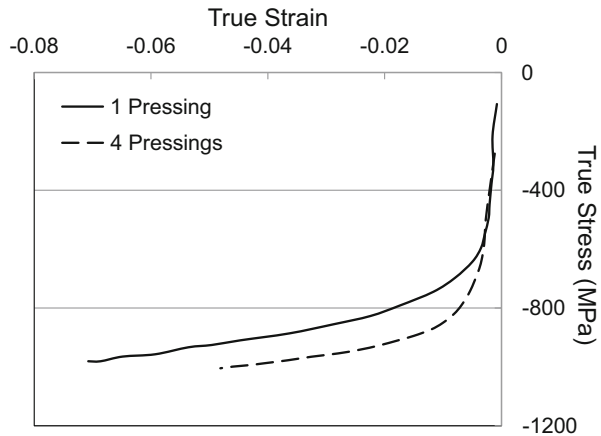
Inaccurate measurement of displacements introduces errors in the true stress calculation using Eq. 1.12 since the conversion from engineering to true stress involves multiplication of the engineering stress by $(1 + e)$. Fortunately, a simple correction is possible under certain idealized conditions. When, for instance, the machine modulus is constant³ and the errors to the measurement of strain solely arise from displacements in the machine frame, the fictitious elastic displacements (engineering strains) can be subtracted from the measured displacements.⁴ In this case the actual elastic strains can be computed using the known specimen modulus.

$$\varepsilon_{e_{\text{act}}} = \varepsilon_{e_{\text{app}}} - \frac{\sigma_e}{E_{\text{app}}} + \frac{\sigma_e}{E_{\text{act}}} \quad (1.15)$$

where the subscript “app” refers to “apparent” and “act” refers to “actual.” Note that the correction is performed on the engineering values of stress and strain and that the signage is very important.

Figure 1.20 shows the stress–strain curves from Fig. 1.18 corrected using Eq. 1.15. In this case, the actual measured apparent moduli for the 1-pass and 4-pass curves are used. As indicated in Fig. 1.18, this was 35 GPa for the 1-pass curve and 74 GPa for the 4-pass curve. The actual modulus was assumed to equal

Fig. 1.20 True stress versus true strain curves from Fig. 1.18 with apparent elastic strains not associated with those in the test specimen removed using Eq. 1.15



³This is an important assumption that may not reflect the actual machine elasticity or “compliance”; testing machines often become stiffer with increasing load, in which case the correction assuming a constant machine modulus will be too large.

⁴The fact that the slopes of the elastic portions of the 1-passing and 4-passing curves are not identical suggests that the high slope does not simply arise from a machine compliance effect. Assuming a constant machine modulus, thus, is an approximation.

192 GPa for both cases. A comparison between the raw data in Fig. 1.18 and the corrected curves in Fig. 1.20 shows that it is mostly the strain values that have changed. The stresses show less of a change since the strains in these tests were fairly low (compared, for instance, to those in Figs. 1.13 and 1.15.) It is worth reemphasizing that Qu et al. believe that the strains are accurate, in which case the stress–strain curves in Fig. 1.18 are accurate and there is no reason to apply the correction above. It is done only as an illustration. For tests carried to large strains, the errors introduced by inaccurate strain measurements can be significant.

1.13 Formation of a Neck in a Tensile Specimen

Figure 1.21 shows another tensile test measurement. This one was reported by Antoun [5] and is also in a 304 stainless steel—but at 344 K (160 °F) instead of room temperature. This stress–strain curve was taken all the way to a true strain of ~ 0.44 . The unloading portion of the curve (as load is reduced to zero) is not shown. It is likely that this test specimen formed a neck and broke (as in Fig. 1.9).

To examine formation of a neck during a tensile test, Fig. 1.22 shows schematically a cross section of a specimen with an “incipient” neck. This could have initiated from a machining defect or simply be a region that for some reason strained slightly nonuniformly. The area within the necked region is less than the area in the

Fig. 1.21 Stress versus strain (tension) measured in 304 SS by Antoun [5] at 344 K (160 °F)

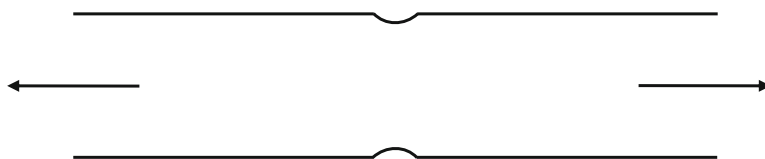
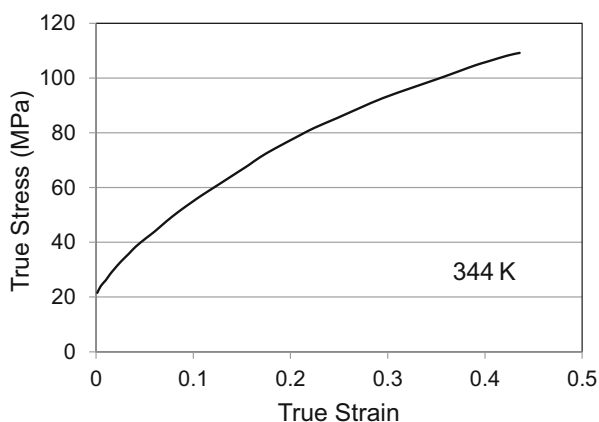


Fig. 1.22 Cross section of a tensile test specimen with an incipient neck region

bulk of the test specimen. Thus, the stress will increase locally, which will lead to even more localized strain and will accentuate the growth of the neck. This will be countered by the fact that the local region that strains nonuniformly will be a little stronger due to the increase in the stress–strain curve.

When the increased stress along the stress–strain curve is no longer sufficient to counter the increased stress due to the area reduction in the neck, the neck will grow. This is a classic instability process. Recall the force F , defined as follows:

$$F = \sigma A$$

Differentiating the force with respect to the strain gives the following:

$$\frac{dF}{d\varepsilon} = \sigma \frac{dA}{d\varepsilon} + A \frac{d\sigma}{d\varepsilon}$$

At the point of instability:

$$\frac{dF}{d\varepsilon} = 0$$

From the constant volume condition:

$$\begin{aligned} V &= A L \\ \frac{dV}{d\varepsilon} &= 0 = A \frac{dL}{d\varepsilon} + L \frac{dA}{d\varepsilon} \\ \frac{dA}{d\varepsilon} &= -\frac{A}{L} \frac{dL}{d\varepsilon} = -A \frac{\frac{dL}{L}}{d\varepsilon} = -A \frac{d\varepsilon}{d\varepsilon} = -A \\ \frac{dF}{d\varepsilon} &= 0 = \sigma \frac{dA}{d\varepsilon} + A \frac{d\sigma}{d\varepsilon} = -\sigma A + A \frac{d\sigma}{d\varepsilon} \end{aligned}$$

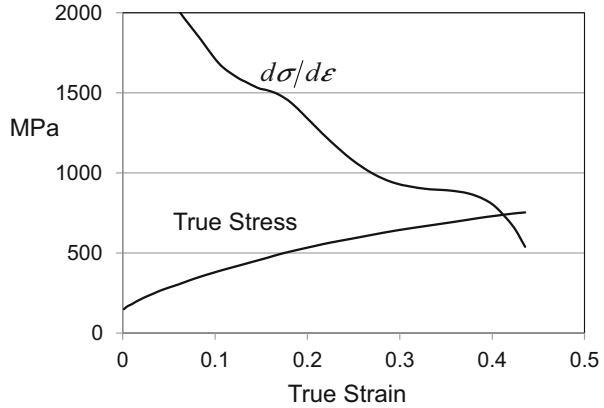
Therefore at the point of instability:

$$\sigma = \frac{d\sigma}{d\varepsilon} \quad (1.16)$$

When the true stress equals the slope of the true stress versus true strain curve, the specimen is prone to undergoing unstable deformation via formation of a neck. The instability condition represented by Eq. 1.16 is referred to as the Considère criterion in recognition of the experimental observations in iron and steel by this French researcher in 1885. Figure 1.23 shows the stress–strain data of Fig. 1.21 plotted along with $d\sigma/d\varepsilon$. Recall that since ε is dimensionless, $d\sigma/d\varepsilon$ has the units of stress.

The two curves in Fig. 1.23 coincide at a strain of ~ 0.41 . Thus, per the instability condition, a neck likely begins to form at this point, and the tensile specimen will soon break. In addition, data is not reported past this point since the stress and strain are no longer uniform in the test specimen. This prediction is consistent with the measurement shown in Fig. 1.21.

Fig. 1.23 Strain hardening rate (slope of the stress-strain curve) versus true stress for the tensile test shown in Fig. 1.21. The point of intersection of these curves is the point of tensile instability



1.14 Strain Rate

In the test results highlighted in Figs. 1.13, 1.16, 1.18, and 1.21, the velocity of the crosshead has not been specified. This actually is an important variable. Typically, the yield stress in a test where the crosshead velocity is high exceeds that in a test where the crosshead is low. The difference can be small, but it is generally measurable.

Figure 1.24 shows a plot of both the engineering strain and the true strain versus time for a tensile test in the nickel-base alloy C-22 [6]. Note that engineering strain varies very close to linearly with time. Recall that:

$$\varepsilon_e = \frac{\Delta L}{L_i}$$

where L is the original length of the test specimen. The strain rate (in this case the engineering strain rate) is defined as the change of strain with time, i.e., the time derivative:

$$\dot{\varepsilon}_e = \frac{d}{dt} \varepsilon_e \quad (1.17)$$

If the engineering strain varies roughly uniform with time, dividing ε_e by time gives the following:

$$\frac{\varepsilon_e}{t} = \frac{\Delta L}{t L_i} = \frac{1}{L_i} \frac{\Delta L}{t} = \frac{1}{L_i} V_{CH} \quad (1.18)$$

where V_{CH} is the crosshead velocity.

Fig. 1.24 Engineering strain and true strain versus time for a tensile test in alloy C-22 [6]

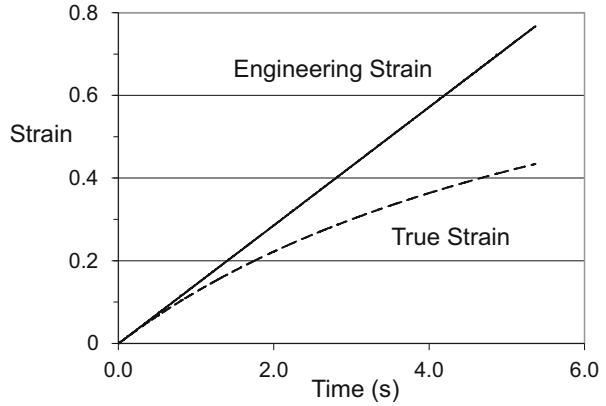
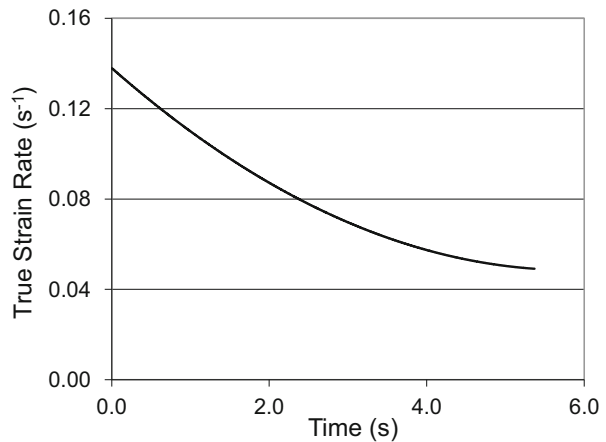


Fig. 1.25 True strain rate versus time for the alloy C-22 tensile test (slope of the true strain versus time curve in Fig. 1.24)



A constant value of ϵ_e/t (slope of the engineering strain versus time line in Fig. 1.24) implies that a constant crosshead velocity has been imposed. The units of strain rate are s^{-1} since strain is dimensionless. Usually, it is the true strain rate rather than the engineering strain rate that is specified.⁵ However, it is easier to operate a test machine with a constant crosshead velocity than to control the motion to yield a constant true strain rate. In the test illustrated in Fig. 1.24, the true strain rate is not constant. Figure 1.25 shows how the true strain rate varies with time in this test.

The true strain rate for this test started at a value nearly equal $0.14 s^{-1}$ at yield but decreased throughout the test. The average true strain rate was approximately equal to $0.08 s^{-1}$.

⁵Test machines with feedback control of the crosshead velocity from a displacement measurement system can operate at a constant true strain rate.

1.15 Summary

The mechanical test is used to measure the strength of materials. This chapter has reviewed the tensile test; introduced definitions of stress, strain, and strain rate; discussed elastic and plastic deformation; and summarized concepts such as compressibility, instability, and errors introduced by imprecise displacement measurement. Several examples of stress–strain curves—in tension as well as compression—were presented. With this introduction, the contributions to the strength measured in a mechanical test can be presented.

Exercises

- 1.1 A copper tensile test specimen is machined with an initial diameter of 5.00 mm and an initial gage length of 40.0 mm. A load of 400 N is applied. (a) At this load, what is the applied stress? (b) If the specimen only deforms elastically, calculate the deflection that would be measured.
- 1.2 Measurements of load versus deflection in a metallic tensile test specimen with an initial diameter of 6.00 mm and an initial gage length of 50.0 mm are given in Table 1.E2. (a) Does this specimen appear to be deforming elastically? (b) From the elastic constants in Table 1.2, determine the metal.
- 1.3 An Al_2O_3 solid cylinder with an initial length of 1.50 cm and an initial diameter of 1.00 cm is loaded in compression. An optical extensometer is used that continuously measures the diameter of the test specimen. Table 1.E3 lists the measured force versus diameter. Assuming that Poisson's ratio for this material is 0.25, compare the elastic modulus with the value listed in Table 1.2. (Note that the forces are listed as negative to reflect the compressive loading.)
- 1.4 Compare the forces required to perform the tensile test in Exercise 1.2 with the forces required to perform the compression test in Exercise 1.3. Instron® and MTS® are two companies that supply mechanical testing machines. Go to either the Instron or MTS web site and research which testing machine would be required to perform these mechanical tests.

Table 1.E2 Deflection and load measurements for a metallic tensile test (Exercise 1.2)

ΔL (μm)	Force (N)
5.4	572
16.2	1662
26.9	2807
37.6	3921
48.4	5089
59.2	6189
69.9	7326
80.7	8457

Table 1.E3 Change in diameter and load measurements for an Al_2O_3 tensile test (Exercise 1.3)

ΔD (μm)	Force (N)
0.36	–3960
1.81	–19,600
3.26	–35,300
4.71	–51,000
6.16	–66,800
7.61	–82,400
9.06	–98,200
10.51	–113,800

Table 1.E5 Deflection and load measurements for a copper tensile test (Exercise 1.5)

ΔL (μm)	Force (N)
4.1	269
7.9	532
12	813
16	1068
19.2	1231
24	1560
28.1	1817
31.9	1973
36.1	2108
40.4	2195
48.1	2407
56.1	2583
64.1	2740
72.2	2903
80	3104
88.3	3182
95.9	3368
112.2	3659
128.2	3845
144.3	4141
160.3	4289
176.5	4507

- 1.5 A copper tensile test specimen is machined with an initial diameter of 5.00 mm and an initial gage length of 40.0 mm. The measured load (N) versus displacement (μm) data is listed in Table 1.E5. (a) Calculate and plot stress versus strain for this test. (b) Has the yield stress been exceeded in this test?
- 1.6 For the test described in Exercise 1.5, (a) estimate the proportional limit and (b) estimate the 0.002 offset yield stress.
- 1.7 The test described in Exercise 1.5 was actually strained to a higher total elongation. Table 1.E7 lists the measured elongation versus force data. Add this data to the data listed in Exercise 1.5. (a) Plot the engineering stress–strain

Table 1.E7 Additional deflection and load measurements for the copper tensile test in Exercise 1.5 (Exercise 1.7)

ΔL (μm)	Force (N)	ΔL (μm)	Force (N)
192.5	4694	1103.0	11,074
208.5	4880	1168.7	11,311
224.5	5142	1234.6	11,655
240.7	5303	1300.7	11,861
256.9	5462	1366.9	12,204
272.9	5608	1433.1	12,466
289.0	5793	1557.5	12,968
321.2	6122	1682.5	13,432
353.5	6416	1807.7	13,830
385.9	6619	1933.3	14,208
418.3	6937	2059.2	14,599
450.5	7164	2185.6	15,017
483.0	7392	2312.4	15,433
515.3	7651	2439.4	15,730
547.6	7937	2567.1	16,081
580.2	8102	2694.9	16,474
612.7	8373	2823.2	16,732
645.0	8574	2951.8	17,095
677.6	8755	3080.8	17,408
710.2	8988	3210.2	17,724
742.8	9138	3340.1	17,912
775.5	9296	3470.3	18,274
808.0	9489	3600.9	18,531
840.7	9742	3732.0	18,727
906.0	10,033	3863.3	19,078
971.5	10,416	3995.1	19,283
1037.2	10,741	4127.4	19,494

curve. (b) Calculate and plot the true stress–strain curve. (Remember that the conversion from engineering strain and stress to true strain and stress needs to be performed only for points beyond the yield stress.)

- 1.8 The highest elongation and force recorded in the test described in Exercise 1.7 were 4127.4 mm and 19,494 N, respectively. If at this point the load were reduced to zero, what would be the final length of the tensile specimen?
- 1.9 Could the tensile test described in Exercise 1.7 deform to the maximum elongation listed without forming a neck?
- 1.10 Table 1.E10 lists displacement versus force for a tantalum cylinder deformed in compression. (Note that the displacement and force values are negative to reflect the compression loading conditions.) The original sample diameter was 8.00 mm, and the original sample length was 12.00 mm. (a) Estimate the proportional limit. (b) Estimate the (–) 0.002 offset strain yield stress.

Table 1.E10 Deflection and load measurements for a tantalum compression test (Exercise 1.10)

ΔL (μm)	Force (N)	ΔL (μm)	Force (N)
-2.4	-1886	-185.7	-23,958
-4.9	-3725	-209.3	-24,651
-7.2	-5571	-233.0	-25,244
-9.6	-7523	-256.4	-25,792
-11.9	-9392	-279.9	-26,247
-14.4	-11,233	-315.0	-27,013
-16.9	-13,040	-350.0	-27,685
-19.3	-14,626	-385.0	-28,310
-21.6	-15,283	-419.8	-28,889
-24.0	-15,654	-454.4	-29,441
-28.8	-16,323	-523.5	-30,429
-33.6	-16,760	-592.1	-31,414
-38.3	-17,215	-660.3	-32,375
-43.2	-17,695	-728.2	-33,187
-52.6	-18,395	-840.3	-34,510
-62.2	-19,108	-951.3	-35,781
-71.8	-19,660	-1061.2	-37,051
-81.3	-20,097	-1170.2	-38,105
-90.8	-20,598	-1277.9	-39,256
-109.8	-21,408	-1384.6	-40,335
-128.9	-22,185	-1490.3	-41,339
-147.8	-22,885	-1594.7	-42,412
-166.8	-23,489	-1698.2	-43,444

- 1.11 Plot the engineering stress–strain curve and the true stress–strain curve for the entire data set listed in Exercise 1.10.
- 1.12 If this material were tested in tension rather than in compression, would the tension specimen be able to elongate to the maximum strain listed without undergoing a tensile instability (i.e., form a neck)?
- 1.13 Table 1.E13 lists the measured displacement versus applied force for a tungsten compression test. The original specimen diameter was 8.00 mm and the original specimen length was 12.0 mm. (a) Plot engineering stress versus engineering strain, and determine the apparent elastic modulus. (b) How does the apparent modulus compare to the value listed in Table 1.2 for tungsten? (c) Can you suggest a rationale for the difference?
- 1.14 Assuming that the true elastic modulus is 411 GPa, perform a correction to remove the artificial elastic strain. Compare the corrected and uncorrected engineering stress–strain curves.
- 1.15 Table 1.E15 lists the measured displacement versus time for a tensile test on a specimen with an initial length of 25.0 mm. (a) Plot the engineering strain versus time and the true strain versus time. (b) Was this test run at a uniform engineering strain rate or a uniform true strain rate? (c) What is this strain rate?

Table 1.E13 Deflection and load measurements for a tungsten compression test (Exercise 1.13)

ΔL (μm)	Force (N)	ΔL (μm)	Force (N)
-23.8	-3916	-528.9	-75,442
-47.7	-8170	-575.4	-76,089
-71.6	-12,216	-624.1	-76,656
-95.4	-15,890	-672.1	-77,415
-119.9	-20,134	-719.5	-77,703
-145.0	-23,989	-767.3	-78,266
-167.5	-28,082	-815.3	-78,835
-192.2	-32,012	-864.5	-79,343
-216.8	-36,201	-912.4	-79,574
-239.3	-40,076	-959.6	-80,102
-264.7	-44,121	-1007.5	-80,259
-287.5	-48,382	-1055.1	-80,934
-312.9	-52,415	-1104.8	-80,983
-335.4	-56,339	-1152.7	-81,591
-360.1	-60,182	-1200.1	-81,797
-384.7	-64,281	-1248.9	-82,345
-407.8	-68,243	-1295.7	-82,626
-432.2	-71,999	-1343.1	-82,794
-480.5	-73,694	-1391.6	-83,012

Table 1.E15 Deflection and load measurements for a tension test (Exercise 1.15)

Time (s)	ΔL (μm)	Time (s)	ΔL (μm)
2.93	0.070	104.79	2.758
8.83	0.216	111.17	2.942
14.99	0.372	116.71	3.098
20.96	0.527	123.12	3.281
27.2	0.674	129.07	3.438
32.79	0.846	134.75	3.610
39.09	0.987	141.21	3.785
45.1	1.161	146.88	3.961
50.87	1.298	153.27	4.129
57.19	1.457	159.04	4.298
62.85	1.619	165.08	4.495
68.88	1.786	171.22	4.662
74.93	1.943	177.03	4.844
80.88	2.105	182.97	5.026
86.8	2.265	189.16	5.195
92.76	2.444	195.1	5.378
98.71	2.604	201.08	5.557

References

1. G.T. Gray III, S.R. Chen “MST-8 Constitutive Properties & Constitutive Modeling,” Los Alamos National Laboratory, LA_CP-07-1590 and LA-CP-03-006 (Must request data from LANL authors.), (2007)
2. E. Krempl, V.V. Kallianpur, Some critical uniaxial experiments for viscoplasticity at room temperature. *J. Mech. Phys. Solids* **32**(4), 301 (1984)
3. B. Becker, M. Dripke, Choosing the right extensometer for every materials testing application. *Adv. Mater. Proc.* **169**(4), 17–21 (2011)
4. S. Qu, C.X. Huang, Y.L. Gao, G. Yang, S.D. Wu, Q.S. Zang, Z.F. Zhang, Tensile and compressive properties of AISI 304L stainless steel subjected to equal channel angular pressing. *Mater. Sci. Eng. A* **475**, 207–216 (2008)
5. B.R. Antoun, in Temperature Effects on the Mechanical Properties of Annealed and HERF 304L Stainless Steel, Sandia National Laboratories, Sandia Report, SAND2004–3090, November 2004
6. B. O’Tolle, Identification of Dynamic Properties of Materials for the Nuclear Waste Package, Technical Report, Task 24, Document ID: TR-02-007, Sept. 2003. See Task 24 documents at the following website: <http://hrcweb.nevada.edu/data/tda/>. Accessed April 2011

Chapter 2

Structure and Bonding



Introduction

In Sect. 1.2 the early stage of a tension test was used to demonstrate that the initial deformation in the specimen was elastic and recoverable. This elastic regime is a consequence of interatomic forces. One can learn about these forces by considering how the forces between two ions depend on their separation distance. Permanent, or plastic deformation, on the other hand, involves dislocations, which are line defects that enable displacements within crystals. This chapter reviews many characteristics of crystal structure, bonding, and dislocations that are essential to the understanding of constitutive behavior.

2.1 Forces and Resultant Energies Associated with an Ionic Bond

Consider a sodium Na and chlorine Cl atom. Sodium has one extra valence electron, whereas chlorine is one electron short of a filled (M) shell. Sodium readily gives up this electron to become a positive ion while chlorine accepts this electron to become a negative ion. (Still, it requires $U_i = 1.12$ eV of energy to make isolated Na^+ and Cl^- ions.) These ions attract through coulombic forces as illustrated in Fig. 2.1. The magnitude of the attractive force is as follows:

$$F_A = \frac{k q_e^2}{r^2} \quad (2.1)$$

Supplementary Information The online version contains supplementary material available at [\[https://doi.org/10.1007/978-3-031-04556-1_2\]](https://doi.org/10.1007/978-3-031-04556-1_2)

Fig. 2.1 Coulombic attraction between two ions

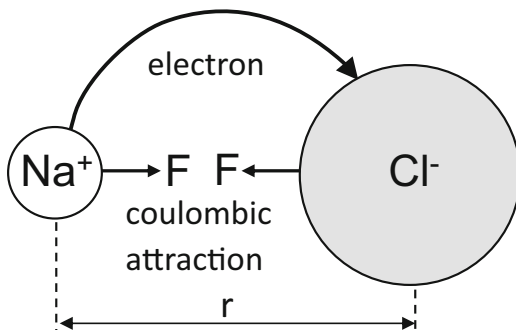
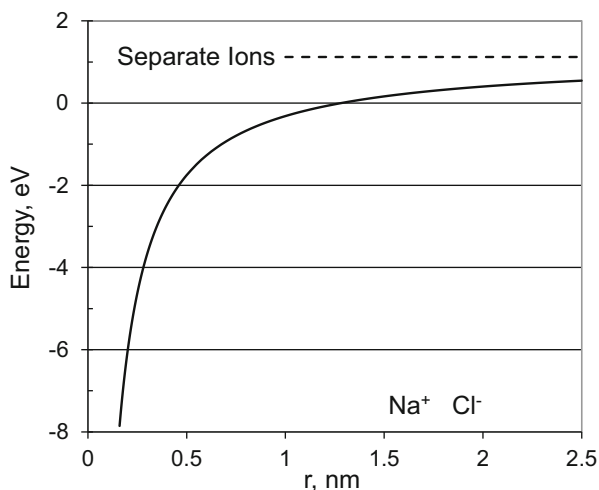


Fig. 2.2 Energy (energy to separate the ions plus the energy gained as the ions approach from Eq. 2.2) of the two-ion (Na^+Cl^-) system



where q_e is the electronic charge on the ions (1.602×10^{-19} C), r is the distance between the ions, and k is a constant. As the ions approach, energy is regained; this energy term (U_A) is as follows:

$$U_A = \int_{\infty}^r F_A dr = \frac{-k q_e^2}{r} \tag{2.2}$$

The net energy of the system as the ions approach is as follows:

$$U = U_i + \int_{\infty}^r F_A dr = 1.12 \text{ eV} - \frac{k q_e^2}{r} \tag{2.3}$$

Figure 2.2 shows how U varies with r .

Of course, the ions cannot approach each other indefinitely. When they become too close, their orbitals will begin to overlap which will generate a repulsive force F_R , schematically illustrated in Fig. 2.3.

Fig. 2.3 A repulsive force grows rapidly when the ions approach too closely

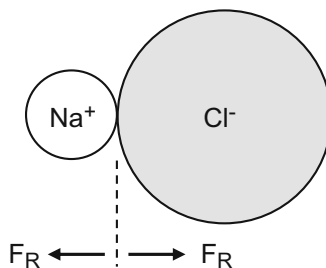
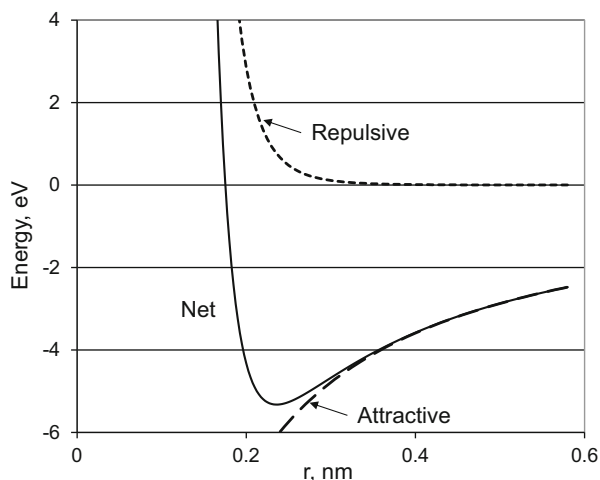


Fig. 2.4 The solid line shows the net force of the two-ion system. The equilibrium separation distance is at the point where the net energy of the system is minimized



This repulsive force increases significantly and the energy of the system once again increases (due to $F_R \times d$ work) as the separation distance between the ions continues to decrease. Figure 2.3 plots the energy due to coulombic attraction together with the energy due to the repulsive force. The sum of these two energies is the net energy of the system, written as follows:

$$U = \int_{\infty}^r F_A dr + \int_{\infty}^r F_R dr \quad (2.4)$$

Figure 2.4 shows the net energy versus separation distance.¹ Note that the energy reaches a minimum and then rises sharply with decreasing r . This minimum is the equilibrium distance between the Na^+ and Cl^- ions. The minimum also represents the bond energy. Note that the energy of the system is less than 0, implying a net energy gain by forming the two ions and bringing them together.

¹The energy required to initially separate the ions is not included in this calculation.

2.2 Elastic Straining and the Force Versus Separation Diagram

Recall that the net force between the ions is as follows:

$$F = \frac{dU}{dr} \quad (2.5)$$

Our interest is how this force varies with r , which is defined as the stiffness S (a quantity directly related to the elastic modulus):

$$S = \frac{dF}{dr} = \frac{d^2U}{dr^2} \quad (2.6)$$

Although it is impossible to see this from inspection of Fig. 2.4 (which shows only a schematic energy-separation distance diagram) when dr is very small and not far from the equilibrium distance r_o , S is roughly constant.

$$\frac{dU^2}{dr^2} \approx S_o$$

In this case:

$$F = S_o \Delta r \quad (2.7)$$

which is the spring equation defined by Eq. 1.1 with $K_S = S_o$. S_o in turn relates (through some geometric factors) to the elastic modulus E in Eq. 1.5.

Metallic bonding is not the same as ionic bonding. However, there are similarities. The metal atoms give up electrons and become ionic in nature, but the electrons are not given up to another atom but form a “sea” of electrons between metal “ions” that form a crystal lattice. The attraction is between the metal ions and the sea of electrons, and once again if brought too close together, a strong repulsive force will be generated. In this sense, the net energy model reflects metallic bonding as well as ionic bonding.

The energy versus distance plot (Fig. 2.4) assumes a key role in properties of condensed matter. The bond energy (minimum, equilibrium distance) is related to the melting point. The asymmetry of curvature around the equilibrium point is related to the thermal expansion coefficient α_v , characterizing the change of dimensions of a solid with respect to temperature:

$$\alpha_v = \frac{1}{V} \frac{\partial V}{\partial T} \quad (2.8)$$

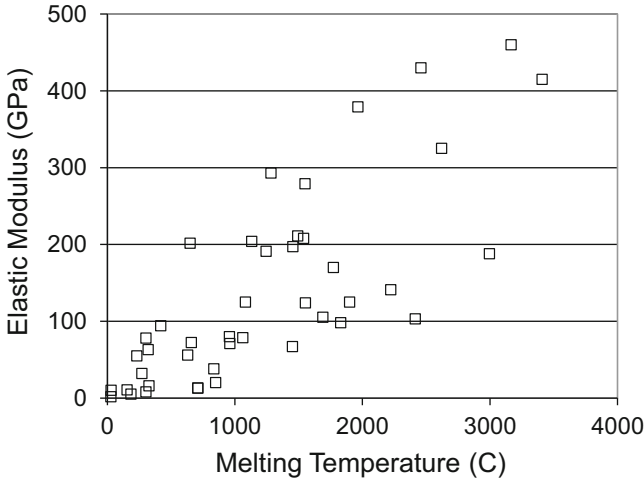


Fig. 2.5 In pure elements, the elastic modulus scales roughly with the melting temperature

And, as described above, the second derivative of the curve around the equilibrium point is related to the elastic modulus. As an example of correlations related to the energy versus distance dependence, Fig. 2.5 shows the variation of the elastic modulus with melting point for the transition metals (groups 3 through 12 in the periodic table) (data from A. Buch [1]). Figure 2.5 shows a general correspondence, indicating that as the bond energy increases (in a negative direction) the second derivative also increases.

To summarize, the elastic modulus and the thermal expansion coefficient follow from the energy balance and equilibrium separation between metal ions. When a force is applied, the energy versus separation curve dictates the elastic strain (either tensile or compressive) in response to the applied force.² Of course, the attraction and repulsion between two ions only serves as a model for the behavior of metallicly bonded ions in a crystal lattice. Metallic crystal structures are described in the next section.

2.3 Crystal Structure

The tendency of metal atoms to give up electrons into a sea of electrons directly influences the tendency of these atoms to assemble in *crystal lattices* rather than in unique (e.g., ionic) molecules. The *simple cubic* structure shown in Fig. 2.6 is the

²It is worthwhile to contrast the role of the energy-separation distance correlation in the influence on physical phenomena—such as the elastic modulus and the thermal expansion coefficient—and the lack of a correlation with conductivities—either electrical or thermal—which are rather affected by valence electrons and bonding.

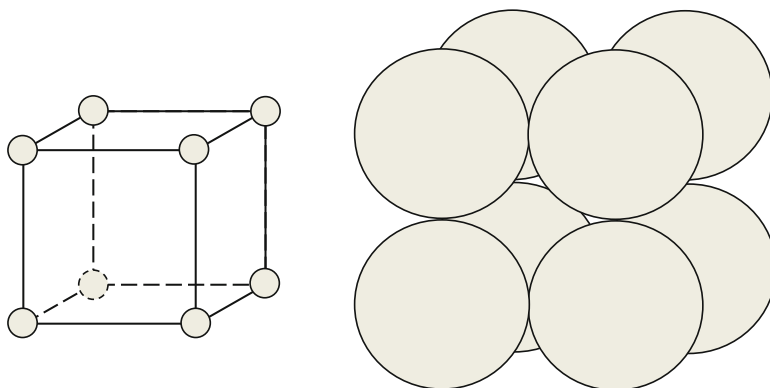
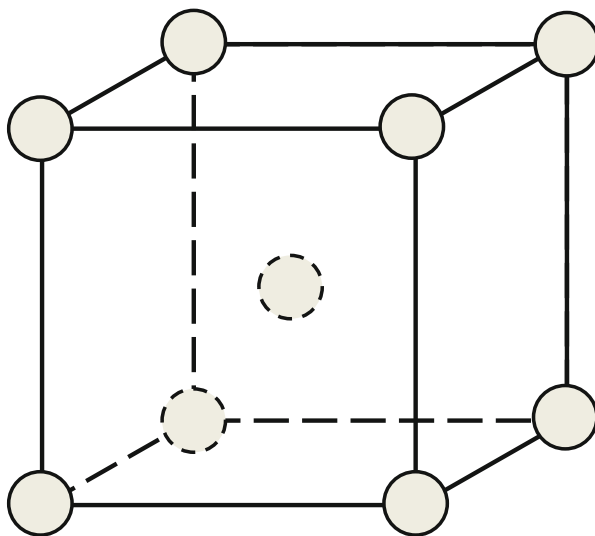


Fig. 2.6 The simple cubic crystal structure with all sides of equal length and one atom at each of the cube corners

Fig. 2.7 The body-centered cubic structure with all sides of equal length and atoms at each of the cube corners plus one in the center of the cube



easiest structure to visualize with atoms at each of the corners of a cube, but this structure is not commonly observed.

The most common crystal lattice structures are (i) *body-centered cubic* (Fig. 2.7), (ii) *face-centered cubic* (Fig. 2.8), and (iii) *hexagonal close-packed* (Fig. 2.9). The unit cells for these structures are drawn with small spheres as atoms located at lattice points. In fact, along certain (*close-packed*) directions, the outer shells are actually touching—as in the structure at the right of Fig. 2.6. (Since this makes it harder to visualize atom positions, the structures are instead drawn with small spheres.) The close-packed direction and the distribution of these in space are important because

Fig. 2.8 The face-centered cubic structure with one atom in each of the cube corners and one at the center of each of the six cube faces

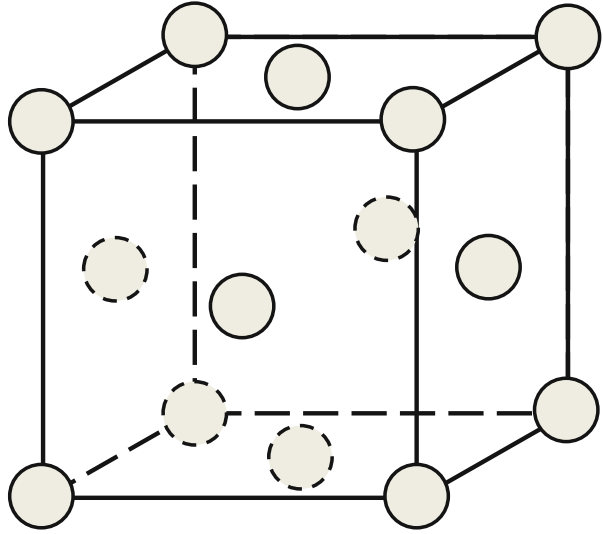
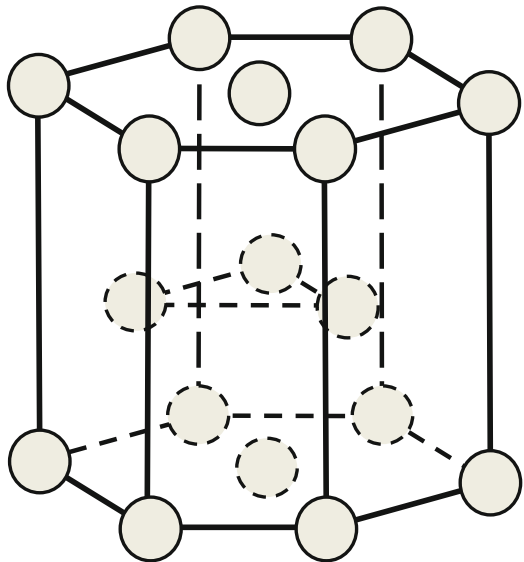
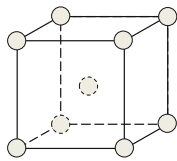
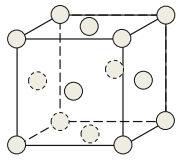
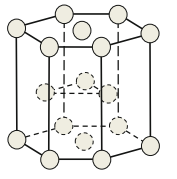


Fig. 2.9 The hexagonal cubic structure with stacked layers of atoms with hexagonal symmetry plus one in the center of the hexagon. The first and third layers line up directly



these are the most likely directions for slip or plastic deformation to be discussed in the next section. Table 2.1 specifies which atoms are touching, lists some common metals that exist (at room temperature), and gives an example of the dimensions of each of these unit cells.

Table 2.1 Key characteristics of the BCC, FCC, and HCP crystal structures

Crystal structure		Atoms in contact	Example metals
Body-centered cubic (BCC)		Along (4) cube diagonals	Fe, Ta, Nb, Mo, W, Cr, V Unit side length for Fe = 0.2866 nm Unit side length for W = 0.2854 nm
Face-centered cubic (FCC)		Along (6) face diagonals (the other 6 face diagonals are repeat directions)	Cu, Al, Ag, Au, Pb, Ni, Pt Unit side length for Cu = 0.3615 nm Unit side length for Pb = 0.3924 nm
Hexagonal close-packed (HCP)		All atoms in “basal” planes, which are the top, bottom, and middle planes of the hexagon. (Also, atoms in top and bottom planes are in contact with atoms in middle plane.)	Zn, Cd, Ti, Mg, Be Unit side length for Ti = 0.2951 nm Height of hexagon for Ti = 0.468 nm

2.4 Plastic Deformation

Elastic deformation simply involves stretching of atoms away from their equilibrium separation. Plastic deformation occurs through collective movement of atom planes. Let us first estimate the stress required to move one plane across another. As an example, take the basal plane in the HCP structure. Figure 2.10 depicts two stacked planes. These are the “basal” planes of the HCP, but more generally, they are the “close-packed” planes that exist in both the HCP and FCC—but not the BCC—structures. (Close-packed implies there is no denser packing of atoms on a plane possible.)

Let’s hypothesize that we can apply a force to each row of atoms on the top plane and slide them over the bottom plane. You can see that this is one way of generating “permanent” strain since this action would create a movement of material in the top plane relative to that in the bottom plane.

Figure 2.11 shows the side view of this process, where it appears as if one row rather than an entire plane of atoms is being slid. Since the motion involves “shearing” of parallel surfaces past each other, the *shear stress* τ is depicted rather than a normal stress (as in a tensile test) σ .

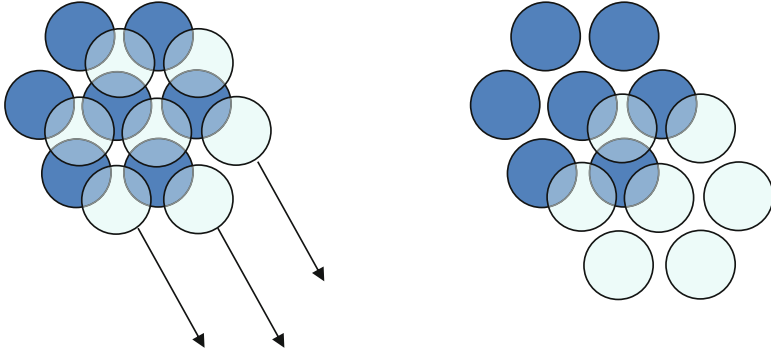


Fig. 2.10 Two close-packed planes with one sliding over the other

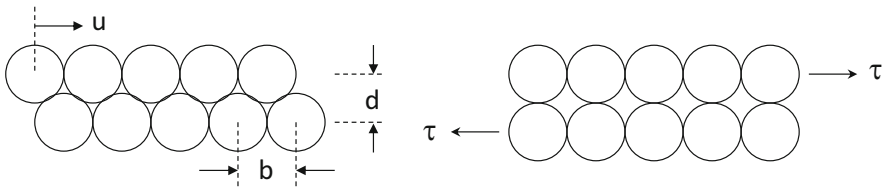


Fig. 2.11 A side view of the configuration shown in Fig. 2.10

According to Fig. 2.11, the shear stress τ will be 0 when $u = 0$ (equilibrium position) and when $u = b/2$ (right-hand side). The stress to impose the elastic motion is related to the strain through:

$$\tau = \mu\lambda = \mu \frac{u}{d} \tag{2.9}$$

where μ is the “shear modulus,” which is another form of the elastic modulus (more on its definition to follow in [Box 6.1](#)), and λ is the “shear strain” defined analogously to ϵ as u/d . An equation that describes the motion of the top plane relative to the bottom plane, given the constraint that $\tau = 0$ at both $u = 0$ and $u = b/2$, is as follows:

$$\tau = C \sin \frac{2\pi u}{d} \tag{2.10}$$

Taking the derivative of Eq. 2.9:

$$\frac{d\tau}{du} = \frac{\mu}{d}$$

and the derivative of Eq. 2.10:

$$\frac{d\tau}{du} = C \frac{2\pi}{b} \cos \frac{2\pi u}{b}$$

and evaluating the latter as $u \rightarrow 0$ gives the following:

$$\left. \frac{d\tau}{du} \right)_{u \rightarrow 0} = C \frac{2\pi}{b}$$

Setting this equal to the derivative of Eq. 2.9 gives the following:

$$\begin{aligned} C \frac{2\pi}{b} &= \frac{\mu}{d} \\ C &= \frac{b\mu}{2\pi d} \end{aligned} \quad (2.11)$$

and Eq. 2.10 becomes as follows:

$$\tau = \frac{b\mu}{2\pi d} \sin \frac{2\pi u}{b} \quad (2.12)$$

The maximum stress τ_{\max} occurs when:

$$\frac{2\pi u}{b} = \frac{\pi}{2}$$

which requires at this point $\mu = b/4$, and from Eq. 2.12, with $\tau = \tau_{\max}$:

$$\tau_{\max} = \frac{b\mu}{2\pi d}$$

Since $d \approx b$:

$$\tau_{\max} \approx \frac{\mu}{2\pi} \quad (2.13)$$

This estimate predicts that the stress to slide one plane over another is $\sim 16\%$ of the shear modulus. Most values of μ are a little less than 50% of E . Thus, the stress to move one plane over another is estimated to be $\sim 8\%$ of E .

Returning to the stress–strain curves of Chap. 1, the yield stress in mild steel (Fig. 1.12) was ~ 270 MPa. Compared to an elastic modulus of 212 GPa, this stress is 0.13% rather than 8% of the elastic modulus. Thus, permanent strain is occurring at a stress much lower than that required to move an entire plane of atoms over another. Table 2.2 lists the percent of theoretical strength of a selection of materials illustrating that the observed strengths are well below the theoretical strength estimate of 8% from Eq. 2.13. Only the value for the nano-laminate Cu-Nb material [2] approaches its theoretical strength. The next section provides insight into why observed

Table 2.2 Observed strength of a variety of materials compared to the theoretical strength

Material	Percent of theoretical strength
Natural diamond single crystal	3
WC-6 Co	1
Al ₂ O ₃	1.1
Low alloy steel (martensitic)	1
Plain carbon steel	0.5
Copper	0.2
10 nm Cu-Nb laminate	10

strengths are well below the theoretical strength. The estimate of τ_{\max} , however, is useful as an estimate of the “theoretical shear stress” possible in crystalline materials. In a sense, this estimate serves as an estimate of potential strength values and has given the materials community a goal for the development of new materials through new alloys or new processing methods.

2.5 Dislocations

Prediction of the theoretical shear stress is a simple calculation, which has likely existed for well over a century. It wasn’t until the 1930s, however, that it was hypothesized how deformations could occur at stresses as low as experimentally observed. In 1934, Orowan [3], Polanyi [4], and Taylor [5] independently concluded that it wasn’t the collective motion of a plane over another plane but rather the incremental motion of rows or partial planes of atoms that are possible at much lower stress. Consider a ripple in a carpet or consider the movement of a snake. In each of these cases, motion is possible (at lower stresses than required to slide the entire carpet or snake) by formation of a “defect” and moving the defect from one location to another—thereby achieving a net motion of the entire body. In materials, these defects are called “dislocations.”

Figure 2.12 shows a perfect (simple cubic) crystal on the left, an edge dislocation in the center, and a dislocated crystal on the right. Note the extra half-plane of atoms forming the dislocation in the center schematic. As the half-plane moves to the right under the applied stress, the top half of the crystal will shift relative to the bottom half by the distance b , which is known as the *Burgers vector* (see Box 2.1). Notice the upside down “T” at the end of the half-plane. This is the symbol for an edge dislocation. The dislocation is a line defect in that it extends in a direction normal to the page and the Burgers vector is normal to the line of the dislocation. Because the lattice planes in the vicinity of the dislocation are distorted, diffraction of electrons, e.g., in an electron microscope thin foil, will create a distinctive image of the dislocation line.

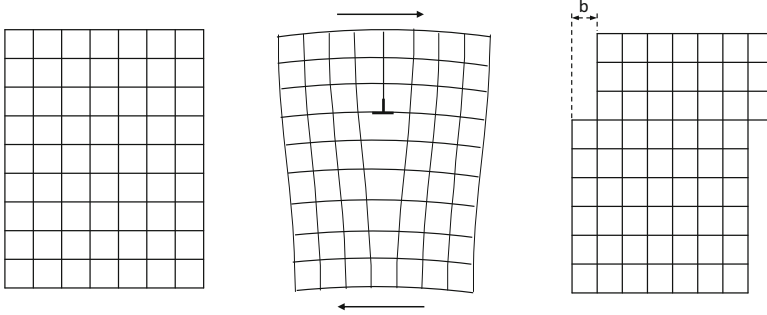


Fig. 2.12 A perfect crystal of unspecified thickness on the left with an edge dislocation formed (see the extra half-plane) in the center and the dislocated crystal on the right

Box 2.1 Calculating the Magnitude of the Burgers Vector

Table 2.1 listed a unit cell side length of 0.3615 nm for Cu and specified that Cu crystallizes in the FCC lattice, which implies that the atoms along a face diagonal are touching. Inspection of the FCC crystal structure suggests that the face diagonal includes one-half of the diameter of a corner atom plus the entire diameter of the atom in the center of the face plus another one-half diameter of a corner atom. This totals to two times the diameter or four times the radius of the copper atom (R_a), and:

$$4R_a = \sqrt{2} a = \sqrt{2} 0.3615 \text{ nm} = 0.5112 \text{ nm}$$

$$R_a = 0.1278 \text{ nm}$$

Since the face diagonal is a close-packed direction, movement of atoms along this direction is energetically most favorable. In fact, the arrows in Fig. 2.10 were drawn in this direction. One slip event entails the motion depicted in Fig. 2.10 which yields Burgers vector equal to $2R$. Thus:

$$b = 2R_a = 0.2556 \text{ nm}$$

If the material were Fe rather than Cu, Table 2.1 indicates that the unit cell length is 0.2866 nm and that the crystal lattice is BCC, which implies the atoms along the cube diagonal (rather than the face diagonal) are touching. In this case:

$$4R_a = \sqrt{3} a = \sqrt{3} 0.2866 \text{ nm} = 0.4964 \text{ nm}$$

$$R_a = 0.12418 \text{ nm}$$

$$b = 0.2482 \text{ nm}$$

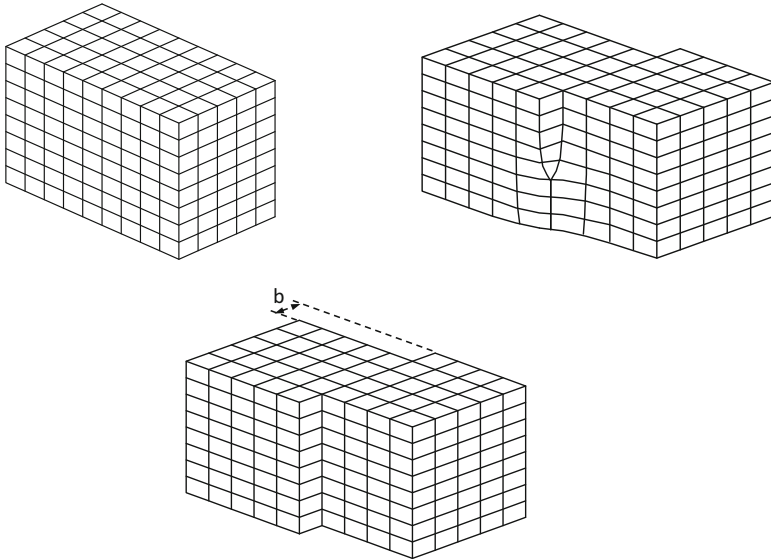


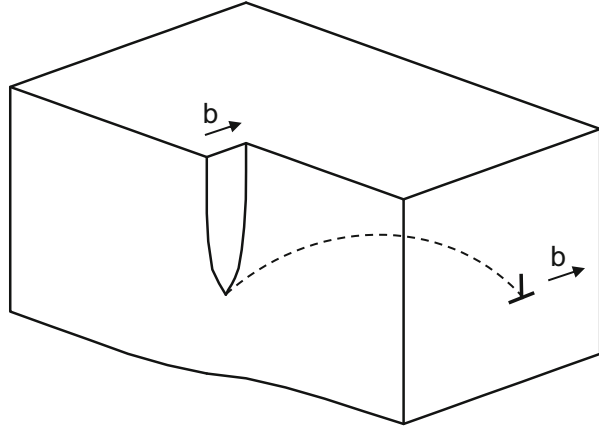
Fig. 2.13 A perfect crystal on the left with a screw dislocation on the right producing a Burgers vector of displacement in the bottom crystal

Figure 2.13 shows a schematic of a perfect (simple cubic) crystal on the left with a screw dislocation active in the center illustration producing a dislocated crystal on the right. (The term “screw” arises from the positioning of atoms around the dislocation line.) In this case the dislocation imparts displacements that shift the top half of the crystal relative to the bottom half of the crystal. As the defect moves toward the bottom of the crystal, the top half will have shifted relative to the bottom half by the same distance b . In this case, the crystal is drawn as an isometric image, and the dislocation line is parallel to the Burgers vector and centered at the point of initiation of the sheared crystal. Again, around this line are distorted crystal planes (when compared with the bulk of the crystal) which will diffract electrons and create an image.

In Figs. 2.12 and 2.13, both the perfect edge and perfect screw dislocation are straight, linear defects, although a volume of distorted crystal is associated with the defect. It is common, however, for a dislocation to be mixed edge and screw, in which case it would still be a linear defect—but with curvature. This is illustrated schematically in Fig. 2.14 with a screw dislocation on the one face of the crystal (as in Fig. 2.13) and an edge dislocation with the same Burgers vector on the other face of the crystal. The dashed line is the mixed edge and screw dislocation on a plane parallel to the top and bottom planes in the figure.

As evident in Figs. 2.12 and 2.13, a “perfect” crystal is dislocation-free. In this sense dislocations represent “defects”—just as a vacancy or an impurity atom can be defects. Dislocations, however, serve a critical role in plastic deformation. It turns out that the stress required to move these dislocations is much less than that required

Fig. 2.14 A dislocation with edge and screw components defining a curved line



to collectively move an entire plane relative to its neighbor. Dislocations enable strain at stresses 10–100× below the theoretical shear stress. The analysis of plastic deformation and the temperature and strain-rate dependence of the stress–strain curve rely on the analysis of the generation and interactions of dislocations. This is the subject of the remaining chapters of this monograph.

The dislocation density ρ_D is the length of dislocation lines (m) per unit volume (m^3). To estimate the strain associated with motion of a dislocation, consider a tensile test specimen with a rectangular cross section of 2.0 mm × 10 mm and a length of 50 mm. Thus, the volume of this specimen is 1000 mm^3 ($1 \times 10^{-6} \text{ m}^3$). Assume the test specimen is copper, which has a Burgers vector of $0.256 \times 10^{-9} \text{ m}$. The strain achieved by the motion of dislocations is as follows:

$$\varepsilon = \rho_D b \ell \quad (2.14)$$

where ℓ is the distance moved by the dislocations. (The time-differentiated form of Eq. 2.14 is referred to as the Orowan equation [6], $d\varepsilon/dt = \dot{\varepsilon} = \rho_D b v$, where v is the average dislocation velocity.)

If the specimen has a single dislocation of length 2 mm (the thickness of the specimen), which moves 10 mm (the entire width of the specimen), the strain would be as follows:

$$\varepsilon = \rho_D b \ell = \frac{0.002 \text{ m}}{10^{-6} \text{ m}^3} (0.256 \times 10^{-9} \text{ m}) (0.010 \text{ m}) = 5 \times 10^{-9}$$

That is, a single dislocation imparts a very small amount of strain. Accordingly, it takes the motion of millions to billions of dislocations to give the level of strain found in mechanical tests.

Figure 2.15 is a photomicrograph of a deformed titanium alloy taken with a transmission electron microscope. Note the micron marker label indicating the level of magnification. The black lines in this figure are the images of dislocations—or the

Fig. 2.15 Transmission electron micrograph of a dislocation structure (dark lines) in a titanium alloy deformed at 400 °C. (Courtesy of James C. Williams)

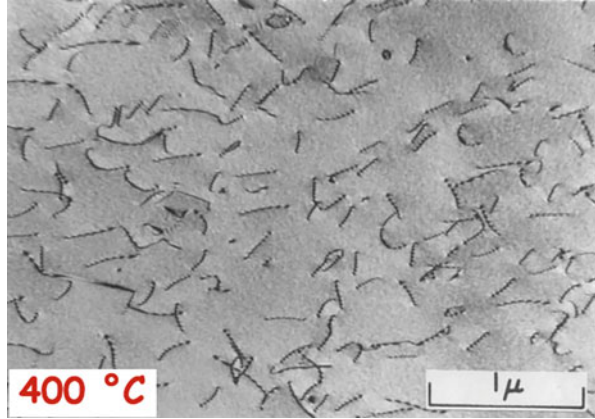
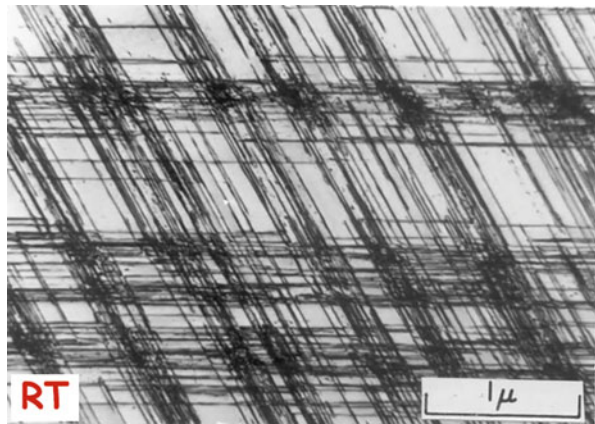


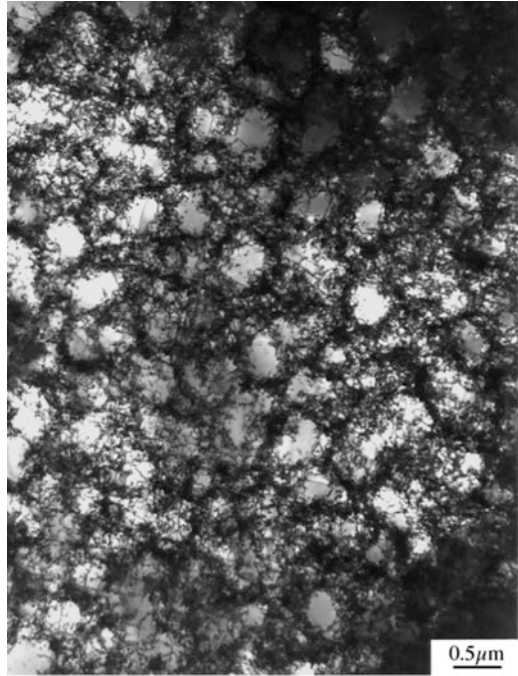
Fig. 2.16 Transmission electron micrograph of a dislocation structure (dark lines) in the same titanium alloy as in Fig. 2.15 deformed at room temperature. (Courtesy of James C. Williams)



distorted lattice planes in the vicinity of the dislocations—referred to above. Many of the dislocations observed in this photomicrograph are not particularly straight—indicating that during transit they have “cross-slipped” from one crystallographic system onto another. This is often referred to as “wavy slip.” Figure 2.16 is a photomicrograph of the same titanium alloy deformed at room temperature rather than at 400 °C. In this case the dislocations demonstrate a far more “planar” appearance; this is often referred to as “planar slip.” Figure 2.17 is a photomicrograph of shock-deformed copper [7]. In this case the sample was heavily deformed, implying an abundance of dislocation generation and motion. All of the black contrast in this figure is due to tangled dislocations, which have assembled into networks—or “subcells.”

These two photomicrographs show that dislocations are prevalent in deformed metal test specimens. Secondly, they illustrate that massive dislocation densities are required to achieve significant strains. These high dislocation densities become critically important, because the movement of a dislocation through a perfect

Fig. 2.17 Transmission electron micrograph showing the dislocation substructure in heavily deformed copper [7]



structure is easier than through a structure with tangled dislocations. (Often, the term “stored” dislocation is used to emphasize that these dislocations lack mobility.) As the dislocation density increases during straining, the stress to continue straining increases. This is the primary explanation for the shape of the stress–strain curves shown in Chap. 1.

2.6 Summary

The intent of this chapter has been to emphasize that properties derive from structure and bonding. This monograph is focused on strength in metals. Strength is shown to depend on forces between ions and the structure of the crystal lattice. The concept of a dislocation has been introduced because the strength of metals is defined largely by the motion and interaction of these defects. More detail on these interactions follows in Chaps. 3 and 4. While the shape of the energy versus ion separation distance curve does not in fact become input to the modeling approach promoted in this monograph, it is useful to ground oneself on the fundamental role these interatomic forces have on material properties (e.g., elasticity) in general. It is useful to remember that interatomic forces affect physical properties such as the elastic modulus and thermal expansion coefficient, while defects—and in particular dislocations—affect strength.

Exercises

2.1 The constant k in Eq. 2.1 is as follows:

$$k = \frac{1}{4\pi\epsilon_0}$$

where ϵ_0 is the permittivity of vacuum, which is 8.854×10^{-12} F/m or 8.854×10^{-12} C²/J·m (F is a farad, C is a coulomb, and J is a joule). Find the attractive force between Na and Cl, when the equilibrium distance between ions is 0.236×10^{-9} m. (Recall that the electron charge for a single electron is 1.602×10^{-19} C.)

- 2.2 The attractive energy is shown in Eq. 2.2 to vary with the reciprocal of r . For the NaCl molecule in Exercise 2.1, compute the attractive energy in units of joules (N·m).
- 2.3 Since in units of N·m, the energy computed in Exercise 2.2 is such a small number, these energies are often given in units of electron volts (eV), where $1 \text{ eV} = 1.602 \times 10^{-19}$ N·m. What is the attractive energy of the NaCl molecule in Exercise 2.1 in units of eV?
- 2.4 The repulsive energy is often assumed to vary with the reciprocal of r to a power of n :

$$U_R = \frac{B}{r^n}$$

where $n > 5$. For the Na Cl molecule, assume that $n = 8$ and that $B = 7.32 \times 10^{-6} \text{ eV}\cdot\text{nm}^8$. Compute the repulsive energy for the NaCl molecule.

- 2.5 What does the negative sign for the total energy in Exercise 2.4 imply?
- 2.6 From the expressions for the attractive and repulsive energies for the NaCl molecule in Exercises 2.3 and 2.4, plot the variation of these energies and the total energy with separation.
- 2.7 The packing density is the volume of atoms within a unit cell divided by the volume of the unit cell. Calculate the packing density of a simple cubic. (Remember to include only the fraction of the atom that is within the unit cell; only one-eighth of each corner atom is within a simple crystal unit cell.)
- 2.8 Calculate the packing density of a body-centered cubic crystal. (In this case, the entire atom in the center of the unit cell is included.)
- 2.9 Calculate the packing density of a face-centered cubic crystal.
- 2.10 Calculate the packing density of a hexagonal close-packed crystal.

The data in Table 2.E11 is a compilation of data published by Buch [1] and ASM International [8]. For the elements listed, the most common crystal structure and values of the melting temperature, elastic modulus, shear modulus, and yield stress are included (where available). The latter three values

Table 2.E11 Crystal structure, melting temperature, elastic modulus, shear modulus, and yield stress (where available) compiled by Buch [1] for a collection of pure metals

Metal	Structure	Melting T, C	E, GPa	G, GPa	YS, MPa
Li	BCC	181	5	4.2	
K	BCC	64			
Na	BCC	710	12.9	2.5	14
Cs	BCC	29	1.7	0.67	
Rb	BCC	39			
Be	HCP	1284	293	147	225
Mg	HCP	650	201.6	17.7	100
Sr	FCC	770			
Ca	FCC	850	20	7.4	14
Ba	BCC	710	12.9	4.86	
Y	HCP	1452	67	26.5	27
Al	FCC	660	72.2	27	30
Ti	HCP	1690	105.2	40	300
V	BCC	1900	125	50	92
Cr	BCC	1550	279	115	175
Mn	Cubic complex	1245	191	76.4	
Fe	BCC	1540	208	80.7	150
Co	HCP	1493	211	82	400
Ni	FCC	1455	197	75	42
Cu	FCC	1083	125	46.4	40
Zn	HCP	420	94	37	40
Ga	Orthorhombic	30	10	4.3–6.7	
Ge	DC	958	80	30	
Zr	HCP	1830	98	37	200
Nb	BCC	2415	103	37.5	150
Mo	BCC	2622	325	122	400
Ru	HCP	2460	430	168	104
Rh	FCC	1966	379	147	300
Pd	FCC	1554	124	47	
Ag	FCC	961	71	27	50
Cd	HCP	321	63	24.6	25
In	FCC	156	10.7	3.8	2
Sn	Tetragonal	232	55	20.6	36
Sb	Rhombic	631	56		
La	Hexagonal	835	38	14.3	
Ce	FCC	793			87
Hf	HCP	2222	141	56	
Ta	BCC	2996	188	69	276
W	BCC	3410	415	161	1200
Re	HCP	3167	460	159	600
Pt	FCC	1773	170	62	2
Au	FCC	1063	78.5	27	20

(continued)

Table 2.E11 (continued)

Metal	Structure	Melting T, C	E, GPa	G, GPa	YS, MPa
Tl	HCP	303	7.9	2.7	
Pb	FCC	327	16	5.6	55
Bi	Rhombic	271	32	12.2	
Th	FCC	303	78	27.6	140
U	Orthorhombic	1133	204	85	270

apply to room temperature. Some of the yield stress estimates are derived from hardness measurements and are not reliable, but for the purposes of Exercises 2.11 and 2.12, the data set is a useful compilation.

- 2.11 Figure 2.5 suggests a general correlation between the elastic modulus and melting temperature. However, there is a lot of scatter in this plot. Create a plot of elastic modulus versus melting temperature for only groups 6, 7, and 8 from the periodic table. Comment on the correlation between these two properties for the smaller data set.
- 2.12 Equation 2.13 was derived as an estimate of the “theoretical strength” of a crystal. Create a plot of yield stress versus $G/2\pi$ (for this, use the noted yield stress, which is likely a value applicable to a uniaxial test, rather than a shear stress and use the polycrystalline value of G rather than the single crystalline value of μ ; the difference between these is discussed in Box 6.1). What can you conclude about the validity of Eq. 2.13? Comment on the magnitude of the yield stress versus $G/2\pi$, on whether there is a general trend that supports this equation and whether the correlations vary with crystal structure.

References

1. A. Buch, *Pure Metals Properties: A Scientific-Technical Handbook* (ASM International, Materials Park, 1999)
2. A. Misra, J.P. Hirth, H. Kung, Single-dislocation-based strengthening mechanisms in nanoscale metallic multilayers. *Philos. Mag. A* **82**, 2935–2951 (2002)
3. E. Orowan, Zur Kristallplastizität. III. *Z. Phys.* **89**, 634–659 (1934)
4. M. Polanyi, Über eine Art Gitterstörung, die einen kristall plastisch machen könnte. *Zeitschrift für Physik* **89**, 660–664
5. G.I. Taylor, Mechanism of plastic deformation in crystals. *Proc. R. Soc. London* **145A**, 362 (1934)
6. P. Veyssièrè, Dislocations and the plasticity of crystals, in *Mechanics and Materials, Fundamentals and Linkages*, ed. by M. A. Meyers, R. A. Armstrong, H. O. K. Kirchner, (Wiley, New York, 1999), p. 293
7. G.T. Gray III, P.S. Follansbee, C.E. Frantz, Effect of residual strain on the substructure development and mechanical response of shock-loaded copper. *Mater. Sci. Eng.* **A111**, 9–16 (1989)
8. H. E. Boyer, T. L. Gall (eds.), *Metals Handbook Desk Edition* (ASM International, Materials Park, OH, 1985) (See, in particular, Chapter 14)

Chapter 3

Contributions to Strength



Introduction

Section 1.9 presented stress–strain curves for an AISI 1018 steel and Sect. 1.11 presented two curves for 304 L stainless steel. The yield stress was described as the point of departure from the elastic to plastic behavior. For the AISI 1018 steel in Fig. 1.12, the yield stress was ~ -265 MPa, whereas for the 304 SS specimen tested by Krempl (Fig. 1.17), the yield stress (0.002 strain offset) was ~ 204 MPa. These were measurements in two very common, readily available materials used for a variety of applications. Their strengths result from the contributions of several strengthening “mechanisms.” This chapter explores these contributions.

3.1 Strength of a Single Crystal

Table 2.1 illustrated how atoms assemble in the FCC, BCC, and HCP crystal structures. The unit cell for each of these structures was specified. The dimension of a single cell was on the order of 0.28 nm. In centimeter-sized samples, many millions of these unit cells have stacked one on top and next to another. Figure 3.1 shows just a $2 \times 2 \times 2$ stacking of FCC unit cells. To achieve a centimeter-sized sample requires

$$\frac{0.01 \text{ m} \frac{10^9 \text{ nm}}{\text{m}}}{\frac{0.28 \text{ nm}}{\text{unit cell}}} = 3.6 \times 10^7 \text{ unit cells}$$

stacked in all 3 directions, giving 4.6×10^{22} unit cells. If these stack together as shown in Fig. 3.1 in a single FCC lattice, the cubic cm of metal would be termed a

Supplementary Information The online version contains supplementary material available at [https://doi.org/10.1007/978-3-031-04556-1_3]

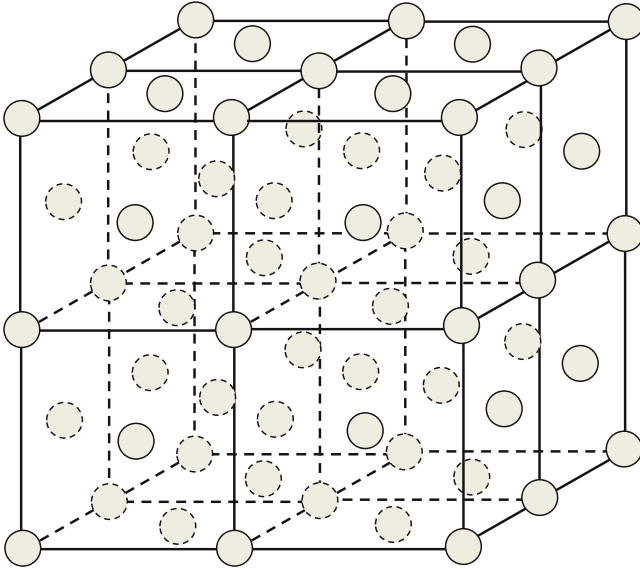
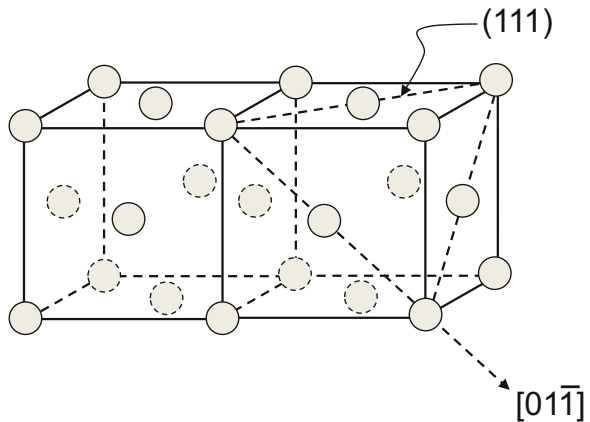


Fig. 3.1 A $2 \times 2 \times 2$ stacking of 8 FCC unit cells

Fig. 3.2 Two FCC unit cells with a single slip plane (111) and slip direction $[01\bar{1}]$ identified



single crystal. Figure 3.2 shows two of these stacked unit cells to illustrate the *slip plane* and *slip direction* in the FCC lattice. The slip plane is the “close packed” plane. One—marked (111)—is identified, although there are several others that could also have been identified (see Box 3.1). This plane is identical to the plane sketched in Fig. 2.10. The slip direction is a “close packed” direction. One—marked $[01\bar{1}]$ —is identified, although there are several others that could also have been marked. The generic direction is the same as the direction sketched in Fig. 2.10.

Box 3.1 A Primer on Crystal Lattice Planes and Directions Convention

A convention has been established—known as “Miller Indices”—for identification of planes and directions in crystal lattices. The easiest to describe are for cubic lattices (FCC or BCC).

Directions: These are enclosed within brackets “[*u v w*].” The vector of interest is positioned so that it passes through zero in a Cartesian coordinate system. *u*, *v*, and *w* are the projections of the vector on the *x*, *y*, and *z* axes, respectively. Whole numbers are used; thus, if the projections are $[1\frac{1}{2}1]$, then the indices are written $[212]$. Negative numbers are specified with a “-” above the number, e.g., $[0\bar{1}1]$, and the negative number is referred to as “bar” one.

Planes: These are enclosed within parenthesis “(*h k l*).” The plane of interest is positioned such that it does not pass through the origin. The intercepts of the plane with the *x*, *y*, and *z* axes become $1/h$, $1/k$, and $1/l$, respectively. That is, if the plane does not intercept the *x*-axis, $1/h = \infty$ and $h = 0$. Again, negative numbers are specified with a “-” above the number, e.g., $(0\bar{1}1)$.

The HCP lattice adds some complexity in that a four-parameter coordinate system is used.

Assume that the single crystal is aligned with the tensile axis parallel to the *y* axis in Fig. 3.2. Using the planes and directions convention of crystallography, this is the $[010]$ direction. Figure 3.3 shows the two stacked unit cells with the tensile axis. Slip occurs due to shear on the slip plane, and slip occurs in the direction of the slip direction. Figure 3.4 shows the scenario at the scale of the tensile specimen. Two

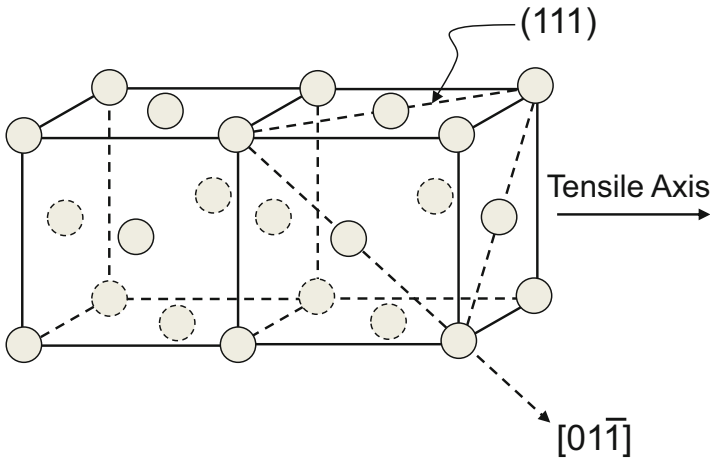
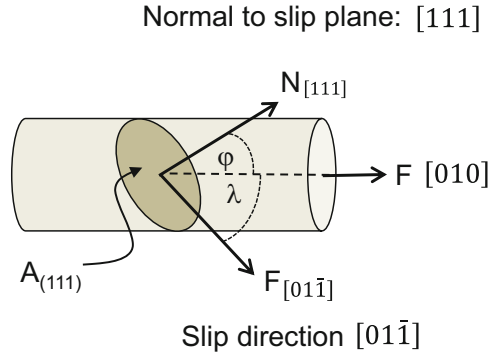


Fig. 3.3 The two unit cells of Fig. 3.2 with a tensile axis identified

Fig. 3.4 Slip planes and directions for a single crystal with a slip plane (actually it's normal) at an angle φ and a slip direction at an angle λ to the stress axis (similar to that shown schematically in Fig. 3.3)



angles have been defined between the load axis and the normal to the slip plane (φ) and between the load axis and the slip direction (λ). The shear stress driving slip is the force in the slip direction divided by the area on the slip plane:

$$\tau = \frac{F_{[01\bar{1}]}}{A_{(111)}} \quad (3.1)$$

This stress is referred to as the *critical resolved shear stress* τ_{CRSS} . Note that in relation to the specimen area, A ,

$$A_{(111)} = \frac{A}{\cos \varphi} \quad (3.2)$$

and that the applied force in the slip direction is

$$F_{[01\bar{1}]} = F \cos \lambda \quad (3.3)$$

Accordingly,

$$\tau_{\text{CRSS}} = \frac{F_{[01\bar{1}]}}{A_{(111)}} = \frac{F \cos \lambda}{\frac{A}{\cos \varphi}} = \frac{F}{A} \cos \varphi \cos \lambda = \sigma \cos \varphi \cos \lambda \quad (3.4)$$

The factor $[\cos \varphi \cos \lambda]$ is referred to as the *Schmidt Factor* [1]; this factor is always less than or equal to one. From vector analysis, it is helpful to remember that the angle θ between two vectors, defined by Cartesian coordinates $[u_1 v_1 w_1]$ and $[u_2 v_2 w_2]$, is:

Direction 1: $[u_1 v_1 w_1]$

Direction 2: $[u_2 v_2 w_2]$

$$\theta = \cos^{-1} \left[\frac{u_1 u_2 + v_1 v_2 + w_1 w_2}{\sqrt{u_1^2 + v_1^2 + w_1^2} \sqrt{u_2^2 + v_2^2 + w_2^2}} \right] \quad (3.5)$$

$$\cos(\theta) = \frac{u_1 u_2 + v_1 v_2 + w_1 w_2}{\sqrt{u_1^2 + v_1^2 + w_1^2} \sqrt{u_2^2 + v_2^2 + w_2^2}}$$

For the example above, the angle φ is between the normal to the slip plane $[111]$ and the loading direction $[010]$:

$$\cos(\varphi) = \frac{1 \times 0 + 1 \times 1 + 1 \times 0}{\sqrt{1^2 + 1^2 + 1^2} \sqrt{0^2 + 1^2 + 0^2}} = \frac{1}{\sqrt{3}} = 0.577$$

and the angle λ is between the slip direction $[01\bar{1}]$ and the loading direction $[010]$

$$\cos(\lambda) = \frac{0 \times 0 + 1 \times 1 + (-1) \times 0}{\sqrt{0^2 + 1^2 + (-1)^2} \sqrt{0^2 + 1^2 + 0^2}} = \frac{1}{\sqrt{2}} = 0.707$$

and the Schmidt Factor is $(0.577 \times 0.707) = 0.408$.

Note the slip plane illustrated in Fig. 3.3 has five other possible slip directions (see the triangle outlining the (111) slip plane). These are direction opposite the $[01\bar{1}]$ which is the $[0\bar{1}1]$, the $[1\bar{1}0]$ and the parallel $[\bar{1}10]$, and the $[10\bar{1}]$ and its parallel $[\bar{1}01]$. Table 3.1 lists the Schmidt Factors for each of these slip systems—made up by the (111) slip plane and each of these six slip directions. The Schmidt Factors listed in Table 3.1 show that slip is favorable, i.e., the Schmidt Factor is highest, on two of the six systems and that, since the Schmidt Factors are equivalent on these two systems, slip is equally likely in the $[01\bar{1}]$ and $[\bar{1}10]$ directions.

With a Schmidt Factor equal to 0.408, and the applied stress along the tensile axis would be $(1/0.408) = 2.45 \times \tau_{\text{CRSS}}$.

The critical resolved shear stress in pure copper (FCC) is 0.48 MPa, while the critical resolved shear stress in pure molybdenum (BCC) is 48 MPa and in pure iron (BCC) is 28 MPa. The next section discusses this difference. A point to emphasize here is that these stresses are significantly less than the yield stresses in 1018 steel

Table 3.1 Calculating the Schmidt Factor for the available slip planes and directions for the single crystal defined in Fig. 3.4

Slip plane	Slip direction	Cos ϕ	Cos λ	Schmidt factor	Slip favorable?
(111)	$[01\bar{1}]$	0.577	0.707	0.408	Yes
	$[0\bar{1}1]$		-0.707	-0.408	No ^a
	$[1\bar{1}0]$		-0.707	-0.408	No ^a
	$[\bar{1}10]$		0.707	0.408	Yes
	$[10\bar{1}]$		0.000	0.000	No
	$[\bar{1}01]$		0.000	0.000	No

^a The negative Schmidt Factor implies that slip is possible in the opposite direction to that specified

(which at RT exists in a BCC structure) and 304 stainless steel (which has an FCC structure). Furthermore, these stresses are much less than the theoretical shear stress estimates made in Sect. 2.4.

3.2 The Peierls Stress

The difference between τ_{CRSS} in pure copper and pure molybdenum is related to the difference in stress required to move a dislocation through a material with an FCC crystal structure compared to that through a material with a BCC crystal structure. In the latter structure, the Peierls stress becomes a dominant factor dictating the ease of dislocation motion [2]. An early estimate of the Peierls stress [3–5] predicted a negative exponential dependence of stress on the width of the dislocation, which characterizes the extent of atomic misorientations in the region encompassing the dislocation. One expression for the Peierls stress τ_p is [6]

$$\tau_p \cong 2\mu \exp\left(-\frac{2\pi w}{b}\right) \quad (3.6)$$

where μ is the shear modulus, b is the Burgers vector, and w is the width of the dislocation.

Wide dislocations are found in ductile metals, which have a low Peierls stress. Narrow dislocations, which are more difficult to move, are found in brittle metals and ceramics. Dislocations move in close packed directions in both BCC and FCC structures, but the slip planes can be shown to be more closely spaced—but more loosely packed—in BCC structures. (Recall that the close packed (111) plane does not exist in the BCC structure.) The spacing within and between slip planes affects the stress required to move a dislocation. A slip plane with more spacing—smaller planar density—promotes narrow dislocations, which, as indicated in Eq. 3.6, have a high Peierls stress. These differences in structure make dislocation motion more difficult in BCC than in FCC crystals. This is reflected in the observed difference in the τ_{CRSS} values.

Table 3.2 lists the areal density and interplanar spacing of slip planes in Mo and Cu (see Boxes 3.2 and 3.3). The large difference in the areal densities of Cu (FCC) and Mo (BCC) supports the notion that the Peierls stress should be higher in Mo than in Cu.

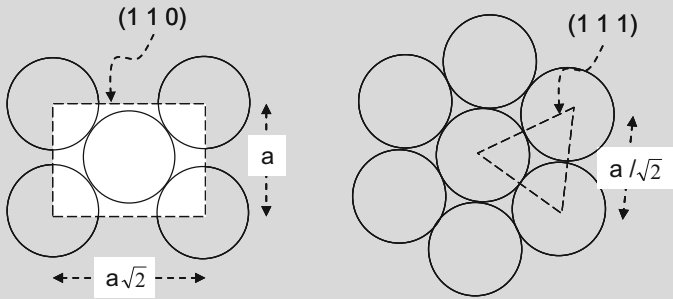
Table 3.2 Comparing the interplanar spacing and the areal density of a common FCC metal with a common BCC metal

Metal	Crystal structure	Slip plane	Distance between parallel planes (nm)	Areal density (atoms/nm ²)	τ_{CRSS} (MPa)
Cu	FCC	(111)	0.209	35.2	0.48
Mo	BCC	(110) ^a	0.222 ^a	14.3	48

^aSlip is also observed on the (112) and (123) planes in the BCC lattice. The interplanar distance on these is 0.128 nm and 0.084 nm, respectively

Box 3.2 Computing Areal Density

The diagrams below illustrates the atom configuration on a (110) BCC plane and on a (111) FCC plane (which is a close-packed plane). It is evident just from inspection that the packing density is higher on the FCC (111) than on the BCC (110)



where a is the length of the unit cell. The areal density is the number of atoms within a repeating unit divided by the area of the repeating unit. On the BCC (110), there are two atoms contained within the dashed area (the repeating unit), and the outer shells of the atoms along the diagonal of this area, the [111] direction, are touching. Thus, the areal density is (for this calculation the relationship between the atom radius and a is required).

$$\frac{2}{a^2\sqrt{2}} = \frac{2}{\left(\frac{4R_a}{\sqrt{3}}\right)^2\sqrt{2}} = \frac{3\sqrt{2}}{16R_a^2}$$

For Mo, $R_a = 0.136$ nm, the areal density is 14.3 atoms / nm^2 .

On the FCC (111), there is one atom within the dashed area (an equilateral triangle), and all atoms are touching. The areal density is

$$\frac{1}{\frac{\sqrt{3}}{4}a^2} = \frac{8}{\sqrt{3}a^2} = \frac{8}{\sqrt{3}(2\sqrt{2}R_a)^2} = \frac{1}{\sqrt{3}R_a^2}$$

For Cu, $R_a = 0.128$ nm and the areal density is 35.2 atoms / nm^2 .

Box 3.3 Computing Planar Spacing

The distance between parallel planes in a cubic system (e.g., the length of a vector normal to the surfaces of and between two parallel planes) is

$$d_{(hkl)} = \frac{a}{\sqrt{h^2 + k^2 + l^2}} \quad (3.B1)$$

where a is the lattice parameter (length of unit cell side) and h , k , and l are the Miller indices of the plane.

For the (111) planes in Cu, where $a = 0.362$ nm,

$$d_{(111)} = \frac{0.362 \text{ nm}}{\sqrt{1^2 + 1^2 + 1^2}} = 0.209 \text{ nm}$$

For the (110) planes in Mo, where $a = 0.314$ nm,

$$d_{(110)} = \frac{0.314 \text{ nm}}{\sqrt{1^2 + 1^2 + 0^2}} = 0.222 \text{ nm}$$

Slip is also observed on the (112) and (123) planes of the BCC lattice. For these, the spacing decreases to 0.128 nm and 0.084 nm, respectively.

3.3 The Importance of Available Slip Systems and Geometry of HCP Metals

The HCP crystal structure has a close-packed plane. In fact, as shown in Fig. 2.9, the HCP crystal is described as the stacking of parallel close-packed planes. An implication of this is that there are fewer “slip systems” available in HCP metals than in FCC metals (or, in fact, in BCC metals). A slip system is the combination of slip plane and direction (e.g., Burgers vector). The available slip systems in an FCC crystal—the collection of (111) planes—comprise an octahedron shape as illustrated in Fig. 3.5.

An octahedron is akin to two pyramids stacked base-to-base. The faces of the pyramids are different (111) planes. In Fig. 3.5, the Miller indices of the four visible (111) planes are indicated. The planes not visible are parallel to one of the planes indicated. Since there are three close-packed directions in each of the (111) planes (see, for instance Fig. 3.2) and there are eight total (111) planes, there are $3 \times 8 = 24$ possible slip directions in the crystal. However, only one-half of these—or 12—are truly unique (or independent). Nonetheless, there are lots of available slip systems in the FCC crystal structure.

In the HCP crystal system, there are only three unique slip directions within each close-packed plane, as illustrated in Fig. 3.6. Since there is only one unique close-

Fig. 3.5 Intersecting (111) planes in a single FCC unit cell illustrating the number of slip systems (planes and directions) available in this crystal structure. Each edge represents a $[110]$ slip direction

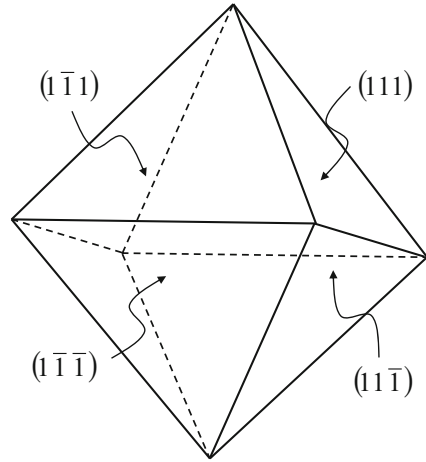
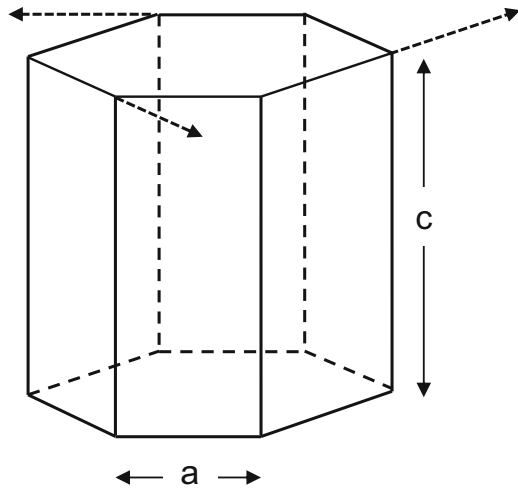


Fig. 3.6 The HCP crystal structure comprises stacked close-packed planes. Each has three close-packed directions, but a single HCP unit cell has fewer available slip systems than a single FCC unit cell



packed plane, this crystal has only three independent slip systems. For this reason, slip is observed on other planes. The *prismatic plane*, which is the plane comprising the side face of the hexagonal polygon, is an active slip plane in some HCP metals. Because slip in HCP metals involves a close-packed plane, the width of the dislocations and, accordingly, the Peierls stress are low. A unique aspect of deformation in HCP metals, however, is the role of the ratio of the dimension a to the dimension c in Fig. 3.6. The ideal c/a ratio based on the packing of spheres can be shown to equal 1.632. However, some HCP metals have a c/a ratio that is higher than the ideal (e.g., 1.856 in Zn and 1.886 in Cd), and others have a c/a ratio that is lower than the ideal (e.g., 1.587 in Ti and 1.59 in Zr). Since this ratio affects the spacing between close-packed planes as well as the spacing between other planes, it becomes a factor in determining the strength of HCP metals. Honeycombe concluded that basal slip is

predominant in HCP metals with c/a ratios close to the ideal value and that there is a correlation between the c/a ratio and the ease to which slip occurs on nonbasal planes [7]. In general, the strength of HCP metals (e.g., comparing the τ_{CRSS} in pure metals at room temperature) is greater than that of FCC metals but still much less than that of BCC metals.

3.4 Contributions from Grain Boundaries

The tensile test specimen above was described as a single crystal. Fabrication of single crystals of this volume is possible—and even desirable for some applications—but most engineering materials are not single crystals. Rather, they exist as *polycrystals* made up of numerous distinct *grains*. Figure 3.7 is an optical photomicrograph showing a polished and etched surface of Inconel 718—a nickel-based superalloy. Note the scale marker, indicating the width of this region is $\sim 330 \mu\text{m}$.

The blocky features in Fig. 3.7 are individual grains. The dark lines separating these grains are grain boundaries. The smallest grains in this photo appear to have a dimension of $\sim 3 \mu\text{m}$, whereas the largest grains have a maximum dimension over $\sim 50 \mu\text{m}$. Individual grains are regions where the individual unit cells are stacked

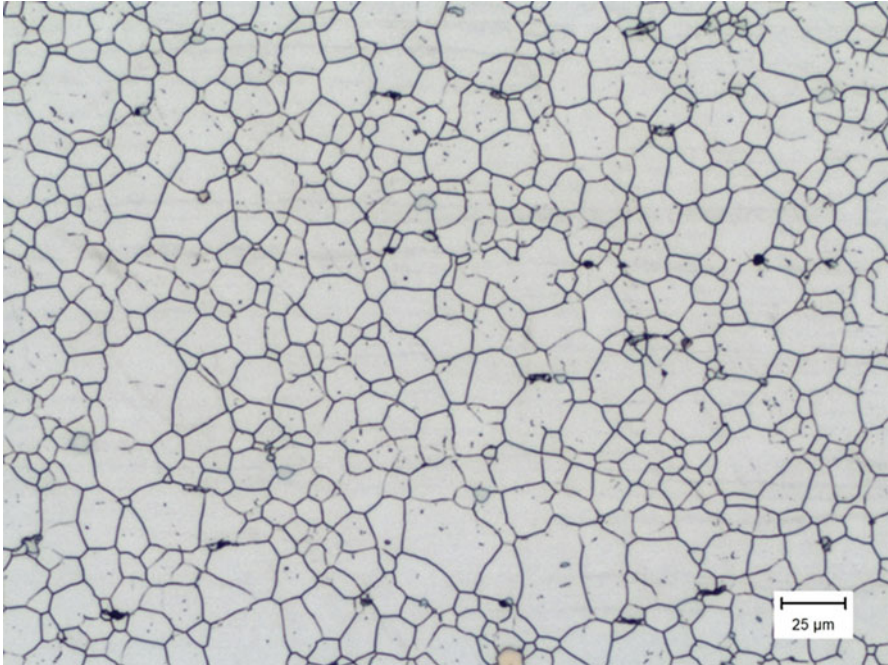


Fig. 3.7 Optical photomicrograph of annealed Inconel 718 showing individual grains. (Courtesy of Product Evaluation Systems, Inc.)

uniformly—just as in the single crystal described previously. In a polycrystal, however, neighboring grains more than likely have different orientations. The crystal planes (e.g., the (111)) and the crystal directions (e.g., the [110]) in one grain do not necessarily line up with the planes and directions in the neighboring grains. Nucleation and growth of solid particles from a liquid melt occur through the simultaneous formation of separate tiny *nuclei* which grow into the liquid, converting more liquid to solid, until only solid remains. These nuclei have random orientations because of the lack of structure in the liquid phase. As the nuclei transition to growing grains, they eventually run into neighboring grains with differing crystallographic orientations. At this point, a *grain boundary* forms between the two regions. Figure 3.7 shows many—perhaps more than 100—of these grains, separated by grain boundaries.

Consider a dislocation traversing one of the grains in Fig. 3.7. When this dislocation reaches a grain boundary, it may find moving into the next grain to be easy or hard. A possible scenario is illustrated schematically in Fig. 3.8. Shown in

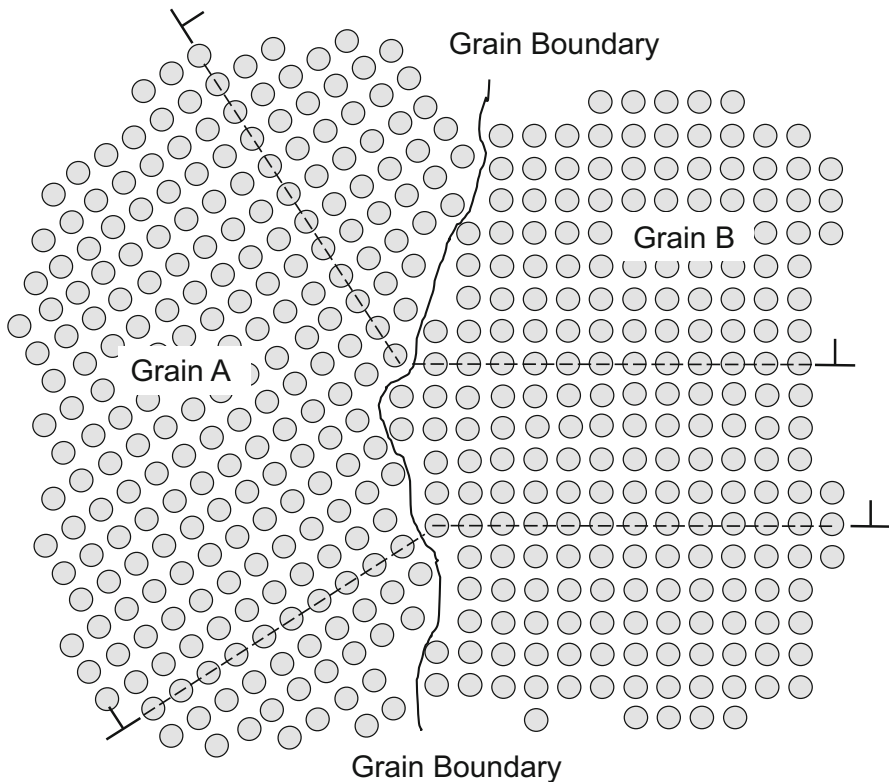


Fig. 3.8 Schematic showing two simple cubic grains (which happen to align in a direction normal to the indicated plane) separated by a grain boundary. The close-packed direction of two edge dislocations from Grain A do not align with a close-packed direction in Grain B

this figure are two simple cubic grains separated by a grain boundary. Dislocations moving along the close-packed direction in one grain do not easily pass to the adjacent grain because the close-packed directions do not align. The dashed lines show the traces of two such scenarios for two edge dislocations. When the dislocations impinge upon the grain boundary, it should be evident that movement of the dislocation into the new grain is not assured.

In fact grain boundaries present formidable obstacles to the motion of dislocations. The presence of grain boundaries in polycrystalline metals is one important contributor to their strength—a strength that rises well above the strength of a single crystal. The obstacle to dislocation motion posed by grain boundaries is the major contributor to the strength increase. This is discussed below. Another contribution arises from the fact that the resolved stress, i.e., the Schmidt Factor, varies from grain to grain. Initiation of yield in a few grains optimally oriented for slip does not imply bulk slip in the polycrystal (see Box 3.4).

Box 3.4 Crystal Plasticity

The Schmidt Factor recognized that slip occurs on unique crystallographic systems, and that the stress in any direction can be related to the stress on the slip system. If in a polycrystal the orientation of every grain is known, then for a specified load direction, it should be possible to sum up the effects of each of these grains to determine the grain-scale distribution of the applied stresses. Indeed, diffraction (x-ray, electron, and neutron) methods have been used to measure the distribution of grain orientations, and computer programs have been developed to process this orientation data.

One of the fascinating aspects of material plasticity is that grains can rotate as strain proceeds, and the measured grain orientations will change. The computer programs are even able to predict this with remarkable accuracy.

While the most predictive models need to account for the actual and evolving collective grain orientations, the sheer number of grains in an engineered product can make this a daunting task. Fortunately, useful approximations exist for averaging the effects of grain orientation for engineering estimates of a polycrystal's strength. These approximations will be used in this monograph.

Sources: S. R. Kalidindi, C. A. Bronkhorst, L. Anand, Crystallographic texture evolution in bulk deformation processing of FCC metals. *J. Mech. Phys. Solids*. **40**, 537-569 (1992).

H.-R. Wenk, S. Matthies, J. Donovan, D. Chateigner, BEARTEX: a Windows based program system for quantitative texture analysis. *J. Appl. Crystallogr.* **31**, 262-269 (1998).

S. I. Wright, U. F. Kocks, "popLA: Preferred Orientation Package – Los Alamos," Los Alamos National Laboratory Software Manual, July 1994.

A rough estimate of the contribution to strength by the presence of grain boundaries can be made by assuming that dislocations can only move across a single grain. Recall from Sect. 2.5 that the strain achieved by the motion of dislocations is

$$\varepsilon = \rho_D b l \quad (2.14)$$

where l is the average distance moved by each dislocation. If this distance is restricted to be the average grain size d , then to achieve the same level of strain (e.g., the 0.002 strain offset) requires the dislocation density to increase inversely to the grain size

$$\rho_D \propto \frac{1}{d} \quad (3.7)$$

Some simple models relate the stress σ to the dislocation density through the following relationship

$$\sigma = \sigma_i + \alpha \mu b \sqrt{\rho_D} \quad (3.8)$$

where α is a geometric factor, μ is the shear modulus, and σ_i is the stress (e.g., related to τ_{CRSS} in a pure metal) in a material with a very low dislocation density. Replacing the dislocation density with the inverse dependence on d_{gs} gives

$$\sigma = \sigma_i + \frac{k_d}{\sqrt{d_{gs}}} \quad (3.9)$$

showing an inverse dependence of the stress with the square-root of the grain dimension. Actually, this relationship is known as the Hall–Petch equation [8, 9] and can be derived more rigorously by modeling the build-up of stresses along a slip plane impeded at a grain boundary. The important point is that grain boundaries restrict dislocation movement, and the strengthening varies with the inverse of the square-root of the grain size.

3.5 Contributions from Impurity Atoms

Recall that in quoting values of τ_{CRSS} in Cu and Mo, it was specified that these were for “pure” materials. In brass, zinc is intentionally added to copper to create an *alloy* that is stronger than either pure copper or pure zinc. However, even when an element is not intentionally added, it is difficult to ensure that 100.000% of the atoms in a metal are of a single element. Impurity elements can exist in the raw ores or be introduced from the atmosphere or fabrication vessels used in production. Impurity additions—whether intentional or not—also present obstacles to the motion of dislocations.

Some impurity atoms can occupy the site of the host atom. This is referred to as a *substitutional* atom. A nickel atom, for instance, readily substitutes for copper in the copper FCC crystal lattice. Small atoms can fit into the “interstices” in the crystal lattice. Hydrogen and carbon are examples. When an atom is missing, the hole is called a vacancy. This occurs naturally (a small population of vacancies is thermodynamically stable) or due to an event, e.g., a high energy particle impinging upon a crystal lattice can actually knock an atom out of its position. Each of these “impurities” creates a discontinuity in the slip plane that affects the movement of dislocations. It is more difficult to move a dislocation through a crystal populated with these impurity atoms (or vacancies). Figure 3.9 shows schematic atom placement on an FCC close-packed plane for the case of a *substitutional* addition, an *interstitial* addition, and a *vacancy*.

Honeycombe [10] reviewed models for solution strengthening and concluded that it is the interaction of mobile dislocations with solute atoms rather than the resistance to the motion of dislocations “locked” by atmosphere of solute atoms that determines the strengthening effect of solutes. According to the theory proposed by Fleischer [11], the increase in stress scales with the square-root of the concentration of these impurity atoms. (Other theories for solution strengthening suggest a linear dependence of strength increase with concentration.) Figure 3.10 shows some data [12] on the strengthening in niobium—which has a BCC crystal structure—with small oxygen additions. The dashed line in this figure has the form

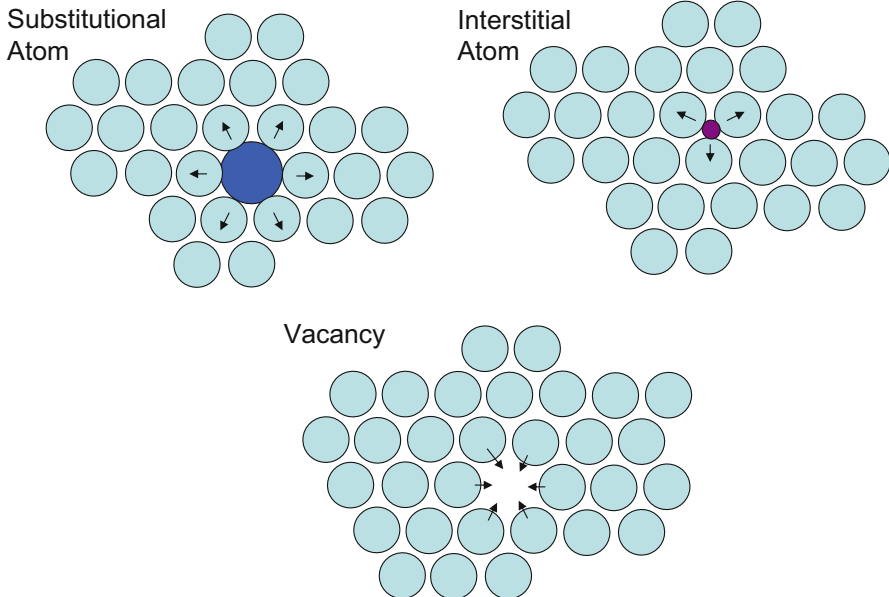
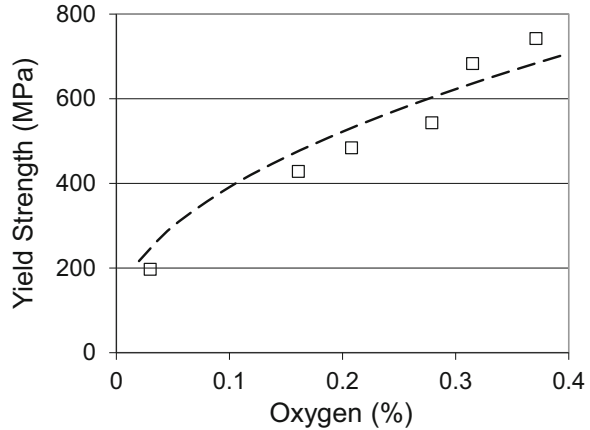


Fig. 3.9 Impurity atoms added to a close packed plane. The atom at the left substitutes for a host atom, whereas the atom on the right squeezes into the interstices between two host atoms. The bottom case is for a missing atom—or a vacancy

Fig. 3.10 Variation of the yield strength in pure niobium as a function of the concentration of oxygen



$$\sigma = \sigma_i + k_c \sqrt{c} \quad (3.10)$$

where c is the oxygen concentration (typically reported in weight percent) and k_c is a proportionality constant (units: $\text{MPa } c^{-1/2}$). The strong influence of relatively small oxygen additions on the strength of niobium is clear in this figure, but it is impossible to confidently conclude whether the hardening follows a linear or square-root dependence on the oxygen concentration.

3.6 Contributions from Stored Dislocations

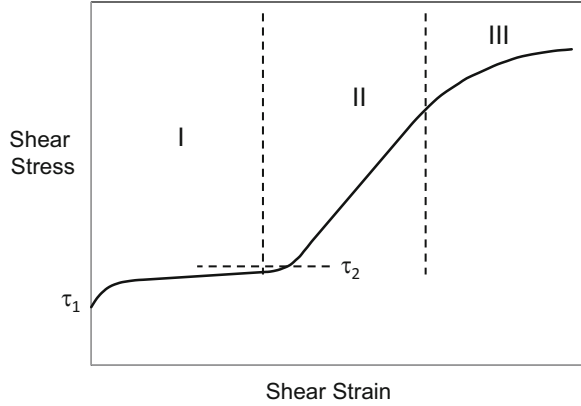
The fact that the stress increases with dislocation density was introduced above in Sect. 3.4. A dislocation represents disruption in the stacking order. Just as the stress increases when a moving dislocation encounters disruption due to a grain boundary or an impurity atom, the stress to force a moving dislocation over or past a stationary dislocation can be significant. This results in the equation given earlier

$$\sigma = \sigma_i + \alpha \mu b \sqrt{\rho_D} \quad (3.8)$$

In well-annealed metals, the starting dislocation density can be very low, making the contribution of this starting dislocation to the crystal strength negligible. With strain, however, this contribution grows quickly.

The increase in dislocation density and addition of obstacles restricting dislocation motion contribute to hardening observed in a stress–strain curve. To begin the discussion of hardening, it is useful to consider how hardening occurs in a single crystal. Figure 3.11 is a schematic stress–strain curve measured in a well-annealed (soft) FCC single crystal (e.g., Copper or Silver). Plotted is shear stress versus shear strain. If the orientation of the single crystal is specified in relation to the tensile axis,

Fig. 3.11 Stress–strain curve for a single crystal showing regions of easy glide, constant Stage II hardening, and Stage III, which is characterized by dislocation storage balanced by recovery



then the stress can be the “resolved” shear stress per Eq. 3.4. This stress–strain curve differs significantly from the curves for AISI 1018 steel and 304 L stainless steel presented in Sects. 1.9 and 1.11. Following the yield stress τ_1 —which would be related to the critical resolved shear stress τ_{CRSS} —the curve rapidly reaches a region of “*easy glide*” where generated dislocations are free to move across the single crystal without encounters with obstacles. Slip is likely occurring on a single slip plane—that which has the highest resolved shear stress. At a stress level of τ_2 , the rate of hardening increases rapidly as the curve enters region II. At this point, other slip planes become active, and the obstacle density increases more rapidly as dislocations encounter and have their motion restricted by dislocations on multiple slip planes. Note that the hardening rate is constant in region II. This hardening rate is referred to as the Stage II hardening rate

$$\frac{d\tau}{d\lambda} = \theta_{II} \quad (3.11)$$

For many single crystals,

$$\theta_{II} \approx \frac{\mu}{200} \quad (3.12)$$

where μ was identified in Eq. 2.9 as the shear modulus. In polycrystals, under uniaxial deformation, Eq. 3.12 is equivalent to [13]:

$$\theta_{II} \approx \frac{E}{50} \quad (3.13)$$

where E is the Young’s Modulus (Eq. 1.5). Thus, the slope of the stress strain curve in this region is $\sim 2\%$ of the slope during elastic loading. Throughout this monograph, stresses are normalized by the shear modulus. A good approximation for many (polycrystalline) materials is:

$$\theta_{II} \approx \frac{\mu}{20} \quad (3.14)$$

Soon, the curve enters a third region, termed region III, where the rate (slope) of hardening decreases. This region is characterized by a balance between dislocation generation and *recovery*, which is a process by which stresses are high enough to assist dislocations past obstacles.

In polycrystals, the initial slip is on multiple slip planes and region I does not exist. In addition, because stress levels are higher in a polycrystal, region II may not exist or may be very short lived. Thus, stress–strain curves in engineering materials exhibit region III behavior. The Voce Law is a convenient equation for region III:

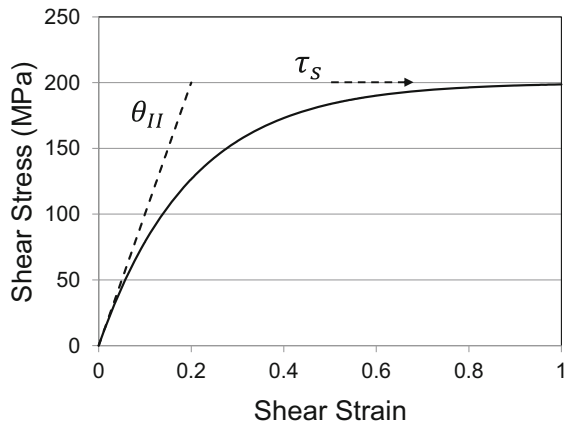
$$\frac{d\tau}{d\gamma} = \theta_{II} \left(1 - \frac{\tau}{\tau_s} \right) \quad (3.15)$$

where τ_s is a “saturation” stress, which is a stress-value where the rate of dislocation generation equals the rate of recovery leading to zero rate of hardening. Equation 3.15 can be integrated to derive the stress (τ) versus strain (γ) curve

$$\tau = \tau_s \left[1 - \exp \left(-\frac{\theta_{II}}{\tau_s} \gamma \right) \right] \quad (3.16)$$

Figure 3.12 shows this plot for a material with $\theta_{II} = 1000$ MPa and $\tau_s = 200$ MPa. Although the yield stress in this curve is 0, which differs from the stress–strain curves in engineering materials presented in Chap. 1 (and which will be addressed in a following chapter), this curve has the general features of these actual stress–strain curves in that the rate of hardening continuously decreases with increasing strain.

Fig. 3.12 Example Voce hardening behavior



3.7 Contributions from Precipitates

Many engineering alloys are strengthened by the presence of hard precipitates. This is a principle strengthening mechanism, in fact, in aluminum alloys. In some metals, ceramic particles are added to the pure metal or alloy to create a metal matrix composite, MMC. The Glidcop® family of alloys are example of copper-based metals with aluminum oxide particle dispersions, manufactured using a powder metallurgy process and internal oxidation of dilute aluminum additions to the copper base [14]. Many aluminum alloys are precipitation strengthened. The precipitation reactions can be quite complicated in these alloys. In the 6XXX series alloys, the precipitates involve a combination (depending on processing conditions) of Guinier–Preston (G-P) zones, and various morphologies of β precipitates, where these are usually of the composition Mg_2Si [15]. A rough estimate of the strengthening due to these precipitates is possible through reference to Fig. 3.13, which shows impenetrable precipitates separated by distance S .

For this simplified system, the yield strength increases with particle density (spacing) according to

$$\Delta\sigma_y = \frac{\mu b}{S_p} \quad (3.17)$$

For instance, an average spacing of 50 nm in an aluminum alloy ($b = 0.286$ nm) with $\mu = 26.2$ GPa produces according to Eq. 3.17 a yield strength enhancement of 150 MPa, which is typical of the magnitude of strength improvement seen in precipitation-hardened aluminum alloys.

3.8 Summary

The sections on strength contributions from grain boundaries, impurity atoms, stored dislocations, and precipitates represent only an introduction to the topic of strengthening mechanisms. Materials are strengthened by introduction of other area, line, and point defects. All combine to produce strengths that can far exceed the critical resolved shear strength of a pure, single crystal by posing obstacles to the free

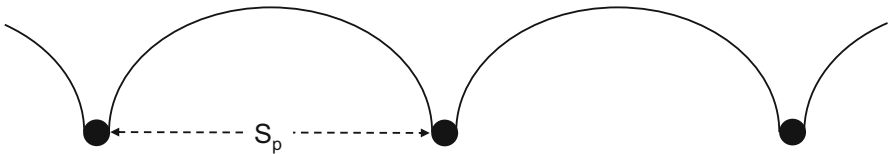


Fig. 3.13 Schematic illustrating a dislocation line blocked by precipitates of spacing S

motion of dislocations. The nature of the interaction between a dislocation and an obstacle defines the strength of the obstacle, e.g., how effective it is in restricting dislocation motion. The strength enhancements introduced in this chapter for the Peierls barrier, grain boundaries, impurity atoms, stored dislocations, and precipitates are most relevant to “low temperature” deformation. (See Box 3.5 entitled “a Note on High Temperatures.”) Moreover, these correlations are introduced briefly and simply without mention of how they are affected by thermal activation. Indeed, deformation kinetics, e.g., how strength varies with temperature and strain rate, is dictated by the interactions of dislocations with these defects. This is explored in more detail in the next chapter.

Box 3.5 A Note on High Temperatures

This discussion on grain boundary strengthening has been most relevant to metals at low temperatures—less than 0.5 of their melting temperature. At high temperatures, diffusion can assist stress in metal deformation. This process is often referred to as “*creep*.” In fact, most of the development in this monograph is limited to low temperature deformation. Chapter 15 includes an assessment of the temperature range represented by the low temperature deformation models described in this monograph.

Because a grain boundary presents an easy path for diffusion, grain boundaries can be detrimental at high temperatures. This is one reason why the highest temperature vanes and blades in aero engines and in some land-based industrial gas turbine engines are now manufactured as single crystals. These components actually have higher creep strengths than polycrystalline components.

Exercises

- 3.1 Molybdenum has a BCC crystal structure. Its critical resolved shear stress is 49 MPa. If a single crystal sample is oriented with the loading axis in the [010] direction, what will be the slip direction? Recall that the slip direction is along one of the [111] directions in the BCC crystal structure.
- 3.2 The (110) is one of the possible slip planes in the BCC crystal structure. Show the (110) plane in relation to the [110] loading direction and [111] slip direction in the example described in Exercise 3.1. What are the angles φ and λ for this scenario?
- 3.3 What would be the angle λ for slip in the $[11\bar{1}]$ direction?
- 3.4 What would be the applied stress to initiate slip in molybdenum on the (110) plane in the [111] slip direction given a [110] loading direction?

- 3.5 If the molybdenum single crystal were instead loaded in the [010] direction, compute the applied stress to initiate slip on the (110) plane in the [111], $[11\bar{1}]$, $[\bar{1}11]$, and $[\bar{1}\bar{1}\bar{1}]$ slip directions?
- 3.6 BCC crystals can also slip on the family of (211) planes. Show this plane in relation to the [100] slip direction. (a) Is slip still likely in the [111] direction? (b) What would be the applied stress to initiate slip in molybdenum on the (211) plane in the [111] slip direction given a [010] loading direction?
- 3.7 Exercises 1.5 and 1.7 described a tensile stress–strain curve in copper. If the initial dislocation density is zero, estimate and plot the variation of the dislocation density during the test. Assume $b = 0.256$ nm, $\mu = 42.2$ GPa, and that the constant α in Eq. 3.8 equal 1. Also, taken σ_i in Eq. 3.8 as the stress at the proportional limit (Exercise 1.6).
- 3.8 Table 3.E8 lists the measured yield stress as a function of oxygen level in a metal alloy. Two measurements at each oxygen level are reported. Determine whether this hardening follows Eq. 3.10 or would be more accurately described by an equation with a linear dependence on oxygen concentration. Propose a governing equation.
- 3.9 Table 3.E9 lists the measured true shear stress as a function of true shear strain in a metal alloy. Determine the values of θ_H and τ_s from Eq. 3.15 that provide a good fit to this data set. (This is easiest done numerically by integrating Eq. 3.15 with possible values of θ_H and τ_s , until a good fit is obtained. A strain increment of 0.001 is sufficiently small for this numerical integration.)

Table 3.E8 Yield stress as a function of oxygen concentration in a metal alloy (Exercise 3.8)

Oxygen concentration (%)	Yield stress (MPa)	
0.05	61.4	59.4
0.1	72.6	68.6
0.25	87.0	93.0
0.5	113.7	107.7
0.75	128.6	126.6
1	139.0	142.0
1.25	149.8	151.8

Table 3.E9 Shear stress as a function of shear strain in a metal alloy (Exercise 3.9)

True shear strain	Stress (MPa)	True shear strain	Stress (MPa)
0.05	66.0	0.345	360.0
0.109	132.4	0.398	381.0
0.148	194.0	0.45	409.0
0.209	232.0	0.498	444.0
0.254	287.0	0.544	458.0
0.306	335.8	0.606	485.9

Table 3.E10 Shear stress as a function of shear strain in a metal alloy that doesn't appear to be in an annealed condition (Exercise 3.10)

True shear strain	Stress (MPa)	True shear strain	Stress (MPa)
0.047	475.5	0.352	735.0
0.093	540.0	0.399	742.0
0.16	612.0	0.456	760.0
0.208	660.0	0.493	762.0
0.249	672.0		
0.304	709.4		

3.10 Even in soft (well-annealed) FCC metals, the initial yield stress is not zero, which is the case in Exercise 3.9. Another data set is shown Table 3.E10. In this case, it was determined that the yield stress at zero strain was 375 MPa. If the governing hardening equation in this case is

$$\tau = \tau_o + \int \theta_{II} \left(1 - \frac{\tau_\epsilon}{\tau_s} \right) d\lambda$$

determine the values of θ_{II} and τ_s from Eq. 3.15 that provide a good fit to this data set.

3.11 Given that the yield strength of an alloy ($\mu = 100$ GPa and $b = 2.5 \times 10^{-4}$ μm) is represented by the following expression:

$$\sigma_{\text{yield}} = 20 \text{ MPa} + \frac{k_d}{\sqrt{d(\text{mm})}} + k_s \frac{\mu b}{S(\mu\text{m})} + k_c \sqrt{C_{\text{oxygen}}(\%)}$$

- (a) What strengthening mechanisms apparently contribute to the strength of this alloy?
- (b) It is further shown that:

$$k_d = 10 \text{ MPa}\sqrt{\text{mm}}$$

$$k_s = 1$$

$$k_c = 100 \text{ MPa}$$

If the grain size d can be decreased to as small as 0.10 mm, the precipitate spacing can be as low as 0.10 μm , and oxygen concentration can be as high as 0.10%, what appears to be the most effective strengthening mechanism in this alloy?

- (c) What would be the yield strength under these conditions?

References

1. G.E. Dieter, Mechanical Metallurgy, in *McGraw-Hill Series in Materials Science and Engineering*, 2nd edn., (McGraw-Hill Book Company, New York, 1976), p. 130
2. J.W. Christian, *The Theory of Transformations in Metals and Alloys*, 2nd edn. (Pergamon Press, Oxford, 1975), p. 278
3. R. Peierls, The size of a dislocation. *Proc. Phys. Soc.* **52**, 34 (1940)
4. F.R.N. Nabarro, Dislocations in a simple cubic lattice. *Proc. Phys. Soc.* **59**, 256 (1947)
5. R.W.K. Honeycombe, *The Plastic Deformation of Metals*, 2nd edn. (Edward Arnold Publishers, Australia, 1984a), p. 108
6. D. Hull, *Introduction to Dislocations*, 2nd edn. (Pergamon Press, Oxford, 1976), p. 231
7. R.W.K. Honeycombe, *The Plastic Deformation of Metals*, 2nd edn. (Edward Arnold Publishers, Australia, 1984b), p. 114
8. E.O. Hall, The deformation and ageing of mild steel: III discussion of results. *Proc. Phys. Soc.* **64B**, 747 (1951)
9. N.J. Petch, The cleavage strength of polycrystals. *J. Iron Steel Inst.* **173**, 25 (1953)
10. R.W.K. Honeycombe, *The Plastic Deformation of Metals*, 2nd edn. (Edward Arnold Publishers, Australia, 1984c), p. 177
11. Fleischer, Substitutional solution hardening. *R. L. Acta Metallurgica* **11**, 203 (1963)
12. A. Buch, *Pure Metals Properties: A Scientific Technical Handbook* (ASM International, Ohio, 1999), p. 31
13. U.F. Kocks, H. Mecking, Physics and phenomenology of strain hardening: the FCC case. *Prog. Mater. Sci.* **48**, 171–273 (2003)
14. SCM Metal Products Incorporated, Research Triangle Park, NC, USA. See Glidcop product information bulletin at: http://www.aps.anl.gov/APS_Engineering_Support_Division/Mechanical_Operations_and_Maintenance/Miscellaneous/tech_info/Glidcop/SCM_Glidcop_product_info.pdf
15. W.F. Miao, D.E. Laughlin, Precipitation hardening in aluminum alloy 6022. *Scr. Mater.* **40**(7), 873–878 (1999)

Chapter 4

Dislocation–Obstacle Interactions



Introduction

The concept of a dislocation was introduced in the previous chapter. The strain rate and temperature dependence of deformation is determined by the interaction of dislocations with obstacles. These obstacles can be, for instance, other dislocations, impurity atoms (whether added intentionally or not), or larger microstructural features such as carbides or precipitates. In this chapter, the kinetic equations defining the thermally activated interactions between dislocations and a variety of obstacles are derived. The importance of the yield stress at absolute zero, which becomes the mechanical threshold stress, is emphasized. Application of these equations to the yield stress versus temperature and strain rate in several pure metals and alloys is demonstrated.

4.1 A Simple Dislocation/Obstacle Profile

Section 2.5 introduced the concept of the dislocation as the mechanism for accommodating permanent (plastic) strain. Figure 2.12 showed an example of a pure edge dislocation, while Fig. 2.13 shows an example of a pure screw dislocation. Consider the edge dislocation moving along the slip plane. (Refer to Figs. 2.10 and 2.11.) A simple model for the variation of stress along the slip plane was introduced in Sect. 2.4 as a sinusoidal function. Although this was introduced as the equation governing the motion of an entire plane of atoms over another, this expression serves as a model as well for the motion of the half plane. Figure 4.1 illustrates schematically how the stress on the slip plane varies with motion of the dislocation along the slip plane—in this case a periodic obstacle resistance [1] involving 12 Burgers vectors of slip.

Supplementary Information The online version contains supplementary material available at [\[https://doi.org/10.1007/978-3-031-04556-1_4\]](https://doi.org/10.1007/978-3-031-04556-1_4)

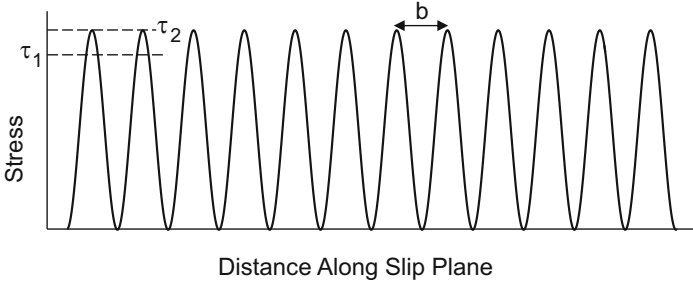
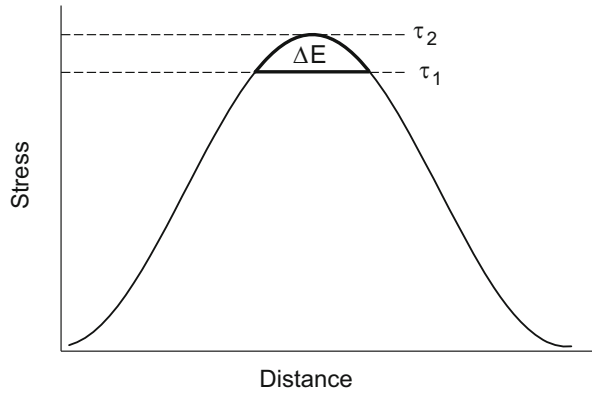


Fig. 4.1 Variation of stress along a slip plane as a dislocation moves a distance equal to 12 Burgers vectors

Fig. 4.2 The area under the stress–distance diagram between the stress levels of τ_1 and τ_2 , marked ΔE , is the energy supplied by thermal activation in overcoming this barrier



At an applied stress of τ_1 , the stress by itself is insufficient to overcome the obstacle, but at a stress level of τ_2 , the dislocation is able to move. At the lower stress level, another source of energy is required to complement the applied stress to enable dislocation motion. Since stress is force per unit slip plane area—which is a constant—the area under the curve in Fig. 4.1 is energy (force \times distance) per unit slip plane area. Figure 4.2 shows a single obstacle with the two stress levels. The area under the curve above the stress level τ_1 , labeled ΔE , is the energy (per unit slip plane area) necessary to overcome this obstacle. *Thermal energy* is the source of this energy. The term *thermal activation* is used when thermal energy assists a dislocation past an obstacle.¹

¹An extremely comprehensive summary of dislocation–obstacle interactions and the kinetics of slip was published by U. F. Kocks, A. S. Argon, and M. F. Ashby in 1975. The reader is referred to Ref. [1] for further information.

4.2 Thermal Energy—Boltzmann's Equation

Recall that for an ideal gas a molecule has an average thermal energy of $3/2kT$ where k is Boltzmann's constant (1.38×10^{-23} J/K) and T is in degrees Kelvin. Although this is the average energy, at any instant a molecule may have a higher or lower thermal energy; the distribution of energies follows the Boltzmann equation

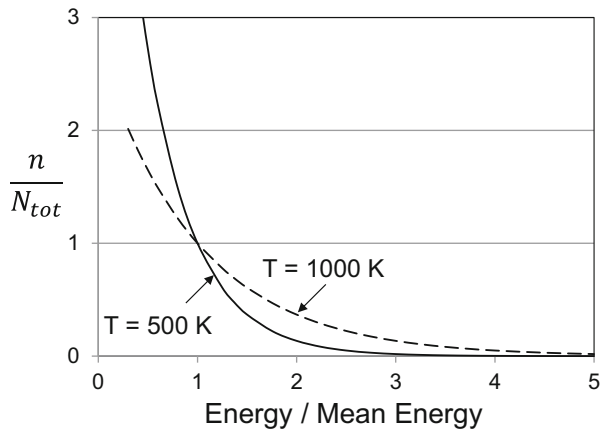
$$\frac{n}{N_{\text{tot}}} \propto \exp\left(-\frac{E - \bar{E}}{kT}\right) \quad (4.1)$$

where n is the number of molecules out of N_{tot} with an energy level of E compared to the average energy level of \bar{E} . Boltzmann's equation applies to condensed matter, where the main interest is the fraction of atoms with high energies

$$\frac{n}{N_{\text{tot}}} \propto \exp\left(-\frac{E}{kT}\right) \quad (4.2)$$

The distribution is shown in Fig. 4.3 for arbitrary values of \bar{E} and temperatures of 500 K and 1000 K. It is evident that the number of atoms with high energy drops quickly and that the number with high energies is higher at the higher temperature. The population, albeit small, of atoms with high thermal energies assumes a critical role in the properties of materials. For slip to occur at applied stresses less than the peak stress τ_2 in Fig. 4.2, thermal energy provides ΔE .

Fig. 4.3 Relative numbers of atoms with higher and lower energies than the mean energy at two temperatures according to the Boltzmann equation



4.3 The Implication of 0 K

The Boltzmann equation suggests that no thermal energy is available at 0 K, which implies that deformation can only proceed at absolute zero if the applied stress is sufficient to drive the dislocation. This stress becomes the fundamental measure of the strength of the obstacle. Recall in Sect. 3.1 the definition of the critical resolved shear stress τ_{CRSS} and the mention of the τ_{CRSS} values for pure copper and molybdenum. The development in this section did not specify the test temperature as 0 K. In fact, since measurements at temperatures approaching 0 K are very difficult, these values were likely room temperature (RT) values. Because they represent a stress at a temperature other than 0 K, thermal energy is available to assist the applied stress, and it is possible that a test at a different temperature would have produced a different τ_{CRSS} . In this sense, the τ_{CRSS} is only meaningful at a specific temperature. The 0 K τ_{CRSS} is thus a more meaningful measure of the “critical resolved shear stress” because it truly represents the strength of the obstacle.

In subsequent sections, a method to experimentally determine the 0 K stress will be presented. For pure, single crystal metals with no dislocation density, this stress would represent τ_{CRSS} . In engineering alloys, this stress is considerably larger than τ_{CRSS} —but still represents a fundamental measure of strength. In this case, the stress is referred to as the *Mechanical Threshold Stress*. In this monograph, the mechanical threshold stress is written with a hat over the Greek letter sigma, $\hat{\sigma}$, and it referred to as “sigma hat.”

4.4 Addition of a Second Obstacle to a Slip Plane

Figure 4.1 treated schematically dislocation motion on a slip plane where the obstacle to dislocation motion was considered to be that restricting the movement of the half plane a single step. Fig. 4.4 shows the stress versus distance moved by a dislocation when encountering this obstacle in addition to an added obstacle, e.g., an impurity atom.

As in Fig. 4.1, the stress versus distance in Fig. 4.4 is highly idealized, but it does serve to demonstrate that the presence of the impurity atom changes the stress versus distance diagram. Furthermore, it is apparent that the 0K stress (τ_2) necessary to move the dislocation in Fig. 4.1 is insufficient to move the dislocation past the added obstacle. Because it is hard to achieve very high purities in metal samples, this schematically illustrates why actual yield stresses exceed τ_{CRSS} by a significant margin.

Referring to Figs. 2.12, 4.1, and 4.4, consider the motion of a dislocation along a slip plane as if the entire dislocation moves in concert, i.e., a pure edge dislocation retains its pure edge character as the half plane shifts from one equilibrium position to the next. In fact—partially due to the role of thermal energy—the motion is far jerkier. This is perhaps easier to visualize by viewing the dislocation line, e.g., as in

Fig. 4.4 Hypothetical variation of stress with distance along a slip plane for a crystal with a strong and weak obstacle

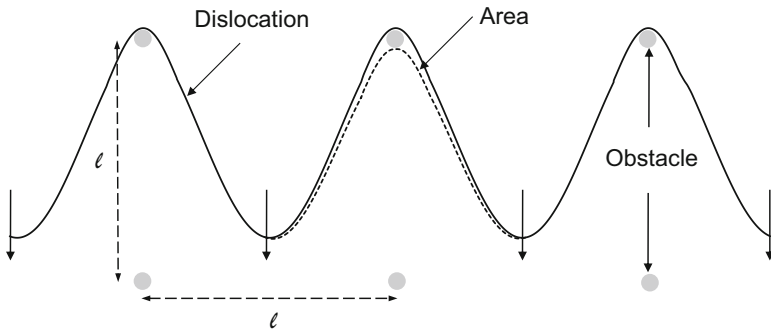
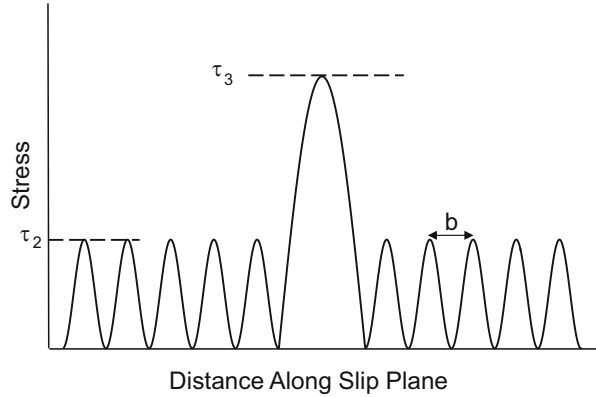


Fig. 4.5 View of a dislocation line impeded by three obstacles. The dashed line shows the area along the slip plane traversed as the dislocation sweeps by one of these obstacles

the photo micrograph in Fig. 2.15. Figure 4.5 shows a schematic of a dislocation line where motion is apparently impeded by three obstacles. The stress is such that the dislocation is trying to move in a downward direction. The dashed line in the vicinity of the middle obstacle illustrates that this section of the dislocation has successfully passed the obstacle and will begin to move until it encounters the next obstacle. The area moved overcoming a single obstacle is the area between these two lines.

The scenario in Fig. 4.5 depicts *jerky glide*, where dislocations spend a great deal of time awaiting thermal activation but, once an obstacle is overcome, the dislocation will move rapidly until it encounters the next obstacle.

4.5 Kinetics

The equation describing jerky glide is

$$\dot{\varepsilon} = \dot{\varepsilon}_o \exp\left(-\frac{\Delta G(\sigma)}{kT}\right) \quad (4.3)$$

where $\dot{\varepsilon}$ is the strain rate $d\varepsilon/dt$ as described in Sect. 1.14, $\dot{\varepsilon}_o$ is a constant, and ΔG is the activation energy characterizing this interaction. Note from Figs. 4.2 and 4.4 that ΔG is a function of stress σ . A simple derivation is given by differentiating Eq. 2.14, giving the Orowan equation defined in Sect. 2.5

$$\begin{aligned} \varepsilon &= \rho_D b \ell \\ \frac{d\varepsilon}{dt} &= \dot{\varepsilon} = \rho_D b \frac{d\ell}{dt} \end{aligned} \quad (4.4)$$

In the dislocation–obstacle interaction depicted in Fig. 4.5, the $d\ell$ is simply l —the distance between subsequent obstacles, and dt , which will be referred to as Δt for this discrete event, is the time spent awaiting thermal energy. The latter follows from the Boltzmann equation

$$\Delta t = \frac{1}{\nu_o \exp\left(-\frac{\Delta G(\sigma)}{kT}\right)} \quad (4.5)$$

where ν_o is the atom “vibrational frequency” or “attempt frequency,” i.e., the number of thermal fluctuations per second—which is on the order of 10^{11} s^{-1} . This gives

$$\dot{\varepsilon} = \rho_D b \ell \nu_o \exp\left(-\frac{\Delta G}{kT}\right) = \dot{\varepsilon}_o \exp\left(-\frac{\Delta G(\sigma)}{kT}\right) \quad (4.6)$$

A rough estimate of $\dot{\varepsilon}_o$ is

$$\begin{aligned} \dot{\varepsilon}_o &= \rho_D b \ell \nu_o \approx (10^{14} \text{ m}^{-2})(2.5 \times 10^{-10} \text{ m})(5 \times 10^{-8} \text{ m})(10^{11} \text{ s}^{-1}) \\ &= 1.2 \times 10^8 \text{ s}^{-1} \end{aligned} \quad (4.7)$$

Defining the stress-dependence of ΔG requires an understanding of the shape of the obstacle profile. The profiles shown in Figs. 4.1 and 4.2 were schematic and drawn (as sine waves) only for illustration. One estimate follows from Fig. 4.5 and the motion of the dislocation under a stress σ through the area identified in this figure as it overcomes the obstacle. The nature of the obstacle is not specified, but it could be, for instance, another dislocation perpendicular to the page. The net distance moved by the obstacle as it overcomes the obstacle can be taken as the Burgers vector b , and the length of the segment of the dislocation that has moved can be taken

as the spacing between the obstacles l . Thus, the force on the dislocation is $\sigma b l$. Because the dislocation has moved a distance b , the work done during this event is $\sigma b^2 l$. If the total activation energy characterizing the dislocation–obstacle interaction is G , then

$$\Delta G = G - \sigma b^2 l \quad (4.8)$$

and

$$\dot{\epsilon} = \dot{\epsilon}_o \exp\left(-\frac{\Delta G(\sigma)}{kT}\right) = \dot{\epsilon}_o \exp\left(-\frac{G - \sigma b^2 l}{kT}\right) \quad (4.9)$$

That is, the work performed by the stress has effectively decreased the required thermal activation energy. As an energy term, the appropriate units for G are Joules (J). Solving for stress gives

$$\sigma = \frac{G}{b^2 l} - \frac{kT}{b^2 l} \ln\left(\frac{\dot{\epsilon}_o}{\dot{\epsilon}}\right) \quad (4.10)$$

When $T = 0$ K, the stress equals $\hat{\sigma}$. Thus

$$\sigma = \hat{\sigma} - \frac{kT}{b^2 l} \ln\left(\frac{\dot{\epsilon}_o}{\dot{\epsilon}}\right) \quad (4.11)$$

It is evident that the specified combination of T and $\dot{\epsilon}$

$$T \ln \frac{1}{\dot{\epsilon}} \quad (4.12)$$

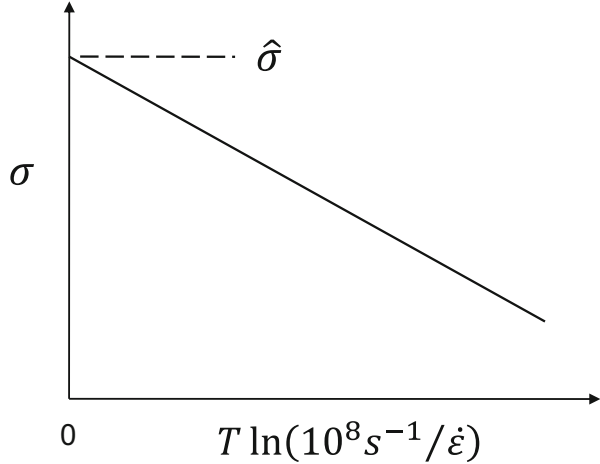
or, more commonly,

$$T \ln \frac{\dot{\epsilon}_o}{\dot{\epsilon}} \quad (4.13)$$

where $\dot{\epsilon}_o$ is taken as 10^8 s^{-1} (see above) has special significance in deformation kinetics. If combinations of T and $\dot{\epsilon}$ are chosen such that $T \ln \dot{\epsilon}_o/\dot{\epsilon}$ is constant, then the stress required to overcome the obstacle is the same. Figure 4.6 shows a plot of stress versus temperature and strain rate using the combination specified above. Plots of this form are particularly useful because they give a graphical representation of how the yield stress varies with temperature and strain rate.

This derivation gives the prediction that a plot of stress (e.g., yield stress) versus temperature and strain rate will give a straight line. The intercept at 0 K (or, equivalently, at an infinite strain rate) is the mechanical threshold stress.

Fig. 4.6 Plot of yield stress versus the function of temperature and strain rate specified by Eq. 4.11



Another, essentially equivalent, form for the stress dependence is written as

$$\sigma = \hat{\sigma} \left[1 - \frac{kT}{G} \ln \left(\frac{\dot{\epsilon}_o}{\dot{\epsilon}} \right) \right] \quad (4.14)$$

In this form, the intercept in Fig. 4.6 is again the mechanical threshold stress, while the slope of the line is proportional to $\hat{\sigma}/G$.

4.6 Analysis of Experimental Data

A wealth of experimental data is available on yield stress as a function of test temperature and strain rate. In fact, data of this nature can be found for almost any metal of interest. In pure niobium, Campbell and Briggs [2] measured yield stress in compression² over the strain rate range of 0.00017 s^{-1} to 100 s^{-1} and the temperature range of 77 K to 400 K. That is, 50 individual tests were run and the yield stress reported at combinations of strain rate and temperature within the range specified. Figure 4.7 shows this data plotted on the coordinates defined in Fig. 4.6.

The data set is characterized by typical scatter observed in experimental measurements. At low values of the abscissa, the data appear to fall on a straight line with an intercept at $\sim 1400 \text{ MPa}$, but at high values of the abscissa (e.g., high temperatures and low strain rates), the data deviate sharply from this line.

Figure 4.8 shows a similar set of data in pure iron reported by Nojima [3]. These measurements were also in compression over the strain rate range of $1.5 \times 10^{-4} \text{ s}^{-1}$

²In Chap. 1, compression tests were characterized by negative strain and stress values. Stresses and strains in Fig. 4.6 (and subsequent figures) will be plotted for convenience as positive values.

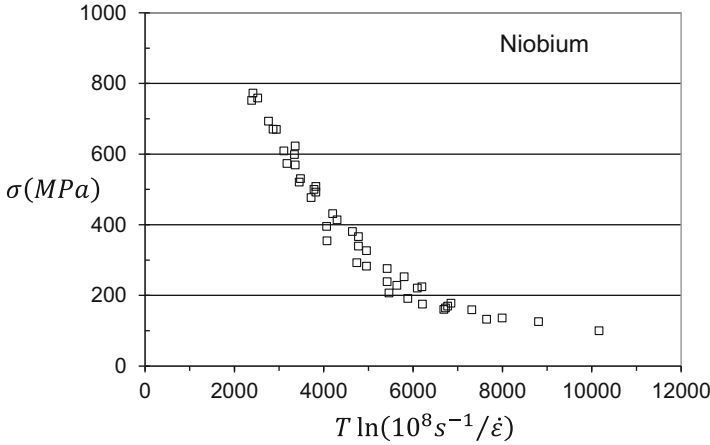


Fig. 4.7 Temperature and strain-rate-dependent yield stress measurements of Campbell and Briggs [2] in polycrystalline niobium plotted on coordinates suggested by Eqs. 4.11 or 4.14

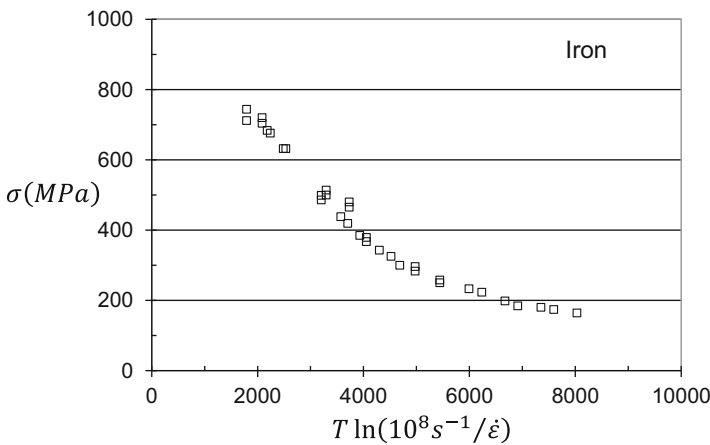


Fig. 4.8 Temperature and strain-rate-dependent yield stress measurements of Nojima [3] in polycrystalline iron

to $1.2 \times 10^2 \text{ s}^{-1}$ and the temperature range of 158–295 K. As in niobium, the low temperature/high strain rate results roughly follow a linear trend with an intercept at $\sim 1100 \text{ MPa}$, but the high temperature and low strain rate data deviate from this trend.

Figures 4.7 and 4.8 showed measurements in two pure metals. Figure 4.9 shows a similar data set in AISI 1018 steel reported by Gray and Chen at Los Alamos National Laboratory [4]. These measurements (also in compression) cover a strain rate range of 10^{-2} s^{-1} to $3.8 \times 10^3 \text{ s}^{-1}$ and a temperature range of 148–823 K.

The data sets shown in Figs. 4.7, 4.8, and 4.9 demonstrate a distinct slope in the line at low values of the abscissa and a tailing off at higher values. Interestingly, all

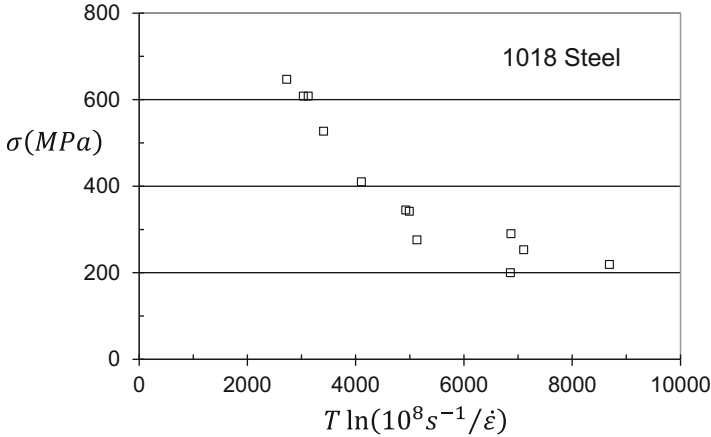


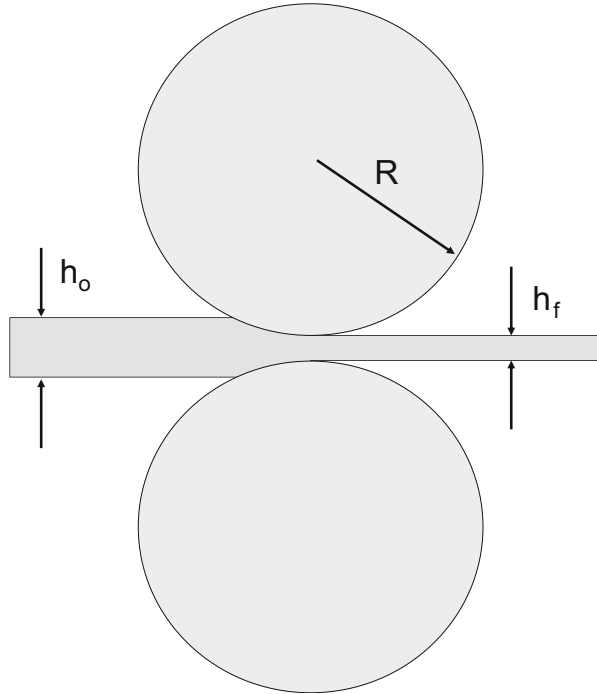
Fig. 4.9 Temperature and strain-rate-dependent yield stress measurements of Gray and Chen [4] in polycrystalline 1018 steel

three of these metals exist in a BCC crystal structure over the range of temperatures plotted. Metals such as copper, silver, gold, aluminum, nickel, etc., that exist in the FCC structure behave very differently. In each of these metals, in the pure and annealed form, the yield stress would be (i) very low and (ii) insensitive of strain rate and temperature. This behavior in fact was already introduced in Sects. 3.1 and 3.2 in the discussion of τ_{CRSS} . Accordingly, a plot of yield stress versus temperature and strain rate in these metals using the coordinates plotted in Fig. 4.7 through 4.9 would have been most uninteresting. However, even in pure form, if the metal is not annealed but is processed to give it a significant dislocation density, then the yield stress would show a dependence on test temperature and strain rate.

A significant dislocation density can be introduced, for instance, using a rolling mill as shown in Fig. 4.10, which shows a plate of metal of thickness h_0 being fed into a rolling mill to thin the plate down to a final thickness of h_f . This process involves significant plastic strain (related to h_f/h_0) which will create a large stored dislocation density. One can machine out test specimens (either a tensile specimen with its axis in the plane of the sheet or compression specimens with axis as desired) and test these to measure the *yield stress* as a function of test temperature and strain rate. Note that this stress is now the yield stress on material that has been processed (with the rolling mill), but the yield stress continues to be defined as the stress at a 0.002 strain offset.

With reference to Fig. 1.13, another way to introduce the dislocation density is with an actual mechanical test. The specimen in Fig. 1.13 was strained at RT and a *Quasi-Static* (QS) strain rate (e.g., 0.001 s^{-1}) to a compression strain of $\epsilon \approx -0.22$, unloaded, and subsequently reloaded at the same temperature and strain rate. If the specimen had instead been reloaded at a different temperature and strain rate, the yield stress (reload yield stress) would have been different. If 10 identical test specimens had all been strained (prestrained) at these conditions (RT, 0.001 s^{-1} ,

Fig. 4.10 Hardening a material by reducing its thickness using a rolling mill



and a true strain of -0.022), then a plot could have been generated of the reload yield stress versus reload temperature and reload strain rate using the same coordinates as used in Figs. 4.7 through 4.9.

Figure 4.11 shows such a plot for copper that has been prestrained at RT and a strain rate of 81 s^{-1} to a true strain of 0.10. (In fact, this prestrain was done in compression, so the true strain would actually be -0.10 .) This was done repetitively to 10 specimens [5]. Each of these specimens was then reloaded (3 at RT and 0.0013 s^{-1} ; 2 at 180 K and 0.0013 s^{-1} ; 3 at 77 K and 0.0013 s^{-1} ; 2 at RT and 81 s^{-1}) and the (reload) yield stress measured. It is this latter yield stress that is plotted versus reload temperature and strain rate in Fig. 4.11. The ten data points in Fig. 4.11 plot roughly on a straight line, but even with the prestrain the slope of this line is much less than the slope of the lines through the left-hand sides of the plots in Figs. 4.7 through 4.9.

A final example is given in Fig. 4.12 for nickel +510 *parts per million* (ppm) carbon [6]. That is, this alloy was pure nickel with small carbon additions (0.051% by weight). In this case, the material was prestrained at a strain rate of 0.0009 s^{-1} to strain levels of 0.048 and 0.297 (in compression). Again, this prestrain was performed to multiple specimens, which were reloaded at temperatures and strain rates similar to those listed for the copper above. As observed in prestrained copper, the reload data points roughly line on lines with a low slope. Naturally, the reload yield stresses on the samples loaded to the higher strain level are much higher than those initially loaded to the lower strain level.

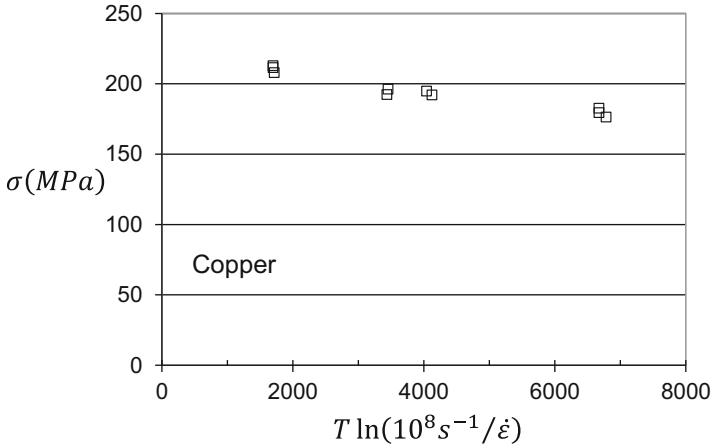


Fig. 4.11 Yield stress (actually reload yield stress) as a function of temperature and strain rate in polycrystalline copper (Follansbee and Kocks [5]) prestrained at RT to a strain level of 0.10 at a strain rate of 81 s^{-1}

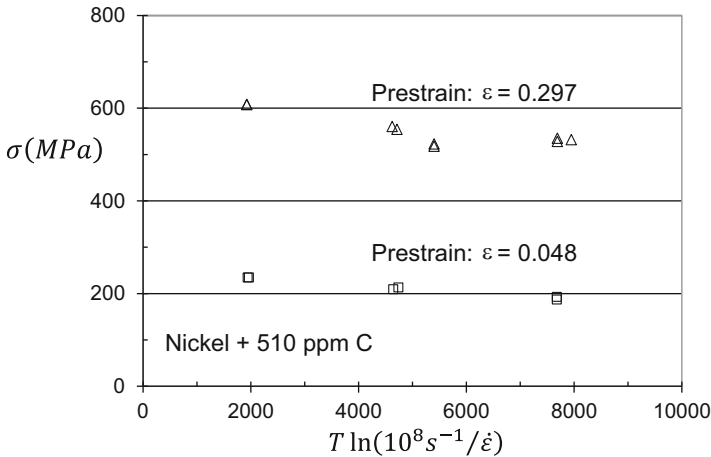


Fig. 4.12 Yield stress (actually reload yield stress) as a function of temperature and strain rate in polycrystalline nickel 510 ppm C prestrained at RT to two strain levels at a strain rate of 0.0009 s^{-1}

4.7 Multiple Obstacles

Section 4.4 introduced a hypothetical obstacle profile for a second obstacle, in this case an impurity atom added to a slip plane. This was a highly idealized example; Fig. 4.4 was drawn as if a larger obstacle “replaced” a few cycles of the weaker obstacle. In fact, the scenario is far more complicated—perhaps more like that drawn in Fig. 4.13 for a weaker obstacle (with a lower amplitude and shorter wave length)

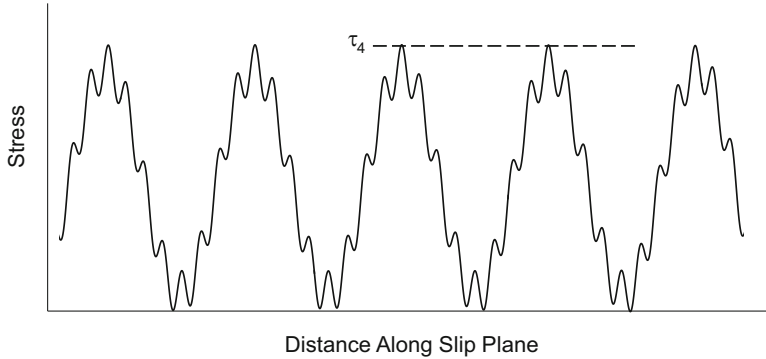


Fig. 4.13 Schematic (but perhaps more realistic than shown in Fig. 4.4) variation of stress with distance along a slip plane for the case of two distinct obstacles

added to a stronger obstacle (with the higher amplitude and longer wave length). In this case the profiles are assumed to add linearly resulting in a small oscillation riding on top of the larger one. The details of how multiple obstacle profiles combine are not well established. A good starting assumption probably is

$$\tau_4 = \tau_2 + \tau_3 \quad (4.15)$$

where τ_2 is the height of the weaker obstacle (see Fig. 4.1), τ_3 is the height of the stronger obstacle (see Fig. 4.4), and τ_4 is the combined height illustrated in Fig. 4.13. A more general model would be

$$\tau_{\text{tot}} = \sum_{i=1}^n \tau_i \quad (4.16)$$

where τ_{tot} is the total stress for n obstacle types. This model represents assumed behavior. There is room for further research on how obstacle profiles for distinct obstacles actually sum to affect the motion of dislocations and define deformation kinetics for real metals.

4.8 Kinetics of Hardening

This chapter has considered deformation kinetics dictated by the interaction of dislocation with obstacles. The premise has been that with a given defect structure—defined by impurity atoms, grain boundaries, and stored dislocations, the yield stress varies with the imposed strain rate and temperature according to Eq. 4.14. Sections 3.6 introduced hardening caused by the stored dislocation density. This was presented by describing first three Regions of behavior in the stress–strain curve of a

single crystal (Fig. 3.11). It was argued that Region III was most applicable to polycrystals. The Voce Equation was introduced

$$\frac{d\tau}{d\gamma} = \theta_{II} \left(1 - \frac{\tau}{\tau_s} \right) \quad (3.13)$$

where τ_s was a “saturation stress,” and this equation was described as one that considered the balance of dislocation generation with stress-assisted recovery—often referred to as “*dynamic recovery*.” One mechanism involved in this process is “*cross slip*.” Since the Burgers vector in a screw dislocation is parallel to the dislocation (see Fig. 2.11)—and screw dislocations do not reside in unique glide planes—a screw dislocation can move from one glide plane to an intersecting glide plane. Doing so offers a mechanism for a screw dislocation to skirt an obstacle. Cross slip is assisted by stress and thermal activation—in a manner similar to that described for a dislocation interacting with a discrete obstacle. An equation for this thermally activated process is

$$\ln \left(\frac{\dot{\gamma}}{\dot{\gamma}_{so}} \right) = \frac{A_{CS}}{T} \ln \left(\frac{\tau_s}{\tau_{so}} \right) \quad (4.17)$$

where $\dot{\gamma}_{so}$, A_{CS} , and τ_{so} are constants [7]. This equation can be used to determine the temperature and strain-rate-dependent saturation stress in Eq. 3.15 (see Fig. 3.12), and introduces the complication that both hardening and yield are thermally activated processes.

4.9 Summary

Chapter 3 introduced strengthening mechanisms that lead to yield strengths well above the critical resolved shear stress. These mechanisms involve interactions between dislocations and defects, such as grain boundaries, solute atoms, interstitial atoms, stored dislocations, precipitates, etc. This chapter reviewed the stress required to move a dislocation past an obstacle. Schematic profiles were introduced that showed the stress versus the distance moved by a dislocation as it encountered an obstacle.

Energy arguments were used to quantify how thermal energy contributed to the force times distance work of the dislocation to enable the dislocation to continue moving. Because thermal energy is nonexistent at 0 K, the stress at absolute zero takes on a special meaning in characterizing the dislocation–obstacle interaction. This stress was termed the mechanical threshold stress—since it is only the mechanical force on the dislocation that is available and a threshold value is necessary to match the energy barrier. A “kinetic factors” equal to

$$T \ln \left(\frac{1}{\dot{\epsilon}} \right) \quad (4.12)$$

was defined, and the following fundamental relation between the (yield) stress and temperature and strain rate was derived

$$\sigma = \hat{\sigma} \left[1 - \frac{kT}{G} \ln \left(\frac{\dot{\epsilon}_o}{\dot{\epsilon}} \right) \right] \quad (4.14)$$

Measurements of temperature and strain-rate-dependent yield stress in niobium, iron, 1018 steel, copper, and nickel +510 ppm C were plotted on axes suggested by Eq. 4.14, and differences between the measurements and model were introduced.

Finally, while the majority of this chapter dealt with the thermally activated overcoming of obstacles by dislocations, thermally activated recovery, which affects the rate of strain hardening, was introduced in Sect. 4.8. These are different but related mechanisms. An example of the interplay between these two processes is given in Chap. 5.

Exercises

- 4.1 A yield stress measurement is made at 298 K and a strain rate of 0.001 s^{-1} . Based on Eq. 4.13, predict the strain rate which would enable the same stress level at (a) 200 K, (b) 400 K, and (c) 500 K. Assume $\dot{\epsilon}_o = 10^8 \text{ s}^{-1}$.
- 4.2 Predict the strain rates for the three temperatures in Exercise 3.1 assuming $\dot{\epsilon}_o = 10^{10} \text{ s}^{-1}$.
- 4.3 Show that the units are consistent for Eq. 4.14 (i.e., that kT/G is dimensionless).
- 4.4 Derive the relation between the slope of the line in Fig. 4.6 and G .
- 4.5 Table 4.E5 lists yield stress measurements as a function of test temperature and strain rate for a metal. Assuming that the kinetics follow Eq. 4.14, estimate $\hat{\sigma}$ and G . Assume $\dot{\epsilon}_o = 10^8 \text{ s}^{-1}$.
- 4.6 Table 4.E6 lists another data set showing yield stress as a function of test temperature and strain rate for a metal. Assuming that the kinetics follow Eq. 4.14, estimate $\hat{\sigma}$ and G . Assume $\dot{\epsilon}_o = 10^8 \text{ s}^{-1}$.
- 4.7 The metal in Exercise 4.5 was tested again and taken to higher temperatures at the strain rate of 0.001 s^{-1} . The test results are summarized in Table 4.E7. First, ignore the measurements at temperatures above 500 K and combine this data set with the data set in Exercise 4.5. How do the “repeat” measurements affect the estimated values of $\hat{\sigma}$ and G ?

Table 4.E5 Yield stress measurements as a function of test temperature and strain rate for a metal (Exercise 4.5)

T (K)	Rate (s^{-1})	Yield stress (MPa)
200	0.001	666
300	0.001	594
400	0.001	481
500	0.001	384
200	1.0	710
300	1.0	665
400	1.0	602
500	1.0	497
200	2000	795
300	2000	750
400	2000	674
500	2000	672

Table 4.E6 Yield stress measurements as a function of test temperature and strain rate for a metal (Exercise 4.6)

T (K)	Rate (s^{-1})	Yield stress (MPa)
200	0.001	376
300	0.001	358
400	0.001	367
500	0.001	335
200	1.0	400
300	1.0	367
400	1.0	360
500	1.0	367
200	2000	394
300	2000	400
400	2000	385
500	2000	383

Table 4.E7 Another data set showing yield stress measurements as a function of test temperature and strain rate for the metal in Exercise 4.5 (Exercise 4.7)

T (K)	Rate (s^{-1})	Yield stress (MPa)
200	0.001	644
300	0.001	585
400	0.001	476
500	0.001	406
200	1.0	749
300	1.0	628
400	1.0	559
500	1.0	509
200	2000	783
300	2000	733
400	2000	723
500	2000	683
600	0.001	260
700	0.001	182
800	0.001	135
900	0.001	110

Table 4.E9 Saturation threshold stress values for the material introduced in Exercises 4.5 and 4.7 (Exercise 4.9)

T (K)	Rate (s^{-1})	Saturation stress (MPa)
200	0.001	733
300	0.001	681
400	0.001	638
500	0.001	588
200	1.0	771
300	1.0	713
400	1.0	688
500	1.0	635
200	2000	791
300	2000	768
400	2000	746
500	2000	714

Table 4.E10 Saturation threshold stress values for the higher temperature measurements (Table 4.E7) for the same material (Exercise 4.10)

T (K)	Rate (s^{-1})	Saturation stress (MPa)
600	0.001	553
700	0.001	527
800	0.001	506
900	0.001	498

- 4.8 Add the four high temperature measurements to the plot created for exercise 4.7. What is the observed trend at these higher temperatures?
- 4.9 Table 4.E9 lists values of the saturation threshold stress (τ_s in Eqs. 3.7 and 4.17) for the material introduced in Exercise 4.5. If it is known that $\dot{\gamma}_{so} = 10^8 \text{ s}^{-1}$ find values of τ_{so} and A in Eq. 4.17.
- 4.10 The saturation stresses for the four higher temperature tests (see Exercise 4.7) are listed in Table 4.E10. Add these data points to the plot created for Exercise 4.9. Do they follow the same trend?

References

1. U.F. Kocks, A.S. Argon, M.F. Ashby, Thermodynamics and kinetics of slip, in *Progress in Materials Science*, ed. by B. Chalmers, J. W. Christian, T. B. Massalski, vol. 19, (Pergamon Press, Oxford, 1975), p. 54
2. J.D. Campbell, T.L. Briggs, *The Effect of Strain Rate and Temperature on the Yield and Flow of Polycrystalline Niobium and Molybdenum*, Department of Engineering Science Report No. 1091 (University of Oxford, Oxford, UK, 1969)
3. T. Nojima, Constitutive equation of some kinds of steels at high rates of strain, in *Impact Loading and Dynamic Behaviour of Materials*, ed. by C. Y. Chiem, H. D. Kunze, L. W. Meyer, (Informationsgesellschaft, Verlag, Bremen, 1988), pp. 357–364

4. G.T. Gray III, S.R. Chen, *MST-8 Constitutive Properties & Constitutive Modeling*. Los Alamos National Laboratory, LA-CP-07-1590 and LA-CP-03-006 (Must Request Data from LANL Authors) (2007)
5. P.S. Follansbee, U.F. Kocks, A constitutive description of the deformation of copper based on the use of the mechanical threshold stress as an internal state variable. *Acta Metall.* **36**, 81–93 (1988)
6. P.S. Follansbee, J.C. Huang, G.T. Gray, Low-temperature and high-strain-rate deformation of nickel and nickel-carbon alloys and analysis of the constitutive behavior according to an internal state variable model. *Acta Metall.* **38**(7), 1241–1254 (1990)
7. U.F. Kocks, Laws for work-hardening and low-temperature creep. *J. Eng. Mater. Technol.* **98**, 76–85 (1976)

Chapter 5

A Constitutive Law for Metal Deformation



Introduction

Equation 4.14 is a type of *constitutive law*, which is an equation that relates variables or physical quantities in a material and offers predictive capability. In this case, Eq. 4.14 related the yield stress to the temperature and strain rate. Equipped with Eq. 4.14, an engineer could predict a yield stress for a specific combination of strain rate and temperature—perhaps even one that was not explicitly part of the data base used to construct the constitutive law. Of course, extreme care must be practiced when these equations are used for extrapolations rather than interpolations. For instance, if the linear part (left side of the abscissa) of the trend observed in the niobium plot (Fig. 4.7) was used to predict a yield strength at temperatures greater than represented by the linear behavior (e.g., the right side of the abscissa), then the stress would be underpredicted. This chapter continues the development of Eq. 4.14 by easing some simplifications made in introduction of this equation. The concept of internal an internal state variable in deformation modeling is introduced. Models for strain hardening are reviewed and the value of implementing an internal state model to describe hardening is emphasized.

5.1 Constitutive Laws in Engineering Design and Materials Processing

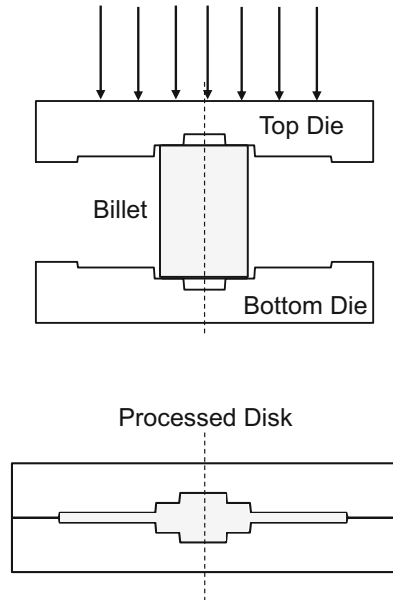
Predictions of temperature- and strain rate-dependent yield strength are valuable in engineering design where the intent is not to exceed an elastic limit and experience plastic deformation. A full constitutive law, such as introduced in this chapter,

Supplementary Information The online version contains supplementary material available at [https://doi.org/10.1007/978-3-031-04556-1_5]

includes the variation of the stress (not just the yield stress) with strain, strain rate, and temperature under a prescribed loading condition. Such a law can be used to model the entire stress–strain curve, which is necessary when deformations are experienced, e.g., in metal-working operations or impact events. It also can be used to predict failure when this results from localized strain, as was described in Sect. 1.13 for a tensile test.

Figure 5.1 shows a schematic of a manufacturing process to create a turbine disk for an aircraft jet engine. This is a single-step forging operation, which involves significant strains, temperatures, strain rates, and temporal variations of these parameters. Forging this part in a single step rather than in multiple sets (with multiple dies) is efficient and cost effective, but the large deformations imposed on the billet material can be highly nonuniform. While these parts are heat treated to create the desired final microstructure and properties, recovery and recrystallization processes depend somewhat on the extent of deformation in the forged piece. To optimize this forging process, the die design and forging conditions (e.g., temperatures and loading rates) rely on computer simulation. Accurate simulations rely on descriptive constitutive models that are valid over the range of temperatures, strains, strain rates, and stress states imposed on the processed disk.

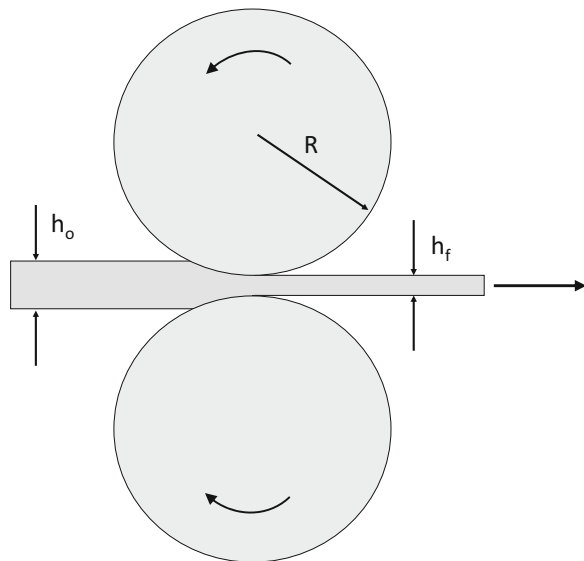
Fig. 5.1 Forging a billet to create a turbine disk



Product failure analysis involving a structural component offers another example where accurate constitutive laws are needed. Whether the part is an automobile bumper, a highway guard rail, a bicycle frame, or crane boom, component failures are commonplace. The automobile bumper and the highway guard rail are designed to fail in a controlled manner to dampen an impact event. Failure of a bicycle frame or crane boom due to design, manufacturing, or overload can result in catastrophic consequences. Design of structural components must balance safety and performance requirements. This is particularly true in the automotive industry, where computer simulation has become an essential element of the design process.¹ Computer predictions rely on accurate specification of boundary conditions (e.g., loads and loading rates) as well as on accurate specification of the material's constitutive behavior.

Rolling is a process used to reduce the thickness of a slab of (usually) metal. Figures 5.2 and 5.3 show schematics of a roll mill with a slab receiving a rolling reduction of roughly 50%. Swaging is a process used to reduce the diameter of a (usually) metal bar. Figure 5.4 shows a photograph of a hot-working operation of a titanium alloy bar. Often metals are rolled and swaged as part of the process to reduce the size of the starting ingot. The deformations also serve to homogenize the

Fig. 5.2 Schematic of a rolling mill



¹Two multi-session symposia at the MS&T'11 Conference (October 16–20, 2011, Columbus, OH) were dedicated to the topic of modeling of automotive components. One was entitled “Measurements and Modeling of Advanced Automotive and Structural Materials at Intermediate and High Strain Rates.” The other was entitled “Characterization and Modeling of the Performance of Advanced Alloys for the Transportation Industry – Bridging the Data Gap II.”

Fig. 5.3 Schematic of a rolling mill showing a slab receiving a rolling reduction of $\sim 50\%$

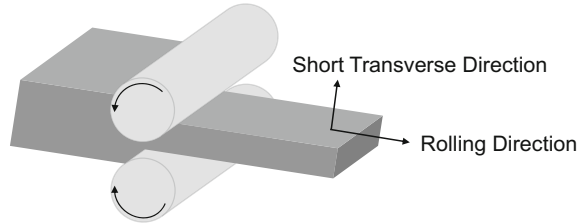


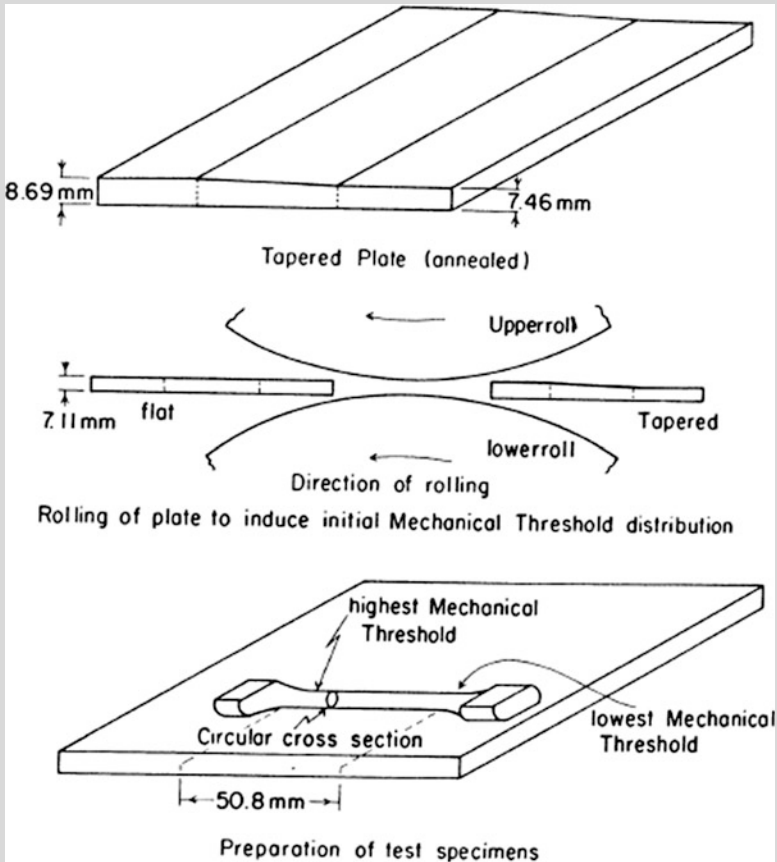
Fig. 5.4 Hot working of a titanium bar (courtesy of TSI Titanium)



structure that is produced in a common foundry ingot. These processes are also routinely used to increase the strength of the metal. That is, posttreatment heat treatments are not always performed because the intended use requires a higher strength than achieved in the annealed condition. Rolling and swaging may impart nonuniform strains in the processed part. Careful choice of the diameter of the roll according to the starting thickness of the part and the minimum rolling reduction can help to ensure uniform strains, but often the suitable equipment (e.g., rolling mill with large enough diameter rolls) is not available. Similar considerations dictate the design of a swaging operation. In suboptimal processing conditions, it may be necessary to simulate the process to ensure that the processed part has the required strength (and ductility) at the desired locations. Box 5.1 describes an experiment [1] where nonuniform strains were purposely introduced into a rolled sheet. Later in this chapter, this experiment will be used to illustrate how nonuniformities of this type are amenable to description using an internal state variable constitutive model.

Box 5.1 The Tapered Plate Experiment

To demonstrate how to simulate deformations in a component with nonuniform deformations, Dawson and Follansbee [1] manufactured a copper plate with a tapered cross section and rolled this plate to induce a gradient of strain (see the following below).



Tensile specimens were machined from the rolled plate. Over the gage length of the tensile specimen, the rolling strain and thus the mechanical threshold stress varied. Simulating the deformation of the tensile specimen poses a challenge due to this gradient. Box 6.3 in Sect. 6.3 describes how Dawson and Follansbee modeled these tensile deformations.

As a final example, Fig. 5.5 is a schematic of an explosively formed penetrator (EFP) before detonation and an example of its shape as determined with dynamic radiography, for instance, after detonation. The deformations and deformation rates

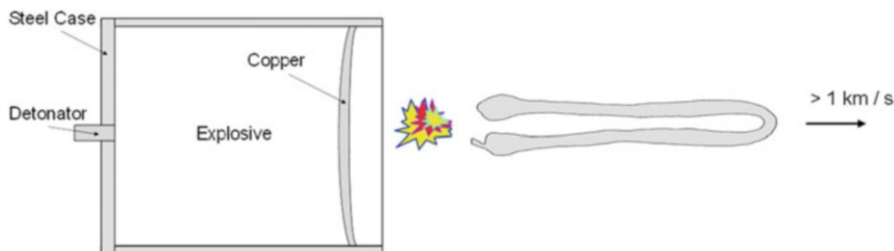


Fig. 5.5 Schematic design of an explosively formed penetrator and shape of the projectile after detonation

are extreme. Again, computer simulation, when equipped with a validated dynamic constitutive model, can assist with EFP designs.

The design process for components such as a turbine disk, an automobile structural component, or a processed metal part is accelerated through the use of computer modeling and simulation codes. These codes need to be equipped with validated constitutive models to enable accurate predictions of process and performance.

5.2 Simple Hardening Models

The simplest model for the entire stress–strain curve is *power law hardening*, written as follows:

$$\sigma = K\dot{\epsilon}^n \quad (5.1)$$

where K and n are constants and n is ~ 0.5 for some coppers and ~ 0.15 for some steels. A disadvantage of Eq. 5.1 is that it predicts zero stress at zero strain. For this reason, this equation has been modified to the Ludwik equation:

$$\sigma = \sigma_o + K\dot{\epsilon}^n \quad (5.2)$$

where σ_o is the yield stress. Note that the dependence on strain rate is not included in Eqs. 5.1 or 5.2. The simplest model for strain rate dependence is as follows:

$$\sigma = C\dot{\epsilon}^m \quad (5.3)$$

where C and m are constants. For austenitic stainless steels, m is on the order of 0.035. Equations 5.1 and 5.3 can be combined, but including the temperature dependence requires yet another term. Numerous integrated equations have been proposed as unified constitutive laws. One example is that proposed by Johnson and Cook [2]:

$$\sigma = (A + B\varepsilon^n) \left[1 - \left(\frac{T - T_r}{T_m - T_r} \right)^m \right] (1 + C \ln \dot{\varepsilon}) \quad (5.4)$$

where T_r is a reference temperature (e.g., RT), T_m is the melting temperature, and A , B , C , n , and m are constants. It is evident that Eq. 5.4 includes a strain-hardening term, a strain rate sensitivity term, and a temperature dependence term. For austenitic stainless steels, the fitted equation has the form:

$$\sigma = (218 \text{ MPa} + 2289 \text{ MPa } \varepsilon^{1.125}) \left[1 - \left(\frac{T - 294\text{K}}{1231\text{K}} \right)^{0.75} \right] (1 + 0.032 \ln \dot{\varepsilon}) \quad (5.5)$$

Figure 5.6 shows stress–strain curves for several combinations of temperature and strain rate predicted using Eq. 5.5. These curves appear to be a reasonable representation of the stress–strain behavior. Imagine, though, that the specimen is strained at RT and a strain rate of 0.001 s^{-1} to a strain of 0.15; then the strain rate was increased to 100 s^{-1} . Figure 5.7 shows the predicted stress–strain curve (solid line) for this two-step loading using Eq. 5.5.

The Johnson-Cook model predicts that at the transition strain, the stress rises from the value on the lower strain rate curve directly to the value on the higher strain rate curve. (Since the stress rises immediately to a higher value, the slope of this rise is the elastic modulus.) Figure 5.8 shows an actual experiment of this sort in copper [3]. Two samples were prestrained² at RT to a strain of 0.15. Specimen A saw a

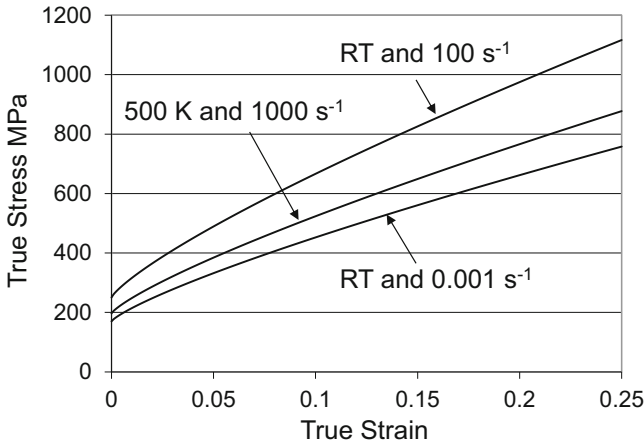


Fig. 5.6 Predicted stress–strain curves in an annealed austenitic stainless steel using the Johnson-Cook deformation model (Eq. 5.5)

²The term “prestrain” is used throughout this monograph to describe straining before a significant change in test temperature or strain rate. The term “reload” is used to describe the straining after this change in test conditions.

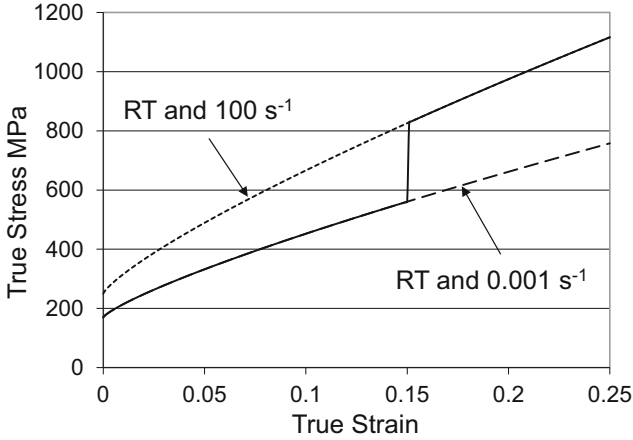


Fig. 5.7 Predicted stress–strain curves in the austenitic stainless steel when a strain rate change is imposed at a strain of 0.15

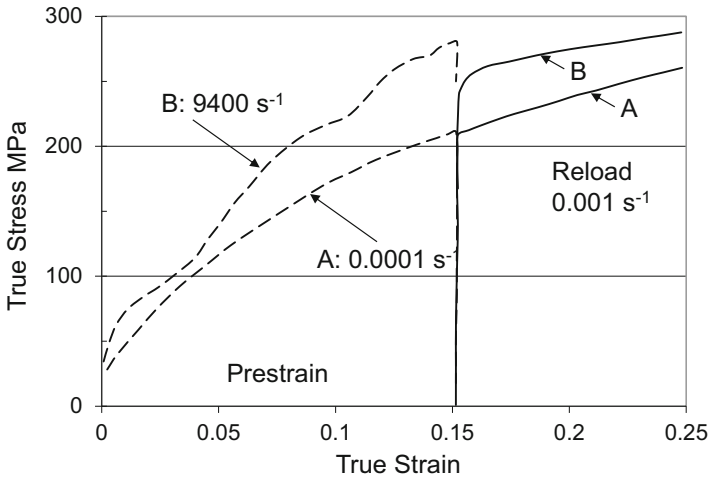


Fig. 5.8 Two RT compression tests at two different strain rates in copper followed by a RT compression test at a uniform strain rate. The observation is that the reload stress–strain curves exhibit different stress levels

strain rate of 0.0001 s^{-1} , whereas specimen B saw a strain rate of 9400 s^{-1} . (The oscillations in the high strain rate test are a result of stress waves produced in the split Hopkinson pressure bar test.) Both samples were unloaded and reloaded at the lower strain rate. Note that upon reloading, specimen B (prestrained at 9400 s^{-1}) reached a yield stress level much higher than did specimen A (prestrained at 0.0001 s^{-1}). This behavior cannot be predicted using a model of the form of Eq. 5.5. One motivation for development of an internal state variable constitutive model is to introduce and

give a mechanistic basis for the observation in Fig. 5.8 and suggest a modeling methodology that is capable of predicting this behavior.

Another way to understand the significance of this experiment is simply consider the dimensions of the test specimens. They started out as identical, and after a strain of 0.15, they still appeared to be identical because their (deformed) dimensions were the same. But, when reloaded at the same temperature and strain rate, one is ~20% stronger than the other, so clearly, these specimens are not the same. Further discussion of this requires introduction of the concept of “state.”

5.3 State Variables

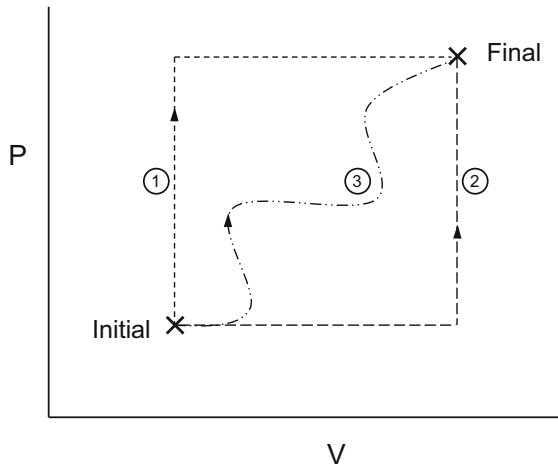
Recall the ideal gas equation:

$$Pv = RT \tag{5.6}$$

where P is pressure, v is the specific volume (inverse of the density), R is the gas constant, and T is the absolute temperature. In this model, P , v , and T are state variables, which uniquely define the state of the gas. Specifying two of these three variables by definition specifies the third through Eq. 5.6. Furthermore, if two states (P_1, v_1, T_1) and ($P_2, v_2, and T_2$) are specified, then the path taken to go from state “1” to state “2” is not important or relevant. This is shown pictorially in Fig. 5.9. The state is uniquely defined by P and v in this figure—and T by Eq. 5.6. In fact, one test of whether a variable is a state variable is whether or not it exhibits path dependence.

Equation 5.6 is a constitutive model—relating P , v , and T . However, just as P , v , and T are state variables, Eq. 5.6 is a state variable model. Equation 5.5 is written as a state variable model; it specifies that a material with the same strain and temperature

Fig. 5.9 Illustrating that the path taken from an initial to a final state in an ideal gas is of no consequence



will have the same stress—regardless of the path taken to achieve this strain. In fact, the path (strain rate) is very important as indicated in Fig. 5.8. Simply stated, strain is not a state variable in materials. Constitutive laws that treat strain as a state variable will be incapable of accurately modeling scenarios where there are large changes in strain rates. The two examples given in Figs. 5.1 and 5.2 are two such scenarios (see Box 5.2).

Box 5.2 When Does the Assumption of Path Independence Lead to Unacceptable Predictions?

The vast majority of stress analysis computer codes used to predict stresses and strains in engineering applications such as those illustrated in Figs. 5.1 and 5.2 in fact does use material models that are of the form $\sigma = f(\epsilon, \dot{\epsilon}, T)$, with the assumption that strain is a state variable. Models of this sort are easy to implement in finite element computer codes. The question of when the path dependence of metal deformation becomes important is difficult to answer. As will be shown in this monograph, the path dependence varies from material to material. Thus, the critical factors become (i) the material being deformed and (ii) the potential for large path changes (strain rate or temperature) during the particular engineering application of interest. The remainder of this monograph presents an approach—a constitutive model—that accounts for path dependence. The model, however, is not as easily implemented in stress analysis.

5.4 Defining a State Variable in Metal Deformation

If two metal samples with the same strain cannot be considered to be in the same state, then the question remains as to what is a valid state variable for metals. Chapter 4 laid the ground work for this through definition of the mechanical threshold stress (MTS), $\hat{\sigma}$ (Sect. 4.3 and Fig. 4.6). Recall that this was defined as the yield stress at 0 K and that this stress characterized the obstacle strength—actually a combination of the height of the obstacle profile and the density of obstacles (which was characterized by the average spacing ℓ). With $\hat{\sigma}$ as a state variable, the constitutive equation—the equation of state—takes the form:

$$\sigma = f(\hat{\sigma}, T, \dot{\epsilon}) \quad (5.7)$$

This equation, which is of the form of Eq. 4.14, is sufficient for specification of the yield stress, but it must be accompanied with an evolution law:

$$\frac{d\hat{\sigma}}{d\epsilon} = f(\hat{\sigma}, T, \dot{\epsilon}) \quad (5.8)$$

which is of the form introduced by the Voce equation (Eq. 3.15) in Sect. 3.6. If this latter function can be defined, then the full stress–strain curve can be derived by integrating this function along the specific strain rate and temperature path.

5.5 The Mechanical Threshold Stress Model

The essential elements of a state variable model have been introduced. Equation 4.14 is rewritten as follows:

$$\sigma = s(\dot{\epsilon}, T)\hat{\sigma} \quad (5.9)$$

where:

$$s(\dot{\epsilon}, T) = \left[1 - \frac{kT}{G} \ln \left(\frac{\dot{\epsilon}_0}{\dot{\epsilon}} \right) \right] \quad (5.10)$$

It is useful to examine Eq. 5.10 and show its correlation with an early “mechanical equation of state” proposed by Zener and Hollomon [4] (see Box 5.3). For a recent application of the Zener-Hollomon equation to analyze deformed copper, see Li et al. [5].

Box 5.3 Comparison with the Zener-Hollomon Equation

Zener and Hollomon [Ref. 5] proposed in 1944 a kinetic equation as an early attempt to define a mechanical equation of state. Their equation is written as follows:

$$\sigma = f(Z) = f(\dot{\epsilon} \exp[\Delta H/RT])|_e \quad (5.B1)$$

where Z is the Zener-Hollomon parameter, ΔH is an activation energy, R is the gas constant, and f signifies that the stress is a function of Z . The equation states that at constant strain, the yield stress is a unique function of Z . It is useful to compare this formulation with that expressed by Eqs. 5.9 with 5.10, which was derived in Sec. 4.5 (see Eq. 4.14):

$$\sigma = \hat{\sigma} \left[1 - \frac{kT}{G} \ln \left(\frac{\dot{\epsilon}_0}{\dot{\epsilon}} \right) \right]$$

where G was also the total activation energy and k is the Boltzmann constant (which recall is the gas constant divided by Avogadro’s number.) With some manipulation:

(continued)

Box 5.3 (continued)

$$\frac{\sigma}{\hat{\sigma}} = \left[1 - \frac{kT}{G} \ln \left(\frac{\dot{\epsilon}_o}{\dot{\epsilon}} \right) \right]$$

$$1 - \frac{\sigma}{\hat{\sigma}} = \frac{kT}{G} \ln \left(\frac{\dot{\epsilon}_o}{\dot{\epsilon}} \right)$$

$$\frac{G}{kT} \left(1 - \frac{\sigma}{\hat{\sigma}} \right) = \ln \left(\frac{\dot{\epsilon}_o}{\dot{\epsilon}} \right)$$

$$\exp \left[\frac{G}{kT} \left(1 - \frac{\sigma}{\hat{\sigma}} \right) \right] = \frac{\dot{\epsilon}_o}{\dot{\epsilon}}$$

$$\dot{\epsilon} \exp \left[\frac{G}{kT} \left(1 - \frac{\sigma}{\hat{\sigma}} \right) \right] = \dot{\epsilon}_o$$

Note the similarity between the above equation and the Zener-Hollomon equation. The difference is that in the above equation the stress dependence is explicit and lies inside the exponent and, in fact, the “ Z ” equals $\dot{\epsilon}_o$ (which is a constant), whereas in the Zener-Hollomon equation, the stress dependence is specified by the function f , which is typically determined experimentally (see, for instance, Li et al. [5]).

Similarly, it is useful to show a correlation of Eqs. 5.9 and 5.10 with the Cottrell-Stokes [6] ratio. This ratio is found by dividing the stresses before and after a temperature change. It is evident from Eq. 5.9 that $\hat{\sigma}$ would cancel and leave only the following:

$$\frac{s_2(\dot{\epsilon}, T)}{s_1(\dot{\epsilon}, T)} = \frac{\left[1 - \frac{kT_2}{G} \ln \left(\frac{\dot{\epsilon}_o}{\dot{\epsilon}} \right) \right]}{\left[1 - \frac{kT_1}{G} \ln \left(\frac{\dot{\epsilon}_o}{\dot{\epsilon}} \right) \right]}$$

which, as predicted by Cottrell and Stokes, would be a constant—as long as the activation energy G remains a constant.

In polycrystals, the strength addition due to interaction of dislocations with grain boundaries is an *athermal* stress σ_a . The term “athermal” implies that thermal activation is unable to assist the dislocation past these obstacles. Recall from Sect. 3.4 the Hall-Petch equation:

$$\sigma = \sigma_i + \frac{k_d}{\sqrt{d_{gs}}} \quad (3.9)$$

where d_{gs} was the grain dimension. It is the grain size-dependent term on the right of Eq. 3.9 that comprises the athermal stress σ_a . In fact, in subsequent developments, the athermal stress could be replaced with $k_d/\sqrt{d_{gs}}$, but to retain generality, σ_a will be used.

$$\sigma = \sigma_a + s(\dot{\epsilon}, T)\hat{\sigma} \tag{5.11}$$

The evolution equation—the Voce law expressed in Eq. 3.15—is rewritten in terms of evolution of the threshold stress $\hat{\sigma}$:

$$\frac{d\hat{\sigma}}{d\epsilon} = \theta_{II} \left(1 - \frac{\hat{\sigma}}{\hat{\sigma}_s(\dot{\epsilon}, T)} \right) \tag{5.12}$$

where the strain rate and temperature dependence of the saturation stress $\hat{\sigma}_s$ is given by Eq. 4.17, which may be rewritten as follows:

$$\ln \hat{\sigma}_s = \ln \hat{\sigma}_{so} + \frac{T}{A_{CS}} \ln \frac{\dot{\epsilon}}{\dot{\epsilon}_{so}} \tag{5.13}$$

An example of application of these equations using a model material is presented in the next section.

5.5.1 Example Material and Constitutive Law

Let us consider a material described by the model parameters listed in Table 5.1. From Eqs. 5.10 and 5.13, s and $\hat{\sigma}_s$ are functions of strain rate and temperature. For the three combinations in Table 5.2, these parameters are computed and listed. (Recall that Boltzmann’s constant $k = 1.38 \times 10^{-23}$ J/K.)

To compute stress–strain curves, note that Eq. 5.12 can be directly integrated, giving the following:

Table 5.1 Hypothetical model parameters for an example metal

Parameter	Value	Units	Equation
G	1.13×10^{-18}	J	5.10
$\dot{\epsilon}_o$	10^8	s^{-1}	5.10
σ_a	50	MPa	5.11
θ_{II}	1000	MPa	5.12
A_{CS}	12,000	K	5.13
$\dot{\epsilon}_{so}$	10^8	s^{-1}	5.13
$\hat{\sigma}_{so}$	1000	MPa	5.13

Table 5.2 Values of $\hat{\sigma}_s$ and s for three test temperature and strain rate combinations for the metal with model parameters specified in Table 5.1

Temp, K	Rate, s^{-1}	$\hat{\sigma}_s$, MPa (Eq. 5.12)	s (Eq. 5.9)
295	0.001	474	0.909
500	0.0001	251	0.831
150	1.0	759	0.966

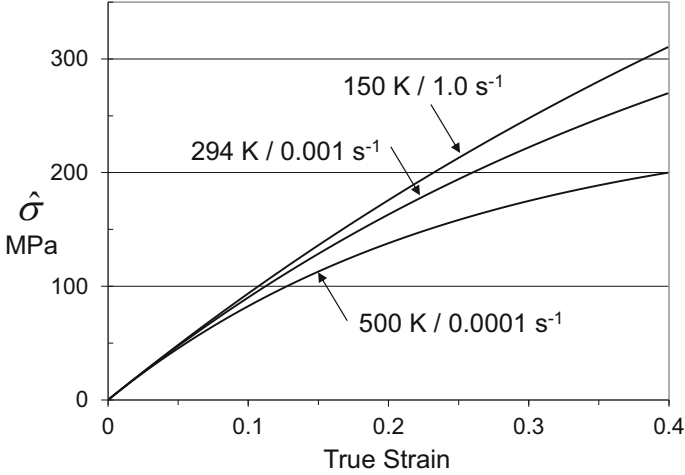


Fig. 5.10 Predicted variation of the threshold stress $\hat{\sigma}$ with strain (from Eqs. 5.14 with 5.13) for different strain rate and temperature combinations

$$\hat{\sigma} = \hat{\sigma}_s \left[1 - \exp \left(-\frac{\theta_{II}}{\hat{\sigma}_s} \varepsilon \right) \right] \quad (5.14)$$

Figure 5.10 shows $\hat{\sigma}$ versus ε for the three temperature and strain rate conditions of interest. Figure 5.10 illustrates that, as expected, evolution of the internal state variable $\hat{\sigma}$ is a function of temperature and strain rate. Stress (rather than $\hat{\sigma}$) is computed using Eqs. 5.11 with 5.10.

In this case, a single equation is derived by substituting Eqs. 5.10 and 5.14 into 5.11, giving the following:

$$\sigma = \sigma_a + \left[1 - \frac{kT}{G} \ln \left(\frac{\dot{\varepsilon}_o}{\dot{\varepsilon}} \right) \right] \hat{\sigma}_s \left[1 - \exp \left(-\frac{\theta_{II}}{\hat{\sigma}_s} \varepsilon \right) \right] \quad (5.15)$$

Figure 5.11 shows example stress–strain curves for the three temperature and strain rate combinations. The curves all start at zero strain at a stress value equal to the athermal stress (50 MPa), which follows from Eq. 5.15 with $\varepsilon = 0$. The rate of strain hardening, however, varies with the test temperature and strain rate.

One advantage of an internal state variable model is the ability to track path changes. Figure 5.12 shows the predicted behavior for a prestrain at 150 K and 1.0 s^{-1} to a strain of 0.20 followed by straining at 500 K and 0.0001 s^{-1} to a strain of 0.40. Equation 5.15 is not valid over the entire two-step straining since $\hat{\sigma}_s$ changes from 759 MPa to 251 MPa when the path change occurs. While careful specification of integration limits enables an explicit solution of Eqs. 5.11 and 5.12, one may find that a numerical solution becomes easier to implement. As shown in Fig. 5.10 at $\varepsilon = 0.20$ for the prestrain at 150 K and 1.0 s^{-1} , $\hat{\sigma} \cong 175 \text{ MPa}$. At this point the path

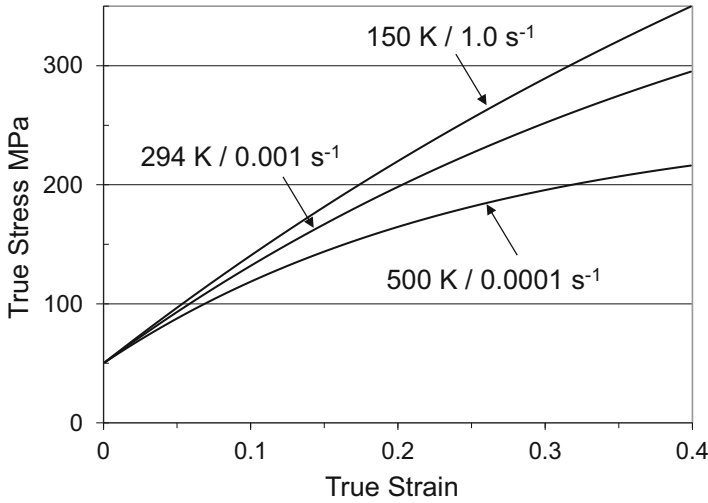


Fig. 5.11 Stress–strain curves at different strain rates and temperatures predicted using Eq. 5.15

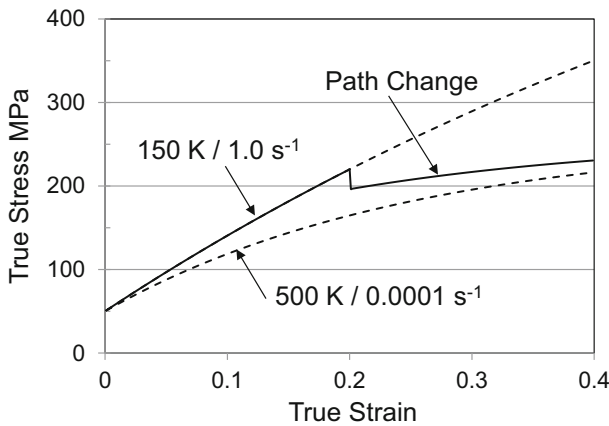


Fig. 5.12 Predicted stress–strain curve when a path change is imposed. Note that in response to the change in temperature and strain rate, the stress–strain curve does not immediately assume the stress level for a monotonic test at the new conditions but does appear to approach these levels with continued strain

change occurs and the temperature and strain rate change to 500 K and 0.0001 s^{-1} . This change in temperature and strain rate implies that, as shown in Table 5.2, s (from Eq. 5.10) becomes 0.831 and $\hat{\sigma}_s$ (from Eq. 5.13) becomes 251 MPa. Since $\hat{\sigma}$ is already ~ 175 MPa, the hardening rate is quite low for the remainder of the straining to $\epsilon = 0.40$. This prediction is quite similar to the scenario depicted in Fig. 5.8. Furthermore, without a state variable model, this behavior is difficult to model.

5.6 Common Deviations from Model Behavior

The example stress–strain curves introduced in Figs. 1.15, 1.16, 1.18, 1.21, and 5.8 were “well-behaved” in that the shape of the curves was consistent with Eq. 5.14 and Region III of the hardening curve shown in Fig. 3.11. Although not as evident in these figures, the variation of strength level (e.g., yield stress) with temperature and strain rate in these materials in general follows the trend described by Eq. 4.14 and illustrated in Fig. 4.7 for niobium and Fig. 4.8 for iron. The constitutive formulation introduced in this chapter relies on knowing that the material of interest is within a mechanistic regime consistent with the model assumptions. Figure 5.13 shows two tensile stress–strain curves measured by Murty [7] in a mild steel (carbon content of 0.06% by weight). These two curves were measured in material before neutron irradiation damage was imposed.

There are several unique aspects of the two curves measured by Murty. Note in the RT (dashed) curve the very slight “bump” at yield, and the extended region of $\sim 5\%$ with no hardening before the curve appears to follow typical Region III hardening behavior. The bump is much more pronounced in the curve measured at 373 K. This curve also has a region ($\sim 2\%$) of almost no hardening followed by a rapid increasing stress level. The higher-temperature curve also exhibits small, short spikes in stress (referred to as “serrations”) not observed at RT. Finally, while the stress level at yield follows the expected temperature dependence, the hardening at 373 K exceeds that at RT, which takes the stress levels at the higher temperature well above those measured at the lower temperature. This temperature dependence is at odds with that modeled by Eq. 5.13.

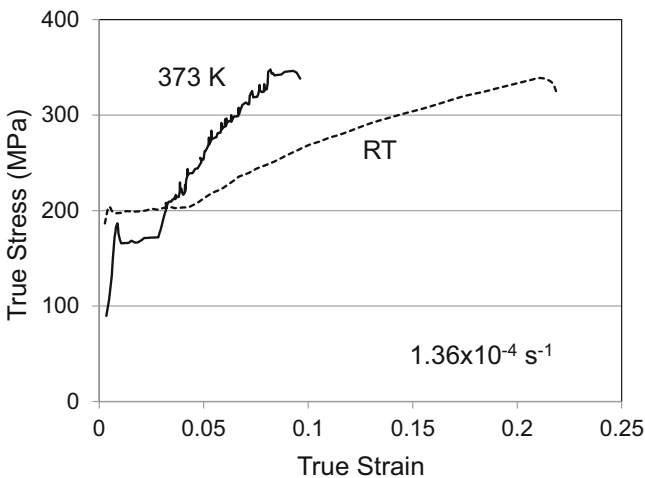


Fig. 5.13 Tensile stress–strain curves in mild steel measured by Murty [7] at two test temperatures

There are actually several contributions to the seemingly “abnormal” behavior in this steel, and, in fact, these behaviors are not at all abnormal but are observed in many materials under certain conditions. The “bump” in the curve at initial yield illustrates an *upper yield point* (the peak stress reached on the bump). The initial yield is thought to relate to the release of a dislocation from an atmosphere of interstitial or substitutional impurities [8]. The flat region that follows is at the *lower yield point*, and the strain incurred at this level is the *yield point elongation*. This behavior is observed in tensile testing of some steels and has been observed in other metals.³ It is thought to represent nonhomogeneous deformation across the gage length of the tensile specimen. That is, yield can initially occur in a single band that occupies only a portion of the gage length. As the yielded region expands to involve the entire gage length, the stress remains at the lower yield point. The bands have been referred to as *Lüders bands*. The upper and lower yield points and the yield point elongation are collectively referred to as “yield phenomena.”

The serrations in the higher-temperature stress–strain curve also relate to the interaction of dislocations with impurity atoms. If the mobility of these impurities is sufficient, they can move to dislocations, which restricts continued dislocation motion resulting in the need for an increased stress level to free the dislocations. It is as if the material must “re-yield” to continue deforming. A good illustration of the effect of defect mobility is to strain (e.g., to 10% strain) a material prone to this effect (such as the mild steel tested by Murty) at low temperature, unload and heat the material at a temperature where the mobility is enhanced (such as at 373 K for this material), and reload at the lower temperature. The yield stress will likely rise above the highest stress reached in the initial straining due to the restriction of dislocation motion posed by the impurity atmosphere. An example of stress–strain curves that illustrates this can be found in ASM’s *Atlas of Stress–Strain Curves* [9]. This is referred to as “strain aging.”

The appearance of serrations on a stress–strain curve has been referred to as the *Portevin-Le Chatelier* effect. Because it also involves mobility of impurities but in this case during straining, it has also been called “dynamic strain aging” (DSA). In Fig. 5.13 it is evident that the mobility of impurities, not present at the lower temperature, has created an additional hardening mechanism, since the stress level has risen above the stresses achieved at the lower temperature. Another example of this showing the variation of stress–strain curves with temperature in a carbon steel is available in the ASM *Atlas of Stress–Strain Curves* [10]. This additional hardening mechanism introduced by dynamic strain aging is not included in the simple kinetic law defined by Eq. 5.11.

³Examples of yield phenomena in metals can be found in the ASM *Atlas of Stress–Strain Curves* (see Refs. [9, 10]) in an aluminum alloy (WA.160), magnesium (Mg.029 and Mg.059), nickel alloys (Ni.010, Ni.063, Ni.108, and Ni.123), beryllium (RM.010), chromium (RM.012 and RM.013), niobium (RM.031), and titanium (Ti.013) where the codes refer to curve numbers in this publication.

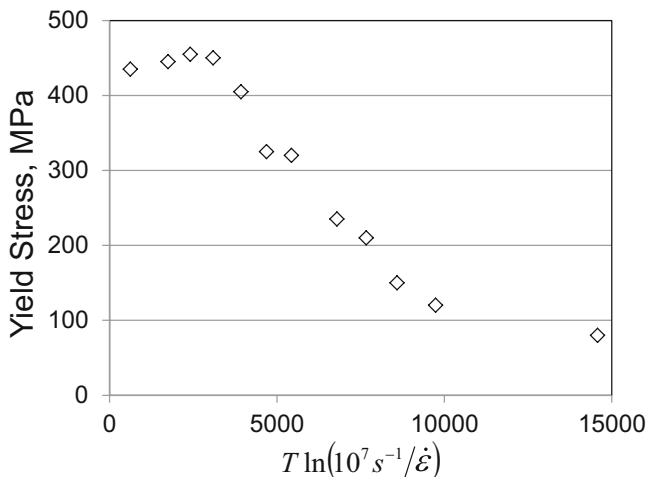


Fig. 5.14 Yield stress versus temperature and strain rate in pure zirconium from Chen and Gray [11]

Another example of measurements that deviate from models described in this chapter is found in the yield stress versus temperature and strain rate in pure zirconium. Chen and Gray [11] reported compression test results, and Song and Gray [12] reported metallography on pure zirconium deformed at temperatures as low as 76 K and strain rates as high as 2800 s^{-1} . Figure 5.14 shows measurements of yield stress versus temperature and strain rate from [11] plotted on similar coordinate to those on Figs. 4.7, 4.8, 4.9, 4.11, and 4.12.

At values of the abscissa greater than ~ 4000 , the curve is similar to curves in the related plots in Chap. 4. To the left of this, however, the stress appears to “saturate” at a value of ~ 440 MPa. The left-most points on this plot are at a temperature of 76 K, whereas the third and fourth data points are at a strain rate of 2800 s^{-1} and temperatures of RT and 373 K. Song and Gray [12] verified through optical metallography that deformation twinning becomes the dominant deformation mechanism at low temperatures and high strain rates. Figure 5.14 shows that when deformation is incurred by a twinning mechanism rather than by a dislocation glide mechanism, the dependence of stress on temperature and strain rate changes markedly.

Erickson and Low [13] observed a similar trend in a 0.04% C steel with a grain size of $20 \mu\text{m}$. Their results are shown in Fig. 5.15, which includes their metallographic observations of the occurrence of twinning in relation to the yield point. In this material the largest departure from the smooth trend observed at temperatures above 100 K occurred in a sample tested at 20 K in which extensive twinning was observed.

The purpose of this section is to emphasize that care is required when analyzing and modeling stress–strain measurements. The models presented in this section and subsequent sections are specific to dislocation glide in the absence of diffusional

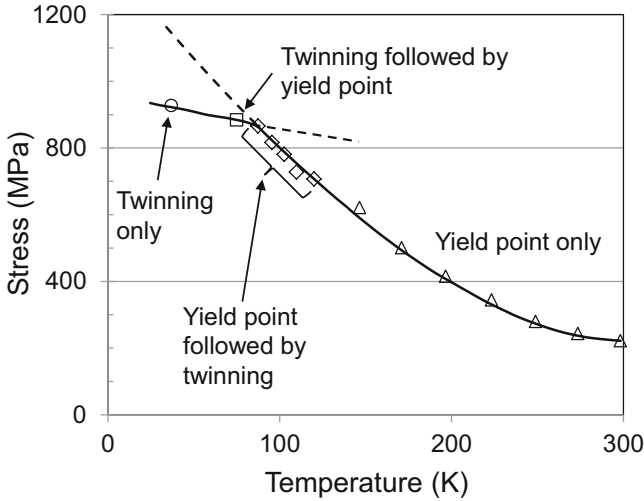


Fig. 5.15 Yield stress measurements at twinning observations by Erickson and Low [13] in a low carbon steel

processes. However, there are several examples of model implementation in FCC, BCC, and HCP metals presented in Chaps. 8, 9, 10, 11, and 12 where deformation twinning, dynamic strain aging, or dynamic recrystallization influence constitutive behavior. Specific examples of how these processes, which are beyond the MTS formalism, manifest themselves in the analysis of stress–strain curves are presented throughout this text. Often, they lead to specific “signatures,” i.e., deviations from typical constitutive behavior, that are noted.

Models for the kinetics of deformation twinning (e.g., twinning [14]) and of dynamic strain aging (e.g., Refs. [15, 16]) that may lead to a more rigorous treatment of the observed trends have been proposed and are under continuous development. Some of these models will be referred to in the following chapters. The objective here has been to demonstrate where the governing equations presented in earlier chapters fail to be descriptive of observed behaviors, show specific “signatures” that appear when analyzing stress–strain curves, and, when possible, suggest a mechanistic basis for these deviations.

5.7 Summary

A constitutive model is simply an equation relating stress (σ) to temperature (T), strain rate ($\dot{\epsilon}$), and strain (ϵ). Although expressions of the form:

$$\sigma = f(\epsilon, \dot{\epsilon}, T) \quad (5.16)$$

are easiest to implement in computer codes, metals exhibit a path dependence—meaning two samples deformed to the same strain along different strain rate and temperature paths may have very different strength levels. This path dependence argues against a constitutive law of the form of Eq. 5.16.

The mechanical threshold stress $\hat{\sigma}$, introduced in Sect. 4.5 as the 0 K yield strength, serves as an internal state variable characterizing dislocation glide in metals and suggests an alternate constitutive law formulation. This model, referred to as the mechanical threshold stress (MTS) model, (i) treats yield stress (at any value of $\hat{\sigma}$) as an explicit function of current temperature and strain rate (Eq. 5.9) and (ii) treats evolution (change) of $\hat{\sigma}$ with strain as an explicit differential function of the current⁴ $\hat{\sigma}$, temperature, and strain rate (Eq. 5.12). Example model formulations for constant strain rate and temperature paths as well as for path changes were given in this chapter.

Examples of commonly observed mechanisms that are not modeled with the analyses presented here were presented to emphasize the range of applicability of these models. The next chapter describes additions and revisions to the model that have been introduced to (i) add additional mechanistic detail and (ii) make the model more predictive for engineering alloys.

Exercises

- 5.1 Assume that a metal follows the hardening law specified by Eq. 5.14 with $\theta_{II} = 2000$ MPa and $\hat{\sigma}_s = 500$ MPa. (a) Find n and K in Eq. 5.1 that gives the closest fit to this hardening law up to a strain of 0.50. (Since the intent of this exercise is to compare the forms of these two equations, ignore the fact that Eq. 5.14 is written in terms of $\hat{\sigma}$ whereas Eq. 5.1 is written in terms of σ .) (b) Plot the difference between the stress predicted by Eqs. 5.14 and 5.1. (c) At what strain levels are the differences the largest?
- 5.2 Repeat Exercise 5.1 but use Eq. 5.11 with $\sigma_a = 250$ MPa and $s = 1$ (and, again, assume this equation applies to σ rather than $\hat{\sigma}$). (a) Find n and K in Eq. 5.1 that gives the closest fit to this hardening law up to a strain of 0.50. (b) Plot the difference between the stress predicted by Eqs. 5.11 and 5.1. (c) At what strain levels are the differences the largest? Include an estimate at a strain level of 0.002 for both equations.
- 5.3 Repeat Exercise 5.1 with $\theta_{II} = 2000$ MPa and (a) $\hat{\sigma}_s = 250$ MPa and (b) $\hat{\sigma}_s = 1000$ MPa. How does the difference between Eqs. 5.1 and 5.14 vary with value of $\hat{\sigma}_s$?

⁴Another term for “current” would be “instantaneous.” In context of Eq. 5.12, the value of $\hat{\sigma}$ would change as strain is incurred. Similarly, the values of T and $\dot{\epsilon}$ could change due to adiabatic heating (to be introduced in Chap. 6) or externally imposed boundary conditions.

Table 5.E6 Threshold stress as a function of strain, strain rate, and temperature for the metal alloy introduced in Exercise 4.5 (Exercise 5.6)

T (K)	Rate (s^{-1})	Strain	$\hat{\sigma}$ (MPa)
300	0.001	0.05	66
		0.10	125
		0.15	171
		0.20	219
		0.30	281
		0.40	318
		0.50	353
600	0.01	0.05	67
		0.10	122
		0.15	163
		0.20	198
		0.30	248
		0.40	283
200	2000	0.05	72
		0.10	128
		0.15	179
		0.20	227
		0.30	303
		0.40	356
		0.50	397

- 5.4 For the material with model parameters listed in Table 5.1, compute the Cottrell-Stokes ratio for a test at a strain rate of $0.001 s^{-1}$ and $T_1 = 295 K$ and $T_2 = 400 K$.
- 5.5 Does the Cottrell-Stokes ratio change for a test at a strain rate of $1.0 s^{-1}$ and the same temperature limits?
- 5.6 Refer to the yield stress versus test temperature and strain rate measurements in Exercise 4.5. Now assume that this experimental campaign included measurements of the threshold stress versus strain for several temperature and strain rate combinations (as in Fig. 5.10). Table 5.E6 lists these results. The goal of this exercise is to derive the model parameters—as in Table 5.1—for this metal. The solution of Exercise 4.5 established G as $3.14 \times 10^{-19} J$, with $\dot{\epsilon}_0 = 10^8 s^{-1}$. Also, since this material was said to follow the deformation kinetics expressed by Eq. 4.14, it also is known that $\sigma_a = 0$. The remaining unknown model parameters for this material are θ_H , A , and $\hat{\sigma}_{s0}$. Estimate values of these parameters, assuming $\dot{\epsilon}_{s0} = 10^8 s^{-1}$.
- 5.7 Using the model parameters derived in Exercise 5.6, plot the stress–strain curve (to 50% strain) along with the $\hat{\sigma}$ versus ϵ data points for (a) a test at 300 K and a strain rate of $0.001 s^{-1}$, (b) a test at 600 K and a strain rate of $0.01 s^{-1}$, and (c) a test at 200 K and a strain rate of $2000 s^{-1}$.

- 5.8 Equation 5.14 gave the closed-form solution for the integral of Eq. 5.12 for the case where $\hat{\sigma} = 0$ when $\varepsilon = 0$. Consider a two-step test with a path change from test temperature and strain rate (starting at $\hat{\sigma} = 0$ and $\varepsilon = 0$) to another test temperature and strain rate. Equation 5.14 can be used to describe the state at the end of the first step:

$$\hat{\sigma}_1 = \hat{\sigma}_{s1} \left[1 - \exp \left(-\frac{\theta_{II} \varepsilon_1}{\hat{\sigma}_{s1}} \right) \right]$$

If for the second step the saturation threshold stress is $\hat{\sigma}_{s2}$, show that the closed-form solution for the evolution of $\hat{\sigma}$ during the second step is as follows:

$$\hat{\sigma} = \hat{\sigma}_{s2} \left\{ 1 - \left(1 - \frac{\hat{\sigma}_1}{\hat{\sigma}_{s2}} \right) \exp \left(-\frac{\theta_{II}(\varepsilon - \varepsilon_1)}{\hat{\sigma}_{s2}} \right) \right\}$$

- 5.9 Using the model parameters derived in Exercise 5.6, plot the stress–strain curve (to 50% strain) for a test at 600 K and a strain rate of 0.01 s^{-1} and a strain of 0.20 followed by a change to 300 K and a strain rate of 0.001 s^{-1} . Include the predicted stress and threshold stress curves.
- 5.10 Using the model parameters derived in Exercise 5.6, plot the stress–strain curve (to 50% strain) for a test at 200 K and a strain rate of 2000 s^{-1} and a strain of 0.30 followed by a change to 600 K and a strain rate of 0.01 s^{-1} . Include the predicted stress and threshold stress curves.

References

1. P.R. Dawson, P.S. Follansbee, The variable threshold rod experiment: A comparison of measured and computed deformations. *J. Eng. Mater. Technol.* **115**, 211–219 (1993)
2. G.R. Johnson, W.H. Cook, A constitutive model and data for metals subjected to large strains, high strain rates, and high temperatures. *Proceedings 7th International Symposium on Ballistics*, The Hague. **541**, 541–547 1983.
3. P.S. Follansbee, The rate dependence of structure evolution in copper and its influence on the stress strain behavior at very high strain rates, in *Impact Loading and Dynamic Behaviour of Materials*, ed. by C. Y. Chiem, H.-D. Kunze, L. W. Meyer, (Informationsgesellschaft, Verlag, Oberursel, 1988), pp. 315–322
4. C. Zener, J.H. Hollomon, Effect of strain rate upon plastic flow of steel. *J. Appl. Phys.* **15**, 22–32 (1944)
5. Y.S. Li, Y. Zhang, N.R. Tao, K. Lu, Effect of the Zener-Hollomon parameter on the microstructures and mechanical properties of Cu subjected to plastic deformation. *Acta Mater.* **57**, 761–772 (2009)
6. A.H. Cottrell, R.J. Stokes, Effects of temperature on the plastic properties of aluminum crystals. *Proc. Royal Soc. A* **233**, 17–34 (1955)
7. K.L. Murty, Is neutron damage exposure always detrimental to metals (steels)? *Lett. Nat.* **308**, 51–52 (1984)

8. G.E. Dieter, *Mechanical Metallurgy*, 2nd edn. (McGraw-Hill, New York, 1976), p. 204
9. Atlas of Stress-Strain Curves, Second Edition, ASM International, Metals Park, OH, 2002, CS.005. The original reference of this curve is: W. T. Lankford, Jr. et al., *The Making, Shaping, and Treating of Steel*. 10th edn. (United States Steel Corporation, 1985), p. 1286.
10. Atlas of Stress-Strain Curves, *ibid*, CS.012. The original reference of this curve is: W. C. Leslie, *The Physical Metallurgy of Metals*. (McGraw-Hill and Hemisphere Publishing, 1981), p. 92.
11. S.-R. Chen, G.T. Gray III, Influence of twinning on the constitutive response of Zr: experiments and modeling. *J. Phys. IV France* 7. Colloque C3, 1997, pp. C3-741 to C3-746 (1997)
12. S.G. Song, G.T. Gray III, Influence of temperature and strain rate on slip and twinning behavior of Zr. *Metall. Trans. A* **26A**, 2665–2675 (1995)
13. J.S. Erickson, J.R. Low Jr., The yield-stress temperature relation for iron at low temperatures. *Acta Metall.* **5**, 405–406 (1957)
14. I.J. Beyerlein, C.N. Tome, A dislocation-based constitutive law for pure Zr including temperature effects. *Int. J. Plast.* **24**, 867–895 (2008)
15. M.A. Soare, W.A. Curtin, Single mechanism rate theory for dynamic strain aging in fcc metals. *Acta Mater.* **56**, 4091–4101 (2008)
16. M.A. Soare, W.A. Curtin, Solute strengthening of both mobile and forest dislocations: the origin of dynamic strain aging in FCC metals. *Acta Mater.* **56**, 4046–4061 (2008)

Chapter 6

Further MTS Model Developments



Introduction

Section 5.5 presented the basic construct of the MTS constitutive model, where deformation was modeled as (i) a temperature- and strain rate-dependent function of the current state—represented by the internal state variable $\hat{\sigma}$ —and (ii) the current temperature- and strain rate-dependent evolution of $\hat{\sigma}$. This chapter introduces some further developments.

6.1 Removing the Temperature Dependence of the Shear Modulus

Equations 5.9 with 5.10 was proposed as a fundamental relation between the flow stress at any temperature and strain rate and the mechanical threshold stress $\hat{\sigma}$:

$$\sigma = \left[1 - \frac{kT}{G} \ln \left(\frac{\dot{\epsilon}_0}{\dot{\epsilon}} \right) \right] \hat{\sigma} \quad (6.1)$$

This equation—the origin of which was described in Sect. 4.5—modeled the dislocation-obstacle interaction and the role of stress and temperature in enabling a dislocation to overcome the obstacle. Dislocation theory has derived the stresses resulting from the interaction of a dislocation with a variety of obstacles. In all of these derivations, the stress is proportional to the shear modulus. For example, dislocation theory predicts that the stress to bend a dislocation to a radius R_d is [1]:

Supplementary Information The online version contains supplementary material available at [\[https://doi.org/10.1007/978-3-031-04556-1_6\]](https://doi.org/10.1007/978-3-031-04556-1_6)

$$\tau \approx \frac{\mu b}{2 R_d} \quad (6.2)$$

where μ is the shear modulus and, as before, b is the Burgers vector.

When considering the temperature dependence of the yield stress, as in Eq. 6.1, it is good practice to remove from Eq. 6.1 any temperature dependence of the shear modulus or from the Burgers vector—since any contribution (either positive or negative) from these are not per say related to the contribution required from thermal activation [2]. The Burgers vector will vary with temperature, but this variation is insignificant. The temperature dependence of the shear modulus, however, while small should nonetheless be factored out of Eq. 6.1. To accomplish this, Eq. 6.1 can be rewritten as follows:

$$\frac{\sigma}{\mu} = \left[1 - \frac{kT}{G} \ln \left(\frac{\dot{\epsilon}_o}{\dot{\epsilon}} \right) \right] \frac{\hat{\sigma}}{\mu_o} \quad (6.3)$$

where μ is the shear modulus at T and μ_o is the shear modulus at 0 K:

$$\mu_o = \mu|_{T=0K} \quad (6.4)$$

Adding the athermal stress, per Eq. 5.11, gives the following:

$$\frac{\sigma}{\mu} = \frac{\sigma_a}{\mu} + \left[1 - \frac{kT}{G} \ln \left(\frac{\dot{\epsilon}_o}{\dot{\epsilon}} \right) \right] \frac{\hat{\sigma}}{\mu_o} \quad (6.5)$$

It also is the case that the activation energy G carries a dependence on shear modulus which should be factored out as well. This is usually accomplished by normalizing G by μb^3 , giving the following:

$$\frac{\sigma}{\mu} = \frac{\sigma_a}{\mu} + \left[1 - \frac{kT}{g_o \mu b^3} \ln \left(\frac{\dot{\epsilon}_o}{\dot{\epsilon}} \right) \right] \frac{\hat{\sigma}}{\mu_o} \quad (6.6)$$

where g_o is referred to as a normalized activation energy. Another benefit of this normalization is that g_o values become (i) dimensionless and (ii) closer to unity. To demonstrate the latter, consider G in Table 5.1:

$$G = 1.13 \times 10^{-18} J = 1.13 \times 10^{-18} \text{ N} \cdot \text{m}$$

Assuming this was for copper at 295 K with $\mu = 42.2$ GPa and $b = 0.256$ nm:

$$g_o = \frac{1.13 \times 10^{-18} \text{ N} \cdot \text{m}}{42.2 \times 10^9 \frac{\text{N}}{\text{m}^2} (0.256 \times 10^{-9} \text{ m})^3} = 1.6$$

Note that dimensions cancel.

Equation 5.13 for the temperature dependence of the saturation stress $\hat{\sigma}_s$ also characterized a thermally activated process, which warrants a normalization by the shear modulus.

$$\ln \hat{\sigma}_s = \ln \hat{\sigma}_{so} + \frac{kT}{\mu b^3 g_{so}} \ln \frac{\dot{\epsilon}}{\dot{\epsilon}_{so}} \tag{6.7}$$

In this case the parameter A was replaced with $\mu b^3 g_{so}/k$ where k is the Boltzmann constant. Again, from Table 5.1:

$$g_{so} = \frac{kA}{\mu b^3} = \frac{1.38 \times 10^{-23} \frac{\text{N}\cdot\text{m}}{\text{K}} 12000\text{K}}{42.2 \times 10^9 \frac{\text{N}}{\text{m}^2} (0.256 \times 10^{-9} \text{m})^3} = 0.23$$

Once again, g_{so} is a dimensionless number close to unity.

For a more detailed discussion of how the shear modulus is defined, see Box 6.1. Temperature dependence of the shear modulus is modeled using an equation evaluated by Varshni [3]:

$$\mu(T) = \mu_o - \frac{D_o}{\exp\left(\frac{T_o}{T}\right) - 1} \tag{6.8}$$

Figure 6.1 shows the variation of μ with T for several materials, and Table 6.1 lists values of μ_o , D_o , and T_o for several metals.

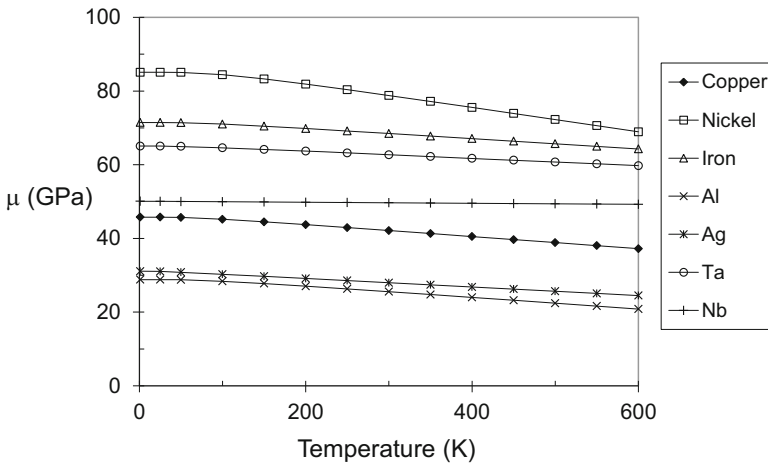


Fig. 6.1 Variation of the shear modulus with temperature for a selection of the metals in Table 6.1

Table 6.1 Coefficients for the temperature dependence of the shear modulus described by Eq. 6.8 for several metals

Material	μ_o (GPa)	D_o (GPa)	T_o (K)
Copper	45.78	3.0	180
Nickel	85.09	9.14	269
Iron	71.46	2.91	204
Al	28.82	3.44	215
Ag	31.1	0.743	64
Ta	65.07	1.40	140
Nb	50.08	0.0207	15
Mo	142.7	6.475	252
W	163.1	10.6	446
V	68.98	0.4098	45
Cr	125.7	1.1	50
Zn	63.5	4.3	125
Cd	33.2	2.8	125
Zr	41.76	1.999	85.04
Mg	18.6	1.92	210
Ti	47.62	5.821	181
Ti6Al-4V	49.02	4.355	198
Be	150	33	680

Box 6.1 The Shear Modulus

Chapter 2 introduced the shear modulus μ in the derivation of the stress required to move an entire plane across another. Normalization of the stress by the shear modulus was presented in Sect. 6.1 as a means to remove a temperature dependence unrelated to thermal activation. However, definition of the shear modulus has heretofore been imprecise.

Section 1.6 introduced Young's modulus in a tensile test. If this is a test in shear, e.g., twisting of a tube, rather than in tension or compression, the elastic modulus would be a "shear modulus"—often referred to as G . For an isotropic material, G is related to E through the Poisson ratio:

$$G = \frac{E}{2(1 + \nu)}$$

Both E and G are relevant to isotropic materials, which are materials characterized by equivalent properties in all directions. They would not be appropriate for a single crystal with, for instance, the tensile axis aligned along the [111] direction. For single crystals, the elastic constants take on a tensor form, e.g., c_{11} , c_{12} , c_{44} , which refer to specific directions in a Cartesian coordinate system. For slip, the shear modulus of interest is that characterizing shear along the slip plane. Kocks, Argon, and Ashby [2, p. 26] recommend the following specific form of the shear modulus for FCC and HCP lattices:

$$\mu = \sqrt{c_{44} \frac{(c_{11} - c_{12})}{2}} \quad (6.B1)$$

It is evident from Fig. 6.1 that the shear modulus varies only slightly with temperature and that the variation depends on the material. Nonetheless, the temperature dependence of μ according to Eq. 6.8 will be included in further analyses.

6.2 Introducing a More Descriptive Obstacle Profile

A simple model was presented in Sect. 4.5 for the stress dependence of the activation energy ΔG . This led to Eq. 4.14 as a general form for the variation of yield stress with temperature and strain rate, which was modified above to Eq. 6.6. It is worth reemphasizing that this expression represents the shape of the obstacle profile and that the form of Eq. 4.14 (and also Eq. 6.6) represents a highly idealized obstacle profile. A further modification to Eq. 4.14 is to introduce parameters that more accurately represent “curvature” of the obstacle profile through the exponents p and q included in Eq. 6.9 [Ref. 2, p. 142]:

$$\left(\frac{\sigma - \sigma_a}{\mu}\right)^p = \left\{1 - \left[\frac{kT}{g_o \mu b^3} \ln\left(\frac{\dot{\epsilon}_o}{\dot{\epsilon}}\right)\right]^{1/q}\right\} \left(\frac{\hat{\sigma}}{\mu_o}\right)^p \quad (6.9)$$

or

$$\frac{\sigma}{\mu} = \frac{\sigma_a}{\mu} + \left\{1 - \left[\frac{kT}{g_o \mu b^3} \ln\left(\frac{\dot{\epsilon}_o}{\dot{\epsilon}}\right)\right]^{1/q}\right\}^{1/p} \frac{\hat{\sigma}}{\mu_o} \quad (6.10)$$

where $0 < p \leq 1$ and $1 \leq q \leq 2$. Eqs. 6.9 and 6.10 represent the form of the “yield stress” equation that will be used in MTS formulations going forth—replacing the earlier simplified expression (Eq. 4.14). Accordingly, Eq. 5.11 becomes as follows:

$$\frac{\sigma}{\mu} = \frac{\sigma_a}{\mu} + s(\dot{\epsilon}, T) \frac{\hat{\sigma}}{\mu_o} \quad (6.11)$$

where:

$$s(\dot{\epsilon}, T) = \left\{1 - \left[\frac{kT}{g_o \mu b^3} \ln\left(\frac{\dot{\epsilon}_o}{\dot{\epsilon}}\right)\right]^{1/q}\right\}^{1/p} \quad (6.12)$$

With these new definitions, it is useful to define the “activation volume” which is a parameter often used in thermal activation experiment and analysis (see Box 6.2).

Box 6.2 Activation Volume

Figure 4.5 showed a schematic of a dislocation encountering multiple obstacles. The position of the dislocation before and after sweeping past the center obstacle via a thermal activation event defines a physical area in the slip plane. This area is referred to as the “activation area.”

The *activation volume* is another parameter that uniquely characterizes a dislocation-obstacle interaction. The activation volume v^* is defined as follows:

$$v^* = -\frac{\partial \Delta G}{\partial \tau} = kT \frac{\partial \ln \left(\frac{\dot{\gamma}}{\dot{\gamma}_0} \right)}{\partial \tau} \quad (6.B2)$$

Since the activation energy has units J (or N · m), dividing by N/m² indeed gives a v^* with units of volume (m³). Contrary to the activation area, it is more difficult to assign a physical, spatial interpretation of the activation volume. Rather, this quantity should be viewed through its definition above. The activation volume is often quoted in experimental studies because the right-hand side of the defining equation is amenable to experimental measure.

For a dislocation-obstacle profile defined by Eq. 6.11 with $\sigma_a = 0$ and Eq. 6.12 and ignoring the temperature dependence of the shear modulus for the special case of $p = 1/2$ and $q = 3/2$, it can be shown that:

$$v^* = kTM \frac{\partial \left(\ln \frac{\dot{\gamma}}{\dot{\gamma}_0} \right)}{\partial \sigma} = \frac{3}{4} b^3 M g_0 \mu_0 \frac{1}{\sqrt{\hat{\sigma}}} \left(1 - \sqrt{\frac{\sigma}{\hat{\sigma}}} \right)^{1/2} \quad (6.B3)$$

where M is the “Taylor factor” relating shear stress to normal stress. It is evident that v^* is not defined at $\sigma = 0$, which follows from the specific form of Eq. 6.12 and the selected values of p and q . When $p = q = 1$, for instance:

$$v^* = kTM \frac{\partial \left(\ln \frac{\dot{\gamma}}{\dot{\gamma}_0} \right)}{\partial \sigma} = \frac{b^3 M g_0 \mu_0}{\hat{\sigma}} \quad (6.B4)$$

which contains no stress dependence. Since Eq. 6.12 with $p = 1/2$ and $q = 3/2$ is more realistic, the more complex definition of v^* will be used, and the v^* at low stress will be evaluated at a constant stress (when comparing different materials) where $\sigma \leq 0.005 \hat{\sigma}$.

Finally, note that for multiple obstacles represented by Eqs. 6.17 and 6.18 it is more difficult to compute an explicit v^* . In this case—which is relevant to most materials and most experimental studies—Sect. 6.4 outlines the procedure used to define activation volumes for each obstacle family.

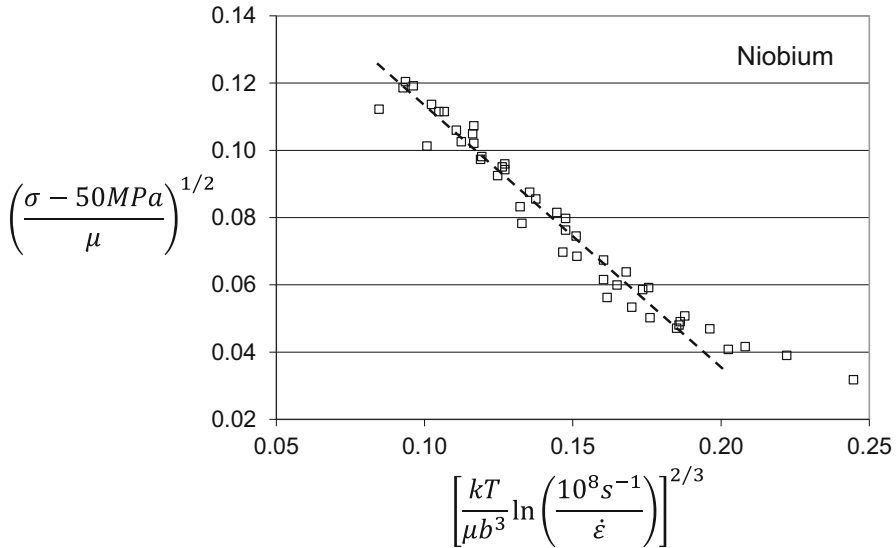


Fig. 6.2 Temperature- and strain rate-dependent yield stress measurements in niobium reported by Campbell and Biggs (Ref. [2] in Chap. 4) plotted on coordinates suggested by Eqs. 6.11 and 6.12

Figure 6.2 is a plot of the niobium data of Campbell and Briggs (Ref. [2] in Chap. 4) plotted on coordinates suggested by Eq. 6.9. Figure 4.7 presented the same data plotted on coordinates suggested by Eq. 4.14. (Note that p and q were chosen as one-half and three-halves, σ_a was chosen as 50 MPa, and $\dot{\epsilon}_o$ was chosen as 10^8 s^{-1} , respectively.) The plots actually are very similar in appearance. Normalization of the temperature-dependent shear modulus (as shown in Fig. 6.1, niobium exhibits insignificant temperature dependence of μ) and use of Eq. 6.9 has had only a subtle influence on the curvature in this plot or the agreement of a model fit according to Eq. 6.9 (dashed line) with the entire data set.

Figure 6.3 plots the iron data of Nojima (see Fig. 4.8) on the same axes and with the same values of p and q as used in Fig. 6.2 (although $\sigma_a = 75 \text{ MPa}$). Once again, the agreement of the model fit (dashed line) with the entire data set is, perhaps, slightly better than one could achieve with a single line in Fig. 4.8, but the model does not fit the entire data set.

6.3 Dealing with Multiple Obstacles

Section 4.7 introduced the challenge of describing multiple dislocation/obstacle interactions in face of multiple strengthening mechanisms. Equation 4.15 defined the assumed behavior which specifies that the total threshold stress is the summation of the threshold stresses characterizing two obstacle populations (the interactions with dislocations of which are influenced by thermal activation) with $\hat{\sigma}_1$ equal to the

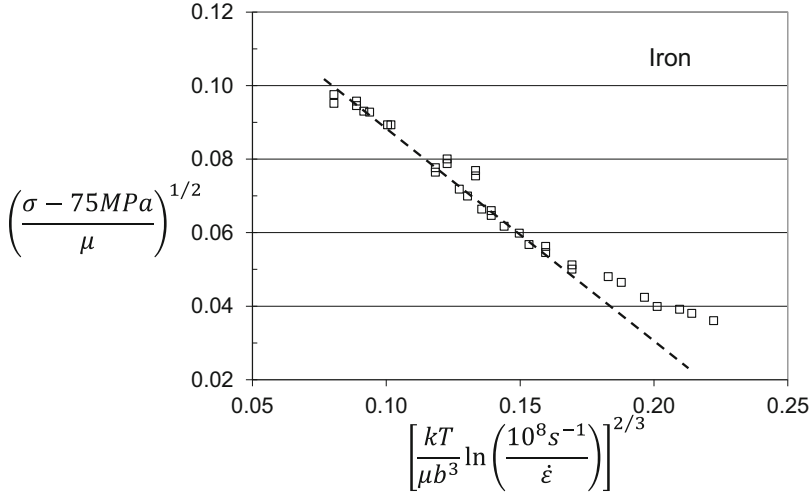


Fig. 6.3 Temperature- and strain rate-dependent yield stress measurements in iron reported by Nojima (Ref. [3] in Chap. 4) plotted on coordinates suggested by Eqs. 6.11 and 6.12

mechanical threshold stress representing one obstacle and $\widehat{\sigma}_2$ equal to the mechanical threshold stress representing a second obstacle:

$$\widehat{\sigma} = \widehat{\sigma}_1 + \widehat{\sigma}_2 \quad (6.13)$$

Following Eq. 6.11, addition of a second obstacle gives the following:

$$\frac{\sigma}{\mu} = \frac{\sigma_a}{\mu} + s_1(\dot{\epsilon}, T) \frac{\widehat{\sigma}_1}{\mu_o} + s_2(\dot{\epsilon}, T) \frac{\widehat{\sigma}_2}{\mu_o} \quad (6.14)$$

where:

$$s_1(\dot{\epsilon}, T) = \left\{ 1 - \left[\frac{kT}{g_{o1}\mu b^3} \ln \left(\frac{\dot{\epsilon}_{o1}}{\dot{\epsilon}} \right) \right]^{1/q_1} \right\}^{1/p_1} \quad (6.15)$$

and

$$s_2(\dot{\epsilon}, T) = \left\{ 1 - \left[\frac{kT}{g_{o2}\mu b^3} \ln \left(\frac{\dot{\epsilon}_{o2}}{\dot{\epsilon}} \right) \right]^{1/q_2} \right\}^{1/p_2} \quad (6.16)$$

Since it is likely that the normalized activation energies g_o characterizing obstacle profiles 1 and 2 will differ and the shapes of the obstacle profiles for obstacle populations 1 and 2 may differ, Eqs. 6.15 and 6.16 specify unique values of g_o , $\dot{\epsilon}_o$, p , and q . When $\dot{\epsilon}_{o1} \neq \dot{\epsilon}_{o2}$, a plotting challenge emerges. Note in Eq. 6.9 that a plot of:

$$\left(\frac{\sigma - \sigma_a}{\mu}\right)^p$$

versus

$$\left[\frac{kT}{\mu b^3} \ln\left(\frac{\dot{\epsilon}_o}{\dot{\epsilon}}\right)\right]^{1/q}$$

on the y -axis and x -axis respectively gives a unique curve, as illustrated in Figs. 6.2 and 6.3. This is no longer the case when $\dot{\epsilon}_{o1} \neq \dot{\epsilon}_{o2}$. To illustrate this, consider the hypothetical model parameters specified in Table 6.2. (This metal is assumed to have the elastic constants of niobium.)

Table 6.3 lists model predictions using the model parameters in Table 6.2 and Eqs. 6.14, 6.15, and 6.16 for several strain rate and temperature combinations. The third column (Obstacle 2) gives predictions only for obstacle 2, i.e., $\hat{\sigma}_1 = 0$ (instead of the value listed in Table 6.2). The fourth column (2 obstacles) gives the predictions for both obstacles.

Figure 6.4 is a plot of these predictions using, on the y -axis:

$$\left(\frac{\sigma}{\mu}\right)^p$$

versus, on the x -axis:

$$\left[\frac{kT}{\mu b^3} \ln\left(\frac{10^8 s^{-1}}{\dot{\epsilon}}\right)\right]^{1/q}$$

The effect of including the contributions of obstacle 1 is evident at low values of the abscissa, but the two predictions converge at high values of the abscissa. This

Table 6.2 Hypothetical parameters selected for Eq. 6.15 and Eq. 6.16

	Parameter	Value
Obstacle	σ_a (MPa)	0
	b (nm)	0.286
Obstacle 1	g_o	0.1
	$\dot{\epsilon}_o$ (s^{-1})	10^{10}
	p	0.5
	q	1.5
	$\hat{\sigma}/\mu_o$	0.03
Obstacle 2	g_o	0.5
	$\dot{\epsilon}_o$ (s^{-1})	10^8
	p	0.5
	q	1.5
	$\hat{\sigma}/\mu_o$	0.03

Table 6.3 Stress predictions using Eqs. 6.14, 6.15, and 6.16 for the material with the model constants listed in Table 6.2

Strain rate (s^{-1})	Temperature (K)	Stress (MPa) (obstacle 2)	Stress (MPa) (2 obstacles)
0.0001	100	1052	1389
	150	928	1072
	200	823	863
	250	732	733
	300	652	652
	350	580	580
	400	516	516
	450	457	457
0.01	100	1099	1513
	150	986	1200
	200	890	980
	250	806	829
	300	731	731
	350	663	663
	400	601	601
	450	545	545
1.0	100	1151	1655
	150	1050	1352
	200	964	1129
	250	888	963
	300	820	842
	350	757	758
	400	700	700
	450	647	647
	500	598	598

The third column lists only the stress contribution from obstacle 2 but the fourth column lists the stress contributions from both obstacles

convergence reflects the fact that obstacle population 1, with its much lower value of g_o , becomes ineffective at restricting dislocation motion at high temperatures and low strain rates. More importantly, note the overlapping symbols for the prediction using both obstacles, but that for the single-obstacle prediction, all symbols lie on a single curve (line). While the overlap appears to be small—and within the typical experimental scatter usually observed—the inability to compare data with a single curve is noted. The source of the overlap is that Eqs. 6.15 and 6.16 have different values of $\dot{\epsilon}_o$ (even though the values of p and q were assumed to be equal for both obstacles) such that a single set of parameters on the abscissa coordinate can't be used to uniquely plot the predictions.

To illustrate this, consider the two overlapping points that lie at the abscissa value ~ 0.10 in Fig. 6.4. Table 6.4 lists values of the various parameters that comprise the estimate of the stress. Note that point A is at a lower strain rate but slightly higher

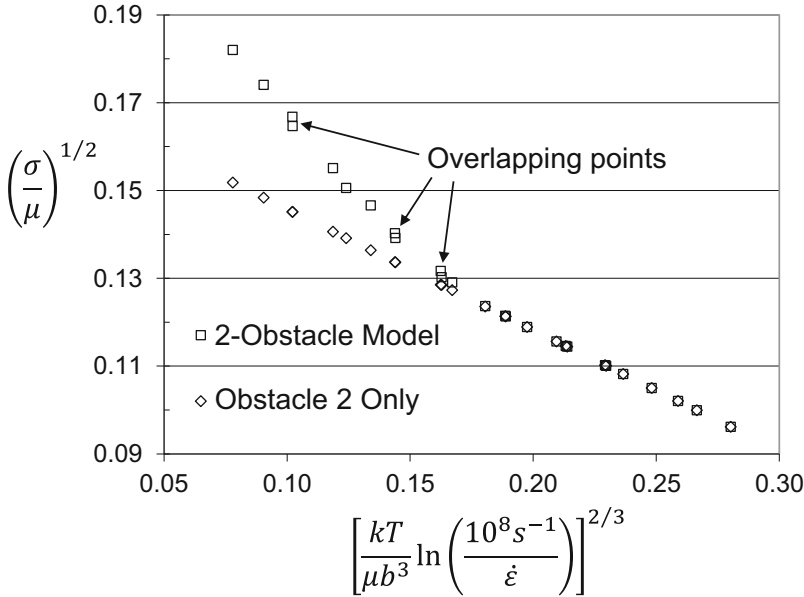


Fig. 6.4 Stresses from Table 6.3 plotted on the same coordinates used in Figs. 6.2 and 6.3

Table 6.4 Computed parameters for the two overlapping points at the left of Fig. 6.4

Parameter	Point A	Point B
$\dot{\epsilon}$ (s^{-1})	0.0001	1
T (K)	100	150
σ_a (MPa)	0	0
μ (GPa)	50.0	49.9
s_1 (Eq. 6.15)	0.225	0.202
s_2 (Eq. 6.16)	0.702	0.702
$\hat{\sigma}_1$ (MPa)	337	302
$\hat{\sigma}_2$ (MPa)	1052	1050
σ (MPa)	1389	1352
$\left[\frac{kT}{\mu b^3} \ln \left(\frac{10^8 s^{-1}}{\dot{\epsilon}} \right) \right]^{2/3}$	0.1022	0.1023
$\left(\frac{\sigma}{\mu} \right)^{1/2}$	0.167	0.165

temperature than point B. However, the computed values of the abscissa coordinate are essentially the same. Because $\dot{\epsilon}_{o1} = 10^{10} s^{-1}$ whereas the x-coordinate values are calculated using $\dot{\epsilon}_o = 10^8 s^{-1}$ (which is the same as $\dot{\epsilon}_{o2}$), the computed ordinate values do not overlap as closely as the abscissa values.

Figure 6.5 is a plot of the Campbell and Briggs data in niobium plotted on the coordinates specified above (with $\dot{\epsilon}_o = 10^8 s^{-1}$ for the abscissa coordinate). Model parameters are based on the work of Follansbee [4], which will be discussed in more detail in Sect. 9.1. Included are the model predictions, plotted with an “x.” To circumvent the problem mentioned above regarding the inability to plot a single

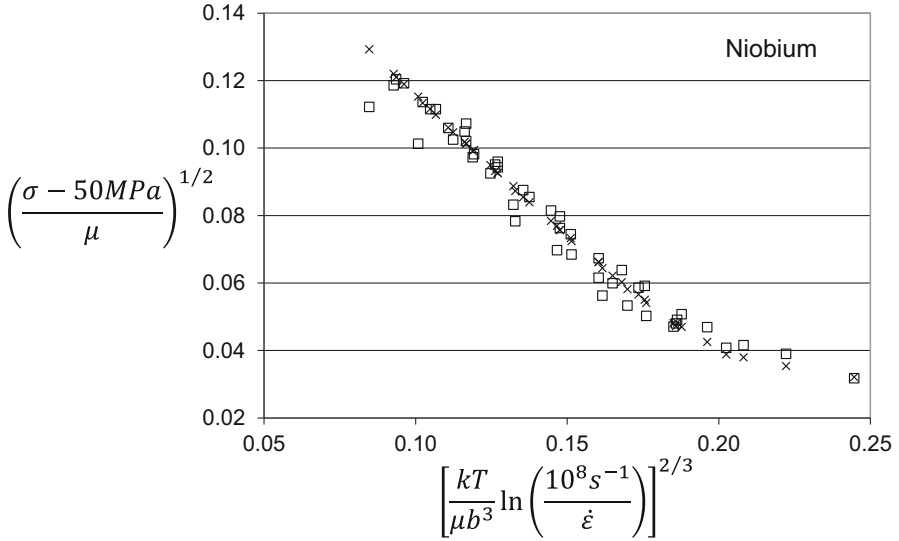


Fig. 6.5 Temperature- and strain rate-dependent data (open squares) in niobium reported by Campbell and Biggs (Ref. [2] in Chap. 4). Accompanying each measured point is a model prediction (x)

smooth curve as the model prediction, a model prediction is given for each value of temperature and strain rate included in the Campbell and Briggs data set. There are examples in Fig. 6.5 of “x” values that show the effects highlighted in Fig. 6.4, but these effects are quite small; it is apparent that a smooth curve could pass through the model predictions.

Comparing the model fit in Fig. 6.5 with that shown in Fig. 6.2 illustrates the benefit of defining a two-obstacle model. Note in particular the agreement at high values of the abscissa, where the single-obstacle model broke down. (Since the objective of this chapter is to describe modifications to the MTS model, the model fits are given only as examples. Interpretation of these results becomes the topic of subsequent chapters.)

Figure 6.6 presents the measurements and model predictions for pure iron. (Model parameters are again based on the work of Follansbee [4] and will be discussed in more detail in Sect. 9.1.) Once again, the open squares represent the Nojima measurements, whereas the “x” represents the model prediction according to the two-obstacle model for each of the temperature and strain rate conditions tested. This figure should be compared to Fig. 6.3, which was the single-obstacle model analysis. The comparison is similar to that observed in niobium.

Equation 6.14 is the model treatment for two-obstacle populations. Addition of a third or more populations can be treated similarly, according to the following:

$$\frac{\sigma}{\mu} = \frac{\sigma_a}{\mu} + \sum_1^n s_i(\dot{\epsilon}, T) \frac{\hat{\sigma}_i}{\mu_o} \tag{6.17}$$

where:

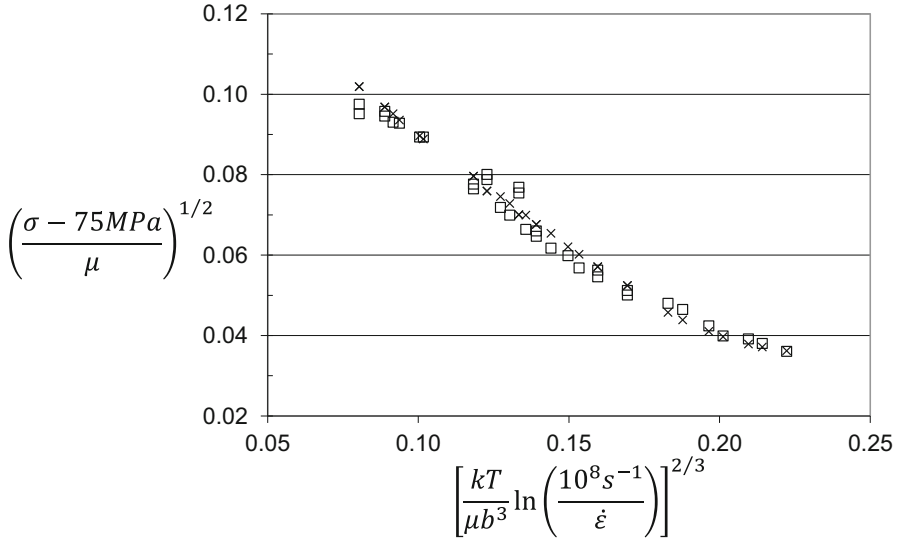


Fig. 6.6 Temperature- and strain rate-dependent data in iron (open squares) reported by Nojima (Ref. [3] in Chap. 4). Accompanying each measured point is a model prediction (x)

$$s_i(\dot{\epsilon}, T) = \left\{ 1 - \left[\frac{kT}{g_{oi}\mu b^3} \ln \left(\frac{\dot{\epsilon}_{oi}}{\dot{\epsilon}} \right) \right]^{1/q_i} \right\}^{1/p_i} \quad (6.18)$$

Several examples of analyses using Eqs. 6.17 and 6.18 will be presented in Chap. 8 through 12. Before moving on to a discussion of developments in the MTS evolution equation, Box 6.3 describes how Eqs. 6.11 and 6.12 are used to assess the variation of state in the tapered plate experiment introduced in Sect. 5.1.

Box 6.3 The Tapered Plate Experiment

This experiment, which was introduced in Sect. 5.1, involved the intentional creation of a variable state in a plate. Predicting the deformation of the tensile specimen machined from this plate requires a finite element method (FEM) code, for instance, programmed with an internal state variable constitutive model. It also requires an assessment of the spatial variation of the state along the plate. To accomplish the latter, compression specimens were machined from the plate at various locations. Specimens were machined with an orientation parallel to the rolling direction (termed L) and transverse (termed T) to the rolling direction (but with the compression axis in the plane of the plate). Figure 6.7 is a plot of the yield stress versus temperature (76 K, 188 K, and 295 K) and strain rate (although each of the reloads was at a strain rate of 0.001 s⁻¹) on coordinates suggested by Eqs. 6.11 and 6.12 with $p = 2/3$ and $q = 1$. (Since the working material was copper which is well-described using a

(continued)

Box 6.3 (continued)

single internal state variable (see Sect. 8.2), it is appropriate to use Eqs. 6.11 and 6.12 with the coefficients for copper.) Measurements for both the L- and T-directions are included.

As in Fig. 6.5 (niobium) and Fig. 6.6 (iron), the intercept at $T = 0$ is the mechanical threshold stress $\hat{\sigma}_\epsilon$ which arises from the interaction of mobile dislocations with stored dislocations. Rolling the tapered plate increased the stored dislocations, so $\hat{\sigma}_\epsilon$ at the hard end (the end receiving the greatest reduction) is above that at the soft end. The right-hand graph in Fig. 6.7 shows the trend with all of the measurements across the gage length of the tensile specimen. With this information an FEM prediction of deformation within the tensile specimen is possible.

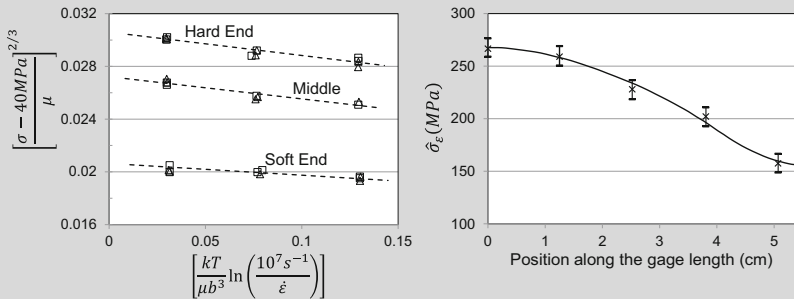


Fig. 6.7 Left: Reload yield stress measurements in two orientations for three positions along the tapered section. Right: Measured variation of $\hat{\sigma}_\epsilon$ along the tensile specimen gage section

Analysis of the variation of the internal state variable in the tapered plate is one example of how the state variable model is applied to a processed part. Additional examples in material subjected to irradiation damage and material that has been fine-grain processed are presented in subsequent chapters.

6.4 Defining the Activation Volume in the Presence of Multiple Obstacles Populations

The activation volume v^* was defined in Box 6.2. For the specific case of deformation determined by the interaction of a dislocation with a single-obstacle population as defined by Eq. 6.11 with $p = 1/2$ and $q = 3/2$ in Eq. 6.12:

$$v^* = kTM \frac{\partial \left(\ln \frac{\dot{\epsilon}}{\dot{\epsilon}_o} \right)}{\partial \sigma} = \frac{3}{4} b^3 M g_o \mu_0 \frac{1}{\sqrt{\widehat{\sigma}} \sigma} \left(1 - \sqrt{\frac{\sigma}{\widehat{\sigma}}} \right)^{1/2} \quad (6.19)$$

This expression is useful in comparing the activation volumes determined for different materials to verify that the obstacle populations are characterized by the same thermal activation parameters. For instance, if v^* is evaluated for several materials at $\sigma = 0.005\widehat{\sigma}$, then Eq. 6.19 simplifies to the following:

$$v^* = kTM \frac{\partial \left(\ln \frac{\dot{\epsilon}}{\dot{\epsilon}_o} \right)}{\partial \sigma} \cong 10.6M\mu_0 b^3 \frac{g_o}{\widehat{\sigma}} \quad (6.20)$$

and a plot of v^* versus $\mu_0 b^3$ should yield a straight line with a slope of $10.6Mg_o/\widehat{\sigma}$. This plot will be generated for several BCC metals in Sect. 9.3 and for austenitic stainless steels in Sect. 11.2 to demonstrate its applicability.

When deformation in a materials system is controlled by the interaction of dislocations with two distinct obstacle populations—as defined by Eqs. 6.14, 6.15, and 6.16—the activation volumes characterizing each obstacle population is of more mechanistic relevance than the overall activation volume. In this case:

$$v_1^* = - \frac{\partial \Delta G}{\partial \tau} = kT \frac{\partial \ln \left(\frac{\dot{\gamma}}{\dot{\gamma}_{01}} \right)}{\partial \tau_1} \quad (6.21)$$

$$v_2^* = - \frac{\partial \Delta G}{\partial \tau} = kT \frac{\partial \ln \left(\frac{\dot{\gamma}}{\dot{\gamma}_{02}} \right)}{\partial \tau_2} \quad (6.22)$$

If $p_1 = p_2 = 1/2$ and $q_1 = q_2 = 3/2$, then the activation volumes are as follows:

$$v_1^* = \frac{3}{4} b^3 M g_{01} \mu_0 \frac{1}{\sqrt{\widehat{\sigma}_1} \sigma} \left(1 - \sqrt{\frac{\sigma}{\widehat{\sigma}_1}} \right)^{1/2} \quad (6.23)$$

$$v_2^* = \frac{3}{4} b^3 M g_{02} \mu_0 \frac{1}{\sqrt{\widehat{\sigma}_2} \sigma} \left(1 - \sqrt{\frac{\sigma}{\widehat{\sigma}_2}} \right)^{1/2} \quad (6.24)$$

If the populations are characterized by different values of p and/or q , then the differentiations in Eqs. 6.21 and 6.22 would give somewhat different expressions than derived for $p = 1/2$ and $q = 3/2$. Comparison of the activation volumes of different obstacle populations and of the activation volumes for similar obstacle populations using Eq. 6.20 offers insight into the operative deformation mechanisms.

6.5 The Evolution Equation

When a metal is deformed, the dislocation density increases, and a third internal state variable function— $\widehat{\sigma}_\varepsilon$ —is added to the governing equation (Eq. 6.14). It is this function that evolves according to Eq. 5.12 with a temperature and strain rate dependence defined by Eq. 5.13, which was revised to Eq. 6.7. These equations were written in a general form in terms of the evolution of a mechanical threshold stress, without addressing which defect population was evolving. In fact, the evolving defect population is the stored dislocation density. As such, these equations are more properly written:

$$\frac{d\widehat{\sigma}_\varepsilon}{d\varepsilon} = \theta_{II} \left(1 - \frac{\widehat{\sigma}_\varepsilon}{\widehat{\sigma}_{\varepsilon s}(\dot{\varepsilon}, T)} \right) \quad (6.25)$$

and

$$\ln \widehat{\sigma}_{\varepsilon s} = \ln(\widehat{\sigma}_{\varepsilon s0}) + \frac{kT}{\mu b^3(g_{\varepsilon s0})} \ln \frac{\dot{\varepsilon}}{\dot{\varepsilon}_{\varepsilon s0}} \quad (6.26)$$

to explicitly specify that the evolution is of $\widehat{\sigma}_\varepsilon$.

While approximating experimentally observed evolution, Eq. 6.25 does not offer as accurate a fit with experimental data as is generally necessary. In the original Follansbee and Kocks experiments with copper [5], Eq. 6.25 was replaced with Eq. 6.27:

$$\frac{d\widehat{\sigma}_\varepsilon}{d\varepsilon} = \theta_{II}(\dot{\varepsilon}) \left(1 - \frac{\tan h \left[2 \frac{\widehat{\sigma}_\varepsilon}{\widehat{\sigma}_{\varepsilon s}(\dot{\varepsilon}, T)} \right]}{\tan h(2)} \right) \quad (6.27)$$

Later, Eq. 6.25 was modified and the generalized form of the evolution equation became [6]:

$$\frac{d\widehat{\sigma}_\varepsilon}{d\varepsilon} = \theta_{II}(\dot{\varepsilon}) \left(1 - \frac{\widehat{\sigma}_\varepsilon}{\widehat{\sigma}_{\varepsilon s}(\dot{\varepsilon}, T)} \right)^\kappa \quad (6.28)$$

where $\theta_{II}(\dot{\varepsilon})$ and κ are empirically derived. (Note that Eq. 6.27 is not used going forth.) Whereas it is possible to derive Eq. 6.25 from a simple balance between dislocation generation and recovery (e.g., see the derivation published by Estrin [7]), it has mostly arisen from analysis of experimental data [8]. The modified evolution law represented by Eq. 6.28 is completely empirical.

Figure 6.8 compares the evolution curves as described using Eq. 6.28 with several values of κ and Eq. 6.27 with some measurements of $\widehat{\sigma}_\varepsilon$ published by Follansbee and Kocks [5] (to be described in Sect. 8.2). For this set of data, Eq. 6.28 with $\kappa = 2$ most

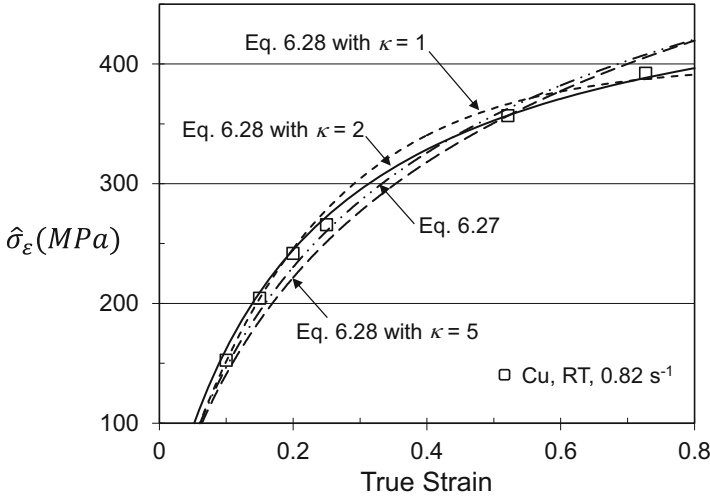


Fig. 6.8 Comparison of evolution predictions described by Eq. 6.28 (with several values of κ) and Eq. 6.27 with one experimental data set (to be detailed in Sect. 8.2). The ordinate scale is chosen to emphasize the slight differences in the predictions. All of the curves approach a stress of zero at a strain of zero

closely represents the experimental results. It will be demonstrated in Chap. 8 through 12 that either $\kappa = 1$ or $\kappa = 2$ achieves good agreement with the measured evolution in the host of metals and alloys considered in this monograph.

The strain rate dependence of θ_{II} has also been empirically defined using an equation of the form

$$\theta_{II} = A_o + A_1 \ln \dot{\epsilon} + A_2 \sqrt{\dot{\epsilon}} \tag{6.29}$$

The second and third terms in Eq. 6.29 are of importance only at very high strain rates.

6.6 Adiabatic Deformation

Recall from general physics that the energy W_d expended in deforming a test specimen is as follows:

$$W_d = \int F dL = \int \sigma A dL = \int \sigma V \frac{dL}{L} = \int \sigma V d\epsilon = \int \sigma \frac{m}{\rho} d\epsilon \tag{6.30}$$

where m is the mass and ρ is the density. Accordingly, the work of deformation is proportional to area under the stress–strain curve. Part of this energy is in the form of the “internal” energy created by defects, where the displacement of atoms in the vicinity of dislocations and the formation of new interfaces represent energy storage mechanisms. But, in fact, most of the energy is expended as heat. The fraction expended as heat is somewhere between 90% and 95%. Consider a tensile or compression test with the ends of the test specimen connected to grips. When the test is performed slowly, the heat generated simply transfers to the grips, and the temperature of the specimen does not change. When the test is performed quickly, there is insufficient time for heat transfer to the grips, and the temperature of the test specimen can rise. This limiting case for the latter scenario is termed “adiabatic deformation,” where the word adiabatic is the thermodynamic term for a process where there is no heat transfer. In this case, the temperature rise may be predicted from a simple energy balance:

$$q = mc_p\Delta T = \psi \frac{m}{\rho} \int \sigma d\epsilon \quad (6.31)$$

or

$$\Delta T = \frac{\psi}{\rho c_p} \int \sigma d\epsilon \quad (6.32)$$

where c_p is the heat capacity—which in most materials varies with temperature (see Box 6.4 and refer to the National Physical Laboratory Kaye and Laby Table of Physical & Chemical Constants [9] for temperature-dependent heat capacity data for a host of materials). Taking the simple material described by the coefficients in Tables 5.1 and 5.2 and the stress–strain curve at the strain rate of 1 s^{-1} and temperature of 150 K, Fig. 6.9 plots the stress and temperature as a function of strain according to Eqs. 5.11, 5.12, 5.13, and 6.32 for the case of adiabatic deformation.

Box 6.4 Temperature Dependence of the Heat Capacity

A material’s heat capacity affects its ability to convert added energy to a temperature rise as defined by Eq. 6.32. In 1819 Dulong and Petit observed experimentally that for many solids at room temperature the heat capacity is $\sim 3R$, where R is the gas constant, or 25 J/K/mol. This value provides a good estimate for many materials. However, measured heat capacities demonstrate strong temperature dependence—approaching a value of 0 at 0 K and approaching a linear temperature dependence at high temperatures. It is desirable to include the temperature-dependent heat capacity when estimating the temperature rise due to adiabatic deformation. Models for this temperature

(continued)

Box 6.4 (continued)

dependence based on quantum theory were proposed by Einstein (1906) and later by Debye (1912). A simplified expression for the observed temperature dependence of the heat capacity which is consistent with the theoretical analyses at low temperatures and experimental observations is as follows:

$$C_p = A_C + BT + \frac{C}{T^2} \quad (6.B5)$$

A very useful compilation of temperature-dependent heat capacity data for a variety of materials, including alloys, is available at the NPL Kaye and Laby web site [9]. Table 6.5 lists values of the constants in this equation for several pure metals and common alloys. Other materials are included in the Kaye and Laby compilation.

A. -T. Petit and P. -L Dulong, 1819, “Recherches sur quelques points importants de la Théorie de la Chaleur,” *Annales de Chimie et de Physique* 10: 395–413.

A. Einstein, 1907, “Die Plancksche Theorie der Strahlung und die Theorie der spezifischen Wärme”, *Annalen der Physik*, 22, pp. 180–190.

P. Debye, 1912, “Zur Theorie der spezifischen Waerme”, *Annalen der Physik* (Leipzig), 39, p. 789.

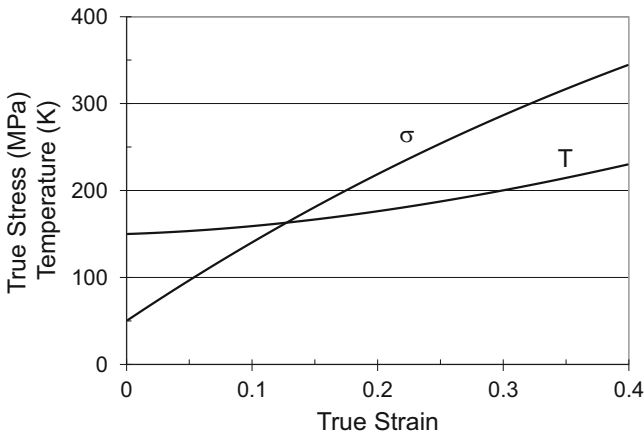


Fig. 6.9 Dynamic stress–strain curve at a strain rate of 1 s^{-1} and a temperature of 150 K for a material with the model constants listed in Tables 5.1 and 5.2 showing the variation of stress and specimen temperature with strain

Table 6.5 Model parameter describing temperature-dependent heat capacity in several metals

Material	A_C (J/g/K)	B (J/g/K ²)	C (J/K/g)
Cu	0.357	9.84×10^{-5}	-77.56
Ni	0.40	2.5×10^{-4}	-1700
Fe (α)	0.334	4.2×10^{-4}	-1350
Ta	0.138	1.95×10^{-5}	-270
Ti	0.485	1.85×10^{-4}	-1700
Al	0.775	4.64×10^{-4}	-2800
Mo	0.245	5.1×10^{-5}	-950
Nb	0.26	4.0×10^{-5}	-572
Co	0.345	2.49×10^{-4}	-1175
Be	1.28	2.0×10^{-3}	-8850
Zr	0.259	1.1×10^{-4}	-660
18Cr 10Ni SS	0.362	4.15×10^{-4}	-1350
Ti 6Al 4 V	0.495	2.3×10^{-4}	-1850
Zircaloy 2	0.26	1.05×10^{-4}	-660

Figure 6.9 should be compared to the prediction at the same temperature and strain rate shown in Fig. 5.11; this prediction assumed the test to be isothermal. Although difficult to see when comparing these stress-strain curve, the stress builds up slightly less in the adiabatic case (Fig. 6.9) than in the isothermal case (Fig. 5.11) due to the temperature rise. Over the 40% strain range in this figure, the temperature has increased ~ 80 K.

Between the isothermal case and the adiabatic case, of course, there is a transition range, where the specimen heats up but less than predicted for fully adiabatic deformation. A full heat transfer analysis would be required (with accurate specimen dimensions and grip geometry) to fully understand the specimen temperature during this transition region. A good approximate for the time to achieve a steady-state thermal distribution at a distance of x is as follows:

$$t \approx \frac{x^2}{\alpha} \quad (6.33)$$

where α is the thermal diffusivity. Taking $x = 5$ mm (e.g., center of a 1 cm long test specimen) and $\alpha = 12$ mm²/s (which is the value for a low carbon steel; copper has a value $10\times$ this) gives $t \approx 2$ s, which corresponds to a strain rate of 0.25 s⁻¹ to achieve a strain of 0.5. Thus, a strain rate of 1 s⁻¹ is a reasonable estimate for the boundary between isothermal and adiabatic conditions. This will be the assumption going forth.

6.7 Summary

This chapter has described the motivation for and the details of modifications made from the simple kinetic and hardening laws introduced in previous chapters.

Including the temperature dependence of the shear modulus is well justified mechanistically. However, the temperature dependence of the shear modulus is typically small, and, in fact, $\mu(T)$ hardly affects model predictions in most cases.

Because most metals are strengthened by more than one strengthening mechanism, writing the kinetic equation to allow for this is an essential modification. Introduction of a second- or third-state variable led to quite good agreement between model predictions and data sets in niobium and iron. The next chapter will detail how these state parameters can be assessed more rigorously.

The activation volume v^* was defined, and an expression for v^* was derived for the special case of $p = 1/2$ and $q = 3/2$ in Eq. 6.12 (and subsequent equations). Use of the activation volume to add insight into operative deformation mechanisms was introduced. Further examples of this are given in subsequent chapters.

A modified hardening law from that introduced earlier is necessary to match experimental results. No theoretical justification for a strain rate-dependent θ_H or an exponent κ other than unity was offered.

An impact of the modifications introduced in this chapter is that numerical methods (as opposed to explicit mathematical solutions) become necessary for model implementation. This becomes more evident in the example described in the next chapter.

Exercises

- 6.1 Exercise 4.5 listed yield stress versus temperature and strain rate measurements for a hypothetical metal. Analysis of the data using Eq. 4.14 led to an estimated value of $\hat{\sigma}$ equal to 866 MPa. Assume now that the material has a temperature-dependent shear modulus equivalent to that of nickel and has a Burgers vector of 0.26 nm. For this exercise, analyze this data set using Eq. 6.6. (Remember that $\sigma_a = 0$.) (a) Plot σ/μ versus $(kT/\mu b^3) \ln(10^8 s^{-1}/\dot{\epsilon})$. (b) If the data set in Exercise 4.6 was created using Eq. 4.14 (with a random number generator to mimic experimental scatter), can you think of a reason why the apparent scatter in the plot just created is greater than the scatter in the plot created in Exercise 4.5?
- 6.2 What is the estimated threshold stress when the data set (Exercise 6.1) is analyzed using Eq. 6.6? Compare this to the value of 866 MPa that was derived in Exercise 4.5.
- 6.3 Table 6.E3 lists yield stress measurements as a function of test temperature and strain rate for a metal. Assuming a Burgers vector of 0.26 nm, a temperature-dependent shear modulus equivalent to that of molybdenum, and an athermal stress of 100 MPa, find $\hat{\sigma}$ and g_o using Eq. 6.6. Assume $\dot{\epsilon}_o = 10^8 \text{ s}^{-1}$.
- 6.4 Table 6.E4 lists single crystal elastic constants for gold. (These are derived from data reported by Collard [10].) Derive the constants to Eq. 6.8 for this material.

Table 6.E3 Yield stress as a function of temperature and strain rate for a metal (Exercise 6.3)

T (K)	Rate (s^{-1})	Yield stress (MPa)
200	0.001	1124
300	0.001	998
400	0.001	897
500	0.001	799
200	1.0	1156
300	1.0	1090
400	1.0	1002
500	1.0	934
200	2000	1203
300	2000	1167
400	2000	1125
500	2000	1065

Table 6.E4 Single crystal elastic constants as a function of temperature for gold (Exercise 6.4)

T (K)	c_{11} (GPa)	c_{12} (GPa)	c_{44} (GPa)
10	201.0	170.0	45.6
50	200.7	169.8	45.5
100	199.5	168.9	45.2
150	198.0	167.7	44.6
200	196.3	166.5	44.0
250	194.7	165.3	43.4
300	193.0	164.0	42.8
350	191.3	162.7	42.1
400	189.6	161.4	41.4
450	187.9	160.1	40.8
500	186.1	158.9	40.1
550	184.4	157.6	39.4
600	182.7	156.3	38.8
650	181.0	155.0	38.1
700	179.2	153.7	37.4
750	177.5	152.4	36.8
800	175.8	151.1	36.1
850	174.1	149.8	35.4
900	172.3	148.5	34.8
950	170.6	147.2	34.1
1000	168.9	145.9	33.4

6.5 Table 6.E5 lists yield stress measurements as a function of test temperature and strain rate for a metal. This metal has a Burgers vector of 0.26 nm, a temperature-dependent shear modulus equivalent to that of molybdenum, and an athermal stress of 100 MPa. (a) Plot $(\sigma - \sigma_a)/\mu$ versus $kT/\mu b^3 \ln(10^8 s^{-1}/\dot{\epsilon})$. Is a straight line a good fit to this data set? (b) Plot

Table 6.E5 Yield stress as a function of temperature and strain rate for a metal (Exercise 6.5)

T (K)	Rate (s^{-1})	Yield stress (MPa)
200	0.001	724
300	0.001	574
400	0.001	454
500	0.001	358
200	1.0	817
300	1.0	681
400	1.0	570
500	1.0	476
200	2000	943
300	2000	833
400	2000	739
500	2000	656

$[(\sigma - \sigma_a)/\mu]^{1/2}$ versus $[kT/\mu b^3 \ln(10^8 s^{-1}/\dot{\epsilon})]^{2/3}$ (i.e., as with Eq. 6.9 with $p = 1/2$ and $q = 3/2$). Is a straight line a good fit now? (c) Compute values for $\hat{\sigma}$ and g_o .

- 6.6 If the athermal stress in Exercise 6.5 is zero, show that $\hat{\sigma} = 1277$ MPa and $g_o = 0.245$.
- 6.7 For the metal described in Exercise 6.6, plot the activation volume versus stress over the stress range of 5 MPa to 800 MPa. Assume $M = 3.1$. (Since the activation volume is a very small number, it is often plotted as v^*/b^3 , which also gives a dimensionless quantity).
- 6.8 Take the data set in Table 6.3 along with the model constants in Table 6.2 and plot $[\sigma/\mu]^{1/2}$ versus $[kT/\mu b^3 \ln(10^8 s^{-1}/\dot{\epsilon})]^{2/3}$ (as in Fig. 6.4). What happens to the value of s_1 for the data points at a strain rate of 0.0001 s⁻¹ and above temperatures of 250 K?
- 6.9 Table 6.E9 lists yield stress measurements as a function of test temperature and strain rate for a metal. This metal has a Burgers vector of 0.26 nm, a temperature-dependent shear modulus equivalent to that of molybdenum, and an athermal stress of 50 MPa. 9a) Plot $[(\sigma - \sigma_a)/\mu]^{1/2}$ versus $[kT/\mu b^3 \ln(10^8 s^{-1}/\dot{\epsilon})]^{2/3}$ (i.e., as with Eq. 6.9 with $p = 1/2$ and $q = 3/2$). A straight line fit provides a pretty good fit, but do you see some lingering curvature in the data set plotted on these axes? (b) From the best linear fit, compute values for $\hat{\sigma}$ and g_o .
- 6.10 For the metal described in Exercise 6.9, assume that deformation is described by Eq. 6.14. It is also known that the athermal stress is 50 MPa and that other model constants are given in Table 6.E10. Find suitable values of $\hat{\sigma}_2$ and g_{o2} . (Note, there is no elegant way to do this; one must program the governing equation (Eq. 6.14) and search for values of these variables that, when combined with the values of other model parameters in Table 6.E10, provide good agreement with the measured stresses.)

Table 6.E9 Yield stress as a function of temperature and strain rate for a metal (Exercise 6.9)

T (K)	Rate (s^{-1})	Yield stress (MPa)
200	0.001	1079
300	0.001	932
400	0.001	818
500	0.001	728
200	1.0	1166
300	1.0	1031
400	1.0	920
500	1.0	828
200	2000	1288
300	2000	1174
400	2000	1077
500	2000	990

Table 6.E10 Model constants for Equation 6.14 for the metal described in Exercise 6.9 (Exercise 6.10)

Parameter	Obstacle 1	Obstacle 2
p	0.5	1
q	1.5	0.667
$\dot{\epsilon}_o$ (s^{-1})	10^8	10^{10}
$\hat{\sigma}$ (MPa)	1000	
g_o	0.15	

References

1. A. Kelly, R.B. Nicholson, *Strengthening Methods in Crystals* (Wiley, New York, 1971), p. 37
2. U.F. Kocks, A.S. Argon, M.F. Ashby, Thermodynamics and kinetics of slip, in *Progress in Materials Science*, ed. by B. Chalmers, J. W. Christian, T. B. Massalski, vol. 19, (Pergamon Press, Oxford, 1975), p. 119
3. Y.P. Varshni, Temperature dependence of the elastic constants. *Phys. Rev. B* **2**(10), 3952–3958 (1970)
4. P.S. Follansbee, Analysis of deformation kinetics in seven body-centered-cubic pure metals using a two-obstacle model. *Metall. Mater. Trans. A* **41A**, 3080–3090 (2010)
5. P.S. Follansbee, U.F. Kocks, A constitutive description of the deformation of copper based on the use of the mechanical threshold stress as an internal state variable. *Acta Metall.* **36**(1), 81–93 (1988)
6. A. Bronkhorst, S.R. Kalidindi, L. Anand, An experimental and analytical study of the evolution of crystallographic texturing in fcc materials. *Text. Microstruc.* **14–18**, 1031–1036 (1991)
7. Y. Estrin, Dislocation-density-related constitutive modeling, in *Unified Constitutive Laws of Plastic Deformation*, ed. by A. S. Krausz, K. Krausz, (Academic Press, San Diego, 1996), pp. 69–106
8. U.F. Kocks, H. Mecking, Physics and phenomenology of strain hardening: the FCC case. *Prog. Mater. Sci.* Pergamon Press **48**, 171–273 (2003)
9. National Physical Laboratory, Kaye & Laby Tables of Physical & Chemical Constants,” 1995. Available through http://www.kayelaby.npl.co.uk/general_physics/2_3/2_3_6.html (accessed on August 2, 2013).
10. S.M. Collard, High-temperature elastic constants of gold single crystals. PhD Thesis, Rice University, 1991, available from <http://www.dspace.rice.edu/bitstream/handle/1911/16433/9136015.PDF?sequence=1>

Chapter 7

Data Analysis: Deriving MTS Model Parameters



Introduction

Chapter 6 presented further developments of the mechanical threshold stress (MTS) constitutive model and defined the basic set of equations that comprise this model. These were Eqs. 6.17 and 6.18 for the yield stress as a function of temperature and strain rate for any combination of obstacle populations (characterized by $\hat{\sigma}_i$), Eqs. 6.25 and 6.26 for evolution of $\hat{\sigma}_\epsilon$, Eq. 6.8 for the temperature-dependent shear modulus, and Eq. 6.32 for the rise of temperature with strain for the case of adiabatic deformation. This chapter outlines how MTS model constants are derived.

7.1 A Hypothetical Alloy

Let's create an alloy FoLLYalloy—an alloy of Fosium (Fo) with additions of Lopper (L) and Lyeria (Ly). Fosium has a BCC crystal structure, while Lopper and Lyeria provide solution hardening. Fosium is formed using *vacuum arc remelting* (VAR) which helps to maintain low levels of undesirable elemental additions (e.g., O, S, and C). After the ingot solidifies, it is heavily worked using mechanical deformation—often referred to as “thermo-mechanical processing,” e.g., *cross rolling*—and annealed at 1280 K for 1 hour to achieve a recrystallized, isotropic structure with an average grain size of 50 μm . The goal is to develop for this alloy a constitutive model based on the MTS formulation.

Supplementary Information The online version contains supplementary material available at [\[https://doi.org/10.1007/978-3-031-04556-1_7\]](https://doi.org/10.1007/978-3-031-04556-1_7)

7.2 Pure Fosium

With its BCC crystal structure, it is anticipated that the Peierls obstacle will serve as an obstacle to dislocation motion at low temperatures and high strain rates. Therefore, the experimental assessment starts with pure Fosium, which, fortunately, can be processed using similar melt and metal working technology to achieve the same isotropic microstructure with a similar grain size. We also take this opportunity to measure some physical properties, which are summarized in Table 7.1.

Test specimens are machined for testing at strain rates of 0.001 s^{-1} , 1 s^{-1} , and 1000 s^{-1} and temperatures from 100 K to 750 K. Table 7.2 lists the test conditions and the measured yield stress (0.002 strain offset). Figure 7.1 is a plot of yield stress versus temperature for testing at the lowest strain rate. Note in Fig. 7.1 as well as in Table 7.2 that the yield stress asymptotically approaches a minimum value of 100 MPa.

This limiting value (100 MPa) which becomes independent of temperature is assumed to be the athermal stress σ_a . Next, the data in Table 7.2 will be plotted on coordinates suggested by Eq. 6.6 with $\dot{\epsilon}_o = 10^8 \text{ s}^{-1}$. Note that all of the data points in this plot, included as Fig. 7.2, fall on a smooth curve and that since σ_a was subtracted from σ the curve asymptotically approaches zero at high temperatures and low strain rates.

Next, this same data set is plotted in Fig. 7.3 on axes suggested by the revisions introduced in Eq. 6.9. It is evident in this figure that choosing $p = 1/2$ and $q = 3/2$ collapses all of the data onto a single line. The agreement between the best-fit line

Table 7.1 Burgers vector and temperature-dependent shear modulus parameters for Fosium

Parameter	Equation	Value	Unit
b		0.26	nm
μ_o	6.8	100	GPa
D_o		15	GPa
T_o		250	K

Table 7.2 Yield stress (0.002 offset) measurements in pure Fosium

Temperature (K)	Yield stress (MPa)		
	$\dot{\epsilon} = 0.001 \text{ s}^{-1}$	$\dot{\epsilon} = 1.0 \text{ s}^{-1}$	$\dot{\epsilon} = 1000 \text{ s}^{-1}$
100	735	799	874
200	538	614	719
300	385	466	584
400	262	350	478
500	184	264	373
550	150	–	–
600	124	190	292
650	113	–	–
700	102	–	–
750	101	–	–

Fig. 7.1 Variation of yield stress with temperature for testing at 0.001 s^{-1} in pure Fosium

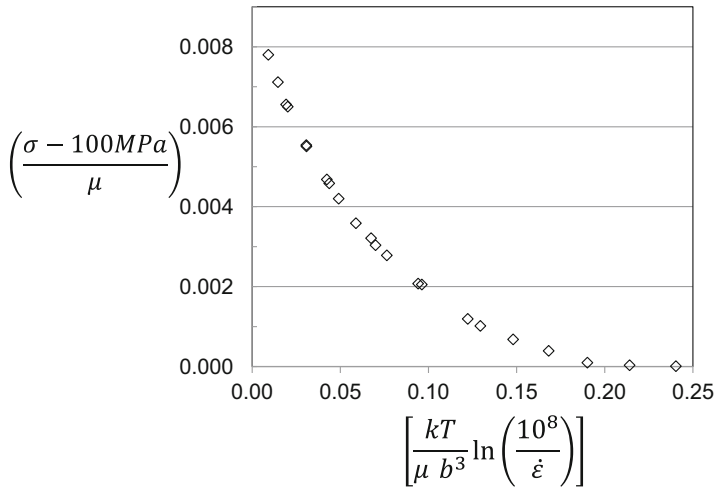
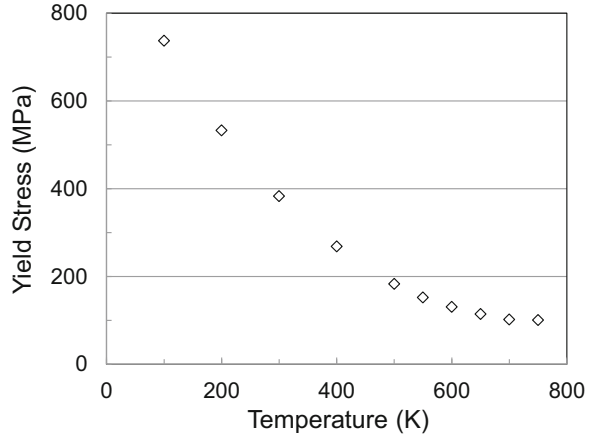


Fig. 7.2 Variation of yield stress with temperature for measurements in pure Fosium plotted on coordinates suggested by Eq. 6.6

and the data points highlights the scatter in the measurements, which is typical of measurements of this nature. The intercept at $T = 0$ is $\sqrt{\hat{\sigma}/\mu_o}$ which equals 0.10, implying that $\hat{\sigma}/\mu_o = 0.001$ or, since $\mu_o = 100 \text{ GPa}$, $\hat{\sigma} = 1000 \text{ MPa}$.

The slope of the line in Fig. 7.3 is related to the normalized activation energy g_o . To see this, assume that the data in Fig. 7.2 is instead plotted on a straight line with a slope m (which is a negative number). From Eq. 6.6:

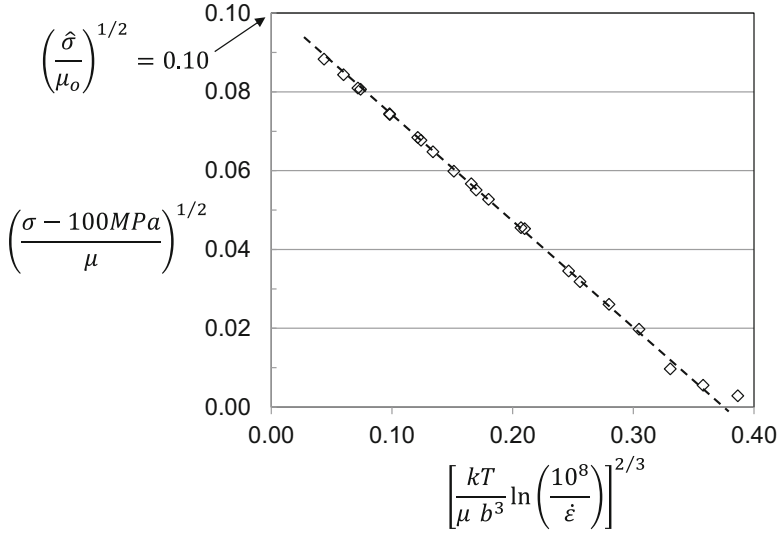


Fig. 7.3 Variation of yield stress with temperature for measurements in pure Fosium plotted on coordinates suggested by Eq. 6.9

$$m = -\frac{1}{g_o} \frac{\hat{\sigma}}{\mu_o} \quad (7.1)$$

The more complex Eq. 6.9 was used in Fig. 7.3:

$$\left(\frac{\sigma - \sigma_a}{\mu} \right)^p = \left\{ 1 - \left[\frac{kT}{g_{op} \mu b^3} \ln \left(\frac{\dot{\epsilon}_o}{\dot{\epsilon}} \right) \right]^{1/q} \right\} \left(\frac{\hat{\sigma}_p}{\mu_o} \right)^p \quad (6.9')$$

Note how the threshold stress $\hat{\sigma}$ in this equation has been replaced with $\hat{\sigma}_p$ and the normalized activation energy g_o has been replaced with g_{op} to acknowledge that it is the Peierls barrier that is restricting dislocation motion in Fo.¹ The correlation between the slope and g_{op} is more difficult to analyze in Eq. 6.9' due to the power $1/q$, but it still can be derived (using a power series approximation or through numerical techniques). For the data in Fig. 7.3, $g_o = 0.2$.

Pure Fo thus is characterized by an obstacle population with $\hat{\sigma} = 1000$ MPa and $g_o = 0.2$. In pure BCC metals, this barrier is the Peierls barrier which is identified with the subscript "p." Thus, $\hat{\sigma}_p = 1000$ MPa and $g_{op} = 0.2$. Along with these values, for this Peierls barrier, $p = 1/2$, $q = 3/2$, and $\dot{\epsilon}_o = 10^8$ s⁻¹.

¹According to the general form of Eq. 6.12 given by Eqs. 6.15 and 6.16, one may wish to also specify q_p , p_p , and $\dot{\epsilon}_{op}$, but to simplify the analyzes, these were taken as $1/2$, $3/2$, and 10^8 s⁻¹, respectively.

7.3 Hardening in Pure Fosium

While Figs. 7.1 through 7.3 plotted only the yield stress as a function of temperature and strain rate, full stress–strain data for the conditions specified in Table 7.2 is available. The measurements at 300 K are shown in Fig. 7.4. It is tempting to begin to analyze the hardening behavior according to Eq. 6.25. However, these measurements were in pure Fo, which has not yet been alloyed. Since this may alter the hardening behavior, it is preferable to proceed with measurements in the unstrained alloy.

7.4 Yield Stress Kinetics in Unstrained FoLLyalloy

The approach for the alloy mirrors the approach taken for pure Fo. Table 7.3 lists the temperature and strain rate conditions for testing and lists the measured yield stresses. Comparison with the measurements in Table 7.2 for pure Fo validates that the addition of L and Ly has strengthened the alloy. Figure 7.5 plots the yield stress data on the coordinates used for Fig. 7.2 (i.e., $p = q = 1$). The athermal stress is assumed to remain at 100 MPa since the grain size has been replicated. Figure 7.6 shows the data plotted on coordinates with Eq. 6.9 with $p = 1/2$ and $q = 3/2$.

Whereas these coordinates yielded a linear dependence for pure Fo in Fig. 7.3, it is evident that the FoLLyalloy data exhibit a distinct curvature at high values of the abscissa. The addition of an additional strengthening mechanism (solution hardening due to L and Ly) implies that the yield stress dependence on strain rate and temperature is modeled with an equation of the form of Eq. 6.14:

$$\frac{\sigma}{\mu} = \frac{\sigma_a}{\mu} + s_p(\dot{\epsilon}, T) \frac{\hat{\sigma}_p}{\mu_o} + s_i(\dot{\epsilon}, T) \frac{\hat{\sigma}_i}{\mu_o} \quad (7.2)$$

Fig. 7.4 Example stress–strain curves measured at various strain rates (at RT) in pure Fosium

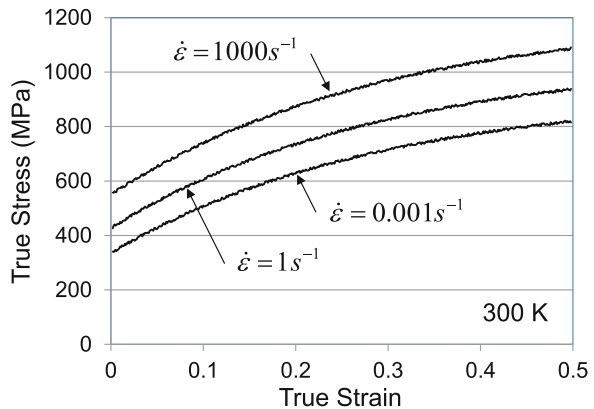


Table 7.3 Yield stress versus temperature and strain rate for unstrained FoLLyalloy

Temperature (K)	Yield stress (MPa)		
	$\dot{\epsilon} = 0.001 \text{ s}^{-1}$	$\dot{\epsilon} = 1.0 \text{ s}^{-1}$	$\dot{\epsilon} = 1000 \text{ s}^{-1}$
100	1038	1106	1197
200	776	872	996
300	560	671	829
400	404	523	673
500	296	400	548
550	258	–	–
600	226	305	442
650	205	–	–
700	187	–	–
750	175	–	–

Fig. 7.5 Yield stress measurements in Fo alloyed with L and Ly plotted on the same coordinates as in Fig. 7.2

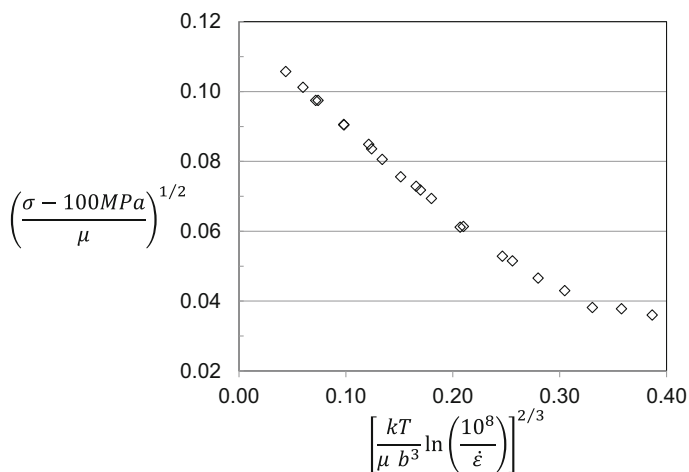
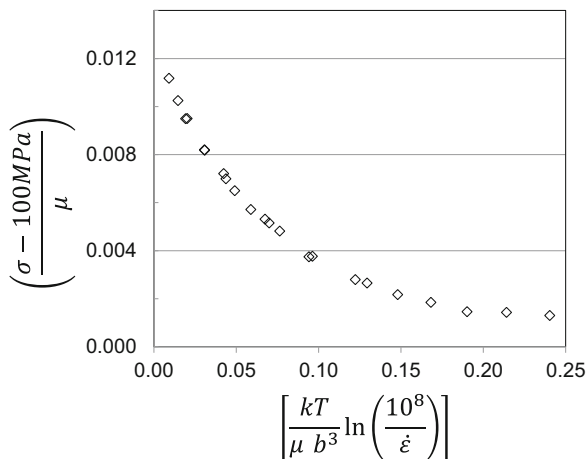


Fig. 7.6 Yield stress measurements in the Fosium alloy plotted on the same coordinates as in Fig. 7.3

where s_p and $\widehat{\sigma}_p$ reflect the Peierls obstacle, described by the model parameters specified in the last paragraph of Sect. 7.2, and the subscript “ i ” refers to the impurity element additions. Even though two hardening elements were added, the obstacle population is treated collectively using a single threshold stress. While the hardening of L may in fact differ from the hardening of Ly, which would necessitate splitting these into two populations, the premise is that the impurity hardening can be treated with a single state parameter. For this population, the parameters comprising s_i are unknown (e.g., g_{oi} , p_i , q_i and $\dot{\epsilon}_{oi}$). While it will be necessary to assume values for some of these based on experience, if sufficient experimental data is available, these parameters can be derived more explicitly. Recall from Eq. 6.16 that:

$$s_i(\dot{\epsilon}, T) = \left\{ 1 - \left[\frac{kT}{g_{oi}\mu b^3} \ln \left(\frac{\dot{\epsilon}_{oi}}{\dot{\epsilon}} \right) \right]^{1/q_i} \right\}^{1/p_i} \quad (7.3)$$

In practice, the sensitivity of the model agreement with experimental data to values of p_i , q_i , and $\dot{\epsilon}_{oi}$ is small, and effort is instead focused on identifying $\widehat{\sigma}_i$ and g_{oi} . Choosing $p_i = 1/2$, $q_i = 3/2$, and $\dot{\epsilon}_{oi} = 10^8 \text{ s}^{-1}$, model predictions (at prescribed temperature and strain rates) can be computed using Eqs. 7.2 and 7.3, and $s_p(\dot{\epsilon}, T)$ as derived from Fig. 7.3. A numerical prediction requires one to assume values of $\widehat{\sigma}_i$ and g_{oi} . The best fit—and therefore the deduced values of $\widehat{\sigma}_i$ and g_{oi} —has the lowest error, as determined, for example, from the square root of the sum of squares of the difference of the measured stress, σ_m , and the model prediction, σ :

$$\text{Error} = \left\{ \sum (\sigma_m - \sigma)^2 \right\}^{1/2} \quad (7.4)$$

Figure 7.7 shows a model prediction for the FoLLyalloy data using $\widehat{\sigma}_i = 400 \text{ MPa}$ and $g_{oi} = 0.8$ (and, of course, $p_i = 1/2$, $q_i = 3/2$, and $\dot{\epsilon}_{oi} = 10^8 \text{ s}^{-1}$). The model

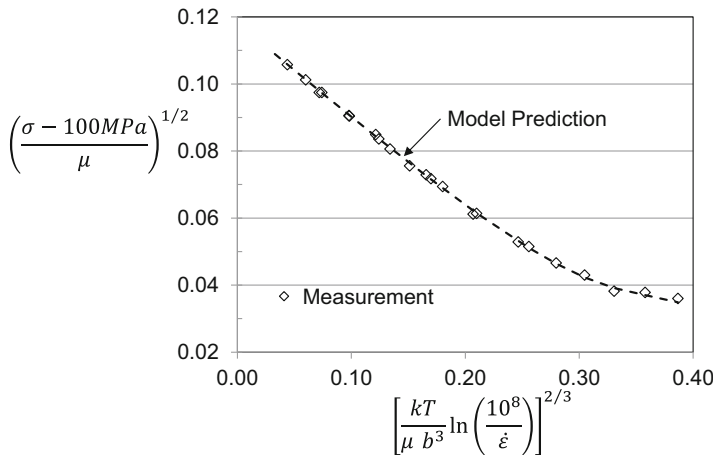


Fig. 7.7 Model prediction for the alloy with $p_p = p_i = 1/2$, $q_p = q_i = 3/2$, $\dot{\epsilon}_{op} = 10^8 \text{ s}^{-1}$, $\dot{\epsilon}_{oi} = 10^8 \text{ s}^{-1}$, $g_{op} = 0.2$, $g_{oi} = 0.8$, $\widehat{\sigma}_p = 1000 \text{ MPa}$, $\widehat{\sigma}_i = 400 \text{ MPa}$, and $\sigma_a = 100 \text{ MPa}$

Table 7.4 Error in the fit of Eq. 7.2 to yield stress measurements evaluated for three combinations of $\hat{\sigma}_i$ and g_{oi}

$\hat{\sigma}_i$ (MPa)	g_{oi}	Error, Eq. 7.4, (MPa)
400	0.8	24
365	1.0	56
460	0.6	106

prediction is shown as a smooth average curve through the actual predicted data points, which exhibit noticeable experimental scatter. Since values of p , q , and $\dot{\epsilon}_o$ are assumed to be the same for both obstacle populations, the plotting difficulty introduced in Sect. 6.3 and illustrated in Fig. 6.4 is absent in this hypothetical alloy.

To demonstrate the sensitivity of the fit to the assumed $\hat{\sigma}_i$ and g_{oi} values, Table 7.4 lists three combinations of these parameters and the associated error, according to Eq. 7.4, summed over all of the data points (e.g., in Fig. 7.7). Errors are shown to rise quickly with values other than $\hat{\sigma}_i = 400$ MPa and $g_{oi} = 0.8$. For FoLLyallyloy in the unstrained condition, Eq. 7.2 becomes the following:

$$\frac{\sigma}{\mu} = \frac{100 \text{ MPa}}{\mu} + s_p(\dot{\epsilon}, T) \frac{1000 \text{ MPa}}{\mu_o} + s_i(\dot{\epsilon}, T) \frac{400 \text{ MPa}}{\mu_o} \quad (7.5)$$

where:

$$s_p(\dot{\epsilon}, T) = \left\{ 1 - \left[\frac{kT}{(0.2)\mu b^3} \ln \left(\frac{10^8 s^{-1}}{\dot{\epsilon}} \right) \right]^{2/3} \right\}^2 \quad (7.6)$$

and:

$$s_i(\dot{\epsilon}, T) = \left\{ 1 - \left[\frac{kT}{(0.8)\mu b^3} \ln \left(\frac{10^8 s^{-1}}{\dot{\epsilon}} \right) \right]^{2/3} \right\}^2 \quad (7.7)$$

Since b and $\mu(T)$ were specified in Table 7.1, the yield stress for any temperature and strain rate (within the range probed experimentally) may be computed.

7.5 Hardening in FoLLyallyloy

Stress–strain curves at strain rates of 0.001 s^{-1} , 1 s^{-1} , and 1000 s^{-1} at temperatures between 100 K and 600 K are shown in Figs. 7.8, 7.9, and 7.10.² (To simplify this discussion, it is assumed that the deformation—even at the higher strain rates—is isothermal. This is possible if the heat capacity of this fictitious alloy is unusually

²The elastic loading portion of the stress–strain curve is omitted, which is sensible given the large strains achieved in these fictitious tests.

Fig. 7.8 Quasi-static stress–strain curves in FoLLyalloy

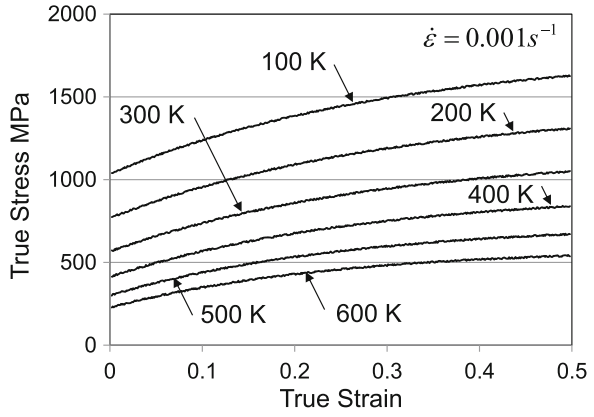


Fig. 7.9 Stress–strain curves in FoLLyalloy at a strain rate of $1.0 s^{-1}$

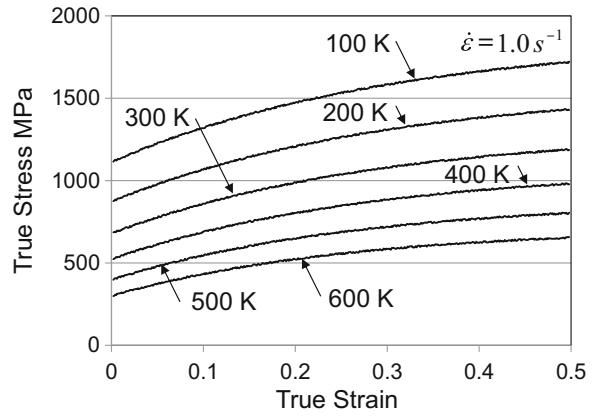
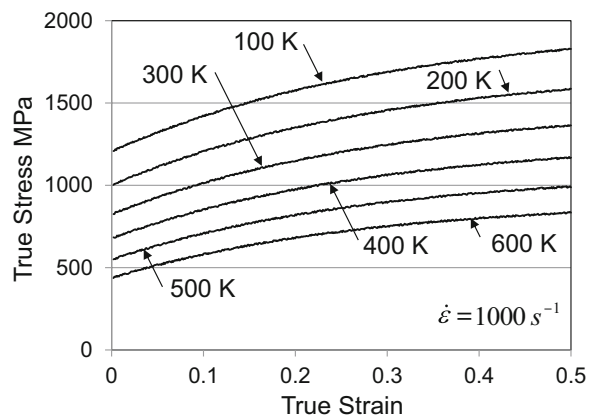


Fig. 7.10 Stress–strain curves in FoLLyalloy at a strain rate of $1000 s^{-1}$



high.) As emphasized in Sect. 6.5, hardening occurs through accumulation of stored dislocations. Thus, these stress–strain curves represent material strengthened with a Peierls obstacle and an impurity obstacle—which have been analyzed—and an evolving stored dislocation obstacle. The governing equation becomes the following:

$$\frac{\sigma}{\mu} = \frac{\sigma_a}{\mu} + s_p(\dot{\epsilon}, T) \frac{\hat{\sigma}_p}{\mu_o} + s_i(\dot{\epsilon}, T) \frac{\hat{\sigma}_i}{\mu_o} + s_\epsilon(\dot{\epsilon}, T) \frac{\hat{\sigma}_\epsilon(\epsilon, \dot{\epsilon}, T)}{\mu_o} \quad (7.8)$$

where $\hat{\sigma}_\epsilon$ is shown to be a function of strain, strain rate, and temperature through the evolution equation:

$$\frac{d\hat{\sigma}_\epsilon}{d\epsilon} = \theta_{II}(\dot{\epsilon}) \left(1 - \frac{\hat{\sigma}_\epsilon}{\hat{\sigma}_{\epsilon s}(\dot{\epsilon}, T)} \right)^\kappa \quad (6.25)$$

In unstrained material $\hat{\sigma}_\epsilon = 0$. With strain, $\hat{\sigma}_\epsilon$ increases while $\hat{\sigma}_p$ and $\hat{\sigma}_i$ are assumed not to change.

Figure 7.11 compares the stress–strain curve in pure Fo with that measured in FoLLyalloy at 300 K and a strain rate of 0.001 s^{-1} . As expected, the alloy is stronger than the pure metal. The difference in stress levels arises from the contribution of $s_i \hat{\sigma}_i$ in Eq. 7.8. In this hypothetical alloy, the rate of strain hardening is identical in the alloy to that in pure Fosium.

7.6 Evaluating the Stored Dislocation Obstacle Population

The procedure to evaluate the obstacle population due to the accumulated dislocation density is to systematically evaluate samples that have been prestrained along prescribed paths. The concept of a prestrain and a reload was introduced in Sect. 5.2 to illustrate path dependence in metal deformation. Figures 7.12, 7.13, and 7.14

Fig. 7.11 Stress–strain curves measured in pure Fo and FoLLyalloy at 300 K and a strain rate of 0.001 s^{-1}

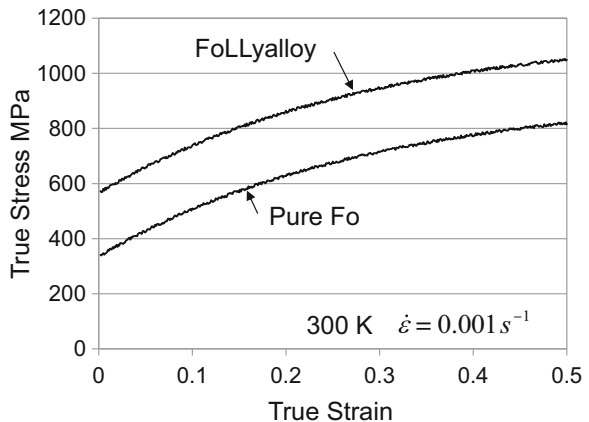


Fig. 7.12 Prestrains of FoLLy alloy at 300 K and a strain rate of 0.001 s^{-1} followed by four reload tests (five if the test at 300 K and a strain rate of 0.001 s^{-1} is also included)

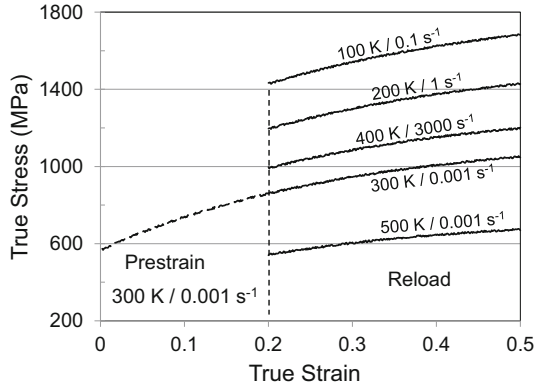


Fig. 7.13 Prestrains of FoLLy alloy at 400 K and a strain rate of 1 s^{-1} followed by four reload tests (five if the test at 400 K and a strain rate of 1 s^{-1} is also included)

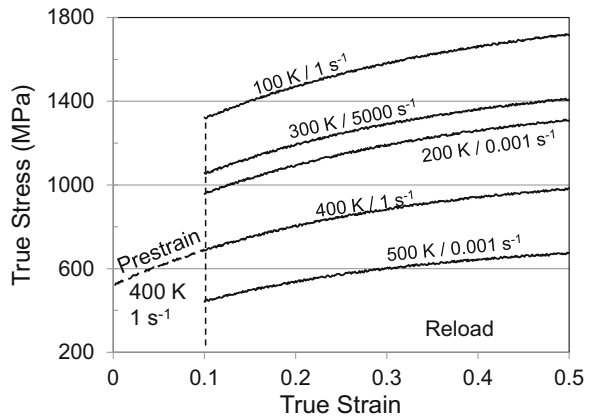
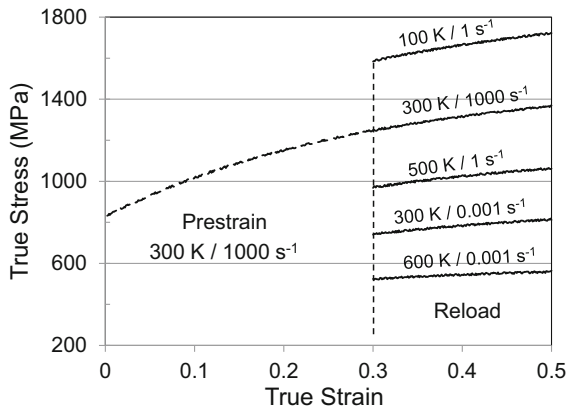


Fig. 7.14 Prestrains of FoLLy alloy at 300 K and a strain rate of 1000 s^{-1} followed by four reload tests (five if the test at 300 K and a strain rate of 1000 s^{-1} is also included)



show three test sequences consisting of a prestrain followed by five (5) reload tests. That is, five samples are prestrained along the specified strain rate and temperature paths to the strains noted and unloaded. This prestrain operation places each of these five samples into the same state. The objective becomes to evaluate the temperature and strain rate dependence of the reload yield stress to assess the state according to Eq. 7.8 (since $\hat{\sigma}_p$ and $\hat{\sigma}_i$ are known). Accordingly, each sample is reloaded at a specified temperature and strain rate. It is the reload yield stress that is of most interest, although the full stress–strain curve during the reload is also meaningful.

For the three prestrain conditions illustrated in Figs. 7.12, 7.13, and 7.14, Table 7.5 lists the reload conditions and measured yield stresses.³ Included in Table 7.5 are the yield stresses for the reload temperatures and strain rates shown in Fig. 7.12 through 7.14 along with a few additional reload conditions not shown in these figures.

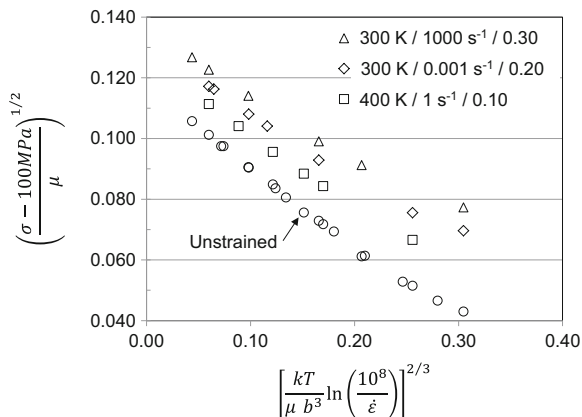
The next step is to plot the reload yield stress measurements using the same coordinates as used in Fig. 7.6 above and in Fig. 6.5 (niobium) and Fig. 6.6 (iron). Figure 7.15 shows this plot. The prestrain conditions are noted for the three data sets. Included is the data for unstrained FoLLyalloy, shown in Fig. 7.6. As expected, the stress levels rise with prestrain due to strain hardening and the accumulated

Table 7.5 Yield stress measurements for the reload tests as a function of the prestrain condition

Prestrain			Reload		
$\dot{\epsilon}$ (s^{-1})	T (K)	ϵ	$\dot{\epsilon}$ (s^{-1})	T (K)	σ (MPa)
0.001	300	0.20	0.001	600	444
			0.001	500	539
			0.001	300	863
			3000	400	996
			1	200	1196
			0.1	100	1433
			1	100	1455
1	400	0.10	0.001	500	441
			1	400	688
			0.001	200	958
			1000	500	701
			1	100	1323
			5000	300	1058
1000	300	0.30	0.001	600	524
			1	500	740
			0.001	300	968
			1000	300	1251
			1	100	1584
			1000	100	1685

³Yield stresses at strain rates as high as $1000 s^{-1}$ are generally unreliable. It is assumed here that Table 7.5 lists accurate yield stresses.

Fig. 7.15 Yield stress and reload yield stress for the three prestrain conditions as a function of test temperature and strain rate. Unstrained data are those listed in Table 7.3, while yield stress measurements on the prestrained samples are those in Table 7.5



dislocation density. At high values of the abscissa, the reload yield stresses tend to tail off the trend line at low values of the abscissa.

Equation 7.8 is the governing equation for the behavior shown in Fig. 7.15, where a third internal state variable— $\hat{\sigma}_e$ —was added to Eq. 7.2. As has been discussed, $\hat{\sigma}_e$ represents the obstacle posed by the evolving, stored dislocation density. Accompanying Eq. 7.8 is the expression for s_e :

$$s_e(\dot{\epsilon}, T) = \left\{ 1 - \left[\frac{kT}{\mu b^3 g_{oe}} \ln \left(\frac{\dot{\epsilon}_{oe}}{\dot{\epsilon}} \right) \right]^{1/q_e} \right\}^{1/p_e} \quad (7.9)$$

The unstrained material ($\hat{\sigma}_e = 0$) has already been analyzed (see Eqs. 7.5 through 7.7), but g_{oe} , $\dot{\epsilon}_{oe}$, q_e , and p_e in Eq. 7.9 are unknown. As concluded earlier when discussing these same parameters for the impurity obstacle population, the parameters $\hat{\sigma}_e$ and g_{oe} carry the most significance. Experience with large data sets in multiple materials (some of which will be summarized in Chap. 8) suggests that for the stored dislocation obstacle population, $\dot{\epsilon}_{oe} = 10^7 \text{ s}^{-1}$, $q_e = 1$, and $p_e = 2/3$. The three prestrain conditions analyzed present three distinct values of $\hat{\sigma}_e$. The procedure to evaluate $\hat{\sigma}_e$ and g_{oe} for each follows the procedure used to identify $\hat{\sigma}_i$. Equation 7.8 is fit to each data set with assumed values of $\hat{\sigma}_e$ and g_{oe} . The most likely values of these parameters are taken as those for the fit with the lowest error, as estimated using Eq. 7.4. Figure 7.16 shows the result for the prestrain condition of 0.001 s^{-1} , 300 K, and 20% strain.

Included in Fig. 7.16 is a best fit model prediction with $\hat{\sigma}_e = 353 \text{ MPa}$ and $g_{oe} = 1.6$. The model predictions and measurements lie close to each other. Table 7.6 shows the sensitivity of the fit to the selected $\hat{\sigma}_e$ and g_{oe} values. It is evident in Table 7.6 that the error depends on the selected parameters and that $\hat{\sigma}_e = 353 \text{ MPa}$ and $g_{oe} = 1.6$ give the smallest error. In fact, since $g_{oe} = 1.6$ will be shown in Chap. 8 to be a common value for this obstacle set, this will be assumed to remain constant for the other set of states to be evaluated.

Fig. 7.16 Reload yield stress versus temperature and strain rate for the 300 K, 0.001 s⁻¹, 0.20 prestrain along with a model prediction (dashed line and “+” symbol)

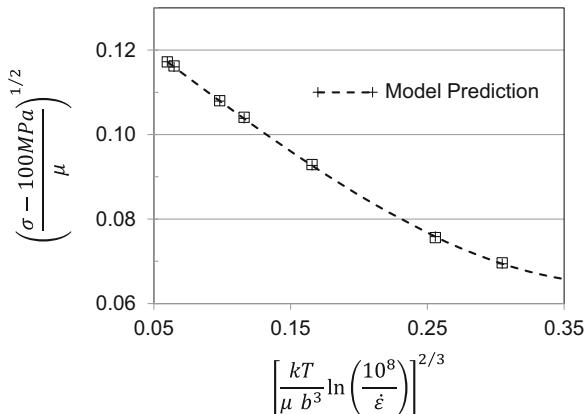


Table 7.6 Errors associated with five combinations of $\hat{\sigma}_\epsilon$ and g_{oe}

$\hat{\sigma}_\epsilon$ (MPa)	g_{oe}	Error, Eq. 7.4, (MPa)
353	1.6	7.6
340	2.0	27.0
342	2.5	21.5
360	1.0	22.4
400	0.5	82.8

Figures 7.17 and 7.18 show the reload yield stress versus temperature and strain rate (as in Fig. 7.16) for the other two prestrain conditions. The fits follow from $g_{oe} = 1.6$ and $\hat{\sigma}_\epsilon = 211$ MPa for the prestrain strain rate of 1 s⁻¹ and $\hat{\sigma}_\epsilon = 485$ MPa for prestrain strain rate of 1000 s⁻¹. The errors for the fits shown were 8.16 MPa and 6.44 MPa, respectively.

While good progress has been made in developing the constitutive law, a lot more work is required. Referring to Figs. 7.8, 7.9, and 7.10, note that only one of the prestrain conditions from each of these figures has been evaluated. This is illustrated in Fig. 7.19, which identifies the state at the 0.001 s⁻¹ prestrain condition. At the state identified, $\hat{\sigma}_\epsilon = 353$ MPa. Developing the full evolution law (Eqs. 6.25 and 6.26) over the range of conditions included in Fig. 7.19 necessitates measurements at additional prestrain conditions. A possible approach is to select the prestrain conditions listed in Table 7.7 for a prestrain strain rate of 0.001 s⁻¹. Similar conditions for other prestrain strain rates, e.g., 1 s⁻¹ and 1000 s⁻¹, would be required. For each prestrain condition, the objective would be to determine $\hat{\sigma}_\epsilon$ as illustrated above. (Note that the one value already determined has been added to the table.) Clearly, this experimental campaign necessitates a great many measurements. If there are six (6) identical test specimens for each prestrain condition, then three (3) strain rates, six (6) temperatures, and five (5) strains amount to 540 prestrains followed by an equal number of reloads—totaling 1080 tests.

Let us assume the project to create a constitutive law for FoLLyalloy has the necessary resources to perform such an experimental study. Table 7.8 lists the

Fig. 7.17 Reload yield stress versus temperature and strain rate for the 400 K, 1 s^{-1} , 0.10 prestrain along with a model prediction

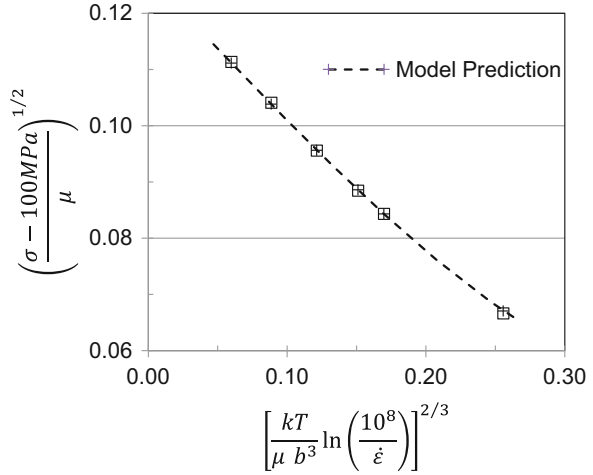


Fig. 7.18 Reload yield stress versus temperature and strain rate for the 300 K, 1000 s^{-1} , 0.30 prestrain along with a model prediction

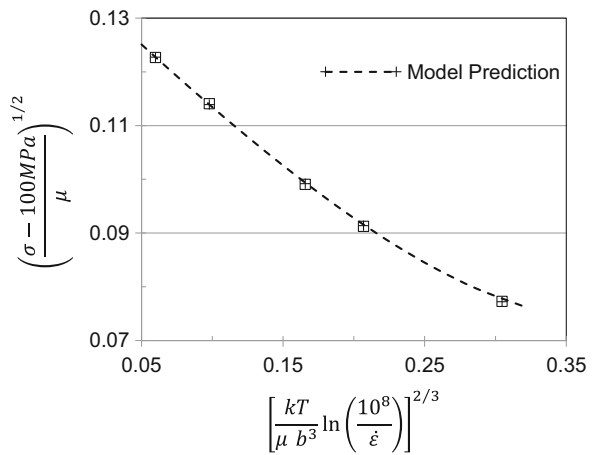


Fig. 7.19 Stress–strain curves at 0.001 s^{-1} as a function of test temperature. Note the symbol designating the one state at this strain rate (and a temperature of 300 K and a strain of 0.20) that was evaluated in Fig. 7.16

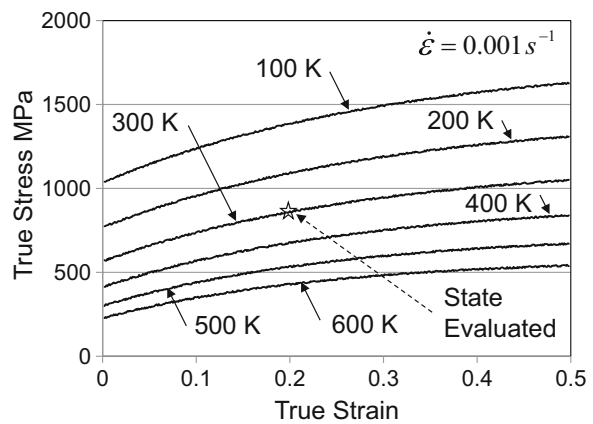


Table 7.7 Possible test matrix for prestrains and reload tests to evaluate hardening ($\hat{\sigma}_\epsilon$ versus ϵ) over a wide range of test temperatures at a test strain rate of 0.001 s^{-1}

Prestrain			$\hat{\sigma}_\epsilon$ (MPa)
$\dot{\epsilon}$ (s^{-1})	T (K)	ϵ	
0.001	100	0.05	
		0.10	
		0.20	
		0.30	
		0.40	
	200	0.05	
		0.10	
		0.20	
		0.30	
		0.40	
	300	0.05	
		0.10	
		0.20	353
		0.30	
		0.40	
	400	0.05	
		0.10	
		0.20	
		0.30	
		0.40	
500	0.05		
	0.10		
	0.20		
	0.30		
	0.40		
600	0.05		
	0.10		
	0.20		
	0.30		
	0.40		

resulting values of $\hat{\sigma}_\epsilon$ for the strain levels specified in Table 7.7 and the prestrain strain rates of 0.001 s^{-1} , 1 s^{-1} , and 1000 s^{-1} . At 40% strain and a temperature of 300 K, $\hat{\sigma}_\epsilon$ varies from 529 MPa at 0.001 s^{-1} to 565 MPa at 1000 s^{-1} . At a strain rate of 0.001 s^{-1} , Table 7.8 shows that at 40% prestrain at a strain rate of 0.001 s^{-1} , $\hat{\sigma}_\epsilon$ varies from 553 MPa at a prestrain temperature of 100 K to 476 MPa at a prestrain temperature of 600 K. While these variations may seem small, they demonstrate a significant dependence of this state variable on the strain rate and temperature of the prestrain. Recall, a simple constitutive law of the form:

Table 7.8 Deduced values of $\hat{\sigma}_\varepsilon$ for the experimental campaign defined in Table 7.7 at prestrain strain rates of 0.001 s^{-1} , 1 s^{-1} , and 1000 s^{-1} . In each case $g_{oe} = 1.6$

Prestrain conditions		$\hat{\sigma}_\varepsilon$ (MPa)		
T (K)	ε	0.001 s^{-1}	1 s^{-1}	1000 s^{-1}
100	0.05	113	116	119
	0.10	209	214	220
	0.20	361	370	378
	0.30	472	482	492
	0.40	553	564	575
200	0.05	112	115	119
	0.10	208	213	219
	0.20	357	367	376
	0.30	464	477	489
	0.40	542	556	570
300	0.05	112	115	118
	0.10	206	212	218
	0.20	353	363	374
	0.30	456	470	485
	0.40	529	547	565
400	0.05	111	115	118
	0.10	204	211	218
	0.20	346	359	372
	0.30	445	463	481
	0.40	514	536	558
500	0.05	111	114	118
	0.10	202	209	217
	0.20	340	354	369
	0.30	433	454	476
	0.40	497	524	551
600	0.05	110	114	118
	0.10	200	208	216
	0.20	331	348	366
	0.30	419	444	470
	0.40	476	509	543

$$\sigma = f(\varepsilon, T, \dot{\varepsilon}) \quad (7.10)$$

is unable to describe this path dependence of the hardening. Rather, an equation of the form of Eq. 5.7:

$$\sigma = f(\hat{\sigma}, T, \dot{\varepsilon}) \quad (5.7)$$

is required.

7.7 Deriving the Evolution Equation

Figure 7.20 shows the increase of $\widehat{\sigma}_\varepsilon$ with increasing strain for prestrains at 300 K and a strain rate of 0.001 s^{-1} . Equation 6.25 is used to model this behavior:

$$\frac{d\widehat{\sigma}_\varepsilon}{d\varepsilon} = \theta_{II}(\dot{\varepsilon}) \left(1 - \frac{\widehat{\sigma}_\varepsilon}{\widehat{\sigma}_{\varepsilon S}(\dot{\varepsilon}, T)} \right)^\kappa \quad (6.25)$$

There are three unknowns in this equation— θ_{II} , $\widehat{\sigma}_{\varepsilon S}$, and κ . For the initial form of this hardening, introduced as the Voce law (Eqs. 3.15 and 5.12), $\kappa = 1$. The parameter κ was introduced in Sect. 6.5 and the use of $\kappa \neq 1$ dictated by the inability of the Voce law to model the curvature of the $\widehat{\sigma}_\varepsilon$ versus ε curve. The analysis will begin, therefore, with the assumption $\kappa = 1$, leaving two unknowns. The procedure is to assume values of θ_{II} and $\widehat{\sigma}_{\varepsilon S}$ (with $\kappa = 1$) and compare the integrated form of Eq. 6.28, which was given in Eq. 5.14, with the data points. The fit with the lowest error, estimated using Eq. 7.4, gives the likely values of θ_{II} and $\widehat{\sigma}_{\varepsilon S}$. Figure 7.21 illustrates this for the data in Fig. 7.20. The fit, with $\theta_{II} = 2434 \text{ MPa}$ and $\widehat{\sigma}_{\varepsilon S} = 709 \text{ MPa}$, agrees well with the data points. The error is determined to be only 0.8 MPa. It is evident that in this case the Voce law fits quite well and there is no need to search for a κ -value other than unity.

Figure 7.21 shows a fit of the evolution equation to the prestrains at 300 K and a strain rate of 0.001 s^{-1} . Plots such as this are required for each of the prestrain temperatures (100 K through 600 K) and strain rates (0.001 s^{-1} , 1 s^{-1} , and 1000 s^{-1}). Doing so gives the results summarized in Table 7.9.

Noted in Table 7.9 is a slight variation of θ_{II} with strain rate, which is consistent with Eq. 6.29 along with very small scatter at each strain rate. Figure 7.22 plots θ_{II} versus the natural logarithm of strain rate, which shows a linear dependence. The equation of the line in Fig. 7.22 is as follows:

Fig. 7.20 Variation of $\widehat{\sigma}_\varepsilon$ with strain for prestrains at 300 K and a strain rate of 0.001 s^{-1}

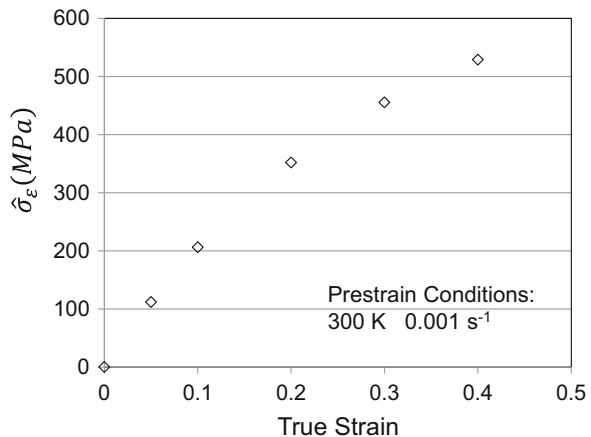


Fig. 7.21 The data of Fig. 7.20 with a Voce law fit

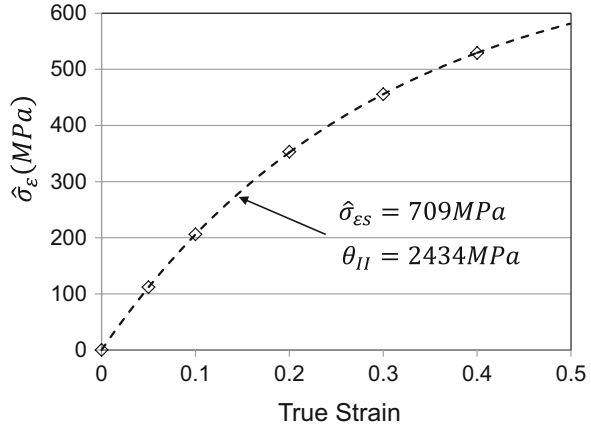


Table 7.9 Tabular summary of the fitting parameters (θ_H and $\hat{\sigma}_{\epsilon_s}$) derived from plots such as shown in Fig. 7.21 for each of the prestrain strain rate and temperature conditions

Prestrain		Equation 6.25 ($\kappa = 1$)		Error, Eq. 7.4
$\dot{\epsilon}$ (s^{-1})	T (K)	θ_H (MPa)	$\hat{\sigma}_{\epsilon_s}$ (MPa)	(MPa)
0.001	100	2439	769	0.44
	200	2432	742	0.28
	300	2434	709	0.97
	400	2432	673	0.37
	500	2433	633	0.23
	600	2433	590	0.27
1	100	2501	781	0.28
	200	2502	759	0.22
	300	2502	735	0.21
	400	2501	709	0.31
	500	2501	680	0.41
	600	2501	647	0.36
1000	100	2570	790	0.35
	200	2571	777	0.29
	300	2570	763	0.32
	400	2571	747	0.25
	500	2571	729	0.24
	600	2571	709	0.29

$$\theta_H = 2500 \text{ MPa} + 10.0 \text{ MPa} \ln[\dot{\epsilon} (s^{-1})] \tag{7.11}$$

Equation 6.26 described the temperature and strain rate dependence of the saturation stress $\hat{\sigma}_{\epsilon_s}$:

$$\ln \hat{\sigma}_{\epsilon_s} = \ln \hat{\sigma}_{\epsilon_{s0}} + \frac{kT}{\mu b^3 g_{\epsilon_{s0}}} \ln \frac{\dot{\epsilon}}{\dot{\epsilon}_{\epsilon_{s0}}} \tag{6.26}$$

Fig. 7.22 Variation of the stage II hardening rate with strain rate and trend line given by Eq. 7.11

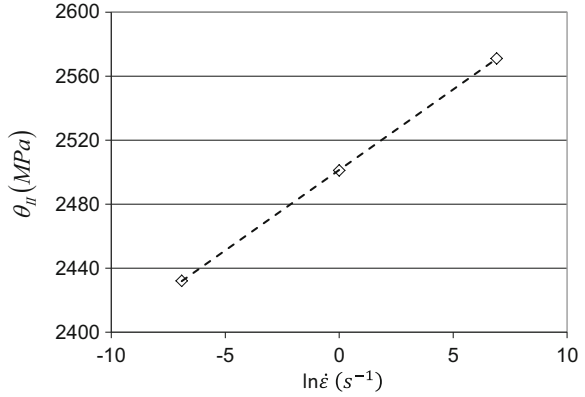
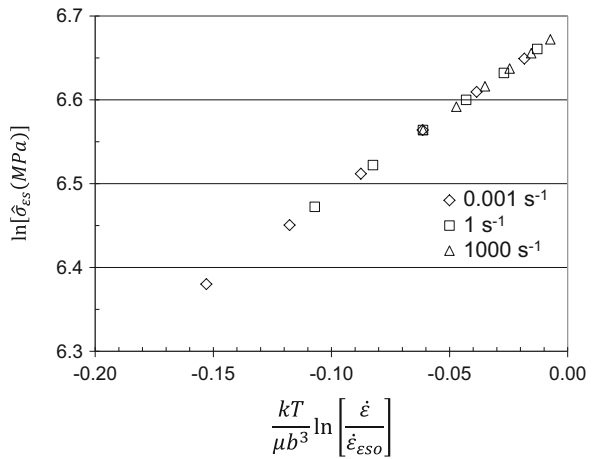


Fig. 7.23 Variation of the saturation stress with temperature and strain rate and trend line according to Eq. 6.26



Unknowns in Eq. 6.26 include g_{ESO} , $\hat{\sigma}_{ESO}$, and $\dot{\epsilon}_{ESO}$. A plot of $\ln \hat{\sigma}_{es}$ versus $kT/\mu b^3 \ln (\dot{\epsilon}/\dot{\epsilon}_{ESO})$ with an assumed value of $\dot{\epsilon}_{ESO}$ should give a linear dependence with an intercept related to $\hat{\sigma}_{ESO}$ and a slope (inversely) related to g_{ESO} . The data points at different strain rates will not fall on the same line if the assumed value of $\dot{\epsilon}_{ESO}$ is not optimum. Figure 7.23 shows this plot with the data in Table 7.9. From the slope of the line, $g_{ESO} = 0.50$, and from the intercept (at $T = 0$), $\hat{\sigma}_{ESO} = 800$ MPa.

7.8 The Constitutive Law for FoLLyalloy

All of the components of the constitutive law for FoLLyalloy have been derived. At any state, the stress is defined by Eq. 7.8, which is rewritten as follows:

$$\frac{\sigma}{\mu} = \frac{\sigma_a}{\mu} + s_p(\dot{\epsilon}, T)(0.01) + s_i(\dot{\epsilon}, T)(0.004) + s_\epsilon(\dot{\epsilon}, T) \frac{\hat{\sigma}_\epsilon(\epsilon, \dot{\epsilon}, T)}{100 \text{ GPa}} \quad (7.12)$$

where $\widehat{\sigma}_p/\mu_o$ and $\widehat{\sigma}_i/\mu_o$ have been replaced by 0.01 and 0.004, respectively—since these state variables do not change. The s -terms in Eq. 7.8 are as follows:

$$s_p(\dot{\varepsilon}, T) = \left\{ 1 - \left[\frac{kT}{(0.2)\mu b^3} \ln \left(\frac{10^8 s^{-1}}{\dot{\varepsilon}} \right) \right]^{2/3} \right\}^2 \quad (7.13)$$

and

$$s_i(\dot{\varepsilon}, T) = \left\{ 1 - \left[\frac{kT}{(0.8)\mu b^3} \ln \left(\frac{10^8 s^{-1}}{\dot{\varepsilon}} \right) \right]^{2/3} \right\}^2 \quad (7.14)$$

and

$$s_\varepsilon(\dot{\varepsilon}, T) = \left\{ 1 - \left[\frac{kT}{(1.6)\mu b^3} \ln \left(\frac{10^7 s^{-1}}{\dot{\varepsilon}} \right) \right]^{3/2} \right\} \quad (7.15)$$

Recall that the temperature dependence of the shear modulus was defined by Eq. 6.8 and that the parameters for this were listed in Table 7.1.

Evolution of the state variable describing dislocation interactions with other (likely stored) dislocations is described by Eq. 6.25 with $\kappa = 1$:

$$\frac{d\widehat{\sigma}_\varepsilon}{d\varepsilon} = \theta_{II}(\dot{\varepsilon}) \left(1 - \frac{\widehat{\sigma}_\varepsilon}{\widehat{\sigma}_{\varepsilon s}(\dot{\varepsilon}, T)} \right) \quad (6.25)$$

where from Eq. 7.11:

$$\theta_{II} = 2500 \text{ MPa} + 10.0 \text{ MPa} \ln[\dot{\varepsilon}(s^{-1})] \quad (7.11)$$

and from Eq. 6.26:

$$\ln \widehat{\sigma}_{\varepsilon s} = \ln(800 \text{ MPa}) + \frac{kT}{\mu b^3(0.5)} \ln \frac{\dot{\varepsilon}}{10^7 s^{-1}} \quad (7.16)$$

For simple *monotonic* (e.g., constant strain rate and temperature) paths, Eq. 6.25 (with Eqs. 7.11 and 7.16) can be directly integrated, and for every value of $\widehat{\sigma}_\varepsilon$, a stress can be computed using Eqs. 7.12 with 7.13 through Eq. 7.15. For arbitrary paths with changes in temperature or strain rate, a numerical solution is most convenient.

7.9 Summary

A fictitious alloy was created to demonstrate how the MTS model constants are determined. The alloy was described as one in which dislocation motion was restricted by a Peierls barrier, solution hardening, and an accumulating density of stored dislocations. The experimental procedure to isolate the effects of these obstacles was described. Determination of MTS model constants requires an intensive experimental survey—including a complement of prestrain/reload tests to create specific “states” for analysis. Fortunately, as experience in a variety of metals has ensued, the experimental requirements have relaxed. Application of the model to several metals and use of the model to understand effects of unique processing routes will be summarized in Chaps. 8 through 14.

Exercises

- 7.1 From the measurements reported in Table 7.2, create the plot of normalized yield stress versus temperature and strain rate shown in Fig. 7.3. Do you get the same values of $\hat{\sigma}/\mu_o$ and g_o ?
- 7.2 From the measurements reported in Table 7.3, create the plot of normalized yield stress versus temperature and strain rate shown in Fig. 7.7. Do you arrive at the same model parameters?
- 7.3 Table 7.E3 lists yield stress values as a function of reload test temperature and strain rate for prestrains at a strain rate of 0.001 s^{-1} and 300 K to a strain level of 0.30. Create the equivalent of Fig. 7.16 for these results and, verify that Table 7.8 lists the correct value of $\hat{\sigma}_\epsilon$.

Table 7.E3 Reload yield stress as a function of temperature and strain rate for a metal prestrained at a temperature of 300 K and a strain rate of 0.001 s^{-1} to a strain of 0.30 (Exercise 7.3)

Reload results		
T (K)	Rate (s^{-1})	Yield stress (MPa)
600	0.001	507
500	0.001	613
300	0.001	944
400	3000	1077
200	1.0	1285
100	0.1	1526
100	1.0	1562

Table 7.E4 Reload yield stress as a function of temperature and strain rate for a metal prestrained at a temperature of 400 K and a strain rate of 1.0 s⁻¹ to a strain of 0.30 (Exercise 7.4)

Reload results		
<i>T</i> (K)	Rate (s ⁻¹)	Yield stress (MPa)
500	0.001	622
400	1.0	879
200	0.001	1190
300	5000	1274
100	1.0	1563

Table 7.E6 Stress versus strain for FoLLyalloy tested at 200 K and a strain rate of 0.001 s⁻¹ (Exercise 7.6)

200 K and 0.001 s ⁻¹			
Strain	Stress (MPa)	Strain	Stress (MPa)
0.01	785	0.075	912
0.02	807	0.1	955
0.03	830	0.125	990
0.04	852	0.15	1026
0.05	869	0.175	1067
0.06	892	0.2	1094
0.07	902	0.25	1143
0.08	922	0.3	1194
0.09	945	0.35	1232
0.1	955	0.4	1258
0.025	826	0.45	1283
0.05	869	0.5	1309

- 7.4 Table 7.E4 lists yield stress values as a function of reload test temperature and strain rate for prestrains at a strain rate of 1.0 s⁻¹ and 400 K to a strain level of 0.30. Create the equivalent of Fig. 7.16 for these results. How does the deduced value of $\hat{\sigma}_e$ compare with the value for a prestrain at 0.001 s⁻¹ and 400 K to the same strain level?
- 7.5 From the results in Table 7.8 at a prestrain temperature of 600 F, create the equivalent of Fig. 7.21. Do the resulting model parameters agree with those listed in Table 7.9?
- 7.6 Table 7.E6 lists stress versus strain in FoLLyalloy for a test at a strain rate of 0.001 s⁻¹ and a test temperature of 200 K. From the model equations listed in Sect. 7.8, derive a predicted stress–strain curve, and compare with the measurements.

Table 7.E7 Stress versus strain for FoLLyalloy tested at 300 K and a strain rate of 1000 s^{-1} to a strain of 0.30 followed by reloading at a temperature of 500 K and a strain rate of 1.0 s^{-1} (Exercise 7.7)

Prestrain: 300 K and 1000 s^{-1}		Reload: 500 K and 1.0 s^{-1}	
Strain	Stress (MPa)	Total strain	Stress (MPa)
0.01	851	0.31	752
0.02	869	0.32	749
0.03	896	0.33	752
0.04	908	0.34	757
0.05	929	0.35	767
0.06	946	0.36	769
0.07	965	0.37	772
0.08	982	0.38	782
0.09	996	0.39	784
0.1	1016	0.4	779
0.025	887	0.325	758
0.05	929	0.35	767
0.075	980	0.375	771
0.1	1016	0.4	779
0.125	1058	0.425	791
0.15	1089	0.45	797
0.175	1127	0.475	803
0.2	1148	0.5	812
0.25	1204	0.55	826
0.3	1246	0.6	836

7.7 Table 7.E7 lists stress versus strain in FoLLyalloy for a test at a strain rate of 1000 s^{-1} and a test temperature of 300 K to a strain of 0.30 followed by a temperature change to 500 K and a strain rate change to 1.0 s^{-1} . From the model equations listed in Sect. 7.8, derive a predicted stress–strain curve, and compare with the measurements.

Chapter 8

Application of MTS Model to Copper and Nickel



Introduction

Chapter 7 described the experiments and analysis necessary to develop MTS parameters using a hypothetical alloy along with a series of mechanical tests. The recommended procedure involved the following:

1. Measurement of yield stress as a function of temperature and strain rate in well-annealed material
2. Multiple tests (termed prestrains) at various temperatures, strain rates, and strains which created prescribed states
3. Reload tests to measure the yield stress as a function of temperature and strain rate for each of the prescribed states

It is evident that a significant experimental campaign is required to fully determine MTS parameters. Pure copper is the material which has been most thoroughly investigated according to this procedure. This chapter begins with a review of the work in pure copper. Application to an FCC metal (nickel) alloyed (with carbon) such that an additional strengthening mechanism is active is then described. The intent of this chapter is not to revisit work already in the published literature but rather to demonstrate how model parameters have been selected and to address the following questions:

1. Does the normalized activation remain (g_o in Eqs. 6.15 or 6.16) constant over a range of conditions?
2. Is the assumption that distinct obstacles add linearly valid?
3. How predictive is the model once model parameters have been selected? In particular, can the model be used to predict experimental results not included in the test matrix used to establish model parameters?

Supplementary Information The online version contains supplementary material available at [https://doi.org/10.1007/978-3-031-04556-1_8]

8.1 Pure Copper

Copper is an FCC metal that has been extensively used as a model material in deformation mechanism research and constitutive model development. Because copper is used in pure form for various applications requiring a high conductivity metal, it is widely available. Its homologous temperature¹ at RT is 0.217 which conveniently places RT tests in the low-temperature regime. Assuming that diffusional mechanisms become active at a homologous temperature of 0.5, testing at temperatures as high as 679 K (406 °C) is possible, giving a wide range of conditions available to researchers. Aluminum has also been routinely used as a model material, but its RT homologous temperature of 0.316 restricts the range of conditions.

Oxygen-free-high-conductivity (OFHC) copper is a generic name for a series of pure copper alloys used for electronic applications. Generally, these materials have purities greater than 99.9%. The primary impurity of interest is oxygen. Oxygen-free-electronic (OFE) copper actually has a purity of 99.99%. When procured as bar stock, a 1 hour anneal at 873 K (600 °C) generates a soft, recrystallized structure with an average grain size on the order of 40 μm .

Low-temperature (as specified above) deformation occurs in copper by the generation of dislocations. Strain-hardening occurs by the storage of dislocations usually in cell structures. (See Fig. 2.16.) Deformation by twinning is possible—but only at very low temperatures or very high strain rates outside of the range of conditions of interest here. In context of the MTS model, the motion of a mobile dislocation in polycrystalline copper is opposed by (i) grain boundaries and (ii) immobile (or stored) dislocations. As a first approximation the contribution from grain boundaries is constant and determined by the grain size (see Eq. 3.9).² The contribution from stored dislocations is referred to as $\widehat{\sigma}_\varepsilon$ which the sole internal state variable in pure copper and is expected to evolve with strain. The constitutive law for pure copper (Eq. 6.14) becomes

$$\frac{\sigma}{\mu} = \frac{\sigma_a}{\mu} + s_\varepsilon(\dot{\varepsilon}, T) \frac{\widehat{\sigma}_\varepsilon}{\mu_o} \quad (8.1)$$

along with Eq. 6.25

$$\frac{d\widehat{\sigma}_\varepsilon}{d\varepsilon} = \theta_{II}(\dot{\varepsilon}) \left[1 - \frac{\widehat{\sigma}_\varepsilon}{\widehat{\sigma}_{\varepsilon s}(\dot{\varepsilon}, T)} \right]^\kappa \quad (8.2)$$

where s_ε , $\widehat{\sigma}_{\varepsilon s}$, and θ_{II} were defined in Eqs. 6.18, 6.26, and 6.29.

Deformation in copper is rate insensitive in that the stress varies only slightly with strain rate—as opposed to what is observed, for instance, in BCC metals. However,

¹The homologous temperature is the dimensionless ratio of the temperature of interest (K) to the melting temperature (K).

²Experimental evidence to support this assumption is presented in Sect. 8.9.

it is a rate-dependent material in that there is a measurable variation of strength with strain rate in deformed copper. This may seem like a subtle distinction, but the origin of the observable strain-rate dependence from the dynamics of dislocation–obstacle interactions is essential to accurately specifying a constitutive law in this material.

8.2 Follansbee and Kocks Experiments

An extensive experimental analysis of RT deformation in OFE copper was published by Follansbee and Kocks [1]. Table 8.1 lists the prestrain conditions included in the study. All of the prestrains were done at RT in compression and ten (10) identical specimens were prepared for each combination of strain rate and strain. This matrix represents 410 compression tests.

Reload tests were performed at a strain rate of 0.001 s^{-1} and temperatures of RT, 180 K, and 76 K. A few reload tests were performed at an RT and a strain rate of 1 s^{-1} . Repeat reload tests were performed giving a total of 410 reload compression tests. Figure 8.1 shows a plot of reload yield stress versus reload test temperature and strain rate for three of the prestrain conditions (indicated on the figure). The plot is made with the same coordinates as in Figs. 6.4, 6.5, and 6.6 with $p = 2/3$, $q = 1$, $\dot{\epsilon}_o = 10^7 \text{ s}^{-1}$, and $\sigma_a = 40 \text{ MPa}$. Straight lines can be drawn through the data points when plotted on these coordinates. It is worth nothing that a plot of the test data with different values of p , q , and $\dot{\epsilon}_o$ would yield straight lines as well. The model parameters specified above represented those that achieved the overall highest regression coefficients.

Recall from Sect. 4.5 Chap. 4 that the intercept at $T = 0$ is related to $\hat{\sigma}_\epsilon$ and the slope is inversely related to g_o (which in this case is g_{oe}). Table 8.2 lists all of the values of $\hat{\sigma}_\epsilon$ and g_o determined for the 41 states.

Figure 8.2 is a plot of all of the $\hat{\sigma}_\epsilon$ measurements in Table 8.2 versus plastic strain. Included are fits according to Eq. 6.28 with $\kappa = 2$. Table 8.3 lists the values of θ_{II} and $\hat{\sigma}_{\epsilon s}$ used as fitting parameters.

Table 8.1 Prestrain conditions (strains at each specified strain rate) for copper test specimens for the Follansbee and Kocks study [1]

Strain rate (s^{-1})	Strain						
0.00014	0.05	0.10	0.15	0.20	0.25	0.468	
0.015	0.05	0.10	0.15	0.20	0.25	0.491	0.96
0.82	0.05	0.10	0.15	0.20	0.25	0.521	0.727
81	0.05	0.10	0.15	0.20	0.25		
1800	0.064	0.107	0.152	0.209	0.253	0.52	
5000	0.065	0.10	0.168	0.211	0.257		
9500	0.087	0.134	0.156	0.189	0.226		

^aA minimum of 10 identical specimens were prepared for each strain rate and strain combination. All prestrains were at RT

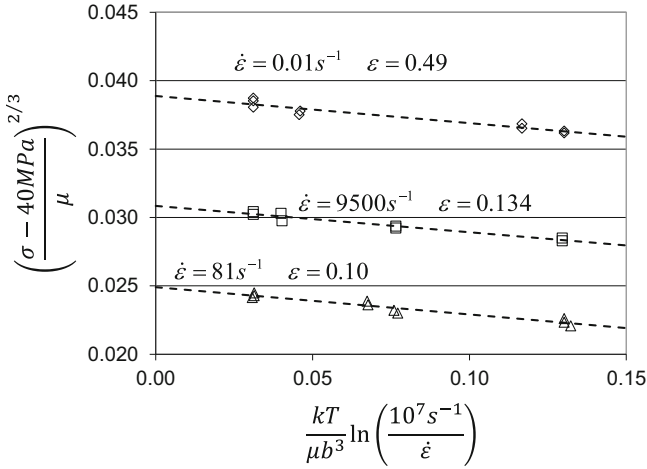


Fig. 8.1 Reload yield stress versus reload temperature and strain rate for the three prestrain conditions identified

Table 8.2 Mechanical threshold stress ($\hat{\sigma}_\epsilon$) and g_o determined for each of the prestrain conditions listed in Table 8.1

Strain rate (s^{-1})	Strain	$\hat{\sigma}_\epsilon$ (MPa)	g_o	Strain rate (s^{-1})	Strain	$\hat{\sigma}_\epsilon$ (MPa)	g_o
0.00014	0.05	83.1	2.3	81	0.05	94.7	1.1
	0.10	141.1	2.7		0.10	163.1	1.3
	0.15	183.2	2.2		0.15	210.3	1.8
	0.20	216.9	2.1		0.20	255	1.5
	0.25	237.6	2.0		0.25	284.2	1.5
	0.468	300.2	1.8		0.468	300.2	1.5
0.015	0.05	87.1	1.8	1800	0.064	133.8	2.3
	0.10	148.5	2.2		0.107	179.1	2.7
	0.15	194.3	2.0		0.152	235.6	1.3
	0.20	228	1.9		0.209	265	1.6
	0.25	251.8	2.0		0.253	300	1.2
	0.491	327.3	1.7		0.52	401.9	1.0
	0.96	395.8	1.3		0.96	395.8	1.0
0.82	0.05	95.9	1.6	5000	0.065	140.6	2.9
	0.10	152.5	2.3		0.1	187.9	1.8
	0.15	204.2	2.0		0.168	241.7	1.4
	0.20	241.7	1.6		0.211	279	1.3
	0.25	265.7	1.6	9500	0.257	310.1	1.1
	0.521	356.8	1.2		0.087	171.6	2.4
	0.727	392.2	1.1		0.134	229.5	1.5
					0.156	254.7	1.3
			0.189	280.8	1.1		
			0.226	297	1.3		

Fig. 8.2 Variation of the mechanical threshold stress ($\hat{\sigma}_\epsilon$) with strain for each of the seven strain rates

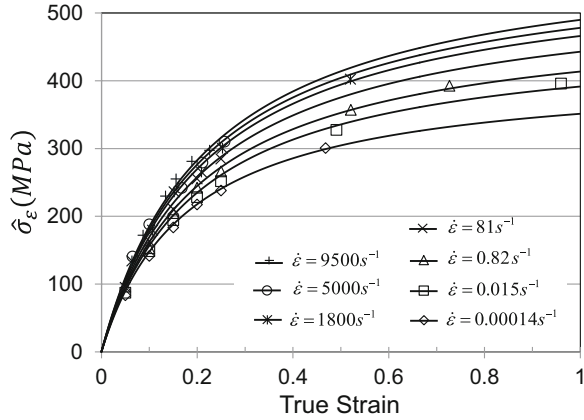


Table 8.3 The parameters θ_{II} and $\hat{\sigma}_{\epsilon s}$ used to generate the curves in Fig. 8.2 according to Eq. 6.28 (with $\kappa = 2$)

Strain rate (s^{-1})	θ_{II} (MPa)	$\hat{\sigma}_{\epsilon s}$ (MPa)
0.00014	2284	415
0.015	2340	470
0.82	2389	500
81	2458	540
1800	2552	570
5000	2612	585
9500	2665	600

Fig. 8.3 Variation of the saturation threshold stress ($\hat{\sigma}_{\epsilon s}$) for each strain rate on coordinates suggested by Eq. 6.26

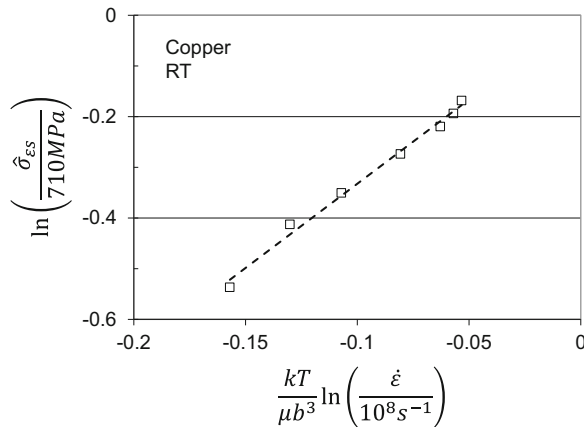


Figure 8.3 shows the variation of $\hat{\sigma}_{\epsilon s}$ with strain rate according to coordinates suggested by Eq. 6.26. Included in the coordinates are best-fit values of $\hat{\sigma}_{\epsilon s0}$ (710 MPa) and $\dot{\epsilon}_{\epsilon s0}$ ($10^8 s^{-1}$). A straight line (with an intercept at the origin) can be drawn through the data points. From Eq. 6.26, $g_{\epsilon s0}$ is the inverse of the slope of this line which gives $g_{\epsilon s0} = 0.301$.

Fig. 8.4 Variation of the Stage II hardening rate (θ_{II}) with strain rate. The line is drawn according to Eq. 6.29

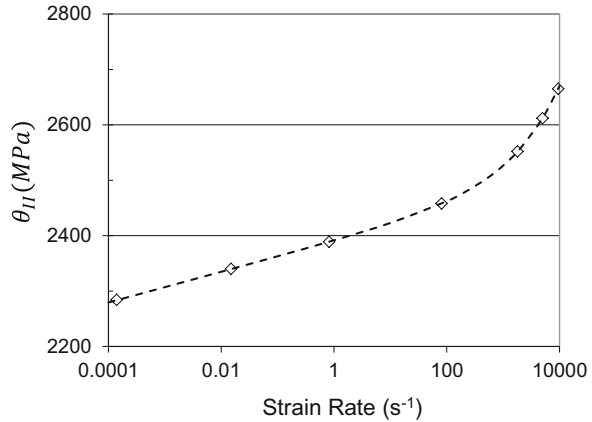


Fig. 8.5 Variation of the normalized activation energy (g_o) with stress

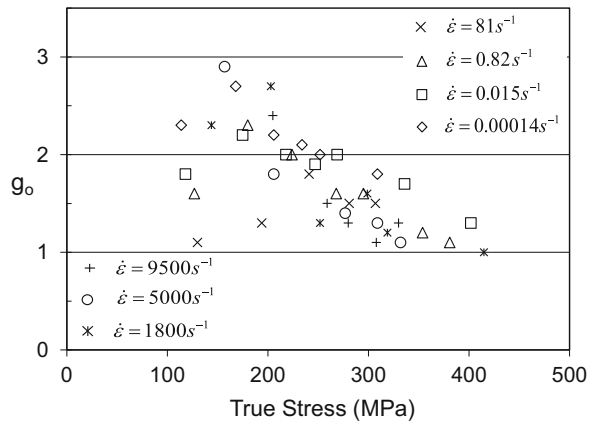


Figure 8.4 is a plot of θ_{II} versus strain rate, where the latter is on a logarithmic scale. The line in this figure is Eq. 6.29 with $A_1 = 2390$ MPa, $A_2 = 12$, and $A_3 = 1.696 s^{-1/2}$.

The results summarized in Figs. 8.2, 8.3, and 8.4 specify the evolution behavior as analyzed according to Eqs. 6.28, 6.26, and 6.29. In addition, all of the parameters except the analyzed activation energy for Eq. 6.18 have been specified. Table 8.2 lists the value of g_o for each of the reload conditions. It is apparent that g_o is not constant. Figure 8.5 shows the variation of g_o with stress for each of the seven strain-rate conditions. (Table 1 in Ref. [1] lists the stress at the noted strains for each of the prestrain strain rates.) There is a lot of scatter in the results and perhaps a strain-rate dependence, but a trend toward decreased g_o values with increasing stress is evident.

In the original Follansbee and Kocks publication [1], the decrease of g_o with stress (and strain) was noted, but an average $g_o = 1.6$ was taken as representative over the range of conditions tested. The change of g_o has been documented previously [2] and represents departure from Cottrell-Stokes behavior with increasing

Table 8.4 Deduced model parameters for the copper investigated by Follansbee and Kocks

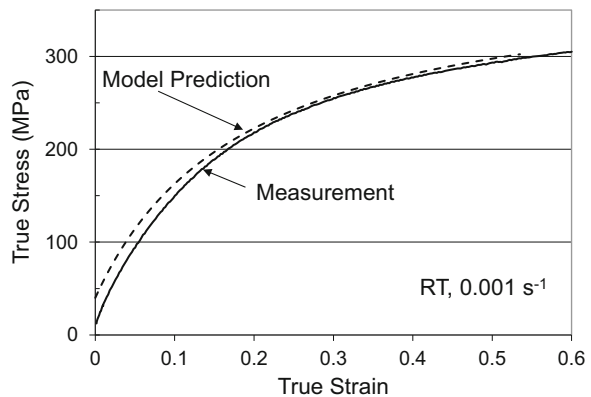
Equation	Parameter	Follansbee and Kocks ^a
6.14	σ_a (MPa)	40
6.15 ^b	g_{oe}	1.6
6.26	$\hat{\sigma}_{eso}$ (MPa)	710
	$\dot{\epsilon}_{eso}$ (s ⁻¹)	10 ⁸
	g_{eso}	0.301
6.28	κ	2
6.29	A_o (MPa)	2390
	A_1^c	12.0
	A_2 (s ⁻¹)	1.696

^aThe parameters in this column represent a reanalysis of the experimental results according to Eqs. 6.28 and 6.29 since Follansbee and Kocks used different equations

^bObstacle 1 in Eq. 6.14 represents dislocation interactions with the stored dislocation density; thus the subscript “1” is replaced with “ ϵ .” For this obstacle population $p_e = 2/3$ $q_e = 1$ and $\dot{\epsilon}_{oe} = 10^7$ s⁻¹

^cThe units of A_1 are awkward since A_1 multiplies the natural logarithm of $\dot{\epsilon}$ (s⁻¹)

Fig. 8.6 Comparison of the model predictions to measurement for a test not part of the original Follansbee and Kocks experimental study



stress. Mecking and Kocks [2] proposed a phenomenological model for this behavior. Application of this model to copper will be described in Chap. 14.

Table 8.4 summarizes the model parameters as described above. The temperature-dependent shear modulus is computed using Eq. 6.8 and the parameters in Table 6.1.

With these model parameters and Eqs. 6.14, 6.15, 6.26, and 6.29 stress–strain curves can be predicted. Figure 8.6 shows a comparison between model predictions and a stress–strain curve measured in copper by Gray and Chen [3]. For this test the stresses at low strains are over-predicted whereas the stresses at high strains closely follow the measurements.

Figure 8.7 shows another comparison with measurements. This experimental result at RT and a strain rate of 0.015 s⁻¹ was reported in by Follansbee and Kocks [1]. Note that in these compression tests the samples were unloaded and re-lubricated and/or remachined into solid cylinders to reduce the effects of barreling

Fig. 8.7 Comparison of the model prediction with the combined stress–strain curve for RT deformation at a strain rate of 0.015 s^{-1} . At every 25% strain increment, the specimen was unloaded and relubricated or remachined and relubricated

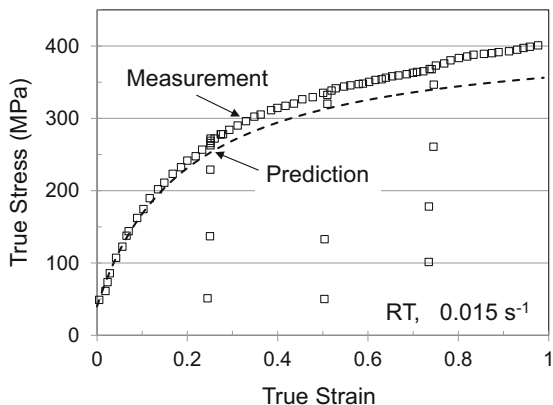
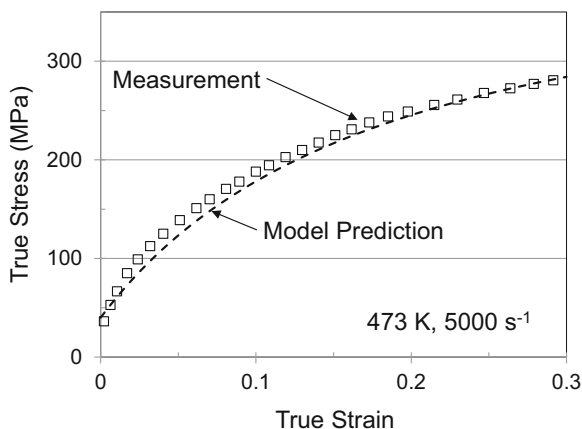


Fig. 8.8 Comparison of the model prediction with a test at 473 K and a strain rate of 5000 s^{-1} which was not part of the original Follansbee and Kocks experimental investigation

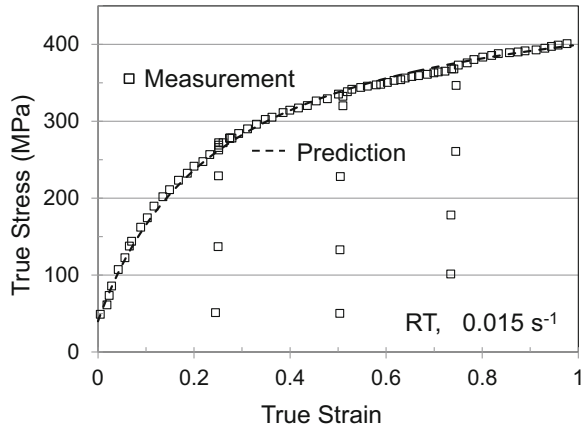


that can plague compression tests when large strains are desired. The predictions at low strains match the measured behavior but the model under-predicts the stresses at high strains.

A third comparison—this time at a temperature of 100°C rather than RT is shown in Fig. 8.8. This represents a prediction at a temperature outside the range of prestrain conditions. The predicted behavior closely matches the measured behavior.

When exercising a constitutive model it can be a temptation to adjust a parameter or two to enable closer agreement with a single experimental result. For instance, Fig. 8.9 compares the measurements shown in Fig. 8.7 with a model prediction with $\hat{\sigma}_{eso} = 850 \text{ MPa}$ instead of 710 MPa and $A_o = 2150 \text{ MPa}$ instead of 2390 MPa . This is not a recommended practice, however, when the desire is to derive a constitutive law that has applicability over a wide range of conditions. Indeed, with these parameters, the comparisons at the conditions shown in Figs. 8.6 and 8.8 would have deteriorated.

Fig. 8.9 Example showing that a slight change in model parameters can improve agreement with the test results shown in Fig. 8.7 (at the expense of agreement with other tests, however)



It is noteworthy that the Follansbee and Kocks measurements all involved RT prestrains. Even though the model equations offer the ability to predict stress–strain curves at other than RT, the temperature dependence is not based on the extensive prestrain and reload testing procedure that was practiced for the strain-rate dependence. Figure 8.8 illustrated predictions are possible at a temperature modestly different than those for which the model was developed. The next section describes how measurements of stress–strain curves at a wider range of temperatures can be analyzed to validate and sometimes adjust model parameters.

8.3 Temperature-Dependent Stress–Strain Curves

A very early experimental study of temperature-dependent stress–strain behavior in pure copper was performed by Carreker and Hibbard [4] (see Fig. 8.10). Their measurements were in 99.999% pure copper wire (762 μm diameter) in tension at temperatures as low as 20 K to as high as 1223 K at an engineering strain rate of 0.00067 s^{-1} (implying a constant cross-head speed). Material annealed at 1023 K (750 C) exhibited an average grain size of 45 μm . At this grain size, there was on average 17 grains across the specimen diameter. Figure 8.10 is a plot of their reported stress–strain curves at 140–1023 K. Because this material was tested in tension, the strains are all less than 30%, whereas it was possible in the compression tests of Follansbee and Kocks to test to larger strains.

Figure 8.11 shows a comparison of the measurements at the three lower temperatures with stress–strain curves predicted using the model parameters in Table 8.4. The predicted curves all lie below the measured curves. (The predicted curve at 300 K happens to match the experimental curve at 140 K.) The origin of the difference between the strength levels in the compression experiments of Follansbee

Fig. 8.10 Stress–strain measurements (tension) as a function of test temperature on copper by Carreker and Hibbard [4]

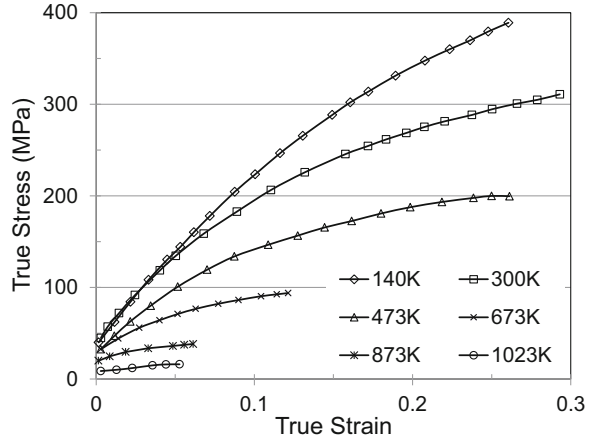
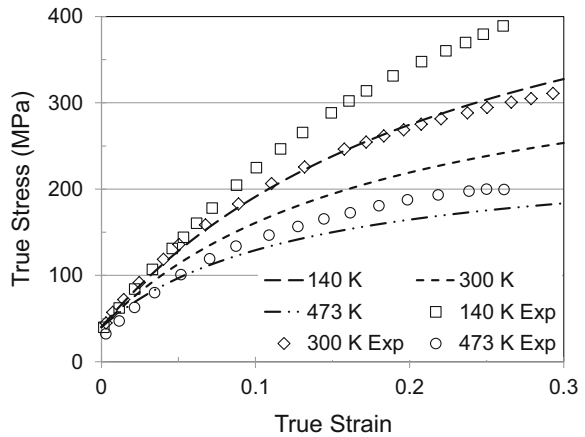
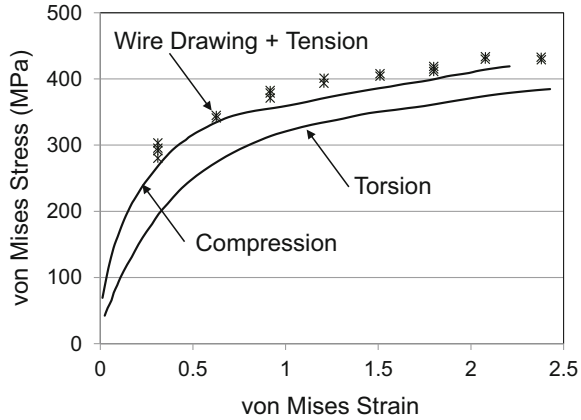


Fig. 8.11 Model predictions using the parameters in Table 8.4 for three of the conditions measured by Carreker and Hibbard. (Note that the good agreement between the prediction at 300 K and the measurement at 140 K is fortuitous)



and Kocks and the tension experiments of Carreker and Hibbard is difficult to assess. The Carreker and Hibbard material was slightly purer but the grain sizes both materials were comparable. The latter is consistent with the observation that the yield stresses in both materials were also comparable (~ 40 MPa). The difference could be due to the tension versus compression orientations and a stress-state effect (see the Box 8.1, which summarizes measurements by Kocks et al. [5]). It is also possible that the limited number of grains across the specimen cross section has influenced the hardening behavior.

Fig. 8.12 Large strain stress–strain measurements at three unique stress states in copper. Plotting the measurements according to the von Mises yield criteria does not force the data onto a single curve



Box 8.1 Stress-State Dependence of Hardening in Copper

Box 1.2 described several scalar quantities of stress and strain used to equate (specifically yield) stresses measured in different stress states. The von Mises stress is perhaps the most common of these. To demonstrate how well this works in large-strain measurements in copper, Fig. 8.12 shows measurements by Kocks et al. [5] in compression, torsion, and wire drawing plus tension. The data are plotted on von Mises stress–strain coordinates.

The curves for the different stress-states do not coincide in Fig. 8.12, which implies that the von Mises coordinates do not, by themselves, serve to equate measurements from different stress states. The explanation for this lies in the details of the strain-hardening mechanism. Recall Box 3.4 entitled “Crystal Plasticity” in Chap. 3 that introduced the relationship between the Schmidt factor and the individual grain-level contributions in a polycrystal. During plastic deformation, these grains are rotating and their rotations are a complicated function of the imposed three-dimensional stresses. Accordingly, the relationship between the collective grain assemblies (texture) and the macro-level stresses are a function of the stress-state history. Box 3.4 listed some of the analytical methods that have arisen to account for these texture and texture evolution effects. These methods are not discussed in any detail in this monograph, but their influence should be considered when comparisons of measurements performed under different stress states are of interest.

To proceed with an analysis of the higher temperature measurements in the Carreker and Hibbard data set, it is necessary to adjust the hardening parameters in Eq. 6.26 ($\hat{\sigma}_{eso}$) and 6.29 (A_0). Figure 8.13 shows how the comparison between predicted and experimental stress–strain curves improves by increasing $\hat{\sigma}_{eso}$ to 950 MPa (from 710 MPa) and by increasing A_0 to 2800 MPa (from 2390 MPa). No other parameters in Table 8.4 were changed.

Fig. 8.13 Improved agreement between the model and the Carreker and Hibbard measurements achieved with changes in two of the model parameters

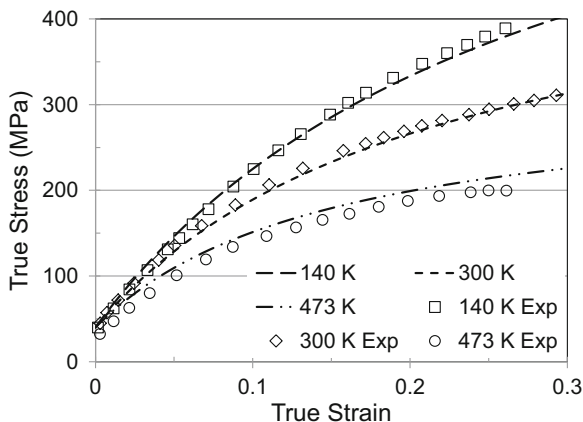
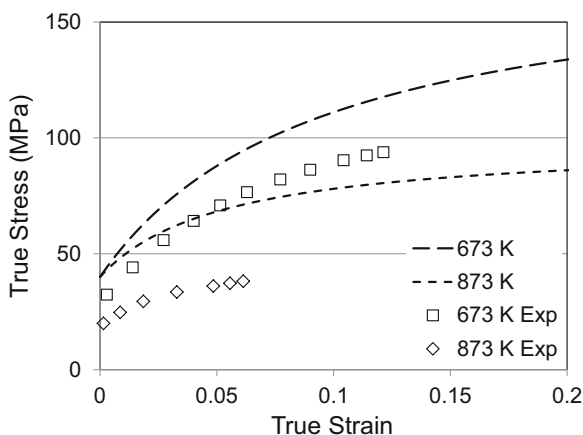


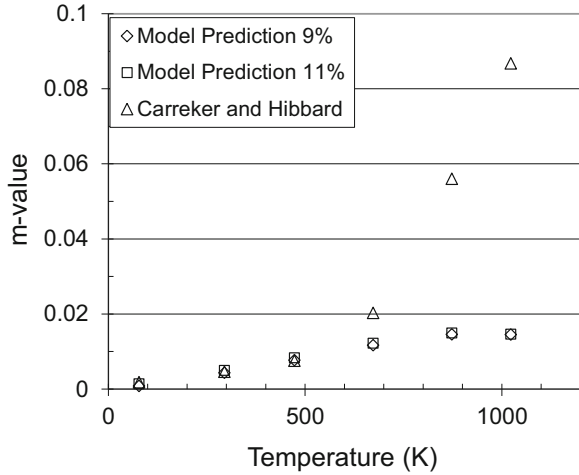
Fig. 8.14 Model predictions at 673 K and 873 K illustrating that at temperatures approaching $T_H/2$ the model loses predictive capability



With this agreement at 140 K, 300 K, and 473 K, Fig. 8.14 compares predictions of the model at 673 K ($T_H = 0.495$) and 873 K ($T_H = 0.643$). At these high temperatures, the model overpredicts the stress levels, with the magnitude of error increasing with increasing temperature. It is also interesting that the measured yield stress, which at lower temperatures hovered around 40 MPa (consistent with an athermal stress) is observed to decrease. This is evidence that the low-temperature model breaks down as the temperature approaches a homologous temperature of 0.5.

In addition to the monotonic tensile tests Carreker and Hibbard performed strain-rate change tests. These were strain-rate changes from 0.00067 s^{-1} to 0.000067 s^{-1} at a strain of $\sim 9\%$ followed by a return to the original strain rate at a strain of $\sim 11\%$. Figure 8.15 compares the measured strain-rate sensitivity—the m -value—defined as

Fig. 8.15 Measurements of the strain-rate sensitivity m -value versus test temperature and comparison of predicted and measured values



$$m = \left. \frac{\partial \ln \sigma}{\partial \ln \dot{\epsilon}} \right|_{\epsilon, T} \tag{8.3}$$

with the predicted m -value. These measurements were in material annealed at 1223 K (950 C) which gave an average grain dimension of 90 μm , which should lead to a slightly smaller athermal stress σ_a than the 40 MPa measured in material annealed at 1023 K (750 C) but likely no effect on the m -value. (Indeed, Carreker and Hibbard showed a higher m -value in material annealed at 523 K (250 C), but this temperature may not have been high enough to yield a fully recrystallized structure.) The measured and predicted m -values agree closely up to a temperature of ~ 600 K ($T_H = 0.442$) where the measured strain-rate sensitivity deviates sharply from the low-temperature curve. This observation offers further insight into the transition between low and high temperature deformation in this material. It should be emphasized that the MTS model as described is limited to low-temperature deformation.

8.4 Eleiche and Campbell Measurements in Torsion

Eleiche and Campbell performed an extensive experimental investigation of large strain deformation in OFHC copper [6]. In copper (OFHC with an average grain size of $\sim 53 \mu\text{m}$), the tests involved the torsion testing of tube geometries at shear strain rates of 0.003 s^{-1} and 900 s^{-1} and temperatures from 123 K (-150 C) to 673 K (400 C). The wall thickness of the copper test specimen was 381 μm . Since this dimension corresponds to seven grains across the wall, a potential complication exists which is similar to that noted for the Carreker and Hibbard tests on wire geometries. Figure 8.16 shows the Eleiche and Campbell measurement at a RT and a shear strain rate of 0.003 s^{-1} . Plotted is shear stress τ versus shear strain γ .

Fig. 8.16 Shear stress versus shear strain measured in torsion at 294 K and a shear strain rate of 0.003 s^{-1} by Eleiche and Campbell [6] in copper

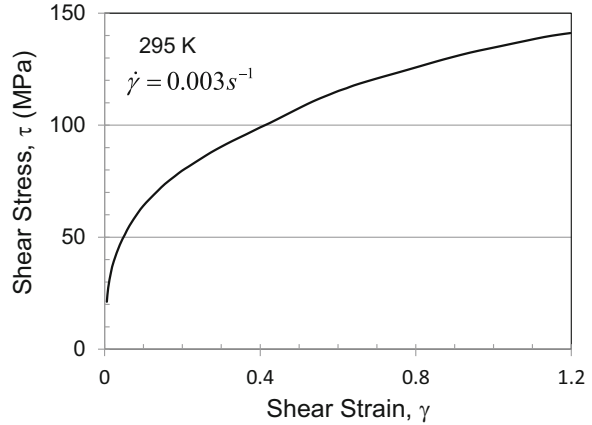
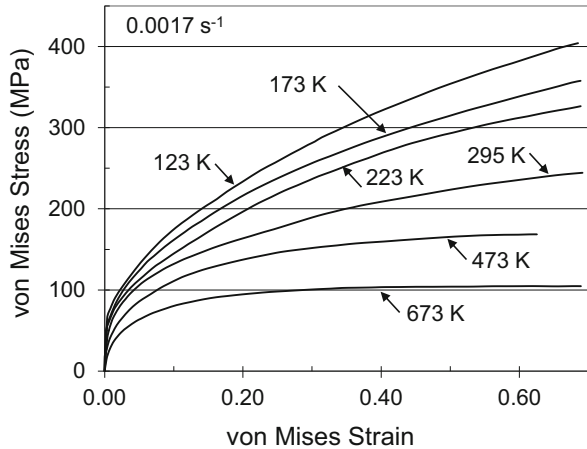


Fig. 8.17 Eleiche and Campbell measurements (on von Mises stress–strain coordinates) at a von Mises strain rate of 0.0017 s^{-1} versus test temperature



To compare shear stress and strain measured in a torsion test with axial stress and strain measured in a uniaxial tensile or compression test, shear stress and strain may be converted to von Mises stress and strain (recall the discussion in the [Box 1.2](#) in [Chap. 1](#) entitled “Scalar Stress Representations”):

$$\begin{aligned}\sigma_v &= \sqrt{3}\tau \\ \epsilon_v &= \gamma/\sqrt{3} \\ \dot{\epsilon}_v &= \dot{\gamma}/\sqrt{3}\end{aligned}\tag{8.4}$$

Note that in a uniaxial tensile or compression test, the von Mises stress and strain are equivalent to the uniaxial stress and strain; thus, the subscript “v” can be dropped. Figures [8.17](#) and [8.18](#) show the Eleiche and Campbell measurements at the axial

Fig. 8.18 Eleiche and Campbell measurements (on von Mises coordinates) at a von Mises strain rate of 520 s^{-1} versus test temperature

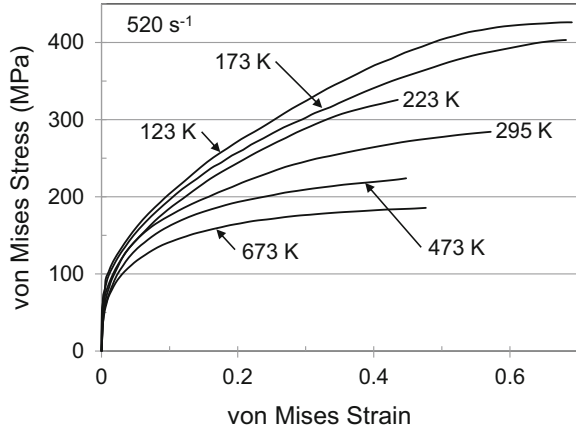
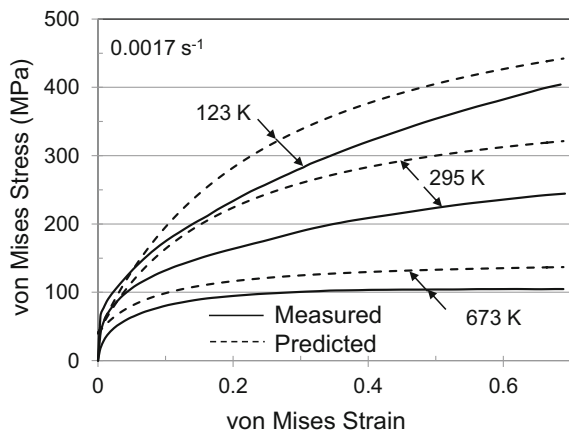


Fig. 8.19 Comparison of measured versus predicted stress–strain curves (using model parameters in Table 8.4) for three of the test temperatures at the lower strain rate investigated by the Eleiche and Campbell



strain rate of 0.0017 s^{-1} (Figs. 8.17) and 520 s^{-1} (Fig. 8.18) for all of the temperatures tested. The curves exhibit a similar shape to those measured by Carreker and Hibbard, although Eleiche and Campbell tested to a maximum temperature of 673 K whereas Carreker and Hibbard reported measurements to temperatures as high as 1023 K.

To compare the Eleiche and Campbell measurements to MTS model predictions, the model parameters listed in Table 8.4 are used to generate stress–strain curves. Three of these predictions are plotted along with measurements at temperatures of 123 K, 295 K, and 673 K and the lower strain rate in Fig. 8.19 and at the same temperatures and the higher strain rate in Fig. 8.20. For each condition the model overpredicts the stress level. For the tests at the higher strain rates, the measured initial strain hardening rate is higher than that predicted. It is noteworthy that the torsion measurements fall beneath the uniaxial predictions, which is in the same direction as noted in Fig. 8.12 from Kocks, Stout, and Rollett. However, at least at

Fig. 8.20 Comparison of measured versus predicted stress–strain curves (using model parameters in Table 8.4) for three of the test temperatures at the higher strain rate investigated by the Eleiche and Campbell

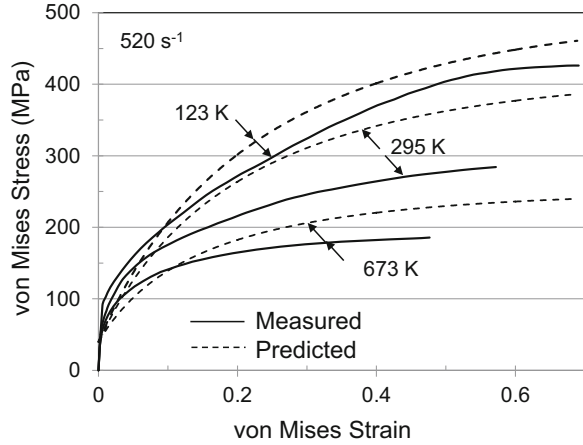
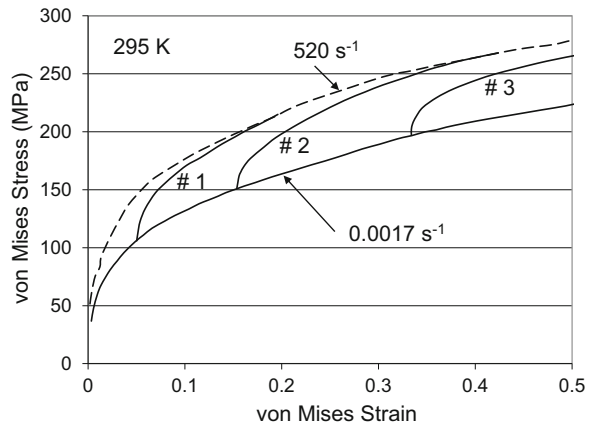


Fig. 8.21 Strain-rate jump tests (0.0017 s^{-1} to 520 s^{-1}) at three strain levels for RT testing measured by Eleiche and Campbell

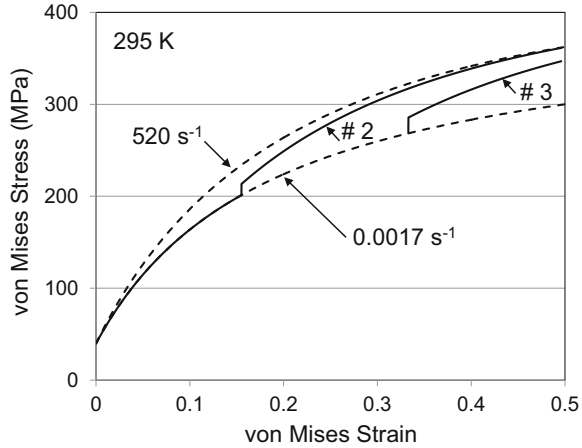


RT, the ratio of the compression to the torsion stresses appears to be higher than that observed by Kocks et al. In the near-yield region, the rate of strain hardening, particularly at the higher strain rates, appears unusually high.

One could adjust model parameters to achieve a closer fit with the experimental curves. However, given (i) an appreciation of stress-state effects, (ii) the question about homogeneous deformation across a gage section when the average grain dimension is not at least an order of magnitude (or more) smaller than the section size, and (iii) experimental observations (e.g., in the near-yield region) that are at odds with other experimental measurements, care should be practiced in over-interpreting a single data set.

In their extensive experimental study, Eleiche and Campbell also performed strain-rate-change tests. These tests were jump tests from the lower to the higher strain rate at several strain levels. Figure 8.21 shows three of their measured responses at RT.

Fig. 8.22 Predicted stress–strain curves for two of the jump conditions in Fig. 8.21



Prediction of the response to a strain-rate change follows naturally from the internal-state variable formulation. For the jump test marked #2 in Fig. 8.21, Eq. 8.2 is integrated, starting with $\hat{\sigma}_\epsilon = 0$ at a strain of zero, for the initial strain rate of 0.0017 s^{-1} and the test temperature of 295 K. At this temperature and strain rate $\hat{\sigma}_{\epsilon s} = 442 \text{ MPa}$ from Eq. 6.26 and $\theta_{II} = 2314 \text{ MPa}$ from Eq. 6.29. The stress at any value of $\hat{\sigma}_\epsilon$ is calculated using Eq. 8.1 (and the same values of strain rate and temperature). At a von Mises strain of 0.156 the strain rate is increased to 520 s^{-1} , where $\hat{\sigma}_{\epsilon s} = 563 \text{ MPa}$ and $\theta_{II} = 2380 \text{ MPa}$. (Note that the change in θ_{II} is small compared to the change in $\hat{\sigma}_{\epsilon s}$.) The integration using Eq. 8.2 continues with the new parameters, and stress is calculated using Eq. 8.1 with the new strain rate. Also, since the higher strain-rate test is under adiabatic conditions, the test temperature is updated using Eq. 6.32. Figure 8.22 shows the predicted strain-rate change test response for jumps # 2 and # 3. The predicted stresses are high, similar to that observed in Figs. 8.18 and 8.19, but the predicted change in stress and the predicted strain hardening following the two strain-rate changes agrees well with the measured response in Fig. 8.21. The ability to describe the response to a change in strain rate validates the form of the adopted hardening law (Eq. 8.2).

The agreement between measurements and model predictions at 673 K is not nearly as good. Figure 8.23 shows the Eleiche and Campbell measurements of strain-rate jumps at three strains. The predicted behavior is shown in Fig. 8.24. At this temperature, the measured increase in stress following each of the strain-rate changes exceeds the predicted increase. This is a similar trend to that observed in the Carreker and Hibbard measurements of strain-rate sensitivity at the higher temperature (Fig. 8.15) where the measured strain-rate sensitivity deviates sharply (toward higher values) than the predicted strain-rate sensitivity. These results offer further evidence that the low-temperature mechanistic model begins to break down as the temperatures approaches a homologous temperature of 0.50.

Fig. 8.23 Strain-rate jump tests (0.0017 s^{-1} to 520 s^{-1}) at three strain levels for 673 K tests measured by Eleiche and Campbell

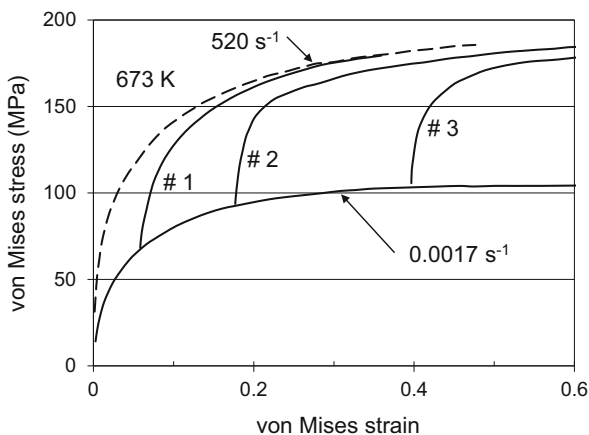
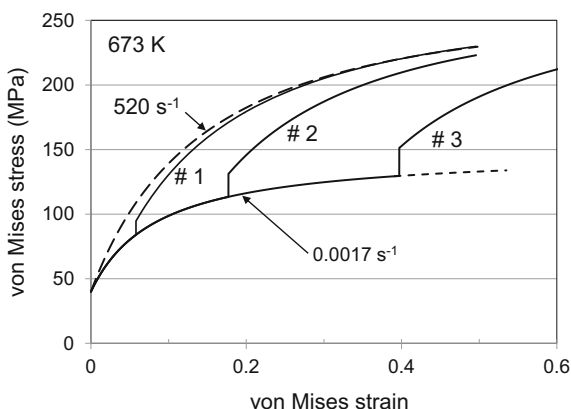


Fig. 8.24 Predicted stress-strain curves for two of the jump conditions in Fig. 8.23



The Follansbee and Kocks measurements in copper construe the most complete set of room temperature prestrains and reloads as a function of prestrain strain rate. Unfortunately, these measurements were never complemented with prestrains at other than room temperature. If strain rate and temperature are related through kinetic equations such as Eq. 6.15 (at constant threshold stress) and Eq. 6.26 (for the strain rate and temperature dependence of $\hat{\sigma}_\epsilon$), then a prestrain plus reload campaign over a wide range of strain rates should provide predictive capability with variations in temperature as long as the deformation mechanism remains uniform. Agreement with several independent measurements at elevated temperatures in copper was demonstrated in this section at temperatures less than one-half the homologous temperature.

The next sections extend the model application to nickel—another metal with an FCC crystal structure—as well as to nickel alloyed with carbon to introduce another deformation mechanism.

8.5 Analysis of Deformation in Nickel

Nickel is another metal that has been the subject of numerous experimental deformation studies. It has an FCC crystal structure and is readily obtained in a commercially pure form. The alloy Ni 270 has a minimum purity level of 0.999. The melting temperature of nickel is 1728 K, which gives a homologous temperature of 0.171 for room temperature tests. Follansbee et al. [7] performed prestrain and reload experiments in Ni 270 processed to give an isotropic structure with an initial grain dimension of 40 μm . Along with experiments in Ni 270, Follansbee et al. procured material with a carbon concentration of 510 wt. ppm (referred to as Ni 510) and another ingot with a carbon concentration of 1900 wt. ppm (referred to as Ni 1900). These latter alloys were used to investigate how introduction of a second strengthening mechanism—in addition to the strengthening associated with the interaction of dislocation with stored dislocations—would affect the constitutive behavior.

The testing matrix for Ni 270 is shown in Table 8.5. This test matrix did not include strains higher than 40% and it included only three prestrain strain rates rather than the seven that made up the copper test matrix shown in Table 8.1. Reload tests were performed at a strain rate of 0.001 s^{-1} and temperatures of RT, 180 K, and 76 K. A few reload tests were performed at a RT and a strain rate of 1 s^{-1} . Repeat reload tests were performed giving a total of 150 reload compression tests.

The constitutive behavior in the three alloys was analyzed according to

$$\frac{\sigma}{\mu} = \frac{\sigma_a}{\mu} + s_i(\dot{\epsilon}, T) \frac{\hat{\sigma}_i}{\mu_o} + s_e(\dot{\epsilon}, T) \frac{\hat{\sigma}_\epsilon}{\mu_o} \quad (8.5)$$

where the $\hat{\sigma}_i$ —term represents the interaction of dislocations with impurity atoms. This term was added to facilitate analysis of the Ni 270 plus carbon alloys. To evaluate the model parameters (g_{oi} and $\hat{\sigma}_i$) in the impurity atom contribution, yield stress measurements in the three materials in the annealed condition were first analyzed. For these tests $\hat{\sigma}_\epsilon$ is assumed to equal zero. Figure 8.25 is a plot of the yield stress versus test temperature and strain rate on the familiar axes.

The model parameters used for the dashed line fits in Fig. 8.25 are listed in Table 8.6. In addition to those listed, $p_i = 0.5$, $q_i = 1.5$, and $\dot{\epsilon}_{oi} = 10^9 \text{ s}^{-1}$. The strain-rate constant $\dot{\epsilon}_{oi}$ differs from the value of 10^7 s^{-1} used for the obstacle representing dislocation interactions with the stored dislocation density (as listed for copper in

Table 8.5 Prestrain conditions (strains at each specified strain rate) for Ni 270 test specimens for the Follansbee, Huang, and Gray [7] study

Strain rate (s^{-1})	Strain				
0.0005	0.0356	0.831	0.185	0.285	0.384
0.8	0.034	0.85	0.187	0.289	0.385
4000	0.052	0.108	0.204	0.306	0.404

A minimum of 10 identical specimens were prepared for each strain rate and strain combination. All prestrains were at RT

Fig. 8.25 Variation of yield stress with temperature and strain rate in Ni 270, Ni 510, and Ni 1900

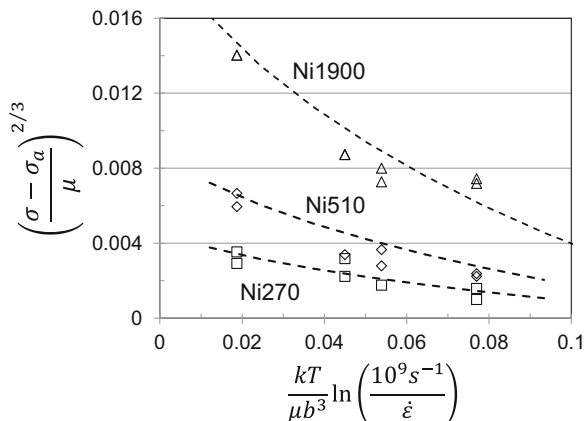


Table 8.6 Deduced values of the athermal stress σ_a and the mechanical threshold stress characterizing interactions of dislocations with the carbon interstitial atoms $\hat{\sigma}_i$ in Ni 270 and the two carbon-containing alloys

Material	Carbon conc. (ppm by weight)	σ_a (MPa)	$\hat{\sigma}_i$ (MPa)	g_{oi}
Ni 270	55	50	28.9	0.20
Ni 510	510	40	76.6	
Ni 1900	1900	60	255	

Table 8.4). The different value has a negligible effect on the curves in Fig. 8.25; a higher value was selected because it, in general, yielded slightly better correlations in FCC alloys (e.g., austenitic stainless steels) and BCC metals. These systems are discussed in subsequent chapters.

The athermal stresses were selected partially according to the measured grain sizes (40 μm for Ni 270, 55 μm for Ni 510, and 45 μm for Ni 1900) and partially from values which achieved agreement in Fig. 8.25. Note that a single value of g_{oi} yielded good agreement with all of the measurements, except perhaps for the RT, 0.001 s^{-1} test in Ni 1900 (the data point on the far right). The small value of g_{oi} is consistent with the expectation that the interaction of dislocations with individual interstitial atoms or even very small clusters should be more thermally activated than the interaction of dislocations with the stored dislocation density. The reason for the deviation between model predictions and the measurements in Ni 1900 at RT and a strain rate of 0.001 s^{-1} is not clear. The deviation may reflect the contribution of dynamic strain aging [8] (due to mobility of carbon at this temperature) which has been observed in Ni-C alloys [9] with similar carbon concentrations to those investigated by Follansbee et al., but this has not been verified in either the Ni 510 or Ni 1900 materials, e.g., with tensile tests showing serrated flow.³

³It is argued in Chap. 13 that DSA should not affect the yield stress in well-annealed materials.

Fig. 8.26 Reload yield stress versus reload temperature and strain rate in Ni 270 for prestrains at room temperature and a strain rate of 0.8 s^{-1} . The prestrain strain levels are, from bottom to top, 0.034, 0.085, 0.187, 0.289, and 0.385

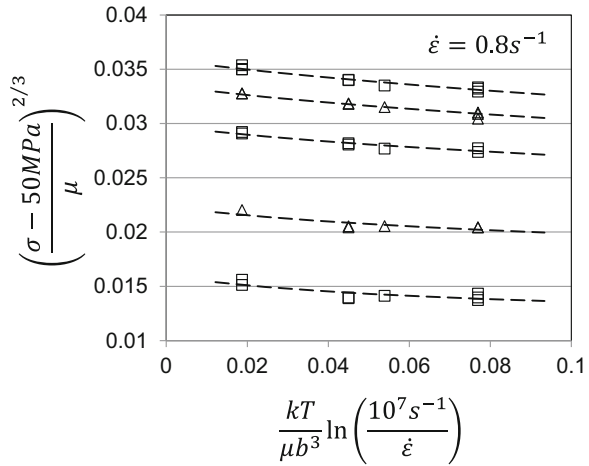


Table 8.7 Model parameters for Ni 270 used for the dashed-line predictions in Fig. 8.26

Equation	Parameter	Ni 270
8.5	σ_a	50 MPa
8.5	$\widehat{\sigma}_i$	28.9 MPa
6.15 ^a	pi	0.5
	qi	1.5
	$\dot{\epsilon}_{oi}$	10^9 s^{-1}
	g_{oi}	0.20
8.5	$\widehat{\sigma}_\epsilon (\epsilon = 0.034)$	145 MPa
	$\widehat{\sigma}_\epsilon (\epsilon = 0.085)$	259 MPa
	$\widehat{\sigma}_\epsilon (\epsilon = 0.187)$	411 MPa
	$\widehat{\sigma}_\epsilon (\epsilon = 0.289)$	495 MPa
	$\widehat{\sigma}_\epsilon (\epsilon = 0.385)$	552 MPa
7.9	$p\epsilon$	2/3
	$q\epsilon$	1
	$\dot{\epsilon}_{o\epsilon} (\text{s}^{-1})$	10^7 s^{-1}
	$g_{o\epsilon}$	1.6

^a $\widehat{\sigma}_i$ represents the dislocation interactions with carbon “impurity” atoms

Figure 8.26 shows the reload yield stress versus reload temperature and strain rate for the prestrains at RT and 0.8 s^{-1} . The data is plotted on coordinates similar to those used for copper in Fig. 8.1 except the athermal stress σ_a is taken as 50 MPa (compared to 40 MPa for copper). The only additional model parameters used to generate the curves shown in Fig. 8.26 are $\widehat{\sigma}_\epsilon$ and $g_{o\epsilon}$. The latter was selected as 1.6—identical to the average value observed in copper (Fig. 8.5). There is insufficient data to observe the trend with stress illustrated for copper in Fig. 8.26. Table 8.7 also lists the values of $\widehat{\sigma}_\epsilon$ at each strain level that enable the model predictions to agree with the reload yield stress measurements. This value affects the level of the curve as well as (subtly) the slope and curvature.

Fig. 8.27 Variation of $\hat{\sigma}_\epsilon$ with strain in Ni 270 for the three prestrain strain rates (data points) with model fits (dashed lines)

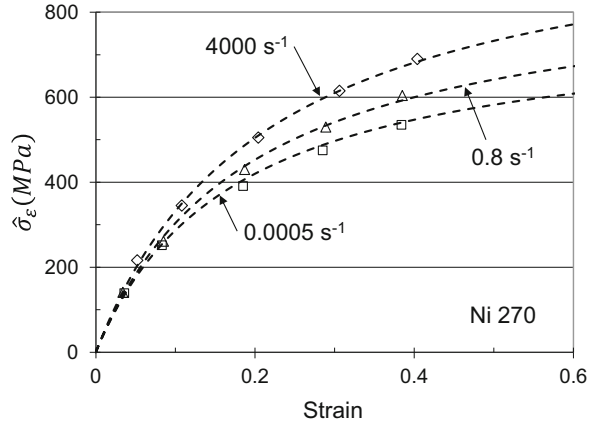


Table 8.8 Values of θ_{II} and $\hat{\sigma}_{es}$ used for the dashed lines in Fig. 8.27

Equation	Parameter	Prestrain strain rate (s^{-1})	Value	
6.28	κ	All	2	
		θ_{II} (MPa)	0.0005	4500
			0.8	4600
	4000		4840	
	$\hat{\sigma}_{es}$ (MPa)	0.0005	757	
		0.8	876	
4000		1030		

Evolution is treated in the same fashion as demonstrated for copper in Fig. 8.2. Figure 8.27 plots $\hat{\sigma}_\epsilon$ versus strain for the three prestrain strain rates.⁴ (Recall that the threshold stress characterizing dislocation interactions with carbon is assumed to remain constant at the value of 28.9 MPa listed in Table 8.7.) The data points at the two lowest strains at a strain rate of $0.0005 s^{-1}$ appear to be low, whereas a few of the data points at a strain rate of $0.8 s^{-1}$ appear to be high, but in general the trends follow those observed in copper in Fig. 8.2. The dashed lines in Fig. 8.27 are drawn according to Eq. 6.26 with the values of θ_{II} and $\hat{\sigma}_{es}$ listed in Table 8.8.

Figure 8.28 is a plot of $\hat{\sigma}_{es}$ versus strain rate and temperature according to Eq. 6.26 similar to that drawn for copper in Fig. 8.3. A straight line through the zero and with $\hat{\sigma}_{eso} = 1260$ MPa can be fit to the three strain-rate-dependent saturation stresses. The slope of the line equates to a g_{eso} -value of 0.168. (Recall from Eq. 6.26 that g_{eso} equals the inverse of the slope of the line in Fig. 8.28.)

⁴As in Ni 270 reanalysis of the original data with different values of $\dot{\epsilon}_{oi}$, g_{oi} , and $g_{o\epsilon}$ has yielded slight differences in Fig. 8.38 compared to Table 5 and Figure 10 of Ref. [7]. Also, see footnote 2 in Table 8.4.

Fig. 8.28 Saturation stress in Eq. 6.28 as a function of temperature and strain rate in Ni 270 for the three prestrain strain rates

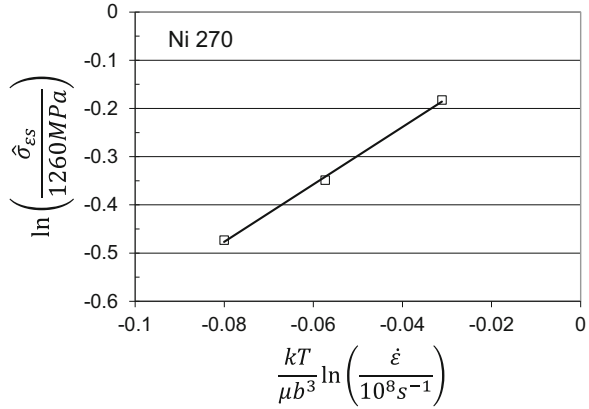


Fig. 8.29 Stage II hardening rate in Ni 270 as a function of strain rate. Solid line is drawn according to Eq. 6.29

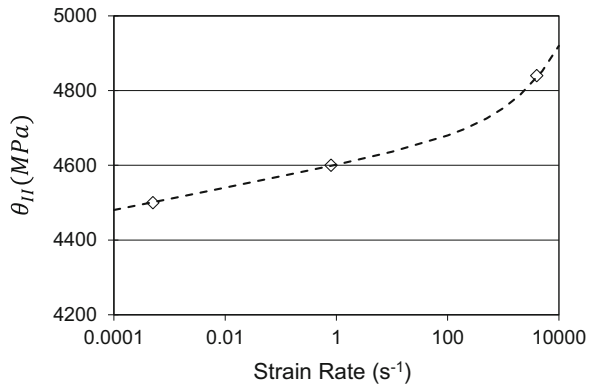


Table 8.9 Evolution parameters for Ni 270 compared to those from Table 8.4 for copper

Equation	Parameter	Ni 270	Copper (Table 8.4)
6.26	$\hat{\sigma}_{\epsilon s o}$ (MPa)	1260	710
	$\dot{\epsilon}_{\epsilon s o}$ (s ⁻¹)	10 ⁸	10 ⁸
	$g_{\epsilon s o}$	0.168	0.301
6.28	κ	2	2
6.29	A_o (MPa)	4600	2390
	A_1^{III}	13	12
	A_2 (s ^{-1/2})	2.0	1.696

The variation of θ_{II} with strain rate is shown in Fig. 8.29. This plot should be compared to the similar one for copper in Fig. 8.4. The three data points do not follow Eq. 6.29 likely due to the suspected low and high $\hat{\sigma}_\epsilon$ values at strain rates of 0.0005 s⁻¹ and 0.8 s⁻¹, respectively. The dashed line through the data points is drawn according to Eq. 6.29.

Table 8.9 lists all of the model parameters for evolution and compares them to those determined for copper. There is a clear correlation between the model parameters and the two materials.

8.6 Predicted Stress–Strain Curves in Nickel and Comparison with Experiment

The MTS model parameters listed in Tables 8.7 and 8.9 along with the equations referenced in these tables comprise the constitutive law for Ni 270. Figure 8.30 compares model predictions (dashed lines) with measured stress–strain curves [1] (solid lines) at RT and strain rates of 0.0005 s^{-1} , 0.8 s^{-1} , and 4000 s^{-1} . The comparison is good at the two lower strain rates, but the predicted curve at the higher strain rate falls below the measured curve at strains exceeding 0.35. The stress–strain curves at the two highest strain rates were calculated assuming adiabatic deformation, which is a very good assumption at these strain rates. The reason for the disagreement at the highest strain rate is not clear. In general, the predictions at strains greater than 0.40 represent an extrapolation since the highest strains investigated with prestrain tests were ~ 0.40 (see Table 8.5). It is also possible that friction on the specimen ends was particularly large at high strains. Typically, friction leads to higher stresses than expected, which is consistent with the test result in Fig. 8.30.

Figure 8.31 compares the model predictions with an elevated temperature (573 K) measurement in Ni 270 [3]. The experimental curve was measured in a Split Hopkinson Pressure Bar (SHPB) and the bumps and wiggles in the data are actual stress waves reverberating in the specimen. Often—as in the RT curve at 4000 s^{-1} in Fig. 8.30—a smooth curve is drawn through the data. Given that 573 K is well above RT which was the temperature of all of the prestrain tests, the agreement shown in Fig. 8.31 between the measurement and the model is quite good.

Muller [10] measured the high strain-rate compressive stress–strain curve in polycrystalline nickel at temperatures from RT to 500 C (773 K). The material was vacuum-melted electrolytic nickel with a purity of 0.9995 and a mean grain diameter of 70 nm. As a baseline, Muller reported a single stress–strain curve measured in tension at RT and a strain rate of 0.00225 s^{-1} . This curve is compared in Fig. 8.32 with a predicted curve using the model parameters in Tables 8.7 and 8.9. The larger grain size and the higher purity in the Muller material—compared to the

Fig. 8.30 Predicted (dashed lines) and measured (solid lines) stress–strain curves at room temperature and the three strain rates

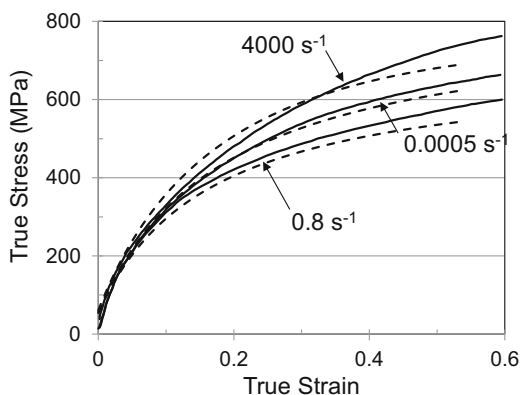


Fig. 8.31 Predicted (dashed line) and measured stress–strain curve in Ni 270 at 300 C (573 K) and a strain rate of 3200 s^{-1}

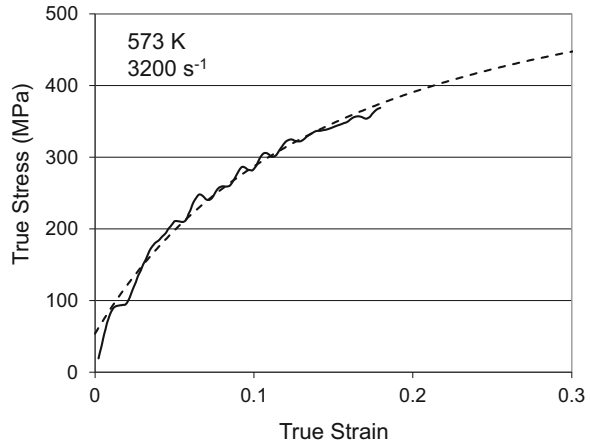
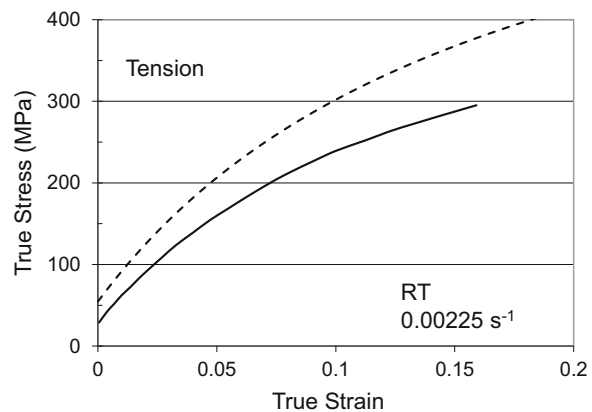


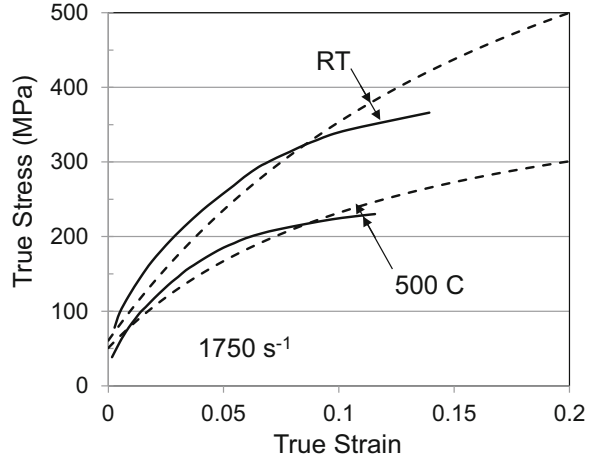
Fig. 8.32 Room temperature, low strain-rate stress–strain curve in tension in pure nickel reported by Muller [10] compared to the model prediction with no change in model parameters



Ni 270 studied by Follansbee, Huang, and Gray—are consistent with the observation that the predicted curve falls above the experimental curve. However, the predicted hardening rate appears high when compared to the measured rate.

Figure 8.33 compares compression curves measured by Mueller at a strain rate of $\sim 1750 \text{ s}^{-1}$ and at test temperatures of RT and 500 C (773 K). Whereas the experimental tensile curve was below the predicted curve, the experimental compression curves in Fig. 8.33 lie above the predicted curves. Of course, the measurements in Fig. 8.33 are at a high strain rate, whereas that in Fig. 8.32 is at low strain rate. It seems unlikely, however, that the strain-rate dependence of the Muller material is that different from the strain-rate dependence of Ni 270. Rather, these comparisons emphasize the difficulty in comparing single measurements. One could adjust model parameters to achieve a closer comparison between these measurements and model predictions. This is not a recommended practice, however. A positive observation in Fig. 8.33 is that the relative temperature dependence is

Fig. 8.33 Compression stress–strain curves measured by Muller [10] in pure nickel at two temperatures compared to model predictions with no change in model parameters



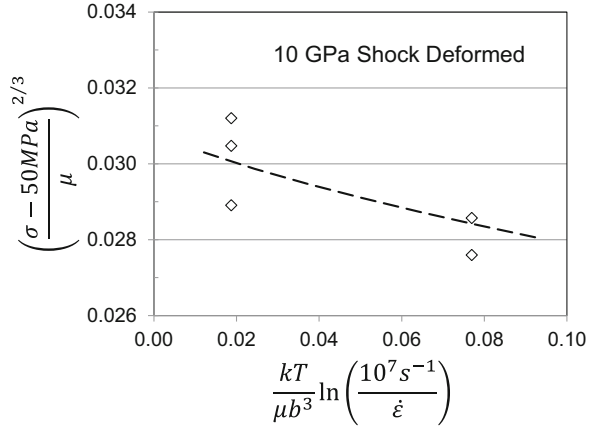
similar in both materials. That is, while the experimental and predicted curves exhibit a different shape, the effect of temperature on the strength level is well-predicted.

8.7 Application to Shock Deformed Nickel

To demonstrate the predictive capability of the MTS model, consider the stress–strain response of Ni 270 exposed to shock deformation. A shock produced by high velocity planar impact creates a stress wave which compresses the impacted material to a higher density until a release wave traverses the sample to decompress the material. The stress wave results in an increment of plastic strain that is offset by an increment of plastic strain of the opposite sign when the sample is decompressed. One might ask whether the decompression process can simply undo or reverse the strain resulting from the compression process yielding an undeformed sample. However, the collective nature of dislocation generation and storage events prohibits this. For a planar shock in a nickel [11] sample produced by impact of a nickel flyer plate propelled at a velocity of 458 m/s a 10 GPa shock wave is produced that yields a total strain (compression plus decompression) of 6.42%. This, of course, occurs at very high strain rates.

Here, the shock deformation is treated as a prestrain. Of interest is whether the reload stress–strain curves can be predicted. Just as in prestrained copper and nickel, compression specimens can be machined from the shock loaded sample to enable measurement of the temperature and strain-rate-dependent yield stress. Fig. 8.34 shows the result on Ni 270 shocked to 10 GPa. Included are measurements at a strain rate of 0.001 s^{-1} and temperatures of 77 K and 295 K. The line through the data points was drawn as in Fig. 8.26, giving $\hat{\sigma}_\epsilon = 434 \text{ MPa}$. For some reason, the

Fig. 8.34 Yield stress versus test temperature and strain rate in material machined from Ni 270 shock deformed at 10 GPa



measurements at the lower temperature (left-hand side of Fig. 8.34) exhibit more scatter than typically observed. However, as in Fig. 8.26, the only adjustable parameter used to derive the fit is $\hat{\sigma}_\epsilon$, and the best fit line in Fig. 8.34 describes well the collective data.

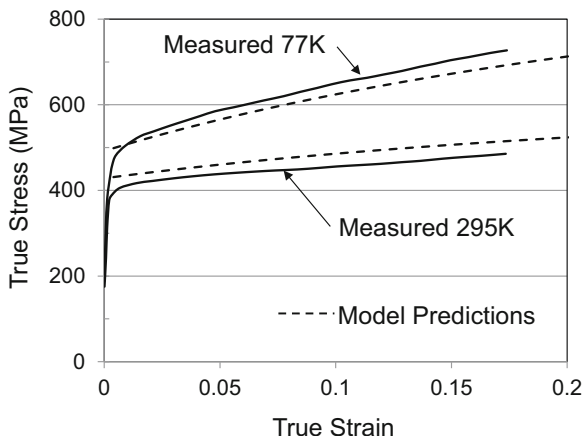
Keeping in mind that the total strain level achieved in the shock is only 6.42%, it is interesting to compare the measured $\hat{\sigma}_\epsilon$ -value to those included in Fig. 8.27. At the same strain level on the curve for the 4000 s^{-1} prestrains, the $\hat{\sigma}_\epsilon$ -value measured in the shock deformed material is approximately 2X the value at 4000 s^{-1} . In fact, a strain level of $\sim 16\%$ at 4000 s^{-1} is required to achieve the same $\hat{\sigma}_\epsilon$ -value (434 MPa) as measured in the shock deformed material. Shock deformation very effectively hardens the material.

The measured $\hat{\sigma}_\epsilon$ -value enables a prediction of the reload stress–strain curves in the shock deformed material. This is of interest since shock waves often accompany explosive events and the initial shock can be followed by large deformations at high strain rates but not as high as experienced during the shock. Simulation of dynamic events such found in projectile impact and penetration requires an understanding of the hardening from the shock event and the constitutive behavior of shock-deformed metal. Once again, the MTS model parameters listed in Tables 8.7 and 8.9 and the model equations referenced in these tables form the constitutive formulation for the reload tests. The difference is that, whereas in annealed material $\hat{\sigma}_\epsilon$ is initially zero, in Ni 270 shock deformed at 10 GPa $\hat{\sigma}_\epsilon$ in Eq. 8.5 is initially set at 434 MPa. In this case, the governing constitutive equation becomes

$$\frac{\sigma}{\mu} = \frac{50\text{MPa}}{\mu} + s_i(\dot{\epsilon}, T) \frac{33.2\text{MPa}}{85090\text{MPa}} + s_\epsilon(\dot{\epsilon}, T) \frac{\hat{\sigma}_\epsilon}{85090\text{MPa}} \quad (8.6)$$

where $\hat{\sigma}_i = 28.9 \text{ MPa}$ is the value for Ni 270 listed in Table 8.6 and $\mu_o = 85,090 \text{ MPa}$ is the value for nickel listed in Table 6.1. The evolution equation (the integrated form of Eq. 6.28) becomes

Fig. 8.35 Reload stress–strain curves (symbols) measured at 10^{-3} s^{-1} and temperatures of 77 K and 295 K compared to model predictions (dashed lines)



$$\hat{\sigma}_\varepsilon = 434\text{MPa} + \int_0^\varepsilon \theta_{II}(\dot{\varepsilon}) \left(1 - \frac{\hat{\sigma}_\varepsilon}{\hat{\sigma}_{es}(\dot{\varepsilon}, T)} \right)^\kappa d\varepsilon \quad (8.7)$$

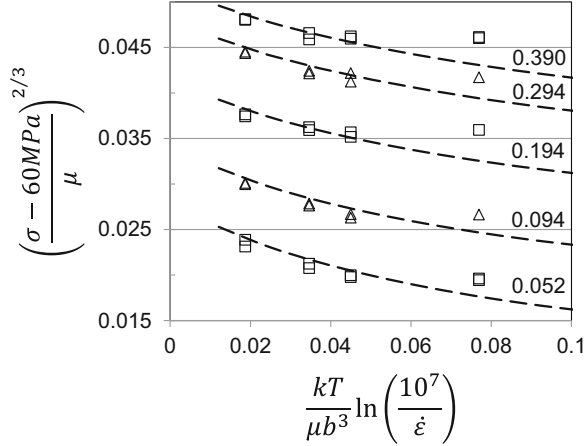
The methodology is analogous to the scenario discussed in [Box 6.3](#) entitled “The Tapered Plate Experiment” where at any point along the tapered plate the initial value of the mechanical threshold stress associated with that point is specified.

Figure 8.35 compares the measured reload stress–strain curves at a strain rate of 0.001 s^{-1} and temperatures of 77 K and 295 K. The yield stresses should agree since these data points were included in Fig. 8.34 and became the basis for determination of $\hat{\sigma}_\varepsilon$. But the agreement between measured and predicted strain hardening is a true test of the model assumptions and validity of the constitutive equations. The agreement between the predictions and measurements in Fig. 8.35 is not perfect, but the trends are adequately described.

8.8 Deformation in Nickel Plus Carbon Alloys

A comparison of the model parameters for nickel in Tables 8.7 and 8.9 with those for copper in Table 8.4 leads to the conclusion that deformation in these materials is very similar. This is sensible in that both are FCC, both of the materials studied had low impurity levels, and the common rate-controlling deformation mechanism is interaction of mobile dislocations with immobile or stored dislocations. To investigate the constitutive behavior of an FCC metal with a second obstacle opposing dislocation motion, Follansbee et al. [7] included two nickel–carbon alloys in the testing matrix introduced in Sect. 8.5. Actually, carbon (likely in the form of interstitial atoms [9]) as an added obstacle was already included in Eq. 8.5 since even Ni 270 had 55 ppm (by weight) of carbon. The analysis of deformation in annealed Ni

Fig. 8.36 Reload yield stress versus reload temperature and strain rate in Ni 1900 prestrained at a strain rate of 0.0009 s^{-1} to strains noted. Dashed lines are model fits using Eq. 8.5



270 summarized in Fig. 8.25 and the model parameters listed in Table 8.6 showed that even this level of carbon had a small, but noticeable effect on the temperature and strain-rate-dependent yield stress. One purpose of the Follansbee et al. study [7] was to study alloys with a higher carbon-content. The two selected alloys along with their carbon contents and the deduced values of σ_a and $\hat{\sigma}_i$ were listed in Table 8.6.

For both Ni 510 and Ni 1900 the full prestrain and reload test matrix was similar to that described for Ni 270. Figure 8.36 shows the variation of reload yield stress with temperature and strain rate for Ni 1900 prestrained at five strain levels (up to 0.39) at a strain rate of 0.0009 s^{-1} . The dashed-line fits in Fig. 8.36 were drawn using Eq. 8.5 with $\hat{\sigma}_i = 255 \text{ MPa}$ and $g_{oi} = 0.20$ (see Table 8.6). As in Fig. 8.26 for Ni 270, the only other fitting parameter is $\hat{\sigma}_\epsilon$.

As specified by Eq. 8.5, the model assumes the contributions of both obstacles add linearly. Follansbee et al. also investigated a model where the obstacles add according to a power law. In this case, Eq. 8.5 is rewritten as

$$\frac{\sigma}{\mu} = \frac{\sigma_a}{\mu} + \left\{ \left[s_i(\dot{\epsilon}, T) \frac{\hat{\sigma}_i}{\mu_o} \right]^n + \left[s_\epsilon(\dot{\epsilon}, T) \frac{\hat{\sigma}_\epsilon}{\mu_o} \right]^n \right\}^{1/n} \tag{8.8}$$

where n is a power between the values of 1 and 2 [12]. Figure 8.37 plots the data at three strains (0.052, 0.194, 0.390) on the same coordinates as in Fig. 8.36 but with $n = 1$ (longer dashes) and $n = 1.5$ (shorter dashes). It is evident that the curves with $n = 1.5$ fit data slightly better than do the curves with $n = 1$. Although agreement with the data points at the highest values of the abscissa is clearly better for $n = 1.5$, the fit over the entire range of the reload temperatures and strain rates is not improved. Recall from the earlier discussion that there is suspicion the right-most values on the abscissa affected by dynamic strain aging (although, see footnote 3). Nakada and Key analyzed the temperature and strain-rate conditions in a nickel plus 1160 ppm (by weight) carbon alloy [9]. Their analysis suggests that a test at a strain rate of 0.001 s^{-1} and a temperature of 295 K (which is the reload condition for the

Fig. 8.37 Analysis of the reload yield stress measurements at the three of the strain levels according to Eq. 8.8 with $n = 1$ (long dashes) and $n = 1.5$ (short dashes)

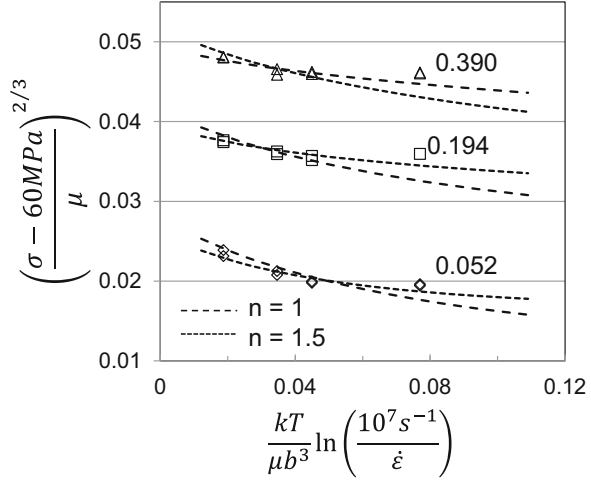


Table 8.10 Effect of n -value on the variation of $\hat{\sigma}_\epsilon$ with strain for Ni 1900 prestrained at a strain rate of 0.0009 s^{-1}

Strain	$\hat{\sigma}_\epsilon$ (MPa)	
	$n = 1$	$n = 1.5$
0.052	170	221
0.094	311	366
0.194	494	579
0.294	672	757
0.390	774	859

points in question) would be in the range where serrated flow is observed but that material tested at this same strain rate or higher and temperatures of 180 K or 77 K (points on the left side of Fig. 8.37) would not. Since Eq. 8.8 is not intended to be applicable when dynamic strain aging is active, there is no reason to expect agreement with the measured stresses and the improved agreement with $n = 1.5$ for these data points must not be misinterpreted.

The modest effect of variations of n in Fig. 8.37 highlights the desire to have a wide range of reload strain rates and temperatures in this analysis to enable an accurate comparison between measurements and model predictions. As useful as this would be, the ability to achieve these conditions can be restricted when the reload conditions take the material into different mechanistic regimes, such as observed when deformation twinning is active, which will be shown to affect the left-hand side of the plot in BCC metals.

Table 8.10 lists the selected values at each level of strain for the results in Fig. 8.36 with $n = 1$ and the results in Fig. 8.37 with $n = 1.5$.⁵ The choice of

⁵As in Ni 270 reanalysis of the original data with different values of $\dot{\epsilon}_{oi}$, g_{oi} , and g_{oe} has yielded slight differences in Fig. 8.38 compared to Table 5 Figure 10 of Ref. [7].

Fig. 8.38 Evolution in Ni 270 and Ni 1900 at room temperature and the quasi-static strain rate illustrating the higher rate of strain-hardening in the c-containing alloy

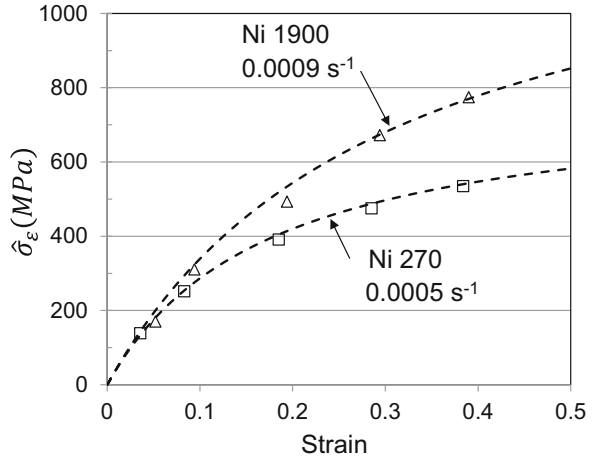
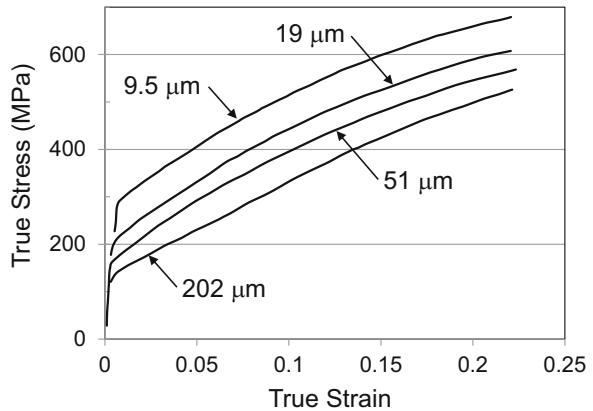


Fig. 8.39 Stress–strain curves as a function of grain size measured in Monel 400 at 298 K and a strain rate of 0.001 s⁻¹ by Gray et al. [13]



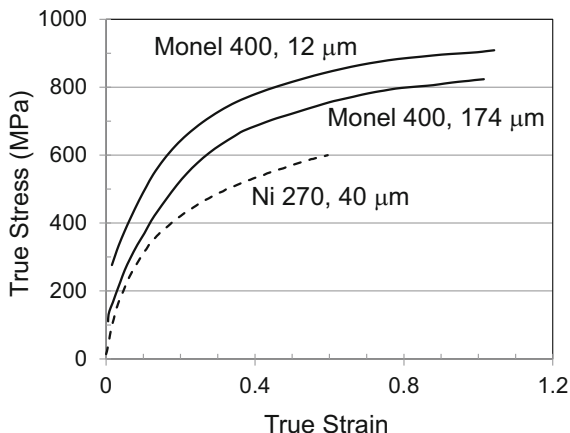
n affects the magnitude of $\hat{\sigma}_\epsilon$. Figure 8.38 compares the evolution of $\hat{\sigma}_\epsilon$ with strain for Ni 270 to that for Ni 1900 with $n = 1$. The addition of carbon increases the evolution rate in nickel. This was described by Follansbee et al., as a possible effect of carbon on the dynamic recovery rate or ability to cross slip.

8.9 Monel 400—Analysis of Grain-Size Dependence

A systematic analysis of the effect of grain size on yield and structure evolution was performed by Gray, Chen, and Vecchio [13]. They used Monel 400⁶ which is a solid-solution strengthened nickel alloy with large additions of copper (32%) and

⁶Monel is a trademark of Inco Alloys International Inc., Huntington, WV.

Fig. 8.40 Large strain compression test results in Monel 400 by Gray et al. [13] at two initial grain sizes and a comparison with a stress–strain curve in Ni 270 (50 μm grain size) at RT and roughly the same strain rate (0.0005 s^{-1} versus 0.001 s^{-1})



smaller additions of iron, manganese, silicon, aluminum, and carbon. Compression tests on material with a starting grain size as small as 9.5 μm to as large as 202 μm were performed as a function of test temperature and strain rate.

Figure 8.39 shows a selection of the stress–strain curves recorded at a 298 K and a strain rate of 0.001 s^{-1} . Measurements on material with an average grain size of 9.5 μm , 19 μm , 51 μm and 202 μm are included. Gray et al. [13] noted that the initial grain size affects the yield stress but not the rate of strain hardening. Similar conclusions are drawn for tests at 77 K and a strain rate of 0.001 s^{-1} and at 298 K and a strain rate of 3000 s^{-1} .⁷

Figure 8.40 shows two stress–strain curves strained through incremental loading to a true strain of ~ 1 . Included are measurements at 298 K and a strain rate of 0.001 s^{-1} for material with starting grain sizes of 12 μm and 174 μm . Also included is a measurement in Ni 270 (Fig. 8.30) at 298 K and a strain rate of 0.0005 s^{-1} . The two Monel alloys are separated by an approximately constant stress level (~ 100 MPa), which reinforces the conclusion that the initial grain size affects the stress level but not the rate of strain hardening. The rate of strain-hardening in pure nickel tracks the hardening in the alloy, and as expected, the stress level in pure nickel is lower than that in the alloy.

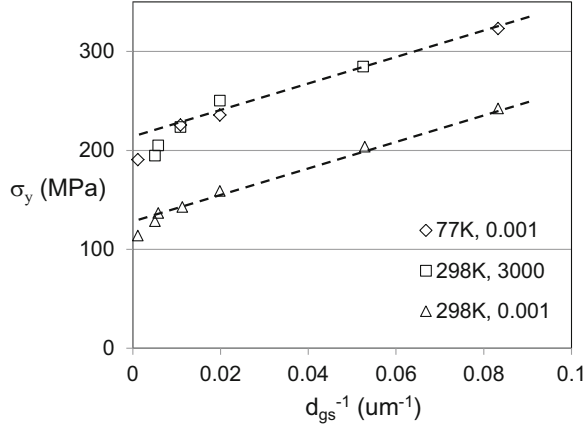
Gray et al. [13] analyzed the grain-size dependence on the stress using a model of the form of Eq. 8.5

$$\frac{\sigma}{\mu} = \frac{\sigma_a(d_{gs})}{\mu} + s_i(\dot{\epsilon}, T) \frac{\hat{\sigma}_i}{\mu_o} + s_\epsilon(\dot{\epsilon}, T) \frac{\hat{\sigma}_\epsilon}{\mu_o} \quad (8.9)$$

where, consistent with the trends observed in the stress–strain curves, the grain-size effect is isolated in the athermal stress σ_a . For annealed material, $\hat{\sigma}_\epsilon = 0$, and Eq. 8.9 becomes a form of the Hall–Petch Equation (Eq. 3.9)

⁷The same conclusion is drawn from measurement by Hughes in Ni–30 Co presented in Fig. 12.9.

Fig. 8.41 Yield stress versus grain size for measurements at three temperature and strain-rate combinations reported by Gray et al. [13]



$$\sigma = \sigma_i(\dot{\epsilon}, T) + \frac{k_d}{d_{gs}^n} \quad (8.10)$$

where σ_i is the sum of σ_a and $s_i\widehat{\sigma}_i$ (and, for simplicity, the shear modulus normalization has been omitted). Figure 8.41 is the plot presented by Gray et al. [13] showing the yield stress in annealed material versus grain size for measurements over the range of strain rates and temperatures considered. Note that the stress levels are coincidentally similar for tests at 77 K and a strain rate of 0.001 s^{-1} to those for tests at 298 K and a strain rate of 3000 s^{-1} . The analysis by these investigators (to subtract $s_i\widehat{\sigma}_i$ from σ_i) leads to the following expression for the athermal stress

$$\sigma_a = \sigma_o + \frac{k_d}{d_{gs}^n} \quad (8.11)$$

where σ_o is a constant (34 MPa) and n is unity rather than the value of one-half normally used in the Hall–Petch Equation. For Monel 400, Gray et al. [13] report a value of k_d equal to 0.0015 MN/m . Interestingly, Eq. 8.10 predicts $\sigma_a = 72 \text{ MPa}$ with these values of σ_o and k_d for a grain size of $40 \mu\text{m}$, which is the grain size of the Ni 270 material discussed in Sect. 8.5. This prediction is a little higher than the value of 50 MPa assumed for Ni 270 (see Table 8.6).

The operative constitutive equation for Monel 400 becomes

$$\frac{\sigma}{\mu} = \frac{\sigma_o + \frac{k_d}{d_{gs}}}{\mu} + s_i(\dot{\epsilon}, T) \frac{\widehat{\sigma}_i}{\mu_o} + s_\epsilon(\dot{\epsilon}, T) \frac{\widehat{\sigma}_\epsilon}{\mu_o} \quad (8.12)$$

The equations for s_i , s_ϵ , and $d\widehat{\sigma}_\epsilon/d\epsilon$ are as specified in Eqs. 6.15 (with “1” = i), 6.16 (with “2” = ϵ), and 8.2, respectively.

Table 8.11 Model parameters for Ni 270 (Sect. 8.5) compared to those proposed by Gray et al. [13] for Monel 400

Parameter		Units	Equation	Value	
				Ni 270	Monel 400
σ_a		MPa	Eq. 8.5	50	–
σ_o		MPa	Eq. 8.10	–	34
k_d		MN/m		–	0.0015
n		–		–	1
s_i	g_{oi}	–	Eq. 6.15 (with “1” = i)	0.20	0.5391
	p_i	–		0.5	
	q_i	–		1.5	
	$\dot{\epsilon}_{oi}$	s^{-1}		1×10^9	1×10^7
$\hat{\sigma}_i$		MPa	Eq. 8.5	28.9	190.2
$s\epsilon$	g_{oe}	–	Eq. 6.16 (with “2” = ϵ)	1.6	
	p_ϵ	–		0.667	
	q_ϵ	–		1	
	$\dot{\epsilon}_{oe}$	s^{-1}		1×10^7	
κ			Eq. 6.28	2	^a
θ_{II}	A_o	MPa	Eq. 6.29	4600	3363
	A_1	MPa ^b		13	4.79
	A_2	MPa $s^{-1/2}$		2.0	7.41
$\hat{\sigma}_{es}$	$\hat{\sigma}_{eso}$	MPa	Eq. 6.26	1260	1030
	g_{eso}	–		0.168	0.37
	$\dot{\epsilon}_{eso}$	s^{-1}		1×10^8	1×10^7
b		nm	Many	0.249	
ρ		g/cm^3	Eq. 6.32	8.9	
ψ		–		0.95	
$\mu(T)$	μ_o	GPa	Eq. 6.8 (see Table 6.1)	85.09	
	D_o	GPa		9.132	
	T_o	K		269	
$c_p(T)$	A_C	J/g/K	See table in Chap. 6 sidebar	0.3	0.157
	B	J/g/K ²		5.0×10^{-4}	7.0×10^{-4}
	C	J K/g		–700	7060 ^c

^aGray et al. [13] used a form of Eq. 6.27 rather than Eq. 6.28 for the differential hardening behavior

^bMPa when strain rate in units of s^{-1}

^cThis may be a typographic error in Ref. [13]. Gray et al. use the same expression for the temperature-dependent heat capacity as proposed in the Box 6.4, entitled Temperature Dependence of the Heat Capacity, but they use a different reference for the data

Model constants derived by Gray et al. [13] are compared to those for Ni 270 (described in Sect. 8.5) in Table 8.11. Many of the constants agree exactly. Others (e.g., $\dot{\epsilon}_{oi}$, $\dot{\epsilon}_{eso}$, A_o , A_1 , A_2 , and $\hat{\sigma}_{eso}$) differ insignificantly. The important differences include $\hat{\sigma}_i$, g_{oi} , and g_{eso} . The differences in $\hat{\sigma}_i$ and g_{oi} are sensible given the two alloy chemistries. The impurity obstacle in Ni 270 was assumed to reflect

carbon or other interstitial impurities. The impurity obstacle in Monel 400 is a combination of all of the solution hardening additions; these are responsible for the increased stress level over pure nickel, which is consistent with the larger value of $\hat{\sigma}_i$. Many of alloying additions are large atoms, which is consistent with the larger value of g_{oi} . The larger value of g_{eso} in Monel 400 compared to Ni 270 is a little puzzling. From Eq. 6.26, the strain-rate and temperature dependence of the saturation threshold stress increases with a decreasing value of g_{eso} . In analyzing data, g_{eso} is related to the slope of the plot of saturation threshold stress versus temperature and strain rate (see Fig. 8.28). The Follansbee et al. measurements included only prestrains at room temperature. The Gray et al. measurements did not include prestrains and reloads but rather a parametric analysis of the hardening behavior (as a function of test temperature and strain rate) using methods discussed in the next section (Cu–Al alloys) and exercised extensively in analysis of the BCC and HCP systems in Chaps. 9 and 10. The inclusion of stress–strain curves at different test temperatures is very important in the estimate of g_{eso} . Thus, the value of g_{eso} for Ni 270 in Tables 8.9 and 8.11 may well be low, although as illustrated in Fig. 8.33 the temperature dependence of hardening appears to be adequately described using this estimate.

The Gray et al. work in Monel 400 is useful in that it supports the assumption that the effect of grain size is on the athermal stress and not on the hardening behavior. Comparison of model parameters deduced for Ni 270 and Monel 400 using different experimental and analysis methods lead to very similar constitutive equations where the differences in model parameters ($\hat{\sigma}_i$ and g_{oi}) are consistent with the differences in alloy chemistries.

8.10 Copper–Aluminum Alloys

The Nickel–Carbon system was interesting in that it enabled analysis of deformation in an FCC metal with two distinct obstacles to dislocation motion. Analysis of deformation in this system led to the observation that the evolution rate was higher in the carbon-containing alloy than in pure nickel.

Another FCC alloy that has been studied extensively is the Cu–Al system. In this case, aluminum is (mostly likely) a substitutional defect rather than an interstitial defect. Addition of aluminum to copper has the useful effect of changing the stacking fault energy (see Box 8.2). The stacking fault energy of pure copper is ~ 78 ergs/cm². The addition of 6% aluminum (by weight) to copper reduces the stacking fault energy to ~ 6 erg/cm² [14]. Deformation studies in the Cu–Al system have been used to isolate the effect of stacking fault energy on strength and strain-hardening.

Box 8.2 Role of the Stacking Fault Energy

The dislocation structures introduced in Chap. 2 were idealized in that they were described and drawn as line defects with edge, screw, or mixed behavior. In the FCC structure, slip occurs on close-packed $\{111\}$ planes, and the observed slip direction is $\langle 110 \rangle$ (a close-packed direction). The unit dislocation—the Burgers vector—is $\frac{1}{2}[110]$. In fact, it is energetically preferable to split this unit dislocation into two partial dislocations. One possible dislocation reaction is

$$\frac{1}{2}[110] \rightarrow \frac{1}{6}[211] + \frac{1}{6}[12\bar{1}]$$

This is known as a Shockley partial dislocation. The common stress fields around these partial dislocations act to separate the dislocations but the added energy associated with the interrupted stacking in the vicinity of the dislocations balances this repulsion. The result is that the partial dislocations will seek an equilibrium separation. The energy associated with this configuration is referred to as the *stacking fault energy* γ_{sf} . The magnitude of the stacking fault energy varies from material to material. In FCC pure metals, it is as low as 22 ergs/cm² in silver and as high as ~ 300 ergs/cm² in aluminum.

The stacking fault energy is important when considering *cross-slip*—which is the motion of a (screw) dislocation onto a slip plane that intersects the dislocation's original slip plane. Cross-slip is one mechanism afforded a dislocation when it encounters an obstacle. The ability of a dislocation to cross-slip and circumvent an obstacle reduces the effectiveness of the obstacle in blocking dislocation motion. An extended dislocation—which is a dislocation separated into partial dislocations—cannot cross-slip, however, without recombining the split dislocation back to the unit dislocation. This process is more difficult with widely spaced partial dislocations than with narrowly spaced dislocations. Accordingly, a material with a low stacking fault energy is less likely to promote cross-slip than is a material with a high stacking fault energy.

It is also observed that materials with low stacking fault energies are more prone to deform by deforming twinning than materials with high stacking fault energies.

Figure 8.42 shows stress–strain curves measured in compression in pure, well-annealed, Cu, Cu–0.2Al, Cu–2Al, and Cu–6Al, where the aluminum additions are all in weight percent. These tests were performed at RT and QS strain rates (10^{-4} s⁻¹ to 10^3 s⁻¹). It is evident that aluminum additions increase the strength (at any particular strain level) as well as the rate of strain hardening. These tests were complemented by tests at a strain rate of ~ 0.1 s⁻¹ and strain rates in the range of 2000 s⁻¹ to $\sim 10,000$ s⁻¹. No tests at other than RT were performed in this test sequence.

Fig. 8.42 Stress–strain curves at RT and a QS strain rate for the three Cu–Al and for pure Copper

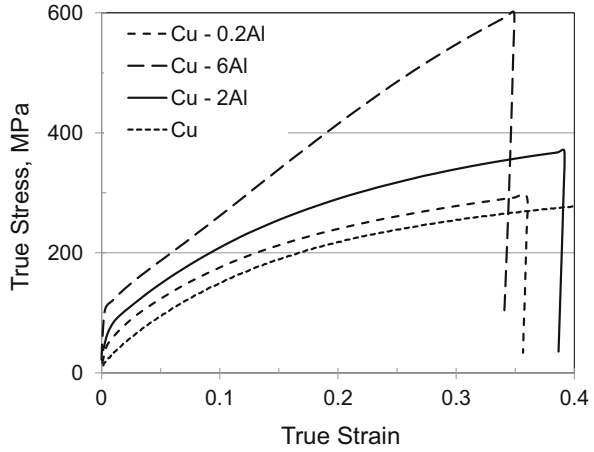


Fig. 8.43 Variation of yield stress with strain rate and temperature (although the measurements included no tests at other than RT) for the three Cu–Al alloys

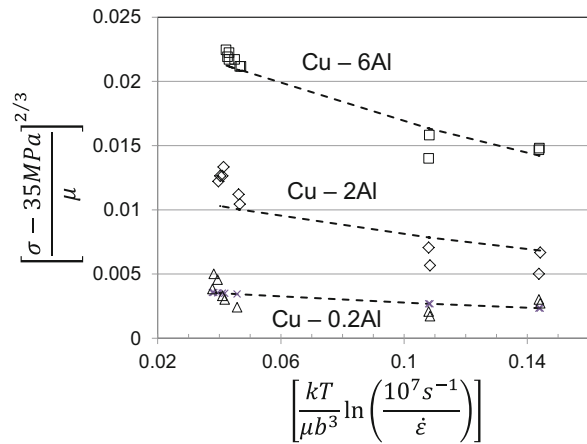


Table 8.12 Model parameters for the kinetic equations relating the yield stress to strain rate and temperature in the three Cu–Al alloys (dashed lines in Fig. 8.43)

Equation	Parameter	Cu-0.2Al	Cu-2Al	Cu-6Al
8.5	σ_a (MPa)	35		
8.5	$\hat{\sigma}_i$ (MPa)	14	69	206
6.16	pi	0.5		
	qi	1.5		
	$\dot{\epsilon}_{oi}$ (s^{-1})	10^7		
	g_{oi}	0.6		

Figure 8.43 shows the variation of the yield stress in the three Al-containing alloys [15] with strain rate—plotted on the same coordinates as used in Fig. 8.25 for the nickel–carbon alloys.⁸ The model fits are shown as dashed lines. Parameters for the fits are listed in Table 8.12.

⁸Yield stress measurement at strain rates above $\sim 1000\text{ s}^{-1}$ are unreliable, which is one reason for the scatter in these data points (left side of the abscissa) in Fig. 8.43.

Note in Fig. 8.43 that Eq. 8.5 with a single value of g_{oi} fits the experimental data (although measurements at other than RT would enable a higher degree of confidence). The selected value of $g_{oi} = 0.6$ is greater than the value of 0.15 used for carbon-strengthening of nickel, but not as high as the value of 1.6 that characterized the interaction of dislocations with stored dislocations in nickel and copper. Interestingly, the value of g_{oi} for solid-solution hardening in Cu Al is similar to that observed by Gray et al. [13] for solid-solution hardening in Monel 400.

These measurements have been full stress–strain curves as a function of strain rate. Prestrain and reload experiments were not performed on these alloys, which implies that the analysis procedure outlined in Chap. 7 and demonstrated in copper, nickel, and nickel–carbon in this chapter cannot be followed. However, assuming the general applicability of Eq. 8.5, much about evolution can still be gleaned from the stress–strain curves. Solving for $\hat{\sigma}_\epsilon$ in Eq. 8.5 gives

$$s_\epsilon(\dot{\epsilon}, T) \frac{\hat{\sigma}_\epsilon}{\mu_o} = \frac{\sigma}{\mu} - \frac{\sigma_a}{\mu} - s_i(\dot{\epsilon}, T) \frac{\hat{\sigma}_i}{\mu_o}$$

and

$$\hat{\sigma}_\epsilon = \frac{\mu_o}{s_\epsilon(\dot{\epsilon}, T)} \left[\frac{\sigma}{\mu} - \frac{\sigma_a}{\mu} - s_i(\dot{\epsilon}, T) \frac{\hat{\sigma}_i}{\mu_o} \right] \quad (8.13)$$

Taking σ in Eq. 8.13 as the measured stress (e.g., from one of the curves in Fig. 8.42) and taking the parameters for s_i from Table 8.12, and those for s_ϵ from Table 8.4, plots of $\hat{\sigma}_\epsilon$ versus ϵ can be generated for the three alloys. The major assumption in this estimate is that the parameters contributing to s_ϵ listed in Table 8.4 for dislocation–dislocation interactions in pure copper are applicable to dislocation–dislocation interaction in the copper–aluminum alloys. Figure 8.44 is a plot of $\hat{\sigma}_\epsilon$ versus ϵ for the three results shown in Fig. 8.42. Included in Fig. 8.44 are model fits (dashed lines) according to Eq. 8.2 with parameter values for each of the alloys given in Table 8.13.

Fig. 8.44 Deduced variation with strain of the threshold stress characterizing dislocation–dislocation interactions for the three Cu–Al alloys

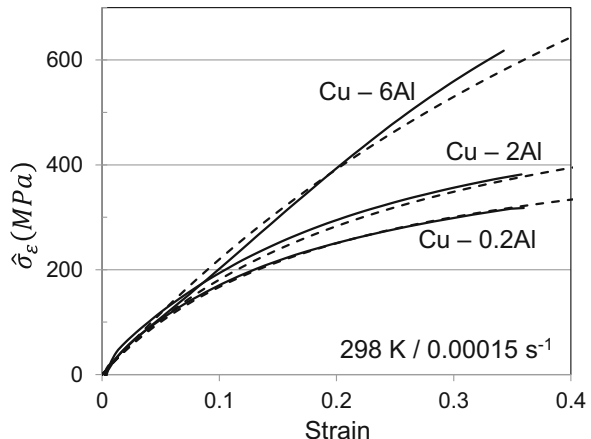
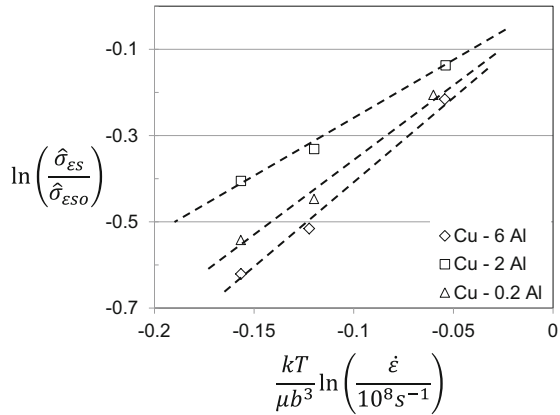


Table 8.13 Model parameters for the modified Voce law (Eq. 8.2) for the dashed lines in Fig. 8.44

Equation	Parameter	Cu–0.2Al	Cu–2Al	Cu–6Al
8.2	θ_{II} (MPa)	2500		
	$\hat{\sigma}_{es}$ (MPa)	500	650	1800
	κ	2		

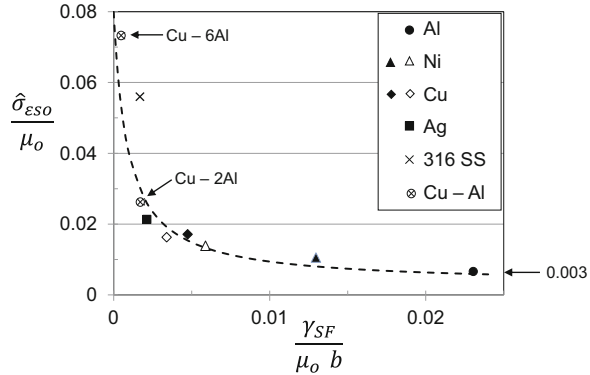
Fig. 8.45 Variation of the value of the saturation threshold stress characterizing dislocation–dislocation interactions with the strain rate. The saturation value at 0 K is listed in Table 8.13. The dashed lines are drawn according to Eq. 6.28



As evident in Table 8.13 variations of $\hat{\sigma}_{es}$ with aluminum level are clear, but variations of θ_{II} with aluminum level are non-existent or too small to be observed. The stress–strain curves in Fig. 8.42 were measured at a quasi-static strain rate. Analysis of the measurements at the other strain rates (0.1 s^{-1} and within the range of 10^3 s^{-1} to 10^4 s^{-1}) following the procedure outlined above gives three values of $\hat{\sigma}_{es}$ for each aluminum level. Figure 8.45 shows a plot of $\hat{\sigma}_{es}$ normalized by $\hat{\sigma}_{eso}$ (which varies with aluminum level) versus strain rate according to the coordinates used, for instance, in Fig. 8.28. For these plots, $\hat{\sigma}_{eso}$ equals 860 MPa, 975 MPa, and 3350 MPa for Cu–0.2Al, Cu–2Al, and Cu–6Al, respectively.

Kocks and Mecking [16] showed a correlation between the saturation threshold stress $\hat{\sigma}_{eso}$ and the stacking fault energy. Figure 8.46 plots their data in Al, Ag, Cu, and Ni (solid points) along with data from the analyses presented in this chapter for Cu, Ni, and the Cu–Al alloys. Included is a data point for AISI 316 stainless steel, which will be described in more detail in Chap. 11. There are two points each for copper and nickel since Kocks and Mecking likely used different values of γ_{SF} than used here, which reflects the fact that the stacking fault energy is difficult to measure accurately and the literature reports conflicting values, even though there is general agreement regarding the order (e.g., γ_{SF} is higher in Ni than in Cu, etc.) shown in this figure. (For an extensive review of stacking fault energy measurements, see Gallagher [17].) The dashed line is drawn according to

Fig. 8.46 Variation with stacking fault energy of the saturation value of the threshold stress characterizing the strength of the dislocation–dislocation obstacle interactions (both axes values are dimensionless quantities). Solid points are measurements reported by Kocks and Mecking [16]. Open points are from work reported here



$$\frac{\hat{\sigma}_{eso}}{\mu_o} = 0.08 - \frac{(0.08 - 0.003)}{1 + 1100 \frac{\gamma_{SF}}{\mu_o b}} \quad (8.14)$$

which is similar to the equation used by Kocks and Mecking. As emphasized by these investigators there is no theoretical basis for this equation.

While Kocks and Mecking only considered pure FCC metals, included in Fig. 8.46 are the two Cu–Al alloys and one result for an austenitic stainless steel. It is interesting that the FCC alloys follow the same behavior as the pure metals.

Rohatgi, Vecchio, and Gray [18] performed a detailed mechanical property and microscopic characterization of Cu–Al alloys covering a similar range of alloys as discussed here. These investigators noted deformation twinning in the Cu–6Al alloy but none in the Cu–2Al alloy and proposed a strength model that accounted for the additional boundaries posed by the increasing twin population. In fact, the stress–strain curve for the high Al alloy in Fig. 8.42 suggests the presence of twinning as evidenced by the apparent increase in hardening rate at strains greater than $\sim 10\%$. Deviations from the modified Voce law fit in Fig. 8.44 are also consistent with twinning contributions. Similarly, the data at the highest strain rate in this alloy (open diamonds) in Fig. 8.43 appears to be trending upward—suggesting that the $\hat{\sigma}_{eso}$ –value is too high, which would bring down the data point for this alloy in Fig. 8.46. (The trends in these plots when twinning becomes active are discussed in more detail in Sect. 9.8, and in Sect. 10.7.1.)

The major contribution to the increased rate of evolution in the Cu–6Al alloy, however, appears to be the effect of the stacking fault energy on dislocation mobility as reflected by the trend in Fig. 8.46. More rigorous measurements of reload yield stress as a function of temperature and strain rate or the use of strain-rate (or temperature) change tests on Cu–6Al samples deformed at RT as a function of strain rate would help to separate the effects of stress contributions from twinning (which presumably are athermal—akin to strengthening from grain boundaries) and dislocation storage.

8.11 Summary

Pure copper and nickel are the two metals that have been most thoroughly investigated using the protocol for measuring the mechanical threshold stress and establishing the evolution rate that was outlined in Chap. 7. All of the prestrain conditions have involved room temperature testing but have spanned many orders of magnitude of strain rate.

This chapter has highlighted the use of plots of reload yield stress (on material of a specified prestrain condition) versus reload temperature and strain rate (see Figs. 8.1, 8.26, 8.34, 8.36, and 8.37). These plots provided the vehicle for establishing the mechanical threshold stress in conjunction with Eq. 8.1 for pure copper or Eq. 8.5 for the nickel plus carbon alloys. Typically, reload temperatures between 77 K and 300 K and reload strain rates of 0.001 s^{-1} to 1 s^{-1} provided a sufficiently wide range of values on the abscissa of these plots. The use of higher temperatures is possible, but the contribution of recovery mechanisms at elevated temperatures complicate interpretation of the measurements.

In copper, the Follansbee and Kocks [1] measurements involved testing to high enough strains to observe (Fig. 8.5) that the activation energy characterizing interactions of glide dislocations with stored dislocations was not constant but rather decreased with stress (or strain). This addresses one of the questions posed at the start of this chapter. Chapter 14 will consider some complications of large-strain constitutive behavior, which will give an opportunity to further consider the variation of g_{oe} with stress.

Upon establishing the MTS model parameters for copper (see Table 8.4) model predictions were compared to published measurements particularly at elevated temperature but also measurements in shear to gage the predictive capability offered by the model. These comparisons demonstrated good agreement between trends (e.g., with strain rate or temperature) while showing that the same material studied by different investigators can show differences in behavior. Such differences can arise from slight differences in chemistry or grain size. Although it was not attempted to “adjust” model parameters to give optimal agreement between the model predictions and data, the model formulation certainly offers the capability to do this if warranted (see Fig. 8.13 compared to Fig. 8.11). The comparisons between model predictions and measurements not included in the prestrain test matrix in both copper and nickel lead to the conclusion that the model offers predictive capability, which was a key question posted at the beginning of this chapter.

The measurements in the nickel and nickel plus carbon alloys addressed the third question posed at the start of this chapter, which dealt with the suitability of the assumption that contributions of two obstacles add linearly as expressed by Eqs. 6.17 and 8.5. The analysis illustrated in Fig. 8.37 using a power-law additive equation (Eq. 8.8) did not lead to a definitive conclusion on this matter. That is, agreement between the model and the data using linear summation was as good (or almost as good) as agreement with $n = 1.5$. The discussions of superposition of multiple obstacles in [12] and [7] offer more insight into this assumption.

Application of the MTS model in BCC and HCP systems described in following chapters will proceed under the assumption that obstacles sum linearly ($n = 1$).

The Gray et al. [13] measurements in Monel 400 show that grain size affects the athermal stress but not the rate of strain hardening. Model parameters reported by these investigators vary systematically from those deduced for Ni 270 in Sect. 8.5.

Analysis of measurements in Cu–Al alloys has emphasized the effect of the stacking fault energy on evolution. An interesting observation is that the trend of the variation of the saturation threshold stress with stacking fault energy observed in pure FCC metals appears to hold for the Cu–Al alloys. A departure in the analysis method applied to these alloys here is that only stress–strain curves were available, which necessitated application of Eq. 8.13. This procedure will be adopted further in subsequent chapters.

The review of measurements in pure copper and nickel should leave the impression that the full analysis as outlined in Chap. 7 necessitates an extensive experimental campaign. Analysis of the stress–strain curves in the Cu–Al alloys introduced the approach when the “full” analysis is not possible. This approach will be further demonstrated in applications of the model to BCC, HCP, austenitic stainless steel, and nickel-based superalloy systems in Chaps. 9, 10, 11, and 12. This is partially made possible by the collective experience that has evolved over the decades with application of this model. The hazard, however, is that the validity of model assumptions become more difficult to assess.

Exercises

8.1 One of the complications in analyzing hardening data is the adiabatic nature of deformation at strain rates exceeding 1 s^{-1} . In the analysis of deformation in FoLLyalloy in Chap. 7, the effect of the temperature rise was ignored. The purpose of this exercise is to review this assumption. Assume that the material is described by the constitutive law summarized in Sect. 7.8 and that it has the density and thermal properties listed in Table 8.E1a.

- (a) For a test at a strain rate of 1000 s^{-1} and an initial temperature of 300 K, compute the adiabatic stress–strain curve and compare it with the isothermal stress–strain curve. Isothermal data up to a strain level of 0.30 was included in Exercise 7.7. Measurements up to a total strain of 0.50 are added and listed in Table 8.E1b.

Table 8.E1a Density and thermal properties of FoLLyalloy (Exercise 8.1)

Property	Unit	Equation	Value
A	J/g/K	See table in Chap. 6 sidebar	0.1345
B	J/g/K ²		0
C	J K/g		0
Ψ		Equation 6.32	0.95
ρ	g/cm ³		19.3

Table 8.E1b Isothermal stress versus strain values for FoLLy alloy at a strain rate of 1000 s^{-1} and a temperature of 300 K to be added to the values specified in Exercise 7.7 (Exercise 8.1)

300 K and 1000 s^{-1}	
Strain	Stress (MPa)
0.35	1285
0.4	1316
0.45	1343
0.5	1365

- (b) What is the temperature at a strain of 0.30?
- (c) What is the value of $\hat{\sigma}_\varepsilon$ reached during the adiabatic test and how does this compare to the value reached during the isothermal test?
- 8.2 Given that the difference in values of $\hat{\sigma}_\varepsilon$ for the isothermal case and the adiabatic case was small in Exercise 8.1, a “worst case” scenario will be analyzed in this exercise. For a prestrain at a strain rate of $10,000 \text{ s}^{-1}$ and a temperature of 100 K to a strain level of 0.50 find the value of $\hat{\sigma}_\varepsilon$ assuming (i) isothermal deformation and (ii) adiabatic deformation. (iii) For the latter, what temperature is reached at a strain of 0.50?
- 8.3 Consider the prestrain conditions in Exercise 8.1 (1000 s^{-1} and a temperature of 300 K to a strain of 0.30). Find the reload yield stress for each of the reload conditions listed in Table 7.5 for this prestrain for (i) the isothermal case and (ii) the adiabatic case. (iii) What is your conclusion about the magnitude of the error introduced by assuming deformation is isothermal?
- 8.4 Based on the results of the above three exercises, what would you conclude is the temperature to use when analyzing the variation of the saturation threshold stress with temperature and strain rate (using Eq. 6.26, such as in Fig. 8.3)? Is it the initial temperature, the final temperature, or the average temperature?
- 8.5 From the results in Table 8.2 for prestrain strain rates of 0.00014 s^{-1} and 0.82 s^{-1} , create plots of $\hat{\sigma}_\varepsilon$ versus strain and find best-fit values of θ_{II} and $\hat{\sigma}_{\varepsilon s}$. Do the resulting model parameters agree with those listed in Table 8.3?
- 8.6 From the results in Table 8.3, create the plot of $\hat{\sigma}_{\varepsilon s}$ versus prestrain temperature and strain rate (Fig. 8.3). Do the resulting model parameters agree with those listed described in the text?

References

1. P.S. Follansbee, U.F. Kocks, A constitutive description of the deformation of copper based on the use of the mechanical threshold stress as an internal state variable. *Acta Metall.* **36**(1), 81–93 (1988)
2. H. Mecking, U.F. Kocks, Kinetics of flow and strain-hardening. *Acta Metall.* **29**, 1865–1875 (1981)
3. G. T. Gray III and S. R. Chen, MST-8 constitutive properties & constitutive modeling, Los Alamos National Laboratory, LA-CP-07-1590 and LA-CP-03-006 (Must request data from LANL authors), 2007

4. R.P. Carreker Jr., W.R. Hibbard Jr., Tensile deformation of high-purity copper as a function of temperature, strain rate, and grain size. *Acta Metall.* **1**, 656–663 (1953)
5. U.F. Kocks, M.G. Stout, A.D. Rollett, Influence of texture on strain hardening, in *8th International Conference on the Strength of Metals and Alloys (ICSMA)*, ed. by P. O. Kettunen, T. K. Lepistö, M. E. Lehtonen, (Pergamon Press, Oxford, 1988), pp. 25–34
6. A. M. Eleiche, and J. D. Campbell, The influence of strain-rate history and temperature on the shear strength of copper, titanium and mild steel, Final report to Air Force Materials Laboratory, Wright-Patterson AFB, OH, AFML-TR-76-90, 1976
7. P.S. Follansbee, J.C. Huang, G.T. Gray, Low-temperature and high strain rate deformation of nickel and nickel-carbon alloys and analysis of the constitutive behavior according to an internal state variable model. *Acta Metall.* **38**(7), 1241–1254 (1990)
8. A. Kelly, R.B. Nicholson, *Strengthening Methods in Crystals* (Wiley, New York, 1971), p. 295
9. Y. Nakada, A.S. Keh, Serrated flow in Ni-C alloys. *Acta Metall.* **18**, 437–443 (1970)
10. T. Muller, High strain rate behaviour of iron and nickel. *J. Mech. Eng. Sci.* **14**(3), 161–167 (1972)
11. P.S. Follansbee, G.T. Gray III, The response of single crystal and polycrystal nickel to quasi-static and shock deformation. *J. Plast.* **7**, 651 (1991)
12. U.F. Kocks, A.S. Argon, M.F. Ashby, in *Thermodynamics and Kinetics of Slip, Progress in Materials Science*, ed. by B. Chalmers, J. W. Christian, T. B. Massalski, vol. 19, (Pergamon Press, Oxford, 1975), p. 226
13. G.T. Gray III, S.R. Chen, K.S. Vecchio, Influence of grain size on the constitutive response and substructure evolution of Monel 400. *Metall. Mater. Trans. A* **30A**, 1235–1247 (1999)
14. L.E. Murr, *Interfacial Phenomena in Metals and Alloys* (Addison-Wesley Publishing Co., New York, 1975), pp. 87–164
15. P.S. Follansbee, M.F. Lopez, W. Wright, Strain-rate dependent stress-strain measurements in three Cu-Al alloys. Los Alamos National Laboratory (1982)
16. U.F. Kocks, H. Mecking, Physics and phenomenology of strain hardening: The FCC case. *Prog. Mater. Sci.* **48**, 171–273 (2003)
17. P.C.J. Gallagher, The influence of alloying, temperature, and related effects on the stacking fault energy. *Metall. Transact.* **1**, 2429–2461 (1970)
18. A. Rohatgi, K.S. Vecchio, G.T. Gray III, The influence of stacking fault energy on the mechanical behavior of Cu and Cu-Al alloys: Deformation twinning, work hardening, and dynamic recovery. *Metall. Mater. Trans. A* **32A**, 135–145 (2001)

Chapter 9

Application of MTS Model to BCC Metals and Alloys



Introduction

Application of the MTS model to several FCC pure metals and alloys was described in Chap. 8. Model development followed the recipe presented in Chap. 7. The procedure included an extensive series of prestrain and reload mechanical tests in both pure copper, pure nickel, and two nickel–carbon alloys. Figures 8.1, 8.26, 8.34, 8.36, and 8.37 gave examples of plots of the reload yield stress as a function of reload test temperature and strain rate. In pure copper and nickel, these plots enabled determination of the mechanical threshold stress characterizing interaction of mobile (glide) dislocations with immobile (stored) dislocations. Alloying nickel with carbon introduced a second deformation mechanism related to interaction of mobile dislocations with the carbon. Assuming these two threshold stresses combined according to Eq. 8.5, the latter mechanical threshold stress could be determined. Analysis of evolution of hardening with strain (as a function of strain rate) was demonstrated in Figs. 8.2, 8.27, and 8.38.

The pure FCC systems are unique in that the yield stress in annealed material is very low and is characterized by an essentially immeasurable temperature and strain rate dependence. The situation in the pure BCC metals and BCC alloys is quite different. Analysis of deformation kinetics in BCC metals and alloys is considered in this chapter. A significant difference between the analyses presented in Chap. 8 for FCC metals and alloys and the implementation in BCC metals and alloys is that in the latter the recipe of Chap. 7 has been applied much less rigorously. The effect of this on the MTS model formulation will be discussed.

Supplementary Information The online version contains supplementary material available at [\[https://doi.org/10.1007/978-3-031-04556-1_9\]](https://doi.org/10.1007/978-3-031-04556-1_9)

9.1 Pure BCC Metals

The temperature dependence of the yield stress in tungsten [1], molybdenum [2], niobium [2], tantalum [3], vanadium [4], and chromium [5] is plotted in Fig. 9.1. For Mo, Nb, Ta, and V the literature data includes measurements over a range of strain rates. The results in Fig. 9.1 are a selection of a more extensive compilation in pure BCC metals compiled by Follansbee [6]. Figure 9.2 shows the variation of yield stress with temperature in pure iron with various amounts of carbon [7–11]. The data in Refs. [7–9] include measurements over a range of strain rates.

Immediately apparent in Figs. 9.1 and 9.2, when compared for instance to the yield stress dependences in prestrained copper (Fig. 4.11) or Ni + 510 ppm C (Fig. 4.12), is that the yield stresses in the BCC systems are much higher than those in copper and that the (absolute value of the) slope of the dependence on these coordinates is much higher in the BCC systems than in these FCC metals. Section 3.2 discussed the contribution of the Peierls stress in the BCC crystal structure. The strong variation of stress with temperature (and strain rate) in Figs. 9.1 and 9.2 is a direct result of the interaction of mobile dislocations with the Peierls stress. This is a contribution to the stress that was non-existent in the FCC systems considered in Chap. 8. Another common observation in Figs. 9.1 and 9.2 evident in all but perhaps the measurements in tungsten is a curvature in the plots with the variation of stress with $T \ln(10^8 s^{-1}/\dot{\epsilon})$ showing a higher (negative) slope at small compared to large values of the abscissa. If the Peierls stress is the only thermally activated deformation in these annealed BCC metals, then one would not anticipate this curvature.

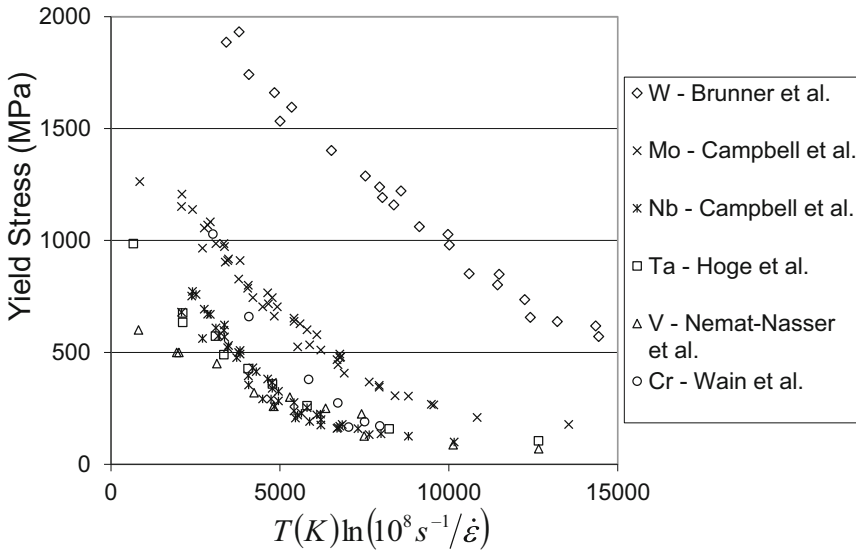


Fig. 9.1 Variation of yield stress with temperature and strain rate in six pure BCC metals

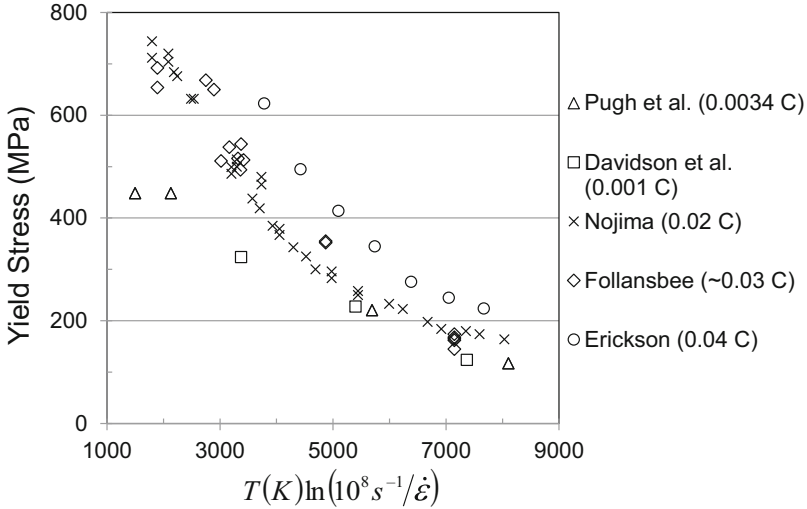


Fig. 9.2 Variation of yield strength with temperature and strain rate in pure iron

Figures 9.1 and 9.2 are plots of the measurements on coordinates of σ versus $T \ln (10^8 s^{-1} / \dot{\epsilon})$. It was argued in Sect. 6.2 that a more descriptive thermal activation expression is

$$\left(\frac{\sigma - \sigma_a}{\mu}\right)^p = \left\{ 1 - \left[\frac{kT}{g_o \mu b^3} \ln \left(\frac{\dot{\epsilon}_o}{\dot{\epsilon}} \right) \right]^{1/q} \right\}^p \left(\frac{\hat{\sigma}}{\mu_o} \right)^p \tag{6.9}$$

which would account for some curvature in plots such as shown in Figs. 9.1 and 9.2. Figure 9.3 plots the molybdenum data of Campbell and Briggs [2] on coordinates consistent with Eq. 6.9 with typical values of p and q . The line shown in this figure is drawn according to Eq. 6.9 with $g_o = 0.1$ and $\hat{\sigma} / \mu_o = 0.019$. Even on the coordinates in Fig. 9.3, the high-temperature (and low strain rate) measurements deviate from the dashed line. The curvature, in fact, cannot be removed through choice of any of the model parameters in Eq. 6.9.

Follansbee proposed in Ref. [6] that a two-parameter model was necessary to model the curvature in Figs. 9.1, 9.2, and 9.3. The governing equation becomes

$$\frac{\sigma}{\mu} = \frac{\sigma_a}{\mu} + s_p(\dot{\epsilon}, T) \frac{\hat{\sigma}_p}{\mu_o} + s_i(\dot{\epsilon}, T) \frac{\hat{\sigma}_i}{\mu_o} \tag{9.1}$$

where the subscript “ p ” denotes the Peierls obstacle and the subscript “ i ” denotes contributions from impurity elements. The latter contribution reflects the difficulty in producing highly pure metals and that even normal levels of impurity elements—particularly in the form of interstitial O, H, N, and C—can introduce measurable strengthening. Figure 9.4 shows the molybdenum data in Fig. 9.3 plotted on the

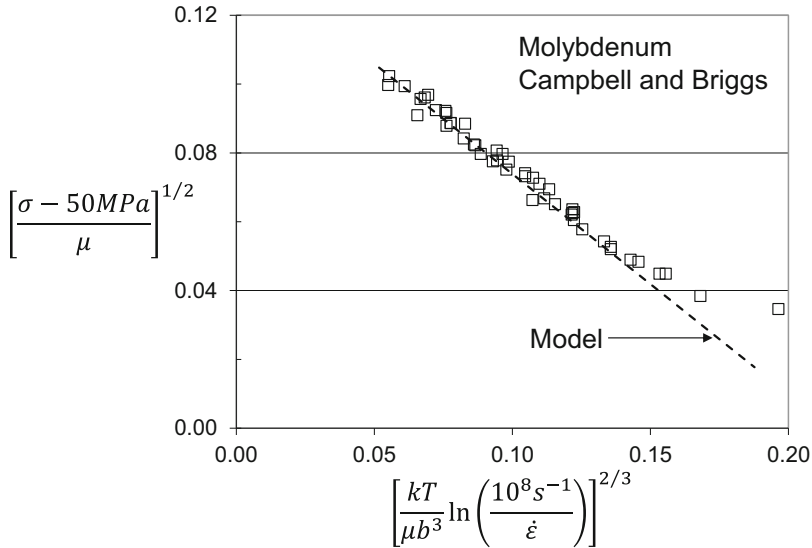


Fig. 9.3 Measurements by Campbell and Briggs in pure molybdenum plotted on coordinates consistent with Eq. 6.9

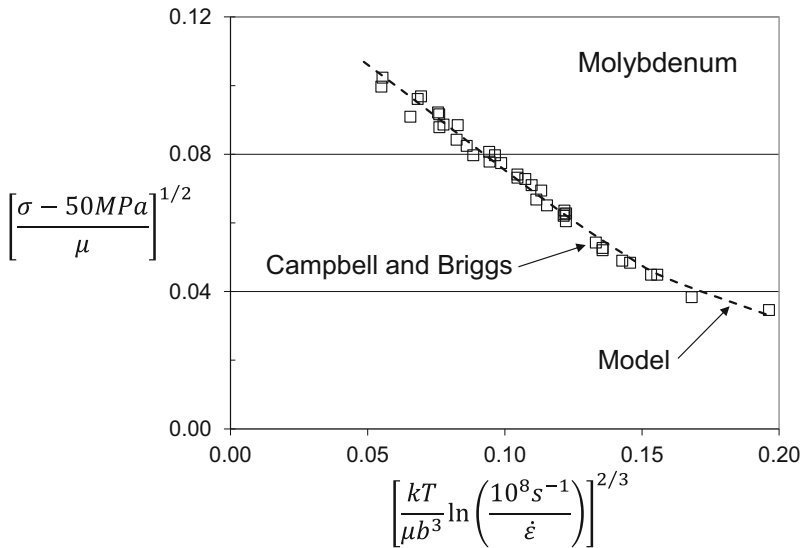
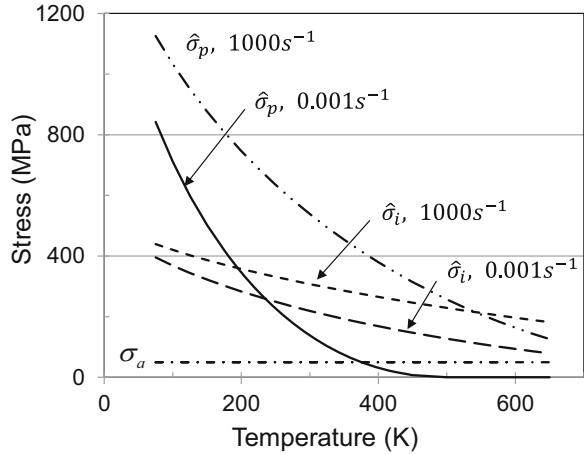


Fig. 9.4 Yield stress measurements of Campbell and Briggs in molybdenum plotted on the same coordinates as is Fig. 9.4 but with a two-parameter model

same coordinates but with a curve fit to Eq. 9.1 with $g_{op} = 0.081$ (see Eq. 6.16 with subscript “p” rather than “2”), $\hat{\sigma}_p/\mu_o = 0.0145$, $g_{oi} = 0.27$ (see Eq. 6.15 with subscript “i” rather than “1”), and $\hat{\sigma}_i = 0.0048$. Note that the Peierls obstacle is a very strong obstacle (as determined by the magnitude $\hat{\sigma}_i/\mu_o$ with a small activation

Fig. 9.5 Variation of the three stress components with temperature at two strain rates illustrating the very strong temperature dependence of the Peierls obstacle



energy (as characterized by the normalized activation energy g_{op}) whereas the impurity obstacle is a weaker obstacle with a large activation energy. Also of interest is the observation that ignoring the contributions of the smaller, impurity obstacle, as in Fig. 9.3, leads to a primary (Peierls) obstacle that is stronger but with a larger activation energy than when both obstacles are considered.

As the governing equation for deformation in molybdenum and other pure FCC metals, Eq. 9.1 sums the contributions of the athermal stress σ_a , the mechanical threshold stress characterizing interactions of dislocations with the Peierls barrier $\hat{\sigma}_p$, and the mechanical threshold stress characterizing interactions of dislocations with impurity elements $\hat{\sigma}_i$. For the values of the parameters selected for molybdenum as reflected in the dashed model line in Figs. 9.4 and 9.5 shows variation of these stress contributions with temperature at strain rates of 0.001 s^{-1} and 1000 s^{-1} . As expected the athermal stress (same for both strain rates) does not vary with temperature. It is evident that at low temperatures the kinetics are dominated by the kinetics defined by the Peierls obstacle and at high-temperatures kinetics are dominated by the kinetics defined by the impurity element obstacle. The stress levels at low temperature represent the sum of all three stress contributors. At high temperature at the lower strain rate the Peierls obstacle loses effectiveness at $\sim 450 \text{ K}$. At the higher strain rates, however, the Peierls obstacle continues to influence the stress level at temperatures as high as 700 K . The point where the stress contribution of both of the thermally activated obstacles are equivalent is $\sim 240 \text{ K}$ at the lower strain rate but rises to $\sim 560 \text{ K}$ at the higher strain rate.

Figures 9.6, 9.7, 9.8, 9.9, and 9.10 show a similar two-parameter model fit to the measurements in pure niobium, tungsten, tantalum, and iron (from Nojima [8]). Table 9.1 lists the fitting parameters used for the model predictions in each of these figures. Included in Table 9.1 is the result for pure vanadium (figure not shown). Note the common values of parameters from Eq. 6.15 (with “1” = p , representing the Peierls obstacle) and Eq. 6.16 (with “2” = i , representing the impurity element obstacle). The parameters in Table 9.1 show several common features. The

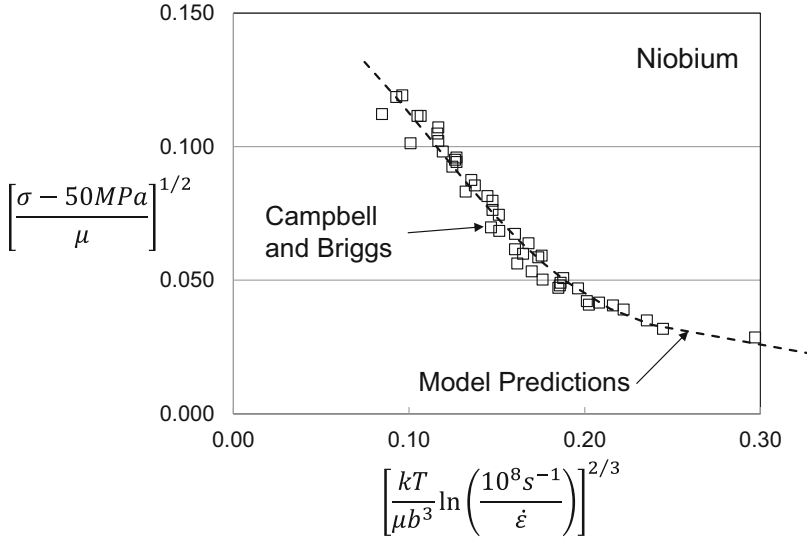


Fig. 9.6 Yield strength measurements of Campbell and Briggs in pure niobium with the two-parameter model prediction

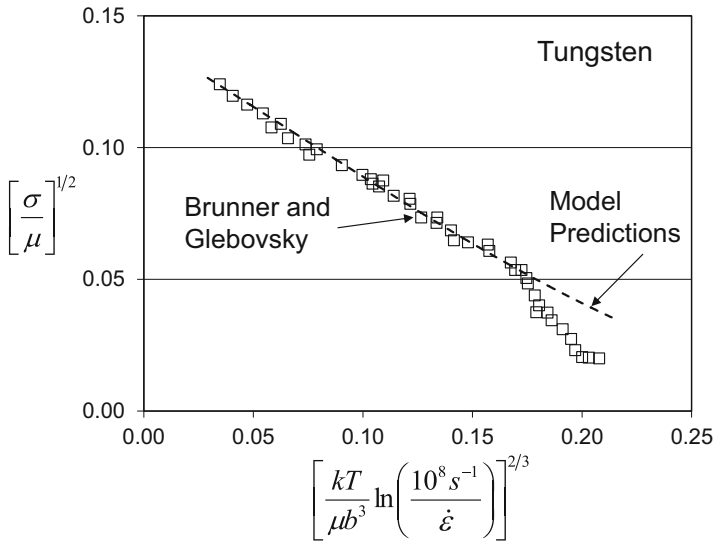


Fig. 9.7 Temperature-dependent yield stress measurements by Brunner and Glebovsky in pure tungsten with a two-parameter model prediction

normalized activation energy for the Peierls obstacle hovers around the value $g_{op} = 0.1$, whereas the corresponding value for the impurity obstacle is $\sim 4X$ this value. Similarly, the strength of the impurity obstacle as characterized by the magnitude of $\hat{\sigma}_i/\mu_o$ is ~ 0.1 the strength of the Peierls obstacle.

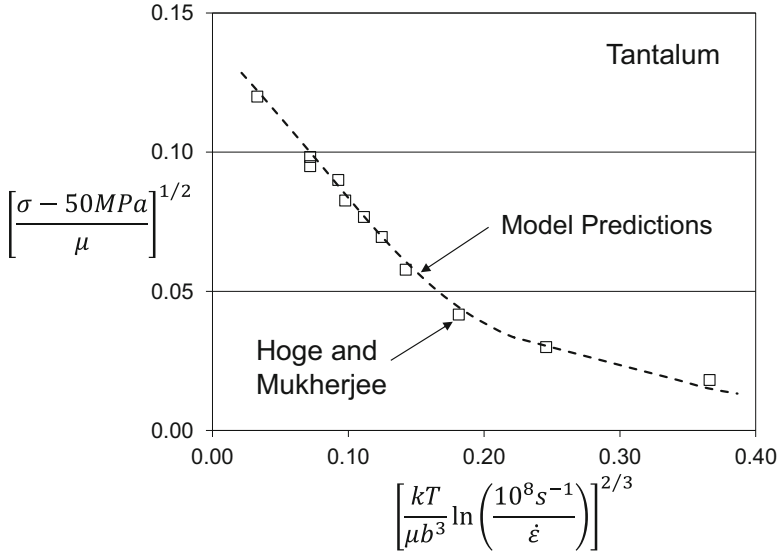


Fig. 9.8 Temperature and strain-rate-dependent yield stress measurements in pure tantalum by Hoge and Mukherjee with the two-parameter model prediction

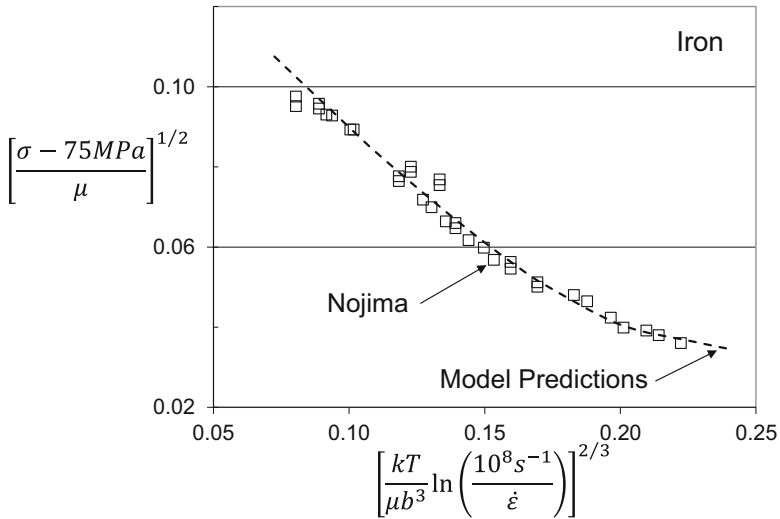


Fig. 9.9 Temperature and strain-rate-dependent yield stress measurements in pure iron by Nojima with the two-parameter model prediction

Table 9.1 lists the model parameters for the Nojima data in iron with 0.02 C. Figure 9.2 includes three other data sets. Equation 9.1 was fit to the other data sets to demonstrate how a variation in carbon concentration affects the model parameters. For these fits, the Pugh and Chang measurements in iron with a carbon

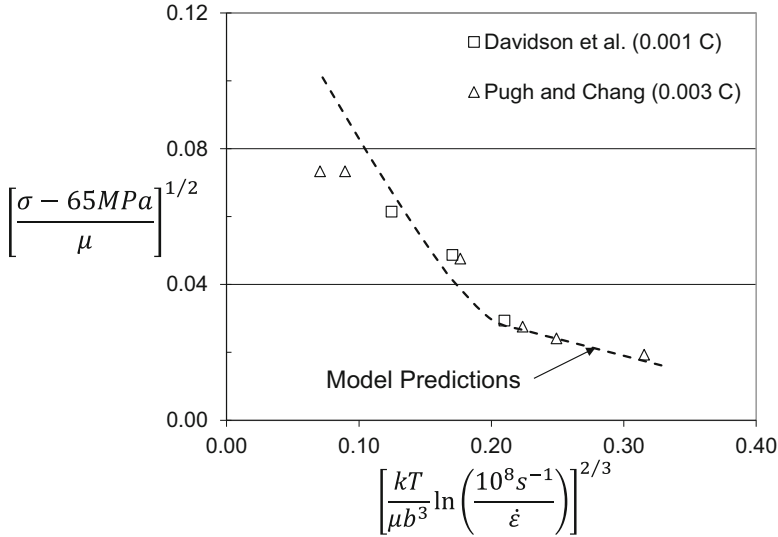


Fig. 9.10 The combined measurements of Pugh and Change [11] and Davidson et al. [7] in pure iron with the two-parameter model prediction

Table 9.1 Model parameters for the two-parameter model predictions in Figs. 9.4, 9.6, 9.7, 9.8, and 9.9

Material	Figure	σ_a (MPa)	g_{op}	$\hat{\sigma}_p/\mu_o$	g_{oi}	$\hat{\sigma}_i/\mu_o$
Mo [2]	9.4	50	0.081	0.0145	0.27	0.0048
Nb [2]	9.6	50	0.10	0.032	0.37	0.0057
W [1] (single crystals)	9.7	0	0.125	0.018	0.52	0.0052
Ta [3]	9.8	50	0.095	0.018	0.4	0.0032
Fe [8]	9.9	75	0.096	0.0193	0.4	0.0046
V [4]	–	25	0.07	0.0185	0.4	0.003

For all materials listed above:

$\dot{\epsilon}_{op}$	10^8 s^{-1}
$p_p = p_i$	0.5
$\dot{\epsilon}_{oi}$	10^{10} s^{-1}
$q_p = q_i$	1.5

concentration of 0.0034% were combined with the Davidson et al. measurements since they exhibited quite similar stress levels. Figure 9.10 shows this combined data set along with the model prediction. The two Pugh and Chang data points at the lower values of the abscissa that deviate from the dashed line demonstrate the contribution of deformation twinning (see Sect. 5.6), which was observed in these tests [11].

Table 9.2 Model parameters for the fits to five pure iron data sets showing the variation with carbon content of the threshold stress characterizing the contributions of impurity atoms

Reference	Carbon	σ_a (MPa)	g_{op}	$\hat{\sigma}_p/\mu_o$	g_{oi}	$\hat{\sigma}_i/\mu_o$
Davidson et al. [7]	0.001	65	0.096	0.0198	0.4	0.0024
Pugh and Chang [11]	0.0034					
Nojima [8]	0.02	75	0.096	0.0193	0.4	0.0046
Follansbee et al. [9]	0.03	75	0.096	0.02	0.4	0.005
Erickson and Low [10]	0.04	75	0.096	0.0185	0.4	0.008

Fig. 9.11 Dependence with carbon concentration of the threshold stress characterizing dislocation interactions with impurity atoms

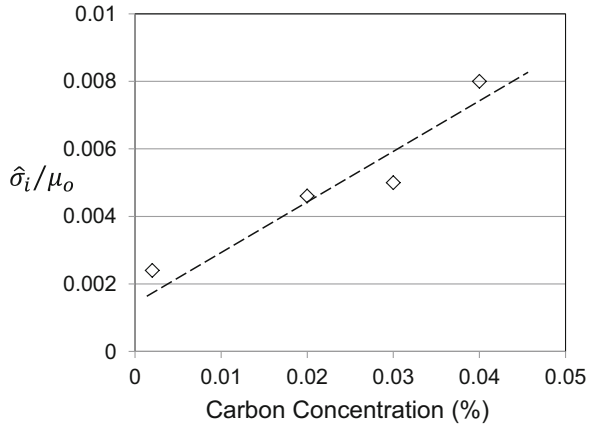


Table 9.2 lists the model parameters for the four pure iron data sets shown in Fig. 9.2. For these predictions, the values of g_{op} and g_{oi} were set at 0.096 and 0.4 respectively. However, the values of $\hat{\sigma}_p/\mu_o$ and $\hat{\sigma}_i/\mu_o$ were allowed to be varied to generate close agreement with the data. It is evident in Table 9.2 that the value of $\hat{\sigma}_p/\mu_o$ for each data set was consistently around 0.0195 whereas the values of $\hat{\sigma}_i/\mu_o$ vary with carbon concentration. Figure 9.11 shows the variation of $\hat{\sigma}_i/\mu_o$ versus carbon concentration with the latter plotted on a linear scale.¹ The conclusion that $\hat{\sigma}_i/\mu_o$ increases with carbon concentration yet $\hat{\sigma}_p/\mu_o$ is invariant to carbon concentration is consistent with the supposition that the latter represents the interactions of mobile dislocations with the Peierls barrier whereas the former represents interactions of mobile dislocations with impurity atoms (predominantly but not solely carbon) which varies from alloy to alloy in Table 9.2.

¹The results in Fig. 9.11 differ slightly from those presented in Figure 13 of Ref. [6]. In the latter work $\hat{\sigma}_p/\mu_o$, $\hat{\sigma}_i/\mu_o$, g_{op} , and g_{oi} were all allowed to vary while in Fig. 9.11 the activation energies were fixed and only the threshold stresses were allowed to vary. The trend in both curves, however, is similar.

9.2 Comparison with Campbell and Ferguson Measurements

Campbell and Ferguson [12] published an extensive series of shear stress measurements as a function of temperature and strain rate in a 0.12% C steel. Figure 9.12 shows their compilation of the yield stress (in shear) versus the shear strain rate. Following a convention established by Rosenfield and Hahn [13] three regions dominated by different deformation mechanisms were defined (see Fig. 9.12). Region I was thought to be a region where deformation was dominated by “long-range internal stress fields.” In Region II, deformation was controlled by “the thermal activation of dislocation motion,” and Region IV involved dislocation motion influenced by a “macroscopic viscosity.”

Applying the approach used in analyzing deformation in molybdenum (Fig. 9.4), niobium (Fig. 9.6), tantalum (Fig. 9.8), and iron (Fig. 9.9), Fig. 9.13 shows a plot of the entire Campbell and Ferguson data set.² As in these other BCC metals, the dashed curve represents the model according to Eq. 9.2,

$$\frac{\tau}{\mu} = \frac{\tau_a}{\mu} + s_p(\dot{\gamma}, T) \frac{\hat{\tau}_p}{\mu_o} + s_i(\dot{\gamma}, T) \frac{\hat{\tau}_i}{\mu_o} \tag{9.2}$$

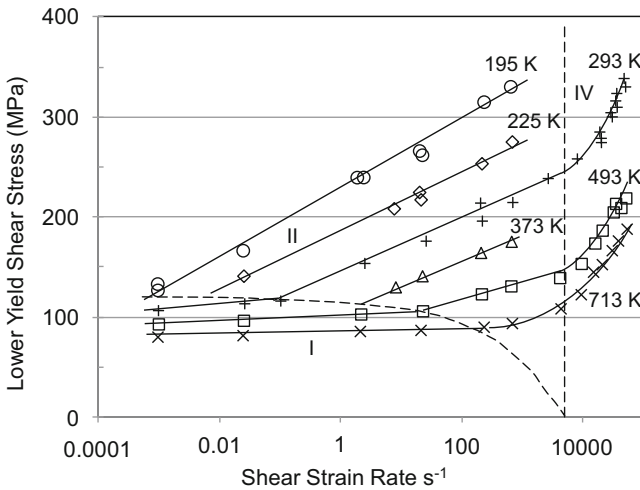


Fig. 9.12 Temperature and strain-rate-dependent yield stress measurements by Campbell and Ferguson in a 0.12% C steel

²Note that the numerator of the logarithmic term in Fig. 9.13 is 10^7 s^{-1} rather than 10^8 s^{-1} as in the prior figures. This follows from the change in $\dot{\epsilon}_o$ terms as listed in Table 9.3.

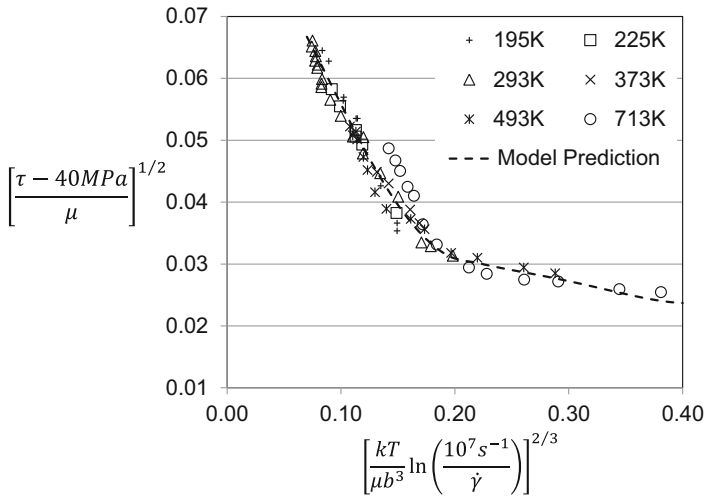


Fig. 9.13 Campbell and Ferguson’s measurements in a 0.12% C steel plotted on coordinates dictated by Eq. 6.9 along with a two-obstacle model prediction

Table 9.3 Model parameters for the two-obstacle prediction in Fig. 9.13

Parameter	Value	Converted to axial stress		Pure Iron (Table 9.2)
τ_a	40 MPa	σ_a	69.3 MPa	65–75 MPa
$\hat{\tau}_p / \mu_o$	0.0075	$\hat{\sigma}_p / \mu_o$	0.013	0.0185–0.02
g_{op}	0.09	g_{op}	0.09	0.096
$\dot{\gamma}_{op}$	10^7 s^{-1}	$\dot{\epsilon}_{op}$	$5.8 \times 10^6 \text{ s}^{-1}$	10^8 s^{-1}
$\hat{\tau}_i / \mu_o$	0.0015	$\hat{\sigma}_i / \mu_o$	0.0026	0.0024–0.008
g_{oi}	1.0	g_{oi}	1.0	0.4
$\dot{\gamma}_{oi}$	10^7 s^{-1}	$\dot{\epsilon}_{oi}$	$5.8 \times 10^6 \text{ s}^{-1}$	10^{10} s^{-1}

which is identical to Eq. 9.1 except that Eq. 9.2 is written in terms of shear stress τ and shear strain rate $\dot{\gamma}$. (Of course, from the von Mises yield criterion, Eq. 8.4 can be used to convert shear stress and shear strain rate to axial stress and axial strain rate.) Table 9.3 lists the model parameters used for the prediction in Fig. 9.13.

It is interesting that decreasing $\dot{\epsilon}_{op}$ and $\dot{\epsilon}_{oi}$ from values used earlier (see Tables 9.1 and 9.3) led to a better overall fit across the entire Campbell and Ferguson data set. This illustrates that these parameters are essentially fitting parameters and there are generally too few data points to discern much effect of an order-of-magnitude change in their values. The Campbell and Ferguson data set may be unique in this regard. However, it cannot be concluded that the values of these parameters are generally applicable beyond the low-carbon steel studied by Campbell and Ferguson. Analysts should choose and report the values that are used in application of the MTS model equations.

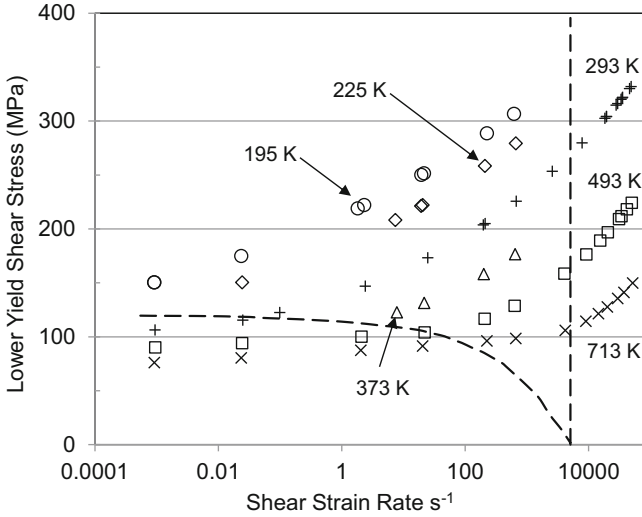


Fig. 9.14 Predicted yield stresses at the temperatures and strain rates used in the Campbell and Ferguson experiments and plotted on the same coordinates used to display their measurements in Fig. 9.12 along with their dashed lines delineating regions with common controlling deformation mechanisms

Figure 9.14 shows model predictions at each strain rate and temperature employed by Campbell and Ferguson on the coordinates used in Fig. 9.12. Included are the lines separating Regions I, II, and IV used by Campbell and Ferguson. On these axes it is apparent the strain-rate sensitivity at the highest strain rates is lower than observed experimentally.³ Good agreement between Figs. 9.12 and 9.14 is found at lower strain rates at all temperatures. Campbell and Ferguson ascribed three separate rate-controlling deformations (Regions I, II, and IV) as identified in Fig. 9.12. The internal-state-variable formulation adopted here specifies two contributing dislocation–obstacle interactions that combine to define the kinetics over the entire range of conditions. An interesting observation is that the dashed line in Figs. 9.12 and 9.14 separating Regions I and II is roughly in the same location as one could draw the line defining where the Peierls obstacle becomes ineffective (see Fig. 9.5). Accordingly, there are points of commonality between the conclusions of Campbell and Ferguson and those resulting from application of the internal-state-variable model and analyses described in this section.

Recall in Chap. 8 that the only plot of yield stress versus temperature and strain rate in annealed FCC metals was that shown in Fig. 8.25 for Ni270. The yield stress in pure FCC metals is rate insensitive. This is in contrast to the measurements in the BCC metals and alloys presented in this section where the yield stress exhibits strong rate (and temperature) dependence. By definition, all of the materials examined in

³It is worth noting that yield stress measurements at these strain rates are unreliable.

this chapter using figures such as Figs. 9.4, 9.6, 9.7, 9.8, 9.9, and 9.10 are at constant structure, as characterized by the annealed initial condition before strain hardening. In the next section, structure evolution in BCC metals and alloys is considered.

9.3 Trends in the Activation Volume for Pure BCC Metals

Table 9.1 listed the model parameters derived for six pure BCC metals using the two parameter model (Eq. 9.1). The activation volume (for $p = 1/2$ and $q = 3/2$ which is applicable here) was given by Eq. 6.19. Table 9.4 lists the activation volumes for the Peierls obstacle population and Table 9.5 lists the activation volumes for the impurity obstacle population for each of these metals calculated using Eq. 6.19 (or Eq. 6.23 for the Peierls obstacle population and Eq. 6.24 for the impurity obstacle population).

Equation 6.20 in Sect. 6.4 gave the expected variation of the activation volume with the product $\mu_o b^3 g_o / \hat{\sigma}$ and it was predicted that measurements of the activation volume on different materials would follow this trend when the model (e.g., Eq. 9.1) correctly assigned the internal-state variables and correctly represented the thermal activation kinetics of each obstacle population. Figure 9.15 is a plot of v_p^* versus $\mu_o b^3$ (Table 9.4) and Fig. 9.16 gives the same plot for v_i^* (Table 9.5).

The dashed lines in Figs. 9.15 and 9.16 are drawn according to Eq. 6.20. It is interesting that the data for the Peierls obstacle in Fig. 9.15 follows the anticipated

Table 9.4 Calculated activation volume for the Peierls obstacle population

Metal	b (nm)	μ_o (GPa)	$\hat{\sigma}_p$ (GPa)	g_{op}	v_p^* (nm ³)
Mo	0.272	142.7	2.07	0.081	3.63
Nb	0.286	50.1	1.60	0.10	2.07
W	0.274	163.1	2.94	0.125	5.52
Ta	0.286	65.1	1.17	0.095	2.97
Fe	0.249	71.5	1.38	0.096	2.01
V	0.263	69.0	1.28	0.07	1.73

v_p^* is evaluated using Eq. 6.19 at $\sigma = 0.01$ GPa^a

^aEvaluation of Eq. 6.19 at a constant stress rather than a constant $\sigma/\hat{\sigma}$ gave lower scatter in Fig. 9.15

Table 9.5 Calculated activation volume for the impurity-atom obstacle population

Metal	$\hat{\sigma}_i$ (GPa)	g_{oi}	v_i^* (nm ³)
Mo	0.684	0.27	38.4
Nb	0.286	0.37	40.3
W	0.848	0.52	96.1
Ta	0.208	0.4	66.1
Fe	0.329	0.4	38.4
V	0.207	0.4	54.5

v_i^* is evaluated using Eq. 6.19 at $\sigma = 0.002$ GPa

Fig. 9.15 Activation volume for the Peierls obstacle population versus $\mu_0 b^3$

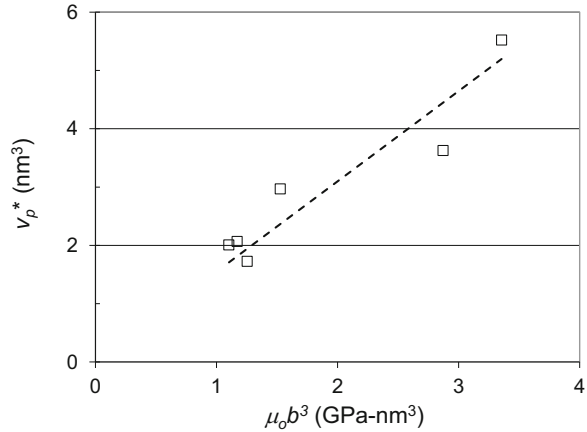
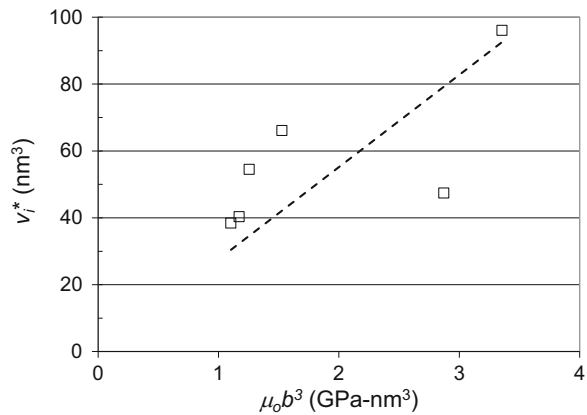


Fig. 9.16 Activation volume for the impurity atom obstacle population versus $\mu_0 b^3$



trend more closely (less scatter) than do the data for the impurity obstacle in Fig. 9.16. This is sensible in that the impurity obstacle may be comprised by a plethora of dislocation–impurity atom interactions in these six FCC metals that may not be ideally described by a single thermal activation equation (e.g., Eq. 7.3) with common values of p_i , q_i , and $\dot{\epsilon}_{oi}$.

The correlation in Fig. 9.15 begs the question as to whether this enables predictive capability, e.g., for deformation in a BCC metals without a comprehensive set of measurements correlating yield stress with temperature and strain rate. The slope of the line in Fig. 9.15 is 1.55 GPa^{-1} . From Eq. 6.20,

$$10.6M \frac{g_{op}}{\hat{\sigma}_p} = 1.55\text{GPa}^{-1} \quad (9.3)$$

Taking $M = 3.1$ gives

$$\frac{\hat{\sigma}_p}{g_{op}} = 21.2\text{GPa} \quad (9.4)$$

Let us assume that a very pure BCC metal exists which follows Eq. 9.1 with $\hat{\sigma}_i = 0$ or at least $\hat{\sigma}_i \ll \hat{\sigma}_p$. In this case,

$$\begin{aligned} \frac{\sigma}{\mu} &= \frac{\sigma_a}{\mu} + \frac{\sigma_p}{\mu} \\ \frac{\sigma_p}{\mu} &= \frac{(\sigma - \sigma_a)}{\mu} = s_p(\dot{\epsilon}, T) \frac{\hat{\sigma}_p}{\mu_o} \\ s_p(\dot{\epsilon}, T) &= \left\{ 1 - \left[\frac{kT}{g_{op}\mu b^3} \ln \left(\frac{\dot{\epsilon}_{op}}{\dot{\epsilon}} \right) \right]^{2/3} \right\}^2 \\ \left(\frac{\sigma_p}{\mu} \right) &= \frac{(\sigma - \sigma_a)}{\mu} = \left\{ 1 - \left[\frac{kT}{g_{op}\mu b^3} \ln \left(\frac{\dot{\epsilon}_o}{\dot{\epsilon}} \right) \right]^{2/3} \right\}^2 \left(\frac{\hat{\sigma}_p}{\mu_o} \right) \end{aligned}$$

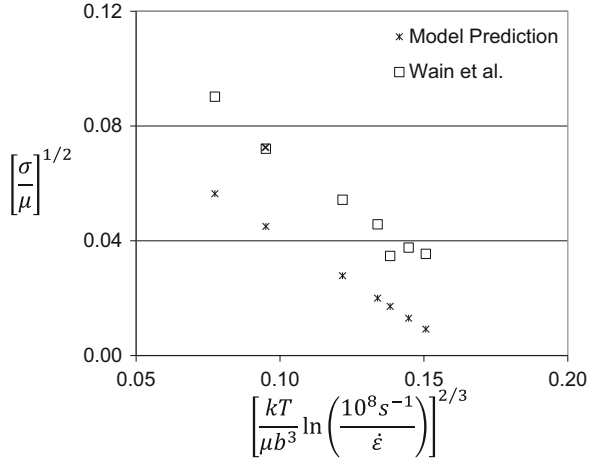
From Eq. 9.4,

$$\left(\frac{\sigma_p}{\mu} \right) = \left\{ 1 - \left[\frac{21.2\text{GPa } kT}{\hat{\sigma}_p(\text{GPa})\mu b^3} \ln \left(\frac{\dot{\epsilon}_o}{\dot{\epsilon}} \right) \right]^{2/3} \right\}^2 \left(\frac{\hat{\sigma}_p}{\mu_o} \right) \quad (9.5)$$

Equation 9.5 relates the Peierls stress ($\sigma - \sigma_a$) to a function with only one unknown— $\hat{\sigma}_p$ —assuming that the Burgers vector and temperature-dependent shear modulus are known. This implies that a single yield stress measurement at a known strain rate and temperature would enable a calculation of $\hat{\sigma}_p$, which would fully specify the deformation kinetics.

To test this, note that measurements in pure chromium were not included in Sect. 9.1, even though limited measurements are available. Wain et al. reported measurements in high purity chromium that had been electrodeposited, arc melted, rolled and recrystallized annealed at 1373 K (2 h) [5]. At 139 K and a strain rate of $1.67 \times 10^{-5} \text{ s}^{-1}$ these investigators reported a yield stress of 660 MPa. With $b = 0.25 \text{ nm}$ and, from Eq. 6.8, $\mu_0 = 125.7 \text{ GPa}$, $D_o = 1.1 \text{ GPa}$, and $T_o = 50 \text{ K}$, a value of $\hat{\sigma}_p$ equal to 1.42 GPa gives (using Eq. 9.5) $\sigma_p = 0.66 \text{ GPa}$. From Eq. 9.4, this in turn gives $g_{op} = 0.067$. These values of $\hat{\sigma}_p$ and g_{op} are in the range of the values for the other

Fig. 9.17 Variation of measured yield stress with temperature (at a strain rate of $1.67 \times 10^{-5} \text{ s}^{-1}$) in chromium. Dashed line is the prediction based on the correlation observed in Fig. 9.15 for six other pure BCC metals



BCC metals listed in Table 9.4. These model parameters can be used to generate a prediction for all of the Wain et al. measurements. Figure 9.17 shows the yield stress plot with the entire data set and the model estimates.

In Fig. 9.17 an “x” has been placed on the one data point used with Eq. 9.5 to compute $\hat{\sigma}_p$. The predicted stresses lie well below the measured stresses, although the temperature dependence is adequately predicted. The lack of agreement in the stress level may relate to the assumption that $\hat{\sigma}_i = 0$. Or it may imply that the scatter in Fig. 9.15 is not simply experimental scatter but rather includes material-to-material differences not included in the model equations. Nonetheless, it is intriguing that a predictive capability appears in reach.

9.4 Structure Evolution in BCC Pure Metals and Alloys

Whereas pure copper, nickel, and the nickel–carbon alloys discussed in Sect. 8.5 benefited from an extensive set of prestrain and reload tests per the recipe described in Chap. 7, this is not the case for any of the BCC metals described above. Instead, to complement the analysis of the temperature and strain-rate dependence of the yield stress discussed in the previous sections, this section describes the analysis of stress–strain curves to identify temperature and strain-rate dependence of $\hat{\sigma}_\varepsilon$. The approach was introduced in Sect. 8.10. To more thoroughly demonstrate the procedure, a fictitious alloy and set of data will be used in the next section. The analysis is based on the model for BCC alloys prescribed by Eq. 9.6

$$\frac{\sigma}{\mu} = \frac{\sigma_a}{\mu} + s_p(\dot{\epsilon}, T) \frac{\hat{\sigma}_p}{\mu_o} + s_i(\dot{\epsilon}, T) \frac{\hat{\sigma}_i}{\mu_o} + s_\varepsilon(\dot{\epsilon}, T) \frac{\hat{\sigma}_\varepsilon}{\mu_o} \quad (9.6)$$

which is identical in form to the governing equation for FCC systems except for the addition of the Peierls obstacle terms.

9.5 Analysis of the Constitutive Behavior of a Fictitious BCC Alloy—UfKonel

It is often the case that an extensive data set documenting reload yield stress as a function of temperature and strain rate—for samples deformed according to a prescribed prestrain temperature, strain rate, and strain—is not available. Instead, researchers may have published full stress–strain curves as a function of temperature and strain rate. It is assumed that this is the case for the fictitious BCC alloy—UfKonel, which is an alloy of Uffium (Uf) and Kopper (Ko). It is known that the alloy has a BCC crystal structure and that it is provided in the annealed condition with an average grain size of 50 μm. The Burgers vector and the variations of the shear modulus and the heat capacity with temperature are taken as the respective values in iron. Figure 9.18 shows the true stress versus true strain curves over a temperature range of 76–673 K and a strain-rate range of 0.001 s⁻¹ to 3000 s⁻¹.

The first step is to analyze the temperature and strain-rate dependence of the yield stress according to Eq. 9.1 and the procedures used to generate Fig. 9.3 and related figures in Sect. 9.1. Figure 9.19 shows the resulting plot. The model parameters for the dashed-line fit in Fig. 9.19 are listed in Table 9.6. From Fig. 9.19 and the model parameters in Table 9.6, UfKonel appears to be very similar to the other FCC metals listed in Table 9.1.

Under the assumption that none of the model parameters listed in Table 9.6 change with strain, Eq. 9.6 can be solved for $\hat{\sigma}_\epsilon$ as per Eq. 8.13, giving

$$\hat{\sigma}_\epsilon = \frac{\mu_o}{s_\epsilon(\dot{\epsilon}, T)} \left[\frac{\sigma}{\mu} - \frac{\sigma_a}{\mu} - s_p(\dot{\epsilon}, T) \frac{\hat{\sigma}_p}{\mu_o} - s_i(\dot{\epsilon}, T) \frac{\hat{\sigma}_i}{\mu_o} \right] \tag{9.7}$$

To proceed, it is necessary to further assume that the parameters for s_ϵ are as established for the FCC systems as summarized in Table 9.7.

Fig. 9.18 Temperature and strain-rate-dependent stress–strain curves in the fictitious alloy UfKonel

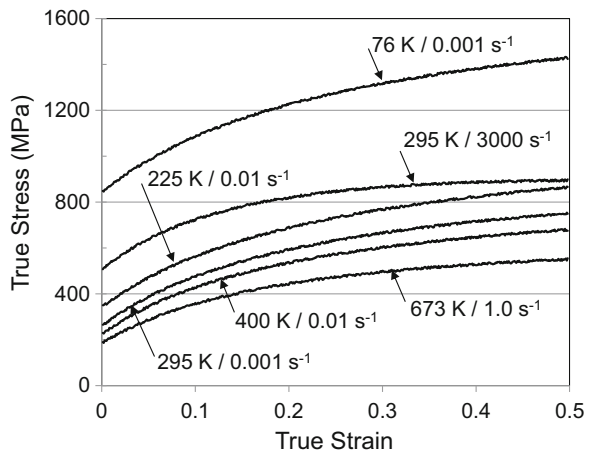


Fig. 9.19 Variation of yield stress in annealed UfKonel with temperature and strain rate

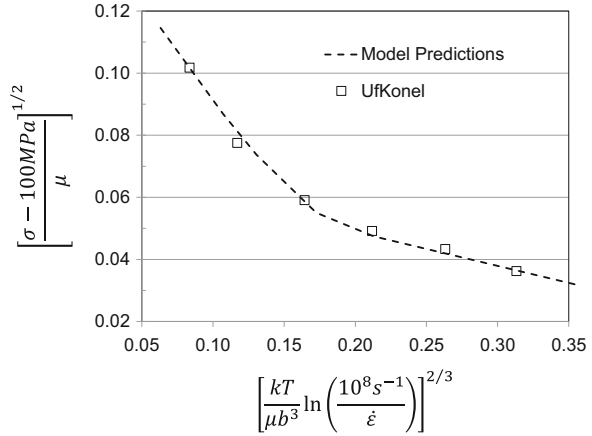


Table 9.6 Model parameters for the dashed-line fit in Fig. 9.19

UfKonel	
$\sigma_a(\text{MPa})$	100
$\dot{\epsilon}_{op} (\text{s}^{-1})$	10^9
$p_p = p_i$	0.5
$\dot{\epsilon}_{oi} (\text{s}^{-1})$	10^{10}
$q_p = q_i$	1.5
g_{oi}	0.65
$\hat{\sigma}_i/\mu_o$	0.005
g_{op}	0.10
$\hat{\sigma}_p/\mu_o$	0.019

Table 9.7 Model parameters for s_ϵ (Eq. 7.9)

Parameter	Equation	Value
$g_{o\epsilon}$	Eq. 7.9	1.6
$\dot{\epsilon}_{o\epsilon}$		10^7 s^{-1}
p_ϵ		0.667
q_ϵ		1

Figure 9.20 shows $\hat{\sigma}_\epsilon$ versus strain for the test at 295 K and a strain rate of 0.001 s^{-1} analyzed according to Eq. 9.7 and the model parameters shown in Tables 9.6 and 9.7. The dashed line—which is barely distinguishable from the solid curve—is the model fit according to the evolution equation (Eq. 6.28) with $\kappa = 2$, $\theta_{II} = 3300 \text{ MPa}$, and $\hat{\sigma}_{\epsilon s} = 830 \text{ MPa}$. Fig. 9.20 for UfKonel is analogous to Fig. 8.2 for copper in that it shows the variation of $\hat{\sigma}_\epsilon$ with strain. In copper, the curve was created from measurements of $\hat{\sigma}_\epsilon$ at various strain levels, while in UfKonel the curve was derived from the measured stress values and reduced to $\hat{\sigma}_\epsilon$ according to Eq. 9.7. Table 9.8 lists the Eq. 6.28 model coefficients for each of the six stress-strain conditions shown in Fig. 9.18 (see Box 9.1).

Fig. 9.20 Variation of $\hat{\sigma}_\epsilon$ with strain in UfKonel for the test at a strain rate of 0.001 s^{-1} and a temperature of 295 K. The dashed line is the fit to the evolution equation (Eq. 6.28)

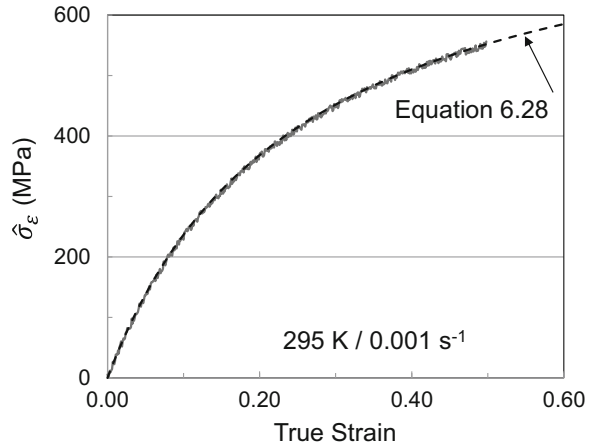


Table 9.8 Model parameters in the evolution equation (Eq. 6.28) for the fits to the six test conditions for UfKonel

Temperature/Strain rate	Eq. 6.28 parameter ($\kappa = 2$)	
	θ_{II} (MPa)	$\hat{\sigma}_{\epsilon s}$ (MPa)
295 K/0.001 s^{-1}	3300	830
400 K/0.001 s^{-1}	3590	760
225 K/0.01 s^{-1}	3500	885
295 K/3000 s^{-1}	3850	860
673 K/1.0 s^{-1}	3520	700
76 K/0.001 s^{-1}	3600	920

Box 9.1 Estimating the Variation of $\hat{\sigma}_\epsilon$ with Strain for Adiabatic Tests

When a test is under adiabatic conditions, the temperature rises according to Eq. 6.32. With tabulated values of measured stress versus strain, the temperature rise is easily computed. Since each of the s -values in Eq. 9.7 is established before evolution is analyzed, the actual, temperature-dependent value of $\hat{\sigma}_\epsilon$ is deduced using this equation. The procedure then calls for fitting Eq. 6.28, rewritten below, to the $\hat{\sigma}_\epsilon$ versus ϵ data set.

$$\frac{d\hat{\sigma}_\epsilon}{d\epsilon} = \theta_{II}(\dot{\epsilon}) \left(1 - \frac{\hat{\sigma}_\epsilon}{\hat{\sigma}_{\epsilon s}(\dot{\epsilon}, T)} \right)^\kappa \quad (6.28)$$

The purpose of this exercise is to derive the temperature and strain-rate-dependent $\hat{\sigma}_{\epsilon s}$ using Eq. 6.26. At issue for an adiabatic test, is that one cannot fit Eq. 6.28 to the $\hat{\sigma}_\epsilon$ versus ϵ data set with a temperature-dependent $\hat{\sigma}_{\epsilon s}$ since

(continued)

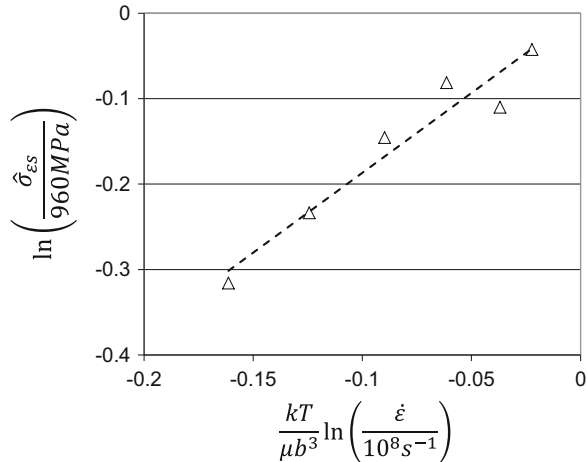
Box 9.1 (continued)

this has not yet been established. Typically, the procedure is to select unique values of θ_{II} and $\hat{\sigma}_{\epsilon_s}$ that best fit the $\hat{\sigma}_{\epsilon}$ versus ϵ data set. This introduces some uncertainty in the $\hat{\sigma}_{\epsilon_s}(\dot{\epsilon}, T)$ correlation. In most cases, the temperature increase is minimal in adiabatic tests and the temperature dependence of $\hat{\sigma}_{\epsilon}$ is small, which implies this uncertainty is second order. However, it is a limitation of the procedure that should be understood and appreciated.

In subsequent chapters when adiabatic test conditions are included in the data set, the initial and final temperatures are noted and the $\hat{\sigma}_{\epsilon_s}(\dot{\epsilon}, T)$ correlation (Eq. 6.26) is made with the initial temperature rather than the final temperature. (Exercises 8.1 through 8.4 provide justification for this assumption, but Exercise 9.9 illustrates the challenge posed by the adiabatic temperature rise.)

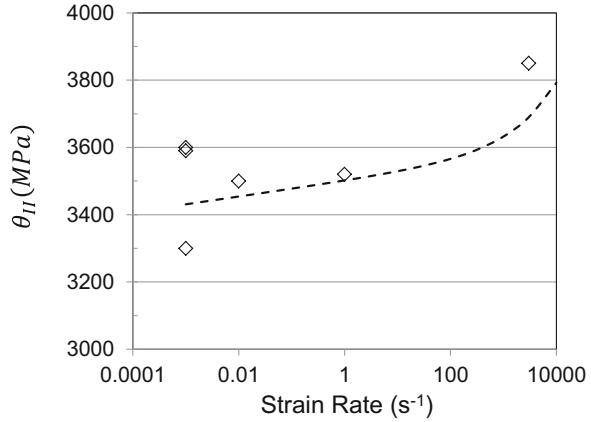
Deriving fits to Eq. 6.26 (for the variation of $\hat{\sigma}_{\epsilon_s}$ with strain rate and temperature) and Eq. 6.29 (for variation of θ_{II} with strain rate) is handled the same as demonstrated for copper in Figs. 8.3 and 8.4. Figure 9.21 shows the fit to Eq. 6.26. The dashed line in this figure is least-squares fit. The inverse of the slope of this line gives the constant $g_{\epsilon_{SO}} = 0.535$ in Eq. 6.26. Note in Fig. 9.21 that $\hat{\sigma}_{\epsilon_{SO}} = 960$ MPa. In fact, the stress–strain curves in Fig. 9.18 were created with $\hat{\sigma}_{\epsilon_{SO}} = 1000$ MPa and $g_{\epsilon_{SO}} = 0.500$. However, a random-number generator was used in the algorithm to vary these parameters (as well as A_o in Eq. 6.29) within a $\pm 5\%$ range to simulate typical experimental scatter.⁴ Accordingly, the deduced values of these parameters are

Fig. 9.21 Variation of $\hat{\sigma}_{\epsilon_s}$ with test temperature and strain rate for the six test conditions in UfKonel. The line is the regression fit according to Eq. 6.26



⁴A random-number generator was also used to give the “noise” in the stress–strain curves shown in Fig. 9.18.

Fig. 9.22 Variation of θ_{II} with strain rate for the six test conditions in UfKonel along with the dashed line fit to Eq. 6.29



reasonable. Similarly, Fig. 9.22 shows variation of the deduced values of θ_{II} with strain rate. The dashed line is drawn according to Eq. 6.29 with $A_o = 3500$ MPa, $A_1 = 10$, and $A_2 = 2 \text{ s}^{-1/2}$ which were the values used to generate the stress–strain curves in Fig. 9.18.

This section has illustrated the procedures used to calculate $\hat{\sigma}_{es}$ versus true strain when given true stress versus true strain curves. Two important assumptions enable use of Eq. 9.7 to accomplish this. The first assumption was that the kinetics of dislocation interactions with stored dislocations (i.e., the model parameters in Eq. 7.9 summarized in Table 9.7) is the same in BCC and FCC systems. The second assumption was that the model parameters in Tables 9.6 and 9.7 are invariant with strain. This assumption was also made when analyzing deformation in FCC systems in Chap. 8; the assumption implies that the material behaves the Cottrell-Stokes Law.

Stress–strain curves from several BCC metals and alloys are next analyzed according to the procedures outlined in this section for the fictitious UfKonel.

9.6 Analysis of the Constitutive Behavior of AISI 1018 Steel

Measurements in annealed AISI 1018 steel by Gray and Chen [14] are analyzed in this section according to the methodology outlined in Sect. 9.5. Table 9.9 lists the test conditions included in this data set. Mechanical tests were in compression. The two tests at the strain rate of 1 s^{-1} included an unloading and reloading step. This is useful because at this strain rate the test is approximately under adiabatic conditions. Thus, the temperatures preceding the unload steps are higher than the temperatures at the start of the reload (148 K and 223 K) steps. Assuming no structural change from the unload and reload steps, the test serves as a temperature–change test, which offers another check on the model equations.

Table 9.9 Test conditions for stress–strain measurements in annealed AISI 1018 steel [14]

Material	Temperature (K)	Strain rate (s^{-1})
AISI 1018 Steel Annealed Condition	148	0.01
	148	1
	223	0.01
	223	1
	298	0.01
	298	2800
	298	3750
	473	2600
	473	3000
	653	2700
	673	2600
	823	2600
	973	2000
	973	2200
973	2600	

Fig. 9.23 Stress–strain curves in AISI 1018 steel at select conditions of strain rate and temperature. The blip at $\sim 27\%$ strain in the test at 298 K and a strain rate of $0.01 s^{-1}$ is an unload plus reload step

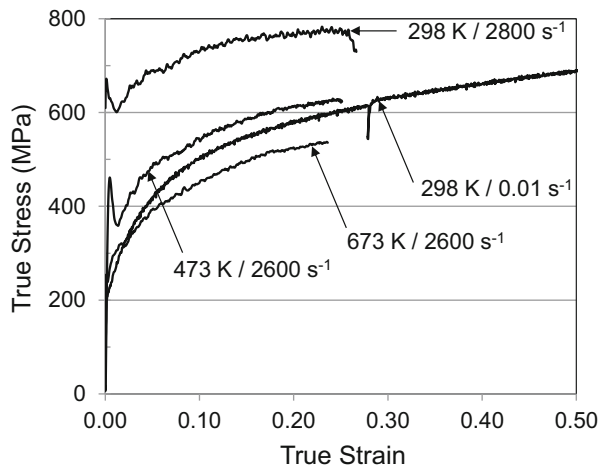


Figure 9.23 shows four of the stress–strain curves from this data set.⁵ Two of the curves in Fig. 9.23 exhibit distinct upper and lower yield points. It is worth re-emphasizing that the stress values shown for these points must be used cautiously since at these strain rates the sample may not be deforming uniformly in the vicinity of yield. Even with the uncertainty in yield stress at high strain rates the first step is to analyze the dependence of yield stress on temperature and strain rate—as was done for UfKoneI in Fig. 9.19. The resulting curve is shown in Fig. 9.24. The star-like

⁵The test at 298 K and a strain rate of $0.01 s^{-1}$ also involved an unloading and (partially shown) reloading operation. Since this is an isothermal test, however, the reload serves no purpose other than to demonstrate that the reload stress returns to the value before unloading.

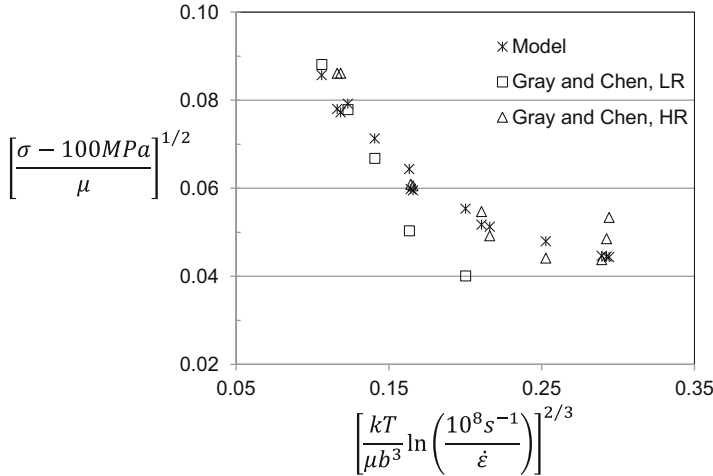


Fig. 9.24 Variation of yield stress with temperature and strain rate (Low Rate and High Rate) for the data set listed in Table 9.9. Model predictions are shown with a star-like symbol for each of the temperature and strain rate combinations. The three HR data points at the abscissa value of ~0.29 are 973 K measurements ($T_H = 0.54$)

symbols in Fig. 9.24 represent model predictions for each of the experimental conditions. The model parameters are identical to those listed in Table 9.6, except that $g_{op} = 0.11$, $\hat{\sigma}_p/\mu_o = 0.014$, $g_{oi} = 1.0$ and $\hat{\sigma}_i/\mu_o = 0.005$ (as in Table 9.6). Measurements at the higher strain rates (HR) and those at strain rates of 0.01 s^{-1} and 1 s^{-1} (lower strain rates [LR]) are plotted with different open symbols in Fig. 9.24. It is evident in this figure that the model predictions follow the measurements although there are some large deviations at several of the conditions. This could be due to difficulty in assessing the yield point in presence of a yield phenomenon or the inaccuracy in assessing yield at the high strain rate conditions.

A separate check on the model parameters is possible by taking advantage of the test conditions noted above where a temperature-change occurred. The temperature rise during deformation is analyzed using Eq. 6.32. This predicted temperature rise relies only on the stress–strain curve and, the heat capacity, and the assumed value of the parameter ψ . Figure 9.25 shows the stress–strain curve for the test at a strain rate of 1.0 s^{-1} and an initial temperature of 148 K.

Before the specimen was unload (the elastic unload and reload steps are not fully shown) the specimen temperature is predicted to have risen to a temperature of 197 K.⁶ The specimen is unloaded, taken to the original temperature of 148 K and reloaded. The stress before unloading is taken from the stress–strain curve to be 813 MPa, whereas upon reloading the yield stress is measured as 921 MPa. This combination of temperatures and stresses gives two points on a plot using the

⁶This is predicted using $\psi = 0.85$ rather than the usual $\psi = 0.95$ to reflect the fact that at this temperature the conditions may not be fully adiabatic.

Fig. 9.25 Stress–strain curves at 148 K and a strain rate of 1.0 s^{-1} in AISI 1018 steel showing the response before and after the unload step. The reload yield stress is higher than the stress subsequent to the unload step because under these approximately adiabatic conditions the specimen temperature has risen to $\sim 197 \text{ K}$

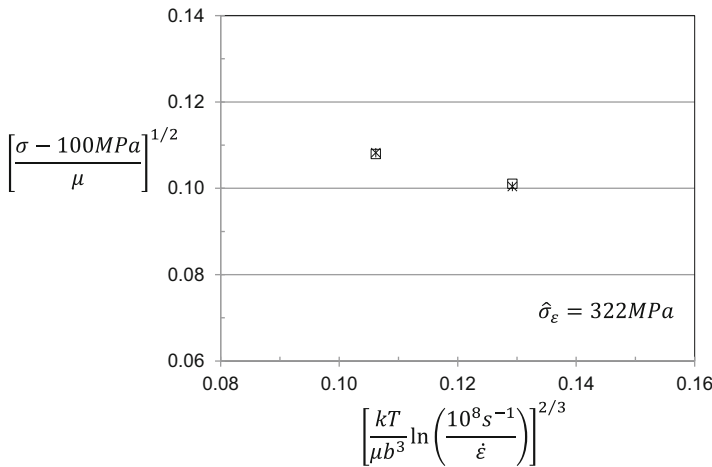
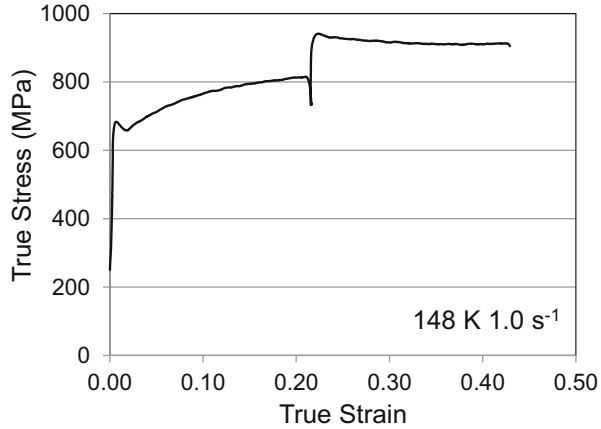


Fig. 9.26 The stress before and after the unload step along with the temperature before and after the unload step along with model predictions

coordinates in Fig. 9.24. Equation 9.6 is the governing equation, where $\hat{\sigma}_\epsilon$ has risen due to strain hardening. The values of $\hat{\sigma}_p$, s_p , $\hat{\sigma}_i$, and s_i are the same as those used in Fig. 9.24 (specified above). Similar to the assumption used in Sect. 9.5, the parameters comprising s_ϵ are assumed to be the same as established for FCC systems and summarized in Table 9.7. The only adjustable parameter becomes $\hat{\sigma}_\epsilon$. Figure 9.26 shows the two data points on an expanded scale. The model predictions with $\hat{\sigma}_\epsilon = 322 \text{ MPa}$ are the star-like symbols which coincide with the open-square data points. The good agreement in Fig. 9.26 gives added confidence to the values of the model parameters.

As with UfKonel the next step is to apply Eq. 9.7 to subtract from the total stress at each strain level the athermal stress and the stress contributions from the Peierls obstacle and the impurity obstacle, leaving $\hat{\sigma}_\epsilon$. For isothermal conditions, the stress

Fig. 9.27 The stress–strain curve at 298 K and a strain rate of 0.01 s^{-1} along with the analyzed contributions to the stress from the Peierls obstacle (which at this condition is close to zero), the impurity obstacle, and the athermal stress

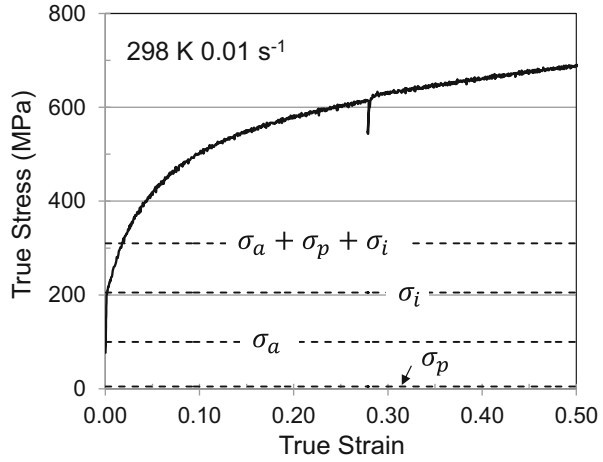
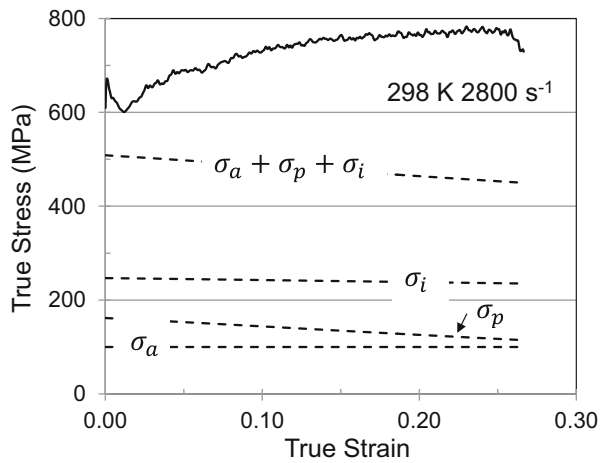


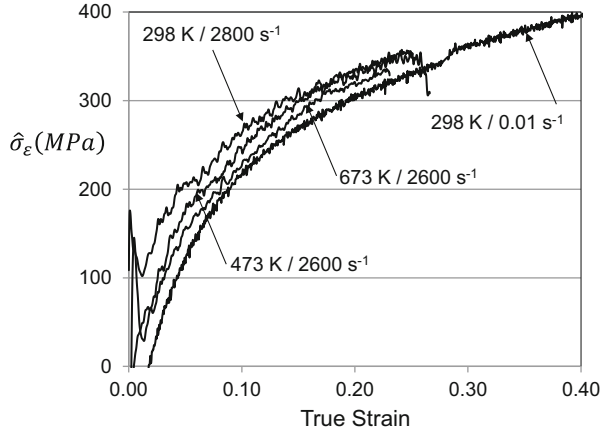
Fig. 9.28 The stress–strain curve at 298 K and a strain rate of 2800 s^{-1} along with the analyzed contributions to the stress from the Peierls obstacle (which at this condition is close to zero), the impurity obstacle, and the athermal stress



contributions subtracted do not vary with strain; for adiabatic conditions, however, the contributions from the Peierls and impurity obstacles decrease as the specimen temperature increases. Figure 9.27 shows the stress–strain curve at 298 K and a strain rate of 0.01 s^{-1} . The dashed lines in this figure show the values of the three stress components to be subtracted from the total stress. Note in this case that the sum of these stresses appears to be $\sim 100 \text{ MPa}$ higher than the apparent yield stress. This illustrates the scatter that accompanies this analysis when a single set of model parameters is selected to describe an entire data set rather than a single curve.

Figure 9.28 shows the full stress–strain curve and the values of the three stress components for the test at 298 K and a strain rate of 2800 s^{-1} . In this case, the athermal stress is invariant with strain, but σ_p and σ_i decrease with strain as the specimen temperature increases due to adiabatic heating. Their variation with strain differs, of course, since each of the obstacle populations exhibit unique kinetics—as

Fig. 9.29 Deduced variation of $\hat{\sigma}_\varepsilon$ with strain using Eq. 9.7 for each of the tests in Fig. 9.23



defined by unique values of s_p and s_i . In this case, the sum of the three stresses to be subtracted is lower than the apparent yield stress, but as emphasized repeatedly, it is difficult to estimate the yield stress in these dynamic tests. In this stress–strain curve, the uncertainty is amplified by the yield phenomenon.

Figure 9.29 shows the analyzed variation of $\hat{\sigma}_\varepsilon$ with strain (using Eq. 9.7) for the four loading conditions shown in Fig. 9.23. No attempt has been made to remove scatter in the measurements or the oscillations that accompany the high strain rate test procedure. The results are reasonable, however, in that the lowest curve is the test at 298 K and a strain rate of 0.01 s^{-1} and the highest curve is at 298 K and the high strain rate whereas the two high strain rate curves at the higher temperatures are in the middle.

The variation of $\hat{\sigma}_\varepsilon$ with strain for the tests under adiabatic conditions is affected by the continuously increasing temperature. No attempt has been made to remove the slight temperature dependence of $\hat{\sigma}_{\varepsilon s}$ (Eq. 6.26). (See the discussion in the Box 8.1.)

The next step is to fit the modified Voce evolution equation (Eq. 6.28) to each of the curves of $\hat{\sigma}_\varepsilon$ versus strain to analyze $\theta_{II}(\dot{\varepsilon})$ and $\hat{\sigma}_{\varepsilon s}(\dot{\varepsilon}, T)$ (Eq. 6.26). It is helpful to remember that the goal of this step is to derive plots such as were shown for UfKonel in Figs. 9.21 and 9.22. When present, the yield phenomenon—particularly when confounded by typical test-to-test scatter—complicates this analysis. Experience with the analysis of data sets such as the 1018 data described in this section, and the niobium and vanadium data sets presented in subsequent sections, has led to several useful guidelines.

1. An accurate description of the yield kinetics in annealed material (e.g., Fig. 9.24) is essential.
2. Fit the modified Voce equation to the entire stress–strain curve, taking note of particular regions of the stress–strain curve where uncertainties (e.g., in the vicinity of yield) or errors (e.g., due to friction for tests taken to large strains) exist.

Fig. 9.30 Computed variation of $\hat{\sigma}_\epsilon$ with strain using Eq. 9.7 for the adiabatic test at 148 K and a strain rate of 1.0 s^{-1} along with the dashed-line fit to the evolution equation (Eq. 6.28)

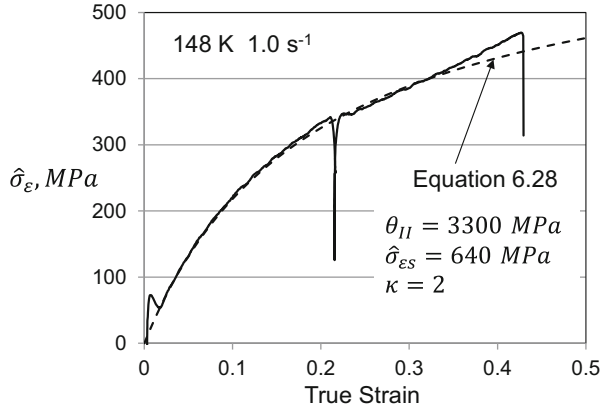
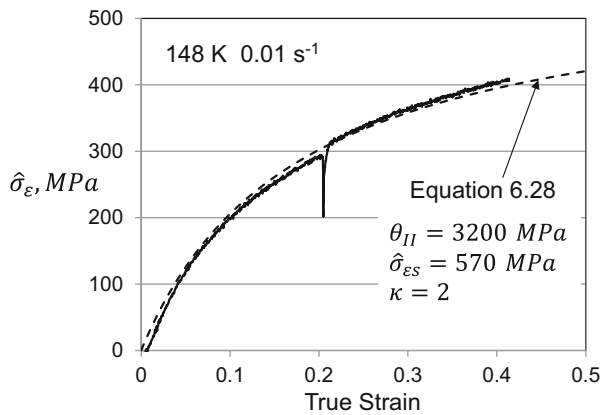


Fig. 9.31 Computed variation of $\hat{\sigma}_\epsilon$ with strain using Eq. 9.7 for the adiabatic test at 148 K and a strain rate of 0.01 s^{-1} along with the dashed-line fit to the evolution equation (Eq. 6.28)



3. Start by analyzing a stress–strain curve that appears to be well-behaved, e.g., one where plots of $\hat{\sigma}_\epsilon$ versus strain show $\hat{\sigma}_\epsilon$ starting at zero and a smooth increase of $\hat{\sigma}_\epsilon$ with strain that enables a good fit to Eq. 6.28. (See Figs. 9.30 and 9.31 below.)
4. Identify a narrow range for the value of θ_{II} . This parameter should not be allowed to vary widely from test to test. A modest increase with strain rate—as shown for FCC metals in Chap. 8—is possible, but widely varying values for tests at the same strain rate is mechanistically illogical and affects the subsequent analysis of the temperature and strain-rate dependence of $\hat{\sigma}_\epsilon$ using Eq. 6.26.
5. When posed with a test exhibiting a yield phenomenon, it appears to be useful to translate the curve along the strain axes to achieve a good fit of the entire stress–strain curve with Eq. 6.28. Often, one may be tempted to translate the stress–strain curve along the stress axes, but this tends not to yield good overall correlations.

Figure 9.30 shows the fit of Eq. 6.28 to the test at 148 K and a strain rate of 1.0 s^{-1} . Even though there is a yield phenomenon in this test, note that Eq. 6.28 can be made to agree with the data closely with the selected parameters. Also evident in this figure, when compared to Fig. 9.23 is that a single smooth curve through both loading steps is achieved, which gives confidence in the model parameters in Eq. 9.7.

Figure 9.31 shows the result for the test at 148 K and a strain rate of 0.01 s^{-1} . Since this is an isothermal test, the slight difference between the stress levels in the two loading steps represents experimental uncertainty. It is also apparent that Eq. 6.28 with the noted parameters fits well with the measurements, although a translation of the curve along the strain axis by a strain of $\sim 1\%$ would force even better agreement with the first loading step—without affecting the choice of model parameters.

Figures 9.30 and 9.31 show application of the guidelines summarized above in analyzing plots of $\hat{\sigma}_e$ versus strain. Table 9.10 lists the values of θ_{II} and $\hat{\sigma}_{eS}$ for all of the conditions listed in Table 9.9. In all cases, $\kappa = 2$. It is worth highlighting the two dynamic tests at 653 K and 673 K where the values of $\hat{\sigma}_{eS}$ range from 420 MPa at the lower temperature to 510 MPa at the higher temperature. This difference represents experimental scatter since these two test conditions were so similar. It is also apparent in Table 9.10 that the tests at 873 K and 973 K do not yield ranges of θ_{II} and $\hat{\sigma}_{eS}$ that are consistent with the lower temperature tests.

Figure 9.32 is a plot of the $\hat{\sigma}_{eS}$ measurements as a function of temperature and strain rate on coordinates defined by Eq. 6.26 (see Fig. 9.21 for UfKonel). The data point at 823 K plots very far away from the trend of all the other data points. The scatter around the dashed line, however, is larger than observed in the FCC systems in Chap. 8. The value of $\hat{\sigma}_{eSO}$ yielding the best-fit (dashed line) is 646 MPa and the slope of the line gives $g_{eSO} = 0.468$.

Table 9.10 Parameters to Eq. 6.28 for each of the tested conditions

Material	T (K)	$\dot{\epsilon}$ (s^{-1})	θ_{II} (MPa)	$\hat{\sigma}_{eS}$ (MPa)
AISI 1018 Steel Annealed Condition	148	0.01	3200	570
	148 (197)	1	3300	640
	223	0.01	3400	600
	223 (255)	1	3600	545
	298	0.01	3600	570
	298 (344)	2800	3800	540
	298 (361)	3750	4000	520
	473 (501)	2600	4300	530
	473 (504)	3000	4200	505
	653 (673)	2700	4300	420
	673 (691)	2600	4200	510
	823 (839)	2600	6800	620
	973 (986)	2000	12,000	680
	973 (989)	2200	12,000	635
973 (986)	2600	8000	350	

Note the final temperature noted for each of the adiabatic tests

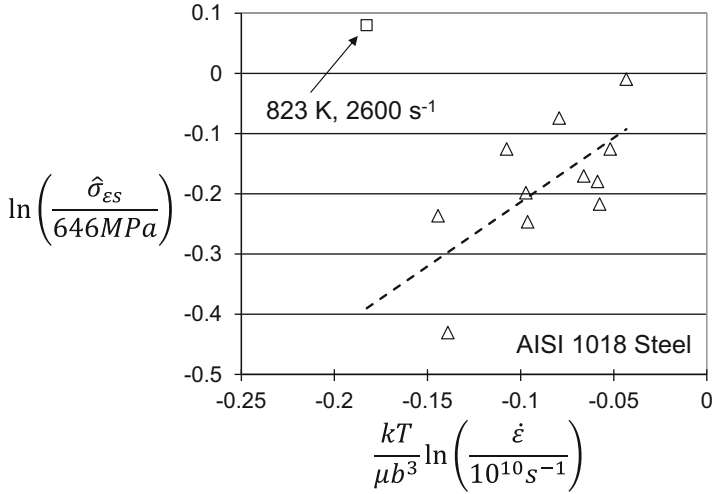
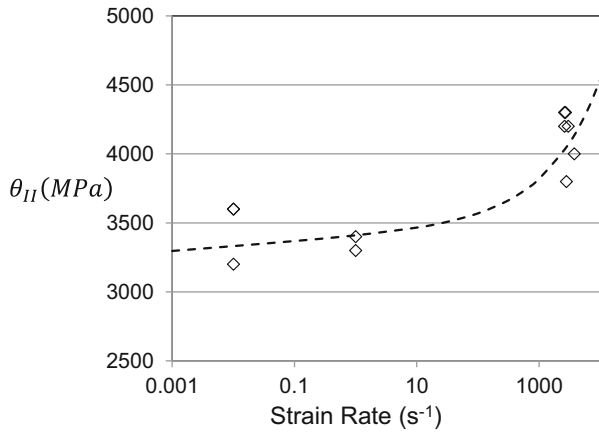


Fig. 9.32 Variation of $\hat{\sigma}_{\epsilon s}$ with strain rate and temperature for each of the tested conditions. The dashed line is the linear fit to the data (excluding the highest temperature data point) according to Eq. 6.26

Fig. 9.33 Variation of θ_{II} with strain rate for each of the test conditions in AISI 1018 steel. The dashed line is the fit to Eq. 6.29



The variation of θ_{II} with strain rate is shown in Fig. 9.33. The dashed line in this figure is Eq. 6.29 with $A_o = 3400 \text{ MPa}$, $A_1 = 15$, and $A_2 = 10 \text{ s}^{-1/2}$. Again there is a lot of scatter in this figure and one could not necessarily conclude that Eq. 6.29 comprises the correct strain-rate-dependent terms, but the agreement with the data is not that different than seen in UfKonel in Fig. 9.22. Table 9.11 summarizes the model parameters and the relevant equation for this AISI 1018 data set.

With these model parameters, predicted stress–strain curves can be generated and compared with the experimentally measured curves. Figure 9.34 shows the result for the test at an initial temperature of 148 K and a strain rate of 1.0 s^{-1} (see Fig. 9.25).

Table 9.11 Full set of model parameters for AISI 1018 steel

Parameter	Equation	Value	Units	
$\sigma_a(MPa)$	Eq. 9.6	100	MPa	
s_p	Eq. 6.15 (with “1” = p)	g_{op}	0.11	–
		pp	0.5	–
		qp	1.5	–
		$\dot{\epsilon}_{op}$	1×10^9	s^{-1}
$\widehat{\sigma}_p$	Eq. 9.6	1000	MPa	
s_i	Eq. 6.16 (with “2” = i)	g_{oi}	1	–
		p_i	0.5	–
		q_i	1.5	–
		$\dot{\epsilon}_{oi}$	1×10^{10}	s^{-1}
$\widehat{\sigma}_i$	Eq. 9.6	357	MPa	
$s\epsilon$	Eq. 7.9	$g_{o\epsilon}$	1.6	–
		p_ϵ	0.667	–
		q_ϵ	1	–
		$\dot{\epsilon}_{o\epsilon}$	1×10^7	s^{-1}
κ	Eq. 6.28	2	–	
θ_{II}	Eq. 6.29	A_o	3400	MPa
		A_1	15	MPa ^a
		A_2	10	MPa $s^{-1/2}$
$\widehat{\sigma}_{es}$	Eq. 6.26	$\widehat{\sigma}_{eso}$	646	MPa
		g_{eso}	0.468	–
		$\dot{\epsilon}_{eso}$	1×10^{10}	s^{-1}
b	Many	0.249	nm	
ρ	Eq. 6.32	7.86	g/cm^3	
ψ		0.95	–	
$\mu(T)$	Eq. 6.8 (See Table 6.1)	μ_o	71.46	GPa
		D_o	2.91	GPa
		T_o	204	K
$c_p(T)$	Eq. 6.B5 See Box 6.4 and Table 6.5	A_C	0.334	J/g/K
		B	4.2×10^{-4}	J/g/K ²
		C	–1350	J K/g

^aUnits are MPa when the strain rate term in Eq. 6.29 has units s^{-1}

The agreement is quite good—up to a strain level of ~ 0.35 where the measured curve deviates upward from the predicted curve, which could signify an effect of friction.

Figure 9.35 shows the predicted curves for each of the conditions included in Fig. 9.23. The stress levels and strain-hardening rates agree well with the measured values, although differences are apparent. For instance, the yield stress in the 298 K test at $2800 s^{-1}$ appears high when compared with the measured value. The presence of a yield phenomenon in the measured curve complicates this comparison, however.

Fig. 9.34 Predicted and measured stress–strain curves for the test at an initial temperature of 148 K and a strain rate of 1.0 s^{-1}

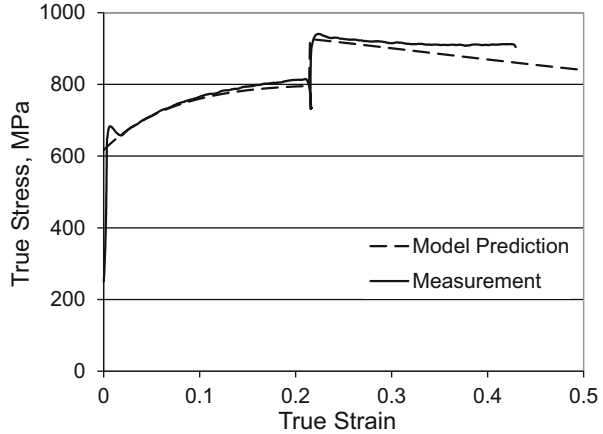
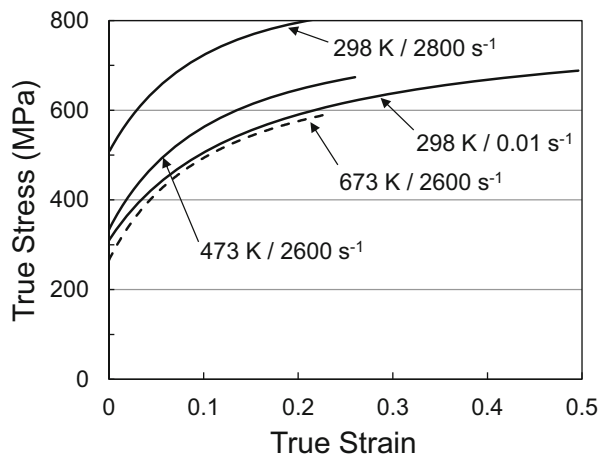


Fig. 9.35 Predicted stress–strain curves for the select temperature and strain rate conditions in Fig. 9.23



9.7 Analysis of the Constitutive Behavior of Polycrystalline Vanadium

Vanadium is another BCC metal that has received some attention as a model BCC system. Nemat-Nasser and Guo performed an extensive experimental study and analysis of deformation in commercially pure vanadium [4]. The testing included compression experiments at strain rates of 0.001 s^{-1} and 2500 s^{-1} and temperatures of 77 K, 190 K, 296 K, 400 K, 500 K, 600 K, and 700 K. Optical metallography was performed to characterize the presence of deformation twins. Figures 9.36 and 9.37 show the stress–strain curves at the low and high strain rate, respectively.

Note in Fig. 9.36 that the experiment at 700 K lies above the measurement at 296 K and the experiment at 600 K is slightly above the measurement at 500 K.

Fig. 9.36 Stress–strain curves as a function of temperature at a strain rate of 0.001 s^{-1} measured in pure, polycrystalline vanadium by Nemat-Nasser and Guo

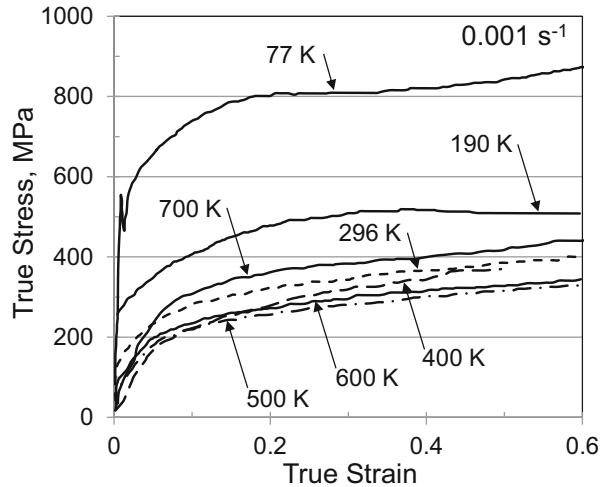
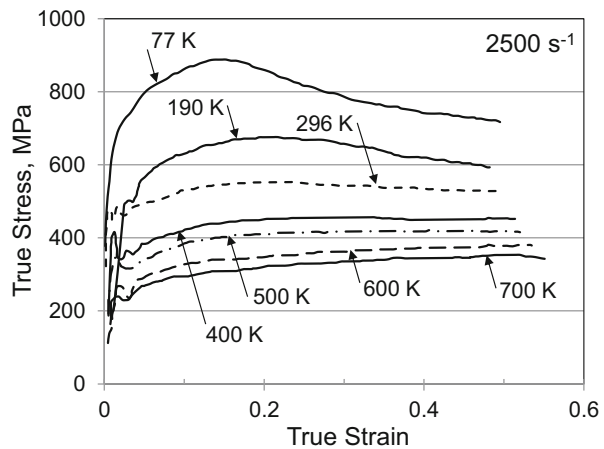


Fig. 9.37 Stress–strain curves as a function of temperature at a strain rate of 2500 s^{-1} measured in pure, polycrystalline vanadium by Nemat-Nasser and Guo



Nemat-Nasser and Guo [4] conclude this is evidence of dynamic strain aging (DSA). A yield phenomenon is visible particularly for material tested at the higher strain rate.

Following the procedure outlined for UfKonel in Sect. 9.5 and AISI 1018 steel in Sect. 9.6, Fig. 9.38 plots the variation of yield stress with temperature and strain rate along with the model fit represented by the star-like symbols. The four data points (open squares) in the center of Fig. 9.38 disagree with the model predictions. However, these data points are at the high strain rate and temperatures of 400 K, 500 K, 600 K, and 700 K. As emphasized previously, accurate yield stress measurements under these conditions are difficult to obtain. Parameters for the model predictions are the same as in Table 9.1 for vanadium, except that $\sigma_a = 50 \text{ MPa}$, $g_{op} = 0.10$, $\hat{\sigma}_p/\mu_o = 0.013$, $g_{oi} = 1.0$, and $\hat{\sigma}_i/\mu_o = 0.002$.

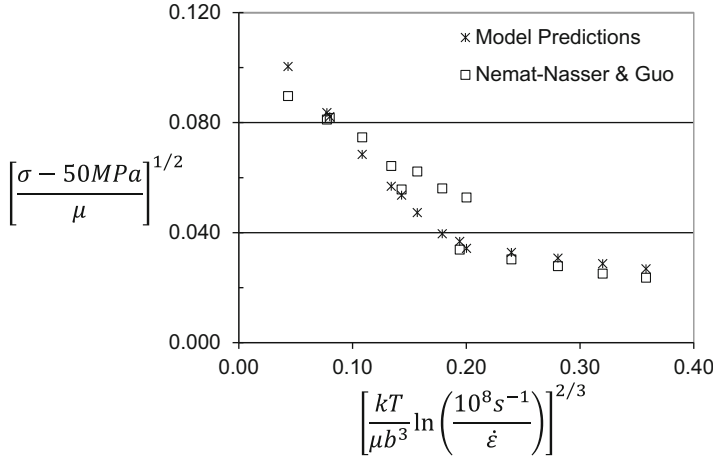
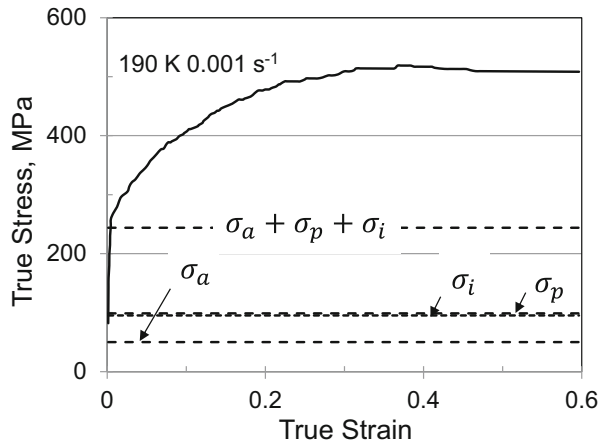


Fig. 9.38 Yield stress as a function of temperature and strain rate in pure vanadium

Fig. 9.39 The stress–strain curve at 190 K and a strain rate of 0.001 s^{-1} along with the analyzed contributions to the stress from the Peierls obstacle, the impurity obstacle, and the athermal stress



The variation of $\hat{\sigma}_\epsilon$ with strain is computed using Eq. 9.7 and the model parameters listed above. Figure 9.39 is a plot of the result for the test at 190 K and a strain rate of 0.001 s^{-1} . In this case, $\sigma_p \cong \sigma_i$, the former exceeding the latter by 3.5 MPa. The sum of the three stress components matches the initial yield point. Figure 9.40 shows the stress contributions for the test at 400 K and a strain rate of 2500 s^{-1} . The sum of the stress components appears low in this case, but given the uncertainty in yield stress at high strain rates, the agreement in the vicinity of yield cannot be accurately assessed. Recall in Fig. 9.38 that the measured yield stress was well above the model prediction at this temperature, which is consistent with the result in Fig. 9.40.

As in AISI 1018 steel, the next step of the analysis is to fit Eq. 6.28—the evolution equation—to the variation of $\hat{\sigma}_\epsilon$ with strain. For these curves a κ -value

Fig. 9.40 The stress–strain curve at 400 K and a strain rate of 2500 s^{-1} along with the analyzed contributions to the stress from the Peierls obstacle, the impurity obstacle, and the athermal stress

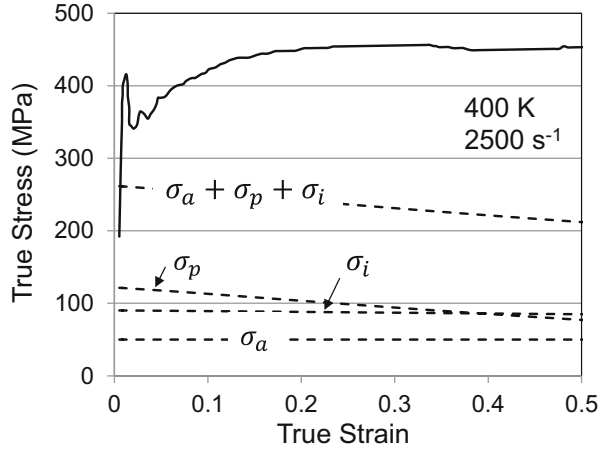
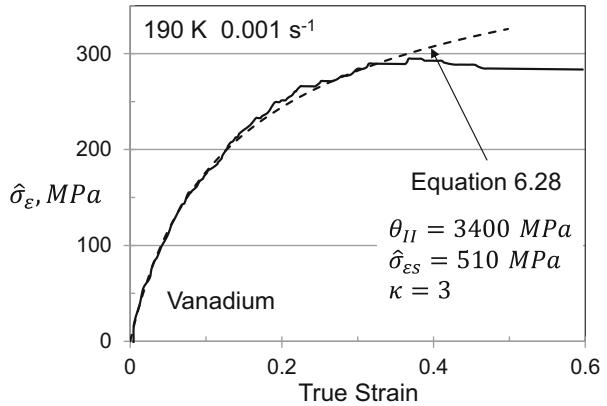


Fig. 9.41 Computed variation of $\hat{\sigma}_{\epsilon_s}$ with strain for the test at a temperature of 190 K and a strain rate of 0.001 s^{-1} . Included as a dashed line is the fit to Eq. 6.28



of 3 was found to match the curves slightly better than a κ -value of 2. Figure 9.41 shows the resulting curve for the test at 190 K and a strain rate of 0.001 s^{-1} (see Fig. 9.39). No strain offset was required to match the model equation with $\hat{\sigma}_{\epsilon}$ versus strain. Good agreement between the model fit and the measurements is observed up to a strain of ~ 0.30 .

For the test at 400 K and a strain rate of 2500 s^{-1} , Fig. 9.42 shows the identical plot. This case is unusual in that a strain offset of 0.02 was required. When the strain offset is dictated by the presence of a yield phenomenon, the offset is less than zero (in the way it is added to the true strain). The need for a positive offset appears to relate to the observation that the apparent lower⁷ yield stress is $\sim 100 \text{ MPa}$ above the value that results from the analysis of the temperature and strain-rate dependence of

⁷“Lower” when used with yield stress refers to the definition of yield stress as that following the fall from the initial, higher yield point—referred to as the “upper” yield stress.

Fig. 9.42 Computed variation of $\hat{\sigma}_{\epsilon_s}$ with strain for the test at a temperature of 400 K and a strain rate of 2500 s⁻¹. Included is the fit to Eq. 6.28

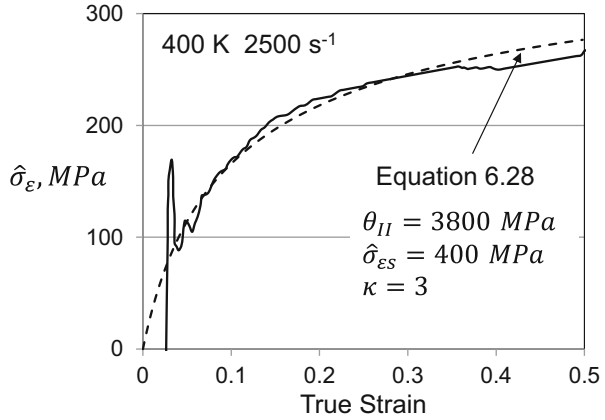
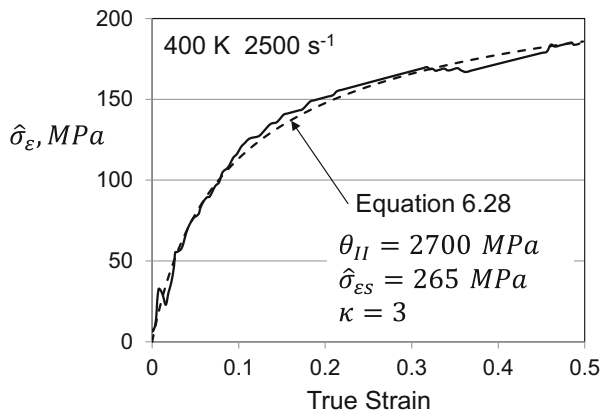


Fig. 9.43 Reanalysis (with a yield stress that more closely matches the experimental value) of the variation of $\hat{\sigma}_{\epsilon_s}$ with strain for the test at a temperature of 400 K and a strain rate of 2500 s⁻¹ along with the fit to Eq. 6.28



yield in Fig. 9.38. Note that if the apparent lower yield stress (~ 345 MPa in Fig. 9.37) were accurate, the plot in Fig. 9.42 would be very different, and the fit to Eq. 6.26 would require very much smaller values of θ_{II} and $\hat{\sigma}_{\epsilon_s}$. Figures 9.43 in fact illustrates this with the sum of the three stress components in (see Fig. 9.40) raised by 75 MPa—as if the yield point were closer to the apparent yield stress—and Eq. 6.26 fit to the adjusted variation of $\hat{\sigma}_{\epsilon}$ with strain. Note in Fig. 9.43 that the value of θ_{II} has dropped to 2700 MPa (from 3800 MPa) and the value of $\hat{\sigma}_{\epsilon_s}$ has dropped to 265 MPa (from 400 MPa). As mentioned in guideline #4 above, widely varying values of θ_{II} are inconsistent with the understanding that this parameter should be approximately constant, although a modest variation with strain rate was observed in the analysis of the copper measurements described in Chap. 8. It is similarly observed that a $\hat{\sigma}_{\epsilon_s}$ equal to 265 MPa would appear quite low on the plot equivalent to Fig. 9.32 (to follow). In this sense each element of the data analysis procedure works in concert to create a plausible constitutive law.

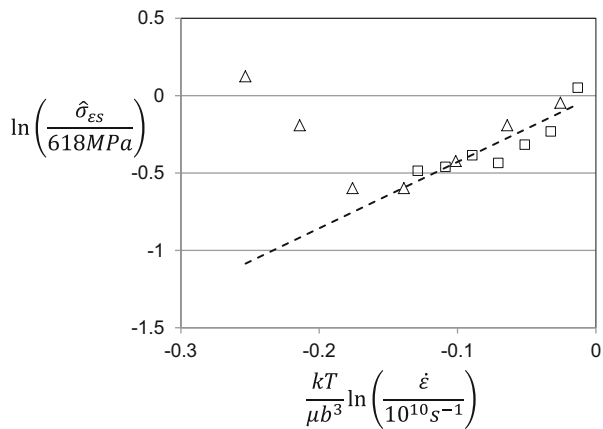
Table 9.12 summarizes the evolution equation analysis (as in Figs. 9.41 and 9.42 but not Fig. 9.43) for all of the measurements. Figure 9.44 shows the variation of $\hat{\sigma}_{\epsilon}$

Table 9.12 Summary of fitted parameters to Eq. 6.28 for each of the test conditions in vanadium

Material	T (K)	$\dot{\epsilon}$ (s^{-1})	θ_H (MPa)	$\hat{\sigma}_{es}$ (MPa)
Vanadium Annealed Condition	77	0.001	3500	590
	190	0.001	3400	510
	296	0.001	3400	405
	400	0.001	3400	340
	500	0.001	3500	340
	600	0.001	3500	510
	700	0.001	3500	700
	77 (204)	2500	4000	650
	190 (286)	2500	4000	490
	296 (381)	2500	4000	450
	400 (472)	2500	4200	400
	500 (567)	2500	3800	420
	600 (660)	2500	4400	390
700 (757)	2500	4400	380	

Final temperatures are shown in parentheses for the dynamic tests

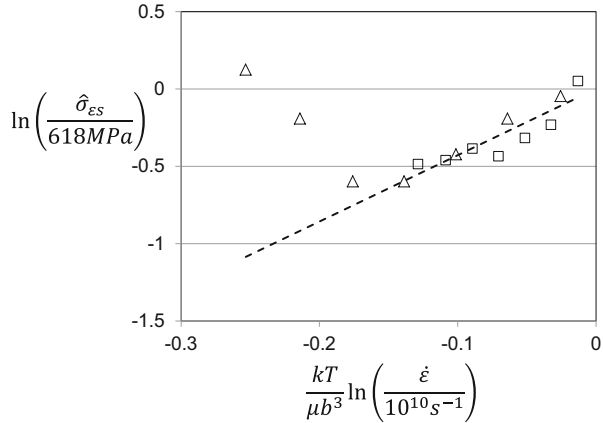
Fig. 9.44 Variation of $\hat{\sigma}_{es}$ with strain rate and (initial) temperature for the measurements in vanadium. The high-strain-rate tests are plotted with open squares whereas the low-strain-rate tests are plotted with open triangles. The line is the best fit to Eq. 6.26



with test temperature (initial temperature for the dynamic tests) and strain rate as in Figs. 9.21 and 9.32. The dynamic tests are plotted in this figure with open squares whereas the quasi-static tests are plotted with open triangles. A clear trend is evident as characterized with the dashed line drawn according to Eq. 6.26 with $\hat{\sigma}_{eso} = 618$ MPa and $\dot{\epsilon}_{eso} = 10^{10} s^{-1}$. The inverse of the slope of this line (drawn through the origin) gives the constant $g_{eso} = 0.233$.

It is interesting that the three points on the left side of the plot, which are measurements at a strain rate of $0.001 s^{-1}$ and temperatures of 500 K, 600 K, and 700 K, deviate from the behavior on the right side of the plot. This is likely the influence of dynamic strain aging, as discussed by Nemat-Nasser and Guo [4]. It is important to note that in the presence of dynamic strain aging Eq. 9.6 is no longer valid. In this case, another term—either a threshold stress or a different s -term (e.g., s_i)—is required to capture the strengthening contribution of strain aging.

Fig. 9.45 Variation of θ_H with strain rate in vanadium. The dashed line is the fit to Eq. 6.29



Accordingly, Eq. 9.7 cannot be used to derive the variation of $\hat{\sigma}_{\epsilon}$ with strain, and the values of $\hat{\sigma}_{\epsilon}$ listed in Table 9.12 and plotted in Fig. 9.44 are not the actual values. Chap. 13 will discuss these complicating factors in more detail.

The variation of θ_H with strain rate is plotted in Fig. 9.45. The dashed line in this figure is plotted according to Eq. 6.29 with $A_o = 3575 \text{ MPa}$, $A_1 = 20$, and $A_2 = 5 \text{ s}^{-1/2}$. Just as in applying Eq. 6.29 to AISI 1018 steel in Fig. 9.33, there is insufficient data in Fig. 9.45 to justify the form of Eq. 6.29. However, the analysis does suggest as in the 1018 steel and the FCC metals discussed in Chap. 8 that a mild strain-rate dependence of θ_H exists.

All of the model parameters for vanadium are summarized in Table 9.13. The similarity between these parameters and those derived for AISI 1018 steel (Table 9.11) is evident.

Predicted stress-strain curves using the model parameters in Table 9.13 are shown in Fig. 9.46 for the tests at a strain rate of 0.001 s^{-1} and in Fig. 9.47 for tests at a strain rate of 2500 s^{-1} . Dashed lines in these figures are the predicted curves whereas the solid lines are the experimental curves (Figs. 9.36 and 9.37). At the lower strain rate the predicted curves at 500 K, 600 K, and 700 K are not shown since dynamic strain aging is not modeled. At low strains there is fairly close agreement between the measured and predicted curves, but at higher strains, particularly at temperatures of 77 K and 190 K, the measured curves fall below the predicted curves. This likely reflects the contribution of deformation twinning which was noted by Nemat-Nasser and Guo [4].

9.8 Deformation Twinning in Vanadium

The analysis of strain hardening in Fig. 9.41 for the test at 190 K and a strain rate of 0.001 s^{-1} offers insight on the effects of deformation twinning. Note how the measurements suggest that hardening essentially ceases at a strain level of ~ 0.35

Table 9.13 Full set of model parameters for pure polycrystalline vanadium

Parameter	Equation	Value	Units	
$\sigma_a(\text{MPa})$	Eq. 9.6	50	MPa	
s_p	Eq. 6.15 (with “1” = p)	g_{op}	0.10	–
		pp	0.5	–
		qp	1.5	–
		$\dot{\epsilon}_{op}$	1×10^8	s^{-1}
$\widehat{\sigma}_p$	Eq. 9.6	897	MPa	
s_i	Eq. 6.16 (with “2” = i)	g_{oi}	1	–
		p_i	0.5	–
		q_i	1.5	–
		$\dot{\epsilon}_{oi}$	1×10^{10}	s^{-1}
$\widehat{\sigma}_i$	Eq. 9.6	138	MPa	
$s\epsilon$	Eq. 7.9	$g_{o\epsilon}$	1.6	–
		p_ϵ	0.667	–
		q_ϵ	1	–
		$\dot{\epsilon}_{o\epsilon}$	1×10^7	s^{-1}
κ	Eq. 6.28	3	–	
θ_{II}	Eq. 6.29	A_o	3575	MPa
		A_1	20	MPa^a
		A_2	5	$\text{MPa s}^{-1/2}$
$\widehat{\sigma}_{\epsilon s}$	Eq. 6.26	$\widehat{\sigma}_{\epsilon s o}$	618	MPa
		$g_{\epsilon s o}$	0.233	–
		$\dot{\epsilon}_{\epsilon s o}$	1×10^{10}	s^{-1}
b	Many	0.263	nm	
ρ	Eq. 6.32	6.00	g/cm^3	
ψ		0.95	–	
$\mu(T)$	Eq. 6.8 (See Table 6.1)	μ_o	68.98	GPa
		D_o	0.4098	GPa
		T_o	45	K
$c_p(T)$	Eq. 6.B5	A_C	0.489	J/g/K
		B	0	J/g/K ²
		C	0	J K/g

^aUnits are MPa when the strain rate term in Eq. 6.29 has units s^{-1}

and $\widehat{\sigma}_\epsilon \approx 280$ MPa. Deformation twinning was observed at this condition, although characterization of the extent of twinning as a function of strain was not performed. It appears, however, that at this point in the test dislocation storage ceases, which implies that strain begins to become fully accommodated by twinning or at least by a slip – twinning partnership where there is no further dislocation storage. Table 9.14 lists the values of total stress, $\widehat{\sigma}_\epsilon$, and strain at the point where strain hardening ceases for each of the conditions where this is observed. Furthermore, the cessation of strain hardening was not observed in conditions where deformation twinning was not observed. The fascinating result is that hardening ceases at roughly the same value of $\widehat{\sigma}_\epsilon$ but at very different values of total stress.

Fig. 9.46 Predicted stress-strain curves (dashed lines) in vanadium at a strain rate of 0.001 s^{-1} and temperatures to 500 K compared to experimental curves (solid lines)

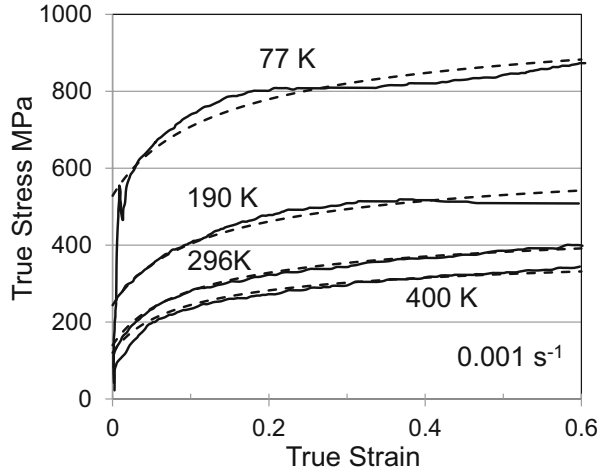


Fig. 9.47 Predicted stress-strain curves (dashed lines) in vanadium at a strain rate of 2500 s^{-1} as a function of temperature compared to experimental curves (solid lines)

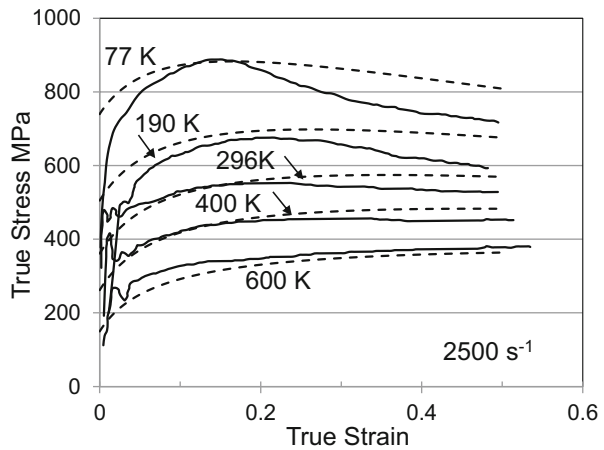


Table 9.14 The strain, total stress, and value of $\hat{\sigma}_\epsilon$ where the rate of strain hardening goes to \sim zero (for each of the conditions where this was observed)

Temperature (K)	Strain rate (s^{-1})	Strain	Stress (MPa)	$\hat{\sigma}_\epsilon$ (MPa)
77	0.001	0.18	800	280
190	0.001	0.35	514	290
77	2500	0.16	885	255
190	2500	0.23	673	245
296	2500	0.21	553	245
400	2500	0.31	456	248

Many theories have ascribed a twinning stress akin to a critical resolved shear stress [15] even though the existence of a twinning stress is not widely acknowledged [16]. Theories of twin formation and motion typically rely upon associated dislocation activity [17]. Since $\widehat{\sigma}_\epsilon$ is a measure of extent of dislocation activity, the observations in Table 9.14 could be considered consistent with the latter requirement. However, the condition where strain becomes completely accommodated by deformation twinning is not the condition that first enables twin formation. Indeed, the observations in Table 9.14 relate to latter stages of deformation twinning rather than initial stages, and these observations shed no light on the existence of a twinning stress.

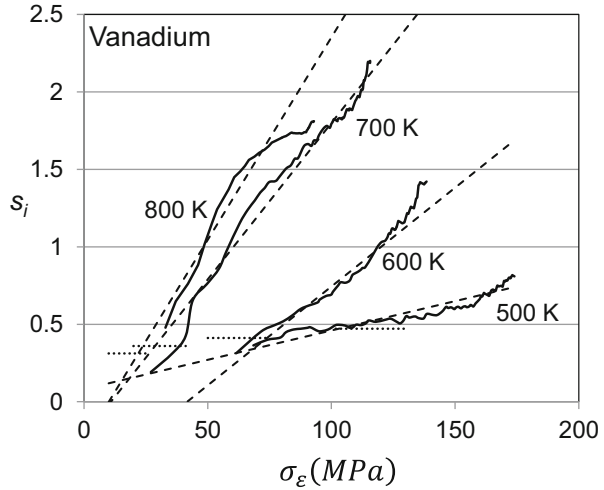
9.9 Signature of Dynamic Strain Aging in Vanadium

Before leaving vanadium, analysis of the stress–strain curves when dynamic strain aging is active offers insight into the kinetics of this process. The curves at 500 K, 600 K, 700 K, and 800 K (not included in Fig. 9.35 and Table 9.12) all show evidence of dynamic strain aging. Assuming that Eq. 9.6 continues as the governing mechanistic equation during dynamic strain aging, it is hypothesized that the term s_i is affected by dynamic strain aging since this term governs the kinetics of dislocation interactions with impurity elements. If it is further assumed that evolution follows the linear behavior in Fig. 9.44—even when dynamic strain aging is underway—then one may compute the variation of s_i with strain for the four tests that exhibited dynamic strain aging by rewriting Eq. 9.6 as

$$s_i = \frac{1}{\widehat{\sigma}_i} \left[\frac{\mu_o}{\mu} (\sigma - \sigma_a) - s_p \widehat{\sigma}_p - s_\epsilon \widehat{\sigma}_\epsilon \right] \quad (9.8)$$

The procedure is to take σ as the measured stress, compute $\widehat{\sigma}_\epsilon$ at the measured strain by integrating Eq. 6.28 with the values of θ_{II} from the dashed line fit in Fig. 9.45 and $\widehat{\sigma}_{\epsilon s}$ from the coefficients for the linear behavior in Fig. 9.44, and solve Eq. 9.8. The result is the variation of s_i versus strain. The more meaningful correlation, however, is s_i versus σ_ϵ . The results for the four tests in vanadium at a strain rate of 0.001 s^{-1} are shown in Fig. 9.48. For temperatures of 500 K, 600 K, 700 K, and 800 K, Eq. 6.16 (with the model parameters in Table 9.13) gives $s_i = 0.471, 0.412, 0.360, \text{ and } 0.312$ respectively. These values are included in Fig. 9.48 as short, horizontal dotted lines. There are two trends to note in Fig. 9.48. For each temperature, the value of s_i begins at the value specified by Eq. 6.16 but as σ_ϵ rises above some value, which varies inversely with temperature, s_i begins to increase with further increases in σ_ϵ . Also, even in light of the scatter in each of the curves in Fig. 9.48 (see Box 9.2), above this threshold value of σ_ϵ the variation of s_i with σ_ϵ is approximately linear. Note that a dashed line has been drawn through each of the four curves in Fig. 9.48.

Fig. 9.48 Computed value of s_i from Eq. 9.8 for the tests in vanadium at 500 K, 600 K, 700 K and 800 K and a strain rate of 0.001 s^{-1}



Box 9.2 Why All the Scatter?

The term “scatter” has been used several times in this chapter in reference to often large point-to-point variations in curves such as Figs. 9.29 and 9.48. The sources of this scatter are manifold.

Some of the data used in this chapter, e.g., the data in AISI 1018 steel, were available in digital form through Ref. [14]. In this case, the stress–strain curves may represent as many as 400 individual measurements. The scatter can reflect electronic noise in the measurement or recording system. In high-strain-rate tests, there are oscillations due to the passage of stress-waves inherent to the split Hopkinson pressure bar experimental method.

Data not available electronically was digitized from plots in the noted references. Many of these curves included scatter from the measurement or recording system. Digitalization introduces some variation not present in the original curves. Of course, some of this variation can be corrected when an obvious digitization error has occurred. The estimate of $\hat{\sigma}_e$ versus strain (e.g., the curves in Figs. 9.29, 9.41, 9.42, and 9.43) are derived using Eq. 9.7 which entails subtracting constant (in isothermal tests) or smoothly varying (in adiabatic tests) quantities from each value of stress. This procedure tends to amplify the scatter in the stress–strain curve. This is also the case for the estimate of s_i versus σ_e (e.g., the curves in Figs. 9.48 and 9.62).

Of course, scatter may reflect an active mechanism such as dynamic strain aging, where serrated yielding can manifest itself as small “yield drops” that repeat during straining (although these are rarely seen in compression testing). Friction in a compression test taken to large strains can lead to stresses that rise

(continued)

Box 9.2 (continued)

above those that would exist absent friction. In the plots of s_i versus σ_e , friction would lead to a curve that rises too rapidly with increasing versus σ_e .

The practice in this chapter—and throughout this monograph—has been to retain the scatter and not attempt to create smooth curves through use of an averaging protocol.

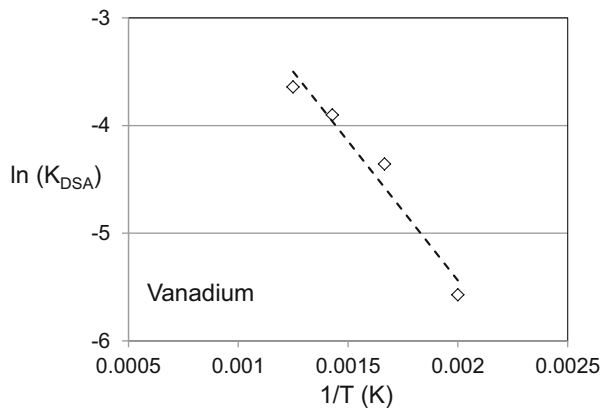
The second trend in Fig. 9.48 is that the slope K_{DSA} of each of the curves varies positively with temperature. Following a standard practice in evaluating kinetic processes, the temperature dependence of K_{DSA} is assumed to vary as the exponent of $1/T$ following the exponential function

$$K_{\text{DSA}}(T) = K_{\text{DSA}_0} \exp\left(-\frac{Q}{RT}\right) \quad (9.9)$$

Figure 9.49 plots the logarithm of the slope K_{DSA} versus $1/T$. The dashed line is the fit according to Eq. 9.9. The slope of this line gives $Q = 21.5$ kJ/mol. As will be discussed in Chap. 13, this activation energy is low for many diffusion assisted processes. This, in fact, calls attention to the general validity of Eq. 9.9. A more rigorous analysis of Dynamic Strain Aging that leads to an equation quite different from Eq. 9.9 is presented in Chap. 13.

The measurements analyzed in Fig. 9.48 were all at the same strain rate, but it is likely that the trends observed in this figure and the slope K_{DSA} are dependent upon strain rate as well as temperature. There was no evidence of dynamic strain aging in the measurements in vanadium by Nemat-Nasser and Guo [4] at a strain rate of 2500 s^{-1} . It would be useful to have measurements at intermediate strain rates to assess the strain-rate dependence.

Fig. 9.49 Temperature dependence of K_{DSA} in Eq. 9.9 from analyses of dynamic strain aging in vanadium



9.10 Analysis of Deformation Behavior of Polycrystalline Niobium

Niobium is another bcc metal that has served as a model system for deformation studies. Figure 9.50 shows measurements of Gray and Chen [14] in pure niobium. The measurements show evidence of significant strain-rate and temperature dependence. A yield drop is very prominent in the high-strain rate measurements at 298 K and 473 K.

Figure 9.51 shows the measurements of Nemat-Nasser and Guo in pure niobium [18] at a strain rate of 0.001 s^{-1} and Fig. 9.52 shows the measurements of these investigators at a strain rate of 3300 s^{-1} . In both figures, stress–strain curves were reported over a wide range of temperatures. The trends at the high strain rate are

Fig. 9.50 Stress–strain curves in commercially pure niobium as a function of test temperature and strain rate [14]

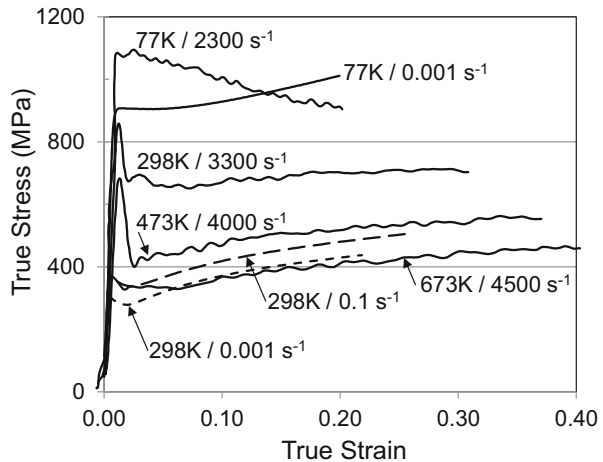


Fig. 9.51 Stress–strain curves in commercially pure niobium as a function of temperature at a strain rate of 0.001 s^{-1} measured by Nemat-Nasser and Guo [18]

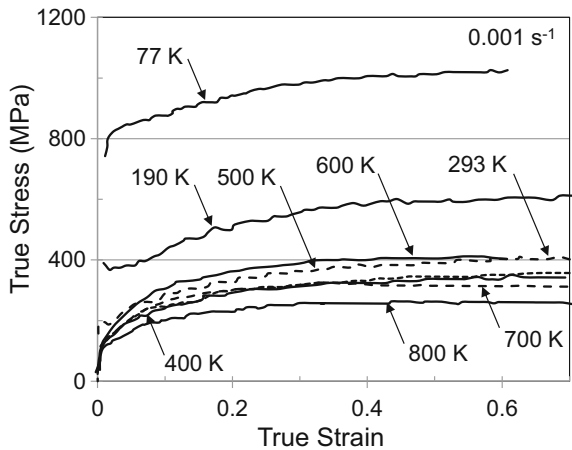


Fig. 9.52 Stress–strain curves in commercially pure niobium as a function of temperature at a strain rate of 3300 s^{-1} measured by Nemat-Nasser and Guo [18]

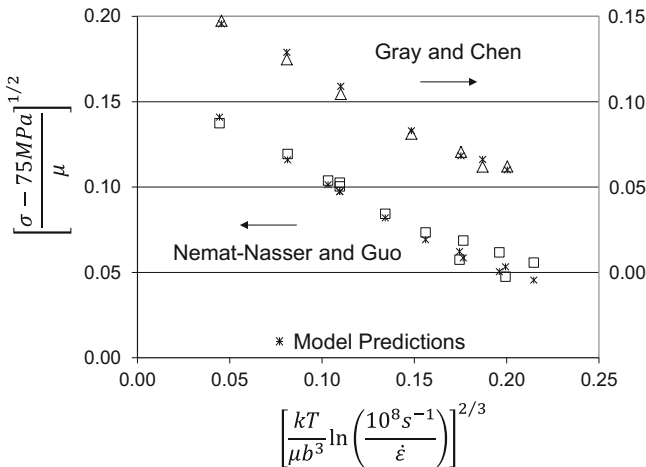
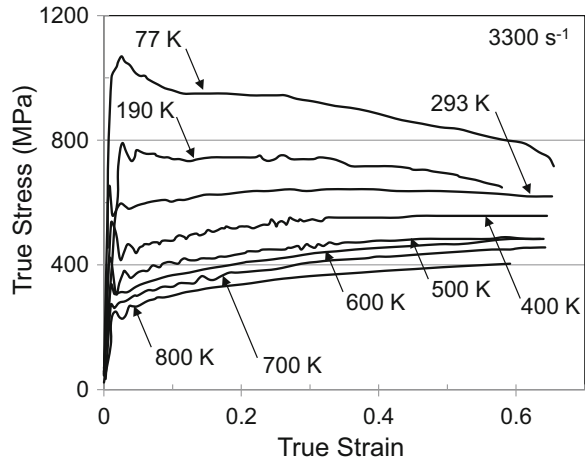


Fig. 9.53 Yield stress versus temperature and strain rate for both the Gray and Chen [14] and Nemat-Nasser and Guo [18] data sets

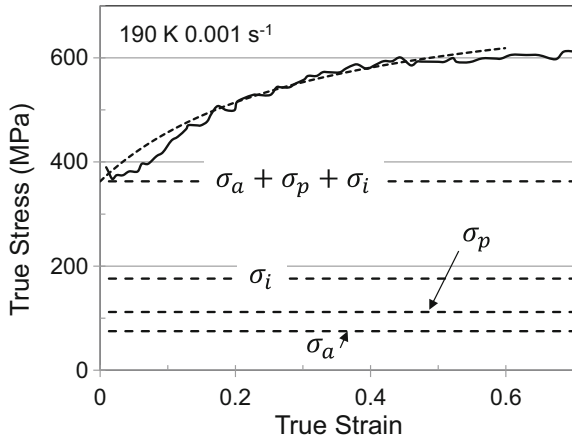
systematic in that as the temperature increases the stress decreases over all strain ranges. At the lower strain rate, however, the curves at temperatures between 293 K and 700 K tend to bunch together.

As in the analyses in AISI 1018 steel, UfKone1, and vanadium, the first step is to characterize the variation of the yield strength with temperature and strain rate in annealed material. Figure 9.53 shows the combined result for the Gray and Chen measurements (open triangles and right ordinate) and the Nemat-Nasser and Guo measurements (open squares and left ordinate). For both sets of data, the model predictions are plotted in star-like symbols for each of the temperature and strain rate combinations. Note again that the model under-predicts the yield stresses for three

Table 9.15 Model parameters for the fits to the niobium data sets in Fig. 9.53

Niobium	Figure	σ_a (MPa)	g_{op}	$\hat{\sigma}_p/\mu_o$	g_{oi}	$\hat{\sigma}_i/\mu_o$
Gray and Chen	9.53	75	0.10	0.023	0.50	0.009
Nemat-Nasser and Guo	9.54 and 9.55	75	0.10	0.023	0.50	0.0065
$\dot{\epsilon}_{op}$	10^8 s^{-1}					
$p_p = p_i$	0.5					
$\dot{\epsilon}_{oi}$	10^{10} s^{-1}					
$q_p = q_i$	1.5					

Fig. 9.54 The stress–strain curve at 190 K and a strain rate of 0.001 s^{-1} (Nemat-Nasser and Guo) along with the analyzed contributions to the stress from the Peierls obstacle, the impurity obstacle, and the athermal stress

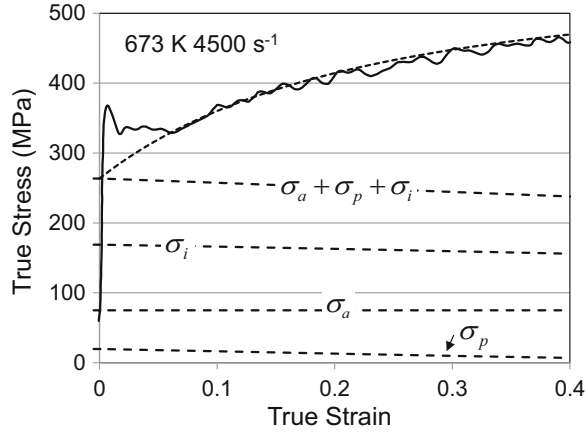


Nemat-Nasser and Guo measurements on the far-right of the abscissa. These measurements are all at high strain rates where confidence in the measured yield stresses is poor.

The model parameters for the model predictions are listed in Table 9.15. A slightly different value of $\hat{\sigma}_p/\mu_o$ is shown in this table that listed in Table 9.1 for niobium; the variation in the parameters, however, is very small. The only parameters changed in evaluating the two sets of measurements in niobium is the value of $\hat{\sigma}_i/\mu_o$. The slightly higher value for the Gray and Chen measurements suggests that this material had higher impurity level than the Nemat-Nasser and Guo material.

Following the procedures demonstrated in other BCC metals, the next step is to assess the strain hardening (evolution) component of the entire stress–strain curve by subtracting the terms unrelated to strain hardening. Figure 9.54 shows the analysis for the stress–strain curve measured by Nemat-Nasser and Guo at a strain rate of 0.001 s^{-1} and a temperature of 190 K. It is worth re-emphasizing that it is assumed in this analysis that the model parameters for σ_p and σ_i do not change from the values listed in Table 9.15.

Fig. 9.55 The stress–strain curve at 673 K and a strain rate of 4500 s^{-1} (Gray and Chen) along with the analyzed contributions to the stress from the Peierls obstacle, the impurity obstacle, and the athermal stress



In Fig. 9.54 the dotted line through the stress–strain curve shows

$$\sigma = \sigma_a + \sigma_i + \sigma_p + s_e \mu \frac{\hat{\sigma}_e}{\mu_o} \tag{9.10}$$

where s_e is defined by Eq. 7.9 (see, for instance, Table 9.13) and $\hat{\sigma}_e$ is calculated by integrating Eq. 6.28 with $k = 2$, $\theta_{II} = 1300 \text{ MPa}$, and $\hat{\sigma}_{es} = 410 \text{ MPa}$. The calculation of $\hat{\sigma}_e$ is identical to that used in deriving the correlations in Figs. 9.42 and 9.43, except in those figures the threshold stress $\hat{\sigma}_e$ is plotted rather than the stress $s_e \hat{\sigma}_e$.

Figure 9.55 shows the identical analysis for the measurement by Gray and Chen at an initial temperature of 673 K and a strain rate of 4500 s^{-1} . In this case, as in Fig. 9.40, the adiabatic temperature rise leads to values of σ_p and σ_i that decrease with strain. The dotted line in Fig. 9.55 shows the total stress calculated using Eq. 9.6 with (from Eq. 6.28) $k = 2$, $\theta_{II} = 1450 \text{ MPa}$, and $\hat{\sigma}_{es} = 430 \text{ MPa}$. An interesting result highlighted in this figure is that the predicted yield stress is well below the stress that might be deduced from the stress–strain curve.

Table 9.16 summarizes the assessed values of θ_{II} and $\hat{\sigma}_{es}$ for all of the measurements in Figs. 9.50, 9.51, and 9.52. The cells with values in parentheses indicate that Eq. 6.28 yielded unreasonable values of the model parameters, which may have reflected the contributions of deformation twinning (e.g., at 77 K and a strain rate of 2300 s^{-1}) or dynamic strain aging (e.g., at a strain rate of 0.001 s^{-1} and temperatures of 600 K, 700 K, and 800 K) [18]. Note, for instance, that the best-fit values of θ_{II} at 500 K and 600 K and a strain rate of 0.001 s^{-1} are well outside the values of this parameter observed at the other conditions. This suggests that a different mechanism—likely dynamic strain aging—is active at this temperature.

Although different values of σ_i (see Table 9.15) were used in analyzing the Gray and Chen versus the Nemat-Nasser and Guo data sets it is suggested that evolution should be similar in both data sets. The variation of $\hat{\sigma}_{es}$ with temperature and strain rate for the Nemat-Nasser and Guo data set is shown in Fig. 9.56 and for the Gray

Table 9.16 Tabulated values of θ_{II} and $\widehat{\sigma}_{es}$ for all of the stress–strain curves in the Gray and Chen and Nemat-Nasser and Guo data sets

Material	T (K)	$\dot{\epsilon}$ (s^{-1})	θ_{II} (MPa)	$\widehat{\sigma}_{es}$ (MPa)
Gray and Chen [14] Annealed condition	77	0.001	1250	600
	298	0.001	1300	440
	298	0.1	1300	470
	77	2300	–	–
	298 (383)	3300	1400	540
	473 (547)	4000	1400	450
	673 (735)	4500	1450	430
Nemat-Nasser and Guo [18] Annealed condition	296	0.001	1200	285
	296	0.1	1200	330
	77	0.001	1300	420
	190	0.001	1300	410
	293	0.001	1200	300
	400	0.001	1200	260
	500	0.001	1800	300
	600	0.001	(4000)	390
	700	0.001	(4500)	280
	800	0.001	(2600)	240
	296 (446)	3300	1400	410
	296 (469)	8000	1500	470
	77 (319)	3300	1500	490
	190 (359)	3300	1350	430
	296 (460)	3300	1400	420
	400 (535)	3300	1400	420
	500 (612)	3300	1400	380
	600 (705)	3300	1400	420
	700 (796)	3300	1500	380
	800 (877)	3300	1500	320

Final temperatures are in parentheses, although the initial temperatures are used to construct Figs. 9.57 and 9.58

Fig. 9.56 Saturation threshold stress versus temperature and strain rate for the Nemat-Nasser and Guo data set. The dashed line is drawn according to Eq. 6.26. The open triangles are data points in parentheses in Table 9.16 not used in establishing the model fit

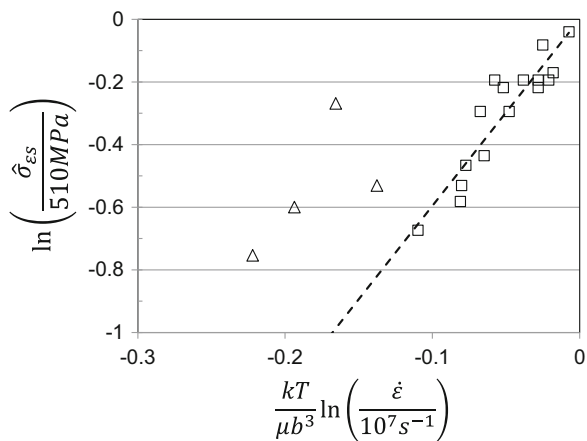


Fig. 9.57 Saturation threshold stress versus temperature and strain rate for the Gray and Chen data set. The dashed line is drawn according to Eq. 6.26

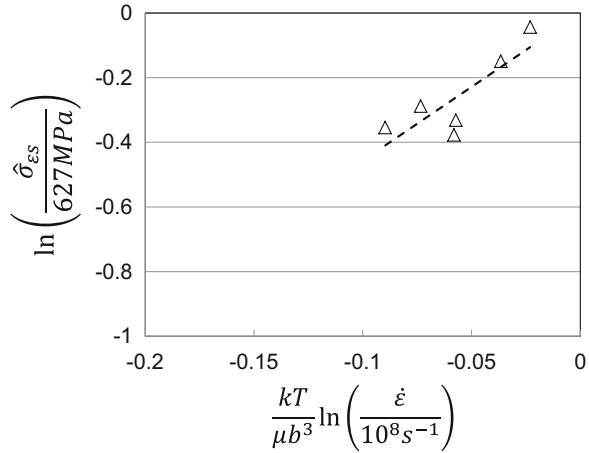
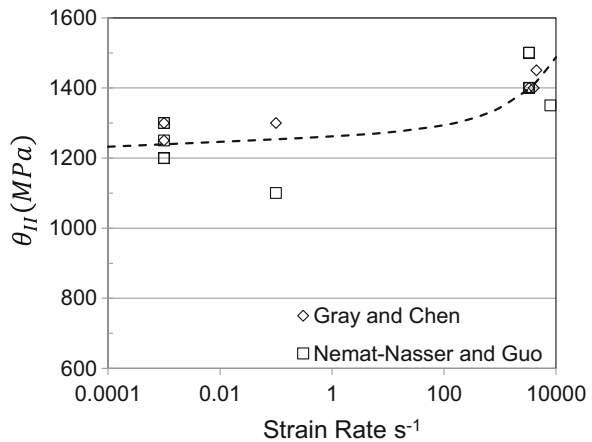


Fig. 9.58 Variation of θ_{II} with strain rate and model fit according to Eq. 6.29



and Chen data set is shown in Fig. 9.57. The plots are on identical axes to illustrate that somewhat different results are derived from these analyses. This is also reflected in the values of the model parameters ($\hat{\sigma}_{ES0}$ and $\dot{\epsilon}_{ES0}$) used for each data set.⁸

The variation of θ_{II} with strain rate for all of the measurements in niobium is shown in Fig. 9.58. As observed in Table 9.16 the θ_{II} values were higher at high strain rates than at low strain rates. The dashed line in Fig. 9.58 is drawn according to Eq. 6.29 with $A_0 = 1260$ MPa, $A_1 = 3$, and $A_2 = 2$ s^{-1/2}.

⁸The Gray and Chen stress–strain curves were taken to lower strains than the Nemat-Nasser and Guo stress–strain curves. It is plausible that the higher strains achieved in the latter tests enabled a different fit to Eq. 6.28 which contributed to the differences noted in Figs. 9.56 and 9.57.

Table 9.17 Full set of model parameters for pure polycrystalline niobium

Parameter	Equation	Value	Units	
σ_a (MPa)	Eq. 9.6	75	MPa	
s_p	Eq. 6.15 (with “1” = p)	g_{op}	0.10	–
		pp	0.5	–
		qp	1.5	–
		$\dot{\epsilon}_{op}$	1×10^8	s^{-1}
$\widehat{\sigma}_p$	Eq. 9.6	1152	MPa	
s_i	Eq. 6.16 (with “2” = i)	g_{oi}	0.5	–
		p_i	0.5	–
		q_i	1.5	–
		$\dot{\epsilon}_{oi}$	1×10^{10}	s^{-1}
$\widehat{\sigma}_i$ (Nemat-Nasser and Guo)	Eq. 9.6	326	MPa	
$\widehat{\sigma}_i$ (Gray and Chen)		451		
s_ϵ	Eq. 7.9	$g_{o\epsilon}$	1.6	–
		p_ϵ	0.667	–
		q_ϵ	1	–
		$\dot{\epsilon}_{o\epsilon}$	1×10^7	s^{-1}
κ	Eq. 6.28	2	–	
θ_{II}	Eq. 6.29	A_o	1260	MPa
		A_1	3	MPa ^a
		A_2	2	MPa $s^{-1/2}$
$\widehat{\sigma}_{es}$ (Nemat-Nasser and Guo)	Eq. 6.26	$\widehat{\sigma}_{eso}$	510	MPa
		g_{eso}	0.168	–
		$\dot{\epsilon}_{eso}$	1×10^7	s^{-1}
$\widehat{\sigma}_{es}$ (Gray and Chen)		$\widehat{\sigma}_{eso}$	627	MPa
		g_{eso}	0.219	–
		$\dot{\epsilon}_{eso}$	1×10^8	s^{-1}
b	Many	0.286	nm	
ρ	Eq. 6.32	8.57	g/cm^3	
ψ		0.95	–	
$\mu(T)$	Eq. 6.8 (See Table 6.1)	μ_o	50.08	GPa
		D_o	0.0207	GPa
		T_o	15	K
$c_p(T)$	Eq. 6.B5	A_C	0.26	J/g/K
		B	4.0×10^{-5}	J/g/K ²
		C	–572	J K/g

^aUnits are MPa when the strain rate term in Eq. 6.29 has units s^{-1}

A summary of the model parameters for niobium is shown in Table 9.17. The model parameters (other than the physical parameters) for niobium in Table 9.17 are similar in magnitude to those for vanadium listed in Table 9.13.

Figures 9.59, 9.60, and 9.61 are plots of predicted and measured stress–strain curves using the model parameters in Table 9.17. In these figures, a representative selection of measurements shown in Figs. 9.50, 9.51, and 9.52 is included. In general, the predictions and measurements follow closely.

Fig. 9.59 Predicted stress-strain curves (dashed lines) versus measured curves for three of the test conditions reported by Gray and Chen [14]

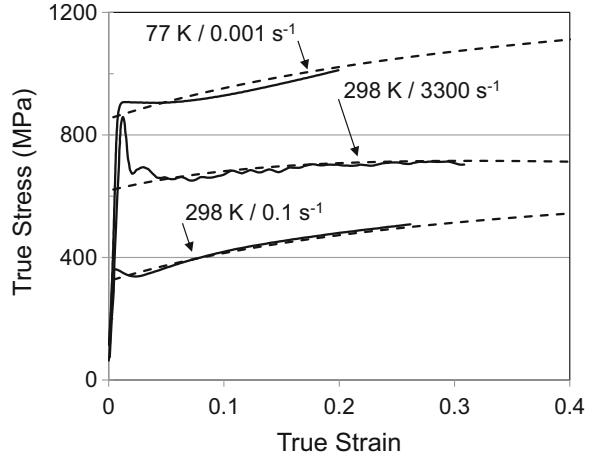


Fig. 9.60 Predicted stress-strain curves (dashed lines) versus measured curves for three of the test conditions reported by Nemat-Nasser and Guo at a strain rate of 0.001 s⁻¹ [18]

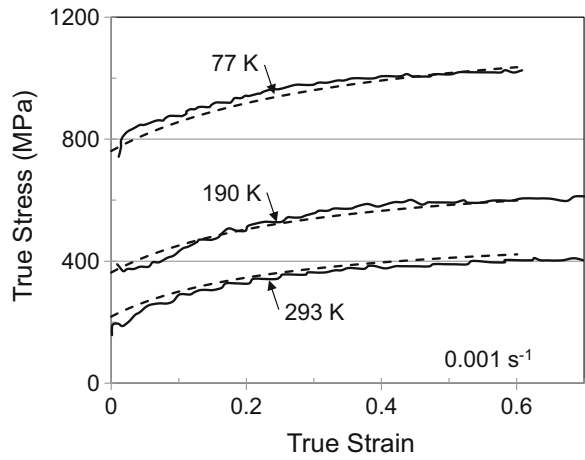


Fig. 9.61 Predicted stress-strain curves (dashed lines) versus measured curves at a strain rate of 3300 s⁻¹ for four of the test conditions reported by Nemat-Nasser and Guo [18]

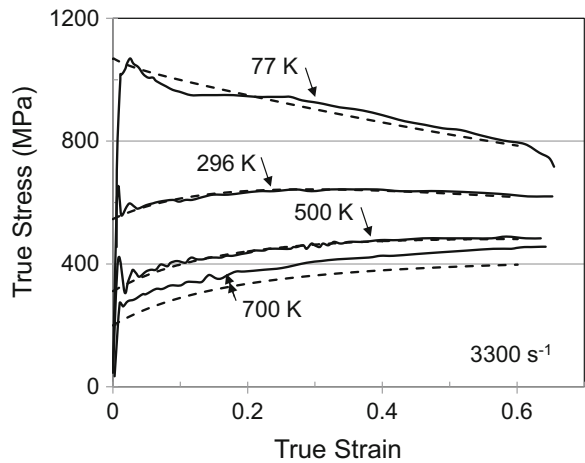
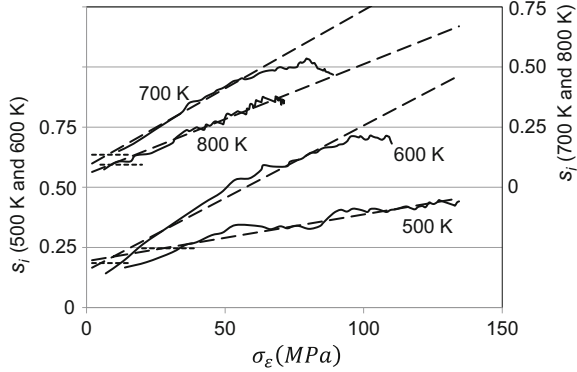


Fig. 9.62 Computed value of s_i from Eq. 9.8 for the tests in niobium at 500 K, 600 K, 700 K and 800 K



The predicted stress–strain curves at a strain rate of 0.001 s^{-1} and temperatures of 500 K and above would not agree particularly well with the measurements. The best-fit values of θ_{II} at 500 K and 600 K and a strain rate of 0.001 s^{-1} in Table 9.16 indicate a change in behavior at these conditions. It was suggested that dynamic strain aging is beginning to become important at temperatures of 500 K and greater. Following the procedure outlined in Sect. 9.9 the variation of s_i with σ_ϵ can be deduced for tests at 500 K through 800 K using Eq. 9.7. Recall that this analysis builds on the assumptions that (i) Eq. 9.6 continues as the governing constitutive equation even when dynamic strain aging becomes active and (ii) evolution continues to follow Eq. 6.26 (the dashed lines shown in Figs. 9.56 and 9.57). Figures 9.62 shows the resulting values of s_i versus σ_ϵ for the four temperatures. (Note that the results at 500 K and 600 K are plotted on the left abscissa whereas the results at 700 K and 800 K are plotted on the right abscissa.) As in Fig. 9.48, dashed lines approximating the linear trend are drawn in these plots and the short, horizontal dotted lines are drawn at the s_i -values predicted by Eq. 6.16 with the model parameters specified in Table 9.15—giving s_i values of 0.246, 0.185, 0.135, and 0.094 at temperatures of 500 K, 600 K, 700 K, and 800 K. The trends in Fig. 9.62 are similar to those observed in vanadium in Fig. 9.48, but the temperature dependencies of the slope K_{DSA} are not as clear as observed in vanadium.

9.11 Summary

The constitutive behavior of the BCC metals analyzed in this chapter is modeled using the same methodology as described for FCC metals in Chap. 8. For copper, nickel, and the Cu–Al and Ni–C alloys, the governing equations were Eqs. 8.5 and 6.28

$$\frac{\sigma}{\mu} = \frac{\sigma_a}{\mu} + s_i(\dot{\epsilon}, T) \frac{\hat{\sigma}_i}{\mu_o} + s_\epsilon(\dot{\epsilon}, T) \frac{\hat{\sigma}_\epsilon}{\mu_o} \tag{8.5}$$

and

$$\frac{d\widehat{\sigma}_\varepsilon}{d\varepsilon} = \theta_{II}(\dot{\varepsilon}) \left(1 - \frac{\widehat{\sigma}_\varepsilon}{\widehat{\sigma}_{\varepsilon s}(\dot{\varepsilon}, T)} \right)^\kappa \quad (6.28)$$

The Peierls obstacle is included in analysis of deformation of BCC metals, which were described using Eq. 9.6 and, once again, Eq. 6.28.

$$\frac{\sigma}{\mu} = \frac{\sigma_a}{\mu} + s_p(\dot{\varepsilon}, T) \frac{\widehat{\sigma}_p}{\mu_o} + s_i(\dot{\varepsilon}, T) \frac{\widehat{\sigma}_i}{\mu_o} + s_\varepsilon(\dot{\varepsilon}, T) \frac{\widehat{\sigma}_\varepsilon}{\mu_o} \quad (9.6)$$

While the measurements in several of the FCC systems followed the recipe outlined in Chap. 7 using the fictitious FoLLyally, the BCC systems analyzed in this chapter did not have such an extensive prestrain plus reload database. Instead, the temperature- and strain-rate-dependent evolution in Eq. 6.28 was treated by analyzing the temperature- and strain-rate-dependent yield stress in annealed material to deduce s_p , s_i , $\widehat{\sigma}_p$, and $\widehat{\sigma}_i$, and solving Eq. 9.6 for $\widehat{\sigma}_\varepsilon$ —as introduced using the fictitious alloy UfKonel. An interesting conclusion resulting from the analyses is that structure evolution is observed to be very similar in the BCC systems and FCC systems. This similarity is evidenced in Table 9.18 which compares model parameters comprising $\widehat{\sigma}_{\varepsilon s}(\dot{\varepsilon}, T)$ (Eq. 6.26) and $\theta_{II}(\dot{\varepsilon})$ (Eq. 6.29) for nickel, copper, 1018 steel, vanadium, and niobium (Nemat-Nasser and Guo material).

In constructing the plots of θ_{II} versus logarithm of strain rate (see Figs. 8.29, 9.45, and 9.58) it was emphasized that there were too few data points with too much scatter to establish with confidence values of A_1 and A_2 in Eq. 6.29. The results in Table 9.18, however, show a common trend with $A_1/\mu_o \sim 200 \times 10^{-6}$ and $A_2/\mu_o \sim 50 \times 10^{-6}$ (with 1018 steel as an outlier).

The similarity observed in dislocation storage rate is perhaps surprising. Often, the strain-rate dependence observed in the dislocation storage in pure FCC metals is not observed in BCC metals [18]. The reason for this may relate to the relative contributions to the total strain-rate sensitivity from the various contributions to stress. From Eq. 9.6, the contributions of each strengthening mechanism to the strain rate sensitivity m (see Eq. 8.3) can be assessed through

Table 9.18 Evolution parameters for FCC metals analyzed in Chap. 8 compared to those for the BCC metals analyzed in this chapter

Equation	Parameter	Ni 270	Copper	AISI 1018 Steel	Vanadium	Niobium
6.26	$\widehat{\sigma}_{\varepsilon so}$ (MPa)	1260	710	646	618	510
	$\dot{\varepsilon}_{\varepsilon so}$ (s^{-1})	10^8	10^8	10^{10}	10^{10}	10^7
	$g_{\varepsilon so}$	0.168	0.301	0.468	0.233	0.168
6.28	κ	2	2	2	3	2
6.29 with $\dot{\varepsilon}$ (s^{-1})	A_o/μ_o	0.0541	0.0522	0.0476	0.0518	0.0255
	A_1/μ_o	153×10^{-6}	262×10^{-6}	210×10^{-6}	290×10^{-6}	100×10^{-6}
	A_2/μ_o	24×10^{-6}	37×10^{-6}	140×10^{-6}	72×10^{-6}	40×10^{-6}

Fig. 9.63 Contribution to the total strain-rate sensitivity, m , from the Peierls, impurity, and storage obstacles (see Eq. 9.11) evaluated for niobium deformed at 295 K at a strain of 0.10

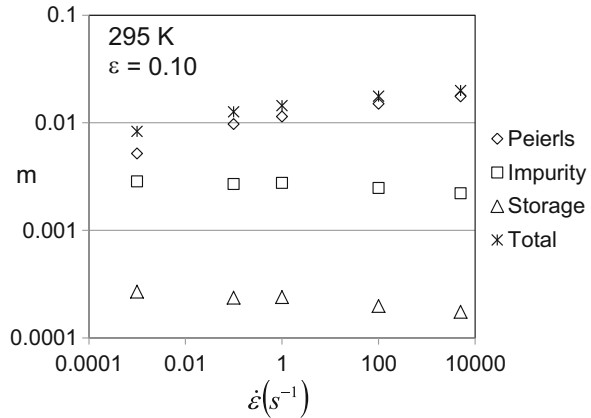
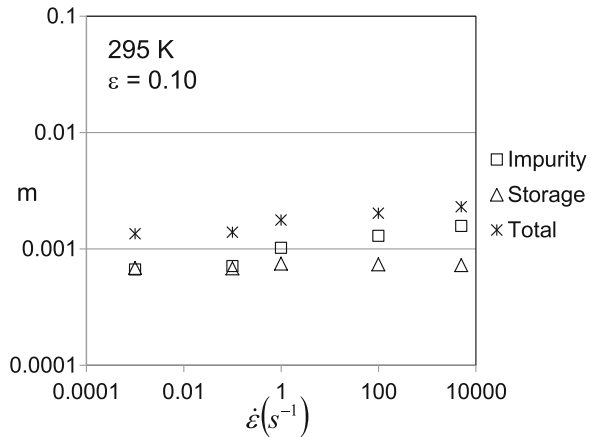


Fig. 9.64 Contribution to the total strain-rate sensitivity, m , from the impurity and storage obstacles (see Eq. 9.11) evaluated for the nickel—500 ppm C alloy deformed at 295 K at a strain of 0.10



$$m = \frac{\partial \sigma_p / \sigma}{\partial \ln \dot{\epsilon}} + \frac{\partial \sigma_i / \sigma}{\partial \ln \dot{\epsilon}} + \frac{\partial \sigma_e / \sigma}{\partial \ln \dot{\epsilon}} = m_p + m_i + m_e \quad (9.11)$$

Figure 9.63 shows the total strain-rate sensitivity and the relative contributions of the Peierls obstacle (m_p), the impurity obstacle (m_i), and the obstacle posed by the stored dislocation density (m_e) for room temperature deformation of (Nemat-Nasser and Guo) niobium evaluated at a strain of 0.10. It is evident that m_e provides a very small part of the total strain-rate dependence. The identical plot for pure copper or nickel would show that the entire strain-rate dependence arises from this term. Even for the nickel—500 ppm C alloy (see Fig. 9.64) the contribution from the dislocation storage term is a significant portion of the entire strain-rate sensitivity.

The implication is that without de-convoluting the various contributions to the stress in the BCC systems, the subtle strain-rate effects associated with the storage term are difficult to observe. This would be particularly problematic when

Table 9.E1a Stress versus strain values at a strain rate of 0.001 s^{-1} and several temperatures in FoLLyalloy (Fig. 7.8) (Exercise 9.1)

0.001 s ⁻¹ Strain	Stress (MPa)					
	100 K	200 K	300 K	400 K	500 K	600 K
0.01	1056	785	583	431	318	243
0.02	1080	807	601	452	332	253
0.03	1103	830	624	470	343	269
0.04	1126	852	646	477	367	282
0.05	1146	869	658	498	375	295
0.06	1166	892	679	508	393	311
0.07	1183	902	695	526	398	318
0.08	1202	922	708	536	417	328
0.09	1223	945	722	553	433	338
0.1	1236	955	739	565	437	351
0.125	1281	990	772	602	471	372
0.15	1322	1026	809	622	492	391
0.175	1357	1067	837	647	517	408
0.2	1386	1094	865	681	538	431
0.25	1443	1143	911	718	574	454
0.3	1492	1194	942	753	595	478
0.35	1540	1232	979	779	618	503
0.4	1576	1258	1011	801	644	521
0.45	1598	1283	1034	827	655	534
0.5	1624	1309	1050	839	674	542

attempting to observe subtle changes in the strain-rate dependence of evolution by comparing full stress–strain curves. The approach applied here isolates this term under the model assumptions described and leads to a conclusion that evolution in the BCC systems is similar to that in FCC systems.

Dynamic strain aging appears to be active in both vanadium and niobium under quasi-static test conditions and temperatures above 400 K. The observed correlation between s_i and σ_ϵ when dynamic strain aging is affecting the stress, as illustrated in Figs. 9.48 and 9.62, and the analyzed temperature dependence of this process illustrated in Fig. 9.49, is a common trend. Chapter 13 will delve more rigorously into the temperature dependence active during Dynamic Strain Aging.

Exercises

9.1 Tables 9.E1a, 9.E1b, and 9.E1c contain data used to construct the stress–strain curves for FoLLyalloy in Chap. 7, Figs. 7.8, 7.9, and 7.10. The objective of this exercise is to apply the procedures outlined in Sect. 9.4 for identifying model constants when reload stress–strain curves are unavailable. Recall that analysis

Table 9.E1b Stress versus strain values at a strain rate of 1.0 s^{-1} and several temperatures in FoLLyalloy (Fig. 7.9) (Exercise 9.1)

1.0 s ⁻¹ Strain	Stress (MPa)					
	100 K	200 K	300 K	400 K	500 K	600 K
0.01	1135	897	698	544	413	317
0.02	1159	917	725	559	436	336
0.03	1182	939	738	584	448	341
0.04	1199	955	763	598	466	360
0.05	1231	981	772	618	484	375
0.06	1248	1001	793	629	493	386
0.07	1268	1015	807	646	502	394
0.08	1289	1037	824	660	526	409
0.09	1303	1052	847	670	538	419
0.1	1319	1066	861	689	543	433
0.125	1365	1107	896	725	573	459
0.15	1400	1145	932	755	605	479
0.175	1440	1176	961	774	632	504
0.2	1474	1203	990	803	645	521
0.25	1536	1267	1037	845	688	561
0.3	1586	1306	1078	885	721	585
0.35	1630	1345	1118	914	743	607
0.4	1664	1385	1139	944	772	622
0.45	1690	1411	1166	963	785	642
0.5	1725	1437	1185	982	798	658

of the yield stress in annealed material in Fig. 7.7 identified the model constants listed in the caption to this figure. For the measurements at both 200 K and 500 K for all three strain rates, compute and plot $\hat{\sigma}_\epsilon$ versus strain using Eq. 9.7.

- 9.2 For the data at a strain rate of 0.001 s^{-1} , add the $\hat{\sigma}_\epsilon$ values listed in Table 7.8, which were found from analysis of prestrain and reload data. How do the results compare?
- 9.3 For the data from Exercise 9.1 at a strain rate of 1000 s^{-1} and temperatures of 200 K and 500 K, fit Eq. 6.25. Do your deduced values of θ_{II} and $\hat{\sigma}_{\epsilon s}$ agree with those listed in Table 7.9?
- 9.4 Table 9.10 lists initial and final temperatures for the dynamic tests. The correlation in Fig. 9.32 was based on the initial temperature. Create the same plot using the final temperature and compare this to Fig. 9.32. What is your assessment of the effect of the assumption regarding temperature?
- 9.5 The analysis of UfKonel described in Sect. 9.5 assumed that there was no adiabatic temperature rise during the dynamic tests. The objective of this exercise is to analyze a dynamic test when a temperature rise is present. Table 9.E5 lists stress versus strain measurements at an initial temperature of 300 K and a strain rate of 5000 s^{-1} in FoLLyalloy. (a) Use Eq. 9.7 to compute $\hat{\sigma}_\epsilon$

Table 9.E1c Stress versus strain values at a strain rate of 1000 s^{-1} and several temperatures in FoLLyalloy (Fig. 7.10) (Exercise 9.1)

Strain	Stress (MPa)					
	100 K	200 K	300 K	400 K	500 K	600 K
0.01	1231	1030	854	697	572	456
0.02	1256	1047	873	714	590	470
0.03	1283	1071	890	735	602	487
0.04	1299	1095	907	755	614	499
0.05	1321	1108	934	768	638	520
0.06	1342	1134	951	794	649	534
0.07	1360	1149	966	803	666	542
0.08	1378	1174	981	821	681	552
0.09	1406	1183	1001	839	698	568
0.1	1420	1210	1021	854	711	585
0.125	1467	1242	1050	884	744	612
0.15	1503	1279	1085	921	769	631
0.175	1539	1316	1118	948	799	655
0.2	1580	1354	1155	979	824	677
0.25	1634	1412	1200	1027	862	723
0.3	1691	1460	1244	1058	893	750
0.35	1732	1496	1281	1097	925	777
0.4	1771	1532	1315	1124	954	800
0.45	1798	1556	1341	1145	976	819
0.5	1829	1586	1361	1169	987	834

Table 9.E5 Stress versus strain values at a temperature of 500 K and a strain rate of 5000 s^{-1} in FoLLyalloy (Exercise 9.5)

Strain	Stress (MPa)	Strain	Stress (MPa)
0.01	543	0.2	826
0.02	579	0.225	838
0.03	607	0.25	854
0.04	624	0.275	862
0.05	647	0.3	871
0.06	667	0.325	878
0.07	688	0.35	890
0.08	703	0.375	891
0.09	712	0.4	897
0.1	727	0.425	896
0.125	767	0.45	906
0.15	791	0.475	901
0.175	803	0.5	908

Table 9.E6b Yield stress versus temperature and strain rate measurements for this BCC alloy (Exercise 9.6)

Strain rate (s^{-1})	Temperature (K)	Yield stress (MPa)
0.001	77	848
0.001	200	525
0.001	300	294
0.001	400	205
0.001	500	108
0.001	600	67
0.001	700	61
1	200	572
1	300	363
1	400	249
1	500	155
1	600	87
2000	77	959
2000	200	680
2000	300	497
2000	400	345
2000	500	220
2000	600	139

Table 9.E6a Physical constants for another BCC alloy (Exercise 9.6)

Parameter	Equation	Value	Units
b		0.275	nm
ρ	6.32	12	g/cm^3
μ_o	6.8	65	GPa
D_o		10	GPa
T_o		125	K
A_C	$c_p(T)$	0.12	J/g/K
B		0	J/g/K ²
C		0	J K/g

versus strain. To do this, you will need to estimate the temperature rise at each point using Eq. 6.32 and use the estimated temperature at each point to assess s_p , s_e , and s_i . (b) Fit Eq. 6.25 to the data points and estimate values of θ_H and $\hat{\sigma}_{es}$. How do your results compare to the values listed in Table 9.8?

9.6 Table 9.E6b lists yield stress versus temperature and strain rate measurements for a BCC alloy. Physical constants for this alloy are in Table 9.E6a. Plot yield stress versus temperature for just the measurements at the lowest strain rate and estimate a value of the athermal stress σ_a .

Table 9.E9 Stress versus strain measurements at various temperatures and strain rates for the BCC alloy introduced in Exercise 9.6 (Exercise 9.9)

T (K)	300	77	500	200	77	500
Strain rate (s^{-1})	0.001	0.001	0.001	0.1	2000	2000
Strain	Stress (MPa)					
0.01	337	855	127	569	970	228
0.02	352	882	131	591	981	239
0.03	371	908	139	618	992	251
0.04	388	933	151	629	1002	256
0.05	401	951	148	655	1010	260
0.06	411	976	156	669	1013	270
0.07	424	998	161	683	1017	273
0.08	430	1017	168	699	1018	282
0.09	438	1030	169	712	1023	282
0.1	455	1047	167	727	1021	282
0.125	467	1088	174	760	1013	298
0.15	488	1122	182	790	1006	296
0.175	502	1145	184	801	991	294
0.2	517	1180	181	827	965	297
0.225	517	1195	178	842	949	285
0.25	526	1221	188	851	922	287
0.275	538	1235	180	866	897	277
0.3	536	1252	182	877	874	275
0.325	546	1264	187	879	843	276
0.35	544	1273	186	894	820	265
0.375	551	1288	179	892	791	259
0.4	554	1293	186	902	766	252
0.425	553	1304	187	908	735	251
0.45	558	1305	184	905	708	238
0.475	560	1307	186	915	679	239
0.5	562	1321	186	913	655	235

9.7 For the yield stress data in Exercise 9.6, plot the yield stress versus temperature and strain rate on normalized coordinates according to Eq. 6.9 (as in Fig. 9.3). Use the value of the athermal stress estimated in Exercise 9.6 and use the same modeling parameters used in Fig. 9.3.

9.8 Now fit Eq. 9.1 to the data set. Assume (as in Table 9.1) that $p_p = p_i = 1/2$, $q_p = q_i = 3/2$, and $\dot{\epsilon}_{op} = \dot{\epsilon}_i = 10^8 s^{-1}$. You will need to identify the model parameters g_{op} , g_{oi} , $\hat{\sigma}_p$, and $\hat{\sigma}_i$. Start with estimates similar to those in Table 9.1, but you will need to adjust these numbers to get an optimum fit.

9.9 Table 9.E9 lists stress–strain measurements for several combinations of temperature and strain rate for the alloy of Exercises 9.6–9.8. For these tests, the measurements at a strain rate of $2000 s^{-1}$ should be considered adiabatic. Construct plots of $\hat{\sigma}_\epsilon$ versus strain for each test condition and estimate values of θ_{II} and $\hat{\sigma}_{\epsilon s}$.

- 9.10 Construct the plot of $\widehat{\sigma}_{es}$ versus strain rate and temperature to estimate $\widehat{\sigma}_{eso}$ and g_{eso} . Assume that $\dot{\epsilon}_{eso} = 10^8 \text{ s}^{-1}$.
- 9.11 Construct the plot of θ_{II} versus strain rate and estimate values of the model parameters to Eq. 6.29.

References

1. D. Brunner, V. Glebovsky, Analysis of flow-stress measurements of high-purity tungsten single crystals. *Mater. Lett.* **44**, 144–152 (2000)
2. J.D. Campbell, T.L. Briggs, *The Effect of Strain Rate and Temperature on the Yield and Flow of Polycrystalline Niobium and Molybdenum* (University of Oxford, Department of Engineering Science Report No. 1091, Oxford, 1969)
3. K.G. Hoge, A.K. Mukherjee, The temperature dependence and strain rate dependence of the flow stress of tantalum. *J. Mater. Sci.* **12**, 1666–1672 (1977)
4. S. Nemat-Nasser, W. Guo, High strain-rate response of commercially pure vanadium. *Mech. Mater.* **32**, 243–260 (2000)
5. H.L. Wain, F. Henderson, S.T.M. Johnston, N. Louat, A study of the room temperature ductility of chromium. *J. Inst. Met.* **86**, 281–288 (1957)
6. P.S. Follansbee, Analysis of deformation in seven body-centered-cubic pure metals using a two-obstacle model. *Metall. Mater. Trans. A* **41A**, 3080–3090 (2010)
7. D.L. Davidson, U.S. Lindholm, L.M. Yeakley, *Acta Metall.* **14**, 703–710 (1966)
8. T. Nojima, Constitutive equation of some kinds of steels at high rates of strain, in *Impact Loading and Dynamic Behaviour of Materials*, ed. by C. Y. Chiem, H.-D. Kunze, L. W. Meyer, (Informationgesellschaft Verlag, 1988), pp. 357–364
9. P. S. Follansbee, J. P. Ledesma, S. Starrett, The temperature and strain-rate dependence of the flow stress of mild steel, unpublished research, University of California at San Diego, 1988
10. J.S. Erickson, J.R. Low Jr., The yield-stress temperature relation for iron at low temperature. *Acta Metall.* **5**, 405–406 (1957)
11. H.L.D. Pugh, S.S. Chang, Tensile properties of a high-purity iron from -196°C to 200°C at two rates of strain. *Philos. Mag.* **8**, 753–768 (1963)
12. J.D. Campbell, W.G. Ferguson, The temperature and strain-rate dependence of the shear strength of mild steel. *Philos. Mag.* **21**, 63–82 (1970)
13. A.R. Rosenfield, G.T. Hahn, Numerical descriptions of the ambient low-temperature and high-strain rate flow and fracture of plain carbon steel. *Transact. Am. Soc. Metals* **59**, 962–980 (1966)
14. G. T. Gray III, S. R. Chen, MST-8 constitutive properties & constitutive modeling, Los Alamos National Laboratory, LA-CP-07-1590 (Contact authors for further information)
15. M.A. Meyers, O. Vohringer, V.A. Lubarda, The onset of twinning in metals: A constitutive description. *Acta Mater.* **49**, 4025–4039 (2001)
16. J. Weertman, J.R. Weertman, Mechanical properties, mildly temperature dependent, in *Physical Metallurgy*, ed. by R. W. Cahn, (Interscience Publishers, New York, 1965), p. 783
17. S. Mahajan, Formation and accommodation at deformation twins in B.C.C. crystals, in *Mechanical Properties of BCC Metals*, ed. by M. Meshii, (Conference Proceedings, Metallurgical Society of AIME, Warrendale, 1982), pp. 225–235
18. S. Nemat-Nasser, W. Guo, Flow stress of commercially pure niobium over a broad range of temperatures and strain rates. *Mater. Sci. Eng.* **A284**, 202–210 (2000)

Chapter 10

Application of MTS Model to HCP Metals and Alloys



Introduction

Section 3.3 summarized several unique characteristics of slip in HCP metals. In particular, the close-packed system—the basal plane (0001) and the close-packed direction $\langle 11\bar{2}0 \rangle$ —has only 3 independent systems compared to the 12 available in the FCC crystal structure. Therefore, slip is observed on other crystal planes. The *prismatic* plane was referred to in Sect. 3.3. In the Miller-Bravais coordinate system, this is the $(10\bar{1}0)$ plane and the close-packed direction $\langle 11\bar{2}0 \rangle$. Slip is also observed on the *pyramidal* system, which is $(10\bar{1}1)$ plane and, once again, the close-packed direction $\langle 11\bar{2}0 \rangle$. The ease of slip in HCP metals as influenced by the dislocation energy and the spacing between parallel slip planes (as discussed in Sect. 3.2 in regard to the Peierls stress) is affected by the active slip system(s). One implication of this is that one should expect less commonality between deformation kinetics in HCP metals and observed in FCC and BCC metals.

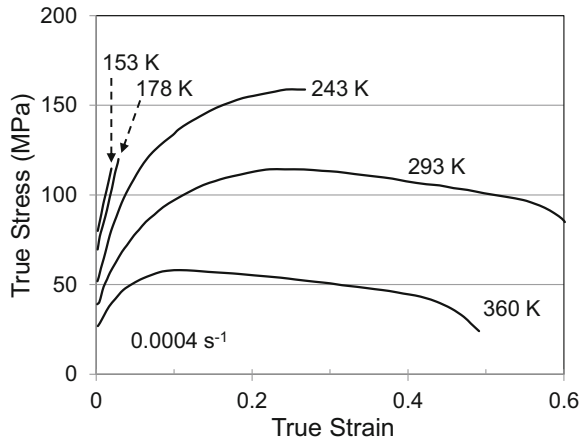
In this chapter the temperature dependence and, in some cases, the strain rate dependence of deformation in pure Cd, Ti, Zn, Mg, and Zr is examined. Deformation in several HCP alloys of Mg, Zr, and Ti also is examined. The analysis presented in these HCP metals is complicated by (i) limited availability of extensive experimental campaigns available for model FCC and BCC systems; (ii) contributions of deformation twinning observed in most of the HCP systems, particularly at low (homologous) temperatures and high strain rates; and (iii) effects of texture evolution on hardening. The last point is important. One tenet of the analyses of FCC metals in Chap. 8 and of BCC metals in Chap. 9 is that deformation in well-annealed, initially isotropic metals can be modeled using isotropic hardening formulations. The development of preferred textures becomes increasingly important with increasing strain,

Supplementary Information The online version contains supplementary material available at https://doi.org/10.1007/978-3-031-04556-1_10

Table 10.1 Variation of some common parameters for the HCP metals considered in this chapter

Metal	T_m (K)	c/a ratio	μ_o (GPa)
Cadmium	594	1.886	33.2
Zinc	693	1.856	63.5
Magnesium	923	1.624	18.6
Zirconium	2128	1.593	41.8
Titanium	1941	1.587	47.6

Fig. 10.1 Stress–strain curves in pure zinc as reported by Risebrough [1]



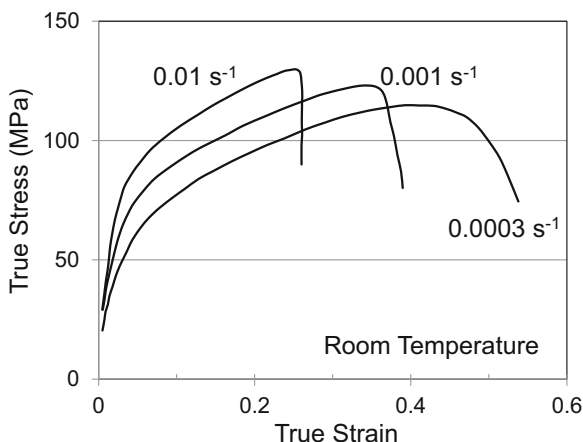
but isotropy offers a good starting assumption. Clearly, the most predictive constitutive equations would include the effects of texture development, and there exist several approaches to accomplish this. In HCP systems, however, the lack of available close-packed slip systems and resulting tendency to slip on non-close-packed planes leads to rapid evolution of preferred crystallographic orientations. In these systems, it is less clear that isotropy is as applicable—even at low strains—as argued above for FCC and BCC metals.

Table 10.1 lists the melting temperature, c/a ratio, and μ_o (Eq. 6.8) for each of the HCP metals included in this chapter.

10.1 Pure Zinc

For his PhD dissertation, Risebrough performed temperature- and strain rate-dependent tensile testing in high purity zinc polycrystals [1]. The material was 99.999% pure and processed to give a grain size of 20 μm . (Testing of material with 400 μm grain size was also performed, but this grain size was on the order of the specimen thickness; thus these results are not discussed here.) Figure 10.1 shows the stress–strain curves at a strain rate of 0.0004 s^{-1} . Note that 360 K is at a homologous temperature (T_H) of 0.52. The tests at 153 K and 178 K exhibited very low ductility values. Risebrough described these tests as below a “ductile-to-brittle” transition. Deformation twinning was observed at all temperatures, but twinning was less

Fig. 10.2 Strain rate-dependent stress–strain curves in pure zinc reported by Liu et al. [2]



extensive in zinc than in cadmium, and the extent of twinning did not appear to vary with temperature. Full stress–strain curves at other than a strain rate of 0.0004 s^{-1} were not published, but Risebrough listed flow stresses at strains between 0.002 and 0.16 for RT tests at strain rates from $4 \times 10^{-5} \text{ s}^{-1}$ to $4 \times 10^{-3} \text{ s}^{-1}$.

In another experimental study, Liu, Huang, Wu, and Zhang [2] measured tensile stress–strain curves in high purity zinc at RT and strain rates of 0.0003 s^{-1} , 0.001 s^{-1} , and 0.01 s^{-1} . This material was also 99.999% pure processed to achieve a grain size of $70 \mu\text{m}$ for the material referred to as “fine grained.” These investigators characterized the fracture surfaces and noted differences in fracture morphology as a function of strain rate and grain size. They did not report on the potential contributions of deformation twinning. Figure 10.2 shows the stress–strain curves at the three strain rates.

Consistent with the approach demonstrated for FCC and BCC metals, the first step in the analysis is to analyze the kinetics of yield in the starting material. Figure 10.3 plots the normalized yield stress versus the normalized temperature and strain rate parameter that has been used extensively in the previous chapters. In Fig. 10.3 the athermal stress is taken to equal 20 MPa for the finer-grain ($20 \mu\text{m}$) Risebrough material and 5 MPa for the Liu et al. material, which was processed to a grain size of $70 \mu\text{m}$. All of the data fall on a single model curve, which is a one-parameter model (e.g., Eq. 8.5 with $\hat{\sigma}_e = 0$) with the model parameters listed in Table 10.2. Note that only the athermal stress differs between the Risebrough and Liu et al. materials.

The analysis of strain hardening in zinc follows from the procedures outlined for UfKoneI (Sect. 9.5). Equation 9.7 is used (with $\hat{\sigma}_p = 0$) along with the model parameters in Table 10.2. Once again, it is assumed that the model parameters for s_e are those specified in Table 9.7. Figure 10.4 shows the computed variation of $\hat{\sigma}_e$ with strain for the Risebrough measurement at 243 K and a strain rate of 0.0004 s^{-1} . The dashed line in this figure is drawn according to Eq. 6.28 with $\kappa = 1$, $\theta_{II} = 1700 \text{ MPa}$, and $\hat{\sigma}_{es} = 137 \text{ MPa}$. Figure 10.5 shows the same analysis for the Liu et al.

Fig. 10.3 Yield stress versus temperature and strain rate in pure zinc. Note that the athermal stress varied between the two data sets

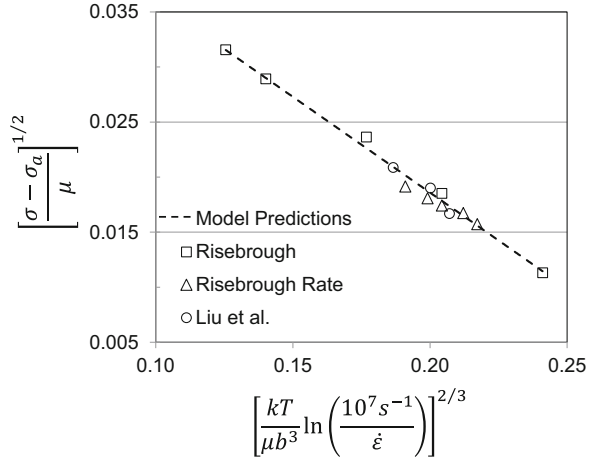


Table 10.2 Summary of model parameters in pure zinc

Equation	Parameter	Risebrough	Liu et al.
8.5	σ_a (MPa)	20	5
8.5	$\hat{\sigma}_i$ (MPa)	181	
6.15	pi	0.5	
	qi	1.5	
	$\dot{\epsilon}_{oi}$ (s^{-1})	10^7	
	g_{oi}	0.17	
	b (nm)	0.267	
6.8	μ_o (GPa)	63.5	
	D_o (GPa)	4.3	
	T_o (K)	125	
6.26	$\hat{\sigma}_{eso}$ (MPa)	1426	
	$\dot{\epsilon}_{eso}$ (s^{-1})	10^7	
	g_{eso}	0.0335	
6.28	κ	1	
6.29	A_o (MPa)	1725	
	$A_1 = 4.3$	4.3	
	A_2 (MPa $s^{-1/2}$)	2	

measurement at 295 K and a strain rate of $0.0003 s^{-1}$. In this case two dashed lines are drawn according to Eq. 6.28. The long-dashed line, with $\kappa = 1$, $\theta_{II} = 1650$ MPa, and $\hat{\sigma}_{es} = 118$ MPa, is drawn to match the low strain behavior as well as the highest stress levels achieved, whereas the short-dashed line, with $\kappa = 1$, $\theta_{II} = 1650$ MPa, and $\hat{\sigma}_{es} = 85$ MPa, is drawn to match the low strain behavior as far as agreement between Eq. 6.28 and the data allows. It is worth noting that trying different values of the κ -variable does not give a curve that agrees with the solid line in Fig. 10.5 over the entire range of strains. The suspicion is that the unique behavior exhibited by the hardening curve in Fig. 10.5 evidences a contribution from deformation twinning. If

Fig. 10.4 Computed variation of $\hat{\sigma}_\epsilon$ with strain and fit to Eq. 6.28 for one of the test conditions reported by Risebrough in pure zinc

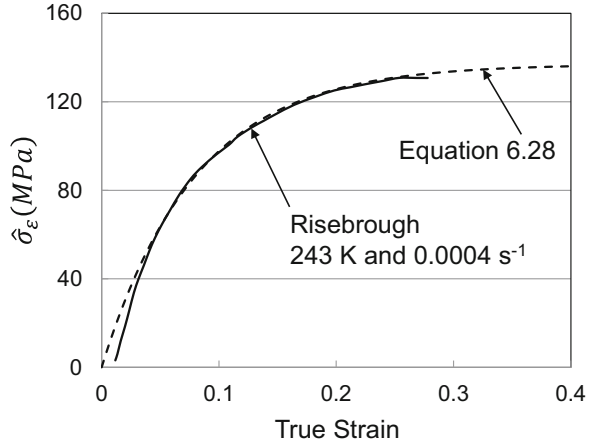
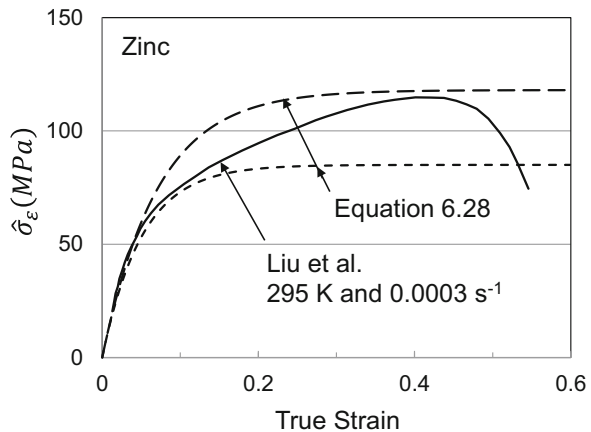


Fig. 10.5 Computed variation of $\hat{\sigma}_\epsilon$ versus strain for one of the Liu et al. tests in zinc. Two possible model lines are drawn according to Eq. 6.28



this is the case, the short-dashed curve may more closely approximate the contribution of dislocation storage, and the long-dashed curve may reflect the total hardening behavior (or the correct curve may lie between the two dashed lines). The challenge is to de-convolute these effects. The analysis of measurements in cadmium presented below may offer a schema to accomplish this objective.

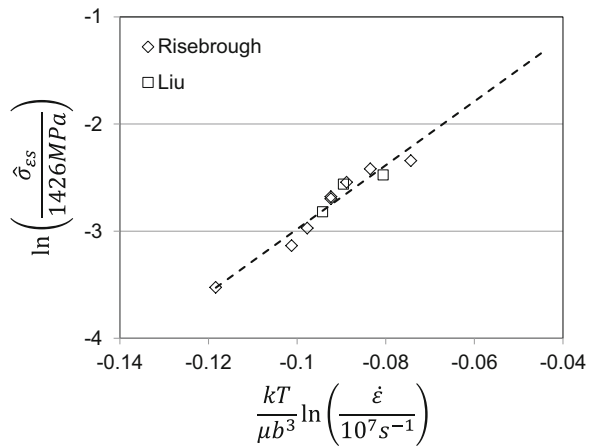
Table 10.3 lists the values of θ_{II} and $\hat{\sigma}_{\epsilon s}$ for each of the Risebrough and Liu et al. stress-strain curves. Note that for consistency, the long-dashed line rather than the lower, short-dashed curve (e.g., Fig. 10.5) was used for cases that presented this choice.

Figure 10.6 shows the evolution plot (normalized $\hat{\sigma}_{\epsilon s}$ versus normalized temperature and strain rate according to Eq. 6.26). As shown in the figure, $\hat{\sigma}_{\epsilon s0} = 1426 \text{ MPa}$ for a $\dot{\epsilon}_{\epsilon s0} = 10^7 \text{ s}^{-1}$. Both the Risebrough and Liu et al. data sets are described by the dashed line fit. The inverse of the slope of this line gives $g_{\epsilon s0} =$

Table 10.3 Model parameters in the evolution equation (Eq. 6.28) for the fits to the measurements in pure zinc

Material	Temperature/strain rate	Equation 6.28 parameter ($\kappa = 1$)	
		θ_{II} (MPa)	$\hat{\sigma}_{es}$ (MPa)
Risebrough [1]	243 K/0.0004 s ⁻¹	1700	137
	293 K/0.0004 s ⁻¹	1700	98
	360 K/0.0004 s ⁻¹	1650	42
	178 K/0.0004 s ⁻¹	1750	–
	153 K/0.0004 s ⁻¹	1750	–
	293 K/0.00004 s ⁻¹	1650	62
	293 K/0.0001 s ⁻¹	1650	73
	293 K/0.0004 s ⁻¹	1700	96
	293 K/0.001 s ⁻¹	1700	112
	293 K/0.004 s ⁻¹	1700	127
Liu et al. [2]	295 K/0.0003 s ⁻¹	1650	85
	295 K/0.001 s ⁻¹	1750	110
	295 K/0.01 s ⁻¹	1750	120

Fig. 10.6 Variation of the saturation threshold stress with temperature and strain rate for the measurements in zinc



0.0335. In comparison to the g_{eso} values observed in FCC and BCC metals, this value is quite small, which suggests that strain hardening in this material is extremely temperature (and strain rate) sensitive.

Figure 10.7 gives the variation of θ_{II} with strain rate. The variation in strain rate is too small to warrant a fit to Eq. 6.29. The dashed line shows a possible fit with $A_o = 1725$ MPa, $A_1 = 4.3$ (MPa when strain rate expressed as s⁻¹), and $A_2 = 2$ MPa s^{-1/2}. The model parameters for Eqs. 6.26 and 6.29 have been added to Table 10.2.

A comparison of the Risebrough stress–strain curves with predicted curves using the model parameters describe above is shown in Fig. 10.8. The predicted curves resulting from application of a single-parameter model formulation are consistent with the measured curves.

Fig. 10.7 Variation of θ_H with strain rate for the measurements in zinc and possible fit according to Eq. 6.29

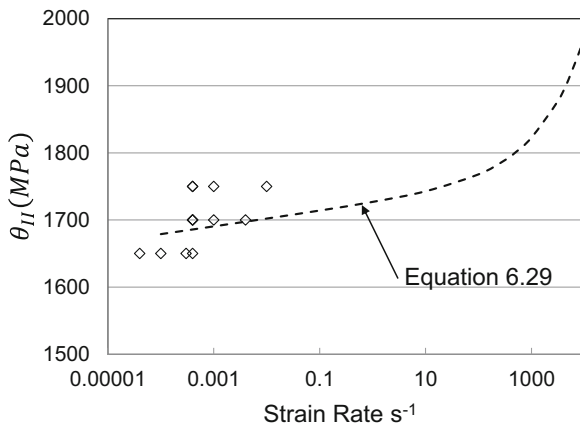
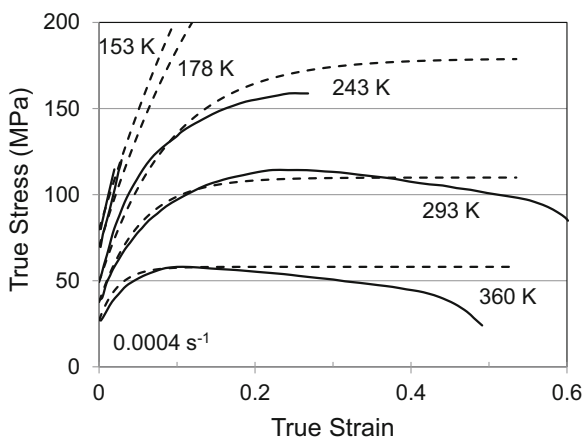


Fig. 10.8 Measured (by Risebrough) and predicted stress–strain curves in zinc



10.2 Kinetics of Yield in Pure Cadmium

Risebrough’s PhD thesis research [1] included measurements in pure cadmium. This metal was also 99.999% pure and in this case was processed to give a grain size of 25 μm . Figure 10.9 shows the tensile stress–strain curves reported by Risebrough. Figure 10.10 plots the variation of the yield stress with temperature. (No measurements at other than a strain rate of 0.0004 s^{-1} were reported in [1].) Included in Fig. 10.10 are model fits according to the one-parameter model with $\sigma_a = 10 \text{ MPa}$, $\hat{\sigma}_i = 86.3 \text{ MPa}$, and $g_{oi} = 0.33$ (and p_i , q_i , and $\dot{\epsilon}_{oi}$ as in Table 10.2). The model fit in Fig. 10.10 appears to agree well with all but the measurement at the highest temperature (at the right side of the abscissa). This test was at temperature of 345 K which is $T_H = 0.581$. The fact that the yield stress at this temperature falls below the model line is problematic since it is difficult to identify a mechanism consistent with this behavior. Note that all deviations from the low-temperature

Fig. 10.9 Stress–strain curves reported by Risebrough [1] in cadmium

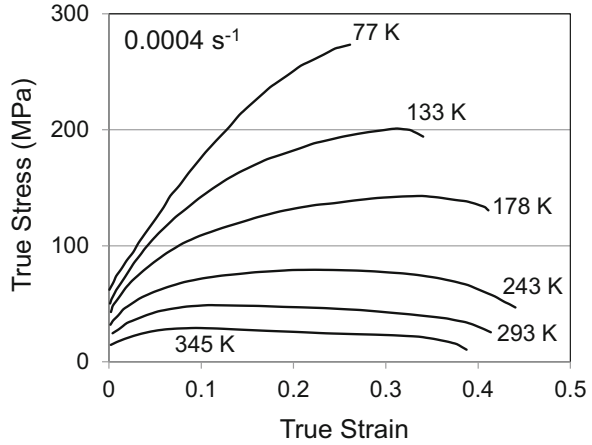
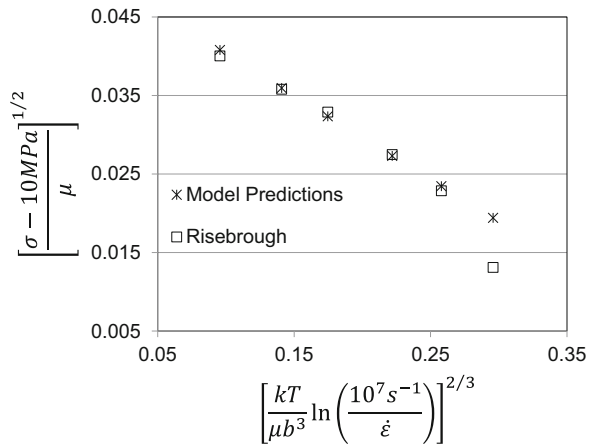


Fig. 10.10 Variation of yield stress with test temperature in cadmium along with a one-parameter model prediction



and/or high strain rate behavior (the left-hand side of Fig. 10.10 and the related figures for other materials presented in earlier chapters) indicate higher stresses than predicted by the model.¹ For pure BCC metals (Sect. 9.1) modeled using a one-parameter formulation (Eq. 8.5), the deviations dictated the need for a second state variable. Similarly, in Ni-1900C, the measured stresses at high temperature rose above the model line (Fig. 8.37). (Further evidence of this is presented in Chap. 11 in analyzing deformation in austenitic stainless steels.) No material discussed so far (except for the one result in tungsten) has shown behavior akin to that in Fig. 10.10 where at high temperature the stress falls below the stress dictated by the kinetics of a dominant deformation mechanism.

¹The data for pure tungsten shown in Fig. 9.7 also trended downward at high temperatures.

It is possible to envisage a set of deformation mechanisms that would lead to the behavior shown in Fig. 10.10. If, for instance, the “dominant deformation mechanism” is not in reality a single deformation mechanism but rather a combination of a dislocation interaction with an impurity element along with something like a diffusion-assisted process, then at a high enough temperature, this additional deformation mechanism would cease, and the stress level would fall to the level dictated by the interaction of the dislocation with the impurity element. Materials hardened by precipitates also show stress levels that fall at temperatures above which diffusion assists dislocations past these precipitates.

However, none of these additional strengthening mechanisms appear to be viable for a metal of this purity. Measurements by Mannan and Rodriguez [3] in pure cadmium offer further insight in the low-temperature behavior. These investigators measured tensile stress–strain curves in 99.99% pure cadmium processed to give grain sizes from 25 μm to 82 μm . Figure 10.11 shows stress–strain curves at a strain rate of $6.56 \times 10^{-5} \text{ s}^{-1}$ in 38 μm grain size material. The yield stresses for these four measurements are added to the Risebrough data and plotted in Fig. 10.12. The Mannan and Rodriguez measurements at 196 K, 255 K, and 298 K agree well with the Risebrough measurements. Their measurement at 77 K, however, falls below the Risebrough measurement at the same temperature. Figure 10.12 includes a very different model equation fit than used in Fig. 10.10. In this case the line is fit to the higher-temperature points. The model parameters in this case are $\sigma_a = 10 \text{ MPa}$, $\hat{\sigma}_i = 249 \text{ MPa}$, and $g_{oi} = 0.20$ (and p_i , q_i , and $\dot{\epsilon}_{oi}$ as in Table 10.2). It is suggested that the deviation from the model line at lower temperatures is due to the contribution of deformation twinning—as discussed in Sect. 5.6 in regard to measurements in zirconium, which is another HCP metal, and in Fig. 9.10 in regard to measurements in pure iron. Although Mannan and Rodriguez did not perform optical metallography to validate the extent of deformation twinning, the variation of $\hat{\sigma}_\epsilon$ with strain

Fig. 10.11 Stress–strain curves reported by Mannan and Rodriguez [3] in polycrystalline cadmium

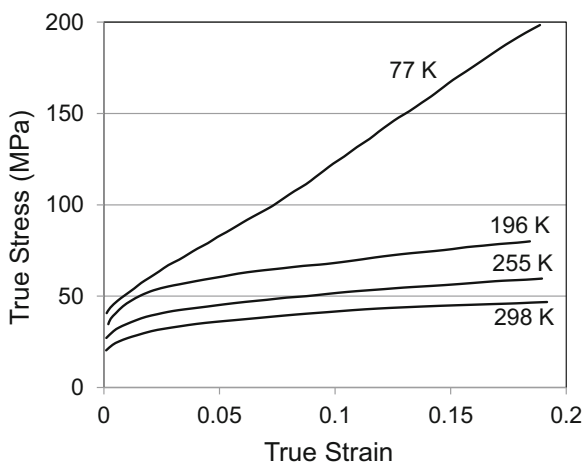


Fig. 10.12 An alternate model fit to both sets of measurements in cadmium

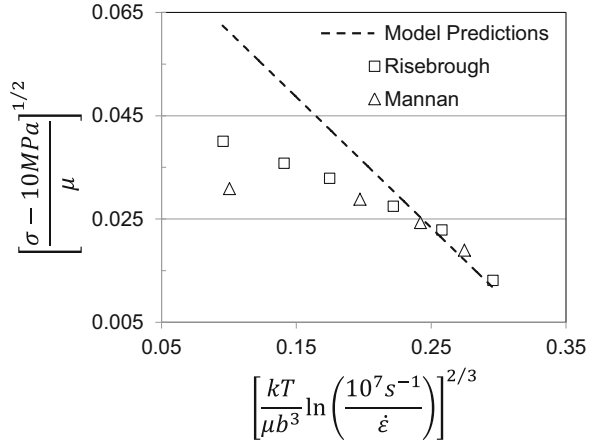


Table 10.4 Summary of model parameters in pure cadmium

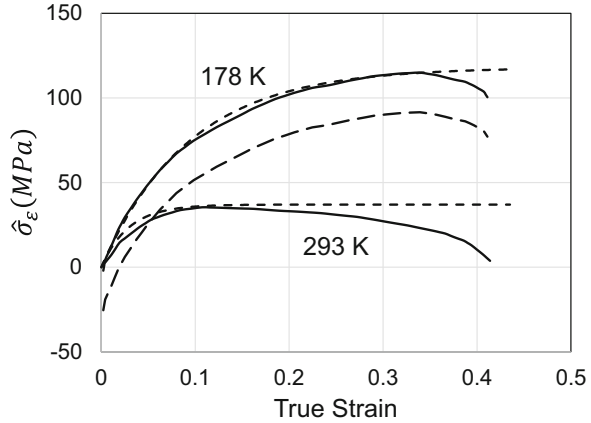
Equation	Parameter	Value
8.5	σ_a (MPa)	10
8.5	$\hat{\sigma}_i$ (MPa)	249
6.15	pi	0.5
	qi	1.5
	$\dot{\epsilon}_{oi}$ (s ⁻¹)	10 ⁷
	g_{oi}	0.20
	b (nm)	0.298
6.8	μ_o (GPa)	33.2
	D_o (GPa)	2.8
	T_o (K)	125
6.26	$\hat{\sigma}_{ESO}$ (MPa)	192
	$\dot{\epsilon}_{ESO}$ (s ⁻¹)	10 ⁷
	g_{ESO}	0.0819
6.28	κ	1
6.29	A_o (MPa)	1340
	$A_1 = 4.3$	5
	A_2 (MPa s ^{-1/2})	2

gives additional insight into the contribution from deformation twinning. Model parameters for the yield stress analysis in cadmium are listed in Table 10.4.

10.3 Structure Evolution in Pure Cadmium

Analysis of structure evolution (strain hardening) in cadmium follows the approach used for zinc in Sect. 10.1 and for UfKonel in Sect. 9.5. Figure 10.13 shows the variation of $\hat{\sigma}_\epsilon$ (analyzed according to Eq. 9.7) with strain for the Risebrough tests at

Fig. 10.13 Computed variation of $\hat{\sigma}_\varepsilon$ with strain for measurements in pure cadmium at 178 K and 293 K. The dashed lines are fits according to Eq. 6.28



178 K and 293 K and a strain rate of $4 \times 10^{-4} \text{ s}^{-1}$. The two dashed lines in Fig. 10.13 are the model fits according to Eq. 6.28. For 293 K, Eq. 6.28 is drawn with $\kappa = 1$, $\theta_{II} = 1250 \text{ MPa}$, and $\hat{\sigma}_{\varepsilon s} = 37 \text{ MPa}$. The agreement between the model fit and measurements at 293 K is good up to the point where a tensile instability likely occurs. The agreement between the model fit and measurements at 178 K shows overestimate of stresses of $\sim 20 \text{ MPa}$. This error is due to the fact that this yield stress value (third open square from the left in Fig. 10.12) is below the model (dashed) line. The model fit with the long dashes in Fig. 10.13 includes this 20 MPa offset, which leads to good agreement between the model and measurements. This model prediction uses Eq. 6.28 with $\kappa = 1$, $\theta_{II} = 1250 \text{ MPa}$ and $\hat{\sigma}_{\varepsilon s} = 118 \text{ MPa}$.

Figure 10.14 shows the analysis of the Mannan and Rodriguez measurement at 298 K and a strain rate of $6.56 \times 10^{-5} \text{ s}^{-1}$. While the stress levels in this measurement are similar to those in the Risebrough measurement at 293 K (Fig. 10.13), the shapes of the stress–strain curves show notable differences. The Mannan curve shows a lower rate of strain hardening, which actually works to delay the point of tensile instability. The stress–strain curve (Fig. 10.11) continues to rise at strain levels as high as 19%. The low initial rate of strain hardening in the Mannan curve is the predominant difference between these two measurements. A hardening rate that dips below that predicted with Eq. 6.28 was observed in zinc (Fig. 10.5) and pure vanadium (Fig. 9.41). It was postulated that this was evidence that strain was being partially accommodated by deformation twinning that develops with straining. With increasing strain it appears as if the rate of hardening then increases. Without detailed microstructural characterization, it is difficult to ascertain whether this subsequent increase is due to traditional dislocation storage or due to interactions of dislocations with a network of twin boundaries.

Figure 10.15 compares the analyzed variation of $\hat{\sigma}_\varepsilon$ with strain for the two tests at 77 K. Although both tests were measured at 77 K, the Risebrough curve was measured at a strain rate of $4 \times 10^{-4} \text{ s}^{-1}$, whereas the Mannan and Rodriguez curve was measured at a strain rate of $6.56 \times 10^{-5} \text{ s}^{-1}$. As at 178 K in the Risebrough measurement, a stress offset must be subtracted from the prediction

Fig. 10.14 Variation of $\hat{\sigma}_\epsilon$ with strain for the Mannan and Rodriguez measurements at 298 K in pure cadmium

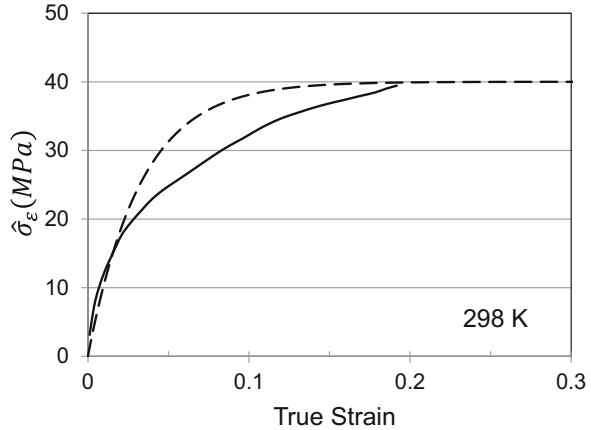
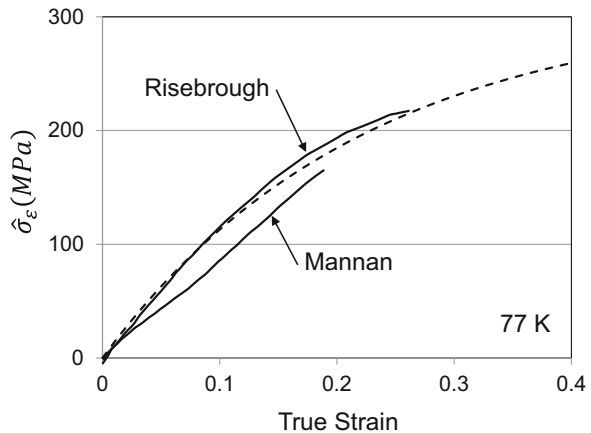


Fig. 10.15 Variation of $\hat{\sigma}_\epsilon$ with strain for the Risebrough and Mannan and Rodriguez measurements at 77 K in pure cadmium



according to Eq. 9.7. For the Risebrough analysis, this was set at 70 MPa, whereas for the Mannan and Rodriguez measurement, this was set at 90 MPa. The model prediction (with $\kappa = 1$, $\theta_{II} = 1400$ MPa and $\hat{\sigma}_{\epsilon S} = 310$ MPa) with these offsets agrees fairly well with the measurements, but the rate of strain hardening in the Mannan and Rodriguez measurement dips below that in the Risebrough measurement. This may reflect the difference in grain size in the two materials (25 μm versus 38 μm), the more than one order of magnitude difference in strain rate, or a subtle difference in the contributions of deformation twinning in these two measurements.

Figure 10.16 shows the $\hat{\sigma}_{\epsilon S}$ values for all of the Risebrough and Mannan and Rodriguez measurements plotted on the coordinates dictated by Eq. 6.26. The unfilled data points are plotted with $\hat{\sigma}_{\epsilon SO} = 485$ MPa, whereas the solid data points are plotted with $\hat{\sigma}_{\epsilon SO} = 192$ MPa and with the four data points on the right side of the abscissa (representing tests at the lower temperatures) excluded from the model fit

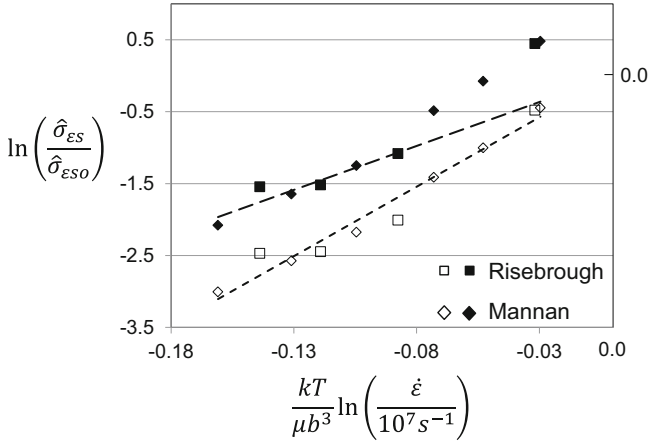


Fig. 10.16 Variation of the saturation threshold stress with temperature and strain rate in pure cadmium for two values of $\hat{\sigma}_{\epsilon_{SO}}$ (192 MPa for the filled in symbols and 485 MPa for the open symbols)

(long-dashed line). The rationale for this latter fit is that one could argue the data points on the right side of the plot trend upward from those on the left side of the plot and that the upward trend represents the contribution of deformation twinning. The fit with the lower value of with $\hat{\sigma}_{\epsilon_{SO}}$ is the preferred solution. The model parameters for this fit are $\hat{\sigma}_{\epsilon_{SO}} = 192$ MPa, $\dot{\epsilon}_{\epsilon_{SO}} = 10^7$ s⁻¹, and $g_{\epsilon_{SO}} = 0.0819$. These model parameters have been included in Table 10.4. Also included are the model fit to Eq. 6.29.

The hardening resulting from deformation twinning has been compared to that due to grain boundaries described by the Hall-Petch equation (Eq. 3.9) [4]. If the Hall-Petch parameters are known, the increase in stress over the stress predicted by the long-dashed line in Fig. 10.16 can be used to predict the equivalent level of grain refinement introduced by the deformation twin boundaries. Mannan and Rodriguez measured the Hall-Petch parameters for cadmium [3]. While they noted some variation of the parameters with strain (and with temperature), at 77 K, the Hall-Petch equation is as follows:

$$\sigma = 9.25\text{MPa} + \frac{212\text{MPa}\sqrt{\mu m}}{\sqrt{d_{gs}(\mu m)}} \tag{10.1}$$

Equation 10.1 predicts a stress of 51.6 MPa for a grain size of 25 μm . Risebrough actually measured a stress of 62.1 MPa at this grain size. While these numbers are close, the implication is that the intercept 9.25 MPa may actually be higher in the Risebrough material. The equivalent grain size resulting in the increased stress level estimated below is predicted assuming the slope of the grain size dependence is as

specified by Mannan and Rodriguez and the difference in grain size follows from the difference in stress.

Prediction of $\hat{\sigma}_\epsilon$ using Eq. 6.28 and the model parameters listed above ($\hat{\sigma}_{\epsilon_{SO}} = 192$ MPa) gives a stress level of 179 MPa at 77 K and a strain rate of 0.0004 s^{-1} and a strain of 26% (the highest strain reached in the Risebrough measurement shown in Fig. 10.15). The measured stress level was 273 MPa. The difference between these stresses (94 MPa) would be the stress increase due to the reduction in grain size incurred through deformation twinning. From Eq. 10.1 this equates to a grain size of $2.4 \text{ }\mu\text{m}$ (compared to the starting grain size of $25 \text{ }\mu\text{m}$). It is not difficult to envision that significant deformation twinning could produce a $\times 10$ reduction in equivalent grain size. Such an effective grain size reduction would have a significant contribution to the total strain-hardening behavior. Based on this analysis, it is suggested that the deviation above the long-dashed line (solid data points) in Fig. 10.16 is due to (athermal) hardening introduced by grain size reduction as a result of deformation twinning. The inclusion of the effect of deformation twinning awaits a model that describes the slip versus twinning transition.

10.4 Pure Magnesium

The low density of magnesium (1.7 g/cm^3) and improvements in alloying and processing technologies have contributed to an increase in the usage of magnesium for gear boxes and transmission cases, wheels, sporting goods, and electronic packages. Deformation in the commonly used magnesium alloy AZ31 is considered in Sect. 10.5.

Suzuki et al. [5] published compression stress–strain curves in 99.96% pure magnesium at test temperatures of 291 K, 473 K ($T_H = 0.512$), 523 K, 573 K, 623 K, 673 K, and 773 K ($T_H = 0.84$) and strain rates from 0.1 s^{-1} to 10 s^{-1} . Actually, only a few test results at 291 K are reported, and these stress–strain curves indicate the material is fairly brittle at this temperature. These tests were performed in a cam plastometer [6], which was a commonly used device to measure high rate deformation behavior before rise in usage of the split Hopkinson pressure bar. Figure 10.17 shows five of the stress–strain curves reported by Suzuki et al. As illustrated in this figure, these investigators do not specify stresses at strains below $\sim 2\%$, which may be associated with limitations of the data acquisition system. Because yield stresses at the traditional 0.002 strain offset are of interest, these stresses are estimated by extrapolating the low strain-hardening behavior. Figure 10.18 shows the normalized yield stress versus temperature and strain rate plot. Measurements at the different strain rates are identified in this figure to determine whether any of the observed scatter is a strain rate effect. Indeed, the scatter does not appear to scale with strain rate. The model fit is a two-parameter model (Eq. 6.14) where the model parameters are listed in Table 10.5. The RT data point (open square at the lowest value of the abscissa) appears to be quite low. The stress–strain curve indicates this sample was able to accommodate a strain of only

Fig. 10.17 Stress–strain curves in pure magnesium reported by Suzuki et al. [5]

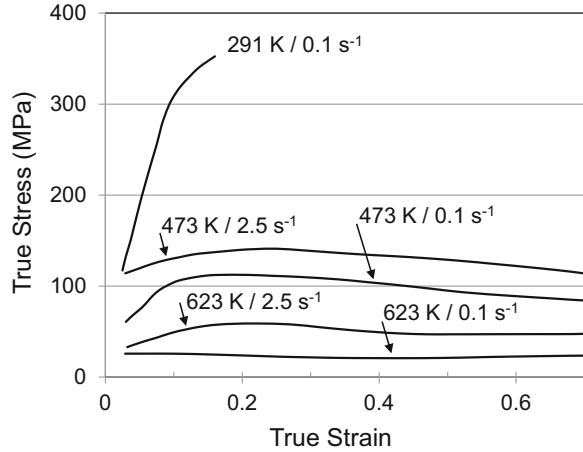
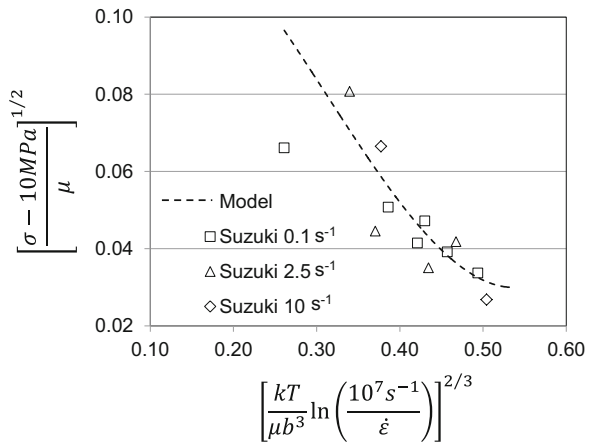


Fig. 10.18 Yield stress versus temperature and strain rate for the Suzuki et al. data set in pure magnesium



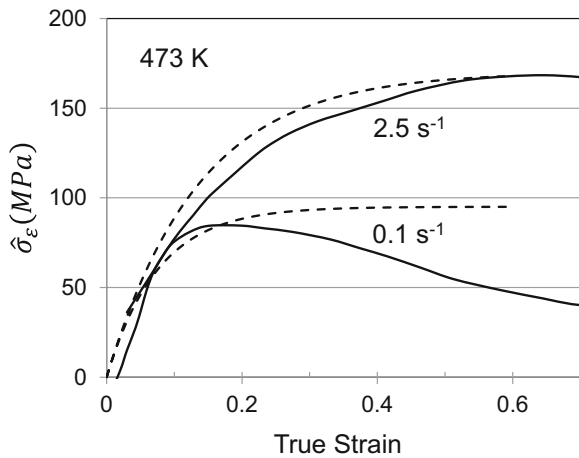
~15%. It may be that deformation twinning is active under these conditions as discussed in relation to measurements in pure cadmium. The overall scatter in Fig. 10.18 likely relates to the uncertainty in the stress–strain curve in and around the yield point.

With the model parameters specified in Table 10.5, the stress–strain curves may be analyzed using Eq. 9.7 (with obstacle “1” and “2” instead of “p” and “i”) to deduce the variation of $\hat{\sigma}_\epsilon$ with strain. Figure 10.19 shows the result for the tests at 200 C (473 K) and strain rates of 0.1 s⁻¹ and 2.5 s⁻¹. (The test at the lower strain rate can likely be considered to be isothermal, whereas the test at the higher strain rate should be treated as adiabatic.) The dashed curves are Eq. 6.28 with $\kappa = 1$ and $\theta_{II} = 1250$ MPa and $\hat{\sigma}_{\epsilon_s}$ set at 95 MPa at the lower strain rate and 170 MPa at the higher strain rate. The curve at the lower strain rate peaks at a strain of ~0.15 and then continuously decreases, which is unusual since this is a compression test where the

Table 10.5 Model parameters for the dashed line fit in Fig. 10.18 for pure magnesium

	Parameter	Value
Obstacle	σ_a (MPa)	10
	b (nm)	0.321
Obstacle 1	g_o	0.35
	$\dot{\epsilon}_o$ (s^{-1})	10^7
	p	0.5
	q	1.5
	$\hat{\sigma}/\mu_o$	0.03
Obstacle 2	g_o	1
	$\dot{\epsilon}_o$ (s^{-1})	10^8
	p	0.5
	q	1.5
	$\hat{\sigma}/\mu_o$	0.005

Fig. 10.19 Variation of $\hat{\sigma}_{\epsilon S}$ with strain for two test conditions in pure magnesium reported by Suzuki. The dashed lines are the fits according to Eq. 6.28



stress should continuously increase. The suspicion is that at this temperature ($T_H = 0.512$) dynamic recrystallization is present, which is consistent with the observation that the test at the higher strain rate does not show this drop. If this is the case, then use of Eq. 9.7 to estimate $\hat{\sigma}_{\epsilon S}$ is suspect since Eq. 6.14 may no longer apply. Furthermore, use of Eq. 9.26 to assess the temperature and strain rate dependence of $\hat{\sigma}_{\epsilon S}$ would be unwarranted. There are no hard and fast rules as to the temperature and strain rate where these equations do not apply. (See discussion in Sect. 15.9.) To gain some insight into this, Table 10.6 lists the test conditions and the values of θ_{II} and $\hat{\sigma}_{\epsilon S}$ (Eq. 6.28) for each of these test conditions—assuming that Eq. 9.7 does apply. Included in Table 10.6 as the last column is the value of $T_i \ln(10^7 s^{-1}/\dot{\epsilon})$. The tests are listed in this table in order of the value of the latter parameter, based on the initial temperature.

Table 10.6 Summary of the model parameters fit to each of the Suzuki et al. stress–strain curves in pure magnesium

Initial temperature (K)	Final temperature (K)	Strain rate (s^{-1})	θ_H (MPa)	$\hat{\sigma}_{es}$ (MPa)	$T_i \ln(10^7 s^{-1}/\dot{\epsilon})$
291	291	0.10	–	–	5360
473	650	2.5	1250	170	7190
573	640	10	1200	112	7920
523	580	2.5	1300	93	7950
473	473	0.1	1250	95	8710
623	640	2.5	1300	52	9470
573	573	0.5	1200	40	9630
523	523	0.1	1250	72	9635
673	685	2.5	1250	15	10,200
573	573	0.10	1200	15	10,560
773	780	10	1300	4	10,780
623	623	0.10	1250	10	11,480
673	673	0.10	1250	5	12,400

Inspection of the $\hat{\sigma}_{es}$ values in Table 10.6 leads to the observation that the low, even single-digit values at the bottom of the table are highly suspect results. The results at the upper rows of the table are more representative of low-temperature behavior documented in other systems. The curve and model fit at an initial temperature of 473 K and a strain rate of $2.5 s^{-1}$ shown in Fig. 10.19 is similar to results in other materials. The result at the same temperature but a strain rate of $0.10 s^{-1}$ also plotted in Fig. 10.19, which has a higher value of $T_i \ln(10^7 s^{-1}/\dot{\epsilon})$, demonstrates significant deviation from expected behavior at strains above ~ 0.10 . There is too little confidence in the results in Table 10.6 to proceed with analysis according to Eq. 6.26. This will be revisited in relation to results in alloy AZ31 in the next section.

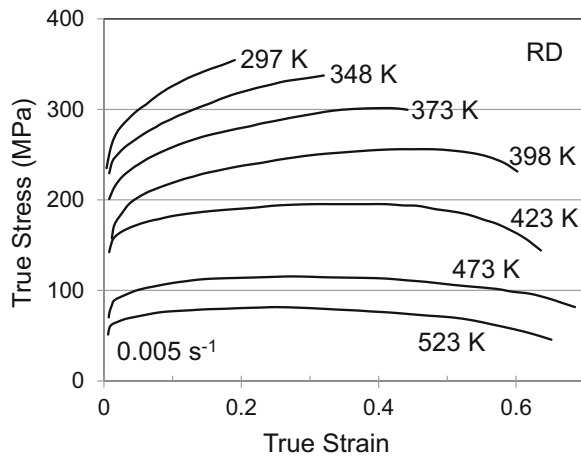
10.5 Magnesium Alloy AZ31

The magnesium alloy AZ31 is a general-purpose alloy with 3% Al and 1% Zn that can be used in the cast or forged (sheet or extrusion) form. The stress–strain behavior of this alloy as a function of test temperature and, to a lesser degree, strain rate has been extensively analyzed. Table 10.7 lists the sources of experimental data along with processing and testing conditions and other information for these three literature sources [7–10].

Figure 10.20 shows stress–strain curves from material oriented in the rolling direction (RD) reported by Agnew and Duygulu [8], while Fig. 10.21 shows stress–strain curves from “cast” material reported by Lukáč and Trojanová [9]. The stress levels in the former are considerably higher than in the latter, but note the substantial

Table 10.7 References, processing conditions, and testing conditions for deformation studies in magnesium alloy AZ31 that are further analyzed here

Reference	Material	Processing conditions	Testing conditions		
				Temperatures	Strain rates
Takuda et al. [7]	AZ31 B-O sheet	Annealed with 25 μm equiaxed grains	Tensile RD	423 K ($T_H = 0.46$) to 573 K ($T_H = 0.62$)	$\sim 0.001 \text{ s}^{-1}$ to $\sim 1 \text{ s}^{-1}$
Agnew and Duygulu [8]	AZ31 B sheet	O temper (1 h 345 C) with 14 μm equiaxed grains	Tensile RD, TD	RT to 523 K ($T_H = 0.57$)	0.005 s^{-1}
Lukáč et al. [9, 10]	AZ31 cast and sheet	Grain size not specified	Tensile RD, TD	298 K to 573 K ($T_H = 0.62$)	$3 \times 10^{-5} \text{ s}^{-1}$

Fig. 10.20 Stress–strain curves in magnesium alloy AZ31B reported by Agnew and Duygulu [8]

difference in strain rates between the two data sets. As expected the stress levels in material tested at the higher strain rate are higher than those tested at the lower strain rate. Figure 10.22 shows measurements reported by Takuda et al. [7] at 473 K and (nominal) strain rates of $\sim 0.001 \text{ s}^{-1}$ through 1 s^{-1} .

The strong temperature dependence and strain rate dependence of the stress–strain behavior is evident in Figs. 10.20, 10.21, and 10.22. These dependencies at zero strain are evaluated using the normalized yield stress plot (as in Figs. 10.12 and 10.18). Figure 10.23 shows this plot for the Takuda et al. measurements. While there is a lot of scatter, the trends are similar to those observed in pure magnesium (Fig. 10.18) and in pure cadmium (Fig. 10.12) in that data at high strain rates and/or low temperature (left side of the abscissa) trend downward below the model line. This was suggested earlier to reflect the contribution of deformation

Fig. 10.21 Stress–strain curves in magnesium alloy AZ31B reported by Lukáč and Trojanová [9]

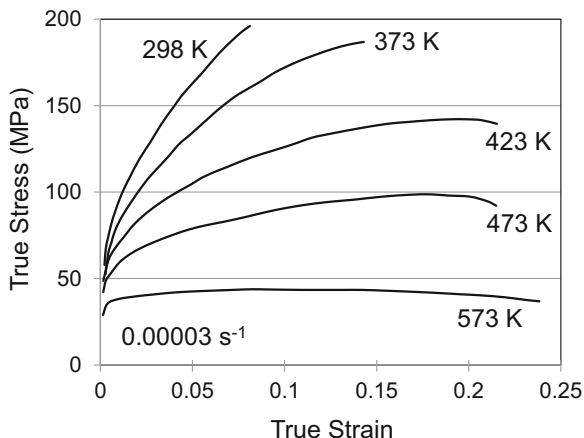
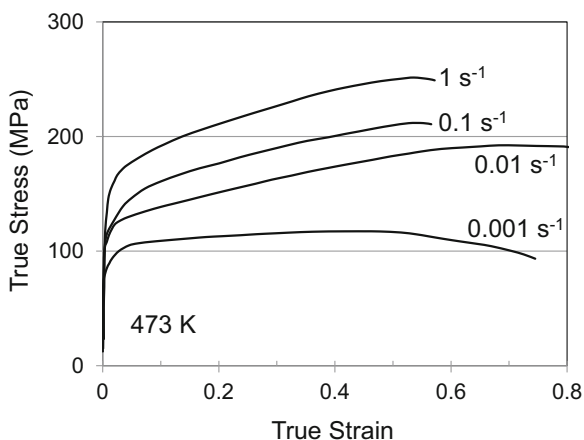


Fig. 10.22 Stress–strain curves in magnesium alloy AZ31B reported by Takuda et al. [7]



twinning. The model predictions² indicated by the dashed line in Fig. 10.23 are derived using a two-parameter model (Eq. 9.6 with obstacle populations “1” and “2” and $\hat{\sigma}_e = 0$) and the model constants given in Table 10.8.

The normalized activation energies for obstacle 1 and 2 are identical to the values used for pure magnesium in Table 10.5. The strength of obstacle sets #1—as specified with $\hat{\sigma}/\mu_o$ —was 0.03 for pure magnesium but increased to 0.08 for AZ31B. Similarly, the strength of obstacle set #2 was 0.005 for pure magnesium but increased to 0.0095 for AZ31B. The strong chemistry dependence on these values suggests neither of these obstacle sets is akin to a Peierls barrier in BCC

²Section 6.3 (see Fig. 6.4) introduced the difficulty of including model predictions as a single line in the presence of multiple obstacle populations. When the strain rate variations are small, the errors in using a single line are small; drawing a model line at an average strain rate eases comparison with measurements.

Fig. 10.23 Yield stress versus temperature and strain rate for the Takuda et al. measurements in magnesium alloy AZ31B

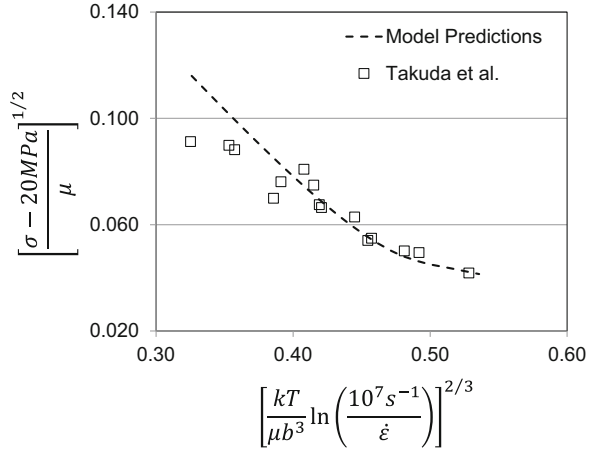


Table 10.8 Model parameters for the dashed line fit in Fig. 10.23 for magnesium alloy AZ31B

	Parameter	Value
Obstacle	σ_a (MPa)	20
	b (nm)	0.321
Obstacle 1	g_o	0.35
	$\dot{\epsilon}_o$ (s^{-1})	10^7
	p	0.5
	q	1.5
	$\hat{\sigma}/\mu_o$	0.08
Obstacle 2	g_o	1
	$\dot{\epsilon}_o$ (s^{-1})	10^8
	p	0.5
	q	1.5
	$\hat{\sigma}/\mu_o$	0.0095

metals since, for the latter, the strength of the Peierls barrier as well as the activation energy was independent of chemistry (see Tables 9.2 and 9.4).

Figure 10.24 adds the Agnew and Duygulu and Lukáč et al. measurements (at yield) to the Takuda et al. measurements in Fig. 10.23. A single model fit to the three data sets is shown as a dashed line. This line uses the same parameters in Table 10.8 except the values of the athermal stress are 20 MPa, 15 MPa, and 25 MPa for Takuda et al., Lukáč et al., and Agnew and Duygulu, respectively. The plot is busy, but one can argue that the single model fit describes these three data sets. Deviation from the model line at the lower values of the abscissa appears to vary somewhat between the three data sets. If this reflects the contribution of deformation twinning as argued earlier, then the variation in point of departure could reflect a grain size or texture difference.

For the case of Ti6Al-4V discussed in Sect. 10.10, a few prestrain/reload measurements are available. However, this is not the case with AZ31B. Analysis of the evolution behavior proceeds as described for UfKonel and as demonstrated for

Fig. 10.24 Yield stress versus temperature and strain rate for all of the measurements in magnesium alloy AZ31B. The athermal stress is varied to account for different grain sizes in the materials tested

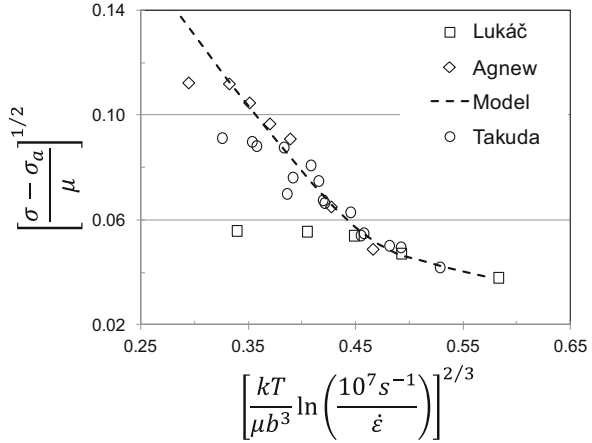
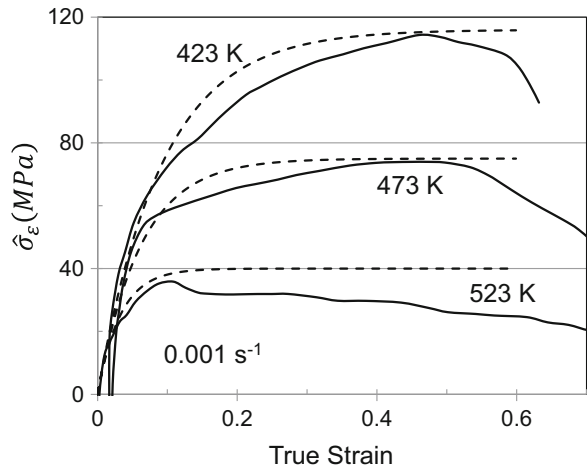


Fig. 10.25 Computed variation of $\hat{\sigma}_\epsilon$ with strain in magnesium alloy AZ31B for three test conditions reported by Takuda et al.



several BCC systems in Chap. 9 and for pure zinc in Sect. 10.1, pure cadmium in Sect. 10.3, and pure magnesium Sect. 10.4. This involves use of Eq. 9.7 (with obstacle “1” and “2” instead of “p” and “i”) and the model parameters specified in Table 10.8 to deduce the variation of $\hat{\sigma}_\epsilon$ with strain from each stress–strain curve. Care is needed when analyzing curves where the combination of temperature and strain rate are such that the actual stress falls beneath the predicted stress (e.g., the dashed line in Fig. 10.24).

Figure 10.25 shows the result for the Takuda et al. measurements at a nominal strain rate of 0.001 s^{-1} and temperatures of 423 K, 473 K, and 523 K. The dashed lines give fits to Eq. 6.28 with $\kappa = 1$ (with θ_{II} and $\hat{\sigma}_{es}$ values listed in Table 10.9). The result at 523 K indicates that dynamic recrystallization takes over at very low strain. Figure 10.26 shows the result for Takuda et al. measurements at 473 K and nominal

Table 10.9 Evolution parameters for the results in magnesium alloy AZ31B shown in Figs. 10.25, 10.26, 10.27, and 10.28 and for the other stress–strain curves reported by the three teams

Investigator	Temperature (K)	Strain rate (s ⁻¹)	θ_{II} (MPa)	$\hat{\sigma}_{\epsilon s}$ (MPa)	$T_i \ln(10^7 s^{-1}/\dot{\epsilon})$
Takuda et al. [7]	423	0.75	1300	180	6940
	473	0.75	1250	165	7760
	523	0.97	1250	148	8440
	573	0.94	1300	106	9270
	423	0.00099	1250	116	10,800
	473	0.0013	1200	75	8860
	523	0.0017	1200	40	11,800
	573	0.0011	1200	8	13,100
	423	0.0080	1250	180	9630
	473	0.012	1250	162	9720
	523	0.011	1250	101	10,800
	573	0.012	1250	50	11,800
	423	0.0088	1300	140	7850
	473	0.069	1300	145	8890
	523	0.103	1300	120	9620
573	0.098	1300	84	10,600	
Agnew and Duygulu [8]	348	0.005	1300	160	7450
	373	0.005	1300	158	7990
	398	0.005	1300	142	8520
	423	0.005	1300	95	9060
	473	0.005	1300	40	10,100
Lukáč et al. [9]	373	0.00003	1400	195	9900
	423	0.00003	1350	145	11,200
	473	0.00003	1300	96	12,600
	573	0.00003	1300	9	15,200

Fig. 10.26 Computed variation of $\hat{\sigma}_{\epsilon}$ with strain in magnesium alloy AZ31B for test results reported by Takuda et al. at three strain rates and a temperature of 473 K

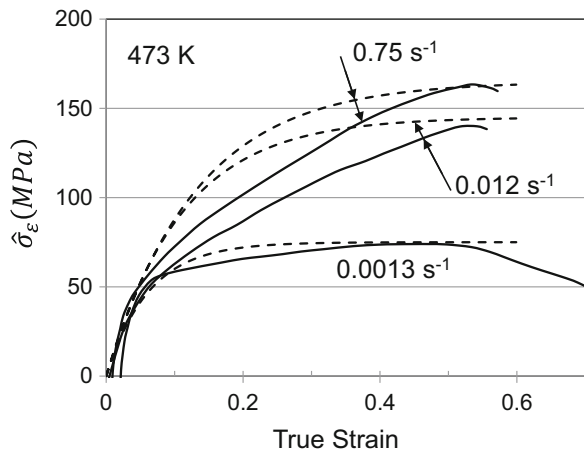


Fig. 10.27 Computed variation of $\hat{\sigma}_\epsilon$ with strain in magnesium alloy AZ31B for test results reported by Agnew and Duygulu

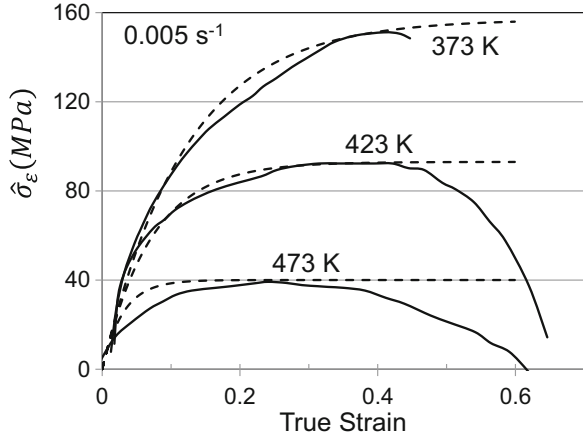
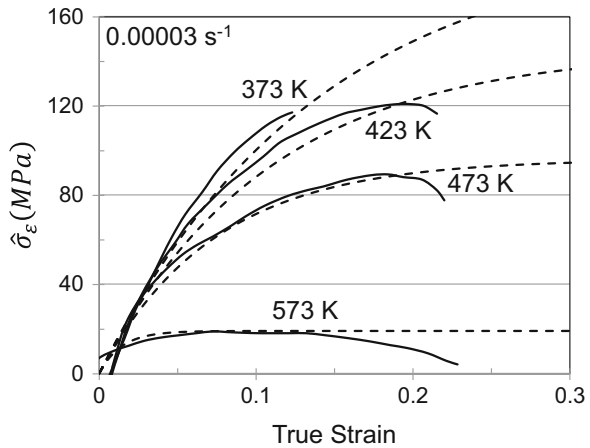


Fig. 10.28 Computed variation of $\hat{\sigma}_\epsilon$ with strain in magnesium alloy AZ31B for test results reported by Lukáč et al.



strain rates from 0.001 s^{-1} to 1 s^{-1} . Evident at the two lowest temperature results in Fig. 10.25 but even more clearly at the two highest strain rate results in Fig. 10.26 is the lack of agreement between the shape of the hardening curve and the shape modeling using Eq. 6.28. This is identical to what was shown in Fig. 10.5 for pure zinc. It was argued there that this evidences the contribution of deformation twinning. Figure 10.27 shows the same plot for the Agnew and Duygulu measurements. In this case the curves more closely follow the form of Eq. 6.28 (the dashed lines).

Three results for measurements by Lukáč et al. are shown in Fig. 10.28. In this case, the dashed curves underpredict the deduced variation of $\hat{\sigma}_\epsilon$ with strain. Better agreement is possible with higher values of θ_{II} (see Table 10.9), but the resulting values of θ_{II} would be much higher than those used for the Takuda et al. and Agnew and Duygulu data sets.

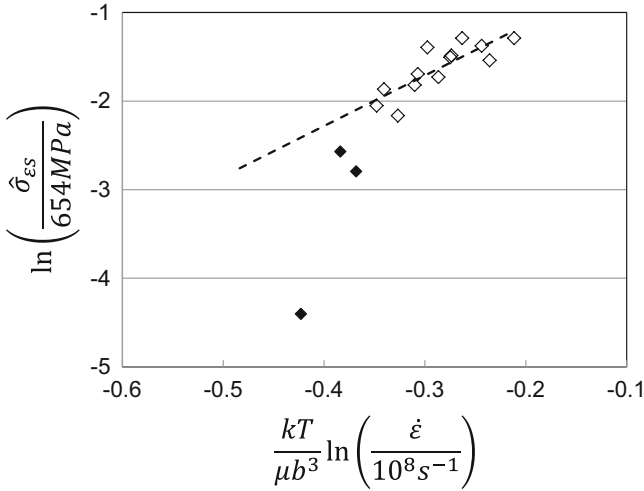


Fig. 10.29 Saturation threshold stress versus temperature and strain rate for the Takuda et al. data set in magnesium alloy AZ31B on coordinates consistent with Eq. 6.28. The filled-in symbols are those with $T_i \ln(10^7 s^{-1}/\dot{\epsilon})$ values in italics in Table 10.9

The dashed lines in Figs. 10.25, 10.26, 10.27, and 10.28 are drawn according to Eq. 6.28 with $\kappa = 1$. Table 10.9 lists values of θ_{II} and $\hat{\sigma}_{\epsilon_s}$ for each of the test conditions reported by Takuda et al., Agnew and Duygulu, and Lukáč et al. The right-hand column lists the value of the parameter $T_i \ln(10^7 s^{-1}/\dot{\epsilon})$. Several of these values are italicized. Generally, they represent test conditions with high values of the listed parameter, and, generally, they represent test results that do not fit the lower-temperature trend represented by Eq. 6.28 (to be described below). Note that a single value of $T_i \ln(10^7 s^{-1}/\dot{\epsilon})$ does not uniquely separate the low-temperature from the high-temperature behavior for each of the data sets. Further inspection suggests that the strain rate dependence of the factor that might uniquely define this separation is larger than modeled using $T_i \ln(10^7 s^{-1}/\dot{\epsilon})$.

The temperature and strain rate dependence of the saturation threshold stress $\hat{\sigma}_{\epsilon_s}$ for the Takuda et al. data set is shown in Fig. 10.29—the evolution plot—using coordinates consistent with Eq. 6.26. The filled-in data points are the test conditions with the italicized values of the parameter $T_i \ln(10^7 s^{-1}/\dot{\epsilon})$. While the open signals demonstrate considerable scatter, a dashed line describes these results, with $\hat{\sigma}_{\epsilon_{SO}} = 654$ MPa. The inverse of the slope of this line gives $g_{\epsilon_{SO}} = 0.175$. Note that there is a high degree of uncertainty in $\hat{\sigma}_{\epsilon_{SO}}$ and $g_{\epsilon_{SO}}$. Including just one more datum point in the fit (the test at 573 K and a strain rate of $0.012 s^{-1}$) gives a best-fit line with $\hat{\sigma}_{\epsilon_{SO}} = 902$ MPa and $g_{\epsilon_{SO}} = 0.145$. Excluding this test point, however, gives a result that is more consistent with the other measurements.

All of the data points for the three data sets are included in Fig. 10.30. Once again, the filled-in data points represent test conditions with italicized values of $T_i \ln(10^7 s^{-1}/\dot{\epsilon})$ in Table 10.9. In each case, the filled-in data points trend downward from the dashed line, which is the same line drawn in Fig. 10.29. The three data

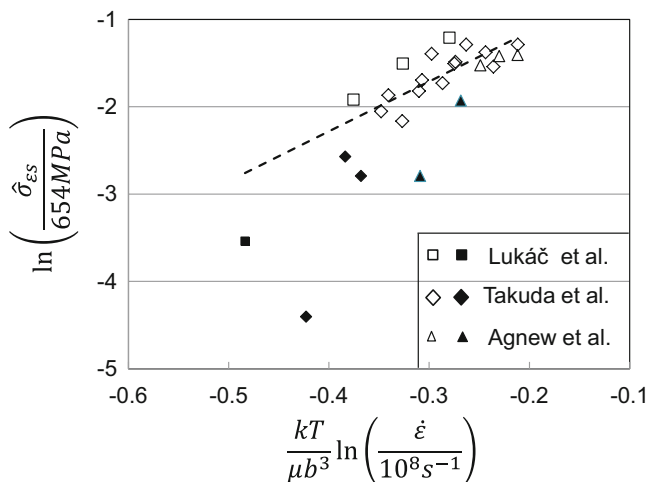


Fig. 10.30 Saturation threshold stress versus temperature and strain rate for all of the measurements in magnesium alloy AZ31B on coordinates consistent with Eq. 6.28. The filled-in symbols are those with $T_i \ln(10^7 s^{-1}/\dot{\epsilon})$ values in italics in Table 10.9

points from the Agnew and Duygulu tests fall right in line with those from the Takuda et al. test conditions. The three data points from the Lukáč et al. test conditions fall slightly above the dashed line, but the slope through the line is quite similar to that represented by the dashed line.

The data points from the Suzuki et al. data set in pure magnesium summarized in Table 10.6 (not italicized) are included with the measurements in AZ31B in Fig. 10.31. For this plot the filled-in symbols in Fig. 10.30 have been excluded. As described in Sect. 10.4, the Suzuki et al. data points exhibit considerable scatter. However, one can argue that these points hover about the dashed line. In the nickel plus carbon alloys described in Sect. 8.8 and the copper plus aluminum alloys described in Sect. 8.10, a variation of dislocation storage with chemistry was observed (see Figs. 8.38 and 8.44). The results in Fig. 10.31 suggest that the magnesium alloy AZ31B exhibits dislocation storage that is similar to that observed in pure magnesium. However, the alloy dependence of storage—if any—could also be within the scatter evident in this figure.

Inspection of the column of values of θ_{II} in Table 10.9 suggests no definitive strain rate dependence according to Eq. 6.29. Accordingly, A_1 and A_2 in Eq. 6.29 are taken as zero and $A_1 = 1250$ MPa.

Summarizing the results in magnesium, the thermal activation parameters for pure magnesium are listed in Table 10.5, and those for AZ31B are listed in Table 10.8. Note that only the values of $\hat{\sigma}_1/\mu_0$ and $\hat{\sigma}_2/\mu_0$ are found to vary between pure magnesium and the alloy. (Recall that $\sigma_a = 20$ MPa, 15 MPa, and 25 MPa for the Takuda et al., Lukáč et al., and Agnew and Duygulu materials, respectively.) As a first approximation, the evolution behavior is modeled for both pure magnesium and the alloy with the model parameters described above, which are listed in Table 10.10.

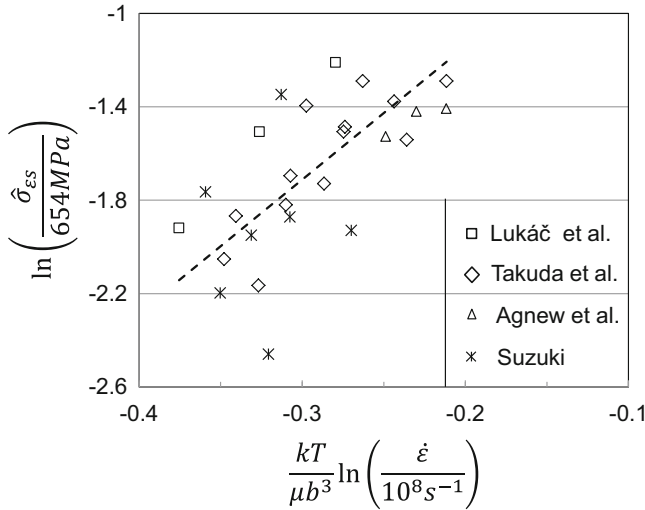


Fig. 10.31 Saturation threshold stress versus temperature and strain rate for all of the measurements in magnesium alloy AZ31B along with the measurements of Suzuki et al. in pure magnesium

Table 10.10 Evolution model parameters for both pure magnesium and magnesium alloy AZ31B

Parameter	Equation	Value	Units
k	6.28	1	
$\hat{\sigma}_{ESO}$	6.26	654	MPa
g_{ESO}		0.175	
$\dot{\epsilon}_{ESO}$		10^8	s^{-1}
A_o	6.29	1250	MPa
A_1		0	
A_2		0	

With these model parameters, Figs. 10.32 and 10.33 compare measured (Suzuki) and predicted stress–strain curves at 473 K and 573 K in pure magnesium. At 473 K the agreement at the lower strain rate is good up to a strain of ~ 0.15 , where the curves deviate sharply. This behavior was also observed in Fig. 10.19, and it was suggested here that dynamic recrystallization may be the source of the divergence. The curve at the higher strain rate agrees to larger strains, although the measured curve does not fall off as rapidly (due to adiabatic heating) as the predicted curve. This may reflect heat transfer conditions that are not ideal at this strain rate such that the temperature is not rising as rapidly as predicted. The measurement and prediction agree closely for the test at a strain rate of $10\ s^{-1}$ at 573 K in Fig. 10.33. At this temperature, however, the test at the lower strain rate does not match the predicted behavior. Note that this test condition is one of the italicized results in Table 10.6, indicating a high-temperature behavior not described using Eq. 6.26.

Measured and predicted stress–strain curves at three temperatures tested by Agnew and Duygulu in AZ31B are shown in Fig. 10.34. Agreement is best at the lower temperature but is poor at the highest temperature. As in pure magnesium, the

Fig. 10.32 Comparison of measured (Suzuki data set) and predicted stress–strain curves in pure magnesium at 473 K and two strain rates

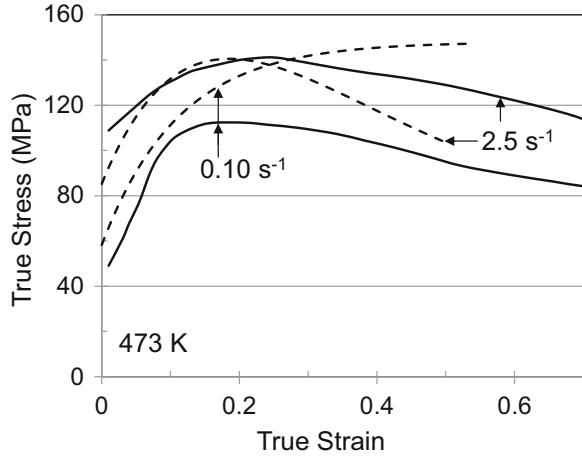


Fig. 10.33 Measured (solid lines) by Suzuki et al. and predicted stress–strain curves at 573 K and two strain rates

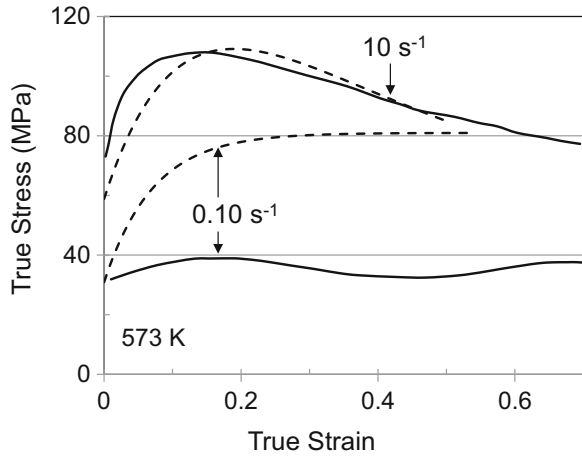
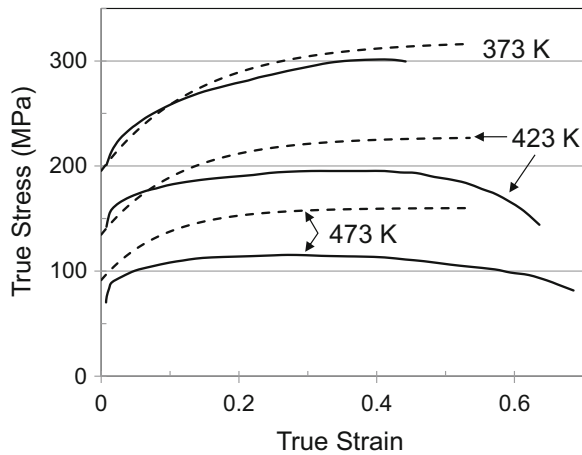


Fig. 10.34 Measured (solid lines) by Agnew and Duygulu [8] and predicted stress–strain curves at three test temperatures



test condition at 473 K in the Agnew and Duygulu data set is one that is italicized in Table 10.9. These comparisons validate that the low-temperature behavior is adequately described using the model formulism developed here. The high-temperature behavior shows consistent and easily recognized deviations from the low-temperature behavior.

10.6 Pure Zirconium

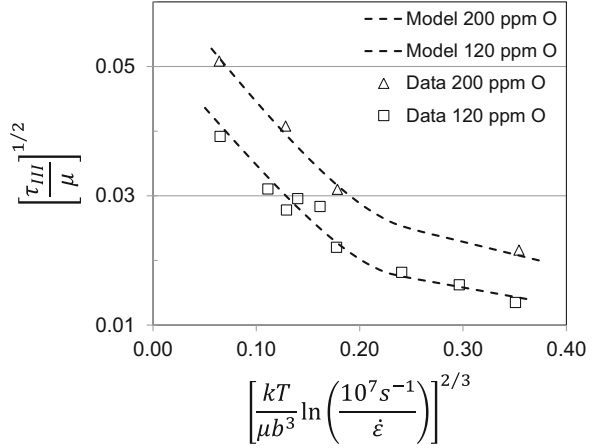
Zirconium is a higher melting point HCP metal than zinc, cadmium, or magnesium (see Table 10.1). It also is a critically important nuclear material in that the zircaloy alloy Zircaloy-2 (Zr—1.5Sn—0.15Fe—0.1Cr—0.05Ni) is widely used as nuclear fuel cladding due to its combination of good corrosion resistance and low neutron absorption [11]. The high melting point (2128 K) implies that the deformation at temperatures even well above room temperature is in the low-temperature regime. Pure zirconium has an HCP structure (alpha) at temperatures below 1143 K ($T_H = 0.538$); above this temperature a transformation to the BCC (beta) structure occurs. The industrial importance of zirconium alloys has led to several fundamental studies of deformation in single and polycrystalline pure zirconium. Table 10.11 lists several data sets that are considered here [12–16].

Figure 10.35 gives the variation of the stress at the onset of stage III hardening (for prismatic slip) as a function of temperature and strain rate for the Akhtar and Teghtsoonian measurements for the high- and low-purity materials. A distinct

Table 10.11 References and test conditions for yield stress and stress–strain measurements in pure zirconium

Reference	Material	Processing conditions	Testing conditions		
				Temperatures	Strain rates
Akhtar and Teghtsoonian [12]	Crystal bar Zr	Annealed single crystals; 120 ppm O and 200 ppm O	Tensile YS measurements	78 K to 623 K ($T_H = 0.293$)	Mostly $1.66 \times 10^{-4} \text{ s}^{-1}$, plus: 0.0044 s^{-1} , 0.18 s^{-1} , 17 s^{-1}
Soo and Higgins [13]	Iodide Zr	Arc-melted single crystals; 135 ppm O to 2000 ppm O	Tensile YS measurements	77 K to 473 K ($T_H = 0.222$)	$1.11 \times 10^{-4} \text{ s}^{-1}$
Buch [14]	Iodide Zr (99.99% pure)	Annealed polycrystals; grain size not specified	Tensile YS measurements	293 K to 873 K ($T_H = 0.410$)	Not specified; assume 0.001 s^{-1}
Chen and Gray [15]	Crystal bar Zr (99.95% pure)	Annealed polycrystals; 25 μm equiaxed grain size [15]	Compression stress–strain curves	76 K to 956 K ($T_H = 0.449$)	0.001 s^{-1} to $\sim 3000 \text{ s}^{-1}$

Fig. 10.35 Yield stress versus temperature and strain rate and model predictions for single-crystal zirconium measurements by Akhtar et al. at two oxygen concentrations



curvature in this plot is evident, which warrants application of a two-parameter model (Eq. 6.14). The model predictions are calculated using the parameters listed in Table 10.12. The values on the ordinate of Fig. 10.35 are small in magnitude when compared, for instance, to those in pure magnesium (see Fig. 10.18), but recall that shear stresses are plotted in Fig. 10.35, whereas tensile stresses are plotted in Fig. 10.18.

The Soo and Higgins [13] measurements of τ_{CRSS} for prismatic slip versus temperature are shown in Fig. 10.36 for oxygen concentrations of 135 ppm, 655 ppm, and 2000 ppm.³ The model predictions are based on the parameters listed in Table 10.12 with the values of $\hat{\tau}_{CRSS_1}/\mu_o$ and $\hat{\tau}_{CRSS_2}/\mu_o$ listed in Table 10.13. The Soo and Higgins results show, particularly at the highest oxygen concentration, a region of higher stress levels than predicted at mid-scale values of the abscissa. These investigators analyzed deformation in pure zirconium as a transition between two mechanisms. At low temperatures, they report that the interactions of dislocations with (single) oxygen atoms were rate controlling but at high temperatures the controlling mechanism shifted to the nonconservative motion of vacancy jogs in screw dislocations. (Note at the highest temperatures of these measurements the homologous temperature only reaches 0.22.) According to these investigators, this scenario was consistent with the shape of the stress versus temperature curve and, in particular, the first plateau at mid-scale in Fig. 10.36 followed by a decreasing stress level with increasing temperature. Interestingly, Akhtar and Teghtsoonian did not observe higher stresses at mid-scale in the lower oxygen-containing materials they investigated. The modeling approach adopted here differs from that proposed by Soo and Higgins in that additive mechanisms are proposed. As discussed in Sect. 10.2

³The stress values for the Akhtar and Teghtsoonian measurements (τ_{111}) for 120 ppm C material and the stress values for the Soo and Higgins measurements (τ_{CRSS}) for 135 ppm C are comparable in magnitude, which is sensible since both investigations specified the stress as that for predominantly prismatic slip.

Table 10.12 Model parameters for yield stress correlation and evolution equations established for Akhtar and Teghtsoonian [12] and Chen and Gray [15] measurements in single-crystal and polycrystalline zirconium

Obstacle	Parameter	Akhtar and Teghtsoonian		Chen and Gray
		ppm O	200	50
	σ_a (MPa)	0		20
	b (nm)	0.323		
Obstacle 1	g_o	0.15		
	$\dot{\epsilon}_o$ (s ⁻¹)	10 ⁸		
	p	0.5		
	q	1.5		
	$\widehat{\tau}_{III}/\mu_o$	0.0022	0.0029	0.044 ^a
Obstacle 2	g_o	1		
	$\dot{\epsilon}_o$ (s ⁻¹)	10 ⁸		
	p	0.5		
	q	1.5		
	$\widehat{\tau}_{III}/\mu_o$	0.0006	0.0012	0.005 ^a
Evolution parameters				
Equation 6.28	k	Units		1
Equation 6.26	$\widehat{\sigma}_{ESO}$	MPa		520
	g_{ESO}			0.28
	$\dot{\epsilon}_{ESO}$	s ⁻¹		10 ⁸
Equation 6.29	A_o	MPa)		8000
	A_1	MPa ($\dot{\epsilon}$ in s ⁻¹)		30
	A_2	MPa s ^{-1/2}		12

^aListed is $\widehat{\sigma}/\mu_o$

Fig. 10.36 Yield stress versus test temperature at model predictions for single-crystal zirconium measurements by Soo and Higgins [13] at three oxygen concentrations

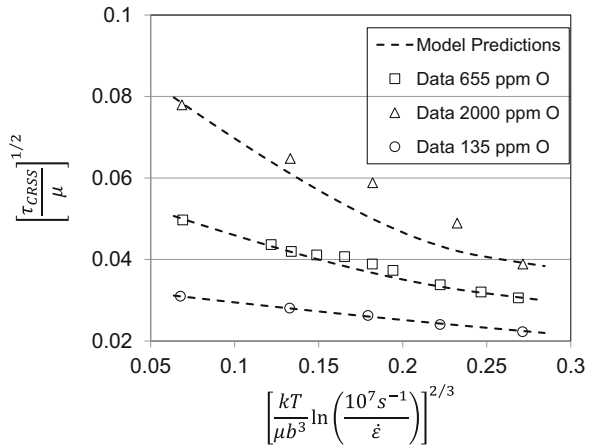
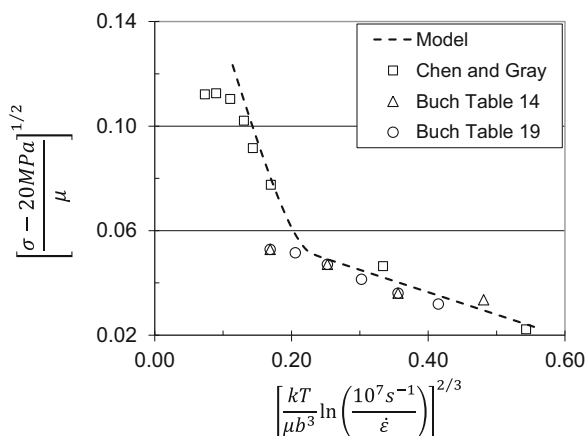


Table 10.13 Summary of the threshold stress values in zirconium determined for obstacle populations 1 and 2 for the single-crystal and polycrystal data sets

Data set	Oxygen content	Obstacle 1	Obstacle 2
Akhtar and Teghtsoonian [12]	120 ppm	$\hat{\tau}_{III}/\mu_o = 0.0022$	$\hat{\tau}_{III}/\mu_o = 0.0006$
	200 ppm	$\hat{\tau}_{III}/\mu_o = 0.0029$	$\hat{\tau}_{III}/\mu_o = 0.0012$
Soo and Higgins [13]	135 ppm	$\hat{\tau}_{CRSS}/\mu_o = 0.00012$	$\hat{\tau}_{CRSS}/\mu_o = 0.00105$
	655 ppm	$\hat{\tau}_{CRSS}/\mu_o = 0.0016$	$\hat{\tau}_{CRSS}/\mu_o = 0.00195$
	2000 ppm	$\hat{\tau}_{CRSS}/\mu_o = 0.0065$	$\hat{\tau}_{CRSS}/\mu_o = 0.0032$
Chen and Gray [15]	50 ppm	$\hat{\sigma}/\mu_o = 0.044$	$\hat{\sigma}/\mu_o = 0.005$

Fig. 10.37 Yield stress versus temperature and strain rate for Chen and Gray measurements in pure polycrystalline zirconium [15] and for Buch data (temperature dependence only) in pure polycrystalline pure zirconium [14]



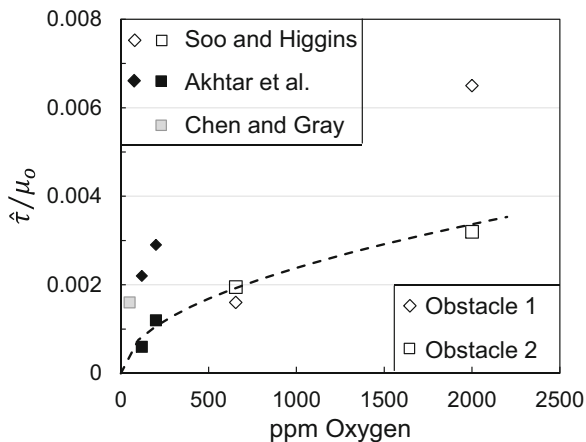
(see the discussion regarding Fig. 10.10), it is difficult to envisage a combination of mechanisms that give the shape of the dependencies (the mid-scale high stress levels) shown in Fig. 10.36.

Figure 10.37 gives the variation of yield stress with temperature and strain rate for the two polycrystalline data sets in Table 10.11. An athermal stress of 20 MPa was selected. Note that both data sets exhibit a peak stress with decreasing values of the abscissa and that the value of the abscissa where this occurs (or, alternatively, the value of the peak stress) varies between the Chen and Gray and Buch data sets. The model predictions were made with the same model parameters as listed in Table 10.12, except that $\sigma_a = 20$ MPa, $\hat{\sigma}_1/\mu_o = 0.044$, and $\hat{\sigma}_2/\mu_o = 0.005$. These model parameters, along with evolution equation model parameters discussed in Sect. 10.7, are included in Table 10.12.

It is interesting that a common set of model parameters—including normalized activation energies for both obstacle populations—enables agreement between model predictions and measurements in the pure zirconium materials listed in Table 10.11. Table 10.13 summarizes the results.

Note in Table 10.13 that the oxygen concentration appears to have a more consistent influence on the threshold stress of obstacle population 2 than of obstacle population 1. Assuming as argued above that $\tau_{III} \cong \tau_{CRSS}$, Fig. 10.38 shows the

Fig. 10.38 Variation of the threshold stress with oxygen concentration in zirconium for the single-crystal data sets



variation of the threshold stresses with oxygen content for the single-crystal results. The solid symbols represent the Akhtar and Teghtsoonian data set. Except for the highest oxygen-containing alloy for the Soo and Higgins data set, the variation of $\hat{\tau}_1$ with oxygen content is uncertain. If the Chen and Gray data point ($\hat{\sigma}/\mu_o = 0.044$) is included in the discussion, e.g., by dividing the normal stress by a factor of 3, it can be concluded that there is a poor correlation between the threshold stress of obstacle population 1 and the oxygen content. On the other hand, Fig. 10.38 shows a possible correlation (in fact, as shown with the dashed line close to a square root dependence) between the threshold stress of obstacle population 2 and the oxygen concentration. The Chen and Gray data point (partially filled square; $\hat{\sigma}/\mu_o = 0.005$; $\hat{\tau}/\mu_o \approx 0.0016$) is perhaps a little high for an oxygen concentration of 50 ppm, but it agrees fairly well with the results for the single crystals.

It is concluded that a two-obstacle model with the model parameters listed in Table 10.12 describes the temperature and strain rate dependence of the yield stress in annealed pure zirconium single and polycrystals. One-obstacle population (referred to as population 2) exhibits a strong dependence on oxygen concentration and is characterized by a normalized activation energy of 1. The other obstacle population is characterized by a much smaller normalized activation energy (0.15) indicating a stronger contribution to the temperature and strain rate dependence—particularly at low temperatures (and/or high strain rates). This obstacle population appears to have a strong dependence on total chemistry.

10.7 Structure Evolution in Zirconium

Chen and Gray [15] reported full stress–strain curves in pure zirconium over a wide range of temperature and strain rates (see Table 10.11). Strain hardening—or structure evolution—is analyzed using Eq. 9.7, with obstacle “1” and “2” instead

Fig. 10.39 Computed variation of $\hat{\sigma}_\epsilon$ with strain for two of the results reported by Chen and Gray [15] at a strain rate of 0.001 s^{-1} along with the fit to Eq. 6.28

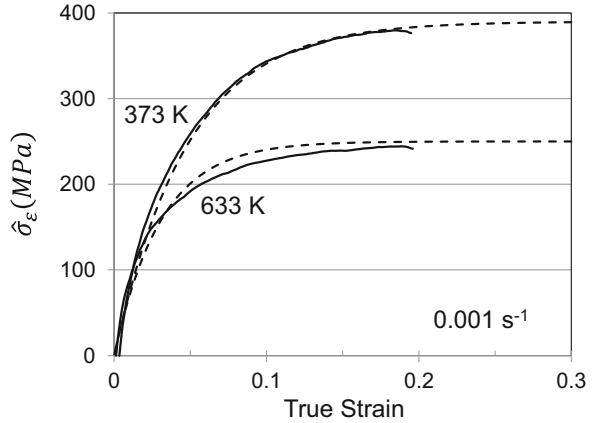


Table 10.14 Tabulation of the model parameters (Eq. 6.28) for each of the stress–strain curves reported by Chen and Gray [15]

Initial temperature (K)	Final temperature (K)	Strain rate (s^{-1})	θ_{II} (MPa)	$\hat{\sigma}_{\epsilon_s}$ (MPa)
298	298	0.001	8000	360
373	373	0.001	8000	390
333	333	0.001	8000	375
295	295	0.10	8000	270
423	423	0.001	8000	345
633	633	0.001	8000	250
956	956	0.001	7500	98
573	633	2800	8500	430
473	539	2500	9000	350
373	440	2500	9000	435
298	379	2800	–	–
76	165	2800	–	–

The italicized test result and the results at the highest strain rate and at 76 K and 298 K are highly suspect

of “*p*” and “*i*” in an identical manner as was demonstrated in pure magnesium (Fig. 10.19). The parameters listed in Table 10.12 are required (along with the parameters for s_ϵ specified in Table 9.7) to compute the variation of $\hat{\sigma}_\epsilon$ with strain. Figure 10.39 shows the result for tests at 373 K and 633 K and a strain rate of 0.001 s^{-1} . The dashed lines are drawn according to Eq. 6.28 with the model constants described below. For the test conditions in Fig. 10.39 and for many of the test conditions in the Chen and Gray data set, Eq. 6.28 provides a good description of the evolution trend.

Table 10.14 summarizes the analysis results for all of the Chen and Gray measurements. Included are values of θ_{II} and $\hat{\sigma}_{\epsilon_s}$ from Eq. 6.28 (with $\kappa = 1$) for each of the test conditions. Several of the values of $\hat{\sigma}_{\epsilon_s}$ are omitted because Eq. 6.28

Fig. 10.40 The evolution plot in pure zirconium showing the variation of $\hat{\sigma}_{es}$ with temperature and strain rate on coordinates consistent with Eq. 6.26. The dashed line is the model fit

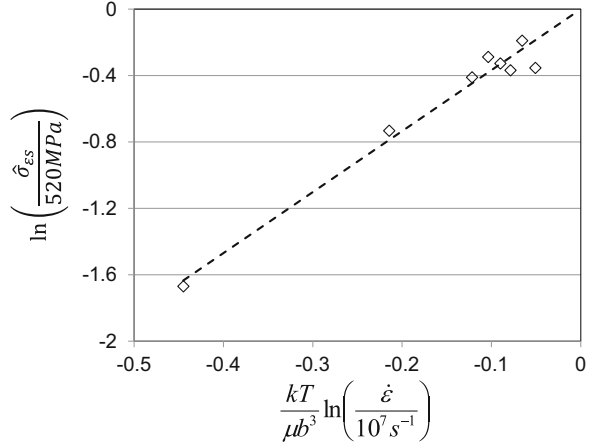
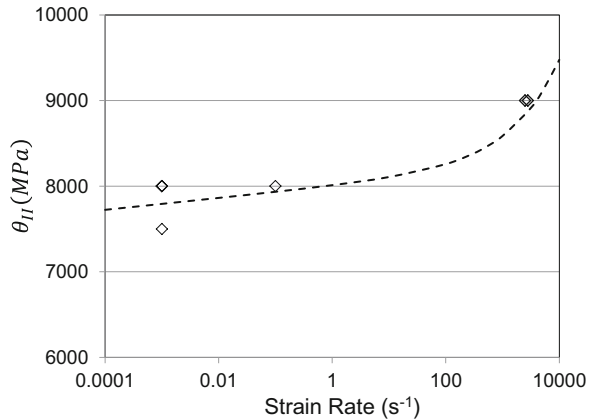


Fig. 10.41 Variation of θ_{II} with strain rate in pure polycrystalline zirconium



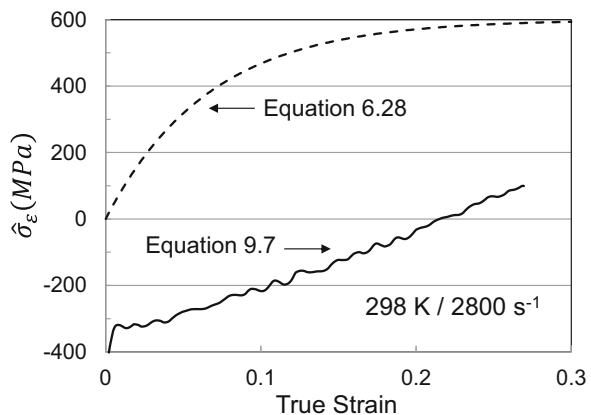
provides such a poor fit (see Sect. 10.7.1). Figure 10.40 shows the variation of the saturation threshold stress $\hat{\sigma}_{es}$ with test temperature and strain rate using the coordinates consistent with Eq. 6.26. The dashed line is a fit according to Eq. 6.26 with $\hat{\sigma}_{eso} = 520$ MPa. The slope of the line gives $g_{eso} = 0.28$. The variation of θ_{II} with strain rate for the results in Table 10.14 is shown in Fig. 10.41. The dashed line in this figure is drawn according to Eq. 6.29 with $A_0 = 8000$ MPa, $A_1 = 30$ MPa (when strain rate is in units of s^{-1}), and $A_2 = 12 \text{ MPa s}^{-1/2}$. As has been the case for many of the similar plots presented in this monograph, there are too few points at different strain rates to establish the constants A_1 and A_2 . However, the dashed line can be forced to fit the data points using values of these constants that are similar to those used in other materials.

10.7.1 The Influence of Deformation Twinning on Hardening

Whereas Eq. 6.28 with Eq. 6.26 provides a good description of hardening for many of the test conditions listed in Table 10.14, these equations produced poor fits for several test conditions. In particular, two problems emerge in analyzing the stress–strain data using Eq. 9.7. The first is not related to the shape of the curve but is related to the deviation from the model predictions at the left-hand side of the abscissa in Fig. 10.37. The s -terms in Eq. 9.7 (and the test temperature and strain rate) define the model predictions in Fig. 10.37. No model has been proposed to describe the observed deviations from model behavior, e.g., due to deformation twinning. Thus, application of Eq. 9.7 results in the subtraction of stresses that are too large from the total stress. Figure 10.42 illustrates this for the test at 298 K and a strain rate of 2800 s^{-1} . The solid curve is the application of Eq. 9.7 as described above. Included in Fig. 10.42 is the prediction based on Eq. 6.28 with the constants listed above. Because this is a test at a high strain rate, the temperature is allowed to increase according to Eq. 6.32. As shown in Fig. 10.42, this application of Eq. 9.7 gives negative $\hat{\sigma}_\varepsilon$ values, and the differences between the analyzed $\hat{\sigma}_\varepsilon$ values and the predicted curve are significant.

It is evident that Eq. 9.7 is invalid when deformation twinning is active. The data points at the far-left side of Fig. 10.37 indicate that the temperature and strain rate dependence of the yield stress decreases dramatically from that at conditions above the transition “point” (which is the combination of the temperature and strain rate at the point on the abscissa where the data points diverge from the dashed line). The kinetics active during deformation twinning were assessed by Meyers et al. in a series of metals and alloys [17]. These authors summarized experimental measurements of the twinning stress as a function of temperature, and they propose a dislocation pileup model (in BCC metals) to predict how deformation kinetics change when deformation transitions from slip to twinning. The model indeed

Fig. 10.42 Computed variation of $\hat{\sigma}_\varepsilon$ with strain for the test result of Chen and Gray at 298 K and a strain rate of 2800 s^{-1} showing the result using Eq. 9.7 and the “expected” curve from Eq. 6.28



predicts a weak temperature dependence of the twinning stress. They also predict that the twinning stress varies strongly with strain rate.

To a first approximation, it can be assumed that twinning is an athermal deformation mechanism (although this may be inconsistent with the limited knowledge of the strain rate dependence). In this case, the yield stress simply becomes the twinning stress σ_t :

$$\sigma = \sigma_t. \quad (10.2)$$

When strain hardening along with the temperature dependence of the shear modulus (as in Eq. 6.8) are included and this equation is rewritten in terms of the mechanical threshold stress, Eq. 10.2 becomes as follows:

$$\frac{\sigma}{\mu} = \frac{\sigma_a}{\mu} + \frac{\sigma_t}{\mu} + s_\varepsilon(\dot{\varepsilon}, T) \frac{\hat{\sigma}_\varepsilon}{\mu_o} \quad (10.3)$$

It is assumed in Eq. 10.3 that the twinning stress is independent of strain. There is no hard evidence to support this assertion. Solving for $\hat{\sigma}_\varepsilon$ gives the following:

$$\hat{\sigma}_\varepsilon = \frac{\mu_o}{s_\varepsilon} \left[\left(\frac{\sigma - \sigma_a}{\mu} \right) - \frac{\sigma_t}{\mu} \right] \quad (10.4)$$

Equation 10.4 replaces Eq. 9.7 in assessing the variation of $\hat{\sigma}_\varepsilon$ with strain. Figure 10.43 shows the predicted variation for the tests at 76 K and 298 K and a strain rate of 2800 s^{-1} . For this prediction the twinning stress was set to 455 MPa for the test at 298 K and 405 MPa for the test at 76 K, which are the values that force $\hat{\sigma}_\varepsilon$ to begin at zero. Whereas $\hat{\sigma}_\varepsilon$ in Fig. 10.42 (298 K and a strain rate of 2800 s^{-1}) was predicted to increase by ~ 400 MPa over the 0.30 strain range of the test, this increasing using Eq. 10.4 is only ~ 200 MPa. A second observation in Fig. 10.43 is the shape of the hardening curves, which differs from that typically observed

Fig. 10.43 Computed variation of $\hat{\sigma}_\varepsilon$ with strain using Eq. 10.4 for test results measured by Chen and Gray at a strain rate 2800 s^{-1} and temperatures of 76 K and 298 K

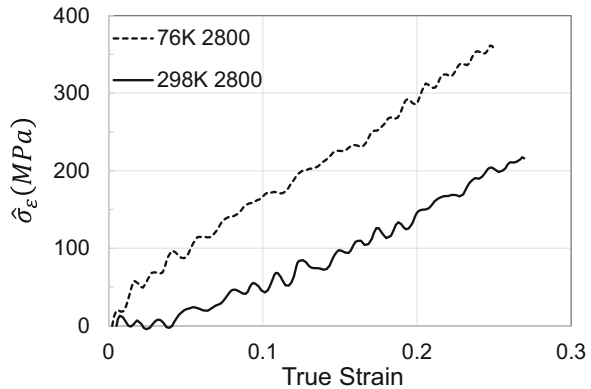
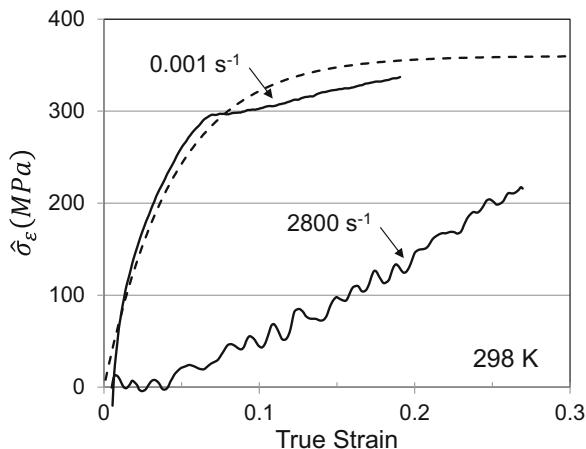


Fig. 10.44 Computed variation of $\hat{\sigma}_\varepsilon$ with strain for the Chen and Gray measurements at 298 K and strain rates of 0.001 s^{-1} and 2800 s^{-1}



(e.g., see Fig. 10.39). The shape of this curve is similar to that observed in Mannan and Rodriguez test in cadmium (Fig. 10.14) and the Takuda et al. measurements in AZ31B (Fig. 10.26).

Figure 10.44 includes the deduced curve from Fig. 10.43 (2800 s^{-1}) along with the result for the test at 298 K and a strain rate of 0.001 s^{-1} . At the lower strain rate, the behavior follows that modeled using Eq. 6.28 up to a strain of ~ 0.07 when the curve dips below the model curve (similarly to the trend observed in Fig. 9.41 in vanadium). At the high strain rate, the hardening is well below that at the lower strain rate. Also, the hardening is shown to vary almost linearly with strain, which is counter to that expected for dislocation storage as described using Eq. 6.28. It is quite possible that the observations in Fig. 10.44 at the higher strain rate are unique signatures of the effects of deformation twinning.

Assessing whether this difference could arise from effective grain size reduction due to mechanical twinning requires knowledge of the Hall-Petch behavior (Eq. 3.9) of this material. Ramani and Rodriguez [18] measured the grain size dependence of the yield stress (and strain-hardening behavior) of pure zirconium at 77 K. Taking $k_d \sim 17.2 \text{ MPa}\cdot\text{mm}^{1/2}$ from their results, a stress increase of 200 MPa (the increase in the stress level for the high strain rate test over the 0.25 strain level) is possible in a material with starting grain size of $25 \mu\text{m}$ if the effective grain size is reduced to $\sim 3 \mu\text{m}$. While this seems to be a large effective reduction in grain size, the characterization of zirconium deformed at 76 K (at quasi-static strain rates) by McCabe et al. [19] showed considerable primary and secondary (finer) twinning. It seems plausible that grain size reduction by extensive deformation twinning could explain the strain-hardening rates in zirconium at high strain rates and low temperatures.

Analysis of measurements in pure zirconium has demonstrated that the basic MTS model formulation provides a good foundation for deformation in this material for conditions where deformation twinning is not dominant. Indications that twinning is contributing to strain accommodation are evident in the plot of yield stress

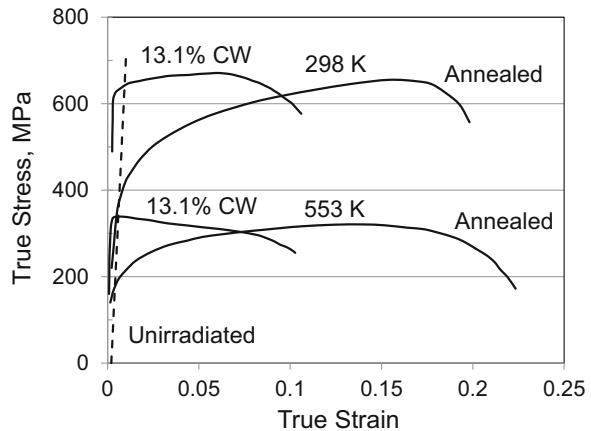
versus temperature and strain rate (Fig. 10.37) and in the analysis of the structure evolution behavior. Model predictions can be both high and low in comparison to measured stresses. Accurate constitutive modeling of a system undergoing combined slip and deformation twinning awaits development of appropriate models for the deformation kinetics and structure evolution.

10.8 Analysis of Deformation in Irradiated Zircaloy-2

In Sect. 8.7 the application of the internal state variable model to a known material (pure nickel) exposed to a unique processing path (shock deformation) was described. An analogous approach is used here to demonstrate application of the model to a zirconium alloy exposed to irradiation damage. Zircaloy-2 is a corrosion-resistant alloy used for nuclear fuel cladding.⁴ The alloy is somewhat stronger and less ductile than unalloyed zirconium. When used as fuel cladding, the material is exposed to high levels of irradiation damage.

Howe and Thomas [20] studied the neutron irradiation damage of Zircaloy-2 and measured stress–strain curves in unirradiated and irradiated material in both the annealed and cold-worked condition. Because the temperature of the fuel cladding during operation can be several hundred degrees centigrade, Howe and Thomas measured the stress–strain curves at RT as well as 280 C (553 K). Figure 10.45 shows the stress–strain curves in annealed and cold-worked (13.1%) material at the two temperatures. Included in the figure is the 0.002 offset strain line.

Fig. 10.45 Stress–strain measurements by Howe and Thomas [20] in unirradiated Zircaloy-2



⁴Some of the analysis in this section was performed by Aaron Weiss as part of his 2012 undergraduate research thesis at Saint Vincent College, Latrobe, Pa.

Fig. 10.46 Temperature dependence of the yield stress in annealed Zircaloy-2 compared with the model curve for pure, polycrystalline zirconium

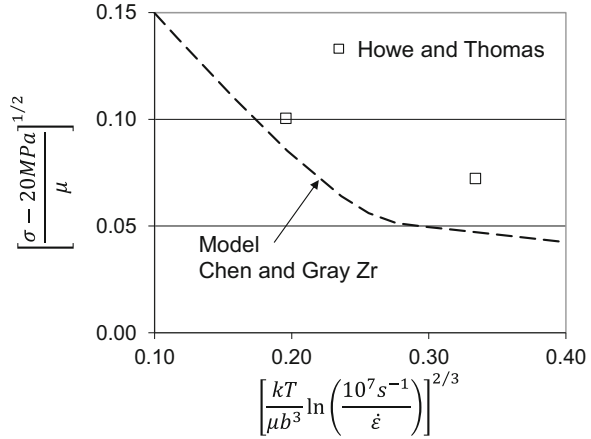
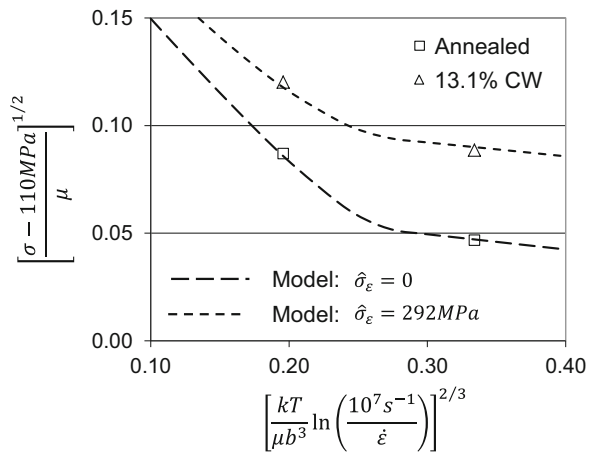


Fig. 10.47 Model predictions for annealed and cold-worked Zircaloy-2 made with the same model parameters used for pure, polycrystalline zirconium except for an increase in the athermal stress from 20 MPa to 110 MPa and, for the cold-worked material, a value of $\hat{\sigma}_\epsilon = 292$ MPa



To compare the strength levels of this alloy with the strength levels in the pure zirconium studied by Chen and Gray, Fig. 10.46 shows the two yield stress measurements in the annealed Zircaloy-2 (open squares) with the model equation established for the Chen and Gray material. The two Zircaloy-2 measurements fall above the model line established for the pure zirconium. The other curious observation is that the temperature dependence in Zircaloy-2 is noticeably less than that in pure zirconium. Under typical processing, the alloying additions in Zircaloy-2 generate a fine, uniform distribution of intermetallic compounds [21]. These precipitates could well create an added athermal stress. In fact, as illustrated in Fig. 10.47, increasing the athermal stress from 20 MPa to 110 MPa gives good agreement between the model equation established for pure zirconium and the measurements in Zircaloy-2. That is, the long-dashed line in Fig. 10.46 is drawn with the parameters listed in Table 10.12 except that $\sigma_a = 110$ MPa, $\hat{\sigma}_1/\mu_o = 0.044$, and $\hat{\sigma}_2/\mu_o = 0.005$. Included in Fig. 10.47 are the yield stress measurements in the

Fig. 10.48 Computed variation of $\hat{\sigma}_\epsilon$ with strain for annealed Zircaloy-2 with fits to Eq. 6.28 (dashed lines)

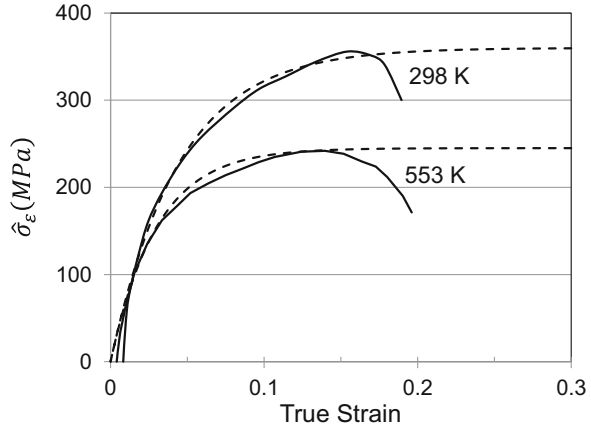
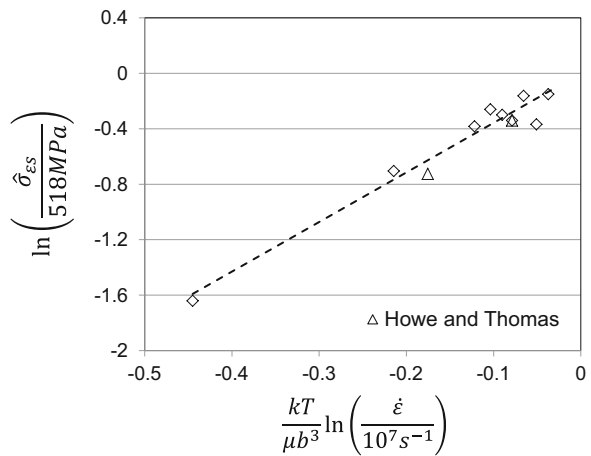


Fig. 10.49 Variation of the saturation threshold stress representing the stored dislocation density ($\hat{\sigma}_{es}$) with temperature and strain rate on coordinates consistent with Eq. 6.26. The open triangles are the Howe and Thomas data points which are added to the data presented in Fig. 10.40



13.1% cold-worked material. In this case the model fit (short-dashed line) assumes the cold work increased $\hat{\sigma}_\epsilon$ from 0 in the case of annealed material to 292 MPa.

The variation of $\hat{\sigma}_\epsilon$ with strain is analyzed using Eq. 9.7 as before. Figure 10.48 shows the result for the two stress–strain curves in unirradiated material. The dashed lines are drawn according to Eq. 6.28 with $\kappa = 1$, $\theta_{II} = 8000$ MPa, and $\hat{\sigma}_\epsilon$ equal 360 MPa at 298 K and 25 MPa at 553 K. These two data points are added to the Chen and Gray data points (Fig. 10.40) in Fig. 10.49 (see open triangles) and displayed with the same model equation as fit to the Chen and Gray material. The Howe and Thomas data fall within the scatter band of Chen and Gray material implying that the strain-hardening behavior of this Zircaloy-2 material is similar to that in pure Zr.

A comparison of predicted stress–strain curves (dashed lines) at the two temperatures with measured curves (solid lines) in unirradiated Zircaloy-2 is shown in Fig. 10.50. The predictions are slightly high, which arises from the observation that the $\hat{\sigma}_{es}$ values for the two Howe and Thomas data points in Fig. 10.49 are slightly below the model line.

Fig. 10.50 Predicted (dashed lines) and measured stress–strain curves in annealed Zircaloy-2

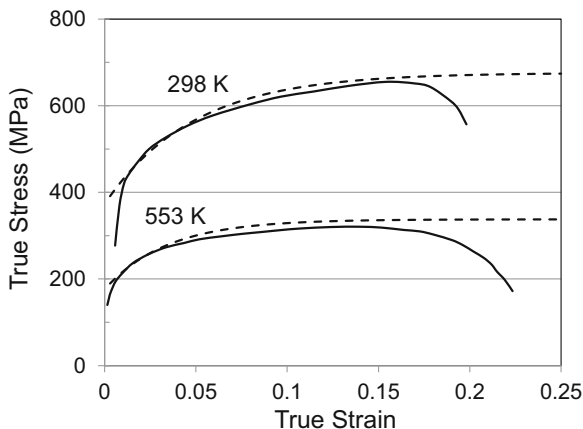


Fig. 10.51 Predicted and measured stress–strain curves in 13.1% cold-worked Zircaloy-2

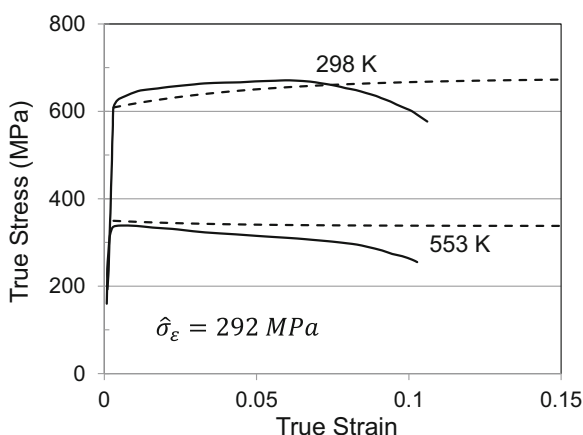


Figure 10.51 compares the measured and predicted stress–strain curves for the cold-worked material at the two test temperatures. As discussed, relative to Fig. 10.46, the cold work introduces a stored dislocation density; the predictions in Fig. 10.51 were made by setting the initial $\hat{\sigma}_\epsilon$ to 292 MPa. Note that the tensile curve at the higher temperature demonstrates negative strain hardening at yield, indicating that this tensile specimen immediately undergoes nonuniform deformation (necking).

Analysis of only two stress–strain curves in Zircaloy-2 and comparison with more extensive analysis of deformation in pure zirconium has illustrated the utility of the model formulation in translating the understanding of deformation in one material to deformation in a related material. Furthermore, this exercise has demonstrated that even though the model consists of what appears to be many adjustable parameters, when carefully applied, only a limited number need to be adjusted. In this case, only one parameter—the athermal stress—was changed in going from pure zirconium to Zircaloy-2.

Fig. 10.52 Stress–strain curves measured by Howe and Thomas [20] in irradiated annealed and cold-worked Zircaloy-2

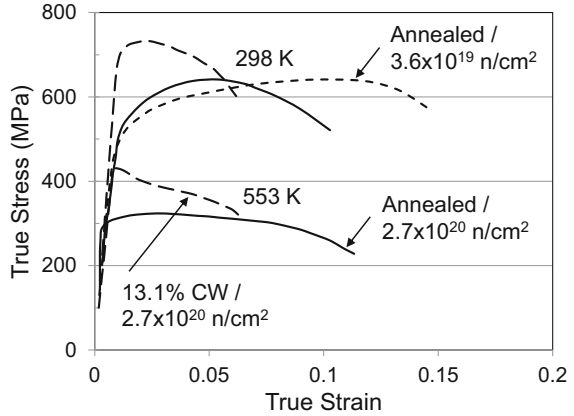


Figure 10.52 shows stress–strain curves measured in irradiated material. It is evident that irradiation leads to significant hardening. The three upper curves are measurements at 298 K, whereas the two lower curves are measurements at 553 K. Annealed material was exposed to two dose levels. The material receiving the higher dose is slightly stronger at 298 K than that receiving the lower dose. Stress–strain curves for cold-worked and irradiated material show negative strain hardening—even at 298 K.

Availability of full stress–strain curves at two test temperatures in irradiated material enables an analysis of the character of the irradiation-induced hardening. The two-parameter model used for magnesium and zirconium in this chapter is a variation of Eq. 9.6:

$$\frac{\sigma}{\mu} = \frac{\sigma_a}{\mu} + s_1(\dot{\epsilon}, T) \frac{\hat{\sigma}_1}{\mu_o} + s_2(\dot{\epsilon}, T) \frac{\hat{\sigma}_2}{\mu_o} + s_\epsilon(\dot{\epsilon}, T) \frac{\hat{\sigma}_\epsilon}{\mu_o} \tag{10.5}$$

For irradiated material, it is possible that irradiation damage resulting, for instance, in large voids would lead to an increase in σ_a . It seems unlikely that irradiation damage would affect either $\hat{\sigma}_1$ or $\hat{\sigma}_2$. It is possible that damage could introduce a new threshold stress—i.e., a fourth state variable term in Eq. 10.5. A final possibility is that irradiation damage manifests itself as a stored dislocation density, which affects $\hat{\sigma}_\epsilon$. In fact, this was the observation of Byun and Hashimoto in 316LN stainless steel [22] and of Byun et al. in a variety of other metals [23].

To illustrate how these options can be probed, Fig. 10.53 shows the measured stress–strain curve for the annealed material exposed to a dose of $3.6 \times 10^{-19} \text{ n/cm}^2$ (solid curve). The short-dashed lines are model predictions. One was made by adjusting the athermal stress (to 185 MPa) to match the experimentally measured yield stress. The other was made by leaving the athermal stress at 110 MPa and adjusting the initial $\hat{\sigma}_\epsilon$ (to 150 MPa) to match the yield stress. Note that the predicted curve with the athermal stress increased provides poor agreement with the strain-hardening behavior, whereas the curve with $\hat{\sigma}_\epsilon$ increased provides a much closer

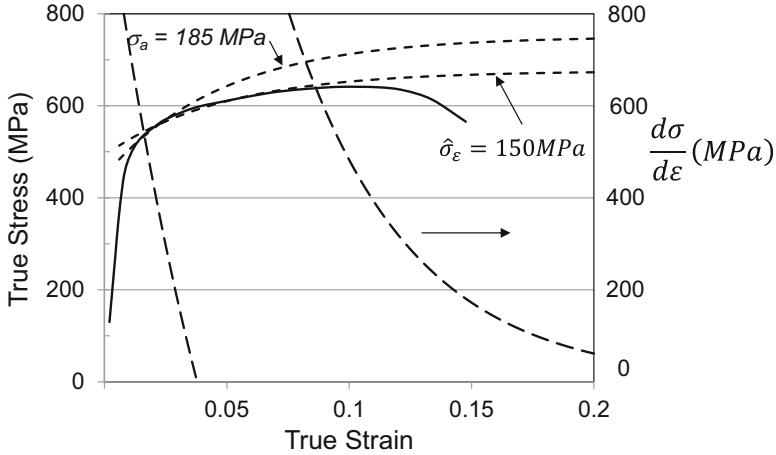


Fig. 10.53 Measured (solid line) and predicted (short-dashed lines) stress–strain curves for the Zircaloy-2 material irradiated at 3.6×10^{19} n/cm². The model predictions are for two model assumptions. The long-dashed line is the rate of strain hardening predicted for the case where $\hat{\sigma}_\epsilon = 150$ MPa

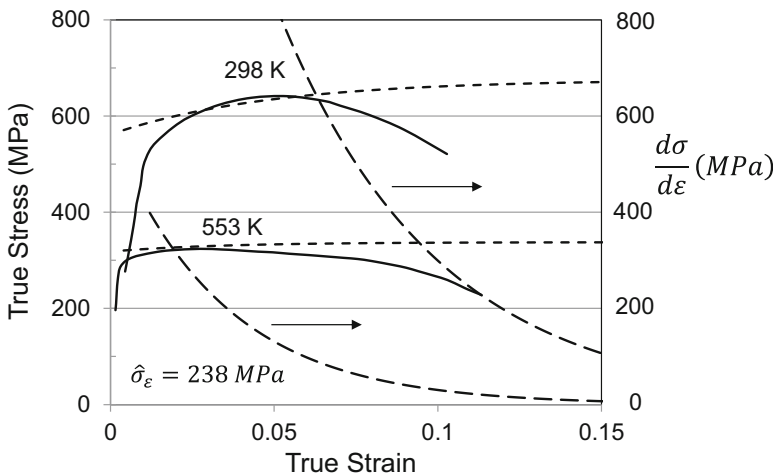
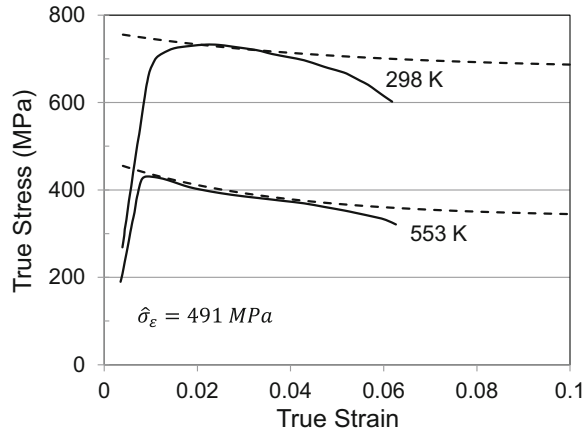


Fig. 10.54 Measured (solid lines) and predicted stress–strain curves for annealed Zircaloy-2 irradiated at 2.7×10^{20} n/cm². The long-dashed lines are the predicted strain-hardening rates

match. This is further evidenced by comparing the predicted point of instability (where the stress equals the hardening rate) to that observed experimentally. The ability to analyze both the stress level and the strain-hardening behavior and compare the predictions with the observations is a very powerful tool.

For Zircaloy-2 irradiated at 2.7×10^{20} n/cm², Fig. 10.54 plots the stress–strain curves measured at 298 K and 553 K along with the model predictions (short-dashed lines) and strain-hardening rate (long-dashed lines). For these model predictions, the

Fig. 10.55 Measured (solid lines) and predicted stress-strain curves for irradiated, 13.1% cold-worked Zircaloy-2



initial value of $\hat{\sigma}_\epsilon$ was set at 238 MPa, which is above the value of 150 MPa used for the lower dosage rate. The stress levels at both reload test temperatures are well-predicted. The predicted instability point (defined by Eq. 1.16) for the test at 298 K is several percent higher than observed, but predicted instability point at the higher temperature agrees well with the stress-strain curve.

Finally, a comparison between the measured and predicted curves in cold-worked material exposed to a dose of $2.7 \times 10^{20} \text{ n/cm}^2$ is shown in Fig. 10.55. The predicted curves at both temperatures begin with a negative strain-hardening rate. The apparent close agreement between the measured and predicted hardening at the higher temperature is fortuitous since the tensile specimen is likely undergoing nonuniform deformation. For these model predictions, the initial value of $\hat{\sigma}_\epsilon$ was set at 491 MPa. Recall from Fig. 10.51 that the cold work introduced an initial $\hat{\sigma}_\epsilon$ value of 292 MPa. The analysis of irradiation damage in annealed material at $2.7 \times 10^{20} \text{ n/cm}^2$ in Fig. 10.54 led to an initial $\hat{\sigma}_\epsilon$ estimate of 238 MPa. If the obstacle population characterizing the stored dislocation density from strain hardening is similar or even identical to that characterizing irradiation damage, then the initial $\hat{\sigma}_\epsilon$ value for the irradiated, cold-worked material should equal the sum of these two quantities—530 MPa—which is not that different from the value of 491 MPa used in Fig. 10.55.

Temperature- and strain rate-dependent stress-strain curves on processed material are valuable because they offer a sensitive test of the understanding of deformation kinetics. Starting with an analysis of pure, polycrystalline zirconium, the deformation of annealed Zircaloy-2 was modeled by adjusting a single model parameter—the athermal stress. The adjustment was consistent with an understanding of changes in the microstructure (the existence of intermetallic compounds) in the alloy. With this change the predicted temperature dependence of the stress-strain curve and the rate of strain-hardening agreed with the measurements. Exposure to neutron irradiation strengthens Zircaloy-2. The nature of the strengthening is very similar to structure evolution by dislocation storage. Adjusting a single model

parameter—the initial value of $\hat{\sigma}_\epsilon$ —led to good agreement between the temperature dependence of the stress–strain curves, the rate of strain hardening, and the point of plastic instability in irradiated material (see Figs. 10.54 and 10.55). Agreement such as achieved in this section between model predictions and experiment requires a model that accurately represents the kinetics at constant structure (temperature and strain rate dependence of the yield stress) and the kinetics of strain hardening (strain, temperature, and strain rate dependence of the stress–strain curve).

10.9 Analysis of Deformation Behavior of Polycrystalline Titanium

Based on its low density (4.51 g/cm³), high melting temperature (1941 K), and excellent oxidation resistance together with its ability to be processed into thin- as well as thick-section components and the development of dual phase (HCP alpha plus BCC beta) alloys (e.g., Ti6Al-4V), titanium use has steadily increased in aerospace, sporting goods, and medical applications. The material has been studied extensively in unalloyed and alloyed forms [24]. (Also, see the collection of articles in Titanium '92 Science and Technology [25].)

To illustrate application of the MTS model formalism in titanium, stress–strain measurements in pure titanium and the Ti6Al-4V alloy from several sources are analyzed [26–30]. Table 10.15 summarizes the processing and testing conditions for these references. In titanium alloys, a convention has to represent the compositions of oxygen, nitrogen, and carbon with the oxygen equivalent (O_{eq}). See the definition of O_{eq} at the bottom of Table 10.15.

Figures 10.56, 10.57, and 10.58 show data reported by H. Conrad and coworkers in a series of publications that paved the way for mechanism studies in pure titanium. As indicated in Table 10.15 (the Yin et al. references), these measurements were in Ti-50A with $O_{\text{eq}} = 0.5\%$. Reference [27] includes measurements at temperatures above $T_H = 0.5$ which are not included in Figs. 10.57 and 10.58 and are not analyzed here.

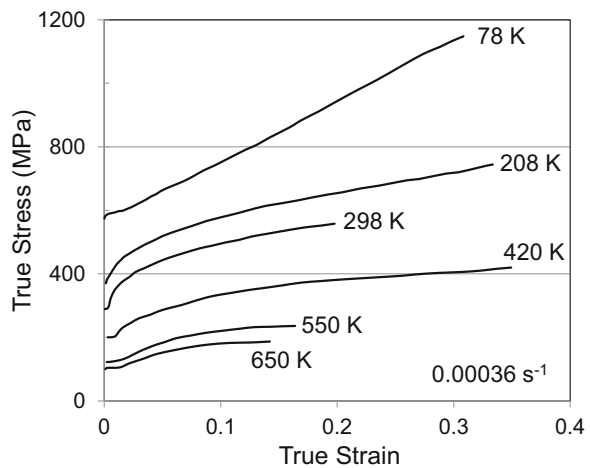
Figure 10.59 shows the variation of yield stress with temperature and strain rate for the measurements in Figs. 10.56, 10.57, and 10.58. As observed in polycrystalline zirconium (Fig. 10.37) and magnesium (Fig. 10.24), the curvature in the yield stress plot warrants application of a two-obstacle model. The dashed line in Fig. 10.59 gives one possible model fit with the model parameters listed in Table 10.16. Similar to the yield stress correlations in zirconium and magnesium, $\hat{\sigma}_1$ represents highly strain rate- and temperature-dependent interactions with dislocations with one-obstacle population, whereas $\hat{\sigma}_2$ represents interactions of dislocations with a considerably less strain rate- and temperature-dependent obstacle population. Analysis of measurements in pure titanium of different purity levels will enable speculation as to the nature of these obstacle populations.

Table 10.15 References and test conditions for yield stress and stress–strain measurements in titanium

Reference	Material	Processing conditions	Testing conditions		
				Temperatures	Strain rates
Yin et al. [26]	Ti-50A 0.5% O_{eq} ^a	Annealed 22 μm grain size	Tensile	78 K to 650 K ($T_H = 0.335$)	$3.6 \times 10^{-4} \text{ s}^{-1}$; $\times 5$ strain rate change tests
Doner and Conrad [27]	Ti-50A 0.5% O_{eq}	Annealed 22 μm grain size	Tensile	600 K to 900 K ($T_H = 0.464$)	$3.3 \times 10^{-5} \text{ s}^{-1}$, $3.3 \times 10^{-2} \text{ s}^{-1}$
Nemat-Nasser et al. [28]	CP-Ti (99.99% pure) 0.09% O_{eq}	Annealed; 40 μm grain size	Compression	77 K to 998 K ($T_H = 0.514$)	0.001 s^{-1} , 0.1 s^{-1} , 2200 s^{-1}
Lederich et al. [29]	EL 60-Ti 0.152% O_{eq}	Annealed; 9–75 μm grain size	Tensile	295 K and 575 K	$2.8 \times 10^{-4} \text{ s}^{-1}$
Follansbee and Gray [30]	Ti6Al-4V 0.703% O_{eq}	As received, 5 μm equiaxed grain size	Compression; prestrains and reloads	Mostly 298 K prestrains; 1 at 495 K; 77 K, 188 K, 298 K reloads	0.001 s^{-1} , 2500 s^{-1}

^a $O_{eq} = O \text{ (at. \%)} + 2 \text{ N (at. \%)} + 0.75\text{C (at. \%)}$

Fig. 10.56 Stress–strain curves in Ti-50A reported by Yin et al. [26]



Lederich et al. [29] measured stress–strain curves in EL 60-grade titanium, which has a lower level of impurities than the material studied by Conrad et al., at 295 K and 575 K as a function of grain size (6–100 μm). Analysis of the temperature-dependent yield stress for 34 μm grain size material using the model parameters in

Fig. 10.57 Stress–strain curves in Ti-50A reported by Doner and Conrad [27]

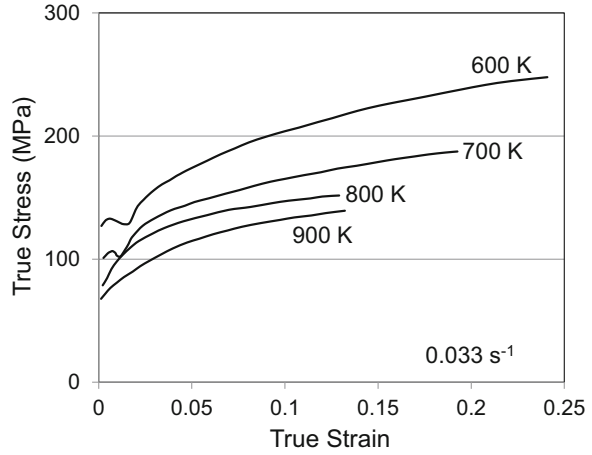


Fig. 10.58 Stress–strain curves in Ti-50A reported by Doner and Conrad [27]

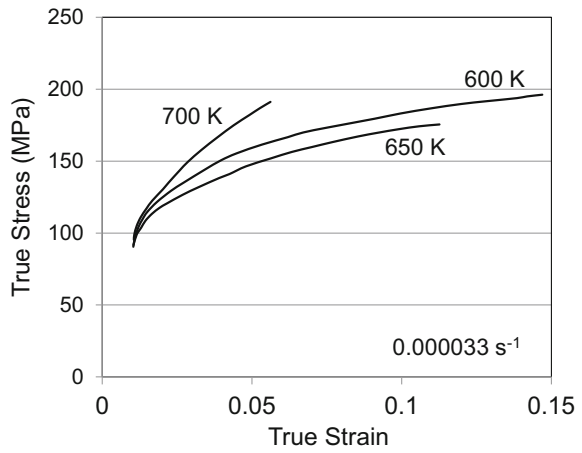


Fig. 10.59 Yield stress versus temperature and strain rate for the stress–strain curves in Figs. 10.56, 10.57, and 10.58

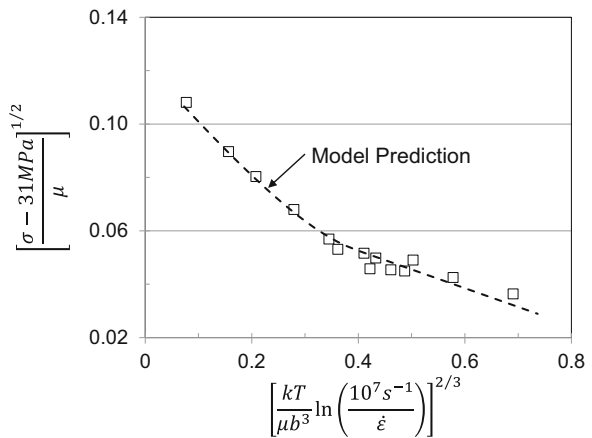


Table 10.16 Model parameters for yield stress correlation established for the Yin et al. [26] and Doner and Conrad [27] measurements in Ti-50A

Obstacle	Parameter	Value
Obstacle 1	σ_a (MPa)	31
	b (nm)	0.295
	g_o	0.25
	$\dot{\epsilon}_o$ (s^{-1})	10^7
	p	0.5
	q	1.5
Obstacle 2	$\hat{\sigma}_1/\mu_o$	0.0085
	g_o	1.6
	$\dot{\epsilon}_o$ (s^{-1})	10^{10}
	p	0.5
	q	1.5
	$\hat{\sigma}_2/\mu_o$	0.0065

Table 10.16 with $\hat{\sigma}_1/\mu_o = 0.0065$, $\hat{\sigma}_2/\mu_o = 0.0012$, and $\sigma_a = 25$ MPa gives agreement with the yield stresses at the two test temperatures.⁵ Recall the governing equation posed in Sect. 6.3 for the yield stress in a material with two obstacle populations:

$$\frac{\sigma}{\mu} = \frac{\sigma_a}{\mu} + s_1(\dot{\epsilon}, T) \frac{\hat{\sigma}_1}{\mu_o} + s_2(\dot{\epsilon}, T) \frac{\hat{\sigma}_2}{\mu_o} \quad (6.14)$$

where s_1 and s_2 were defined by Eqs. 6.15 and 6.16. In Sect. 5.5, the athermal stress σ_a was equated to the factor $k_d/\sqrt{d_{gs}}$ in the Hall-Petch equation (Eq. 3.9). Replacing σ_a (25 MPa at a grain size of 34 μm) in Eq. 6.14 with this term in Eq. 6.14 gives the following:

$$\sigma = \frac{146\text{MPa} - \mu m^{1/2}}{\sqrt{d_{gs}(\mu m)}} + \left[s_1 \frac{\hat{\sigma}_1}{\mu_o} \mu + s_2 \frac{\hat{\sigma}_2}{\mu_o} \mu \right] \quad (10.6)$$

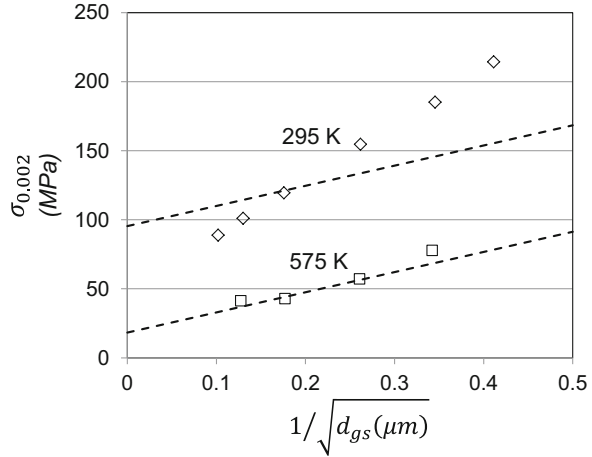
and substituting the model parameters listed in Table 10.16 into Eqs. 6.15 and 6.16, 10.6 becomes at 295 K and a strain rate of $0.00028 s^{-1}$ (the conditions of the one of the Lederich et al. measurements):

$$\sigma = \frac{146\text{MPa} - \mu m^{1/2}}{\sqrt{d_{gs}(\mu m)}} + 95.4\text{MPa} \quad (10.7)$$

and at 575 K and the same strain rate:

⁵Since there are only two data points (one strain rate and two temperatures) in the Lederich et al. data set, there is not as much confidence in these model parameters as in analysis of the Conrad et al. data set.

Fig. 10.60 Yield stress versus grain size measurements in EL-60 Ti reported by Lederich et al. [29] and model fits (dashed lines) drawn to Eqs. 10.7 and 10.8



$$\sigma = \frac{146\text{MPa} - \mu m^{1/2}}{\sqrt{d_{gs}(\mu m)}} + 18.3\text{MPa} \quad (10.8)$$

Figure 10.60 compares the Lederich et al. measurements at these two temperatures (and a strain rate of 0.00028 s^{-1}) with Eqs. 10.7 and 10.8. It is evident that the slope of the best-fit lines to the two data sets does not have the same slope, which is counter to the model expressed by Eq. 10.6. Lederich et al. observed extensive deformation twinning at the 295 K but only dislocation substructures at 575 K and suggested that deformation twinning was influencing the grain size effect at the lower temperature. The decrease in stress level with increasing grain size is consistent with the expected dependence of twinning stress on grain size [31]. Equation 10.8 at 575 K provides a good fit to the higher temperature results. For subsequent analyses in titanium and in Ti6Al-4V, the athermal stress will be taken as follows⁶:

$$\sigma_a = \frac{146\text{MPa} - \mu m^{1/2}}{\sqrt{d_{gs}(\mu m)}} \quad (10.9)$$

Nemat-Nasser et al. [28] performed an extensive experimental study of the strain rate and temperature dependence of deformation in commercially pure titanium ($O_{eq} = 0.09\%$). This data set includes measurements at strain rates as high as 8000 s^{-1} . Figures 10.61, 10.62, and 10.63 show the stress–strain curves at strain rates of 0.001 s^{-1} , 0.1 s^{-1} , and 2200 s^{-1} . A unique feature of these results is the occurrence of a region of increased strain hardening at temperatures between $\sim 300 \text{ K}$ and $\sim 800 \text{ K}$. Nemat-Nasser et al. [28] describe this as the contribution of dynamic strain aging. They also conclude that deformation twinning, while prevalent at lower

⁶In fact, the value of 31 MPa for the Ti-50A material was computed using Eq. 10.9 and the reported grain size of 22 μm.

Fig. 10.61 Stress–strain curves at a strain rate of 0.001 s^{-1} reported by Nemat-Nasser et al. [28] in CP-Ti

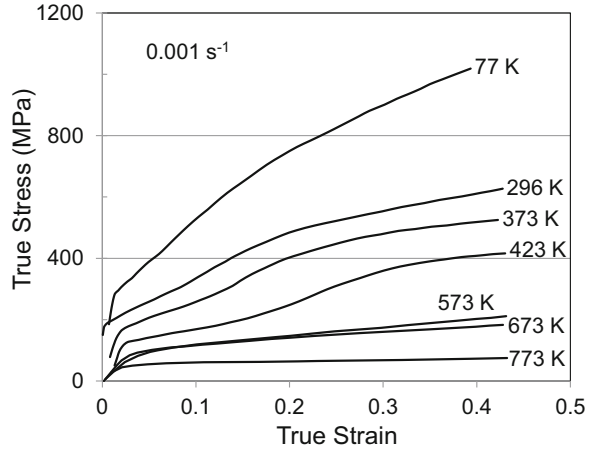
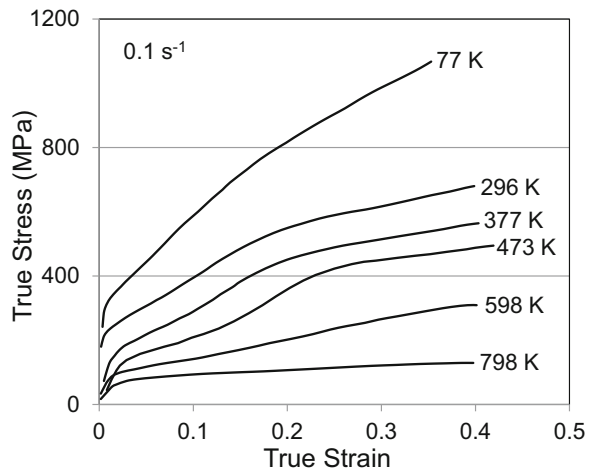


Fig. 10.62 Stress–strain curves at a strain rate of 0.1 s^{-1} reported by Nemat-Nasser et al. [28] in CP-Ti



test temperatures and higher strain rates, does not contribute significantly to hardening.

Figure 10.64 shows the variation of yield stress with temperature and strain rate for measurements at strain rates of 0.001 s^{-1} , 0.1 s^{-1} , and 2200 s^{-1} (only at the lower test temperatures where there was confidence in the yield stress estimate). The dashed line is the model fit with $\hat{\sigma}_1/\mu_o = 0.0036$, $\hat{\sigma}_2/\mu_o = 0.0042$, and $\sigma_a = 23 \text{ MPa}$ (all other model parameters as listed in Table 10.16). The scatter in the plot is likely related to the difficulty in defining a 0.002 strain offset yield stress. There also may be a slight plateau in stress level at the lowest temperatures, which when observed in other materials (e.g., zirconium; see Fig. 10.37) has been associated with deformation twinning.

Table 10.17 lists model parameters (other than those in Table 10.16 that have not changed) for the Conrad et al. and Nemat-Nasser et al. data sets. The magnitude of

Fig. 10.63 Stress–strain curves at a strain rate of 2200 s^{-1} reported by Nemat-Nasser et al. [28] in CP-Ti

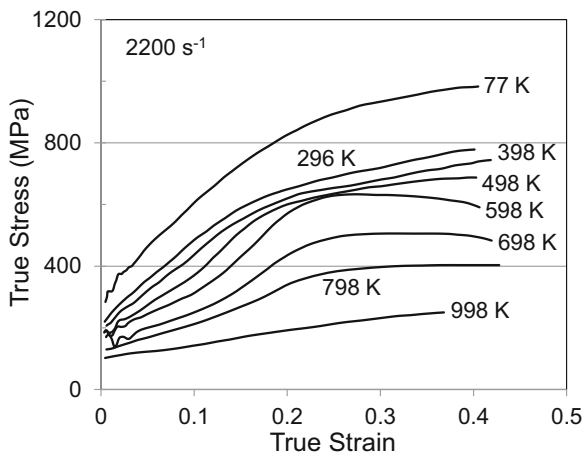


Fig. 10.64 Yield stress versus temperature and strain rate for the Nemat-Nasser et al. measurements in CP-Ti

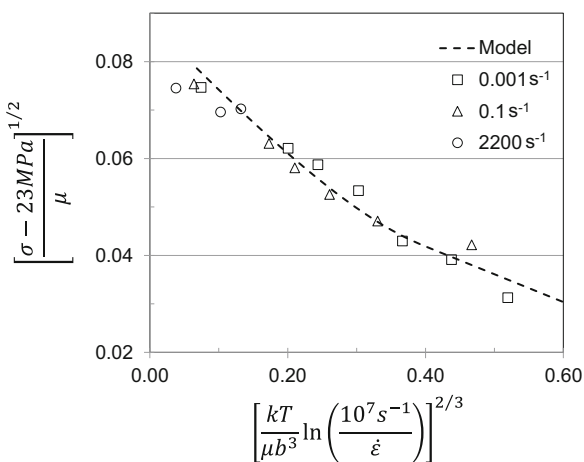
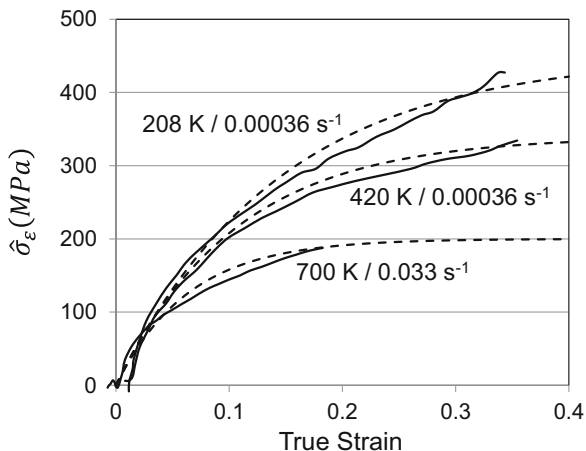


Table 10.17 Threshold stress values used for the model fit to the Conrad et al. Ti-50A data set (Fig. 10.59) and the Nemat-Nasser et al. CP-Ti data set (Fig. 10.64)

Reference	O_{eq}	Parameter	
		$\hat{\sigma}_1/\mu_o$, MPa	$\hat{\sigma}_2/\mu_o$, MPa
Conrad et al. [24]	0.5%	0.0085	0.0065
Nemat-Nasser et al. [28]	0.09%	0.0036	0.0042

the state variables varies with O_{eq} , suggesting both are related to interstitial content. This is a similar observation as made in zirconium (see Table 10.13 and Fig. 10.38), but it differs from the conclusion in iron where the obstacle population referred to as the Peierls barrier did appear to vary with composition, whereas a strong dependence

Fig. 10.65 Variation of $\hat{\sigma}_\epsilon$ with strain for three stress-strain curves reported by Conrad et al. along with the model fit to Eq. 6.28



on carbon concentration was observed for the obstacle population referred to as “i” (see Fig. 9.11).

Structure evolution in titanium is analyzed using the same procedure described for the other HCP and BCC metals in earlier sections and introduced in Sect. 9.5 for UfKone1. Equation 9.7 is used with the model parameters established for the yield stress correlation to deduce the variation of $\hat{\sigma}_\epsilon$ with strain. Then, Eq. 6.28 is fit to this curve to first estimate κ , which once established is not varied, and then estimate the values of θ_{II} and $\hat{\sigma}_{es}$ for each test condition. Figure 10.65 shows three of the results in Conrad et al. material for the test conditions indicated. The dashed lines are drawn according to Eq. 6.28 with $\kappa = 1$. The values of θ_{II} and $\hat{\sigma}_{es}$ for these tests are listed in Table 10.18 along with model parameters for other test conditions analyzed in the Conrad et al., Nemat-Nasser et al., and Lederich et al. data sets.

Whereas the dashed lines follow the three curves in Fig. 10.65, the two curves from the Nemat-Nasser et al. data set in Fig. 10.66 exhibit notable differences. The solid curve for the test at 296 K and a strain rate of 0.001 s^{-1} (left ordinate) agrees with the dashed line up to a strain of ~ 0.2 at which point the curve deviates to higher stress levels. The result at 598 K and a strain rate of 2200 s^{-1} (right ordinate) is even more interesting in that the solid curve follows the predicted trend up to a strain of ~ 0.1 at which point the solid curve deviates very strongly to higher stress levels. This behavior is similar to that observed in vanadium and niobium when dynamic strain aging (DSA) becomes active. This will be discussed more below.

The analyzed variation of $\hat{\sigma}_\epsilon$ with strain for the measurement by Nemat-Nasser et al. at 473 K and a strain rate of 0.001 s^{-1} is shown in Fig. 10.67. This result is typical of several of the measurements in this data set. A dashed line is drawn according to Eq. 6.28, but this line doesn't particular well coincide with the solid curve.

The parameters for Eq. 6.28 for each of the stress-strain curves analyzed from the Conrad et al., Lederich et al., and Nemat-Nasser et al. data sets are listed in

Table 10.18 Summary of the evolution analysis (Eqs. 6.26 and 6.28) for the Conrad et al., Lederich et al., and Nemat-Nasser et al. stress–strain curves in titanium

	Initial temperature (K)	Strain rate (s ⁻¹)	θ_{II} (MPa)	$\hat{\sigma}_{\epsilon s}$ (MPa)
Conrad et al. [24]	208	0.00036	3100	450
	298	0.00036	3200	440
	420	0.00036	3200	340
	550	0.00036	3200	215
	600	0.000033	3100	185
	650	0.000033	3100	210
	650	0.00036	3200	210
	600	0.033	3200	225
	700	0.000033	3100	400
	700	0.033	3100	200
	800	0.033	3200	220
Lederich et al. [29]	295	0.00028	3200	325
	575	0.00028	3300	180
Nemat-Nasser et al. [28]	296	0.001	3200	480
	296	2200	4000	600
	473	0.001	3200	(280)
	598	2200	4000	400
	673	0.001	3300	150

Fig. 10.66 Variation of $\hat{\sigma}_{\epsilon}$ with strain for two stress–strain curves reported by Nemat-Nasser et al. along with the model fit to Eq. 6.28

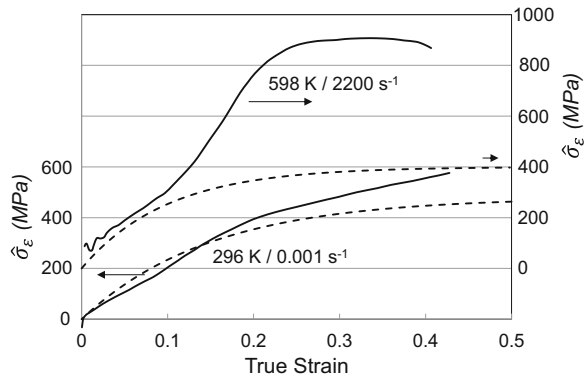


Table 10.18. The saturation stress value for the result shown in Fig. 10.67 is in parenthesis for reasons that will be detailed below. In fact, analysis of the Nemat-Nasser et al. data at each of the conditions described in Table 10.18 carries a great deal of uncertainty as evidenced by the model fits in Figs. 10.66 and 10.67. In analyzing these curves, more weight was given to the behavior at low strains than at high strains.

Following the procedure used in analysis of the evolution behavior in each of the materials studied earlier, Fig. 10.68 shows the variation of the saturation threshold

Fig. 10.67 Variation of $\hat{\sigma}_\epsilon$ with strain for the stress-strain curve at 473 K and a strain rate of 0.001 s^{-1} reported by Nemat-Nasser et al. along with a possible model (dashed line)

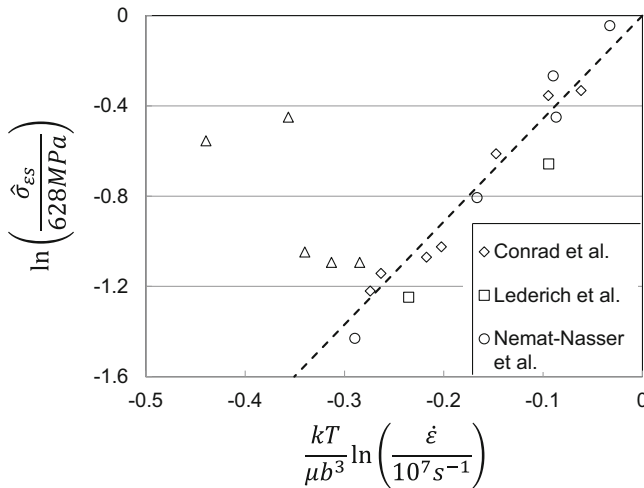
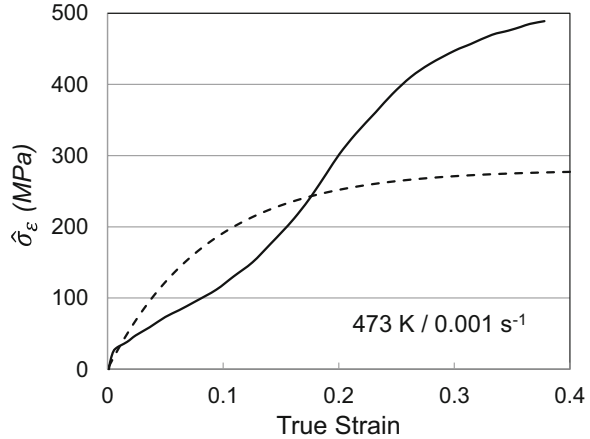
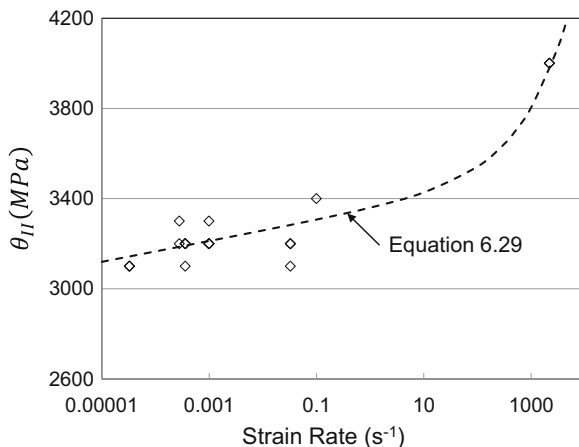


Fig. 10.68 Variation of $\hat{\sigma}_{\epsilon s}$ with temperature and strain rate for the three data sets in pure titanium. The model fit according to Eq. 6.26 is drawn through the Conrad et al. data points. Note that the open triangles are from the Conrad et al. measurements but are excluded from the model fit

stress with test temperature and strain rate on coordinates consistent with Eq. 6.26. The dashed line is a best-fit line through the Conrad et al. points represented with open diamonds. The model parameters for this fit are $\hat{\sigma}_{\epsilon s 0} = 628 \text{ MPa}$ and $\dot{\epsilon}_{\epsilon s 0} = 10^7 \text{ s}^{-1}$. From the slope of the line, $g_{\epsilon s 0} = 0.216$. Similar to the result earlier in vanadium (Fig. 9.44), the tests from the Conrad et al. data set that appear to be affected by dynamic strain aging (open triangles) trend upward off of the line. It is interesting that even though the Lederich et al. data points were not included in establishing the dashed line, they do exhibit a similar temperature dependence. The

Fig. 10.69 Variation of the stage II hardening rate with strain rate for the three pure titanium materials with a model fit according to Eq. 6.29



temperature and strain rate dependence observed in the Nemat-Nasser et al. data points, shown as open circles in Fig. 10.68, also tracts the dashed line. For the test at 473 K and a strain rate of 0.001 s^{-1} , the saturation stress was selected as that defined by the dashed line. It is this saturation stress which established the dashed line in Fig. 10.67.

The strain rate dependence of θ_{II} is shown in Fig. 10.69. The dashed line in this figure is drawn according to Eq. 6.29 with $A_0 = 3350 \text{ MPa}$, $A_1 = 20 \text{ MPa}$ (when strain rate is in units of s^{-1}), and $A_2 = 10 \text{ MPa s}^{-1/2}$. The full set of model parameters for the Conrad et al. material is listed in Table 10.19.

For other titanium materials listed in Table 10.15, the values of σ_a , $\hat{\sigma}_1$, and $\hat{\sigma}_2$ take on slightly different values than listed in Table 10.19 presumably due to slightly different chemistries. These values were detailed in the text.

Figure 10.70 compares predicted (dashed lines) with measured stress–strain curves for a selection of test conditions reported by Conrad et al. The agreement between the model predictions and the measurements is quite acceptable.

Yin et al. [26] also measured the change in stress due to a $5 \times$ change in strain rate. Figure 10.71 compares their measurement at 5% strain with model predictions (open boxes). Yin et al. noted some scatter in their measurements. The double-ended arrows in Fig. 10.71 give the mean plus and minus an estimated standard error. Except for the peak at 400 K, the predicted change in stress follows the measured trend over the temperature range tested. The source of the disagreement at 400 K is not clear. In general, however, it is satisfying to observe agreement between the model predictions and a set of measurement not included in development of model parameters.

Table 10.19 Full set of model parameters for Ti-50A titanium (Conrad et al. material)

Parameter	Equation	Value	Units
σ_a (MPa)	Eq. 10.5	31	MPa
s_1	Eq. 6.15	g_{o1}	0.25
		$p1$	0.5
		$q2$	1.5
		$\dot{\epsilon}_{o1}$	1×10^7
$\widehat{\sigma}_1$	Eq. 10.5	405	MPa
s_2	Eq. 6.16	g_{o2}	1.6
		p_2	0.5
		q_2	1.5
		$\dot{\epsilon}_{o2}$	1×10^{10}
$\widehat{\sigma}_2$	Eq. 10.5	310	MPa
s^E	Eq. 7.9	g_{oE}	1.6
		p_E	0.667
		q_E	1
		$\dot{\epsilon}_{oE}$	1×10^7
κ	Eq. 6.28	1	–
θ_{II}	Eq. 6.29	A_o	3400
		A_1	20
		A_2	5
$\widehat{\sigma}_{ES}$	Eq. 6.26	$\widehat{\sigma}_{ESO}$	628
		g_{ESO}	0.216
		$\dot{\epsilon}_{ESO}$	1×10^7
b		0.295	nm
ρ	Eq. 6.32	4.51	g/cm^3
ψ		0.95	–
$\mu(T)$	Eq. 6.8 (See Table 6.1)	μ_o	47.62
		D_o	5.821
		T_o	181
$c_p(T)$	See Table 6.5 in Box 6.4	A_C	0.485
		B	1.85×10^{-4}
		C	–1700

10.9.1 Dynamic Strain Aging in Polycrystalline Titanium

The existence of dynamic strain aging in titanium is well acknowledged [28]. In the Conrad et al. material, DSA is evidenced by the open triangles in Fig. 10.68 showing saturation stresses that deviate above those found in the absence of DSA (the dashed line). Nemat-Nasser et al. [28] interpreted the enhanced hardening at intermediate temperatures for the tests at a strain rate of $2200 s^{-1}$ as evidence of DSA. Following the approach used in analyzing DSA in vanadium in Sect. 9.9, it is assumed that DSA involves mobility of interstitials (likely oxygen) that are characterized by obstacle population 1, and Eq. 9.8 is rewritten as follows:

Fig. 10.70 Comparison between measurements and predictions for three test conditions reported by Conrad et al.

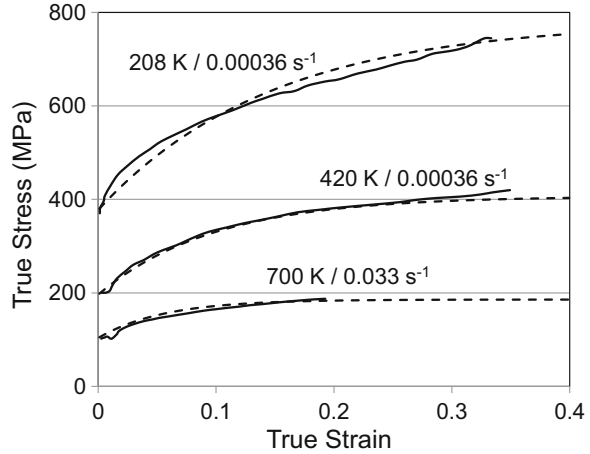
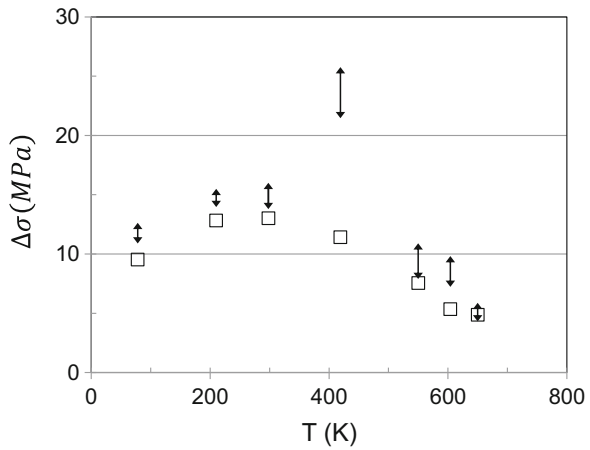


Fig. 10.71 Stress increase following a 5× increase in strain rate (double arrows) as a function of test temperature reported by Yin et al. [26] compared to the predicted stress increase (open squares)



$$s_1 = \frac{1}{\widehat{\sigma}_1} \left[\frac{\mu_o}{\mu} (\sigma - \sigma_a) - s_2 \widehat{\sigma}_2 - s_\epsilon \widehat{\sigma}_\epsilon \right] \quad (10.10a)$$

Taking $\widehat{\sigma}_\epsilon$ as determined by integrating Eq. 6.28 with the model parameters listed in Table 10.19, the variation of s_1 with σ_ϵ can be computed. (Recall that $\sigma_\epsilon = s_\epsilon \widehat{\sigma}_\epsilon \mu / \mu_o$.) For the Conrad et al. material at 650 K and a strain rate of 0.33 s^{-1} , s_1 is computed to equal zero. This implies that obstacle population 1 cannot affect DSA. Assuming that it is obstacle population 2, Eq. 10.10a becomes the following:

$$s_2 = \frac{1}{\widehat{\sigma}_2} \left[\frac{\mu_o}{\mu} (\sigma - \sigma_a) - s_1 \widehat{\sigma}_1 - s_\epsilon \widehat{\sigma}_\epsilon \right] \quad (10.10b)$$

Fig. 10.72 Computed variation of s_1 with σ_ϵ for three test conditions from the Conrad et al. data set in Ti-50A

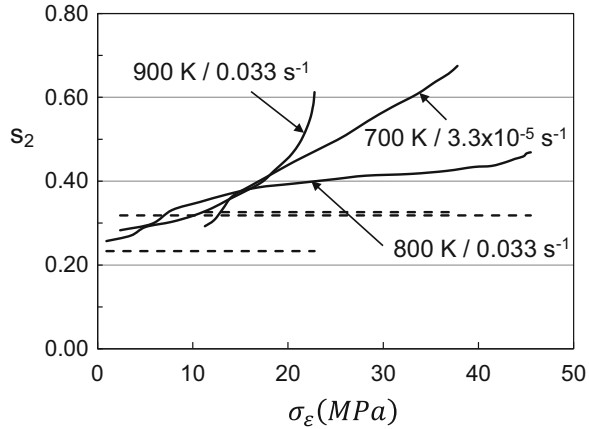


Fig. 10.73 Computed variation of s_1 with σ_ϵ for two test conditions from the Nemat-Nasser et al. data set in CP-Ti

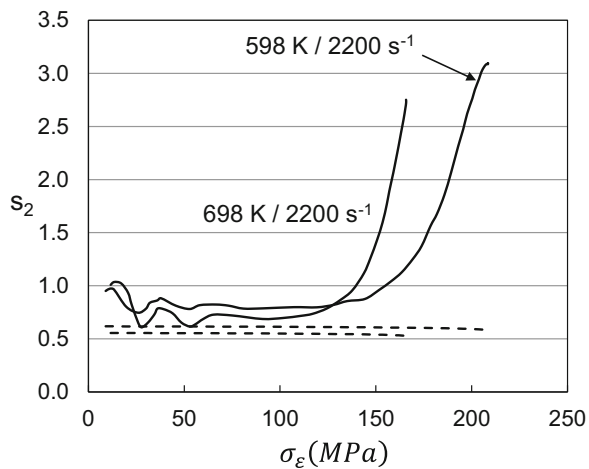
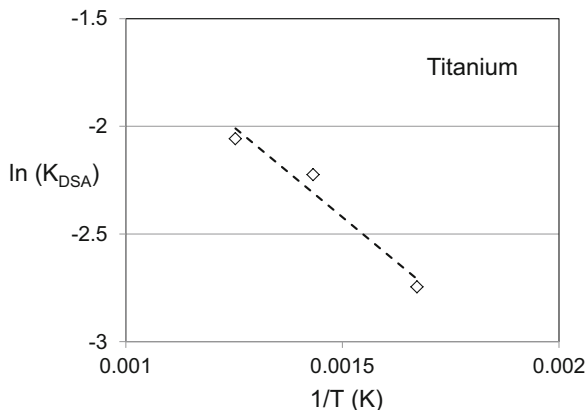


Figure 10.72 shows three results for Conrad et al. material. Consistent with the trends observed in vanadium, s_2 begins to rise almost linearly when σ_ϵ exceeds some value, and this value decreases with increasing temperature, which is evident by comparing the two results at the strain rate of 0.033 s^{-1} . In addition the slope of the dashed line increases with increasing temperature.

Figure 10.73 shows two results from the Nemat-Nasser et al. material. At this strain rate, and for these temperatures s_1 is slightly greater than zero. However, for consistency, Eq. 10.10b is applied. Once again, the value of σ_ϵ characterizing the departure from the baseline value of s_2 decreases with increasing temperature, and the slope of the dashed line increases with increasing temperature. One difference between the results in Fig. 10.73 and those in Fig. 10.72 is that the compression test conditions (test temperature and strain rate) in the former enable higher strains and thus higher s_2 values than achieved in the tension test conditions in the latter.

Fig. 10.74 Variation of K from Eq. 9.9 with reciprocal temperature for the three data points from the Conrad et al. data set in Ti-50A



Following Eq. 9.9, the slopes of the two curves in Fig. 10.73 (and one additional result at a temperature of 798 K not included in Fig. 10.73) for the Nemat-Nasser et al. data set at a strain rate of 2200 s^{-1} are plotted on logarithm K_{DSA} versus inverse temperature coordinates in Fig. 10.74. The dashed line is the fit according to Eq. 9.9. The slope of this line gives $Q = 13.9 \text{ kJ/mol}$. As observed in the equivalent plot for measurements in vanadium (Fig. 9.49), this Q value is low for a diffusion-assisted process.

Deviations from model behavior when DSA becomes active in pure titanium have been shown to be similar to those observed in vanadium and niobium. In each case stresses have risen above those predicted. Analysis of the variation of the kinetic factor s_2 with σ_e was approximately linear with a slope that was inversely related to test temperature. Chapter 13 will present an analysis of DSA based on solute diffusion that shows that this slope should not be directly related to an activation energy for diffusion.

10.10 Analysis of Deformation Behavior of Titanium Alloy Ti6Al-4V

The alloy Ti6Al-4V is a commercially important two-phase, heat-treatable titanium alloy that accounts for over 50% of titanium metal usage. Follansbee and Gray [30] used this alloy as an early test of application of the MTS model formalism to an alloy with multiple strengthening mechanisms. This study included analysis of the strengthening of pure titanium with aluminum, from the work of Paton et al. [32], and a collection of prestrain and reload measurements such as described in Sect. 7.6 and used in the analysis of deformation in copper, nickel, and nickel-carbon alloys in Sect. 8.2. This section will update the earlier study by ensuring consistency with the analysis of deformation in the pure titanium metals in Sect. 10.9.

Fig. 10.75 Yield stress versus temperature and strain rate for Ti6Al-4V measurements reported by Follansbee and Gray [30]

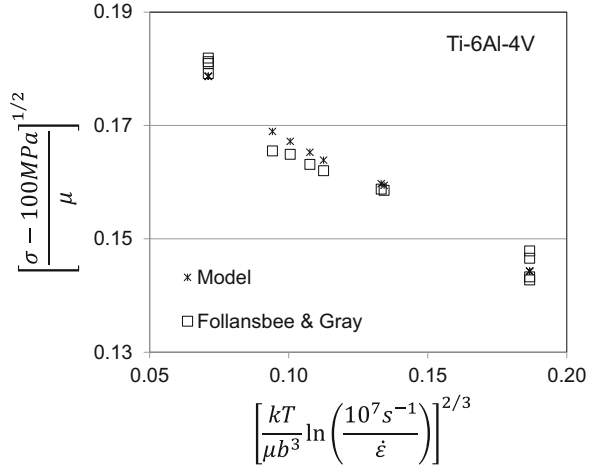


Figure 10.75 shows the variation of yield stress with temperature and strain rate (see Table 10.15) in unstrained material. The model predictions for each temperature and strain rate condition are indicated the “*” symbols. The model constants used for these predictions are as in Table 10.19⁷ except $\sigma_a = 100$ MPa, $\hat{\sigma}_1 = 882$ MPa, and $\hat{\sigma}_2 = 1103$ MPa. The athermal stress is the same used in the original Follansbee and Gray work. It is somewhat higher than the value of 64 MPa suggested by Eq. 10.9 for material with a 5 mm grain size, but it was suggested in [30] that blocky β might contribute to the athermal stress. Both $\hat{\sigma}_1$ and $\hat{\sigma}_2$ are higher than the values used for the Conrad et al. and Nemat-Nasser et al. materials (see Table 10.17) which is consistent with the fact that the Ti6Al-4V alloy had a higher O_{eq} than either of the pure titanium metals.

The variation of yield stress with temperature for the three Ti-Al alloys tested by Paton et al. is shown in Fig. 10.76. (While data is included for an alloy with 0% Al, this data was obtained by extrapolation.) Model parameters were established first for the hypothetical 0% Al material; this gave except $\sigma_a = 26$ MPa (computed using Eq. 10.9 and the reported 30 μm grain size), $\hat{\sigma}_1 = 429$ MPa, and $\hat{\sigma}_2 = 86$ MPa. These parameters establish the dashed line prediction for the 0% Al material in Fig. 10.76.

The dashed line model predictions for the three Al-containing alloys were obtained by varying the magnitude of $\hat{\sigma}_2$. The values selected were 205 MPa, 362 MPa, and 571 MPa for the 3.5% Al, 6.9% Al, and 10.2% Al materials, respectively. Figure 10.77 shows the variation of $\hat{\sigma}_2$ with Al content. Ignoring the 0% Al result, the threshold stress varies almost linearly with Al content.

The dashed line model predictions in Fig. 10.76 were derived by varying $\hat{\sigma}_2$ but maintaining the other model parameters—including σ_a and $\hat{\sigma}_1$ —at the values used for 0% Al. To show that this is not an arbitrary decision, Fig. 10.78 shows the 0% Al

⁷Another small difference is that the temperature-dependent shear modulus in the alloy is described using $\mu_o = 49.02$ GPa, $D_o = 4.335$ GPa, and $T_o = 198$ K.

Fig. 10.76 Yield stress as a function of temperature for Ti-Al alloys reported by Paton et al. [32]. Dashed lines are model fits

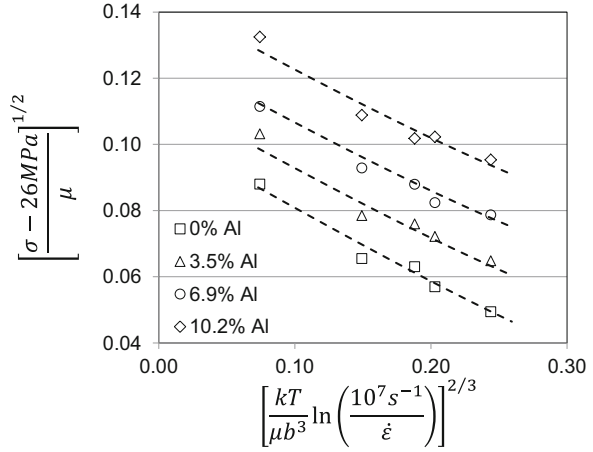


Fig. 10.77 Variation of $\hat{\sigma}_2$ with aluminum content in the binary Ti-Al alloys

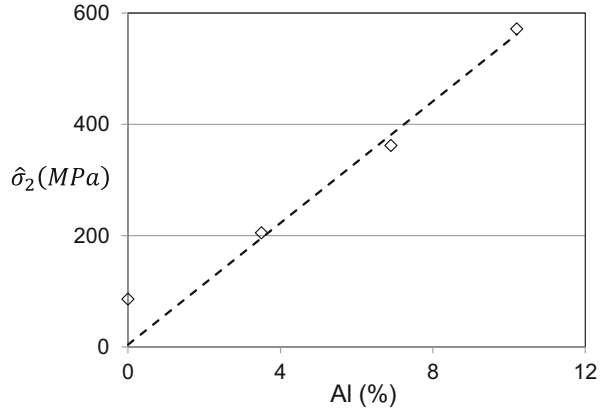


Fig. 10.78 Demonstration of the sensitivity of model fits to the Ti-10.2% Al measurements according to model assumptions

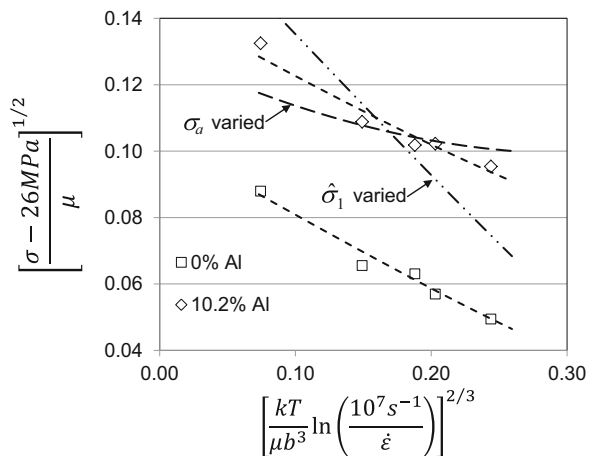


Table 10.20 Prestrain and reload test conditions for the Follansbee and Gray measurements in Ti6Al-4V

Reload conditions			Prestrain conditions	
Temperature (K)	Strain rate (s^{-1})	Strain	Strain rate (s^{-1})	Temperatures (K)
295	0.001	0.101	0.0015	76, ~183, 295
295	0.001	0.185	0.0015	76, ~180, 295
295	0.001	0.281	0.0015	76, 183, 295
495	0.001	0.100	0.0015	76, 295
295	2500	0.084	0.0015	76, ~188, 295

data points along with the dashed line fit (same as in Fig. 10.76) and the 10.2% Al data points with model predictions for analysis (i) assuming $\hat{\sigma}_1$ is allowed to vary while $\hat{\sigma}_2$ and σ_a remain constant and (ii) assuming σ_a is allowed to vary while $\hat{\sigma}_1$ and $\hat{\sigma}_2$ remain constant. For the former, it is evident that the predicted temperature dependence is well above the measured behavior, whereas for the latter the predicted temperature dependence is too low. This reinforces the importance of the selection of state variables and that, when the appropriate selections are made, even complex behavior—such as the variation of strength with aluminum content—can be modeled with ease.

A limited number of prestrain and reload tests were performed by Follansbee and Gray [30]. The conditions tested are summarized in Table 10.20. For the reload experiments, multiple tests were performed at all combinations of reload temperature and strain rate, except that only one test was performed at 183 K for the sample prestrained at 295 K and a strain rate of $0.001 s^{-1}$ to a strain of 0.281. Figure 10.79 shows the yield stress versus temperature and strain rate for the $0.001 s^{-1}$ and 295 K prestrains.

The dashed line model predictions are drawn according to Eq. 10.5 with σ_a 100 MPa, $\hat{\sigma}_1 = 882$ MPa, and $\hat{\sigma}_2 = 1103$ MPa (as in Fig. 10.78) and all other parameters as listed in Table 10.19. The value of $\hat{\sigma}_\epsilon$ is the only fitting parameter. Values of 270 MPa, 363 MPa, and 461 MPa were used for prestrains of 0.101, 0.185, and 0.281, respectively. Just as for the analysis of the Ti-Al alloys in Fig. 10.76, matching the stress level as well as the temperature dependence of the reload yield stress through variation of a single parameter—in this case $\hat{\sigma}_\epsilon$ —requires that the model parameters, in this case s_ϵ , be descriptive of the deformation behavior.

Figure 10.80 shows the variation of $\hat{\sigma}_\epsilon$ with true strain along with a fit (the dashed line) according to Eq. 6.28 with $\kappa = 1$, $\theta_{II} = 3400$ MPa, and $\hat{\sigma}_{\epsilon so} = 540$ MPa. Only one prestrain strain condition ($\epsilon = 0.084$) was tested at the strain rate of $2500 s^{-1}$. Figure 10.81 is a plot of reload yield stress versus reload test temperature. The dashed line through the data points is the model prediction, as described for Fig. 10.79, with $\hat{\sigma}_\epsilon = 225$ MPa. For a measurement under similar conditions (298 K and $2000 s^{-1}$), the variation of $\hat{\sigma}_\epsilon$ with strain was analyzed directly from the stress–strain curve using Eq. 9.7 as described for UfKonel in Sect. 9.5 and used for many of the evolution analyses in Chap. 9 for BCC metals and in this chapter for

Fig. 10.79 Reload yield stress versus reload test temperature (all at 0.0015 s^{-1}) for prestrains of Ti6Al-4V at a strain rate of 0.001 s^{-1} to three strain levels

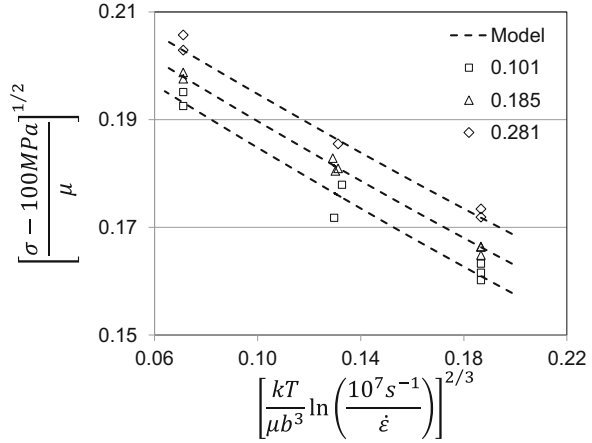


Fig. 10.80 Variation of $\hat{\sigma}_\epsilon$ with prestrain level for the 0.001 s^{-1} prestrains in Ti6Al-4V

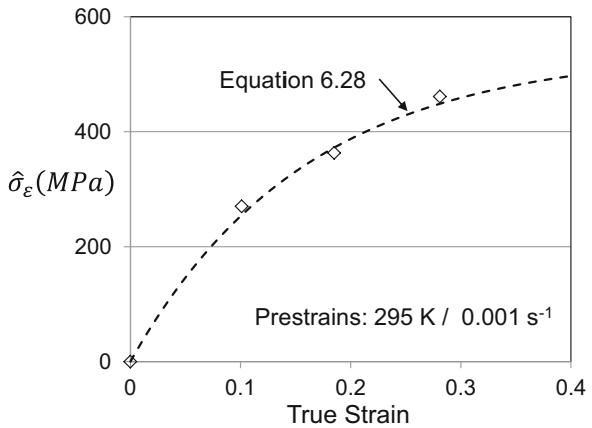


Fig. 10.81 Variation of reload yield stress versus reload temperature (all at 0.001 s^{-1}) for Ti6Al-4V prestrained at 2500 s^{-1} to a strain of 0.084 along with model fit (dashed line)

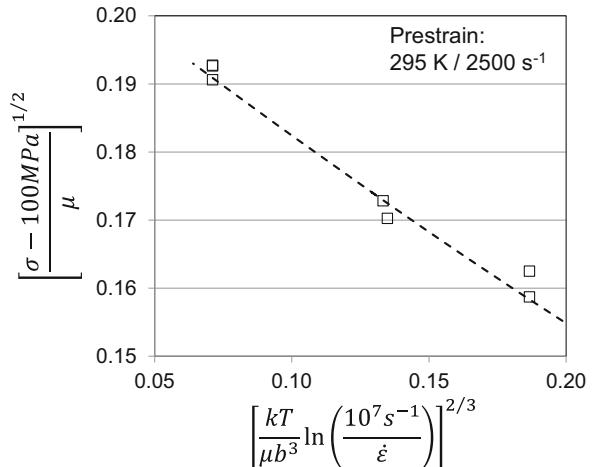
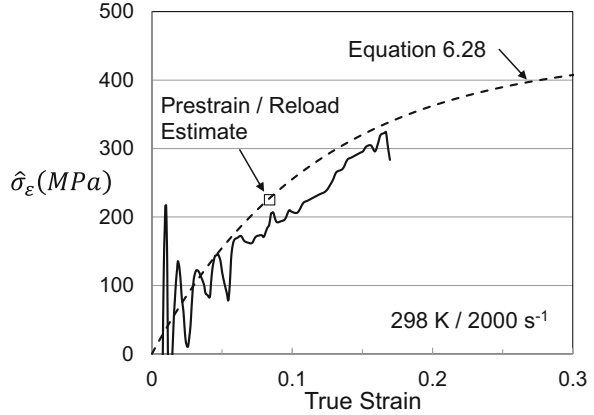


Fig. 10.82 Computed variation of $\hat{\sigma}_\varepsilon$ with strain for a measurement at 298 K and a strain rate of 2000 s^{-1} following the procedure outlined for UfKoneI in Sect. 9.5

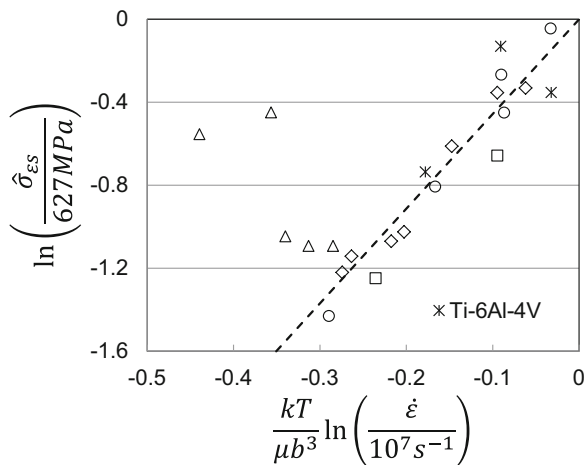


HCP metals. The result is shown in Fig. 10.82. The dashed line in this figure is Eq. 6.28 with $\kappa = 1$, $\theta_{II} = 3800 \text{ MPa}$, and $\hat{\sigma}_{\varepsilon_{so}} = 440 \text{ MPa}$. The open square is the result from the prestrain plus reload tests described in Fig. 10.81. Agreement between the two analyses is excellent.

Note that $\hat{\sigma}_\varepsilon$ for the dynamic test (2500 s^{-1} to a strain of 0.084) is only 225 MPa, whereas the value for the quasi-static test (0.001 s^{-1} to a strain of 0.101) was estimated to be 270 MPa. Similarly, the saturation threshold stress for the dynamic test (Fig. 10.82) was estimated as 440 MPa, whereas the value for the quasi-static test (Fig. 10.80) was estimated to be 540 MPa. The expectation from Eq. 6.26 is that the saturation threshold stress increases with increasing strain rate. The observation in Ti6Al-4V likely relates to the existence of deformation twinning, which is consistent with the observations by Follansbee and Gray [30] and is consistent with the tendency for the solid curve in Fig. 10.82 to dip below the dashed curve. This was discussed earlier in relation to measurements in zinc (Fig. 10.5), zirconium (Fig. 10.44), and vanadium (Fig. 9.41).

The saturation threshold stress values for the three prestrain strain rate and temperature conditions in Table 10.20 have been added to the plot of saturation threshold stress versus temperature and strain rate for pure titanium presented in Fig. 10.68 and shown in Fig. 10.83. (See Fig. 10.68 for identification of the open symbols). The measurement at 295 K and 0.001 s^{-1} (the symbol at an abscissa value of -0.09) is a little above the best-fit line (same line as in Fig. 10.68), whereas the measurement at 495 K (the symbol at an abscissa value of -0.18) falls close to the line and the measurement at 295 K and a strain rate of 2500 s^{-1} (abscissa value of -0.03) falls below the line, which is consistent with the effect of deformation twinning discussed above. In general, the evolution behavior in Ti6Al-4V is very similar to that observed in pure titanium.

Fig. 10.83 Saturation threshold stress analysis in pure titanium (Fig. 10.68) with the Ti6Al-4V results included



10.11 Summary

The HCP metals analyzed in this chapter offered a full slate of confounding mechanisms that taxed application of the MTS model formulation. This included the roles of deformation twinning, dynamic strain aging (DSA), and dynamic recrystallization. The experience gained through analysis of FCC systems in Chap. 8 and the BCC systems in Chap. 9 enabled the identification of signatures of twinning, DSA, and dynamic recrystallization.

Dynamic recrystallization was thought to be occurring in pure magnesium at high homologous temperatures. Stress–strain curves (even those in compression) that exhibited thermal softening (a stress level that decreases with increasing strain as in Fig. 10.25) gave strong evidence of dynamic recrystallization. The effects were also observed in the saturation stress plot, where the apparent saturation stress dipped below the low-temperature behavior (as in Fig. 10.29). Note that for the three solid diamonds in Fig. 10.29, the homologous temperature is 0.567 at 523 K and 0.621 at 573 K. These temperatures are well above the rule of thumb estimate that the recrystallization temperature is at roughly one-half of the melting point ($T_H = 0.5$).

The effects of deformation twinning were introduced in Sect. 9.8 in analyzing deformation in pure, polycrystalline vanadium. Deformation twinning can affect the yield stress correlation (as in Zirconium in Fig. 10.37) and the strain-hardening behavior. Evidence is that the latter can be a dislocation storage rate that is initially lower than expected, as in zinc (Fig. 10.5), cadmium (Figs. 10.14 and 10.15), magnesium AZ31 (Fig. 10.26), pure zirconium (Fig. 10.42), and pure titanium (Fig. 10.67). It is important to note that microscopic evidence of twinning exists in some but not all of these systems. The shape of the stress–strain curve and the evidence of a low initial dislocation storage rate lead to the general conclusions proffered here.

Deformation twinning also leads to enhanced hardening, as evident in many of the figures listed above (see, for instance, the measurement in titanium in Fig. 10.67). However, the presence of deformation twinning in niobium (see Table 9.16 and the related discussion) and Ti6Al-4V (see Fig. 10.82 and the related discussion) leads to lower hardening than anticipated. Thus, deformation twinning must be fairly extensive to lead to enhanced hardening. When present, the enhanced hardening may well reflect an increase in the athermal stress due to effective grain refinement by deformation twins. Estimates of the extent of grain refinement were made for zirconium (see Sect. 10.7.1) and cadmium (see Sect. 10.3). Salem et al. reported an extensive analysis of the strain hardening in titanium using microstructure characterization [33]. They conclude that deformation twinning is first observed at a strain level of 5% and that pronounced twinning leads to the observed increased rate of strain hardening. It is suggested here that the initial effect of deformation twinning is a lower rate of dislocation storage—and this is all that is observed in some systems. In other systems, deformation twinning can actually lead to an increased hardening rate due to grain refinement. A good example of this is found in the stress–strain measurements by El-Danaf et al. [31] in 70/30 brass with an initial grain size of 30 μm . Figure 10.84 shows the strain-hardening rate divided by the shear modulus versus true strain measured in a compression test at a strain rate of 0.001 s^{-1} . Also included in this figure is the strain-hardening rate predicted using the Voce equation, Eq. 5.12. At low strains, the hardening follows the Voce equation. At strains greater than 5%, however, significant deviations from Voce behavior are noted. These deviations are described as indicating a transition to “primary twinning,” a conclusion that is supported with extensive microscopic evidence [31]. It is further suggested that the twinning inhibits dynamic recovery processes such as cross slip.

Dynamic strain aging also has led to some common signatures. An increased rate of hardening is observed in stress–strain curves. Several analyzed systems have yielded a common observation. This was introduced in Sect. 9.9 in analysis of measurements in vanadium. Analysis of measurements in niobium (see Fig. 9.62)

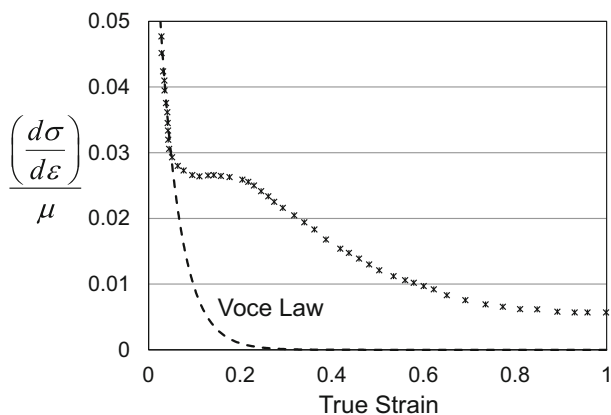


Fig. 10.84 Normalized rate of strain hardening versus plastic strain measured in 70/30 brass [31]

Table 10.21 Model parameters for the kinetics of yield defined by Eqs. 6.15 and 6.16 for the HCP metals studied in this chapter and for several FCC and BCC metals analyzed in Chaps. 8 and 9

Material	Table	Obstacle 1				Obstacle 2			
		g_o	$\dot{\epsilon}_o$	p	q	g_o	$\dot{\epsilon}_o$	p	q
HCP metals									
Zirconium	10.12	0.15	10^8	0.5	1.5	1	10^8	0.5	1.5
Cadmium	10.4	0.20	10^7	0.5	1.5	None			
Magnesium AZ31	10.5 10.8	0.35	10^7	0.5	1.5	1	10^8	0.5	1.5
Zinc	10.2	0.17	10^7	0.5	1.5	None			
Titanium/Ti6Al-4V	10.16	0.25	10^7	0.5	1.5	1.6	10^{10}	0.5	1.5
FCC metals									
Nickel-C	8.6	0.20	10^9	0.5	1.5	None			
Copper-Al	8.12	0.6	10^7	0.5	1.5	None			
Monel	8.11	0.539	10^7	0.5	1.5	None			
Austenitic SS	11.2	0.2	10^8	0.5	1.5	1.7	10^8	0.5	1.5
BCC metals									
Niobium	9.15	0.1	10^8	0.5	1.5	0.5	10^{10}	0.5	1.5
1018 steel	9.11	0.11	10^9	0.5	1.5	1	10^{10}	0.5	1.5
Vanadium	9.13	0.1	10^8	0.5	1.5	1	10^{10}	0.5	1.5

and titanium (see Figs. 10.72 and 10.73) affirmed the signatures. It is observed that upon the onset of DSA, one of the kinetic terms, e.g., s_1 , begins to increase almost linearly with σ_e at a slope that is inversely related to temperature. A more rigorous analysis of these trends is described in Chap. 13.

With the measurements presented in this chapter in five HCP systems, it is useful to compile these results and search for commonalities. Table 10.21 lists parameters for Eqs. 6.15 and 6.16 for the HCP metals analyzed. Included in this table are select values of FCC and BCC systems from Chaps. 8 and 9. It is worth emphasizing that in all cases the parameters for dislocation-dislocation interactions ($\hat{\sigma}_e$) are those listed in Table 9.7. Note that for some of the metals listed in Table 10.21 there was no need for a second obstacle population, but for many metals, this was necessary. Also note that, where two obstacle populations are identified, the protocol has been to identify obstacle 1 with the more rate-sensitive (smallest activation volume) obstacle population and obstacle 2 with the less rate-sensitive obstacle population.

In a similar fashion, Table 10.22 summarizes the evolution equation parameters (Eqs. 6.26, 6.28, and 6.29) for these same systems. These results offer many opportunities to search for correlations. It is interesting that θ_{II}/μ_o is close to 0.05 (which is well above the rule-of-thumb value given in Eq. 3.12), but there is considerable variation around this value. Also of note is that $\kappa = 1$ was suitable for all of the HCP systems, but a higher value of κ was necessary for the other metals.

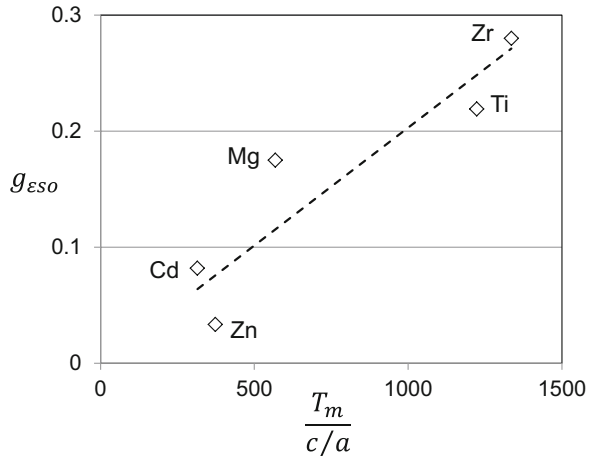
Of the potential correlations among the parameters in Table 10.22, perhaps the most interesting is the observation that, in HCP metals, g_{eso} increases with increasing melting temperature but decreases with the c/a ratio (from Table 10.1). The

Table 10.22 Model parameters for structure evolution defined by Eqs. 6.26, 6.28, and 6.29 for the HCP metals studied in this chapter and for several FCC and BCC metals analyzed in Chaps. 8 and 9

Material	Table	$\hat{\sigma}_{\epsilon_{SO}}/\mu_o$	$\dot{\epsilon}_{\epsilon_{SO}} \text{ (s}^{-1}\text{)}$	$g_{\epsilon_{SO}}$	θ_{II}/μ_o^a	κ
HCP metals						
Zirconium	10.12	0.0124	108	0.280	0.191	1
Cadmium	10.4	0.00578	10 ⁷	0.0819	0.0404	1
Magnesium AZ31	10.10	0.0352	10 ⁸	0.175	0.0672	1
Zinc	10.2	0.0225	10 ⁷	0.0335	0.0272	1
Titanium/Ti6Al-4V	10.19	0.0132	10 ⁷	0.216	0.0714	1
FCC metals						
Nickel	8.11	0.0148	10 ⁸	0.168	0.0541	2
Monel 400	8.11	0.0121	10 ⁷	0.37	0.0395	
Copper	8.4	0.0155	10 ⁸	0.301	0.0522	2
Austenitic SS	11.6	0.0364	10 ⁷	0.258	0.0437	2
BCC metals						
Niobium	9.17	0.0125	10 ⁸	0.219	0.0252	2
1018 steel	9.11	0.00904	10 ¹⁰	0.468	0.0476	2
Vanadium	9.13	0.00896	10 ¹⁰	0.233	0.0518	3

^aThe numerator is actually A_0 in Eq. 6.29

Fig. 10.85 Variation of $g_{\epsilon_{SO}}$ with the ratio of T_m divided by the c/a ratio (both from Table 10.1)



correlation is shown in Fig. 10.85. It is unclear why these parameters should correlate in this manner, but the trend is fairly strong.

This chapter ended with the analysis of deformation kinetics in the commercially important titanium alloy Ti6Al-4V to demonstrate how the understanding of a complex system builds from the understanding of the pure metal. In the next chapter, deformation in austenitic stainless steels—another broadly used set of commercial alloys—is addressed.

Exercises

- 10.1 From the model parameters for zinc listed in Table 10.2 (assume $\sigma_a = 20$ MPa) and the hardening parameters listed in the paragraphs following Table 10.3, assume that the metal is further alloyed, which introduces a second obstacle population. This population is characterized by $p = 0.5$, $q = 1.5$, $g_o = 1.0$, $\dot{\epsilon}_o = 10^{10} \text{ s}^{-1}$, and $\hat{\sigma} = 159$ MPa. (a) Compare stress–strain curves at 295 K and a strain rate of 0.001 s^{-1} for the two materials. (b) Generate and compare plots of yield stress versus temperature and strain rate at zero strain. (c) Generate and compare plots of yield stress versus temperature and strain rate at a strain level of 0.20. For (b) and (c), include temperatures between 100 K and 400 K and strain rates between 0.0004 s^{-1} and 4 s^{-1} .
- 10.2 The data sets in Table 10.E2 for two tests in a cadmium-based material at two sets of conditions. Included in the table are stress–strain values in pure cadmium for one of the conditions, which indicates that the unknown material is stronger. (a) Determine whether the additional strengthening is due to strain hardening or by alloying. Hint: plot yield stress versus temperature and strain rate using the model parameters for pure Cd described in Sect. 10.2 (assume no deformation twinning). (b) Add the yield stresses for the unknown material at

Table 10.E2 Yield stress versus strain for pure Cd at one test temperature and strain rate and an unknown Cd alloy at two temperatures and strain rates

Strain	Stress (MPa)		
	Unknown Cd-based material		Pure Cd
	190 K/ 0.01 s^{-1}	225 K/ 0.001 s^{-1}	190 K/ 0.01 s^{-1}
0.002	92.2	50.5	71.8
0.01	101.2	59.3	80.0
0.015	105.8	63.4	84.6
0.02	110.1	67.1	88.9
0.025	114.0	70.4	92.8
0.03	117.7	73.4	96.5
0.035	121.1	76.1	99.9
0.04	124.2	78.5	103.0
0.045	127.1	80.7	105.9
0.05	129.7	82.7	108.5
0.055	132.2	84.4	111.0
0.06	134.5	86.0	113.3
0.065	136.6	87.5	115.4
0.07	138.5	88.8	117.3
0.08	141.9	91.0	120.7
0.09	144.9	92.7	123.7
0.010	147.4	94.2	126.2
0.011	149.5	95.4	128.3

Table 10.E4 Stress versus strain measurements at 373 K and a strain rate of 0.005 s^{-1} on magnesium alloy AZ31B exposed to a wire-drawing operation

Strain	Stress (MPa)	Strain	Stress (MPa)
0.003	283	0.09	300
0.01	287	0.1	298
0.015	290	0.11	302
0.02	288	0.12	302
0.025	288	0.14	306
0.03	288	0.16	301
0.035	294	0.18	303
0.04	293	0.2	306
0.045	292	0.25	309
0.05	291	0.3	310
0.055	294	0.35	311
0.06	294	0.4	312
0.065	292	0.45	312
0.07	296	0.5	313
0.08	295	0.55	313

the two conditions, and find model parameters that provide a good fit. Compare the deduced model parameters with typical model parameters for strain hardening and for solution hardening.

- 10.3 From your answer to Exercise 10.2, compare the predicted and measured stress–strain curves at both loading conditions. Assume (as usual) that for the stored dislocation population, $p_\epsilon = 0.667$, $q_\epsilon = 1.0$, $g_{o\epsilon} = 1.6$, and $\dot{\epsilon}_{o\epsilon} = 10^7 \text{ s}^{-1}$.
- 10.4 Table 10.E4 lists stress–strain data measured at 373 K and a strain rate of 0.005 s^{-1} on magnesium alloy AZ31B exposed to a wire-drawing operation. (a) Estimate the equivalent strain imposed by this operation. Refer to the model parameters in Tables 10.8 and 10.10. (b) Compare the measured and predicted stress–strain curves.
- 10.5 Table 10.E5 lists stress–strain data measured at 298 K and a strain rate of 1.0 s^{-1} on pure zirconium. (a) Plot this data set along with predictions of the model developed in Sects. 10.6 and 10.7. Use $\sigma_a = 20 \text{ MPa}$ (to start) and the model parameters for the Chen and Gray material (see Tables 10.12 and 10.13). Assume this deformation is under isothermal conditions. (b) Compared to what is presented in Sect. 10.7, what is your assessment of this plot? (c) If the grain size dependence of the stress follows:

$$\sigma \propto \frac{17.2 \text{ MPa} - \text{mm}^{1/2}}{\sqrt{d_{gs}(\text{mm})}}$$

and it is assumed that the increased rate of hardening at strains exceeding 0.25 is caused by a decrease in the effective grain size due to deformation twinning, estimate the grain size at a strain of 0.55.

Table 10.E5 Stress versus strain measurements at 298 K and a strain rate of 1.0 s^{-1} on pure zirconium.

Strain	Stress (MPa)	Strain	Stress (MPa)
0.003	453	0.09	541
0.01	458	0.1	562
0.015	460	0.11	568
0.02	464	0.12	588
0.025	475	0.14	604
0.03	483	0.16	624
0.035	487	0.18	650
0.04	491	0.2	681
0.045	498	0.25	765
0.05	499	0.3	798
0.055	509	0.35	858
0.06	510	0.4	910
0.065	523	0.45	981
0.07	530	0.5	1042
0.08	542	0.55	1100

Table 10.E6 Hypothetical stress versus strain measurements at 700 K and a strain rate of 0.001 s^{-1} on Ti-50A

Strain	Stress (MPa)	Strain	Stress (MPa)
0.003	103	0.09	217
0.01	109	0.1	227
0.015	111	0.11	231
0.02	116	0.12	235
0.025	121	0.14	236
0.03	133	0.16	242
0.035	140	0.18	246
0.04	152	0.2	246
0.045	162	0.25	251
0.05	175	0.3	250
0.055	181		
0.06	189		
0.065	197		
0.07	199		
0.08	211		

10.6 Table 10.E6 lists (hypothetical) stress–strain data measured at 700 K and a strain rate of 0.001 s^{-1} on Ti-50A. (a) Create the plot of $\hat{\sigma}_\epsilon$ versus strain. Assume that this material has model parameters similar to the Conrad et al. material listed in Table 10.19. Include on the plot the model prediction for $\hat{\sigma}_\epsilon$ versus strain according to the model parameters in Table 10.19. (b) Using

Table 10.E7 Saturation threshold stress and stacking fault energy (as well as values normalized by the shear modulus and Burgers vector) in FCC and a few other metals

Material	$\hat{\sigma}_{\text{ESO}}$ (MPa)	γ_{SF} (ergs/cm ²)	$\frac{\gamma_{\text{SF}}}{\mu b}$	$\frac{\hat{\sigma}_{\text{ESO}}}{\mu_0}$
Cu	710	40	0.0034	0.0155
Cu – 2 Al	975	25	0.0021	0.0213
Cu-6Al	3350	6	0.0005	0.0732
Ni	1180	125	0.0059	0.0139
SS	4000	30	0.0017	0.0560
Al	From Ref. [34]		0.0231	0.0066
Ni			0.0130	0.0105
Cu			0.0048	0.0171
Ag			0.0018	0.0263
Mg	654	125	0.0209	0.0352
Zr	506	240	0.0178	0.0121
W	735	50	0.0011	0.0045
Zn	1426	140	0.0083	0.0225
Cd	192	175	0.0177	0.0058

Eq. 10.7, create a plot of s_1 versus s_e —as in Figs. 10.75 and 10.76. (c) How do the slope and intercept in this curve compare to the values listed in Table 10.19?

- 10.7 Table 10.E7 lists the data used to establish Fig. 8.46, showing the correlation between the 0 K saturation threshold stress and the stacking fault energy in FCC metals. Included are several of the results from this chapter in HCP metals (and one result in W). For these metals, values of the stacking fault energy were taken from Murr [34]. Add the other metals to the FCC systems in a plot akin to Fig. 8.46. Does the correlation (dashed line in Fig. 8.46) continue to hold?

References

1. N. R. Risebrough, The Deformation Characteristic of Zinc and Cadmium, PhD Thesis, Department of Metallurgy, University of British Columbia, 1965
2. J.H. Liu, C.X. Huang, S.D. Wu, Z.F. Zhang, Tensile deformation and fracture behaviors of high purity polycrystalline zinc. *Mater. Sci. Eng. A* **490**, 117–125 (2008)
3. S.L. Mannan, P. Rodriguez, Grain size dependence of the deformation behaviour of cadmium. *Acta Metall.* **23**, 221–228 (1975)
4. C.A. Yablinsky, E.K. Ceretta, G.T. Gray III, D.W. Brow, S.C. Vogel, The effect of twinning on the work-hardening behavior and microstructural evolution of hafnium. *Metall. Mater. Trans. A* **37A**, 1907–1915 (2006)
5. H. Suzuki, S. Hashizume, Y. Yabuki, Y. Ichihara, S. Nakajima, K. Kenimochi, Studies on the flow stress of metals and alloys, Report of the Institute of Industrial Science, The University of Tokyo, Vol. 18, No. 3, Serial No. 117, 1968, p. 59

6. J.E. Hockett, Compression testing at constant true strain rates. *Proc. Am. Soc. Test. Mater.* **59**, 1309–1319 (1959)
7. H. Takuda, T. Morishita, T. Kinoshita, N. Shirakawa, Modeling of formula for flow stress of a magnesium alloy AZ31 sheet at elevated temperatures. *J. Mater. Proc. Technol.* **164–165**, 1258–1262
8. S.R. Agnew, Ö. Duygulu, Plastic anisotropy and the role of non-basal slip in magnesium alloy AZ31B. *Int. Journal of Plasticity* **21**, 1161–1193 (2005)
9. P. Lukáč, Z. Trojanová, Hardening and softening in magnesium alloys, in *Magnesium Alloys – Design, Processing, and Properties*, ed. by F. Czerwinski, (In Tech, Rijeka, 2011) pp. 1–20
10. P. Lukáč, J. Balík, Z. Trojanová, Deformation behaviour of AZ31 magnesium alloy, in *Proceedings, Metal 2011, 20th Anniversary International Conference on Metallurgy and Materials*, (Brno, Czech Republic, 2011), pp. 915–920
11. J.A.L. Robertson, Zirconium – An international nuclear fuel. *J. Nucl. Mater.* **100**, 108–118 (1981)
12. A. Akhtar, K.A. Teghtsoonian, Plastic deformation of zirconium single crystals. *Acta Metall.* **19**, 655–663 (1971)
13. P. Soo, G.T. Higgins, The deformation of zirconium-oxygen single crystals. *Acta Metall.* **16**, 177–186 (1968)
14. A. Buch, *Pure Metals Properties* (ASM International, Materials Park, 1999) (see Table 14, p. 144, and Table 19, p. 147)
15. S.-R. Chen, G. T. Gray III, Influence of Twinning on the Constitutive Response of Zr: Experiments and Modeling, International conference on mechanical and physical behavior of materials under dynamic loading (EURO/DYMAT), Toledo (Spain), 1997, pp. C3-741 to C3-746
16. L. Addessio, E.K. Cerreta, G.T. Gray III, Mechanical behavior of zirconium and hafnium in tension and compression. *Metall. Mater. Trans. A* **36A**, 2893–2903 (2005)
17. M.A. Meyers, O. Vöhringer, V.A. Lubarda, The onset of twinning in metals: A constitutive description. *Acta Materialia* **49**, 4025–5039 (2001)
18. S.V. Ramani, P. Rodriguez, Grain size dependence of the deformation behavior of alpha zirconium. *Can. Metall. Q.* **11**(1), 61–67 (1972)
19. R.J. McCabe, E.K. Cerreta, A. Misra, G.C. Kaschner, C.N. Tomé, Effects of texture, temperature and strain on the deformation modes of zirconium. *Philos. Mag.* **86**(23), 3595–3611 (2006)
20. L.M. Howe, W.R. Thomas, The effect of neutron irradiation on the tensile properties of Zircaloy-2. *J. Nucl. Mater.* **2**(3), 248–260 (1960)
21. H. E. Boyer, T. L. Gall (eds.), *Metals Handbook Desk Edition* (ASM International, Materials Park, 1985), pp. 20–35
22. T. Byun, N. Hashimoto, Strain localization in irradiated materials. *Nucl. Eng. Technol.* **38**(7), 619–638 (2006)
23. T.S. Byun, K. Farrell, N. Hashimoto, Plastic instability behavior of bcc and hcp metals after low temperature neutron irradiation. *J. Nucl. Mater.* **329–333**, 998–1002 (2004)
24. H. Conrad, M. Doner, B. deMeester, Investigations to understand the plastic deformation and strengthening mechanisms of solid solution phases of titanium, Air Force Technical Report AFML-TR-72-04, Air Force Materials Laboratory, 1972, available from NTIS <http://www.dtic.mil/cgi-bin/GetTRDoc?AD=AD0744711>
25. F.H. Froes and I. Caplan, editors, Titanium '92 Science and Technology, Proceedings of the Seventh World Conference on Titanium in San Diego, California, June 28 – July 2, 1992, TMS, Warrendale
26. C.-A. Yin, M. Doner, H. Conrad, Deformation kinetics of commercial Ti-50A (0.5 at. pct O_{eq}) at low temperatures ($T < 0.3 T_m$). *Metall. Trans. A.* **14A**, 2545–2556 (1983)
27. M. Doner, H. Conrad, Deformation mechanisms in commercial Ti-50A (0.5a at. pct O_{eq}) at intermediate and high temperatures (0.3 – 0.6 T_m). *Metall. Transact.* **4**, 2809–2817 (1973)

28. S. Nemat-Nasser, W.G. Guo, Y.Y. Cheng, Mechanical properties and deformation mechanisms of a commercially pure titanium. *Acta Materialia* **47**, 3705–3720 (1999)
29. R.J. Lederich, S.M.L. Sastry, J.E. O’Neal, B.B. Rath, The effect of grain size on yield stress and work hardening of polycrystalline titanium at 295 K and 575 K. *Mater. Sci. Eng.* **33**, 183–188 (1978)
30. P.S. Follansbee, G.T. Gray III, An analysis of the low temperature, low and high strain-rate deformation of Ti-6Al-4V. *Metall. Trans. A.* **11989**, 863–874 (20A)
31. E. El-Danaf, S.R. Kalidindi, R.D. Doherty, Influence of grain size and stacking fault energy on deformation twinning in FCC metals. *Metall. Mater. Trans. A* **30A**, 1223–1233 (1999)
32. N.E. Paton, J.C. Williams, G.P. Rauscher, The deformation of alpha-phase titanium, in *Titanium Science and Technology*, ed. by R. I. Jaffee, H. M. Burte, (Plenum Press, New York, 1973), pp. 1049–1069
33. A.A. Salem, S.R. Kalidindi, R.D. Doherty, Strain hardening regimes and microstructure evolution during large strain compression of high purity titanium. *Scr. Mater.* **46**, 419–423 (2002)
34. L.E. Murr, *Interfacial Phenomena in Metals and Alloys*, Table 3.9 (Addison-Wesley Publishing Company, Reading, 1975), pp. 145–148

Chapter 11

Application of MTS Model to Austenitic Stainless Steels



Introduction

Austenitic stainless steels are an industrially important class of metals that have found use in a myriad of applications.¹ These metals are characterized by their inherent corrosion resistance and excellent strength and ductility. The latter properties arise from their FCC crystal structure that results from the expansion of the austenite phase field transformation primarily due to large nickel additions and the increased sluggishness of the gamma to alpha phase caused by the large chromium and nickel additions [1]. The hardening in austenitic stainless steels is a combination of solution hardening, interstitial hardening (nitrogen and oxygen additions in particular), precipitate hardening (MC carbides, where M is one of the metal alloy additions), and, after straining, hardening from the stored dislocation density.

11.1 Variation of Yield Stress with Temperature and Strain Rate in Annealed Materials

Because austenitic stainless steels are often used at cryogenic temperatures as well as temperatures well above room temperature (RT, where $T/T_m = 0.163$), a constitutive description of the strength properties over a wide range of temperatures assists component design analysis. Figure 11.1 shows the tensile yield stress versus tem-

Supplementary Information The online version contains supplementary material available at https://doi.org/10.1007/978-3-031-04556-1_11.

¹Much of the content in this chapter was originally published in Reference [1]. This chapter contains minor revisions and some new material (e.g., Sect. 11.5).

perature (measured at quasi-static strain rates²) in annealed AISI 304 and 304L stainless steel reported by Clauss [2], the Sandmeyer Steel Company [3], and the Alruqee Group [4] and similar data for annealed AISI 316 and 316L stainless steel reported by Clauss [2] and the Sandmeyer Steel Company [5].

The data in Fig. 11.1 are typical of all measurements in annealed AISI 304/304L/316/316L in that the variation in strength with temperature at low temperatures is quite high but the temperature dependence decreases with increasing temperatures up to the maximum temperature shown in these figures, which is at a $T/T_m = 0.552$.

Following the work described in Chap. 8 for pure FCC metals and some binary alloys, and with the analysis of deformation in pure HCP metals and select HCP alloys (Zircaloy-2 and Ti-6Al-4V) in Chap. 10, this chapter will consider deformation in the austenitic stainless steels. Table 11.1 gives a partial list of published sources for measurements in the AISI 304/304L/316/316L family of alloys. Included are measurements reported by Steichen [6, 7], Gray and Chen [8], Conway et al. [9], Swindeman [10], Albertini and Montagnani [11], Hammond and Sikka [12], Norström [13], Clauss [2], Brynes et al. [14], Byun et al. [15], Dai et al. [16], and Stout and Follansbee [17]. Several of these sources were used for the analyses presented in this chapter.

With the list of contributing deformation mechanisms given above, it is not expected that a one-obstacle population model will describe the dependence of yield stress on temperature and strain rate over a wide range of conditions.

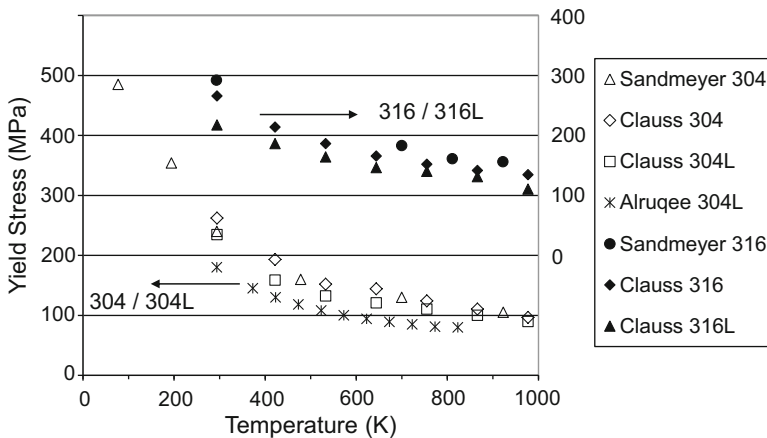


Fig. 11.1 Yield stress versus test temperature for 304 and 304L (open symbols, left ordinate) and for 316 and 316L (closed symbols, right ordinate) stainless steels reported by several sources

²The strain rate for measurements reported in product bulletins is rarely specified. However, the capabilities of standard testing machines imply that these strain rates (usually constant cross head velocity rather than true strain rate) are in the range 10^{-4} s^{-1} to 10^{-2} s^{-1} .

Table 11.1 Selection of published references in the AISI 304/304L/316/316L stainless steels with temperature- and strain rate-dependent yield stress and stress–strain measurements

Reference	Material	Processing conditions	Testing conditions		
			Mode	Temperatures	Strain rates (s ⁻¹)
Steichen [6, 7]	304 0.052% N	HT: 1339 K, 1 hr; ASTM GS 5	Tension	Stress–strain curves: RT, 811 K YS measure- ments: RT to 1033 K ($T_H = 0.57$)	Stress–strain curves: 3×10^{-5} and 10^2 YS measure- ments: 3×10^{-5} to 10^2
Gray and Chen [8]	304L annealed; 316L mill- annealed		Compression	RT	0.001, 0.1, 2500
Conway et al. [9]	304 and 316	Stress relief anneal	Tension	294 K, 703 K, 923 K, 1089 K	4×10^{-5} 0.004
Swindeman [10]	304 0.031% N	HT: 1366 K for 30 min; 120 μm to 250 μm GS	Tension	RT to 760 K	1.5×10^{-6} to 8.3×10^{-3}
Albertini and Montagnani [11]	304L, 316L, 321	“Virgin,” welded, and irradiated	Tension	RT to 1223 K	0.01 to 1000
Hammond and Sikka [12]	304 and 316; 8 separate heats; with chemistry	Mill-annealed and re-annealed 1338 K for 30 min	Tension SS curves to 4% strain	RT to 589 K	0.0005
Norström [13]	316L 0.05% N, 0.11% N, and 0.18% N	Annealed to give GS of $\sim 25 \mu\text{m}$, $\sim 70 \mu\text{m}$, and $\sim 150 \mu\text{m}$	Tension YS meas.	RT	0.001
Claus [2]	304, 304L, 316, 316L	Annealed	Tension YS meas.	RT to 1000 K	Not specified
Brynes et al. [14]	Fe-.27Cr- .32Ni- .0325Mo- .015C; 0.04–0.36% N	Annealed at 1423 K	Tension YS meas.	78 K to 875 K	7×10^{-5}
Byun et al. [15]	304, 316, 316LN	HT: 1323 K for 30 min	Tension	123 K to 723 K	0.001
Dai et al. [16]	316 LN	HT: 1323 K for 30 min; Unirradiated and irradiated	Tension	RT to 673 K	0.001
Stout and Follansbee [17]	304L	HT: 1323 K, 1 hr	Compression	RT	0.0002, 0.02, 1, 100, 8000

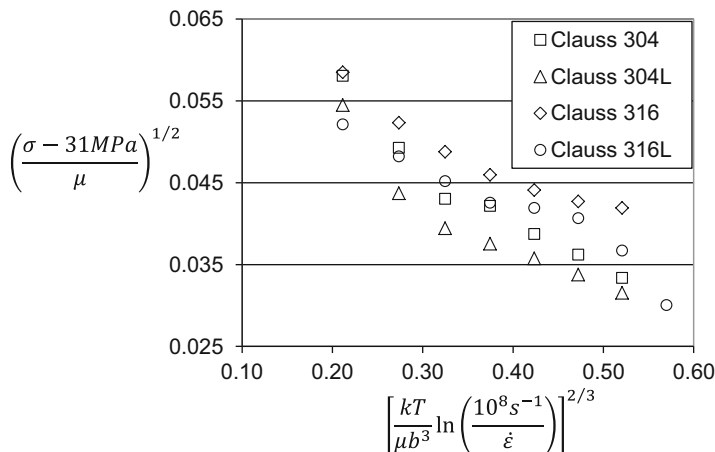


Fig. 11.2 Yield stress versus temperature and strain rate (which for data shown in unchanging) plotted on coordinates suggested by Eqs. 6.11 and 6.12

Figure 11.2 shows the normalized plot of these variables for the Claus data for AISI 304, 304L, 316, and 316L stainless steel³ with $\dot{\epsilon}_0 = 10^8 \text{ s}^{-1}$, $p = 1/2$, $q = 3/2$, and $\sigma_a = 31 \text{ MPa}$.

The observation in Fig. 11.2 is that at low temperatures, the data appear to fall on a line—perhaps even a line of constant slope but a stress level that varies from alloy to alloy. At higher temperatures the data deviates from the low temperature behavior.

Although the Claus data is at a single quasi-static (QS) strain rate, measurements in 304 SS by Steichen and Paxton [7] over a wide temperature (RT to 932 K) and strain rate ($3 \times 10^{-5} \text{ s}^{-1}$ to 10^2 s^{-1}) range in Fig. 11.3 yield a similar conclusion. Starting with the assumption that deformation kinetics are driven by interaction of dislocations with a single-obstacle population, the model line in Fig. 11.3 is derived from Eqs. 6.11 and 6.12 with $g_0 = 0.4$, $\hat{\sigma} = 529 \text{ MPa}$, and all the constants listed above (except for an insignificant difference in the athermal stress). The departure between the low temperature (and high strain rate) and high temperature (and low strain rate) behavior is evident in Fig. 11.3. This, in fact, is a consistent trend observed in other AISI 304, 304L, 316, and 316L temperature-dependent yield stress measurements [18, 19].

The departure from the behavior on the left-hand side to the right-hand side of Figs. 11.2 and 11.3 suggests strongly that deformation in these alloys over the range of conditions considered is not adequately described by a single mechanism. The question addressed here is what might be the competing or additive mechanism. Several factors could contribute to the departure. One possibility is that the change in behavior results from changes in the microstructure. The point of departure in Fig. 11.3 is at a value of the abscissa of ~ 0.35 . At a QS strain rate, this corresponds

³Claus reports in [2] that these data are from U.S. Steel.

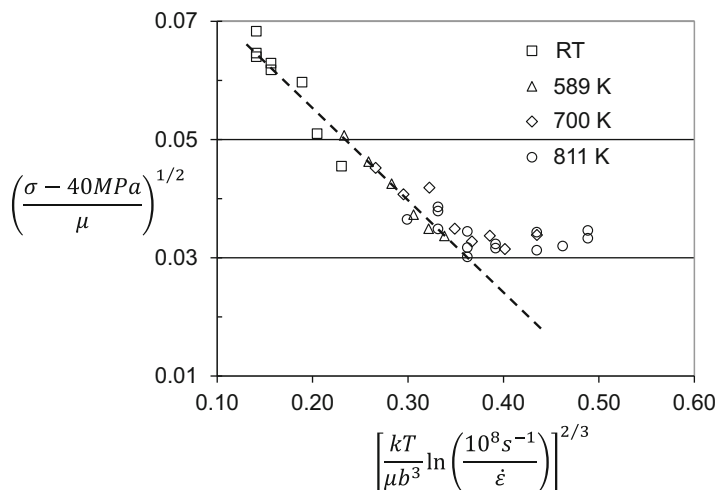


Fig. 11.3 Measurements by Steichen and Paxton [7] of yield stress in 304 stainless steel over a wide range of temperature and strain rate

to temperatures greater than ~ 600 K ($0.33 T_m$), where some investigators have reported the precipitation of $M_{23}C_6$ carbides [20]. However, Morris concluded that the precipitates do not contribute to a friction stress that inhibits dislocation glide [21]. A second possibility is that the departure represents the contribution of diffusional processes, although this seems unlikely in annealed material at a homologous temperature as low as 0.33.

The stability of austenite in these alloys is another consideration. At low temperatures (e.g., 77 K) and/or high strain rates, austenite can transform through a martensite reaction to ferrite [22]. Such a transformation, if present, would be observed at the lower values of the abscissa in Figs. 11.2 and 11.3. Another indication of this reaction is stress-strain curves that exhibit an extremely high strain-hardening rate. Several stress-strain curves will be presented in Sect. 11.4; all of the curves reported for the 304 and 316 systems of alloys are well behaved, indicating a stable austenite structure.

A final possibility is that Eq. 6.11 with Eq. 6.12 does not accurately represent the rate-controlling thermal activation mechanism. Austenitic stainless steels are strengthened by solute atom additions (primarily Ni and Cr, but also Mn and Si in the 304 and 316 alloys and Mo in 316) and interstitial atom additions (primarily C and N). Carbide precipitation can occur during slow cooling (e.g., from a recrystallization heat treatment at 1273 K or from extended service at elevated temperature), but these carbides are not relied upon for strengthening [2]. The primary strengthening mechanism, therefore, is created by the stress fields around solute and interstitial atoms that restrict dislocation motion. In this case, a model that considers the contributions from multiple obstacle populations is appropriate. Equations 6.14, 6.15, and 6.16 presented the two-parameter model, which, as detailed in Sect. 6.3, assumes that these contributions add linearly rather than, for instance, as the sum of

squares (see Sect. 8.8). Derivation of the model parameters for these equations using a suite of prestrain and reload tests—as introduced in Chap. 7—would require an extensive experimental campaign. Fortunately, experimental investigations of the variation of strength with one interstitial alloying addition—N—have been performed. Measurements from two of these investigations will be reviewed in the next section.

11.2 Nitrogen in Austenitic Stainless Steels

In a 1989 review article [23], Reed summarized the influence of nitrogen on metallurgical stability, stacking fault energy, corrosion resistance, strength, and creep and fatigue of austenitic stainless steels. The dependence of yield strength on alloying was shown to be highest for N additions than for any other interstitial or solute addition (and roughly twice the dependence on C additions). The variation of yield stress with N did not follow a single power law but fell between square-root and linear dependence. Reed reviewed theories for the origin of the strengthening effect and concluded that this remained an open question. The observation of a change in dislocation geometry with increasing N content (along with the observation that the stacking fault energy did not vary with N content) pointed to the influence of long-range or local ordering on strength.

Turan and Koursaris published another extensive review of the effects of nitrogen alloying on the properties of austenitic stainless steels [24]. One of the papers referenced by both Reed and Turan and Koursaris was a publication by Norström [13], who measured the dependence of yield stress on nitrogen content (0.05% N, 0.11% N, and 0.18% N) and grain size ($\sim 25\ \mu\text{m}$, $\sim 70\ \mu\text{m}$, and $\sim 150\ \mu\text{m}$) in AISI 316L stainless steel. Figure 11.4 shows the Norström measurements for the material with a $\sim 70\ \mu\text{m}$ grain size. The temperature dependence exhibits similar behavior as illustrated in Fig. 11.1, but a significant variation of strength with nitrogen level is evident. Another extensive evaluation of the effect of nitrogen content on properties of an austenitic stainless steel was published by Brynes et al. [14]. In this case these investigators selected an alloy chemistry high in both chromium and nickel that yielded a very stable austenitic phase field not prone to a martensitic transformation. The grain size of the alloy is not specified, but the heat treatment coincides with the heat treatment conditions that produced the $\sim 70\ \mu\text{m}$ grain size in the Norström alloys. Included in Fig. 11.4 is the variation of 0.002 strain offset stress with temperature reported by Brynes et al. (left ordinate). This data set, which spans a temperature range from liquid nitrogen temperature to $\sim 0.5 T_m$, shows similar trends to those seen in the other austenitic alloys included in Fig. 11.1. Figure 11.5 combines the Norström measurements for the 0.11% N material with other measurements in 316/316L. The trend in the Norström data is similar to that seen in the other materials.

With grain-size- and nitrogen-content-dependent data available, it is possible to separately investigate these contributions in context of the model outlined above.

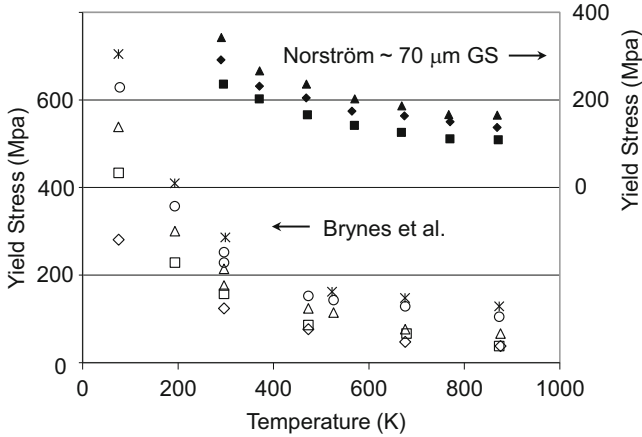


Fig. 11.4 Measurements of yield stress as a function of nitrogen content and test temperature reported by Norström [13] (0.05% to 0.18% N) in 316L stainless steel for material heat treated to give an average grain size of $\sim 70 \mu\text{m}$ (solid symbols, right ordinate) and by Brynes et al. [14] (0.045% to 0.35%) in a very stable, high chromium- and nickel-containing, stainless steel (open symbols, left ordinate)

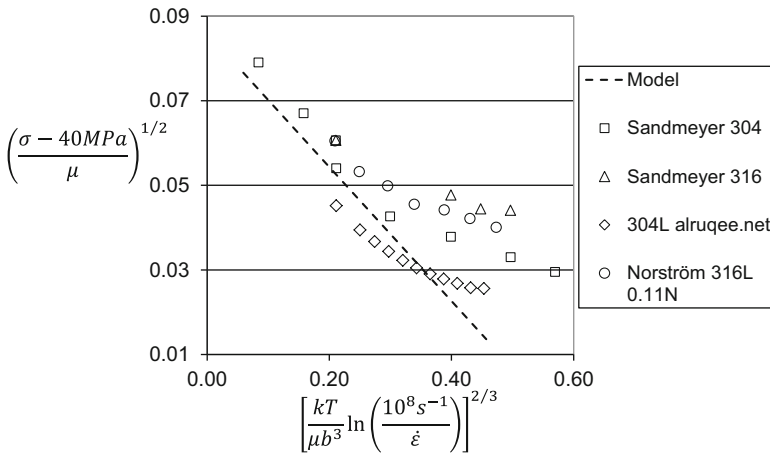


Fig. 11.5 Literature data shown in Fig. 11.1 along with the Norström data shown in Fig. 11.4 plotted on coordinates suggested by Eqs. 6.11 and 6.12

Norström [13] and Brynes et al. [14] argue that nitrogen additions affect both the thermal and athermal component of the yield stress. This is evident in Fig. 11.4 where nitrogen additions do not raise the stress levels uniformly. Rather the increase in stress is slightly larger at low temperatures than at high temperatures.

To analyze the separate contributions of grain size, interstitial and solid solution hardening, and the additional contribution to strength provided by nitrogen, Eq. 6.14 is rewritten in an analogous fashion to Eq. 10.6 in pure titanium

$$\frac{\sigma}{\mu(T)} = \frac{k_d}{\sqrt{d_{gs}}} + s_i(\dot{\epsilon}, T) \frac{\hat{\sigma}_i}{\mu_o} + s_N(\dot{\epsilon}, T) \frac{\hat{\sigma}_N}{\mu_o} \quad (11.1)$$

where the athermal stress σ_a has been replaced by $k_d/\sqrt{d_{gs}}$ where k_d is a constant and d_{gs} is the grain size. The single thermally activated stress term in Eq. 6.11 has been separated into two terms, where $\hat{\sigma}_N$ represents the contribution of nitrogen strengthening and $\hat{\sigma}_i$ represents the contribution of all other “impurity” (e.g., not iron) interstitial and substitutional atoms—which might include contributions from nitrogen interstitial strengthening. In this case there must be two s -terms:

$$s_i(\dot{\epsilon}, T) = \left\{ 1 - \left[\frac{kT}{\mu(T)b^3 g_{oi}} \ln \left(\frac{\dot{\epsilon}_{oi}}{\dot{\epsilon}} \right) \right]^{1/q_i} \right\}^{1/p_i} \quad (11.2)$$

$$s_N(\dot{\epsilon}, T) = \left\{ 1 - \left[\frac{kT}{\mu(T)b^3 g_{oN}} \ln \left(\frac{\dot{\epsilon}_{oN}}{\dot{\epsilon}} \right) \right]^{1/q_N} \right\}^{1/p_N} \quad (11.3)$$

Although Norström and Brynes et al. conclude that nitrogen additions contribute to a variable athermal stress, Eq. 11.1 with Eq. 11.3 does not at the outset presume this. If this is found to be the case, then g_{oN} will be observed to be very large, when compared to g_{oi} . (A high activation energy is associated with a lower temperature and strain-rate dependence.) In assessing Eq. 11.1 with Eq. 11.2 and Eq. 11.3, it is assumed that $\dot{\epsilon}_{oi} = \dot{\epsilon}_{oN} = 10^8 \text{ s}^{-1}$ and that $q_i = q_N = 1.5$ and $p_i = p_N = 0.5$ which are values similar or identical to those used in previous studies [18, 25] and is consistent with the values used in a plethora of metals in this monograph (see Table 10.21) This leaves k_d (in Eq. 11.1) and the two g_o terms and two $\hat{\sigma}$ terms as fitting parameters. The intent is to identify the single k_d , g_{oi} , and g_{oN} values and the (three) $\hat{\sigma}_i(N)$ and $\hat{\sigma}_N(N)$ values that best fit the entire data set⁴. Recall that the Norström data set includes three grain sizes, three nitrogen contents, and multiple measurements (3 at the smallest and largest grain sizes and 10 at the medium grain size) of yield stress as a function of test temperature for each grain size and nitrogen content. The Brynes et al. data set includes 5 to 8 yield stress measurements at each of the five nitrogen levels. A total of 78 separate measurements comprises the combined data set. Table 11.2 lists the k_d , g_{oN} , and g_{oi} values that resulted from this numerical analysis, which involves trial and error selection of the values that provide the optimal fit.

Figure 11.6 shows model fits for one data set—Norström measurements for 0.11% N and a 75 μm grain size. To illustrate the sensitivity of the fit to the selected parameters, five curves are drawn through the data points. Table 11.3 lists the values

⁴The Norström measurements were at a single strain rate; thus the choice of $\dot{\epsilon}_o$ is moot. Selecting constant values of these coefficients is consistent with the commitment not to use these as fitting parameters.

Table 11.2 Parameters for Eqs. 11.1, 11.2, and 11.3 selected for optimal fit of these equations to the Norström data set

$k_d = 13.7 \text{ (MPa mm}^{0.5}\text{)}$	Eqs. 11.2 and 11.3			
Obstacle	g_o	$\dot{\epsilon}_{oES} \text{ (s}^{-1}\text{)}$	p	q
Obstacle i	$g_{oi} = 0.2$	10^8	0.5	1.5
Obstacle N	$g_{oN} = 1.7$	10^8	0.5	1.5

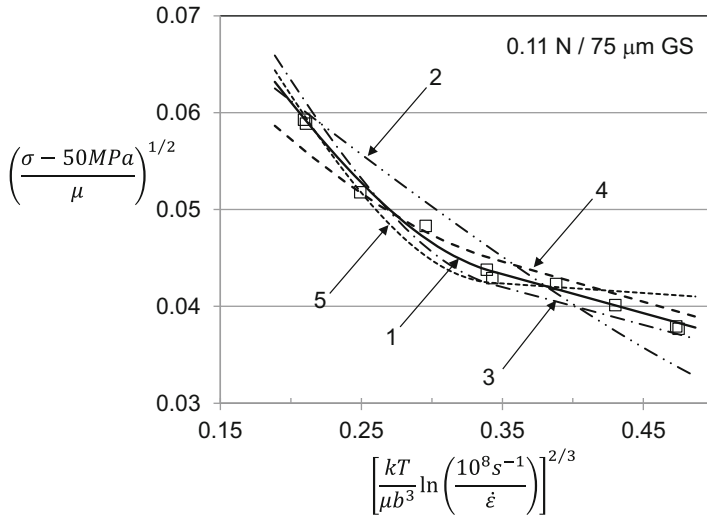


Fig. 11.6 Comparison of model predictions for parameters listed in Table 11.3 with measurements of Norström for 0.11% N and a 75 μm grain size

Table 11.3 Fitting parameters selected for Eqs. 11.1, 11.2, and 11.3 to illustrate the sensitivity of the agreement between experiment and model predictions to the values of these parameters (see Fig. 11.6)

Parameter	Fit 1	Fit 2	Fit 3	Fit 4	Fit 5
g_{oi}	0.2	0.5	0.2	0.2	0.2
g_{oN}	1.7	5	1.7	1.7	10
$\hat{\sigma}_i \text{ (MPa)}$	536	429	715	286	786
$\hat{\sigma}_N \text{ (MPa)}$	236	79	222	250	150
$(\sigma_{Meas} - \sigma_{MTS})_{Avg} \text{ (MPa)}$	4.1	16.2	10.5	12.4	10.1

of g_{oN} , g_{oi} , $\hat{\sigma}_i$, and $\hat{\sigma}_N$ used with Eqs. 11.1, 11.2, and 11.3. These values represent a range of possible values and were selected to demonstrate sensitivity of fits to these parameters. Included in Table 11.3 is the average difference between the predicted stress and the measured stress according to

$$(|\sigma_{Meas} - \sigma_{MTS}|)_{Avg} = \sqrt{\frac{\sum (\sigma_{Meas_i} - \sigma_{MTS_i})^2}{n}} \tag{11.4}$$

Table 11.4 Values of $\hat{\sigma}_i$ and $\hat{\sigma}_N$ selected for optimal fit of Eqs. 11.1, 11.2, and 11.3 with Norström and Brynes et al. data sets. Included is a measure of the average error calculated using Eq. 11.4

N (%)	d_{gs}	Data points	$\hat{\sigma}_i$ (MPa)	$\hat{\sigma}_N$ (MPa)	$(\sigma_{Meas} - \sigma_{MTS})_{Avg}$ (MPa)
Norström [13]					
0.05	S	3	486	157	5.7
0.05	M	10	500	171	5.9
0.05	L	3	464	186	1.2
0.11	S	3	572	229	4.1
0.11	M	10	536	236	4.1
0.11	L	3	557	222	1.3
0.18	S	3	657	314	3.7
0.18	M	10	607	275	5.4
0.18	L	3	643	279	3.7
Brynes et al. [14]					
0.045	M ^a	5	264	193	4.0
0.11		6	493	200	14.0
0.19		8	593	250	18.7
0.29		8	621	322	24.7
0.35		6	643	386	25.1
Total:		78			

^a Assumed based on the heat treatment temperature

^b Included is a measure of the average error calculated using Eq. 11.4

where n is the number of data points in the data set. The agreement between the model predictions and the measurements for Fit 1 is much better than for the other fits, which is also evident in Fig. 11.6. This illustrates the sensitivity of the agreement to the model parameters. The values of g_{oN} and g_{oi} for Fit 1 are the same as those listed in Table 11.2.

Table 11.4 lists the values of $\hat{\sigma}_i$ (N) and $\hat{\sigma}_N$ (N) for each alloy. Included in Table 11.4 is the average difference between the predictions and measurements according to Eq. 11.4. It is evident in Table 11.4 that both $\hat{\sigma}_i$ and $\hat{\sigma}_N$ vary with nitrogen content and that there is some variability in the estimates, as evidenced by the variation in these stresses for alloys of identical nitrogen content but differing grain size. Since there is no consistent trend with grain size, this variability appears to be random and to reflect typical experimental scatter. The agreement between the model predictions and the measurements is not as good for the Brynes et al. data set when compared to the Norström data set. The Brynes et al. data includes several repeat measurements at room temperature where it is observed that measurements under identical conditions vary by as much as 23 MPa to 38 MPa. Thus, some of the variability may indeed be experimental scatter.

Model assumptions may also affect the observed variation in agreement between the model and the measurements. While in analyzing the Brynes et al. data the values of g_{oN} and g_{oi} were maintained at the values observed and to provide the best fit to the

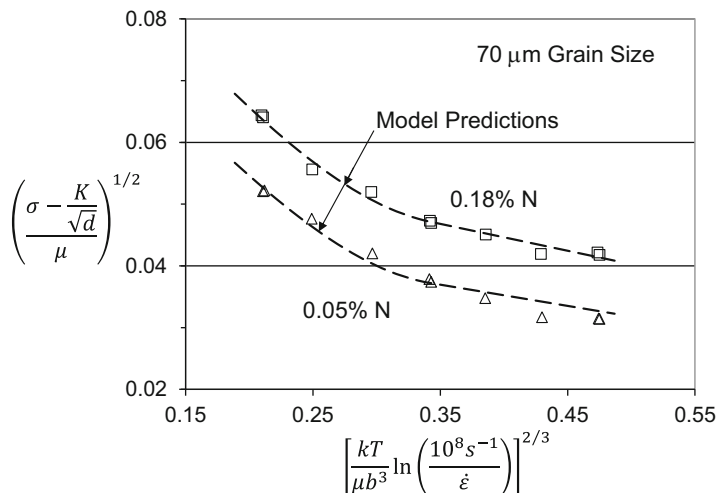


Fig. 11.7 Comparison of model predictions with two of Norström’s data sets. The value of K is specified in Table 11.2

Norström data with g_{oN} and g_{oi} equal to 0.2 and 1.7, respectively, the Brynes et al. alloys had a very different composition than the Norström alloys. In fact, changing g_{oN} from 0.2 to 0.17 decreases the difference between the measured and predicted stresses for the 0.19 N alloy from 18.7 MPa (see Table 11.4) to 12.6 MPa.

Figure 11.7 compares predictions of the model with Norström measurements for the medium-grain-sized material⁵ ($\sim 70 \mu\text{m}$) and the highest and lowest nitrogen levels. Consistent with the results in Table 11.4, the agreement between the predictions and the measurements is better at the higher than the lower nitrogen content. While there is some scatter in the measurements, the measured and predicted temperature-dependent yield stress values follow each other.

Figure 11.8 shows the variation of $\hat{\sigma}_i$ and $\hat{\sigma}_N$ with the nitrogen level for both the Norström and the Brynes data sets. The value of $\hat{\sigma}_i$ at the lowest nitrogen content in the Brynes data set appears to be low. Brynes et al. questioned measurements at the lowest nitrogen content and even repeated these measurements but were unable to explain the discrepancy [14]. There are three values of $\hat{\sigma}_i$ and $\hat{\sigma}_N$ for each nitrogen level in the Norström data set since there were materials with three grain sizes, and each set of data was fit to Eqs. 11.1, 11.2, and 11.3 to give independent values of $\hat{\sigma}_i$ and $\hat{\sigma}_N$. The scatter in these three estimates at each nitrogen level gives an indication of the uncertainty in the estimate of $\hat{\sigma}_N$. Inspection of the individual data points in Table 11.4 shows no trend in $\hat{\sigma}_i$ or $\hat{\sigma}_N$ with grain size at a given nitrogen level. The lines in Fig. 11.8 are

⁵The grain size was measured for each lot of material. Thus, the target grain size for the medium-grain-sized material was $70 \mu\text{m}$, but the actual measured grain size was used in Equation 11.1.

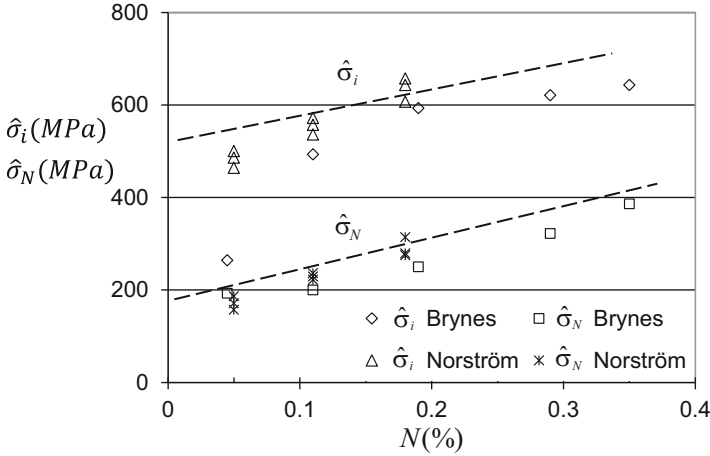


Fig. 11.8 Variation of the two mechanical threshold stresses with nitrogen content for both the Norström and Brynes et al. measurements

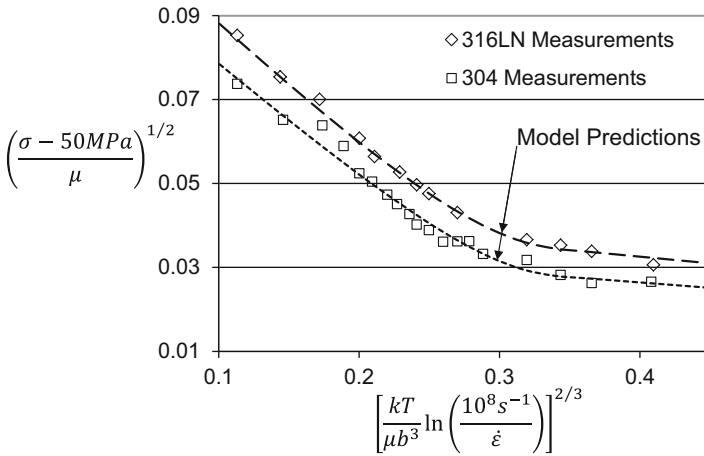


Fig. 11.9 Comparison of measurements by Byun et al. [15] in 316 LN and 304 stainless steels with model predictions

$$\hat{\sigma}_N(N) = 148 \text{ MPa} + 672 \text{ MPa} \times N(\%) \tag{11.5a}$$

$$\hat{\sigma}_i(N) = 478 \text{ MPa} + 593 \text{ MPa} \times N(\%) \tag{11.5b}$$

Figure 11.9 compares model predictions with data from Byun et al. [15] in 316 LN and 304 stainless steels. The same values of g_{oi} and g_{oN} as listed in Table 11.3 were used for the model predictions. The values of $\hat{\sigma}_i$ and $\hat{\sigma}_N$ for 316 LN (0.11% N) were 843 MPa and 147 MPa, and those for 304 (0.058% N)

were 715 MPa and 96 MPa, respectively. For both calculations $\sigma_a = 50$ MPa. Although the agreement between the measurements in predictions in both alloys is good, these $\hat{\sigma}_i$ values are higher than found for the Norström and Brynes materials as shown in Fig. 11.8, whereas these $\hat{\sigma}_N$ values are smaller than those shown in Fig. 11.8, which suggests the correlations shown in Fig. 11.8 and Eqs. 11.5a and 11.5b may not be universal.

Separating the contributions of nitrogen additions using a nitrogen-dependent threshold stress provides a useful model of deformation kinetics of yield in annealed austenitic alloys. The threshold stress termed $\hat{\sigma}_i$ represents the interactions of dislocations with solute and interstitial atoms that are highly localized—as indicated by the small value of g_{oi} . The threshold stress termed $\hat{\sigma}_N$ represents the interaction of dislocations with a second obstacle created by nitrogen additions. These interactions are weaker than the latter and are much less localized, as evidenced by the large value of g_{oN} . However, interactions of dislocations with this set of obstacles are assisted by thermal activation energy; in fact the g_{oN} value is almost the same as that observed for the interaction of dislocations with stored dislocations [26]. This conclusion differs from that reached by Norström [13] and Brynes et al. [14]. Although it is not a significant difference given the large observed g_{oN} value, the agreement between model predictions and measurements is better when the obstacle characterized by $\hat{\sigma}_N$ is considered to be thermally activated (see, for instance, the poor fit in Fig. 11.6 when g_{oN} is set equal to 10 for Fit 5).

The variation of the activation volume v^* with stress is one measure of the obstacle character. For the obstacle characterized by $\hat{\sigma}_i$,

$$\frac{\sigma_i}{\mu} = s_i(\dot{\epsilon}, T) \frac{\hat{\sigma}_i}{\mu_o} \quad (11.6)$$

$$s_i(\dot{\epsilon}, T) = \left\{ 1 - \left[\frac{kT}{\mu b^3 g_{oi}} \ln \left(\frac{\dot{\epsilon}_{oi}}{\dot{\epsilon}} \right) \right]^{\frac{1}{q_i}} \right\}^{\frac{1}{p_i}} \quad (11.7)$$

and by definition [27],

$$v_i^* = kT \frac{\partial \ln \left(\frac{\dot{\epsilon}}{\dot{\epsilon}_{oi}} \right)}{\partial \sigma_i} \quad (11.8)$$

Replacing the subscript “*i*” with “*N*” gives a similar set of equations for the activation volume of the obstacle characterized by $\hat{\sigma}_N$. Setting aside the temperature dependence of the shear modulus (which was described as being small) in Eqs. 11.6 and 11.7 simplifies differentiation, giving

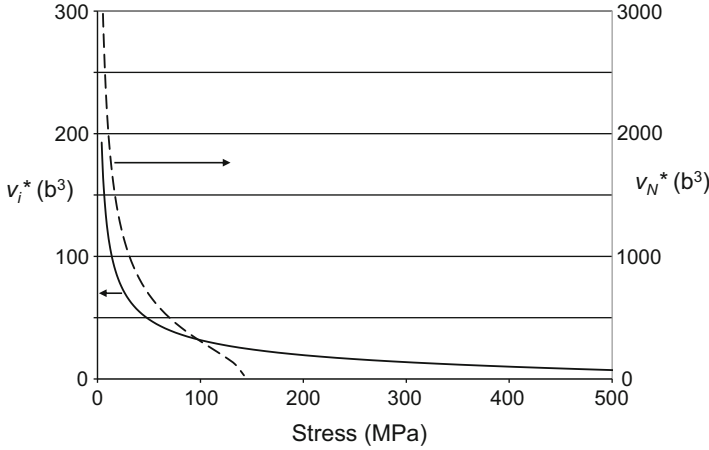


Fig. 11.10 Variation of the activation volume for the “*i*” obstacle population (solid line, left ordinate) and the “*N*” obstacle population (dashed line, right ordinate) versus stress calculated from Eqs. 11.9 and 11.10

$$v_i^* = \frac{3}{4} b^3 g_{oi} \mu_o \frac{1}{\sqrt{\hat{\sigma}_i \sigma_i}} \left(1 - \sqrt{\frac{\sigma_i}{\hat{\sigma}_i}} \right)^{\frac{1}{2}} \quad (11.9)$$

And similarly for the second obstacle,

$$v_N^* = \frac{3}{4} b^3 g_{oN} \mu_o \frac{1}{\sqrt{\hat{\sigma}_N \sigma_N}} \left(1 - \sqrt{\frac{\sigma_N}{\hat{\sigma}_N}} \right)^{\frac{1}{2}} \quad (11.10)$$

Figure 11.10 shows the variation of the activation volume with stress for both obstacles for the case where $\hat{\sigma}_i = 715$ MPa and $\hat{\sigma}_N = 143$ MPa. Indeed, the activation volume for the obstacle characterized by $\hat{\sigma}_N$ is considerably larger than that characterized by $\hat{\sigma}_i$ (note the scale difference between the left and right ordinates in this figure). The large activation volume for the former suggests a long-range obstacle, which is consistent with the suggested contributions of local or long-range ordering.

11.3 The Hammond and Sikka Study in 316

Hammond and Sikka [12] performed a detailed study of the temperature-dependent strength of AISI 304 and AISI 316 stainless steels. They procured eight mill-annealed lots of each of these materials and observed considerable variability in the yield strength between lots in the as-received condition. This variability decreased significantly but not totally in material that received a re-anneal heat

Table 11.5 Carbon content, nitrogen content, grain size, and yield stress reported by Hammond and Sikka [12] on seven lots of 316 stainless steel and prediction of the yield stress based on Eqs. 11.1 and 11.5a

Lot designation	C (%)	N (%)	d_{gs} (mm)	0.002 offset yield stress (MPa)	Predicted yield stress (MPa)
613	0.063	0.042	0.034	243	260
509	0.053	0.074	0.060	243	257
212	0.055	0.053	0.060	238	247
297	0.065	0.031	0.090	215	226
160	0.041	0.021	0.029	206	257
694	0.043	0.021	0.048	190	239
695	0.039	0.019	0.050	190	237

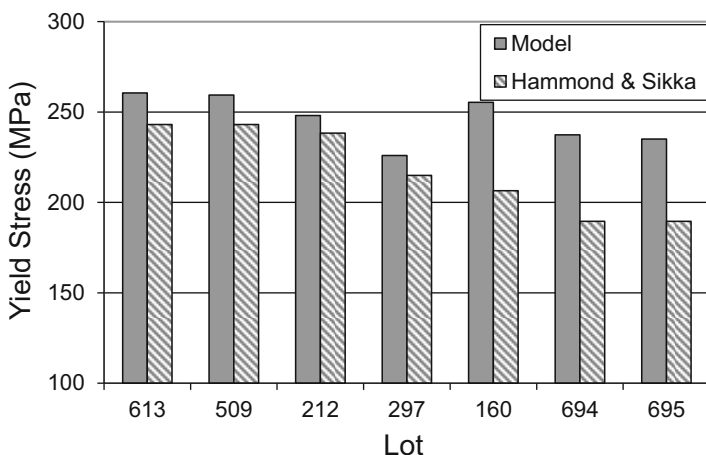


Fig. 11.11 Estimate of the yield stress (solid bars) for each of the lots of 316 stainless steel analyzed by Hammond and Sikka [12] according to the nitrogen content and grain size specified by these investigators. The estimates are compared to the measured yield stresses

treatment. For 316, Table 11.5 lists the carbon and nitrogen contents and grain sizes (after the re-anneal heat treatment) for each of the lots. The materials are listed from the strongest to the weakest. Included in Table 11.5 are the measured and predicted yield stresses. The latter are calculated using Eq. 11.1 with $\hat{\sigma}_N$ and $\hat{\sigma}_i$ given by Eqs. 11.5a and 11.5b. All other model parameters are as specified in Table 11.2 and the discussion preceding Table 11.2.

Figure 11.11 is a bar chart comparing the measured and predicted yield stress for each of the materials. The measured variation in yield stress from the strongest (lot 613) to the weakest (lot 695) is larger than predicted, and the measured stresses are in general slightly less than the predicted stresses, but it is apparent that at least some of the variation is accounted for by consideration of the specific grain size and nitrogen content of the materials.

11.4 Modeling the Stress–Strain Curve

Equation 11.1 has been applied to the variation of yield stress with temperature and strain rate of annealed material. In annealed material the dislocation density is expected to be very low. The dislocation density increases rapidly with strain, and the interaction of dislocations with stored dislocations leads to strain hardening. This strength contribution can be accounted for by adding another mechanical threshold stress— $\widehat{\sigma}_\varepsilon$ —to the governing equation:

$$\frac{\sigma}{\mu(T)} = \frac{k_d}{\sqrt{d_{gs}}} + s_i(\dot{\varepsilon}, T) \frac{\widehat{\sigma}_i}{\mu_o} + s_N(\dot{\varepsilon}, T) \frac{\widehat{\sigma}_N}{\mu_o} + s_\varepsilon(\dot{\varepsilon}, T) \frac{\widehat{\sigma}_\varepsilon(\varepsilon)}{\mu_o} \quad (11.11)$$

Accompanying Eq. 11.11 is an expression for s_ε similar to those for s_i (Eq. 11.2) and s_N (Eq. 11.3). Recall that s_ε was prescribed by Eq. 7.9 with model parameters listed in Table 9.7.

As demonstrated in UFKonel (Sect. 9.5) and several metals and alloys in Chap. 10, analysis of evolution entails solving for $\widehat{\sigma}_\varepsilon$ versus strain using Eq. 9.7 (with the Peierls obstacle replaced by $\widehat{\sigma}_N$) and the fit of Eq. 6.28 to this result giving $\widehat{\sigma}_{\varepsilon S}$ and θ_{II} . This procedure is repeated for a variety of test temperatures and strain rates [28]. Figure 11.12 shows $\widehat{\sigma}_{\varepsilon S}$ versus test temperature and strain rate on coordinates defined by Eq. 6.26. This plot has data from eight sources and includes measurements in AISI 304, AISI 304L, AISI 316, AISI 316L, and AISI 316LN materials. Only parameter values for g_{oN} and g_{oN} have been altered for some of these systems. One source of the scatter observed in Fig. 11.12 may originate from subtle differences in these materials. However, the general trend and agreement with

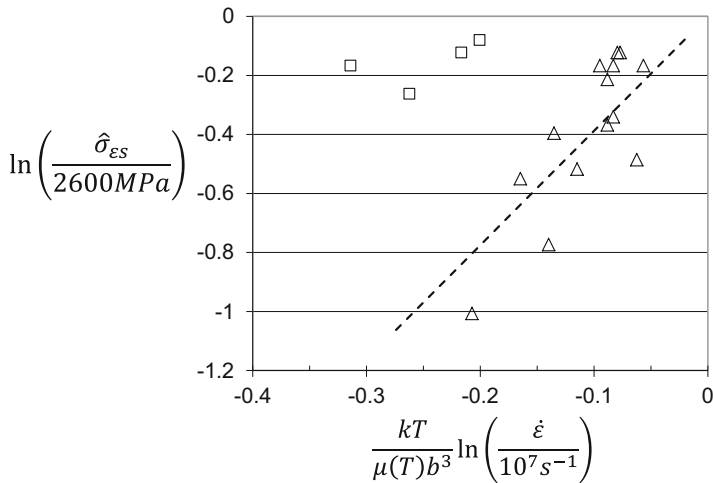


Fig. 11.12 Computed values of $\widehat{\sigma}_{\varepsilon S}$ versus test temperature and strain rate for a collection of austenitic stainless steels

Table 11.6 Model parameters selected for comparisons between experiment and model prediction in Figs. 11.13, 11.14, 11.15, and 11.16

Parameter	Equation	Value	Units
κ	6.28	2	–
A_0	6.29	3120	MPa
A_1		32	MPa ($\dot{\epsilon}$ in s^{-1})
A_2		0	MPa $s^{-1/2}$
g_{oes}	6.26	0.258	–
$\hat{\sigma}_{eso}$		2600	MPa
$\dot{\epsilon}_{oes}$		10^7	s^{-1}
g_{oi}	11.2 ^a	0.2	–
g_{oN}	11.3 ^a	1.7	–
μ_o		71.46	GPa
b		0.249	nm

^aRemaining parameters for Eqs. 11.2 and 11.3 were specified in the discussions following these equations

Eq. 6.26 are apparent. As observed in AISI 1018 steel (Fig. 9.32), vanadium (Fig. 9.44), niobium (Fig. 9.56), and titanium (Fig. 10.68), four data points in Fig. 11.12 fall well above the trend according to Eq. 6.26. As described in these other materials, this is a clear signature of dynamic strain aging. The model constants for the trend line in Fig. 11.12 as well as for the fit to Eq. 6.29 for $\theta_{II}(\dot{\epsilon})$ are listed in Table 11.6.

To demonstrate implementation of the model and compare model predictions with measurements, Fig. 11.13 shows data in 316L stainless steel (nitrogen content wasn’t specified) by Albertini and Montagnani [11] compared with model predictions (dashed line). These predictions were made with the model parameters listed in Table 11.6. The values of the parameters listed in Table 11.6 will be held constant for all model predictions described below. Remaining model parameters— $\hat{\sigma}_i$ and $\hat{\sigma}_N$ which are the only parameters varied in the comparisons below—are listed in Table 11.7.

Included in Fig. 11.13 is another example, which is the comparison of model predictions with measurements of Conway et al. [9] in 316 SS (nitrogen content specified as 0.05%) at room temperature and a strain rate of $0.004 s^{-1}$. For this prediction the value of one parameter— $\hat{\sigma}_N$ —was changed (from 243 MPa to 179 MPa); all other parameters remained the same as for the prediction for the Albertini and Montagnani measurement. Note in Fig. 11.13 that it is difficult to discern the model prediction from the measurement.

Figure 11.14 compares the model predictions with measurements reported by Byun, Hashimoto, and Farrell [15] in 316 SS (nitrogen content specified as 0.031%) at a strain rate of $0.001 s^{-1}$ and temperatures of 223 K, 293 K, 373 K, 473 K, and 673 K. In this case the model and measurements track at the lower temperatures, but at 473 K and, particularly 673 K, the measurements (e.g., see dotted line in Fig. 11.14) display a higher hardening rate than predicted or than measured at the lower temperatures.

Fig. 11.13 Comparisons of the predicted stress strain curves with that measured by Albertini and Montagnani [11] in 316L (left ordinate) and by Conway et al. [9] (right ordinate) in 316 stainless steel at the specified temperature and strain rate

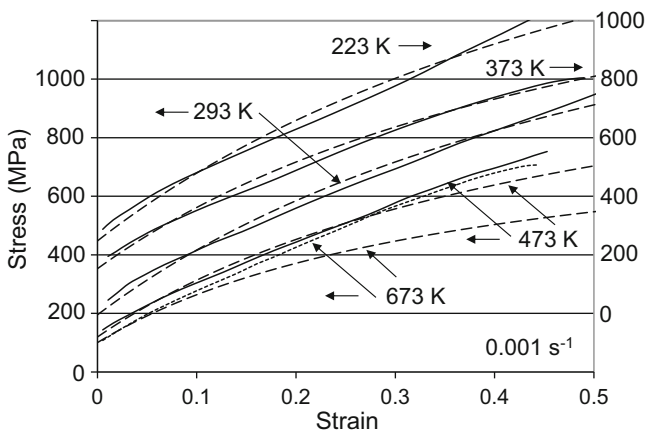
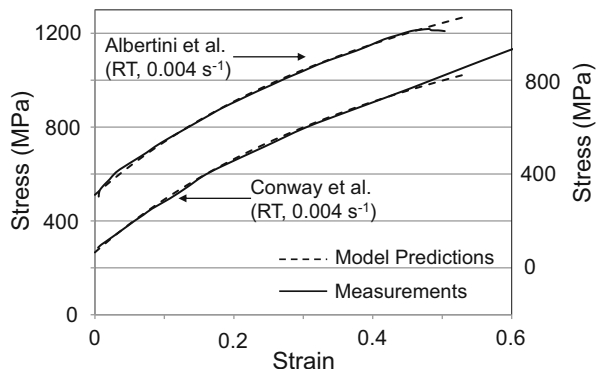


Fig. 11.14 Comparison of the predicted stress strain curves with those measured by Byun et al. [15] in 316 stainless steel at the specified temperatures and strain rate

Figure 11.15 shows room temperature measurements from Gray and Chen in 316L SS [8] and Stout and Follansbee in 304L SS [17] (nitrogen contents not specified) along with model predictions at various strain rates. The comparisons in Figs. 11.13, 11.14, and 11.15 suggest that the model predictions agree well with measurements in these austenitic alloys over a wide range of strain rates and temperatures up to ~ 500 K. Deviations from the model are apparent at higher temperatures. This is further demonstrated in Fig. 11.16, which compares model predictions with measurements at elevated temperature by Albertini and Montagnani [11], Conway et al. [9], and Steichen [6] (nitrogen content of 0.052 N). As shown in Fig. 11.14 at 673K, the measured hardening rate far exceeds the predicted hardening rate, although the measured and predicted yield stresses agree.

Fig. 11.15 Comparison of the predicted stress strain curves (dashed lines) with those measured (solid lines) by Gray and Chen (316L, left ordinate) and Stout and Follansbee (304L, right ordinate) at room temperature and the specified strain rates

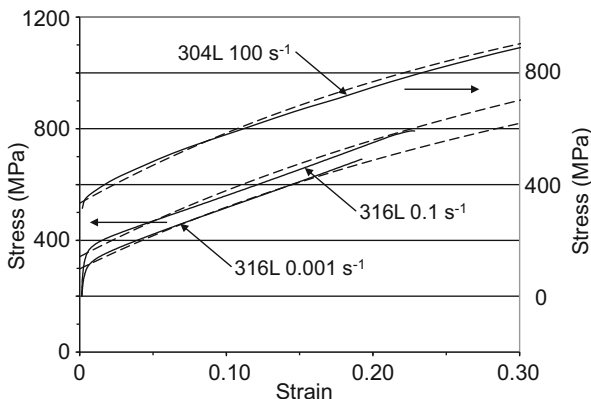
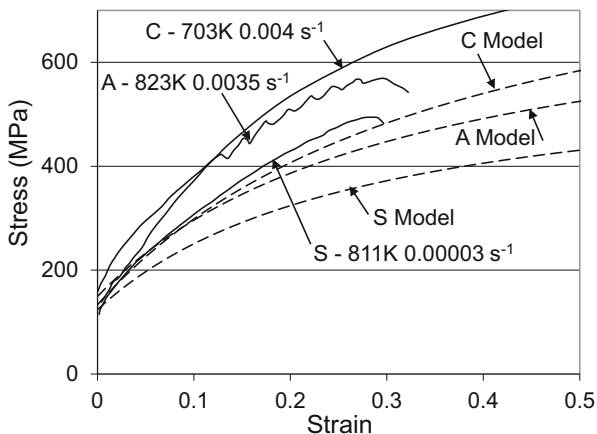


Fig. 11.16 Comparison of the predicted and measured stress strain curves for various austenitic stainless steels (see Table 11.7) at the specified strain rates and temperatures



11.5 Dynamic Strain Aging in Austenitic Stainless Steels

The curve measured by Albertini and Montagnani (identified as “A” in Fig. 11.16) shows evidence of serrated yielding. Indeed, dynamic strain aging (DSA) has been observed in austenitic stainless steels. Samuel et al. [29] studied serrated yielding in AISI 316 stainless steel. Peng et al. [30] documented serrations in tensile stress-strain curves in an 18-8-type austenitic stainless steel (similar in chemistry to 304 SS) over the temperature range of 298 K to 973 K and the strain rate range of $5 \times 10^{-4} \text{ s}^{-1}$ to $5 \times 10^{-2} \text{ s}^{-1}$. Both of these investigations reported serrations (and a negative strain-rate sensitivity [29]) in two distinct temperature and strain-rate regimes which were considered to arise from different solute-dislocation interactions. The elevated temperature measurements in Figs. 11.14 and 11.16 span the conditions where dynamic strain aging has been observed in austenitic stainless steels.

Dynamic strain aging was observed in vanadium and niobium in Chap. 9 and in titanium in Chap. 10. It was observed in these systems that DSA-induced hardening exhibited common trends. When DSA appears to become active, an effective s_1 was computed using Eq. 9.8, and plots of s_1 versus σ_ϵ were created (see Fig. 9.48, Fig. 9.62, Fig. 10.72, and Fig. 10.73). At low values of σ_ϵ , the value of s_1 was indeed the value predicted using Eq. 6.15 or equivalent, but with increasing σ_ϵ the values of s_1 increased with σ_ϵ . The increase was approximated as a linear dependence, and the slope of the line K_{DSA} was found to increase exponentially with increasing temperature. This trend was analyzed using Eq. 9.9 to determine the effective “activation energy” (see Fig. 9.49 and Fig. 10.74).

To investigate whether DSA in the austenitic stainless steels follows a similar trend, one can revise Eq. 9.8 to reflect the contributions of obstacle populations 1 and 2

$$s_1 = \frac{1}{\hat{\sigma}_1} \left[\frac{\mu_o}{\mu} (\sigma - \sigma_a) - s_2 \hat{\sigma}_2 - s_\epsilon \hat{\sigma}_\epsilon \right] \quad (9.8i)$$

which is written as if obstacle population 1 is contributing to DSA. This is an assumption. It is possible that obstacle population 2 is involved, in which case Eq. 9.8 becomes

$$s_2 = \frac{1}{\hat{\sigma}_2} \left[\frac{\mu_o}{\mu} (\sigma - \sigma_a) - s_1 \hat{\sigma}_1 - s_\epsilon \hat{\sigma}_\epsilon \right] \quad (9.8ii)$$

Although it isn't known with certainty which obstacle population is contributing to DSA, there is an important consideration. The s-factors are functions of temperature and strain rate defined by Eq. 7.3

$$s_j(\dot{\epsilon}, T) = \left\{ 1 - \left[\frac{kT}{g_{oj}\mu b^3} \ln \left(\frac{\dot{\epsilon}_{oj}}{\dot{\epsilon}} \right) \right]^{2/3} \right\}^2 \quad (7.3)$$

where j can refer to either obstacle population 1 or 2. The s_j factors are strong functions of temperature, and actually fall to zero at high enough temperatures, which implies that the obstacle is no longer effective in blocking dislocation motion. In 316L stainless steel with the model constants listed in Table 11.6 and Table 11.7, s_1 is indeed zero at 703 K and a strain rate of 0.004 s^{-1} . This implies that obstacle population 1 cannot be involved in DSA at these conditions. But DSA was clearly evident in the Conway et al. measurement at these conditions shown in Fig. 11.16. Accordingly, it is instead assumed that obstacle population 2 is actively involved in DSA.

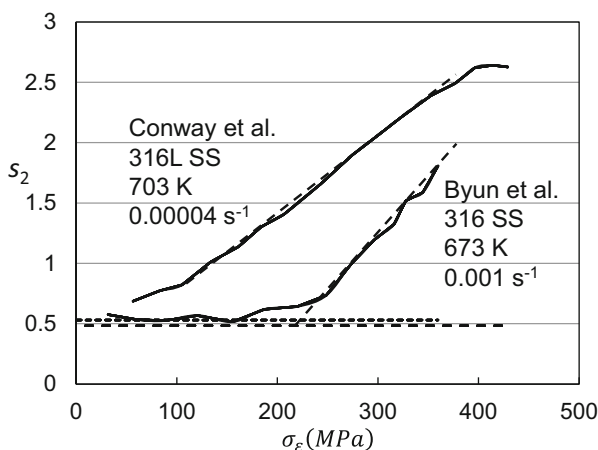
The variation of s_2 with σ_ϵ is computed as before using Eq. 9.8ii where σ is the measured stress and $\hat{\sigma}_\epsilon$ is computed using Eqs. 6.28, 6.26, and 6.29 and the model parameters listed in Table 11.6. Figure 11.17 shows the result for the Conway et al.

Table 11.7 Fitting parameters used for the predictions and comparisons with measured stress-strain curves in Figs. 11.13, 11.14, 11.15, and 11.16. Note that the values of $\hat{\sigma}_i$ and $\hat{\sigma}_N$ are chosen to provide the optimum fit; these are consistent with but don't necessary equal those predicted using Eqs. 11.5a and 11.5b

Figure	Material	N (%)	$\hat{\sigma}_i$ (MPa)	$\hat{\sigma}_N$ (MPa)
11.13 and 11.16 "A"	316L	–	572	243
11.13 and 11.16 "C"	316	0.05	572	179
11.15	316	0.031	500	107
11.15	316L	–	572	243
11.15	304L	–	572	121
11.16 "S"	304	0.052	572	200

Note that the values of $\hat{\sigma}_i$ and $\hat{\sigma}_N$ are chosen to provide the optimum fit; these are consistent with but don't necessary equal those predicted using Eqs. 11.5a and 11.5b

Fig. 11.17 Computed variation of s_i with σ_e for a measurement in 316L (Conway et al.) and one in 316 SS (Byun et al.) illustrating behavior consistent with Eq. 9.8

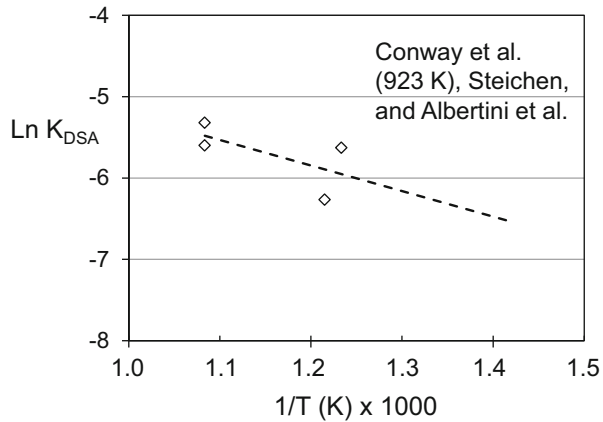


measurement in 316L SS at 703 K and a strain rate of 0.00004 s^{-1} and for the Byun et al. measurement in 316 SS at 673 K and a strain rate of 0.001 s^{-1} . Both curves show trends consistent with observations in pure titanium (Fig. 10.72 and Fig. 10.73), vanadium (Fig. 9.48), and niobium (Fig. 9.62). At low values of σ_e , s_2 equals the value defined by Eq. 7.3 (horizontal dashed lines). At some value of σ_e , s_2 begins to rise in proportion to σ_e . The point of departure from the expected value of zero is higher for the test at the lower temperature and higher strain rate (the Brun et al. test) than for the Conway et al. test. This is similar to the result shown in Fig. 9.48 for vanadium. The slope K_{DSA} is roughly the same for each analysis. Table 11.8 lists the results for these two tests and five others that evidenced dynamic strain aging.

Comparisons of the K_{DSA} values in Table 11.8 lead to no simple trends with temperature or strain rate. The analysis of the temperature dependence of K_{DSA} according to Eq. 9.9 is shown in Fig. 11.18. A few—but not all—of the data from Table 11.8 fall along a line. The equation for the dashed line for these higher temperature measurements in Fig. 11.18 is

Table 11.8 Measurements in austenitic stainless steels showing evidence of dynamic strain aging and the analyzed values K (Eq. 9.9)

Investigator	Material	Temperature (K)	Strain rate (s^{-1})	K_{DSA} (MPa^{-1})
Conway et al.	316	703	0.00004	0.0062
		703	0.004	0.0033
		923	0.00004	0.0049
		923	0.004	0.0037
Albertini et al.	316L	823	0.0035	0.0019
Steichen	304	811	0.00003	0.0036
Byun	316	673	0.001	0.0082

Fig. 11.18 Variation of K versus inverse temperature for the tests in austenitic stainless steel showing evidence of dynamic strain aging

$$K_{DSA} = 0.125MPa^{-1} \exp\left(-\frac{26.1kJ/mol}{RT}\right) \quad (11.12)$$

In these austenitic stainless steels, if the diffusion species is assumed to be nitrogen, the expected activation energy would be 145 kJ/mole, which is significantly greater than the value of 26.1 kJ/mole observed in Fig. 11.18. In the high-temperature region, Peng et al. reported an activation energy of 172.93 kJ/mol⁶. A more descriptive model for DSA outlined in Sect. 13.4 may offer an explanation for why the activation energies deduced from Fig. 11.18 differ from activation energies characterizing solute diffusion in austenitic stainless steels.

It is concluded that DSA in these austenitic stainless steels shows similar trends to those observed in the BCC metals AISI 1018 steel, vanadium, and niobium and HCP metal titanium.

⁶These investigators suggest that it is C and Ni solution atom atmospheres that pin dislocations at lower temperatures and C and Cr solution atoms that are involved at the higher temperatures [30].

11.6 Application of the Model to Irradiation-Damaged Material

As an illustration of how a mechanism-based model adds insight into an unknown process, this section analyzes stress–strain curves measured in an unirradiated and irradiated austenitic stainless steel. Dai et al. [16] reported tensile test measurements in a 316LN stainless steel (with 0.067% nitrogen) that had received a mixed proton and neutron irradiation dose in the SINQ spallation neutron source. Because the temperature at which the irradiation damage is imposed varies according to the dosage, these investigators measured the post irradiation stress–strain curves at both room temperature and the temperature relevant to the imposed damage. Figure 11.19 shows the stress–strain curves in unirradiated material at RT, 150 C, and 350 C. For the model predictions (dashed lines), $\hat{\sigma}_i = 572$ MPa, $\hat{\sigma}_N = 243$ MPa, and the athermal stress was set at 50 MPa. The agreement between the measured and predicted curves is good at the lower temperatures but shows the same deviation at the higher temperature that was illustrated in Figs. 11.14 and 11.16 due to the contribution of dynamic strain aging. In general, the agreement between the measured and predicted curves is better than in an earlier study, which treated deformation using a single-obstacle population [31].

Figure 11.19 also shows the RT and 150 C stress–strain curves measured on material irradiated at 5.3 displacements per atom (dpa) along with model predictions (dashed lines—to be described below). Figure 11.20 shows the RT reload stress–strain curves for material irradiated at 3 dpa and 7.6 dpa. One expects the increase in strength to scale (although not necessarily linearly) with dpa [32]. The measurements in Figs. 11.19 and 11.20 are consistent with this expectation.

Fig. 11.19 Comparison of the predicted (dashed lines) stress strain curves at various temperatures with those measured (solid lines) by Dai et al. in unirradiated 316 LN stainless steel and material irradiated to 5.3 dpa

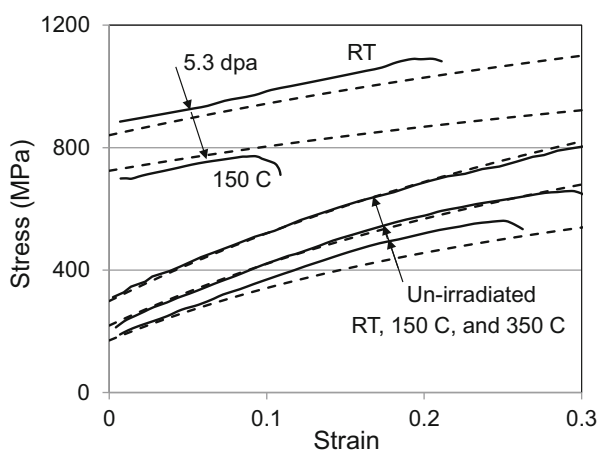


Fig. 11.20 Comparison of the predicted (long- and short-dashed lines) stress strain curves at RT with those measured (solid lines) by Dai et al. in 316 LN stainless steel irradiated to 3 and 7.6 dpa

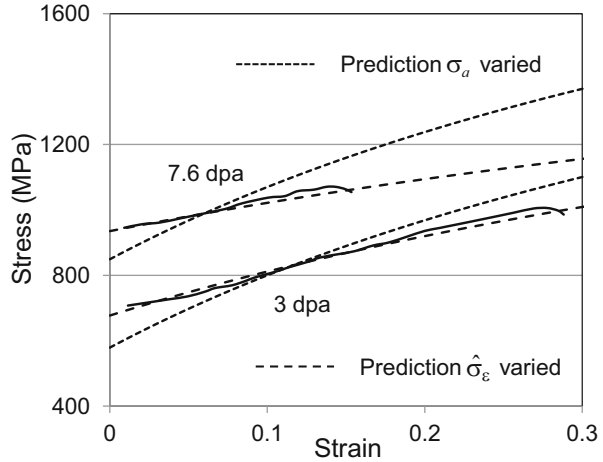


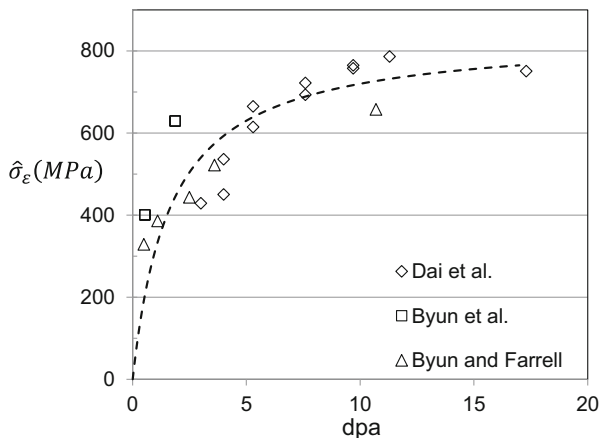
Table 11.9 Model parameters giving the short- and long-dashed lines in Figs. 11.19 and 11.20. No other model parameters from those listed in Table 11.6 have been altered

Adjusted state parameter	Damage (dpa)		
	3	5.3	7.6
σ_a (see short-dashed lines)	330 MPa		600 MPa
$\hat{\sigma}_\epsilon$ (long-dashed lines)	429 MPa	665 MPa	722 MPa

Availability of a physically based constitutive law provides the opportunity to analyze which state parameter is altered by irradiation damage—or to conclude that a new state parameter needs to be added to the formulation. In Fig. 11.19 the model predictions for damage in material exposed to 5.3 dpa were made by setting $\hat{\sigma}_\epsilon = 615$ MPa. The dashed lines for the predictions follow the trends of the curves at RT and 150 C. It is not known whether the slightly higher temperature dependence seen in the data represents scatter or a real trend.

Figure 11.20 compares model predictions with the experiments assuming (i) an increase with dpa in the athermal stress, σ_a , with damage and (ii) an increase in the threshold stress characterizing interaction of dislocations with the stored dislocation density, $\hat{\sigma}_\epsilon$. (That is, the initial value of $\hat{\sigma}_\epsilon$ at 0 strain has been adjusted and hardening during the tensile loading modeled by integrating Eq. 6.28 with this initial condition.) Table 11.9 lists the values of the parameters for each case. It is evident in Fig. 11.20 that simply increasing the athermal stress does not give very good agreement between the measurements and predictions. Byun and Farrell concluded that the irradiation-induced defect structure is similar to a strain-induced structure [33]. The closer agreement between measurements and predictions in Figs. 11.19 and 11.20 observed when $\hat{\sigma}_\epsilon$ has been adjusted supports the Byun and Farrell contention.

Fig. 11.21 Evolution of $\hat{\sigma}_\epsilon$ with dpa and fit to Eq. 6.28



Analysis of the reload stress–strain curves in irradiated material leads to the conclusion that the irradiation-induced defect has similarity to the stored dislocation density—particularly in how the strain-hardening rate decreases with increased damage. The variation of irradiation-induced hardening with dosage offers further insight into this process. Figure 11.21 shows the results of the analysis of the Dai et al. measurements as discussed above along with similar analyses of results reported by Byun and Farrell [33] in 316 SS and Byun et al. [34] in 304L. Whereas in Fig. 11.19 and Table 11.9, a single value of $\hat{\sigma}_\epsilon$ was selected for the tests with reloads at more than one temperature (e.g., 5.3 dpa at RT and 150 C), the best fit value of $\hat{\sigma}_\epsilon$ for each reload temperature is shown in Fig. 11.21, which is why there are two symbols at some dpa conditions.

The dashed line in Fig. 11.21 is drawn according to Eq. 6.28 with $\kappa = 2.0$ —just as listed in Table 11.6. It seems as if evolution of irradiation damage follows a similar law to dislocation storage. The equation for this line is

$$\frac{d\hat{\sigma}_\epsilon}{ddpa} = 500\text{MPa} \left[1 - \frac{\hat{\sigma}_\epsilon}{840\text{MPa}} \right]^{2.0} \tag{11.13}$$

There is not enough information to draw firm conclusions regarding the irradiation-induced defect populations. However, analysis of the reload measurements using the mechanistic model described here for unirradiated material has enabled considerable insight into the induced damage. Furthermore, the combination of temperature-dependent yield and temperature-dependent strain hardening in irradiation-damaged material offers valuable information.

11.7 Summary

The deformation as a function of temperature, strain rate, and strain of a number of austenitic stainless steels from the 304 and 316 families of alloys has been analyzed using the mechanical threshold stress (MTS) constitutive model. All of these alloys exhibit a curvature in plots of yield stress versus $T/\ln \dot{\epsilon}$ which is observed in both the annealed and cold-worked conditions. For annealed material, analysis of yield stress measurements as a function of temperature in alloys of varying nitrogen contents and grain size led to the conclusion that nitrogen additions are a major contributor to strength. This contribution is defined by a nitrogen-dependent internal state variable—the mechanical threshold stress—with a small activation volume and a second nitrogen-dependent mechanical threshold stress with a much larger activation volume. In context of the MTS model, the interactions of dislocations with the evolving stored dislocation density developed during straining were represented with a third mechanical threshold stress. The total stress is the sum of these three components plus a small athermal stress due to the interaction of dislocations with grain boundaries. The stress at a given strain rate and temperature is computed by multiplying each mechanical threshold stress by a factor representing the role of thermal activation in assisting dislocations past the specific obstacles. The modeling approach exercised was similar to that demonstrated for pure BCC metals, where a mechanical threshold stress representing the Peierls barrier and one representing the strengthening due to impurity atoms were considered [35].

For the austenitic stainless steels, the more strain rate- and temperature-dependent obstacle (that is represented by the smaller activation volume) is thought to be due to the interaction of dislocations with solute or interstitial atoms. These are short range in character. Because of compositional differences between alloys, one would expect the strength of this obstacle to vary from alloy to alloy. Indeed, some variation was observed. The less strain rate- and temperature-dependent obstacle (that is represented by the larger activation volume) varied strongly with the nitrogen content. The large activation volume suggests a longer-range obstacle. It has been proposed that nitrogen additions enhance long or short-range ordering in these alloys [23]. This proposal is consistent with the large activation volume observed here.

Implementation of the constitutive model was demonstrated on several data sets. Included were measurements at varying strain rates and temperatures on alloys with varying nitrogen concentrations (see Table 11.1 and Figs. 11.13, 11.14, and 11.15). Over a wide range of temperatures and strain rates, good agreement between model predictions and measurements is observed. As the temperature rises above 600 K, however, the stress levels measured experimentally consistently exceed those predicted, which was assumed to represent the contribution of dynamic strain aging.

It is important to emphasize that, although there are numerous, supposedly “adjustable” parameters included in the model equations (e.g., Eqs. 11.2, 11.3, 11.11, 6.26, 6.28, and 6.29) only three parameters were in fact allowed to vary in the predictions referred to above. One of these was the athermal stress σ_a . An explicit dependence of this stress on grain size (see Eq. 11.1) was deduced from the

Norström [13] measurements; this correlation was used whenever possible. Certainly, given the small value of the athermal stress (compared with the mechanical threshold stresses) and the small changes used in the predictions above, the effect of this stress on the predictions is limited. The two internal state variables, $\hat{\sigma}_N$ and $\hat{\sigma}_i$, however, were allowed to vary to enable better agreement with experimental results. The variation of $\hat{\sigma}_N$ with nitrogen content illustrated in Fig. 11.8 offered a good starting point for selection of $\hat{\sigma}_N$ —when the nitrogen concentration was known. But, the correlation shown in Fig. 11.8 and represented by Eq. 11.5a is likely specific to the materials studied by Norström [13] and Brynes et al. [14]. Thus, the value of $\hat{\sigma}_N$ was allowed to vary outside of Eq. 11.5a. Similarly, the value of $\hat{\sigma}_i$ was selected as that which gave a good fit between experiments and predictions. The variation of chemistry between alloys provides strong justification for this practice. None of the other model parameters—including all of the parameters in the evolution law (Eqs. 6.26, 6.28, and 6.29) and the normalized activation energies (g_{oi} , g_{oN} , and g_{oe})—was allowed to vary. The observation of good agreement between measurements and model predictions for such a wide range of alloys and experimental conditions with only two adjustable parameters supports the proposed modeling approach.

In addition, the observation that some of the variation of stress level reported by Hammond and Sikka [12] in different lots of material could be explained by the nitrogen levels in the alloys (and the reported grain size) tends to validate the modeling approach adopted here.

Observation of dynamic strain aging at elevated temperatures in austenitic stainless steel enabled analysis following the procedure applied to AISI 1018 steel, vanadium, niobium, and titanium in earlier chapters. Common behavior observed in both BCC and HCP metals is observed in the austenitic stainless steels.

Finally, demonstration of application of the model to material that is exposed to irradiation damage illustrated how insight can be obtained regarding the irradiation-induced defect population. The comparisons between model predictions and measurements in Figs. 11.19 and 11.20 show that the defect population is similar to a stored dislocation density. Application of the state variable model to material unique processes—in this case using irradiation damage—illustrates how the model can be exploited.

Exercises

- 11.1. The Dai et al. stress–strain curve at 350 C in unirradiated 316LN SS shown in Fig. 11.19 indicates the contribution of dynamic strain aging. Data for this test are listed in Table 11.E1. Using $\hat{\sigma}_i = 572$ MPa and $\hat{\sigma}_N = 243$ MPa (see Sect. 11.6), the model parameters listed in Table 11.6, and the values of p , q , and $\dot{\epsilon}_o$ that have been consistently used in this chapter, (a) create a plot of s_{i2} versus σ_e . (Note that obstacle population “2” rather than “1” is selected since at this temperature and strain rate $s_{i1} = 0$, whereas $s_{i2} > 0$.) (b) Compare the slope of the best fit line with the values listed in Table 11.8.

Table 11.E1 Stress versus strain values for the Dai et al. tensile test at 623 K (350 C) and a strain rate of 0.001 s^{-1} in unirradiated 316LN stainless steel (Exercise 11.1)

Strain	Stress (MPa)	Strain	Stress (MPa)
0.007	190	0.118	400
0.012	204	0.124	413
0.019	218	0.136	432
0.027	233	0.147	451
0.037	250	0.159	469
0.046	271	0.172	488
0.057	287	0.184	500
0.067	307	0.196	515
0.072	320	0.209	531
0.083	337	0.223	542
0.092	354	0.232	552
0.103	374	0.241	557
0.111	389	0.246	559

Table 11.E2 Several of the stress versus temperature and strain rate measurements reported by Steichen in 304 SS (see Fig. 11.3) (Exercise 1.2)

Strain rate (s^{-1})	Temp (K)	Stress (MPa)	Strain rate (s^{-1})	Temp (K)	Stress (MPa)
0.00003	294	192	0.00003	700	122
0.0032	294	228	0.00079	700	112
0.050	294	294	0.0035	700	121
10.00	294	321	0.020	700	117
10.00	294	312	0.101	700	126
100.0	294	334	1.03	700	160
100.0	294	370	10.1	700	154
0.0035	589	123	0.00003	811	120
0.020	589	129	0.0003	811	113
0.101	589	140	0.003	811	116
1.00	589	167	0.1	811	112
10.15	589	188	1	811	113
103.0	589	216	10	811	135

11.2. Table 11.E2 lists a selection of the data points shown in Fig. 11.3 from Steichen in 304 SS. (a) Create a plot of normalized yield stress versus normalized temperature and strain rate (as in Fig. 11.9) for a model that includes $\hat{\sigma}_i$ and $\hat{\sigma}_N$. Except for these latter threshold stresses, use the model parameters dictated in Exercise 11.2. (b) Table 11.2 lists a nitrogen content of 0.052% for this material. How do your values of $\hat{\sigma}_i$ and $\hat{\sigma}_N$ compare with those specified by the correlations in Eqs. 11.5a and 11.5b?

11.3. Table 11.E3 lists stress–strain data for the Conway et al. alloy (316 SS, Fig. 11.17) tested at 703 K and a strain rate of 0.00004 s^{-1} . Using $\hat{\sigma}_i = 572 \text{ MPa}$ and $\hat{\sigma}_N = 243 \text{ MPa}$ (see Sect. 11.6), the model parameters listed in Table 11.6, and the values of p , q , and $\dot{\epsilon}_o$ that have been consistently used in

Table 11.E3 Stress versus strain measurements reported by Conway et al. in 316 SS at 703K and a strain rate of 0.00004 s^{-1} (see Figure 11.17) (Exercise 1.3).

703 K and 0.00004 s^{-1}			
Strain	Stress (MPa)	Strain	Stress (MPa)
0.005	153	0.163	477
0.008	165	0.210	553
0.012	176	0.259	623
0.017	183	0.306	676
0.021	192	0.351	719
0.027	202	0.425	778
0.033	214	0.497	818
0.042	235	0.567	858
0.051	255	0.640	879
0.067	284	0.714	892
0.090	342	0.762	900
0.115	390	0.811	921
0.138	438	0.835	924

Table 11.E4 Stress versus strain measurements reported by Albertini and Montagnani in Irradiated 316L SS at 293K and a strain rate of 0.004 s^{-1} (Exercise 11.4)

293 K and 0.004 s^{-1}			
Strain	Stress (MPa)	Strain	Stress (MPa)
0.0051	442	0.199	811
0.0075	458	0.212	825
0.011	472	0.225	842
0.015	489	0.237	853
0.022	508	0.250	870
0.030	528	0.261	883
0.038	542	0.272	893
0.047	563	0.285	908
0.057	582	0.301	923
0.074	611	0.311	932
0.090	637	0.321	938
0.107	667	0.328	941
0.124	696	0.338	945
0.137	719	0.349	944
0.149	736	0.359	940
0.161	754	0.368	930
0.174	776	0.378	932
0.186	791	0.383	923

this chapter, (a) create a plot of s_{i2} versus σ_e . (Note that obstacle population “2” rather than “1” is selected since at this temperature and strain rate $s_{i1} = 0$, whereas $s_{i2} > 0$.) (b) Compare the slope of the best fit line with the values listed in Table 11.8.

- 11.4. Table 11.E4 lists stress–strain data measured at 293 K and a strain rate of 0.004 s^{-1} by Albertini and Montagnani (see Table 11.1) in irradiated (2.2 dpa) 316L SS. a) Estimate the equivalent level of hardening ($\hat{\sigma}_e$) induced by the

Table 11.E5 Stress versus strain measurements reported by Albertini and Montagnani in Irradiated 316L SS at 293K and a strain rate of 27 s^{-1} (Exercise 11.5)

293 K and 27 s^{-1}			
Strain	Stress (MPa)	Strain	Stress (MPa)
0.0024	508	0.181	859
0.0060	540	0.190	870
0.013	569	0.201	880
0.019	593	0.212	889
0.031	623	0.229	901
0.044	647	0.238	904
0.056	678	0.246	898
0.067	694	0.261	899
0.076	708	0.271	898
0.088	727	0.287	884
0.094	738	0.297	869
0.104	762	0.305	856
0.117	775	0.310	830
0.127	791		
0.136	804		
0.143	812		
0.159	831		
0.169	843		

irradiation, and plot the predicted stress–strain curve along with the measurements. Use the model parameters specified for the “A” material in Table 11.7 along with the parameters in Table 11.6.

- 11.5. Albertini and Montagnani also measured the reload response of the same material as described in Exercise 11.4 at higher strain rates. Table 11.E5 lists stress–strain data measured at 293 K and a strain rate of 27 s^{-1} a) Plot the predicted stress–strain curve along with the measurements using the same value of $\hat{\sigma}_\epsilon$ that you deduced in Exercise 11.5. How do the curves compare?
- 11.6. Table 11.E6 lists the data used to construct Fig. 11.21. Included along with the dose is the irradiation temperature reported by these research groups. Compare the data point for the Albertini and Montagnani measurements described in Exercises 11.6 and 11.7 with the data in this table. Albertini and Montagnani report an irradiation temperature of 400 C. Is this relatively high temperature consistent with the difference between the value of $\hat{\sigma}_\epsilon$ estimated for the Albertini and Montagnani and those listed in Table 11.E6?

Table 11.E6 Estimated values of versus irradiation dose used to construct Fig. 11.21 (Exercise 11.6)

Research group	Irradiation conditions		$\hat{\sigma}_e$ (MPa)
	Dose (dba)	Temperature (C)	
Dai et al.	3	77 to 91	429
	4	107 to 126	536
	5.3	142 to 167	615
	7.6	204 to 240	722
	9.7	265 to 311	757
	11.3	309 to 364	772
	4	107 to 126	450
	5.3	142 to 167	615
	7.6	207 to 244	693
	9.7		765
	17.3		750
Byun et al.	0.54	RT	322
	0.54	165	386
	1.87	RT	443
	1.87	164	522
Byun and Farrell	0.5	RT	322
	1.1	RT	386
	2.5	RT	443
	3.6	RT	522
	10.7	RT	657

References

1. P.S. Follansbee, An internal state variable constitutive model for deformation of austenitic stainless steel. *Trans. ASME J. Eng. Mater. Technol.* **134**, 41007-1–41007-10 (2012)
2. F.J. Clauss, *Engineer's Guide to High-Temperature Materials* (Addison-Wesley, Reading, MA, 1969)
3. Sandmeyer Steel Company, "304 Spec Sheet", Philadelphia, PA, <http://www.sandmeyersteel.com/304.html>
4. The Alruqee Group, <http://www.alruqee.net/userfiles/file/SpecialMetalAlloys/304L.pdf>
5. Sandmeyer Steel Company, "304L Spec Sheet", Philadelphia, PA, <http://www.sandmeyersteel.com/304L.html#1>
6. J.M. Steichen, "High strain rate mechanical properties of types 304 stainless steel and nickel 200 (RM-14)," Hanford Engineering Development Laboratory, HEDL-TME-71-145, Richland, WA (September, 1971)
7. J.M. Steichen, M.M. Paxton, "Interim Report – Effect of Strain Rate on the Mechanical Properties of Austenitic Stainless Steels," Hanford Engineering Development Laboratory, HEDL-TME-71-56 (May 1971)
8. G.T. Gray III, S.R. Chen, "MST-8 constitutive properties & constitutive modeling", LA-CP-07-1590 and LA-CP-03-006 (Must request data from LANL authors) (2007)
9. J.B. Conway, R.H. Stentz, J.T. Berling, "Fatigue, tensile and relaxation behavior of stainless steels," Report commissioned by the U. S. Atomic Energy Commission Division of Reactor Research and Development, Available from: NTIS, TID26135, (June 1974)

10. R.W. Swindeman, Representation of high-temperature tensile behavior of reannealed type 304 stainless steel by the Voce equation. *ASME J. Eng. Mater. Technol.* **97**, 98–106 (1975)
11. C. Albertini, M. Montagnani, Dynamic uniaxial and biaxial stress–strain relationships for austenitic stainless steels. *Nucl. Eng. Des.* **57**, 107–123 (1980)
12. J.P. Hammond, V.K. Sikka, “Predicted strains in austenitic stainless steels at stresses above yield”, ORNL Report, Available thru <http://www.osti.gov/energycitations/> as Conf-771120-18, 1977
13. L.-Å. Norström, The influence of nitrogen and grain size on yield strength in type AISI 316L austenitic stainless steel. *Metal Sci.* **11**, 208–212 (1977)
14. M.L.G. Brynes, M. Grujcic, W.S. Owen, Nitrogen strengthening of a stable austenitic stainless steel. *Acta Metall.* **37**(7), 1853–1862 (1987)
15. T.S. Byun, N. Hashimoto, K. Farrell, Temperature dependence of strain hardening and plastic instability behaviors in austenitic stainless steels. *Acta Mater.* **52**, 3889–3899 (2004)
16. Y. Dai, G.W. Egeland, B. Long, Tensile properties of ECX316LN irradiated in SINQ to 20 dpa. *J. Nucl. Mater.* **377**, 109–114 (2008)
17. M.G. Stout, P.S. Follansbee, Strain rate sensitivity, strain hardening, and yield behavior of 304L stainless steel. *Trans. ASME J. Eng. Mater. Technol.* **108**, 344–353 (1986)
18. P.S. Follansbee, “A lower-bound strength model for AISI 304 SS,” Proceedings, MS&T 2010, Houston, TX (October 2010)
19. P.S. Follansbee, D.J. Gross, J. Minichiello, E. Rodriguez, “A lower-bound temperature and strain-rate dependent strength model for AISI 304 SS,” PVP2011-57399, ASME Pressure Vessel and Piping Conference, Baltimore, MD (2011)
20. M.D. Mathew, M. Sundararaman, S.L. Mannan, Dislocation substructure and precipitation in type 316 stainless steel deformed in creep. *Mater. Trans. JIM* **38**, 37–42 (1997)
21. D.G. Morris, Creep in type 316 stainless steel. *Acta Metall.* **26**, 1143–1151 (1978)
22. G.W. Powell, E.R. Marshall, W.A. Backofen, Strain hardening of austenitic stainless steel. *Trans. Am. Soc. Metals* **L**, 478–497 (1958)
23. R.P. Reed, Nitrogen in austenitic stainless steels. *JOM* **41**, 16–21 (1989)
24. Y.N. Turan, A. Koursaris, Nitrogen-alloyed stainless steels and their properties. *J. South Afr. Inst. Min. Metall.* **93**, 97–104 (1993)
25. P.S. Follansbee, G.T. Gray III, An analysis of the low temperature, low and high strain-rate deformation of T-6Al-4V. *Metall. Trans. A* **20A**, 863–874 (1989)
26. P.S. Follansbee, U.F. Kocks, A constitutive description of the deformation of copper based on the use of the mechanical threshold stress as an internal state variable. *Acta Metall.* **36**, 81–93 (1988)
27. A. Kelly, R. B. Nicholson (eds.), *Strengthening Methods in Crystals* (John Wiley and Sons, New York, 1971), p. 293
28. P.S. Follansbee, Structure evolution in austenitic stainless steels—a state variable model assessment. *Mater. Sci. Appl.* **6**(6), 457–463 (2015)
29. K.G. Samuel, S.L. Mannan, P. Rodriguez, Serrated yielding in AISI 316 stainless steel. *Acta Metallurgica* **36**(1988), 2423–2327 (1988)
30. K. Peng, K. Qian, W. Chen, Effect of dynamic strain aging on high temperature properties of austenitic stainless steel. *Mater. Sci. Eng. A* **379**, 372–377 (2004)
31. P. S. Follansbee, “Characterizing the defect population introduced by radiation damage,” Proceedings MS&T 2010, TMS, Warrendale, PA (2010)
32. F.A. Garner, M.L. Hamilton, N.F. Panayotou, G.D. Johnson, The microstructural origins of yield strength changes in AISI 316 during fission or fusion irradiation. *J. Nuclear Mater.* **103 & 104**, 803–808 (1981)
33. T.S. Byun, K. Farrell, Plastic instability in polycrystalline metals after low temperature irradiation. *Acta Mater.* **52**, 1597–1608 (2004)
34. T. S. Byun, K. Farrel, E. H. Lee, L. K. Mansur, S. A. Maloy, M. R. James, and W. R. Johnson, “Temperature effects on the mechanical properties of candidate SNS target container Materials after proton and neutron irradiation,” Oak Ridge National Laboratory, SNS-101060100-TR0003-R00 (2001)
35. P.S. Follansbee, Analysis of deformation kinetics in seven body centered cubic pure metals using a two-obstacle model. *Metall. Mater. Trans. A* **41A**, 3080–3089 (2010)

Chapter 12

Application of MTS Model to Nickel-Base Superalloys



Introduction

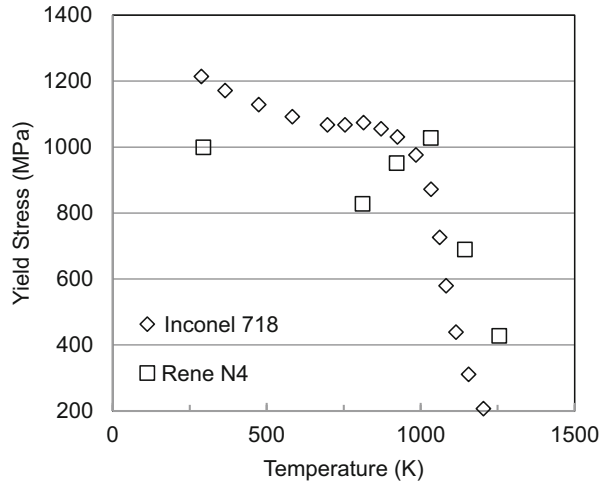
This chapter applies the MTS modeling formalism to the analysis of yield stress and evolution kinetics in nickel-based superalloys [1]. There are two confounding factors when assessing deformation in superalloy systems. The first is the influence of anomalous hardening resulting from the ordered intermetallic phase found in these materials. The second is the influence of DSA. One objective in this chapter will be to demonstrate how to deconvolute these contributions. This offers another example of how the internal state variable formalism can be used to gain insight into deformation kinetics in more complex metallurgical systems.

12.1 Deformation in Nickel-Based Superalloys

The next several sections will consider deformation in a remarkable class of advanced alloys—nickel-based superalloys. In their list of the top 50 “Greatest Moments in Materials Science and Engineering,” the Minerals, Metals, and Materials Society includes the 1926 patent by Paul Merica, which described the addition of small amounts of aluminum to a Ni-Cr alloy creating the first “superalloy” [2]. Indeed the evolution of these alloys, including the advances in chemical composition and processing, has revolutionized air transport and gas and steam turbine commercialization. One fascinating metallurgical feature of this alloy is their ability to form an ordered intermetallic phase (referred to as gamma prime, γ') based on the $L1_2$ structure. In many superalloys these precipitates are a combination of Ni (or Co) and Al (or Ti), e.g., Ni_3Al . These precipitates have a small lattice

Supplementary Information The online version contains supplementary material available at https://doi.org/10.1007/978-3-031-04556-1_12

Fig. 12.1 Yield stress versus test temperature in Inconel 718 [3] and Rene N4 [4] showing the influence of anomalous hardening



mismatch with the ductile and disordered FCC host phase (referred to as gamma). One result of this is the ability to form very high volume fractions of fine precipitates, which in modern airfoil alloys now approach volume fractions of 70%. The presence of these precipitates and the difficulty of transmitting dislocations through an ordered structure give superalloys some very unique mechanical properties. In particular, the variation of the yield stress with increasing temperature shows a regime at elevated temperature where yield stress actually increases with increasing temperature. This is illustrated in Fig. 12.1, which shows the variation of yield stress with temperature in precipitation-hardened Inconel 718 [3] and in Rene N4 [4].

This behavior, which is at odds with the temperature dependence typically observed in metals, is larger in the higher Ni₃Al containing alloy N4 than in the lower Ni₃Al containing alloy Inconel 718. Interestingly, in pure Ni₃Al, the behavior is quite pronounced; at 900K (627 °C), the critical resolved shear stress exceeds that at 300K (27 °C) by a factor of six [5] (see Fig. 12.12).

In superalloys, the enhanced hardening at elevated temperatures is known as the “stress anomaly.” The origin of the effect arises from a self-locking mechanism in dislocations cross-slipping onto non-glide cube planes. This is known as the Kear-Wilsdorf locking mechanism [6]. Detailed models for the dislocation interactions have been proposed and long debated [7].

Another observation related to elevated temperature deformation of superalloys is the presence of dynamic strain aging (DSA). This was topic of an extensive study by Mulford and Kocks in Inconel 600 [8]. These investigators used elevated temperature strain-rate change tests to probe the instantaneous strain-rate sensitivity. Hänninen et al. measured elevated temperature stress–strain curves in Inconel 600 and Inconel 690 and observed jerky flow (serrations) over a wide range of conditions [9]. In addition to the appearance of jerky flow, which often accompanies DSA, another effect of DSA is to increase the flow stress levels during deformation.

While the stress anomaly and the presence of DSA in superalloys have individually been studied in depth, the possibility that both may simultaneously contribute to the extraordinary elevated temperature flow stress levels in these materials is not widely acknowledged. One reason for this is that the stress anomaly has been studied in material in a starting microstructural condition—e.g., solution annealed or precipitation hardened—whereas DSA does not become active until some accumulation of dislocations is in a material [10]. Models of the stress anomaly have not considered the presence of a large density of stored dislocations.

The objective of the following sections is to analyze deformation in example superalloy systems using the MTS formalism. Certainly, the model as currently developed is unable to account for the stress anomaly or for dynamic strain aging, but it may be possible deconvolute the effects of these mechanisms and to look for signatures or trends that could shed further light on these mechanisms. The variation of yield stress with temperature and strain rate (when data is available) in various superalloys will first be considered. Focus will be on the regime of conditions in which the stress anomaly is not active. Strain hardening will then be considered. Again, focus will be on a temperature and strain rate regime where DSA is not active. Predictions over a wider range of temperature and strain rate will then be compared to measurements to analyze deviations from model behavior in the presence of the stress anomaly and DSA. In the former case, deviations from model behavior are compared to the measured variation of strength with temperature in Ni₃Al when the stress anomaly is active. In the latter case, the signature of DSA in the superalloy system is compared to signatures observed in the systems described in earlier chapters.

12.2 Yield Stress Kinetics

It is assumed that in the regime outside where the stress anomaly is active, the yield stress obeys the following constitutive law, which is a form of Eq. 6.14

$$\frac{\sigma}{\mu} = \frac{\sigma_a}{\mu} + s_i(\dot{\epsilon}, T) \frac{\hat{\sigma}_i}{\mu_o} + s_{\gamma'}(\dot{\epsilon}, T) \frac{\hat{\sigma}_{\gamma'}}{\mu_o} \quad (12.1)$$

In Eq. 12.1 $\hat{\sigma}_i$ is the mechanical threshold stress characterizing the interaction of dislocations with impurity atoms (interstitial or solid solution additions) and $\hat{\sigma}_{\gamma'}$ is the mechanical threshold stress characterizing the interactions of dislocations with the precipitates and, perhaps, carbides. Following Eqs. 6.15 and 6.16, s_i and $s_{\gamma'}$ are the kinetic factors, given by

$$s_i(\dot{\epsilon}, T) = \left\{ 1 - \left[\frac{kT}{\mu b^3 g_{oi}} \ln \left(\frac{10^8 s^{-1}}{\dot{\epsilon}} \right) \right]^{\frac{2}{3}} \right\}^2 \quad (12.2)$$

and

$$s_{\gamma'}(\dot{\epsilon}, T) = \left\{ 1 - \left[\frac{kT}{\mu b^3 g_{oj'}} \ln \left(\frac{10^8 s^{-1}}{\dot{\epsilon}} \right) \right]_{\text{th}}^2 \right\}^2 \quad (12.3)$$

where the g_{oj} values are the normalized activation energies characterizing the specific dislocation—obstacle interactions. The assumption here is that along with an athermal stress, there exist two obstacle populations that define the kinetics in the regime outside where the stress anomaly is active. The use of a two-obstacle model follows the approach used in many of the pure metals and alloys described in Chaps. 8, 9, and 10 as well as in the austenitic stainless steels described in Chap. 11.

Figure 12.2 shows the familiar plot of normalized yield stress versus the combination of temperature and strain presented for so many of the metals and alloys in these previous chapters. This data is for Inconel 600 [9] and Inconel 625 [11]. Included in this plot is data for Ni 510 ppm C (Sect. 8.5). For this plot, an athermal stress of 50 MPa was selected. The temperature dependence of the shear modulus is taken as that of pure nickel, represented by (see Eq. 6.8 and Table 6.1)

$$\mu(T) = 85.09 \text{GPa} - \frac{9.132 \text{GPa}}{\exp \left(\frac{269 \text{K}}{T} \right) - 1} \quad (12.4)$$

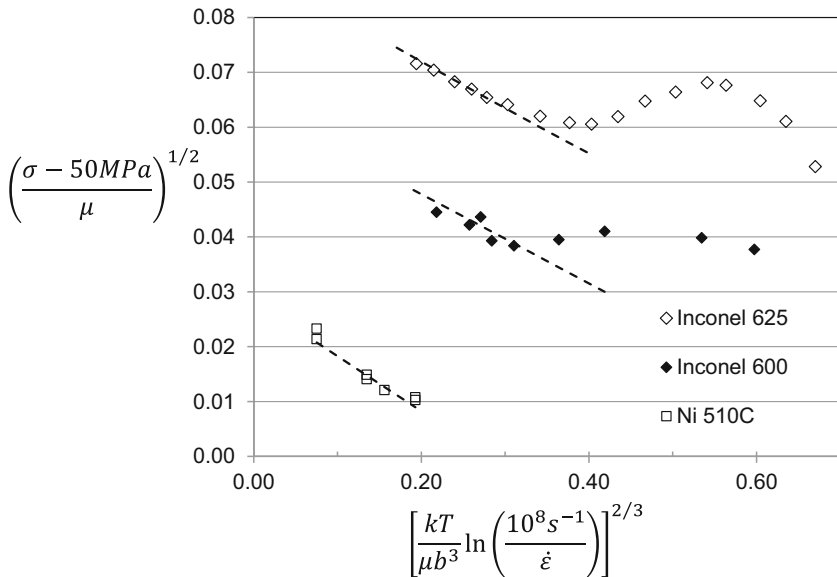


Fig. 12.2 Yield stress versus temperature and strain rate in two Inconel alloys and in Ni 510 C plotted on coordinates consistent with Eq. 12.1 showing in the Inconel alloys a region at low temperatures where Eq. 12.1 is followed

Table 12.1 Values of model constants in Eq. 12.1, Eq. 12.2, and Eq. 12.3 for the linear (dashed lines) regions of Fig. 12.2 (Inconel 600), Fig. 12.3 (Inconel 718), and Fig. 12.14 (C-276)

Superalloy	g_{oi}	$\hat{\sigma}_1/\mu_0$	$g_{oy'}$	$\hat{\sigma}_{y'}/\mu_0$
Inconel 600	0.7	0.0041	2	0
Inconel 625		0.0045		0.0035
Ni 510 C		0.0008		0
Inconel 718 Special Metals, Joshi, AMMT, ASM, Nalawade		0.0045		0.0135
Inconel 718 Lee et al.		0.0045		0.005
C-276	0.9	0.0015	3	0.00375

and the Burgers vector is taken as that in pure nickel (0.249 nm). Both of the Inconel alloys in Fig. 12.2 show a regime characterized by an approximately linear trend followed by the stress anomaly regime. The more heavily alloyed Inconel 625 material has higher yield stresses than observed in Inconel 600. The three dashed lines are model fits. The four fitting parameters are $\hat{\sigma}_i$ and $\hat{\sigma}_{y'}$ from Eq. 12.1, g_{oi} in Eq. 12.2, and $g_{oy'}$ in Eq. 12.3. For the dashed lines in Fig. 12.2, Table 12.1 lists the selected model parameters. Note that single values of both g_{oi} (0.7) and $g_{oy'}$ (2) were selected for the superalloys. (For Ni 510 ppm C, the g_{oi} value was taken as 0.20, consistent with the value listed in Table 8.7). The value for the impurity obstacle population is similar to the value selected for the impurity population in Monel 400 ($g_{oi} = 0.54$) (Table 8.11), somewhat larger than the value selected for the Ni-C system ($g_{oi} = 0.20$, Table 8.7), and also larger than the value selected for austenitic stainless steel ($g_{oi} = 0.20$) (Tables 11.2 and 11.6). In general, g_{oi} values of this magnitude reflect a short-range obstacle to dislocation motion, such as would be imposed by an interstitial or solute atom. The $g_{oy'}$ value of 2, on the other hand, reflects a longer-range obstacle. This is consistent with the suggestion that this parameter reflects the precipitate obstacle. While the activation energies have been held constant, the threshold stress values have been adjusted to enable good agreement with the measurements. Even better agreement is possible by further refinements in the activation energy values, but the measurements do not warrant this. It is noteworthy that, under the assumptions outlined, this relatively simple kinetic model is shown to agree well with the measurements in these three alloys in absence of the stress anomaly. Another result that supports the application of this simple model is the fact that the threshold stress values for the impurity obstacle are almost identical, which reflects that fact that these are all heavily alloyed metals, whereas the threshold stress values for the precipitate obstacle population increase according to the expected gamma prime volume fraction.

Figure 12.3 shows the compilation of measurements in Inconel 718 [3, 12–15]. For these measurements, there is a very limited range of conditions outside of the stress anomaly regime. The dashed line is a model prediction with the same model parameters used in Fig. 12.2 except that the dimensionless threshold stress characterizing dislocation interactions with the precipitates has been increased to 0.0135. The Nalawade et al. [15] measurements are at a strain rate of $6.5 \times 10^{-5} \text{ s}^{-1}$ and test temperatures of 473 K to 923 K. Only tests at temperatures of 473 K, 573 K, and

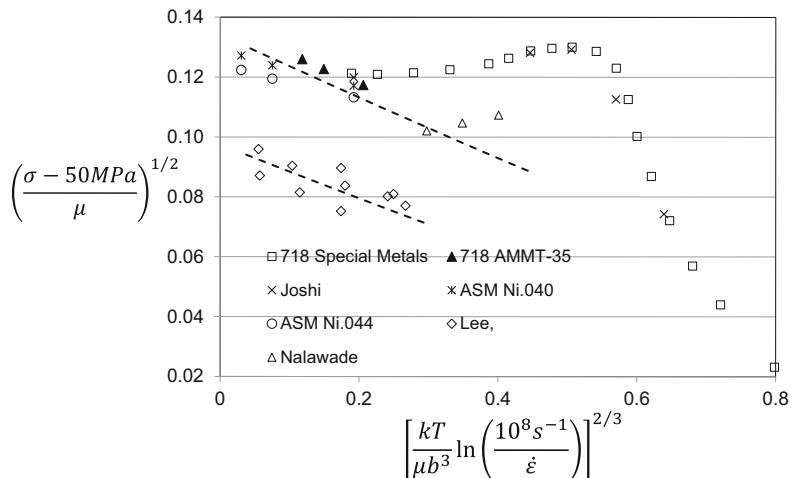


Fig. 12.3 Yield stress versus temperature and strain rate in Inconel 718 plotted on coordinates consistent with Eq. 12.1 showing a region at low temperatures (and, in case of the Lee measurements [14], at high strain rates) where Eq. 12.1 is followed

673 K are included in Fig. 12.3 as open triangles. The 473 K test result falls close to the dashed line in this figure. The tests at higher temperatures all trend upward as demonstrated by the Special Metals measurements. Included in Fig. 12.3 are measurements by Lee et al., who published stress–strain measurements in Inconel 718 under dynamic test conditions [14]. This study considered strain rates of 1000 s^{-1} to 5000 s^{-1} measured in a split Hopkinson pressure bar system over a temperature range of 123 K ($-150 \text{ }^\circ\text{C}$) to 823 K ($600 \text{ }^\circ\text{C}$). However, the Lee et al. material is somewhat softer than the Nalawade et al. material. Lee et al. report a solution treatment at 1323 K ($1050 \text{ }^\circ\text{C}$) for 1 hour followed by an air cool and an aging treatment at 1048 K ($775 \text{ }^\circ\text{C}$) for 8 hours followed by an air cool. This is in contrast to the solution treatment imposed by Nalawade et al. at 1373 K ($1100 \text{ }^\circ\text{C}$) for 1 hour followed by a water quench and an aging treatment at 993 K ($720 \text{ }^\circ\text{C}$) for 50 hours with a water quench. It may well be that the different aging heat treatment created a different precipitate volume fraction and/or morphology.

While the internal state variable representing the interaction of dislocations with precipitates is referred to as $\hat{\sigma}_\gamma$, Inconel 718 also is strengthened by the ordered BCT phase Ni_3Nb , which is designated γ'' [16]. The total fraction of γ' and γ'' in this alloy is on the order of 0.2 [17]. It is assumed that one internal state variable represents both of these strengthening contributions. Note that the total fraction of γ' and γ'' in Inconel 625 is ~ 0.09 [17]. The 923 K ($650 \text{ }^\circ\text{C}$) yield stress in Inconel 718 is ~ 2.5 times that in Inconel 625, which offers a good example of the role precipitation and the associated stress anomaly play in the strengthening in nickel-base superalloys.

It is evident in Fig. 12.3 that the yield stress kinetics in the more highly alloyed Inconel 718 system also are well represented by the simple model above with a single (and sensible) parameter variation—outside of the regime of the stress

anomaly. The next section considers strain hardening—or structure evolution—to begin to separate the effects of the stress anomaly from the contributions of DSA.

12.3 Strain Hardening in Several Nickel-Base Superalloys

The analysis of strain hardening follows the procedures described earlier and demonstrated for a host of FCC, BCC, and HCP metals and alloys. The governing equation for deformation becomes

$$\frac{\sigma}{\mu} = \frac{\sigma_a}{\mu} + s_i(\dot{\epsilon}, T) \frac{\widehat{\sigma}_i}{\mu_o} + s_{\gamma'}(\dot{\epsilon}, T) \frac{\widehat{\sigma}_{\gamma'}}{\mu_o} + s_{\epsilon}(\dot{\epsilon}, T) \frac{\widehat{\sigma}_{\epsilon}}{\mu_o} \tag{12.5}$$

With the values of the model parameters for both obstacle populations specified in the previous section and the usual values of the model parameters for s_{ϵ} in Eq. 7.9 ($g_{oe} = 1.6, p_{\epsilon} = 2/3, q_{\epsilon} = 1,$ and $\dot{\epsilon}_{oe} = 10^7 \text{ s}^{-1}$), Eq. 12.5 is solved for $\widehat{\sigma}_{\epsilon}$ to generate a family of plots of $\widehat{\sigma}_{\epsilon}$ versus strain over a range of test temperatures and strain rates

$$\widehat{\sigma}_{\epsilon} = \frac{\mu_o}{s_{\epsilon}(\dot{\epsilon}, T)} \left(\frac{\sigma - \sigma_a}{\mu} - s_i(\dot{\epsilon}, T) \frac{\widehat{\sigma}_i}{\mu_o} - s_{\gamma'}(\dot{\epsilon}, T) \frac{\widehat{\sigma}_{\gamma'}}{\mu_o} \right) \tag{12.6}$$

This requires a collection of stress–strain curves at varying test temperatures and strain rates.

For Inconel 600 the measurements reported by Hänninen et al. [9] are used. Figure 12.4 shows a collection of stress–strain curves published by these authors. The almost linear hardening demonstrated by this material is somewhat unusual (when compared to other metals analyzed in this monograph) and will complicate the analysis of $\widehat{\sigma}_{\epsilon}$ versus ϵ according to Eq. 6.28.

Fig. 12.4 Stress–strain curves reported by Hänninen et al. [9] in Inconel 600

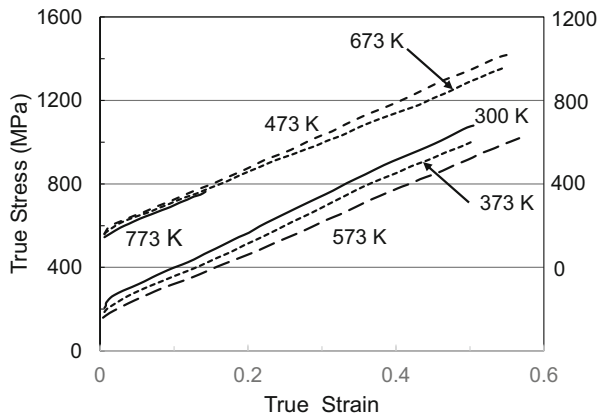


Fig. 12.5 Stress–strain curves reported by Lee et al. [14] in Inconel 718

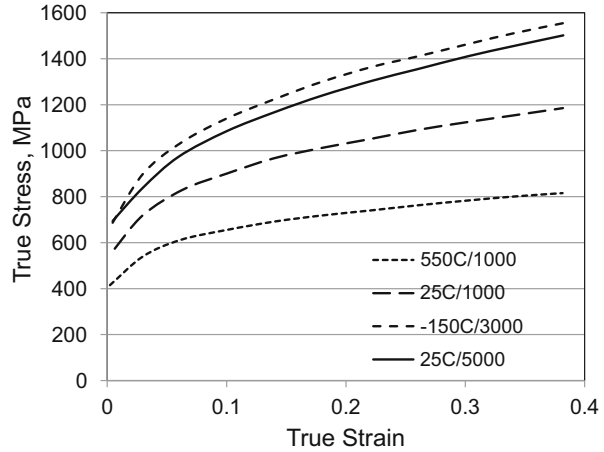
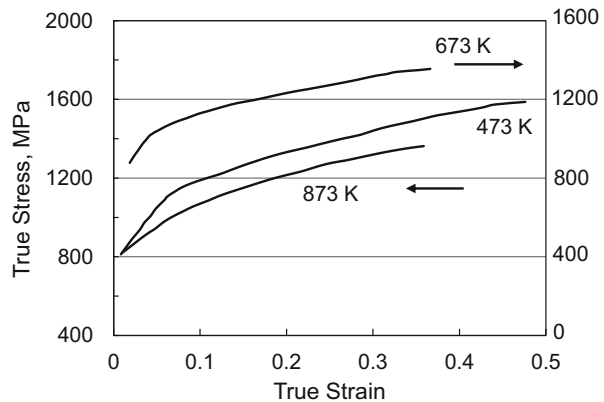


Fig. 12.6 Stress–strain curves reported by Nalawade et al. [15] in Inconel 718



For Inconel 718 the measurements reported by Lee et al. [14] are used. These were at high strain rates as a function of test temperature. Several of these stress–strain curves are shown in Fig. 12.5. The stress–strain curves published by Nalawade et al. [15] also are used. These stress–strain curves are shown in Fig. 12.6. Another useful set of stress–strain curves are the results reported by Roy et al. in C-276 [18]. The strengthening contributions in this alloy reportedly include solution hardening and hardening by the various carbide phases [19]. These stress–strain curves are shown in Fig. 12.7. As in Inconel 600 the rate of strain hardening in this alloy is remarkably linear.

Fig. 12.7 Stress–strain curves reported by Roy et al. [18] in nickel-based alloy C-276

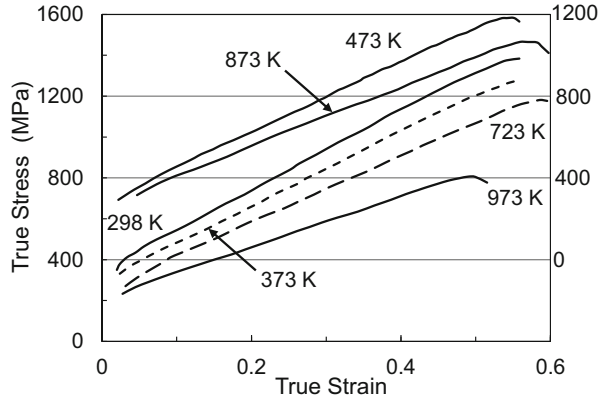
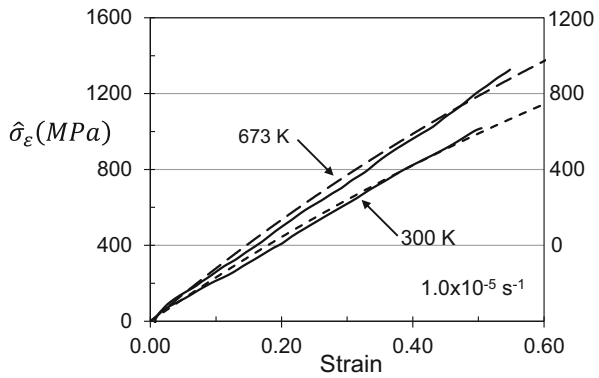


Fig. 12.8 Plots of $\hat{\sigma}_\epsilon$ versus ϵ for two measurements in Inconel 600. The test at 300 K is plotted on the right ordinate, whereas the test at 673 K is plotted on the left ordinate



12.3.1 Strain Hardening in Inconel 600

Figure 12.8 shows plots of $\hat{\sigma}_\epsilon$ versus ϵ by Hänninen et al. measurements in Inconel 600 at temperatures of 27 K and 673 K. These plots are computed using Eq. 12.6 and the model constants listed in Table 12.1. The stress–strain curves shown in Fig. 12.4 demonstrated remarkably linear hardening. This is shown as well for both temperatures in Fig. 12.8. The yield stress correlation for this material (Fig. 12.2) shows a region where the yield stresses follow the dashed model-fit line. Above temperatures of 473 K, however, the data points trend above the dashed line. This likely reflects the contribution of the stress anomaly. Note in Table 12.1, the value of $\hat{\sigma}_\gamma/\mu_0$ is listed as zero. It was argued earlier that this threshold stress represented the contribution of the gamma prime precipitates. A zero value would suggest that the stress anomaly shouldn't be observed. However, one can achieve as good a model-fit agreement using a non-zero—but still small (e.g., < 0.001)—value of $\hat{\sigma}_\gamma/\mu_0$. The application of Eq. 12.6 to the raw data at test temperatures greater than 473 K would yield starting values of $\hat{\sigma}_\epsilon$ (at $\epsilon = 0$) that are less than 0 because the model fit does not include the contribution of the stress anomaly. This plot needs to start at a zero initial value of $\hat{\sigma}_\epsilon$ in order to evaluate Eq. 6.28. The solution is simply to add an offset stress

to the model-fit stress that yields an initial $\hat{\sigma}_\epsilon$ value of zero. At 673 K, this offset stress is only 47 MPa, which supports the observation that the stress anomaly is fairly small in Inconel 600.

The remarkably linear strain hardening observed in both the raw stress–strain curves and the plots of $\hat{\sigma}_\epsilon$ versus ϵ in Fig. 12.8 further complicates the analysis of hardening. Without an indication of the transition to Stage III hardening (indicated by a bending over of the stress–strain curve), one cannot deduce a value of a saturation stress. The variation of the saturation stress with test temperature and strain rate enables creation of plots such as shown in Fig. 9.44 for vanadium, Fig. 9.56 for niobium, Fig. 10.68 for titanium, and Fig. 11.12 for AISI 316L stainless steel. Another curious observation in Fig. 12.8 is that the slope of the curves—the Stage II hardening rate—appears to increase at the higher test temperature. Recall for all of the analyses presented in earlier chapters, this Stage II hardening rate did not show a variation with test temperature. It has been argued that a variation with strain rate exists, as represented using Eq. 6.29, but a variation with test temperature was not evident in any of these systems.

Table 12.2 lists the model parameters for best fits of Eq. 6.28 with the $\hat{\sigma}_\epsilon$ versus ϵ data for the Hänninen et al. measurements in Inconel 600. A value of $\kappa = 1$ was used for these fits. The offset stress values are consistent with the differences between the measured stresses and model-fit stresses in Fig. 12.2. A slight temperature dependence of θ_{II} is evident. The saturation stress values, however, are not meaningful; they reflect the fact that the linear hardening observed does not enable a fit to Eq. 6.28. Nonetheless, Fig. 12.9 shows the standard plot of the saturation stress with temperature and strain rate. As in other similar plots, a dashed line extrapolating through the origin has been drawn. To make this plot, the value of the 0 K saturation threshold stress, $\hat{\sigma}_{\epsilon_{SO}}$, was arbitrarily selected as 5000 MPa. This value has no significance. This plot looks nothing like the plots in other materials analyzed in this monograph. The one significant feature evident in Fig. 12.9 is the three data points on the left side of the plot, which deviate significantly from the behavior demonstrated in the data points on the right side of the plot. It is very likely that these deviations reflect the contribution of DSA. Table 12.3 lists the full sets of model parameters for Inconel 600.

Table 12.2 Fits to Eq. 6.28 for measurements in Inconel 600. The offset stresses are the stress differences between the yield stress measurements and the dashed-line fit in Fig. 12.2

T, K	Offset stress, MPa	θ_{II} , MPa	$\hat{\sigma}_{\epsilon_s}$, MPa
300	0	2400	3000
373	0	2300	3000
398	0	2400	3100
423	0	2500	3000
473	0	2500	3200
573	21	2500	4000
673	47	2900	3500
873	63	3500	3000

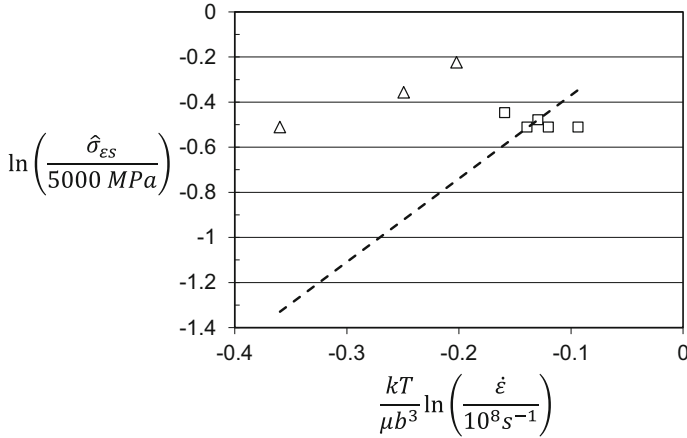


Fig. 12.9 Saturation stress versus temperature and strain rate for Inconel 600 plotted on coordinates consistent with Eq. 6.26. The lack of agreement with Eq. 6.26—evidenced by the lack of a linear relationship extrapolating through the origin—reflects the linear stress–strain behavior that shows no tendency for saturation

12.3.2 Strain Hardening in Inconel 718

Figure 12.3 showed that Inconel 718 follows a consistent variation of yield stress with temperature and strain rate when the temperatures are low and/or the strain rates are high (the left side of the plot). At some point the yield stresses deviate upward. It has been suggested that this deviation reflects the stress anomaly. It is known that DSA is active in Inconel 718 at elevated temperatures. The stress–strain curves published by Nalawade et al. show serrated flow at temperatures of 573 K through 823 K. These are not represented in the stress–strain curves reproduced in Fig. 12.6 due to the difficulty inherent in digitizing the original curves. A consistent observation regarding the initiation of DSA has been that DSA does not influence the yield stress in relatively dislocation-free materials (see, for instance, Figs. 9.48, 9.62, and 11.17). Rather DSA requires the generation of dislocations that attract solute atoms.

Two data sets included in Fig. 12.3 will be analyzed further to assess strain hardening. These are the Lee et al. data set and the Nalawade et al. data set. Note from Fig. 12.3 that all of the yield stresses in the dynamic test results of Lee et al. fall on the (lower) dashed line. That is, the stress anomaly does not appear to be affecting these measurements. While the Nalawade et al. yield stress measurements are at a higher stress level—presumably due to the different solution heat treatments applied—the data sets are complementary. Note in Fig. 12.3 that the yield stress at the lowest test temperature (473 K) used by Nalawade et al. falls close to the dashed line. As temperatures rise above this, the yield stresses deviate strongly upward.

Figure 12.10 shows the variation of $\hat{\sigma}_\epsilon$ versus ϵ for the Lee et al. measurements at 823 K and strain rates of 1000 s^{-1} and 5000 s^{-1} . These plots are computed using

Table 12.3 Full set of model parameters for Inconel 600

Parameter	Equation	Value	Units
σ_a (MPa)	Eq. 12.1	50	MPa
s_i	Eq. 12.2	g_{oi}	0.7
		pi	0.5
		qi	1.5
		$\dot{\epsilon}_{oi}$	1×10^8
$\widehat{\sigma}_i$	Eq. 12.1	349	MPa
$s_{\gamma'}$	Eq. 12.3	$g_{\gamma'}$	2.0
		$p_{\gamma'}$	0.5
		$q_{\gamma'}$	1.5
		$\dot{\epsilon}_{o\gamma'}$	1×10^8
$\widehat{\sigma}_{\gamma'}^{-1}$	Eq. 12.1	0	MPa
$s\epsilon$	Eq. 7.9	$g_{o\epsilon}$	1.6
		p_ϵ	0.667
		q_ϵ	1
		$\dot{\epsilon}_{o\epsilon}$	1×10^7
κ	Eq. 6.28	1	–
θ_{II}	Eq. 6.29	A_o	3000
		A_1	20
		A_2	0
$\widehat{\sigma}_{\epsilon s}$	Eq. 6.26	$\widehat{\sigma}_{\epsilon so}$	5000
		$g_{\epsilon so}$	0.1271
		$\dot{\epsilon}_{\epsilon so}$	1×10^8
b		0.249	nm
ρ	Eq. 6.32	8.9	g/cm^3
ψ		0.95	–
$\mu(T)$	Eq. 6.8 (See Table 6.1)	μ_o	85.09
		D_o	9.132
		T_o	269
$c_p(T)$	See Table 6.5 in Box 6.4	A_C	0.1565
		B	7.00×10^{-5}
		C	7060

¹Parameters for the 2nd obstacle population consistent with those listed in Table 12.1 are shown, even though the threshold stress for this population in Inconel 600 was very small

Eq. 12.6 and the model constants listed in Table 12.1.¹ The dashed lines are drawn according to Eq. 6.28 with $\kappa = 2$. Figure 12.11 shows the variation of $\widehat{\sigma}_\epsilon$ versus ϵ for the Nalawade et al. measurements at 473 K and 773 K. Because these curves

¹The model parameters listed in the Lee et al. row in Table 12.1 are used for this data set. For analysis of the Nalawade et al. data, the model parameters for the Inconel 718 Special metals, etc., are used.

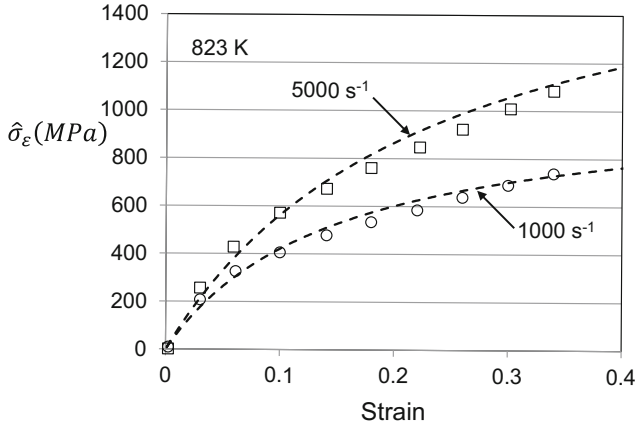


Fig. 12.10 Plots of $\hat{\sigma}_\epsilon$ versus ϵ for two measurements by Lee et al. [14] in Inconel 718

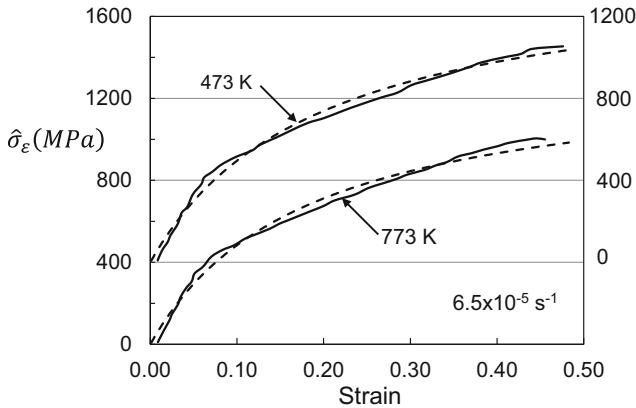


Fig. 12.11 Plots of $\hat{\sigma}_\epsilon$ versus ϵ for two measurements by Nalawade et al. [15] in Inconel 718. The test at 473 K is plotted on the right ordinate, whereas the test at 773 K is plotted on the left ordinate

approximately coincide, the 473 K results are plotted on the right ordinate with a 400 MPa offset. In analyzing the Inconel 600 measurements, the stress anomaly at temperatures greater than 473 K introduced inaccurate $\hat{\sigma}_\epsilon$ predictions according to Eq. 12.6. An offset stress is required so that the $\hat{\sigma}_\epsilon$ versus ϵ curve starts at zero. At 773 K, this offset stress is 270 MPa, which is much larger than the offset stress required in analyzing Inconel 600. Table 12.4 lists the resultant model parameters for Eq. 6.28 for both the Lee et al. and the Nalawade et al. measurements. Because the specimen temperature rises during dynamic straining, Table 12.4 lists both the starting temperature and the average temperature during the test.

The offset stresses (Nalawade et al. data set) added to the predicted stress to enable agreement with the measured stress are listed in Table 12.4. These offset

Table 12.4 Fits to Eq. 6.28 for measurements in Inconel 718. The offset stresses are the stress differences between the yield stress measurements and the dashed-line fit in Fig. 12.3

Data set	Temperature, K		Strain rate s^{-1}	Offset Stress MPa	θ_{II} , MPa	$\hat{\sigma}_{ES}$, MPa
	Starting	Average				
Lee et al.	123	254	3000	-80	7000	2200
	123	269	5000	35	7000	2600
	298	395	1000	-80	6500	1400
	298	415	5000	30	6500	2200
	573	658	3000	30	7000	1500
	573	664	5000	70	7000	1900
	823	874	1000	25	7000	1050
	823	889	3000	50	7000	1450
	823	894	5000	40	8000	1880
Nalawade et al.	473	473	6.5×10^{-5}	-25	7500	1450
	573	573		85	7000	1500
	673	673		186	7500	1300
	773	773		270	7500	1600
	823	823		316	7500	1600
	873	873		460	7000	1950

¹Offset stresses for the Lee et al. measurements are introduced to counter the scatter in the yield stress measurements

²Because these are dynamic tests, the temperature arises as straining proceeds. This column lists the average temperature during the test

stresses increase with test temperature, which also is evidenced by the growing difference between the measured yield stresses and the model behavior (dashed line) in Fig. 12.3 due to the stress anomaly. Figure 12.12 compares the yield stress measured in Ni₃Al as a function of temperature [20, 21] with the offset stresses from Table 12.4. In this plot the measured critical resolve shear stresses are multiplied by a Taylor factor of 3.1. It is intriguing that the temperature dependence estimated in Inconel 718 using these analyses presented here follows that in Ni₃Al.

The saturation threshold stress values for both the Lee et al. and Nalawade et al. data sets are plotted in Fig. 12.13 on coordinates used to assess the correspondence to Eq. 6.26. Although the measurements are plagued with a lot of scatter, the Lee et al. measurements (open diamonds) loosely follow Eq. 6.26 with $\hat{\sigma}_{ES0} = 3500$ MPa. Only the lowest temperature measurement in the Nalawade et al. data set (473 K) lies close to the dashed-line model fit; measurements at higher temperatures trend upward—indicative of the contribution of DSA. It is noteworthy that although these two materials were heat treated differently and exhibit different yield stresses, the hardening (Eq. 6.26) appears to be described with a single set of model parameters. A full set of MTS model constants for Inconel 718 are listed in Table 12.5.

Fig. 12.12 Variation of yield stress with temperature for Ni₃Al compared to the variation of the offset stress listed in Table 12.4. These offset stresses are the difference between the yield stresses in Fig. 12.3 (Nalawade et al. data set) and the dashed line

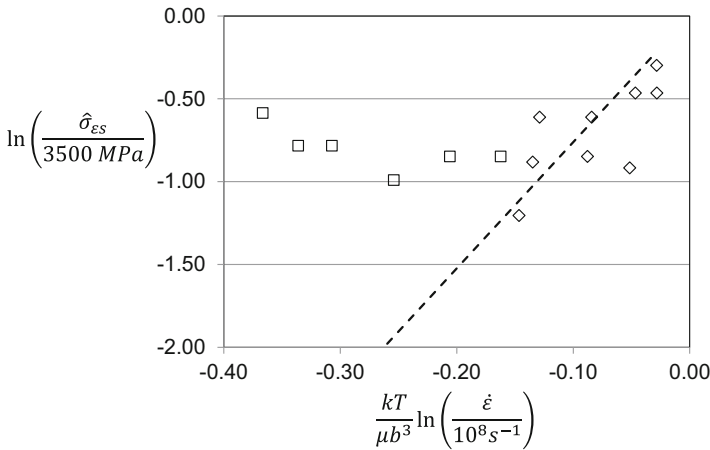
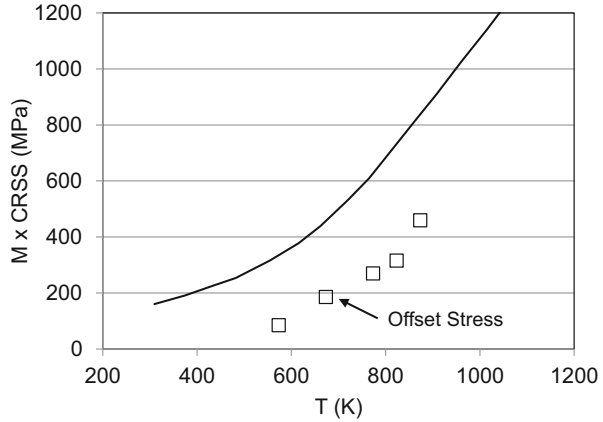


Fig. 12.13 Saturation stress versus temperature and strain rate for Inconel 718 plotted on coordinates consistent with Eq. 6.26

12.3.3 Yield Stress Kinetics and Strain Hardening in C-276

Alloy C-276 is a solution strengthened nickel-based alloy that has seen recent consideration as a material for nuclear power system components [22]. A select set of stress–strain curves, measured in tension at a strain rate of $5 \times 10^{-4} \text{ s}^{-1}$, were shown in Fig. 12.7. Another set of tensile stress–strain curves in this material at a strain rate of $3 \times 10^{-4} \text{ s}^{-1}$ was reported by Pu et al. [19]. These investigators analyzed stress–strain behavior in both the solution treated (ST) and the solution treated and aged (STA) conditions. Figure 12.14 shows yield stress versus temperature and strain rate in these materials. The Pu et al. measurements in material in the STA condition and the Roy et al. measurements show similar trends. The data follow

Table 12.5 Full set of model parameters for Inconel 718

Parameter		Equation	Value	Units
σ_a (MPa)		Eq. 12.1	50	MPa
s_i	g_{oi}	Eq. 12.2	0.7	–
	pi		0.5	–
	qi		1.5	–
	$\dot{\epsilon}_{oi}$		1×10^8	s^{-1}
$\hat{\sigma}_i$		Eq. 12.1	383	MPa
$s_{\gamma'}$	$g_{\gamma'}$	Eq. 12.3	2.0	–
	$p_{\gamma'}$		0.5	–
	$q_{\gamma'}$		1.5	–
	$\dot{\epsilon}_{o\gamma'}$		1×10^8	s^{-1}
$\hat{\sigma}_{\gamma'}$ Special Metals, Nalawade, . . .		Eq. 12.1	1149	MPa
$\hat{\sigma}_{\gamma'}$ Lee			425	MPa
s_{ϵ}	$g_{o\epsilon}$	Eq. 7.9	1.6	–
	p_{ϵ}		0.667	–
	q_{ϵ}		1	–
	$\dot{\epsilon}_{o\epsilon}$		1×10^7	s^{-1}
κ		Eq. 6.28	2	–
θ_{II}	A_o	Eq. 6.29	2800	MPa
	A_1		100	MPa
	A_2		0	$MPa s^{-1/2}$
$\hat{\sigma}_{\epsilon s}$	$\hat{\sigma}_{\epsilon s o}$	Eq. 6.26	3500	MPa
	$g_{\epsilon s o}$		0.131	–
	$\dot{\epsilon}_{\epsilon s o}$		1×10^8	s^{-1}
b			0.249	nm
ρ		Eq. 6.32	8.9	g/cm^3
ψ			0.95	–
$\mu(T)$	μ_o	Eq. 6.8 (See Table 6.1)	85.09	GPa
	D_o		9.132	GPa
	T_o		269	K
$c_p(T)$	A_C	See Table 6.5 in Box 6.4	0.1565	J/g/K
	B		7.00×10^{-5}	J/g/K ²
	C		7060	J K/g

typical low temperature behavior (left side of the plot) and then trend upward. In the ST material analyzed by Pu et al., the stresses are lower, but the slope of trend at low temperature is very similar to that demonstrated by the STA material. In fact, a good model fit (dashed line) is achieved by simply decreasing the value of $\hat{\sigma}_{\gamma'}/\mu_0$. The ST material shows a higher tendency toward increased stress levels with increasing temperatures. Pu et al. refer to the upward trend as a “stress anomaly” related to the formation of $M_{23}C_6$ carbides as well as the contribution of DSA [19]. It has been argued here that DSA should not affect yield in material with a low initial dislocation density. Attributing the stress anomaly to carbide precipitates is unusual since these

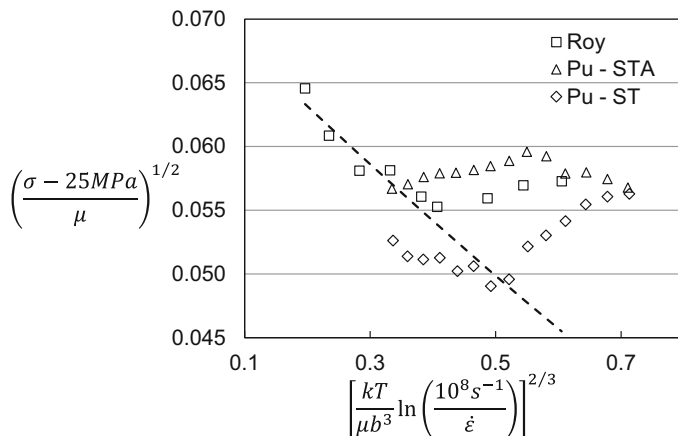


Fig. 12.14 Yield stress versus temperature and strain rate in C-276 plotted on coordinates consistent with Eq. 12.1. Results for both solution-treated (ST) and solution-treated and aged (STA) materials are shown. The dashed line is the model fit

precipitates are quite large compared to the intermetallic γ' precipitates found in nickel-based superalloys, and the Kear-Wilsdorf locking mechanism that is presumed responsible for anomalous hardening wouldn't be relevant to dislocation interactions with carbide precipitates. The Pu et al. material reportedly contained 0.22 weight percent Al, which is on the order of the aluminum concentrations in, for instance, Inconel 718 (0.3 max) or Inconel 600 (<0.35). No aluminum content in the Roy et al. material was reported. Nonetheless, it seems likely that the stress anomaly observed in C-276 is related to the presence of γ' . These precipitates would not be visible using the SEM characterization reported in both the Pu et al. and Roy et al. publications.

The model parameters selected for the dashed-line fit in Fig. 12.14 are included in Table 12.1. The athermal stress was decreased to 25 MPa since, as heat treated, these materials exhibit a large grain size [19]. The activation energy for the "precipitate phase" ($g_{\gamma'}$) has been increased to 3.0, showing an even longer-range obstacle than was found in Inconel 600 or Inconel 718.

Figure 12.15 shows the increase of $\hat{\sigma}_\varepsilon$ with ε for measurements at 373 K and 873 K. These have been calculated using Eq. 12.6 with the model parameters listed in Table 12.1. As observed in Inconel 600, the plots are remarkably linear. This introduces the same complexity as reported in Inconel 600 in fitting the evolution equation (Eq. 6.28). The dashed lines are drawn according to this equation (with $\kappa = 1$). For the test at 373 K, $\theta_{II} = 2500$ MPa and $\hat{\sigma}_{\varepsilon_s} = 5000$ MPa. For the test at 873 K, these become 3500 MPa and 5000 MPa, respectively. That is, the value of $\hat{\sigma}_{\varepsilon_s}$ is artificially high to account for the apparent lack of transition to Stage III hardening, and it doesn't vary with test temperature. Also of interest in Fig. 12.15 is that the slope of the line (θ_{II}) for the test at 873 K is noticeably greater than that at 373 K. This trend also was observed in Inconel 600 (Sect. 12.3.1).

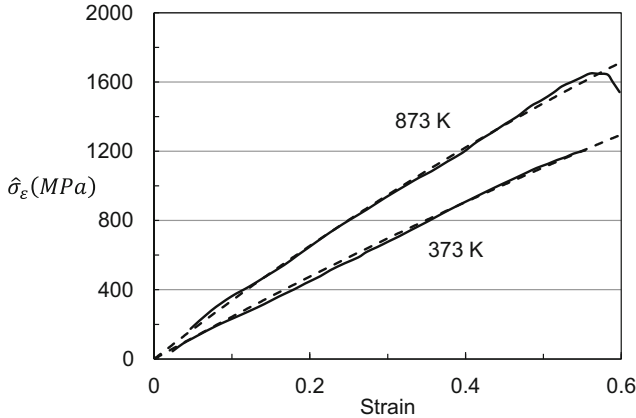


Fig. 12.15 Plots of $\hat{\sigma}_\varepsilon$ versus ε for two measurements by Roy et al. [18] in C-276

12.3.4 Yield Stress Kinetics and Strain Hardening in C-22

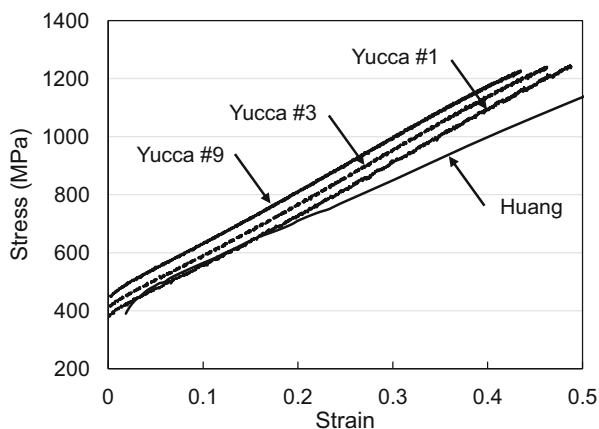
Alloy C-22 (variants referred to as Inconel 622, Alloy 22, and Hastelloy 22) offers yet another superalloy for comparison. This is a nickel-based alloy with outstanding corrosion resistance that has become a prime candidate for waste storage vessels, e.g., for the Yucca Mountain project [23–26]. Alloy C-22 is an alloy with significant chromium (21% by weight) and molybdenum (17% by weight) additions. The alloy exhibits excellent corrosion resistance, which has motivated its use in low- and moderate-temperature applications where corrosion resistance is desired. Table 12.6 compares the chemical composition of Hastelloy C-22 [27], Inconel 622 [28], Inconel 718 [29], and AISI 304 SS. It is evident that Hastelloy C-22 is similar to Inconel 622. Along with all of the alloys in Table 12.6, C-22 exhibits a Face-Centered-Cubic (FCC) crystal structure. The alloy has the UNS designation UNS N06022 and is included in the ASTM B575-10 specification [30]. Recent modifications to the alloy have increased the strength levels, as evidenced by the Hastelloy C-22HS alloy developed by Haynes International [31].

Alloy C-22 can be age-hardened which produces a precipitate phase. Age hardening requires annealing (e.g., 16 hours at 978 K) followed with a lower-temperature aging (e.g., 32 hours at 878 K) [32]. In the annealed condition, the material exhibits a higher yield strength (376 MPa) than AISI 304 SS (207 MPa). In the aged condition, the yield strength rises to 690 MPa due to precipitation reactions. Age hardening in this alloy system is related to the precipitation of the $\text{Ni}_2(\text{Cr, Mo})$ precipitates [32] although the presence of long-range ordering (LRO) after aging at intermediate temperatures has also been documented [26]. While the strength increases significantly with aging, work in C-22 has shown that the reduction of area in a tensile test decreases in the aged condition compared to the annealed condition [26]. Another compelling factor limiting the use of precipitation-hardened material involves

Table 12.6 Chemical compositions of several nickel-base superalloys

Alloy	Inconel alloy 622	Hastelloy C-22	Inconel 718	Inconel 600	C-276
Ni	Base	Base	52.5	Base	Base
Cr	20.0–22.5	20.0–22.5	19.0	14.0–17.0	15.6
Mo	12.5–14.5	12.5–14.5	3.0		16.1
Fe	2.0–6.0	2.0–6.0	18.5	6.0–10.0	5.2
W	2.5–3.5	2.5–3.5	5.1		3.8
Co	2.5 max	2.5 max			0.02
C	0.015 max	0.010 max	0.08 max	0.05–1.50	0.01
Mn	0.50 max	0.50 max		1.0 max	0.5
V	0.35 max	0.35 max			
S	0.02 max	0.010 max		0.015 max	0.002
Si	0.08 max	0.08 max		0.5 max	0.08
P	0.02 max	0.025 max		0.015 max	0.005
Al			0.5	0.3 max	0.22
Ti			0.9	0.3 max	
Cu			0.15 max	0.5 max	
B				0.006 max	
Crystal	FCC	FCC	FCC	FCC	FCC

Fig. 12.16 Stress–strain curves in C-22, including three measurements from the Yucca Task 24 project (#1, 352 K and $1.52 \times 10^{-4} \text{ s}^{-1}$; #3, 352 K and $1.49 \times 10^{-2} \text{ s}^{-1}$; #9, 294 K and $1.43 \times 10^{-1} \text{ s}^{-1}$) and a measurement by Huang (295 K and $1.0 \times 10^{-3} \text{ s}^{-1}$)



fabrication. Achieving the stronger precipitation-hardened strength of welded pipe and storage vessels could be challenging. Thus, material in the annealed condition is most typically considered for waste storage applications.

Figure 12.16 shows a collection of stress–strain curves in material in an annealed condition [32, 33]. These tests include conditions over a range of temperatures and strain rates. As in Inconel 600 (Fig. 12.4) and Alloy C-276 (Fig. 12.7), this alloy demonstrates remarkably linear hardening. This may well indicate contribution from a strain-assisted precipitation reaction.

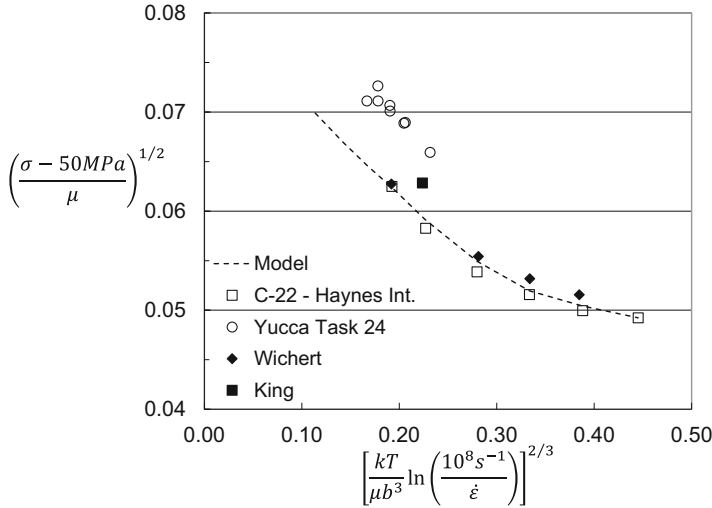


Fig. 12.17 Yield stress versus temperature and strain rate in C-22 plotted on coordinates consistent with Eq. 12.1. The dashed line is the model fit

Several investigators have reported yield stress measurements as a function of test temperature and even strain rate in annealed material. In addition to the stress-strain curves shown in Fig. 12.16, Wichert et al. reported measurements at a strain rate of 10^{-3} s^{-1} and temperatures from 293 K to 693 K [34]. King et al. reported a measurement at 294 K and a very slow strain rate (10^{-6} s^{-1}) [35]. Hayne International has published data on Alloy C-22 over wide temperature range (294 K to 811 K) [36]. Figure 12.17 compiles yield stress versus temperature and strain rate for these measurements. The Yucca Task 24 measurements are at a slightly higher stress level than the other measurements, but all follow the simple model behavior shown with the dashed line. The model parameters for this model fit have been added to Table 12.1. As in the other superalloys listed in Table 12.1, a two-parameter model with a short-range obstacle population ($g_{oi} = 0.23$) and a long-range obstacle population ($g_{o\gamma'} = 1.5$) describes the trends well.

Of interest in Fig. 12.17 is the lack of the indication of a stress anomaly; the yield stresses uniformly decrease over the entire test regime. The compositions for this alloy in Table 12.6 indicate no aluminum additions. This would imply that the ordered intermetallic Ni_3Al , which is the source of the anomaly, will not form. Indeed, Reed lists the total fraction of γ' and γ'' in Hastelloy C-22 as zero [17]. Thus, reference to this obstacle population in Table 12.1 as $\hat{\sigma}_{\gamma'}$ is inaccurate. Instead, this is simply a long-range obstacle. Figure 12.18 compares the yield stress versus test temperature (and strain rate) measurements in Alloy C-22 (open symbols) with measurement presented for Alloy C-276 (closed symbols). The different behavior at the higher temperatures (right-hand side of the plot) is quite evident.

The high rate of strain hardening introduces the same complication that was encountered in Inconel 600 and C-276. Equation 6.28 cannot be used to describe the variation of $\hat{\sigma}_{\epsilon}$ with ϵ to find the variation of the saturation stress with temperature

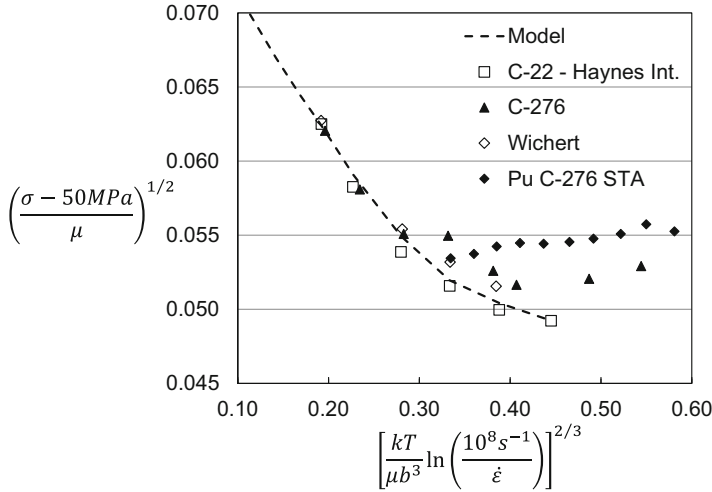


Fig. 12.18 Yield stress versus temperature and strain rate in C-22 (open symbols) compared to measurements in C-276 (closed symbols). The dashed line is the model fit to the C-22 data set

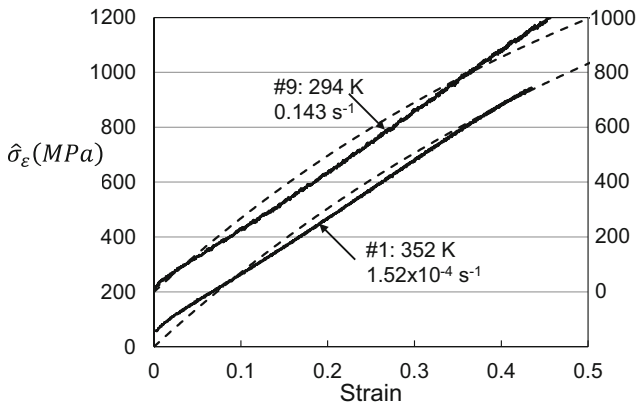


Fig. 12.19 Plots of $\hat{\sigma}_\epsilon$ versus ϵ for two of the Yucca Task 24 measurements in C-22

and strain rate. Nonetheless, one can derive the $\hat{\sigma}_\epsilon$ versus ϵ curve using Eq. 12.6. Figure 12.19 shows two of these curves for measurements in the Yucca Task 24 data set. Because the two curves essentially overlie, the lower temperature test is plotted on the right-hand ordinate, whereas the higher temperature test is plotted on the left-hand ordinate. The dashed lines are the fit to Eq. 6.28 with $\kappa = 1$. For both of these curves, the Stage II hardening rate is selected as $\theta_{II} = 2900$ MPa, which is close to the values found for Inconel 600 (2500 MPa) and C-276 (2800 MPa). Interestingly, these values are less than that found for Inconel 718 (7000 MPa). Inspection of the range of ratios of θ_{II} to μ_0 listed in Table 10.22 for other materials considered in this monograph shows that this variation is not unusual.

12.3.5 Potential Origins of High Hardening Rates

Clearly, Eq. 6.28 cannot be used to describe hardening in materials such as Inconel 600, C-276, and C-22 that exhibit such high rates of strain hardening. Application of this equation has led to observation of an apparent temperature dependence of (θ_H) which has not been observed in any of the metals and alloys examined in this monograph.

High rates of strain hardening have been observed in cadmium (Fig. 10.11) and titanium (Fig. 10.56 and Fig. 10.66). Tests in cadmium and titanium were at 77 K, and the high hardening rates were attributed to deformation twinning. The titanium test analyzed in Fig. 10.66 was at a high strain rate, and the enhanced hardening was attributed to the contribution of DSA. In each of these cases, it was impossible to fit Eq. 6.28 to establish $\hat{\sigma}_{es}$.

High hardening rates are not uncommon in many material systems. Often high hardening rates are desirable because they achieve increased strength levels and can delay the onset of a tensile instability and lead to increased elongations in a tensile test. Researchers have gone to great lengths to design materials that achieve high hardening rates. In an austenitic stainless steel, He et al. documented high rates of strain hardening in tests at 1073 K and 1273 K [37]. Continuous strain hardening in the former case is attributed to strain-induced martensite, whereas enhanced strain hardening in the latter was due to deformation twinning. Brozek et al. applied transformation-induced plasticity (TRIP) and twinning-induced plasticity (TWIP) concepts to enhance the hardening in a β -titanium alloy [38]. Again, they concluded that twin networks decreased the dislocation mean-free path which led to high, essentially linear, strain hardening. Gao et al. also studied deformation microstructures in a β -titanium alloy [39]. They also attributed the high, linear rate of strain hardening to interaction of multiple deformation twinning systems and the formation of orthorhombic α' martensite and the ω phase within these twin networks. K. Tao et al. used neutron diffraction to analyze the source of a high rate of strain hardening in an ultrafine-grained steel [40]. They attributed the high strain hardening to the formation of martensite and the load partitioning between the austenite and martensite phases. Suh et al. studied the effect of transformation-induced transformation of austenite to martensite in manganese-containing steels on the creation of high rates of strain hardening in specific temperature regimes [41]. Wong et al. proposed a crystal plasticity model to explain high strain hardening rates in steels resulting from TRIP and TWIP mechanisms [42]. They compare model predictions to measured stress-strain curves and show excellent agreement. They conclude activation of martensite transformations at low temperatures and deformation twinning at high temperatures lead to the high rates of strain hardening.

In each of the studies summarized above, high rates of strain hardening arose from a strain- and/or stress-induced transformation. Such mechanisms are not going to be well-described using the simple form of Eq. 6.28.

The high rate of strain hardening observed in Inconel 600 and nickel-base C-276 alloy likely is not associated with a martensitic phase transformation or deformation twinning. Precipitation strengthening and aging kinetics in alloy C-276 were studied

in detail by Pu et al. [19]. They observed a large increase of the yield stress as a function of aging treatment and concluded that precipitates impeded the motion of dislocations. It may be that the aging treatment does not solely establish precipitation and that straining at elevated temperatures may further contribute to the precipitation microstructures. The increase in the slope of the $\hat{\sigma}_\epsilon$ versus ϵ curve observed in C-276 at 873 K compared to that observed at 373 K (Fig. 12.15) is consistent with this hypothesis.

12.4 Signatures of Dynamic Strain Aging

Figure 9.48 showed a common trend when DSA is affecting hardening. This figure is a plot of the “apparent” s_i as a function of σ_ϵ in vanadium computed using Eq. 9.8. (Fig. 13.7 shows the variation of σ_{DSA} with σ_ϵ for the same measurements in vanadium computed using Eq. 13.2, where s_{ia} in this equation is the s_i computed using Eq. 9.8.) In order to compute s_{ia} , one needs $\hat{\sigma}_\epsilon$ computed using Eq. 6.28 with the temperature and strain rate dependence of the saturation stress defined by Eq. 6.26. Establishing a fit to Eq. 6.26 for Inconel 600 (Fig. 12.9) was not ideal because the shape of the stress–strain curves did not enable fits to Eq. 6.28. Figure 12.9 presented a possible fit and the model constants. (Eq. 6.26 in Table 12.3 lists the model parameters for this line). A suitable fit for Inconel 718, however, was shown in Fig. 12.13. These results suggest that DSA is active in the Nalawade et al. measurements at temperatures exceeding 473 K. Figure 12.20 shows the variation of s_i , and Fig. 12.21 shows the variation of σ_{DSA} with σ_ϵ in this material. The plots are similar to those presented, for instance, for vanadium in Fig. 9.48 and Fig. 13.7. The s_i curves in Fig. 12.20 start at low values of σ_ϵ at the s_i values predicted using Eq. 6.18 with the model parameters listed in Table 12.1. The s_i values increase rapidly with σ_ϵ , and the rate of increase rises with increasing test temperature. As in

Fig. 12.20 Variation of s_i with σ_ϵ in three high-temperature tests in Inconel 718 where DSA is active

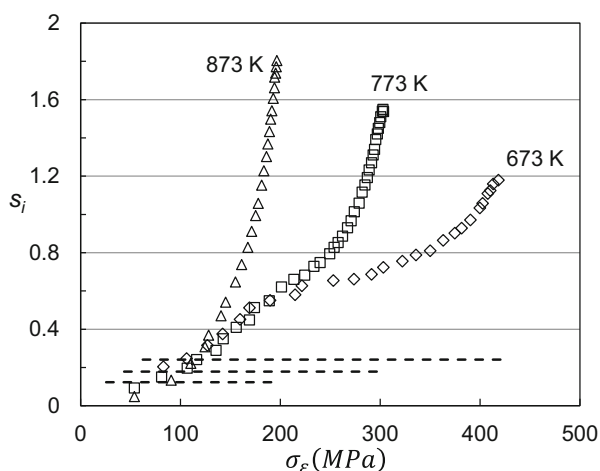


Fig. 12.21 Variation of σ_{DSA} with σ_e in three high-temperature tests in Inconel 718 where DSA is active

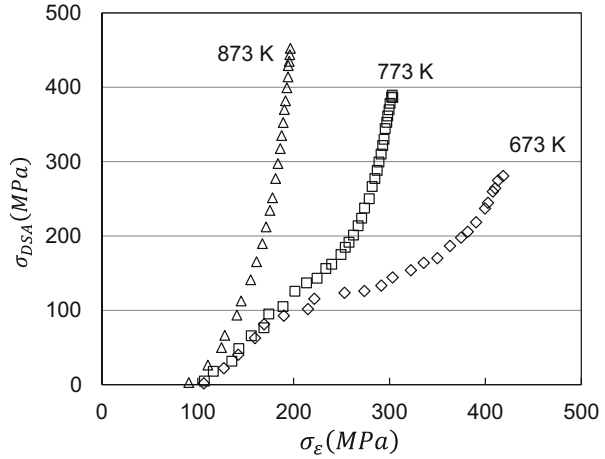
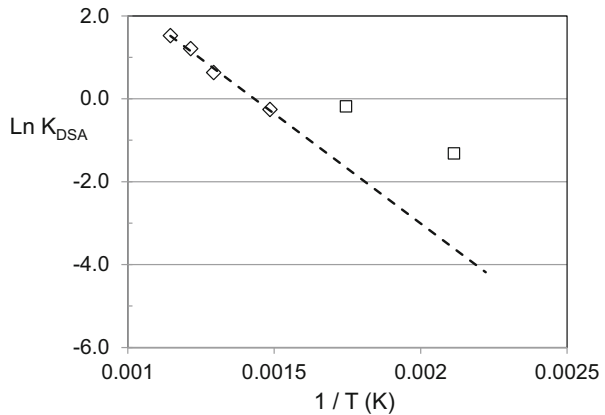


Fig. 12.22 Analysis according to Eq. 9.9 of the slopes of the lines drawn through the curves in Fig. 12.21



Figs. 9.49, 10.74, and 11.18, the temperature dependence is assessed by assuming a linear increase of function of σ_{DSA} with σ_e (Fig. 12.21), and fitting the slope of these, $K_{DSA\sigma}$ lines to Eq. 9.9

$$K_{DSA}(T) = K_{DSA\sigma} \exp\left(-\frac{Q}{RT}\right) \tag{9.9}$$

Figure 12.22 shows the resulting variation. The measurements at the highest temperatures (673 K, 773 K, 823 K, and 873 K) fall along a line on this plot. From the slope of this line, a Q value of 44.0 kJ/mole is estimated. The following chapter will consider whether Eq. 9.9 should be used to assess the temperature dependence when DSA is active.

12.5 Summary

The development—and continued development—of nickel-base superalloys offers a fascinating chapter in modern metallurgical practice. Anomalous hardening observed in these alloys which is a result of the formation of a coherent, ordered intermetallic strengthening contribution enables very high stress levels at elevated temperatures. This has in turn contributed—along with the development of modern fabrication methods, e.g., directional solidification and the production of single crystal airfoils, and thermal barrier coatings—to the continued increase of engine operating temperatures, engine efficiencies, and thrust to weight ratios.

The objective of this chapter has been to demonstrate application of the MTS constitutive modeling formalism to this remarkable class of alloys. The unusual temperature dependence of the yield stress seen in Ni₃Al certainly introduces a complexity to the application of the standard MTS equations. As seen in several other systems, the contribution of DSA introduces a second, confounding, deformation mechanism.

Given that the continuous matrix in nickel-base superalloys is FCC, analysis of the yield stress versus temperature and strain rate shows that at low temperatures and high strain rates, a regime exists where the behavior is well behaved; that is, it follows Eq. 6.14 where two-obstacle populations are introduced. The population with the low value of the normalized activation energy, g_{oi} (e.g., 0.7), likely reflects solid solution strengthening. The population with the high value of this activation energy, $g_{o\gamma'}$ (e.g., 2), likely reflects dislocation interactions with the ordered precipitate γ' .

With increasing temperature, however, the yield stress is observed to strongly deviate upward from the low temperature behavior. In material with a low initial dislocation density, which is certainly the case in modern investment cast airfoils, this increase reflects the contribution of anomalous hardening. The measurements in pure Ni₃Al (Fig. 12.12) show the remarkable yield stress dependence. Of course, the actual contribution of anomalous hardening will vary with the volume fraction of γ' present in each alloy system. The hardening in Inconel 718 was less than that in Rene N4 (Fig. 12.12), which in turn is less than that in pure Ni₃Al. Assuming that this stress increase is not a function of strain (which has not been rigorously validated), it was relatively simple to deconvolute the measured yield stress dependence from the model behavior (Eq. 12.1) and the contribution of anomalous hardening.

Another complexity introduced in this chapter was the very high rate of strain hardening observed in Inconel 600 (Fig. 12.4), C-276 (Fig. 12.7), and C-22 (Fig. 12.16). It was suggested that this enhanced hardening results from a strain-induced transformation. Nonetheless, because the shape of the strain hardening curve is not well-described using Eq. 6.28, it was impossible to assess the kinetics of the saturation stress (Eq. 6.26). Furthermore, attempt to apply Eq. 6.28 to the $\hat{\sigma}_\varepsilon$ versus ε curves for these materials led to an unusual dependence of θ_{II} with temperature (see Table 12.2). This dependence has nothing to do with Stage II hardening. (See Appendix 13.A2.)

Inconel 718 stress–strain curves demonstrate the typical saturation stress behavior. Thus, it was possible to fit Eq. 6.26 to the saturation stress values (Fig. 12.3). The plot showed a region (at high strain rates) which provided an adequate correlation to Eq. 6.26 and a region at low strain rates and increasing temperature with large deviations from Eq. 6.26. This has been taken as a “signature” of DSA. Indeed, it was possible to analyze the increase of both the “apparent” s_i value as well as σ_{DSA} with increasing with σ_e . It was noted that both of these model parameters increased more rapidly as the temperature increased, which is consistent with the observations in vanadium, niobium, austenitic stainless steel, and titanium.

Because there do not exist independent models for the contribution of the stress anomaly as a function of alloy chemistry or for the contribution of DSA with strain, a self-consistent constitutive equation for nickel-base superalloys cannot be recommended. However, this chapter has demonstrated how insight into these confounding deformation mechanisms can be assessed through application of the MTS formalism.

Exercises

- 12.1. Table 12.E1 lists yield stress versus test temperature and strain rate for a hypothetical superalloy—HypoSuperalloy. Plot the yield stress versus temperature and strain rate according to Eq. 12.1. Use the model constants listed in Table 12.5 for Inconel 718. You will need to adjust the values of $\hat{\sigma}_i$ and $\hat{\sigma}_{\gamma'}$ so that the model predictions agree with the measurements. Report your estimated values of these threshold stresses. Remember to fit Eq. 12.1 only to the data points that follow this equation.

Table 12.E1 Yield stress versus temperature and strain rate for the hypothetical HypoSuperalloy (Exercise 12.1)

Temperature, K	Yield stress, MPa	
	0.001 s ⁻¹	1 s ⁻¹
100	1876	
200	1661	
300	1479	1535
400	1270	
500	1242	1250
550	1131	
600	1153	
700	1166	
800	1192	
900	1176	
1000	1138	
1100	1096	

Table 12.E3 True stress versus true strain for the hypothetical HypoSuperalloy at 300 K and a strain rate of 0.001 s⁻¹ (Exercise 12.3)

300 K and 0.001 s ⁻¹			
Strain	Stress (MPa)	Strain	Stress (MPa)
0.025	1516	0.325	1818
0.050	1555	0.350	1832
0.075	1592	0.375	1846
0.100	1618	0.400	1864
0.125	1645	0.425	1878
0.150	1673	0.450	1886
0.175	1690	0.475	1903
0.200	1720	0.500	1913
0.225	1737	0.525	1928
0.250	1761	0.550	1933
0.275	1779	0.575	1943
0.300	1803	0.600	1956

- 12.2. The “Offset Stresses” listed in Table 12.2 for Inconel 600 and Table 12.4 for Inconel 718 (Nalawade et al. data) are the differences between the Eq. 12.1 model fits and the measured yield stresses. From your analysis in Exercise 12.1, deduce these differences for the hypothetical superalloy and produce a plot (akin to Fig. 12.12) of offset stress versus test temperature for these three materials. How does the anomalous hardening in the hypothetical superalloy compare to that in Inconel 600 and Inconel 718? What might you conclude about the extent of precipitate hardening (γ' and γ'') in the hypothetical superalloy?
- 12.3. Table 12.E3 lists the true stress versus true strain for a temperature of 300 K and a strain rate of 0.001 s⁻¹. Create a plot of $\hat{\sigma}_\epsilon$ versus strain using Eq. 12.6 and the model constants you used in Exercise 12.1. Fit Eq. 6.28 with $\kappa = 2$ to the hypothetical data. Report the values of $\hat{\sigma}_{\epsilon_s}$ and θ_{II} used in applying Eq. 6.28.
- 12.4. Table 12.E4 lists the true stress versus true strain for a temperature of 400 K and a strain rate of 0.001 s⁻¹. As you did in Exercise 12.3, create a plot of $\hat{\sigma}_\epsilon$ versus strain using Eq. 12.6 and the model constants you used in Exercise 12.1. Report the values of $\hat{\sigma}_{\epsilon_s}$ and θ_{II} used in applying Eq. 6.28.
- 12.5. Table 12.E5 lists the true stress versus true strain for a temperature of 500 K and a strain rate of 0.001 s⁻¹. As you did in Exercise 12.3 and Exercise 12.4, create a plot of $\hat{\sigma}_\epsilon$ versus strain using Eq. 12.6 and the model constants you used in Exercise 12.1. Report the values of $\hat{\sigma}_{\epsilon_s}$ and θ_{II} used in applying Eq. 6.28.
- 12.6. Create the equivalent of Fig. 12.13 for the HypoSuperalloy using the estimates of $\hat{\sigma}_{\epsilon_s}$ at 300 K, 400 K, and 500 K. Recall Eq. 6.26. Use the model constants listed in Table 12.5 for Inconel 718. Of course, the value of $\hat{\sigma}_{\epsilon_{SO}}$ may need to change to force a line through the three data points to go through the origin.

Table 12.E4 True stress versus true strain for the hypothetical HypoSuperalloy at 400 K and a strain rate of 0.001 s^{-1} (Exercise 12.4)

400 K and 0.001 s^{-1}			
Strain	Stress (MPa)	Strain	Stress (MPa)
0.025	1349	0.325	1597
0.050	1372	0.350	1609
0.075	1403	0.375	1615
0.100	1431	0.400	1634
0.125	1453	0.425	1639
0.150	1481	0.450	1650
0.175	1492	0.475	1660
0.200	1518	0.500	1670
0.225	1538	0.525	1676
0.250	1546	0.550	1688
0.275	1561	0.575	1694
0.300	1581	0.600	1708

Table 12.E5 True stress versus true strain for the hypothetical HypoSuperalloy at 500 K and a strain rate of 0.001 s^{-1} (Exercise 12.5)

500 K and 0.001 s^{-1}			
Strain	Stress (MPa)	Strain	Stress (MPa)
0.025	1182	0.325	1392
0.050	1209	0.350	1399
0.075	1241	0.375	1405
0.100	1263	0.400	1417
0.125	1281	0.425	1429
0.150	1295	0.450	1434
0.175	1317	0.475	1434
0.200	1328	0.500	1442
0.225	1347	0.525	1455
0.250	1361	0.550	1454
0.275	1374	0.575	1461
0.300	1377	0.600	1474

Also note that if you create the plot using the coordinates shown in Fig. 12.13, g_{eso} is the reciprocal of the slope of the best fit line.

- 12.7. Table 12.E7 lists the true stress versus true strain for a temperature of 700 K and a strain rate of 0.001 s^{-1} . As you did in Exercise 12.3 and Exercise 12.4, create a plot of $\hat{\sigma}_\varepsilon$ versus strain using Eq. 12.6 and the model constants you used in Exercise 12.1. Report the values of $\hat{\sigma}_{\varepsilon s}$ and θ_{II} used in applying Eq. 6.28. Note that this temperature is well into the anomalous hardening regime identified in Exercise 12.1. You will need to adjust Eq. 12.6 to subtract the “offset stress” you identified in Exercise 12.2. Equation 12.6 becomes

$$\hat{\sigma}_\varepsilon = \frac{\mu_o}{s_\varepsilon(\dot{\varepsilon}, T)} \left(\frac{\sigma - \sigma_a - \sigma_o}{\mu} - s_i(\dot{\varepsilon}, T) \frac{\hat{\sigma}_i}{\mu_o} - s_{\gamma'}(\dot{\varepsilon}, T) \frac{\hat{\sigma}_{\gamma'}}{\mu_o} \right) \quad (12.7)$$

where σ_o is the offset stress.

Table 12.E7 True stress versus true strain for the hypothetical HypoSuperalloy at 700 K and a strain rate of 0.001 s^{-1} (Exercise 12.7)

700 K and 0.001 s^{-1}			
Strain	Stress (MPa)	Strain	Stress (MPa)
0.025	1189	0.325	1381
0.050	1219	0.350	1389
0.075	1245	0.375	1396
0.100	1268	0.400	1410
0.125	1286	0.425	1408
0.150	1297	0.450	1419
0.175	1317	0.475	1428
0.200	1336	0.500	1431
0.225	1347	0.525	1438
0.250	1359	0.550	1437
0.275	1365	0.575	1445
0.300	1373	0.600	1442

12.8. Add the estimated value of $\hat{\sigma}_{es}$ at 700 K to the saturation stress plot you created in Exercise 12.6. You will want to plot this value using a different symbol, i.e., create separate column in the spreadsheet for the 700 K test. Comment on the deviation from the dashed-line trend. You may wish to refer to Fig. 12.13 and the related discussion.

References

1. P.S. Follansbee, Analysis of deformation in Inconel 718 when the stress anomaly and dynamic strain aging coexist. *Metall. Mater. Trans. A* **47A**, 4455–4466 (2016)
2. The Minerals, Metals & Materials Society (2007), <http://www.materialmoments.org/index.html>
3. Inconel Alloy 718, Special Metals Corporation, Publication Number SMC-045 (Sept, 2007), <http://www.specialmetals.com/documents/Inconel%20alloy%20718.pdf>
4. Nickel Development Institute, High-temperature high-strength nickel base alloys, Supplement, No. 393 (1995), <http://www.stainless-steel-world.net/pdf/393.pdf>
5. S. Miura, S. Ochiai, Y. Oya, Y. Mishima, T. Suzuki, in “*High Temperature Ordered Intermetallic Alloys III*”, *MRS Symposium Proceedings*, ed. by C. T. Lie, A. Taub, N. S. Stoloff, C. C. Koch, vol. 133, (Materials Research Society, Pittsburgh, 1989), p. 241
6. P. Veyssi ere, G. Saada, in *Dislocations in Solids*, ed. by F. R. N. Nabarro, M. S. Duesbery, vol. 10, (North-Holland, Amsterdam, 1996), p. 254
7. P.B. Hirsch, Report of the discussion at the “Round Table on the Yield Stress Anomaly”. *J. Phy. III* **1**, 989–996 (1991)
8. R.A. Mulford, U.F. Kocks, New observations on the mechanisms of dynamic strain aging and of jerky flow. *Acta Metall.* **27**, 1125–1134 (1979)
9. H. H anninen, M. Ivanchenko, Y. Yagodzinskyy, V. Nevdacha, U. Ehrnst en, and P. Aaltonen, in T.R. Allen, P.J. King, L. Nelson, eds., *Proceedings of the 12th International Conference on Environmental Degradation of Materials in Nuclear Power System – Water Reactors*, 2005, The Minerals, Metals & Materials Society, pp. 1423–1430 (2005)
10. R. A. Mulford, U. F. Kocks, The effect of solute on the obstacle profiles for dislocation interaction and solution strengthening in Ni alloys. *Scripta Metal.*, vol. 13 (1979), pp. 729–732

11. Inconel Alloy 625, Special Metals, <http://www.specialmetals.com/documents/Inconel%20alloy%20625.pdf>
12. R.A. Lane, C. Fink, "High strain rate characterization of materials," Advanced Materials, Manufacturing and Testing Information Analysis Center (AMMTIAC), Report AMMT-35, (2009)
13. D. Joshi, "Finite-Element Simulation of Machining a Nickel-Based Superalloy – Inconel 718," MS Dissertation, Oklahoma State University (2004)
14. W.-S. Lee, C.-F. Lin, T.-H. Chen, H.-W. Chen, Dynamic impact response of Inconel 718 alloy under low and high temperatures. *Mater. Trans. Japan Ins. Metals* **52**(9), 1734–1740 (2011)
15. S.A. Nalawade, M. Sundararaman, R. Kishore, J.G. Shah, The influence of aging on the serrated yielding phenomena in a nickel-base superalloy. *Scr. Mater.* **59**(2008), 991–994 (2008)
16. C.T. Sims, W.C. Hagel, *The Superalloys* (John Wiley & Sons, New York, 1972), p. 123
17. R.C. Reed, *The Superalloys – Fundamentals and Applications* (Cambridge University Press, Cambridge, UK, 2006), p. 238
18. A.K. Roy, J. Pal, C. Mukhopadhyay, Dynamic strain ageing of an austenitic superalloy – temperature and strain rate effects. *Mater. Sci. Eng. A* **A474**, 363–370 (2008)
19. E. Pu, W. Zheng, Z. Song, K. Zhang, S. Liu, W. Shen, H. Dong, The effect of aging on the serrated yielding and intermediate temperature embrittlement of nickel-base C-276 alloy. *Mater. Sci. Eng. A* **A 714**, 59–67 (2018)
20. D. Golberg, M. Demura, T. Hirano, Effect of Al-rich off-stoichiometry on the yield stress of binary Ni3Al single crystals. *Acta Mater.* **46**, 2695 (1988)
21. M. Demura, D. Golberg, T. Hirano, An athermal deformation model of the yield stress anomaly in Ni3Al. *Intermetallics* **15**, 1322–1331 (2007)
22. E.X. Pu, W.J. Zheng, Z.G. Song, H. Feng, F. Yang, H. Dong, Effects of temperature and strain rate on tensile deformation behavior of superalloy UNS N10276. *Mater. Sci. Eng. A* **A699**, 88–98 (2017)
23. U. S. Nuclear Waste Technical Review Board, 1997 Findings and Recommendations, Report to The U. S. Congress and The Secretary of Energy, Arlington, Virginia (April 1998)
24. A.A. Sagtlds, Paper QQI4.1 in Proceedings of the Symposium on Scientific Basis for Nuclear Waste Management XXII, Materials Research Society, Boston, Nov. 30–Dec. 4, 1998, 556
25. D.S. Dunn, Y.-M. Pan, K.T. Chiang, L. Yang, G.A. Cragolino, X. He, "The Localized Corrosion Properties of Alloy 22 Waste Package Outer Containers," JOM, The Minerals, Metals, and Materials Society (January, 2005), p. 49
26. R.B. Rebak, T.S.E. Summers, R.M. Carranza, Mechanical properties, microstructure, and corrosion performance of C-22 alloy aged at 260°C to 800°C. *Mater. Res. Soc. Symp. Proc.* **608**, 109–114 (2000)
27. High Temp Metals, <http://www.hightempmetals.com/techdata/hitempHastC22data.php>
28. Inconel Alloy 22, Special Metals, Publication Number SMC-049, <http://www.specialmetals.com/documents/Inconel%20alloy%2022.pdf>
29. ASM Metals Handbook Desk Edition (1985)
30. ASTM B575-10, "Standard Specification for Low-Carbon Nickel-Chromium-Molybdenum, Low-Carbon Nickel-Chromium-Molybdenum-Copper, Low-Carbon Nickel-Chromium-Molybdenum-Tantalum, Low-Carbon Nickel-Chromium-Molybdenum-Tungsten, and Low-Carbon Nickel-Molybdenum-Chromium Alloy Plate, Sheet, and Strip," ASTM International, West Conshohocken, PA
31. L.M. Pike, P.E. Manning, "A new high-strength, corrosion-resistant alloy for oil and gas applications," NACE Corrosion 2010, Paper No. 10319
32. E.W. Huang, "Fundamental mechanical-behavior studies of annealed and nano-particle-strengthened nickel-based alloys using in-situ neutron-diffraction experiments," PhD Dissertation, University of Tennessee, Knoxville, TN, December, http://trace.tennessee.edu/utk_graddiss/608

33. B. O'Tolle, "Identification of dynamic properties of materials for the nuclear waste package," Technical Report, Task 24, Document ID: TR-02-007, Sept. 2003 (Also see Task 24 documents at following web site: <http://hrcweb.nevada.edu/data/tda/>)
34. W. Wichert, J.W. Tackett, J.-D. Schobel, Mechanical properties of Hastelloy alloy C-22. *Zeitschrift Fur Werkstofftechnik* **18**(12), 422–427 (1987)
35. K.J. King, L.L. Wong, J.C. Estill, R.B. Rebak, "Slow strain rate testing of alloy 22 in simulated concentrated ground waters," UCRL-PROC-200661, Corrosion 2004 (Oct. 2003)
36. Hastelloy C-22 alloy, Haynes Corrosion-Resistant Alloys, H-2019F, <http://www.haynesintl.com/pdf/h2019.pdf>
37. Y.M. He, Y.H. Wang, K. Guo, T.S. Wang, Effect of carbide precipitation on strain-hardening and deformation mechanism of metastable austenitic stainless steel after repetitive cold rolling and reversion annealing. *Mater. Sci. Eng. A* **708**, 248–253 (2017)
38. C. Brozek, F. Sun, P. Vermaut, Y. Millet, A. Lenain, D. Embury, P.J. Jacques, F. Prima, A β -titanium alloy with extra high strain-hardening rate: Design and mechanical properties. *Scr. Mater.* **114**, 60–64 (2016)
39. J. Gao, Y. Huang, D. Guan, A.J. Knowles, L. Ma, D. Dye, W.M. Rainforth, Deformation mechanisms in a metastable beta titanium twinning induced plasticity alloy with high yield strength and high strain hardening rate. *Acta Mater.* **152**, 301–314 (2018)
40. K. Tao, H. Choo, H. Li, Transformation-induced plasticity in an ultrafine-grained steel: An in situ neutron diffraction study. *Appl. Phys. Lett.* **90**, 101911-1–101911-3 (2007)
41. D.W. Suh, J.H. Ryu, M.S. Joo, H.S. Yang, K.Y. Lee, H.K.D.H. Bhadeshia, Medium-alloy manganese rich transformation-induced plasticity steels. *Metall. Mater. Trans A.* **46A**, 286–293 (2013)
42. S.L. Wong, M. Madivala, U. Prahl, F. Roters, D. Raabe, A crystal plasticity model for twinning- and transformation-induced plasticity. *Acta Mater.* **118**, 140–151 (2016)

Chapter 13

A Model for Dynamic Strain Aging



Introduction

Dynamic strain aging (DSA) was observed in several of the systems analyzed in this monograph. The objective of this chapter is to review the observations—the signatures—described in these systems. A simple model is proposed to describe the flux of solute atoms to a dislocation core and predict the stress increase. This model enables an evaluation of the dependence of the stress increase on test temperature (Eq. 9.9) that was presented in earlier chapters and shows that the operative kinetics during DSA are more complicated than represented by this simple equation. Comparison with strain hardening and strain-rate sensitivity measurements in Inconel 600 gives credence to the proposed model.

13.1 Review of Signatures of DSA

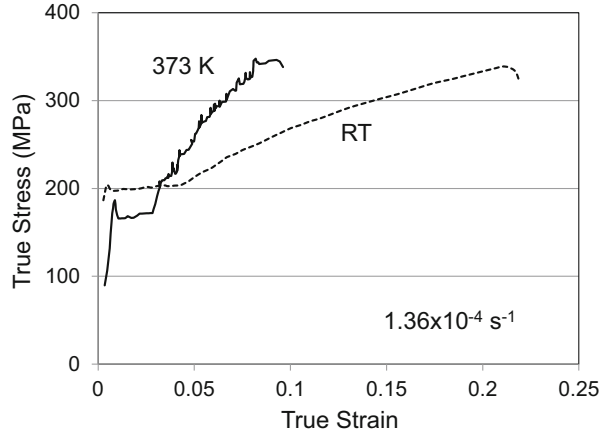
The classic signature of DSA was shown in Fig. 5.13, included here as Fig. 13.1, from measurements in mild steel by Murty [1]. DSA leads to a high rate of hardening over a range of elevated temperatures. In this measurement, it also leads to serrations along the stress–strain curve. The effects of DSA were observed in vanadium (Fig. 9.36), niobium (Fig. 9.51), titanium (Fig. 10.58), austenitic stainless steel (Fig. 11.16), and Inconel 718 (Fig. 12.6).¹

An important question in understanding DSA is whether the high hardening rates reflect an increase in the stored dislocation density or whether they instead reflect a

Supplementary Information The online version contains supplementary material available at https://doi.org/10.1007/978-3-031-04556-1_13

¹ While the 673 K and 873 K curves in Figure 12.6 are plotted on different ordinates, the stress levels essentially overlap, which suggests that DSA is affecting the 873 K curve.

Fig. 13.1 Tensile stress-strain curves in mild steel measured by Murty [1] at two test temperatures



change (increase) in one or more of the s_i values in Eq. 6.17. None of the measurements included in this monograph provide a definitive answer to this question.² To do so would necessitate a prestrain in a condition where DSA is prevalent followed by a campaign of reloads, as introduced in Sect. 5.2 and described in Sect. 7.6 and Sect. 8.2 (and elsewhere), to establish $\hat{\sigma}_{es}$. Figure 9.44, included here as Fig. 13.2, shows the saturation threshold stress plot in vanadium where the $\hat{\sigma}_{es}$ —alues are derived using Eq. 9.7. (See Fig. 9.56 for the equivalent plot in niobium, Fig. 10.68 for the equivalent plot in titanium, Fig. 11.12 for the equivalent plot in austenitic stainless steel, and Fig. 12.13 for the equivalent plot in Inconel 718.) The three open triangles at values of the abscissa less than ~ -0.16 in Fig. 9.44 are at conditions where DSA is likely active. Here, the $\hat{\sigma}_{es}$ —values are very much larger than represented by the dashed-line fit (Eq. 6.26). The traditional understanding of DSA is that at these temperatures the mobility of one or more of the impurity species is sufficient to allow impurities to travel to dislocations and restrict their motion. It seems unlikely that this increased strengthening should lead to increased dislocation storage rates, in which case the high values of $\hat{\sigma}_{es}$ in Fig. 13.2 are an artifact of the analysis.

The supposition is that DSA affects one of the s-values in Eq. 6.17. The analyses of stress-strain curves in the presence of DSA proceeded through use of Eq. 9.8

$$s_i = \frac{1}{\hat{\sigma}_i} \left[\frac{\mu_a}{\mu} (\sigma - \sigma_a) - s_p \hat{\sigma}_p - s_\varepsilon \hat{\sigma}_\varepsilon \right] \quad (9.8)$$

²Exercise 14.2 involves analysis of ECAP processed Ti-6Al-4 V in which the processing conditions were likely in a regime where DSA was active. The fact that the reload stresses in this material matched the predicted stress levels using a model that did not include a DSA subroutine offers evidence that DSA does not affect dislocation storage. However, a more definitive experimental verification of this would be useful.

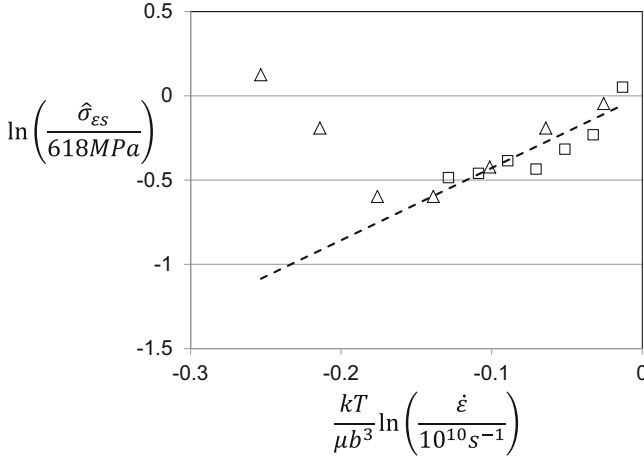
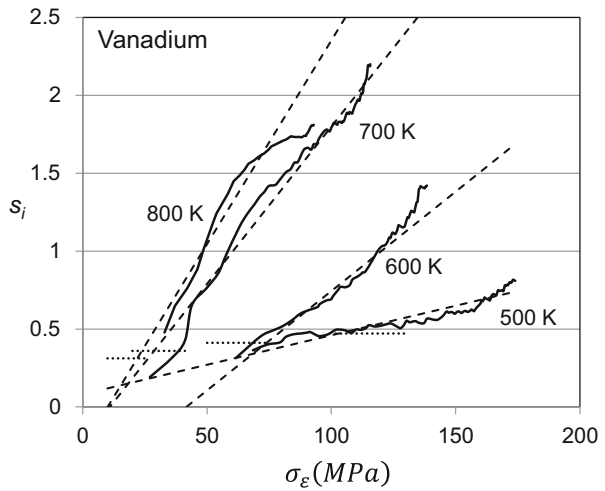


Fig. 13.2 Variation of $\hat{\sigma}_{\epsilon s}$ with strain rate and (initial) temperature for the measurements in vanadium. The high-strain-rate tests are plotted with open squares, whereas the low-strain-rate tests are plotted with open triangles. The line is the best fit to Eq. 6.26

Fig. 13.3 Computed value of s_i from Eq. 9.8 for the tests in vanadium at 500 K, 600 K, 700 K and 800 K and a strain rate of 0.001 s^{-1} . The dashed lines are fits according to Eq. 9.9



which is written for a BCC system (because of the inclusion of a Peierls term). Dislocation storage is assumed to proceed according to Eq. 6.28 with $\hat{\sigma}_{\epsilon s}$ set by the fit to Eq. 6.26 (e.g., the dashed line in Fig. 13.2 for vanadium). An interesting observation in all of the systems analyzed was that the resulting plots of s_i versus σ_e exhibited common features. Figure 9.48, presented here as Fig. 13.3, shows the result for vanadium. In this case the values of s_i predicted by Eq. 6.18 with the model parameters from Table 9.13 are indicated by short horizontal dotted lines. At some value of σ_e , s_i is observed to increase roughly linearly with σ_e . Plots similar to

Fig. 13.4 Stress–strain curve in AISI 1018 steel at a temperature of 823 K and a strain rate of 2800 s^{-1}

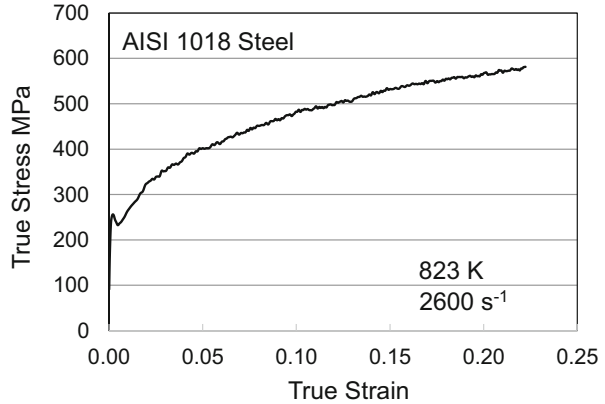


Fig. 13.3 were generated for niobium (Fig. 9.62), titanium (Fig. 10.72), austenitic stainless steel (Fig. 11.17), and Inconel 718 (Fig. 12.20).

A common observation in each of the plots of s_i versus σ_e is that in these materials, which are all initially annealed with a low dislocation density, s_i starts at the value determined by Eq. 6.18. In these figures, this value is indicated by the dashed line. This is sensible in that dislocation generation must precede initiation of DSA.

Although not analyzed in Sect. 9.6, Fig. 9.32 showed in the plot of normalized saturation stress versus normalized temperature and strain rate for AISI 1018 steel a data point at 823 K and a strain rate of 2600 s^{-1} [2] that deviated from the trend established by the other data points in the same fashion as indicated for vanadium in Fig. 13.2. Figure 13.4 shows the true stress versus true strain data set for this measurement. As in many steels, a slight yield drop is observed. The MTS model formalism does not enable capturing this yield drop in the stress versus strain predictions. Applying Eq. 9.8 and the model parameters in Table 9.11 to this data set yields a plot of s_i versus σ_e . The result is shown in Fig. 13.5. As in the other analyses, the (almost) horizontal dashed line is the predicted s_i from Eq. 6.18 with the model parameters in Table 9.11 for obstacle “ i ”. The values decrease slightly with increasing σ_e because this is an adiabatic test and the temperature is rising. In this material under these test conditions, s_i is seen to increase approximately linearly beginning near the yield point. The slope K_{DSA} is a little less than observed in vanadium (Fig. 13.3) but on the order of what was observed in stainless steel (discussed below and in Table 11.8).

Each of the s_i versus σ_e plots referred to above showed an approximately linear trend. In many cases, the slope, referred to as K_{DSA} , of the trend increased with increasing temperature. In many metallurgical processes where kinetics are defined by thermal activation, the process can be modeled using Eq. 9.9, where K_{DSA_0} is a constant and Q is the activation energy

Fig. 13.5 Computed value of s_i from Eq. 9.8 for the stress–strain curve measured in AISI 1018 steel at a temperature of 823 K and a strain rate of 2800 s^{-1}

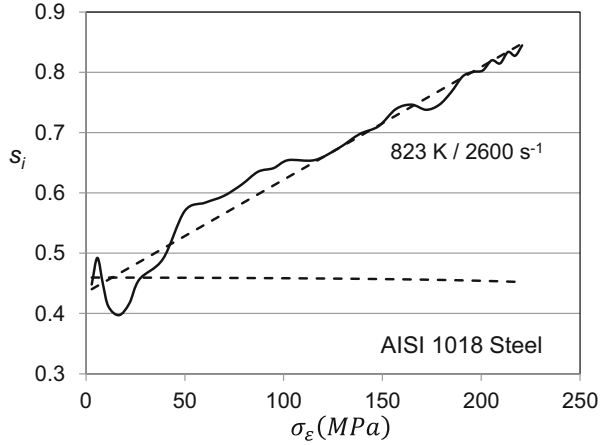
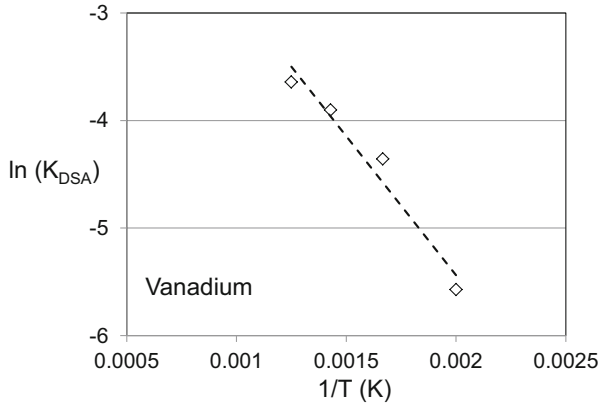


Fig. 13.6 Temperature dependence of K_{DSA} in Eq. 9.9 from analyses of dynamic strain aging in vanadium



$$K_{\text{DSA}}(T) = K_{\text{DSA}0} \exp\left(-\frac{Q}{RT}\right) \tag{9.9}$$

Figure 9.49, included here as Fig. 13.6, shows a plot of $\ln(K_{\text{DSA}})$ versus inverse temperature for the measurements in vanadium. Similar plots were produced for titanium (Fig. 10.74), austenitic stainless steel (Fig. 11.18), and Inconel 718 (Fig. 12.22). The slope of this line is proportional to Q . As discussed in Sect. 9.9 and in the discussions related to the results in titanium and austenitic stainless steels, the activation energies estimated from these plots did not coincide with known activation energies for diffusion of the likely solute elements involved in strain aging. As will be detailed below, this arises from the suggestion that Eq. 9.9 is not an accurate description of the temperature dependence during dynamic strain aging.

13.2 Focusing on the Increased Stress Levels Accompanying DSA

Plots such as that shown in Fig. 13.3 and Fig. 13.5 showed s_i versus σ_e . With the objective of introducing a model for the kinetics active during dynamic strain aging, it is useful to show how the additional stress over and above that predicted without the influence of DSA varies with σ_e . The total stress due to the contribution of obstacle population i is

$$\frac{\sigma_i}{\mu} = s_{ia} \frac{\widehat{\sigma}_i}{\mu_0} = s_i \frac{\widehat{\sigma}_i}{\mu_0} + \frac{\sigma_{DSA}}{\mu} \quad (13.1)$$

That is, the stress σ_i due to obstacle population i is equal to the product of s_{ia} —the apparent value of s_i , which is what has been plotted in Fig. 13.3 and Fig. 13.5—and the value of the threshold stress characterizing this obstacle population $\widehat{\sigma}_i$. This in turn equals the sum of two contributions. The first is the product of the actual value of s_i —which is the value calculated using Eq. 6.18—and the threshold stress characterizing this obstacle population $\widehat{\sigma}_i$. The second term is σ_{DSA} , the stress introduced from DSA. As usual, these stresses are normalized using the appropriate value of the shear modulus. These stress contributions all relate to obstacle population i . It would be possible to fold σ_{DSA} into $\widehat{\sigma}_i$. Separating σ_{DSA} is a convenient way to isolate and investigate the influence of diffusion of solute to the dislocation core which increases σ_i . Solving Eq. 13.1 for σ_{DSA} gives

$$\sigma_{DSA} = \mu \left(s_{ia} \frac{\widehat{\sigma}_i}{\mu_0} - s_i \frac{\widehat{\sigma}_i}{\mu_0} \right) \quad (13.2)$$

Since in Fig. 13.3 s_{ia} is greater than s_i when DSA is active, application of Eq. 13.2 gives positive values of σ_{DSA} . Figure 13.7 plots these calculations for the tests in vanadium shown in Fig. 13.3. The curves in these figures are quite similar in shape. Figure 13.7, however, shows how the stresses exceed those predicted without the contribution of DSA. Figure 12.21 presented the same analysis for Inconel 718.

Figure 13.8 gives the result for the Conway et al. measurement in AISI 316L stainless steel at a temperature of 703 K and a strain rate of $4 \times 10^{-5} \text{ s}^{-1}$ [3]. In this case σ_{DSA} rises to 300 MPa. Equation 11.5a specified the dependence of the threshold stress characterizing dislocation interactions with nitrogen solutes, $\widehat{\sigma}_N$, and the nitrogen concentration (%). Equation 11.5a showed a linear dependence of these variables. However, a square-root dependence following Eq. 3.10 fits the limited set of data points equally well

$$\widehat{\sigma}_N = 6630 \text{ MPa} \sqrt{C_N} \quad (13.3)$$

Fig. 13.7 Computed value of σ_{DSA} from Eq. 13.2 for the tests in vanadium at 500 K, 600 K, 700 K and 800 K and a strain rate of 0.001 s^{-1}

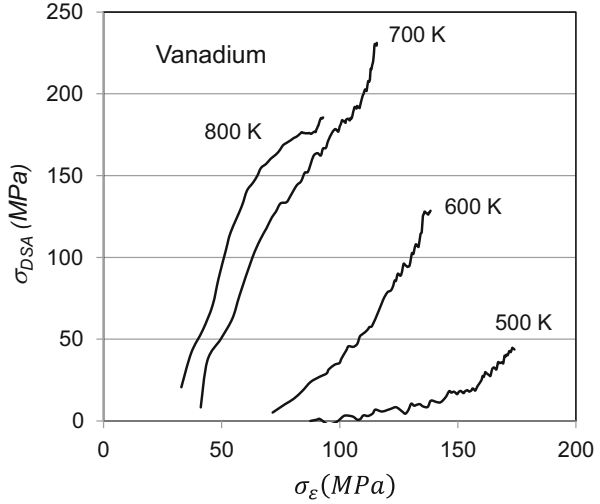
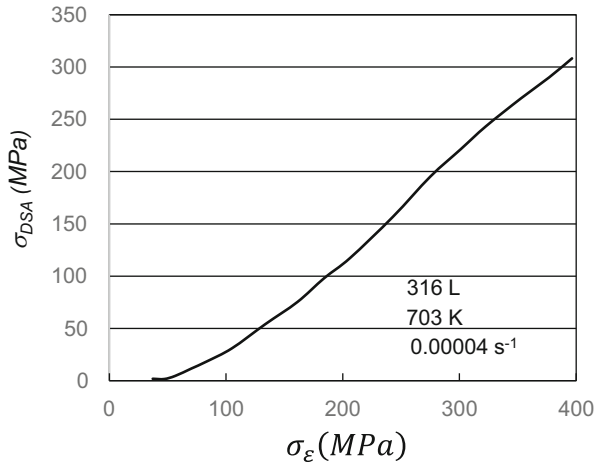


Fig. 13.8 Computed value of σ_{DSA} from Eq. 13.2 for the test in 316L stainless steel at 703 K and a strain rate of 0.00004 s^{-1}



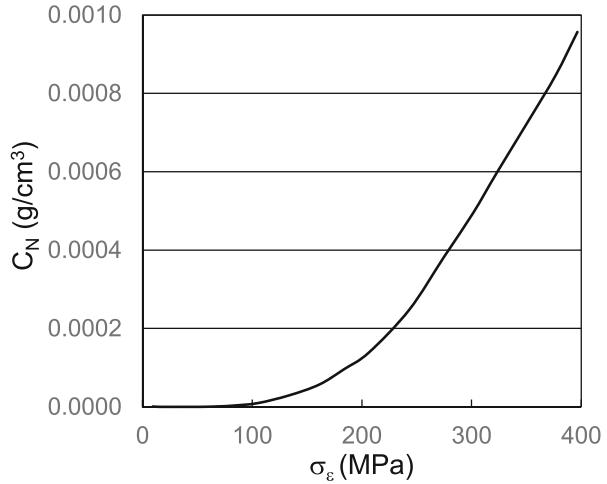
This equation expresses concentration in percent. Since Fig. 13.8 plotted the stress at the test temperature rather than the mechanical threshold stress at 0 K, the equation is rewritten as

$$\frac{\sigma_N}{\mu} = s_i \frac{\hat{\sigma}_N}{\mu_0} = \frac{s_i}{\mu_0} 6630 \text{MPa} \sqrt{C_N} \tag{13.4}$$

$$\sigma_N = s_i \frac{\mu}{\mu_0} 6630 \text{MPa} \sqrt{C_N} = s_i \mu K \sqrt{C_N} \tag{13.5}$$

where K is a dimensionless constant. For a dilute concentration, a concentration in C_N (%) can be converted to a concentration C'_N (g/cm^3) using

Fig. 13.9 Computed variation of the solute concentration at the dislocation core with stress that yields the values of σ_{DSA} shown in Fig. 13.8



$$C'_N \left(\frac{\text{g}}{\text{cm}^3} \right) = \left(\frac{C_N}{100 - C_N} \right) \rho \cong 0.01 C_N \rho \quad (13.6)$$

Combining Eq. 13.6 with Eq. 13.5 gives

$$C'_N \cong 0.01 \left(\frac{\sigma_N}{s_i K \mu} \right)^2 \rho \quad (13.7)$$

which is the desired correlation between the concentration in g/cm^3 and the stress contribution from nitrogen solutes. The stress in this case is σ_{DSA} . For the test in 316 L presented in Fig. 13.8, Eq. 13.7 has been used to convert σ_{DSA} to C'_N (g/cm^3), shown in Fig. 13.9. This is the additional solute concentration (over and above the average solute concentration) which contributes to the increased stress level.³ According to this prediction, the concentration rises $\sim 0.001 \text{ g/cm}^3$ above the average solute concentration.

13.3 Toward a Mechanistic Understanding

The common understanding is that DSA involves transport of solutes to the cores of dislocations. This results in a net reduction of internal (strain) energy, which is the driving force for the process. However, DSA also requires that diffusion is fast enough to enable transport, which is integral to understanding the kinetics of the

³Because of the square-root dependence of stress on the solute concentration, it is not mathematically rigorous to separate the two concentration terms as specified by Eq. 13.1. Because these concentrations are $\ll 1.0$, the mathematical error is insignificant.

process. Several comprehensive experimental and theoretical reviews of DSA have been published [4–8]. The objective here is to present a model that describes the underlying kinetic processes and that is consistent with the departures from the mechanical threshold stress model predictions summarized in the introduction to this chapter. Several models have been developed [9–15] that compare well to experimental observations. The approach followed here is to propose a model in the context of the mechanical threshold stress constitutive formalism [16].⁴

A model of DSA needs to consider diffusion of solutes to mobile dislocations. Shewmon presented a model for stress-assisted diffusion of solutes to a dislocation core [17]. For solute transport to a screw dislocation, the (short time) solution to the transport equation gives for the amount of solute q_s per unit length of dislocation (g/m) removed from the matrix at a time t as

$$q_s = C_0 \pi \left(\frac{3D\beta t}{kT} \right)^{2/3} \quad (13.8)$$

where C_0 is the initial solute concentration in the matrix, D is the diffusion coefficient, β is a constant, k is the Boltzmann constant, and T is the temperature. Solute concentrations are typically expressed in units of weight percent or weight fraction. Since weight percent was used in Eq. 13.4, these units are used here. Applying this conversion to Eq. 13.8 (as in Eq. 13.6) gives

$$q_s = \left(\frac{C_0}{100 - C_0} \right) \rho \pi \left(\frac{3D\beta t}{kT} \right)^{2/3} \quad (13.9)$$

where ρ is the density of the alloy and C_0 is the average solute concentration (weight percent). Assuming $\beta = 10^{-25} \text{ N cm}^2$ [17] and introducing conversion factors, Eq. 13.9 reduces to

$$q_s \left(\frac{\text{g}}{\text{cm}} \right) = \frac{C_0}{100 - C_0} (5.269) \rho \left(\frac{Dt}{T} \right)^{2/3} \quad (13.10)$$

To define the concentration of solutes transported to the dislocation core in units of g/cm^3 , the right side of Eq. 13.10 is multiplied by the mobile dislocation density ρ_m (cm^{-2}). Solute may diffuse to stored dislocations, which comprise the total dislocation density ρ_t , but these do not contribute to DSA.

$$q_s \left(\frac{\text{g}}{\text{cm}^3} \right) = \frac{C_0}{100 - C_0} (5.269) \rho \left(\frac{Dt}{T} \right)^{2/3} \rho_m \quad (13.11)$$

⁴Much of the work presented in this chapter was published in [16]. Some of the material in this prior publication was omitted from this chapter.

The time t can be related to the mobile dislocation density,⁵ ρ_m ; the Burgers vector b ; the average distance moved by dislocations during their glide phase, ℓ ; and the strain rate $\dot{\epsilon}$ through the Orowan equation (Eq. 4.4)

$$t = \frac{b\rho_m\ell}{\dot{\epsilon}} \quad (13.12)$$

where the dislocation velocity $d\ell/dt$ has been replaced by ℓ/t . An approximation for the average distance ℓ is

$$\ell = \frac{1}{\sqrt{\rho_t}} \quad (13.13)$$

where ρ_t is the total dislocation density. Clearly, this is a lower limit for ℓ which does not account for the fact that stored dislocations are locked up in, for instance, cell structures. The total dislocation density is related to the threshold stress $\hat{\sigma}_\epsilon$ characterizing the stored dislocations through (as in Eq. 3.8⁶)

$$\sigma_\epsilon = s_\epsilon \hat{\sigma}_\epsilon \frac{\mu}{\mu_0} = s_\epsilon M \alpha \mu b \sqrt{\rho_t} \quad (13.14)$$

where μ is the shear modulus, M is the Taylor factor (taken as 3.1), α is a constant (taken as $\alpha = 0.3$), and b is the Burgers vector.

Replacing ρ_t in Eq. 13.13 with Eq. 13.14, ℓ in Eq. 13.12 with the revised Eq. 13.13, and t in Eq. 13.11 with the revised Eq. 13.12 gives

$$C' \left(\frac{g}{cm^3} \right) = \frac{C_0}{100 - C_0} (2.446 \times 10^{-9}) \rho \left(\frac{D}{T} \right)^{2/3} \left(\frac{b}{\dot{\epsilon}} \right)^{2/3} \left(\frac{s_\epsilon M \alpha \mu b}{\sigma_\epsilon} \right)^{2/3} (\rho_m)^{5/3} \quad (13.15)$$

The constant 2.446×10^{-9} is computed assuming that the units of the variables are as defined as in Eq. 13.10 with the applicable Burgers vector b (nm), temperature-dependent shear modulus μ (MPa), and stress σ_ϵ (MPa). Table 13.1 summarizes variables and units used to derive Eq. 13.15. Equation 13.15 includes the diffusion coefficient, D (m²/s). This would be the diffusion coefficient for the element that is diffusing to and locking up dislocations. The temperature dependence of the diffusion coefficient is generally expressed using the Arrhenius equation

⁵In Eq. 2.14 and Eq. 4.4, the dislocation density was specified as ρ_D . Now, the only dislocations of interest are those moving—the mobile dislocation density ρ_m —which will be distinguished from the total dislocation density ρ_t .

⁶Equation 3.8 was a general form illustrating the relation between the stress and the dislocation density. Equation 13.14 is more rigorous in that the stress of interest is the mechanical threshold stress due to the stored dislocation density and the 0 K shear modulus and Taylor factor are introduced.

Table 13.1 Description, units, and, where applicable, value of the model parameters used in the derivation of Eq. 13.15

Parameter	Description	Units	Value
C_o	Bulk solute concentration	wt. %	
D	Diffusion coefficient	m^2/s	
β	Constant in Eq. 13.8	$N\ cm^2$	10^{-25}
t	Time	sec	
ρ	Density	g/cm^3	
κ	Boltzmann constant	Nm/K	1.381×10^{-23}
T	Temperature	K	
ℓ	Distance moved by a dislocation	nm	
ρ_m	Mobile dislocation density	cm^{-2}	
ρ_t	Total dislocation density	cm^{-2}	
$\dot{\epsilon}$	Strain rate	s^{-1}	
s_e	Kinetic factor for $\hat{\sigma}_e$	Dimensionless	
α	Constant	Dimensionless	0.3
M	Taylor factor	Dimensionless	3.1
μ	Shear modulus	MPa	

$$D\left(\frac{m^2}{s}\right) = D_0\left(\frac{m^2}{s}\right) \exp\left(-\frac{Q_D\left(\frac{J}{mole}\right)}{RT(K)}\right) \quad (13.16)$$

where D_0 is a constant and Q_D is the activation energy. This should be the diffusion coefficient in a heavily dislocated material. However, this diffusion coefficient is rarely available. Diffusion data is generally available only for relatively dislocation-free metals. Accordingly, there is significant uncertainty in this parameter.

Equation 13.15 gives the solute concentration transported to the dislocation core, C' , as a function of the mobile dislocation density, ρ_m , and the stress representing the stored dislocation density, σ_e . Given the variation of σ_{DSA} with σ_e , as found from Eq. 13.2 and as shown in Figs. 13.7 and 13.8, and the variation of σ_{DSA} with C' , as defined by Eq. 13.7, it is possible to compute the variation of ρ_m with σ_e . The consistent experimental observation has been that σ_{DSA} varied approximately linearly with σ_e , as illustrated in Figs. 13.7 and 13.8. Also, Eq. 13.7 specified a square-root dependence of σ_N (or σ_{DSA} in for the model presented here) and the solute concentration. Taking the square root of the right side of Eq. 13.15 leads to the conclusion that the temperature dependence of this process may be far from what was assumed in Eq. 9.9. Of course, introduction of the mobile dislocation density ρ_m in Eq. 13.15 confounds this assessment. The next section considers several sets of data that shed light on how this dislocation density varies with σ_e —at least in context of the model assumptions introduced.

13.4 Model Predictions

In this section application of Eq. 13.15 is demonstrated on stress–strain curves measured in niobium, Inconel 600, AISI 316 L SS, AISI 1018 steel, and titanium. These stress–strain curves were selected because it was determined they all were in a regime where DSA was active. Table 13.2 lists the source of the selected stress–strain curves, the source of the MTS model constants for these materials, and the model constants required to exercise Eq. 13.15. Included in this table is the assumed solute that participates in DSA and the temperature-dependent diffusion coefficient for diffusion of this solute in the host material. This diffusion coefficient likely does not relate to pipe diffusion of solute in dislocated materials, which implies a high level of uncertainty in this important parameter. The solute concentration is usually the typical concentration found in alloys. The value of K , from Eq. 13.5, is sometimes known (e.g., N in 316L SS), but is unknown in other cases; an estimated value is used here.

Table 13.2 Source of stress–strain curves and model constants used to demonstrate application of Eq. 13.15

Material	AISI 316L SS	Niobium	Inconel 600	AISI 1018 Steel	Titanium
Temperature (K)	823	500, 600, 700, 800	573, 673, 873	823	700, 800, 900
Strain rate (s^{-1})	0.0035	0.001	10^{-5}	2600	0.033, 3.3×10^{-5}
Source	[3]	[18]	[19]	[2]	[20]
MTS model constant source	Tables 11.6 and 11.7	Table 9.17	Table 12.3	Table 9.11	Table 10.19
Assumed diffusing element	N	O	C	C	O
D_0 in Eq. 13.16 (m^2/s)	0.0034	3.17×10^{-8}	2.482×10^{-4}	2.0×10^{-6}	4.78×10^{-5}
Q in Eq. 13.16 (J/mol)	144800	112600	166300	84100	200900
Diffusion equation source	[21]	[22]	[23]	[24]	[25]
Temperature range	623 K–773 K	300 K–700 K		238 K–473 K	573 K–1473 K
Alloy density (g/cm^3)	8.0	8.6	8.9	7.86	4.508
Bulk solute concentration (wt. %)	0.03	0.01	0.01	0.18	0.02
K in Eq. 13.5	0.0928	0.4	0.1	0.035	0.1
Source for K	Equation 11.5a ⁵	Estimate	Estimate	Figure 9.11 ^a	Estimate
K_{ρ_m} ($cm^{-2} MPa^{-2}$)	9.81×10^3	5.01×10^6	52.0×10^3	1.90×10^6	112.5×10^6

^aReanalyzed according to Eq. 13.5

Fig. 13.10 Computed value of σ_{DSA} from Eq. 13.2 for the stress–strain curve measured in AISI 1018 steel at a temperature of 823 K and a strain rate of 2800 s^{-1}

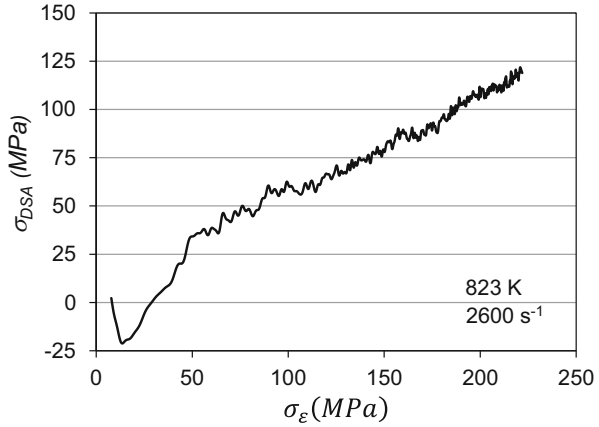
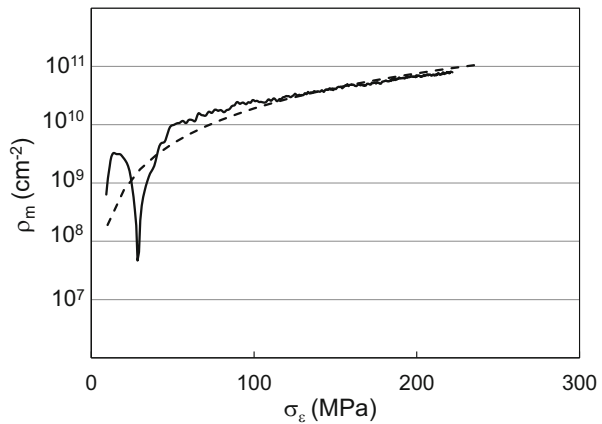
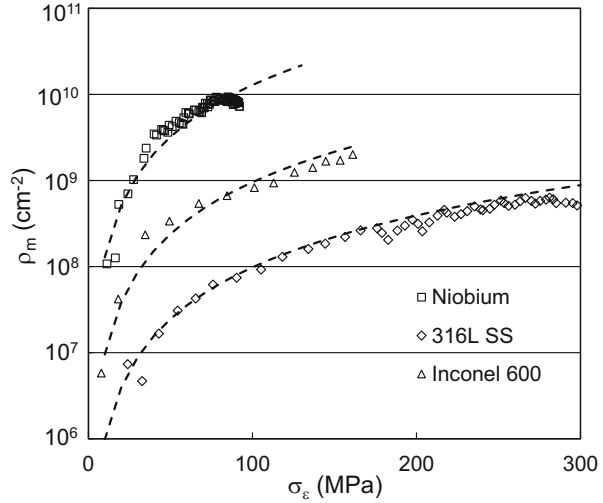


Fig. 13.11 Computed variation of the mobile dislocation density with stress according to Eq. 13.15 for the stress–strain curve measured on AISI 1018 steel at a temperature of 823 K and a strain rate of 2800 s^{-1} . The dashed line is drawn according to Eq. 13.17



First, the analysis is demonstrated in AISI 1018 steel to review and demonstrate the steps required to generate the curve. The first step in the analysis is to generate the plot of “apparent s_i ” versus σ_ϵ using Eq. 9.8. This plot was presented as Fig. 13.5. The second step is to generate the variation of σ_{DSA} with σ_ϵ using Eq. 13.2. Recall that σ_{DSA} is the stress increment over and above that predicted assuming DSA is not active. Figure 13.10 shows the resulting prediction. Because Eq. 13.2 is the difference between two stresses, the experimental scatter evident in Fig. 13.4 is amplified. Also, the effect of the yield drop is visible in that it leads initially to some negative values of σ_{DSA} , which results from having selected the upper rather than lower yield stress as the yield point. The final step is to use Eq. 13.15 to compute the variation of the mobile dislocation density with σ_ϵ . Since this is a dynamic test where the test temperature rises with strain due to adiabatic heating, the temperature-dependent parameters in Eq. 13.15 (μ , s_i , s_ϵ , T , and D) must be updated throughout the calculation. With the model constants listed in Table 13.2, Fig. 13.11 gives the resulting plot.

Fig. 13.12 Computed variation of the mobile dislocation density with stress according to Eq. 13.15. Estimates for niobium, Inconel 600, and 316 L stainless steel are shown. The dashed lines are drawn according to Eq. 13.17



Application to niobium and AISI 316L SS follows the procedure outlined above. The MTS model constants and the variation of σ_{DSA} with σ_ϵ have been described previously. Application to Inconel 600, however, is hampered by the inability to establish the saturation stress correlation (Eq. 6.26). Figure 12.9 showed the saturation stress versus temperature and strain rate as dictated by Eq. 6.26. While the fit of Eq. 6.26 was less than ideal, this correlation is required in order to exercise Eqs. 9.8 and 13.2; the latter equation estimates the stress increment over that predicted by the Eq. 6.26 in absence of DSA. The dashed line in Fig. 12.9 reflects the approximate stress levels of the saturation stresses in the absence of DSA.

Figure 13.12 shows the dependence of the mobile dislocation density ρ_m on σ_ϵ for niobium (800 K), AISI 316L SS, and Inconel 600 (873 K). (The model constants for Inconel 600 were listed in Table 12.3.) As in Fig. 13.11 for AISI 1018 steel, the curves loosely follow a power of 2 dependence of ρ_m with σ_ϵ (dashed lines)

$$\rho_m = K_{\rho} \sigma_\epsilon^2 \quad (13.17)$$

Given the uncertainty in some of the variables in Eq. 13.15, it is difficult to draw conclusions regarding the magnitudes of ρ_m in these figures or how these vary from material to material.

Figure 13.12 showed example calculations for niobium, Inconel 600, and AISI 316L SS for specific stress–strain curves. Table 13.2 indicated, however, that for niobium, Inconel 600, and titanium, stress–strain curves were available at several test temperatures and/or strain rates. Each of these stress strain curves exhibited signatures of DSA. In titanium, for instance, Fig. 10.68 showed two data points that were well off the model behavior (dashed line). These tests were at a strain rate of 0.033 s^{-1} and test temperatures of 800 K and 900 K. One of the other open triangles closer but still deviating from the model behavior was also selected; this was at a strain rate of $3.5 \times 10^{-5} \text{ s}^{-1}$ and a test temperature of 700 K. In Inconel 600, tests at

Fig. 13.13 Computed variation of the mobile dislocation density with stress according to Eq. 13.15 for three titanium tests. The dashed line is drawn according to Eq. 13.17

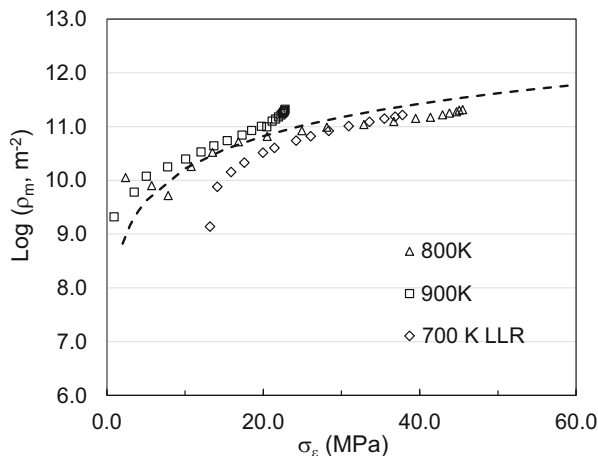
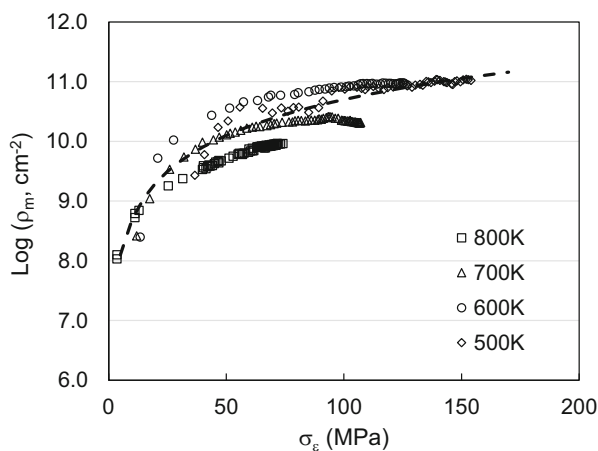


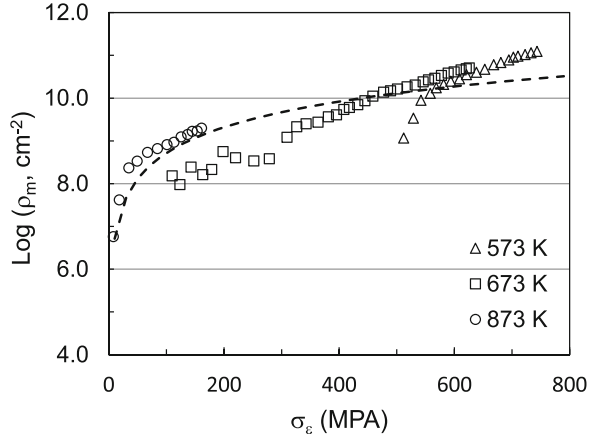
Fig. 13.14 Computed variation of the mobile dislocation density with stress according to Eq. 13.15 for four niobium tests. The dashed line is drawn according to Eq. 13.17



temperatures of 573 K, 673 K, and 873 K were selected because the similar plot (Fig. 12.9) showed they deviated sharply from the assumed model behavior (dashed line). For niobium, the four tests (temperatures of 500 K, 600 K, 700 K, and 800 K) shown to the left of the model line in Fig. 9.56 were selected. Each of these stress-strain curves was analyzed as described above to see whether consistent trends were found.

Figure 13.13 shows the result for the three tests in titanium. The results in niobium and Inconel 600 are shown in Figs. 13.14 and 13.15, respectively. The trends mirror those shown in Fig. 13.12. A single dashed line according to Eq. 13.17 adequately describes the combined set of curves in each case. The $K_{\rho m}$ model constants are included in Table 13.2. Recall that in order to exercise Eq. 13.15, the temperature (and strain rate dependence) of the MTS model constants as well as the temperature dependence of the diffusion coefficient must be included. The result that

Fig. 13.15 Computed variation of the mobile dislocation density with stress according to Eq. 13.15 for three Inconel 600 tests. The dashed line is drawn according to Eq. 13.17



measurements at different test temperatures tend to congregate along a single ρ_m versus σ_e curve provides validation that the temperature-dependencies implicit to Eq. 13.15 have been well represented.

13.5 Predicting the Stresses When DSA is Active

Prediction of stresses when DSA is active follows from combining Eq. 8.5, for the case of a single-obstacle population,

$$\frac{\sigma}{\mu} = \frac{\sigma_a}{\mu} + s_i(\dot{\epsilon}, T) \frac{\widehat{\sigma}_i}{\mu_o} + s_\epsilon(\dot{\epsilon}, T) \frac{\widehat{\sigma}_\epsilon}{\mu_o} \tag{8.5}$$

or Eq. 10.5, for the case of two-obstacle populations,

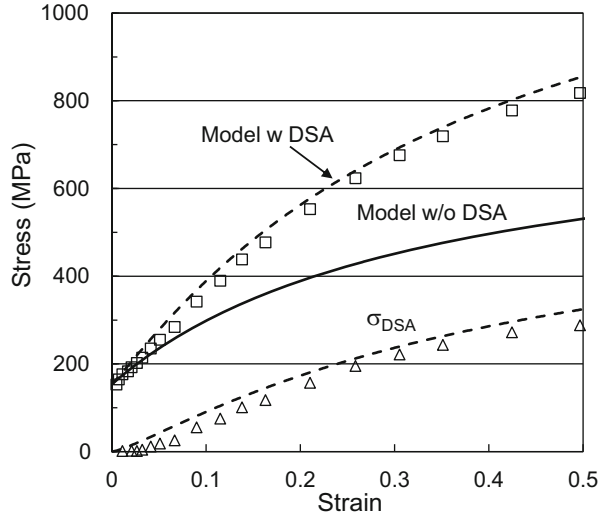
$$\frac{\sigma}{\mu} = \frac{\sigma_a}{\mu} + s_1(\dot{\epsilon}, T) \frac{\widehat{\sigma}_1}{\mu_o} + s_2(\dot{\epsilon}, T) \frac{\widehat{\sigma}_2}{\mu_o} + s_\epsilon(\dot{\epsilon}, T) \frac{\widehat{\sigma}_\epsilon}{\mu_o} \tag{10.5}$$

with Eq. 13.1 substituted for the threshold stress of the species that contributes to DSA. If this is population “2,” then the governing equation becomes

$$\frac{\sigma}{\mu} = \frac{\sigma_a}{\mu} + s_1(\dot{\epsilon}, T) \frac{\widehat{\sigma}_1}{\mu_o} + s_2(\dot{\epsilon}, T) \frac{\widehat{\sigma}_2}{\mu_o} + \frac{\sigma_{\text{DSA}}}{\mu} + s_\epsilon(\dot{\epsilon}, T) \frac{\widehat{\sigma}_\epsilon}{\mu_o} \tag{13.18}$$

In Eq. 13.18 s_2 is the s-factor computed using Eq. 6.16, i.e., without the contribution from DSA. The stress σ_{DSA} is computed using Eq. 13.7

Fig. 13.16 Predictions using Eq. 13.15 of stress for the measurement in AISI 316 SS at 703 K and a strain rate of 0.00004 s^{-1} . The solid curve is the prediction without the DSA model. The lower curve is the prediction of σ_{DSA} compared to the estimates of σ_{DSA} . The upper curve shows the model prediction with DSA compared to the measured stress–strain curve



$$C'_2 \cong 0.01 \left(\frac{\sigma_{\text{DSA}}}{s_i K \mu} \right)^2 \rho \tag{13.7}$$

where σ_{DSA} has been substituted for σ_N and the concentration C'_2 has been substituted for C'_N in this equation. The concentration is computed using Eq. 13.15 with ρ_m from Eq. 13.17.

Figure 13.16 presents these calculations for the Conway et al. measurement in AISI 316 SS at 703 K and a strain rate of 0.00004 s^{-1} . All model constants (listed in Table 13.2) used to analyze the 316L SS data in Fig. 13.12 listed in were kept constant. This included the value of $K_{\rho m}$ although this was determined through analysis of another set of data in AISI 316L SS. The nitrogen concentration for these calculations was set at 0.05%, which was the value in Table 11.7. Figure 13.16 includes as the solid curve the MTS model prediction assuming DSA was not active. The measurements are shown as open squares. The presence of DSA leads to higher stress levels. The bottom dashed-line curve shows the predicted values of σ_{DSA} computed as described above. The dashed curve through the open square data points shows the total stress. The agreement between measurements and predictions is quite good.

Figure 13.17 shows another example of this analysis for measurement in Inconel 600. This stress strain curve is that reported by Hänninen et al. [19] at a temperature of 673 K and a strain rate of 10^{-5} s^{-1} . The same model constants used in Fig. 13.12 were used for this test (Table 12.3). The model again predicts higher stress levels when DSA is active (dashed line). The open squares represent the measured stress–strain curve. The predicted stresses exceed the measured stresses but the agreement is noteworthy. Of interest in the predictions shown in Fig. 13.17 are the periodic strain rate changes. These were strain rate increases from 10^{-5} s^{-1} to 10^{-4} s^{-1} . The “blips” are the model predictions for these strain-rate changes. As expected, in the

Fig. 13.17 Predictions using Eq. 13.15 of stress for the measurement in Inconel 600 at 700 K and a strain rate of 0.00001 s^{-1} . The lower curve is the prediction without the DSA model. The upper curve shows the model prediction with DSA compared to the measured stress-strain curve. The blips are predictions of the stress response to a $\times 10$ strain rate increase

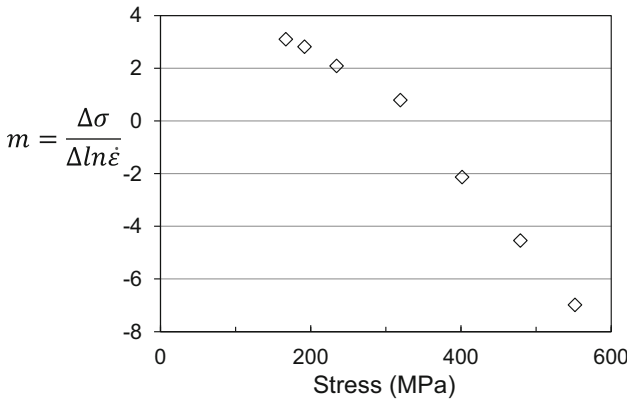
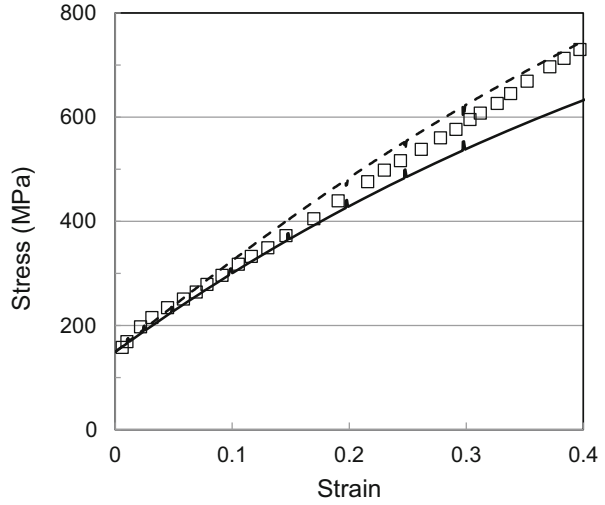
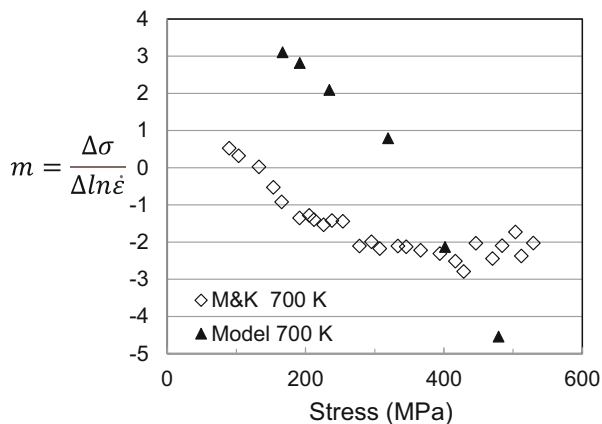


Fig. 13.18 Predicted strain-rate sensitivity values for the test in Inconel 600 at 700 K and a strain rate of 0.00001 s^{-1}

model predictions without DSA, the brief strain rate increases lead to stress increases. In the predictions with the DSA model, these stress increments are quite small—barely visible on the dashed line. Figure 13.18 plots the strain-rate sensitivity as a function of stress computed with application of Eq. 13.15, where the strain-rate sensitivity m is defined

$$m = \frac{d\sigma}{d\ln\dot{\epsilon}} \tag{13.19}$$

Fig. 13.19 Comparison of measured and predicted strain-rate sensitivity values for Inconel 600 at 700 K and a strain rate of 0.00001 s^{-1}



As shown in Fig. 13.18, the m -value starts at a positive value, but with increasing stress the m -values fall and become negative. Negative strain-rate sensitivity is a hallmark observation when DSA is active [5].

Mulford and Kocks performed X10 strain rate change tests in Inconel 600 [26]. Figure 13.19 compares the measured m -values from Mulford and Kocks with the model predictions for the Inconel 600 at a temperature of 700 K and a strain rate of 10^{-5} s^{-1} . The computed m -values initially exceed the measured values. At higher stresses as the m -values fall below zero, the computed and measured values coincide. The comparison in Fig. 13.19 is not ideal, but the agreement using the model summarized in Eq. 13.15 tends to validate the modeling approach.

13.6 Summary

The object of this chapter was to re-examine the signatures of DSA in steels, austenitic stainless steels, niobium, vanadium, and titanium. Similar trends were observed in each of these systems when DSA was active. A simple model based on transport of solutes to the dislocation core led to a correlation between several model variables along with the mobile dislocation density. This model suggested that the simple Arrhenius correlation expressed by Eq. 9.9 did not accurately describe the operative kinetics. This explains why plots based on Eq. 9.9 (e.g., Figs. 13.6, 10.74, 11.18, and 12.22) did not yield activation energies which coincided with known solute diffusion rates. Although there is great uncertainty regarding the rate of diffusion of solutes in a heavily dislocation metal, use of literature diffusion correlations (as shown in Table 13.2) led to predictions of stress (e.g., Figs. 13.16 and 13.17) and, in the case of Inconel 600, predictions of strain-rate sensitivity (e.g., Fig. 13.19) that agreed with experimental data. An underlying assumption of the analyses was that the additional hardening observed when DSA was active was due

to the hardening induced by the extra concentration of solutes at the dislocation core. This was represented by σ_{DSA} as defined by Eq. 13.2. The comparison of model predictions with estimated σ_{DSA} values and strain-rate sensitivity supports this assumption, although the uncertainty in several of the model constants leaves this as an open issue. The availability of additional experimental measurements, including measurements of strain-rate sensitivity, could help to resolve this question.

The results suggest, however, that the high rate of evolution observed when DSA is active (e.g., as seen in Fig. 13.2 and in the corresponding figures for niobium (Fig. 9.56), AISI 316L SS (Fig. 11.12), titanium (Fig. 10.68), and Inconel 713 (Fig. 12.13)) arises from the contribution of σ_{DSA} . This re-emphasizes the need to derive an accurate solution to Eq. 6.26—the saturation stress versus temperature strain rate correlation—in a regime where DSA is not active. As described in Sect. 13.5, an inaccurate solution here can introduce errors in the prediction of σ_{DSA} .

One of the interesting results of the application of Eq. 13.15 was the observed variation of the mobile dislocation density with σ_e , given by Eq. 13.17. While no physical justification for this correlation was offered and the fit of this equation to the analyzed measurements was not ideal, Figs. 13.13, 13.14, and 13.15 show that this correlation may have some validity. A common feature of many of the models of DSA (e.g. [5, 10–12]) is the use of an Omega term, which is the ratio of the mobile to forest dislocation densities

$$\Omega = \frac{\rho_m b}{(\rho_f)^{1/2}} \quad (13.20)$$

The Ω term is allowed to vary. Combining Eq. 13.17 with Eq. 13.14 gives

$$\Omega = \frac{K_{\rho m} \sigma_e \mu b^2 M \alpha}{s_\epsilon} \quad (13.21)$$

which is a prediction for the variation of Ω with stress.

In many of the metals examined in this monograph, DSA was shown to be a confounding deformation mechanism at elevated temperature. This model represented by Eq. 13.15 presents a possible MTS model enhancement that correlates well with many of the “signatures” of DSA documented in earlier chapters.

Appendix 13.A1 The Effect of an Incorrect Assumption on the Analysis Using Eq. 13.15

In an earlier publication where Eq. 13.15 was introduced and evaluated [16], the conclusions in Inconel 600 were tainted by an incorrect assumption related to the evaluation of Eq. 6.26. The issue was discussed when describing the $\hat{\sigma}_\epsilon$ versus ϵ plots in this material (Fig. 12.8). Because these curves demonstrated no tendency toward

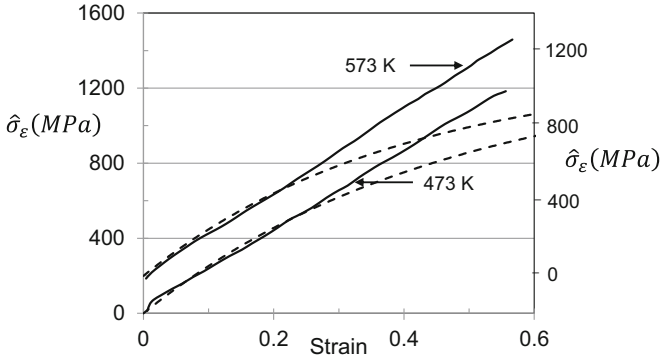


Fig. 13.A1.1 Plots of $\hat{\sigma}_\varepsilon$ versus ε for two measurements in Inconel 600 at 473 K (left ordinate) and 573 K (right ordinate) from earlier work [16]. The dashed-line model fit for both sets of data was incorrectly assumed to tend toward saturation which led to an overestimate of σ_{DSA}

saturation, one could not establish a temperature-dependent saturation stress which could be fit to Eq. 6.26. In the earlier work, a hardening curve that did converge on a saturation stress was assumed. The incorrect model fits at 473 K and 573 K are shown in Fig. 13.A1.1. This assumption was partially driven by the expectation that stress–strain curves must show this behavior and the observation in so many materials that this was the case. Comparing the model fits in Fig. 13.A1.1 with those presented in Fig. 12.8 (at 300 K and 673 K) highlights the effect of this model assumption. In Fig. 13.A1.1 the σ_{DSA} values (related to the difference between the solid and dashed curves) will be quite large compared to those computed when the hardening is correctly assumed to be almost linear (as in Fig. 12.8). That is, the representation of saturation stress behavior in Fig. 12.9 was less than ideal, but at least the behavior in absence of DSA was approximated. Furthermore, the stress–strain curves in Inconel 600 at temperatures less than 573 K did not show evidence of DSA, which implies that the assumed model fit at 473 K in Fig. 13.A1.1 should have coincided closely with the measurements, i.e., shouldn't have deviated at all from the measured data points.

With this incorrect assumption, values of σ_{DSA} were overestimated, and Eq. 13.15 gave high values of the solute concentration. This, in turn, gave overestimated (negative) m -values (Fig. 13.19). In this earlier work, the solute concentrations that yielded good agreement with the measured m -values were estimated, and it was concluded that most of the σ_{DSA} contribution did not arise from solute diffusion to the dislocation core. This was the correct conclusion in light of the incorrect assumption that the dashed line in Fig. 13.A1.1 (e.g., at 473 K) represented the hardening behavior in absence of DSA. When a different assessment of hardening in absence of DSA is made—as in Fig. 12.8—the model leads to lower σ_{DSA} values and closer agreement with the measured m -values.

Appendix 13.A2 The Effect of DSA on the Stage II Hardening Rate

One of the curious results in the analysis of strain hardening in Inconel 600 (Sect. 12.4.1), and to a lesser degree in the analysis of strain hardening in Inconel 718 (Sect. 12.4.2), was the suggestion that the stage II hardening rate increased as DSA became active. This was evident in Table 12.2, where at temperatures exceeding 600 K, a temperature dependence of θ_{II} was noted in Inconel 600. Figure 13.A2.1 shows a plot of θ_{II} versus test temperature. The temperature dependence θ_{II} was unusual and had not been observed in any of the other metal systems examined in this monograph. Exercise 12.7 sheds light on this apparent temperature dependence. All of the exercises in Chap. 12 involved a hypothetical superalloy. In Exercise 12.7 a table of true stress versus true strain measurements at a temperature of 700 K and a strain rate of 0.001 s^{-1} is provided, and the student is asked to generate a plot of $\hat{\sigma}_\varepsilon$ versus strain (using Eq. 12.6) and to fit Eq. 6.28—the modified Voce law—to the data points.

The base stress versus strain data for HypoSuperalloy was created using the model constants listed in Table 13.A2.1. To introduce the effects of anomalous hardening and DSA, an “offset stress” of $\sigma_o = 286 \text{ MPa}$ (assumed to be independent of strain) was added to the base stresses. To further complicate the test, the contributions of DSA were introduced by adding a σ_{DSA} term. With these modifications, the stresses listed in Table 12.E7 were computed using the following equation

$$\sigma = \sigma_a + \mu \left(s_i(\dot{\varepsilon}, T) \frac{\hat{\sigma}_i}{\mu_o} + s_{\gamma'}(\dot{\varepsilon}, T) \frac{\hat{\sigma}_{\gamma'}}{\mu_o} + s_\varepsilon(\dot{\varepsilon}, T) \frac{\hat{\sigma}_\varepsilon}{\mu_o} \right) + \sigma_o + \sigma_{\text{DSA}} \quad (13.A2.1)$$

Fig. 13.A2.1 Apparent variation of the Stage II hardening rate θ_{II} observed in Inconel 600

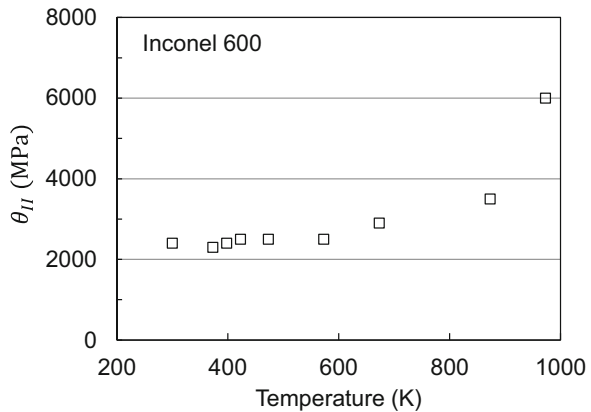
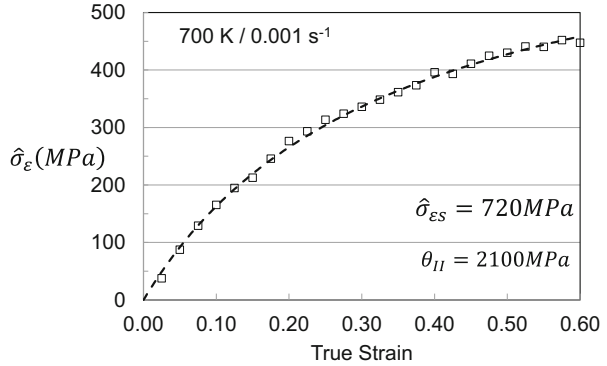


Table 13.A2.1 Full set of model parameters for the hypothetical superalloy used in Chap. 12 Exercises

Parameter	Equation	Value	Units	
σ_a (MPa)	Eq. 12.1	100	MPa	
s_i	Eq. 12.2	g_{oi}	0.7	
		p_i	0.5	
		q_i	1.5	
		$\dot{\epsilon}_{oi}$	1×10^8	s^{-1}
$\widehat{\sigma}_i$	Eq. 12.1	600	MPa	
$s_{\gamma'}$	Eq. 12.3	$g_{\gamma'}$	2.0	
		$p_{\gamma'}$	0.5	
		$q_{\gamma'}$	1.5	
		$\dot{\epsilon}_{o\gamma'}$	1×10^8	s^{-1}
$\widehat{\sigma}_{\gamma'}$	Eq. 12.1	1500	MPa	
s_{ϵ}	Eq. 7.9	$g_{o\epsilon}$	1.6	
		p_{ϵ}	0.667	
		q_{ϵ}	1	
		$\dot{\epsilon}_{o\epsilon}$	1×10^7	s^{-1}
κ	Eq. 6.28	1	–	
θ_{II}	Eq. 6.29	A_o	2500	MPa
		A_I	100	MPa
		A_2	0	MPa $s^{-1/2}$
$\widehat{\sigma}_{\epsilon s}$	Eq. 6.26	$\widehat{\sigma}_{\epsilon s o}$	2000	MPa
		$g_{\epsilon s o}$	0.15	–
		$\dot{\epsilon}_{\epsilon s o}$	1×10^8	s^{-1}
b		0.249	nm	
ρ	Eq. 6.32	8.9	g / cm^3	
ψ		0.95	–	
$\mu(T)$	Eq. 6.8 (See Table 6.1)	μ_o	85.09	GPa
		D_o	9.132	GPa
		T_o	269	K
$c_p(T)$	See Table 6.5 in Box 6.4	A_C	0.1565	J / g / K
		B	7.00×10^{-5}	J / g / K ²
		C	7060	J K / g

The model parameters and equation numbers for each of these terms are listed in Table 13.A2.1 and in the value of σ_o specified above. The term not specified is σ_{DSA} . For this, the correlation between σ_{DSA} and σ_{ϵ} for AISI 316L stainless steel shown in Fig. 13.8 was assumed. In addition to the result in AISI 316L stainless steel, the dependence of σ_{DSA} on σ_{ϵ} for vanadium (Fig. 13.7) and AISI 1018 steel (Fig. 13.10) showed similar trends; they all start at zero and increase uniformly with increasing σ_{ϵ} .

Fig. 13.A2.2 Variation of $\hat{\sigma}_\epsilon$ with strain computed in Exercise 12.7 showing an unusually high Stage II hardening rate



For the calculation of stresses using Eq. 13.A2.1, the strain hardening absent DSA was computed using Eq. 6.28 with Eq. 6.29 for θ_{II} and Eq. 6.26 for $\hat{\sigma}_{\epsilon S}$. From Eq. 6.29 with the parameters specified in Table 13.A2.1, θ_{II} is calculated to equal 1809 MPa at a strain rate of 0.001 s^{-1} . Figure 13.A2.2 shows the plot of $\hat{\sigma}_\epsilon$ versus strain that the student is asked to compute, along with the fit to Eq. 6.28. Interestingly, the fit of Eq. 6.28 yields a $\theta_{II} = 2100 \text{ MPa}$, which is much higher than the value of 1809 MPa used to generate the stresses.

The source of this discrepancy follows from the addition of σ_{DSA} . Recall that the student computes $\hat{\sigma}_\epsilon$ versus strain using Eq. 9.7

$$\hat{\sigma}_\epsilon = \frac{\mu_o}{s_\epsilon(\dot{\epsilon}, T)} \left[\frac{\sigma}{\mu} - \frac{\sigma_a}{\mu} - s_p(\dot{\epsilon}, T) \frac{\hat{\sigma}_p}{\mu_o} - s_i(\dot{\epsilon}, T) \frac{\hat{\sigma}_i}{\mu_o} \right] \quad (9.7)$$

While the student is reminded to subtract σ_O —the anomalous stress addition—from σ , they haven’t subtracted σ_{DSA} , as in Eq. 13.A2.1. Because σ_{DSA} generally is a smoothly increasing function of σ_ϵ , the combination of σ plus σ_{DSA} should not necessary be well described by the modified Voce law (Eq. 6.28); the fit of this equation becomes a simple curve fit, and the significance of both θ_{II} and $\hat{\sigma}_{\epsilon S}$ is diminished.⁷ For the case of the hypothetical superalloy, the initial Stage II hardening rate appears to be higher than that used to generate the base stresses. Thus, the high value of θ_{II} observed when DSA is active is not related to the actual Stage II hardening rate but is an artifact produced by the contribution of DSA.

⁷This also may explain why, in many of the examples where Equation 6.28 was fit to σ plus σ_{DSA} , the agreement of the model fit to the data was not as good as when σ_{DSA} was not active. Figure 12.11 12.11 was a good example of this.

Exercises

- 13.1. Refer to Exercise 11.1, where a plot of s_2 versus σ_ϵ for the Dai et al. stress-strain curve at 350 C in unirradiated 316LN SS was created. Data for this test were listed in the Table 11.E1. Using $\hat{\sigma}_i = 572$ MPa and $\hat{\sigma}_N = 243$ MPa (see Sect. 11.6), the model parameters listed in Table 11.6, and the values of p , q , and $\dot{\epsilon}_o$ that have been consistently used in this chapter, (a) create a plot of σ_{DSA} versus σ_ϵ . (b) From the value of K for Eq. 13.5 listed in Table 13.2, create a plot of the solute concentration versus σ_ϵ .
- 13.2. Create a plot of stress versus strain and σ_{DSA} versus strain for titanium at a strain rate of 0.001 s^{-1} and a temperature of 700 K. Use the MTS model constants in Table 10.19. For this calculation, use Eq. 13.15 for σ_{DSA} , Eq. 13.17 for ρ_m , and the model constants for titanium listed in Table 13.2. b) Create a plot of the sum of $\hat{\sigma}_\epsilon$ plus σ_{DSA} versus strain. Find the best fit of Eq. 6.28, which requires you to adjust θ_{II} and $\hat{\sigma}_{\epsilon s}$ to align Eq. 6.28 with the summed stresses.
- 13.3. Repeat the calculations of Exercise 13.2 for a strain rate of 0.001 s^{-1} and a temperature of 500 K.
- 13.4. Repeat the calculations of Exercise 13.2 for a strain rate of 0.001 s^{-1} and a temperature of 900 K.
- 13.5. Repeat the calculations of Exercise 13.2 for a strain rate of 0.0001 s^{-1} and a temperature of 600 K.
- 13.6. Table 13.E.6 contains the saturation threshold stress versus temperature and strain rate data points used to create Fig. 10.68. Recreate this plot according to Eq. 6.26 and the model variables listed in Table 10.19. Add the four data sets from Exercises 13.2 through 13.5. Comment on how these data compare.
- 13.7. Comment on the trends to θ_{II} observed in the fits to Eq. 6.28 found in Exercises 13.2 through 13.5. You may want to review the discussion in Appendix 13.A.2.

References

1. K.L. Murty, Is neutron damage exposure always detrimental to metals (steels)? Lett. Nat. **308**, 51–52 (1984)
2. G.T. Gray III, S.R. Chen, “MST-8 constitutive properties & constitutive modeling,” Los Alamos National Laboratory, LA-CP-07-1590 (Contact authors for further information)
3. J.B. Conway, R.H. Stentz, J.T. Berling, “Fatigue, tensile, and relaxation behavior of stainless steels”, U. S. Atomic Energy Commission, Division of Reactor Research and Development, NTIS, TID26135, 1974
4. U.F. Kocks, R.E. Cook, R.A. Mulford, Strain aging and strain hardening in Ni-C alloys. Acta Metall. **33**, 623–638 (1985)
5. L.P. Kubin, Y. Estrin, Dynamic strain ageing and the mechanical response of alloys. J. Phys. III **1**, 929–943 (1991)
6. P.G. McCormick, Model for Portevin-Le Chatelier effect in substitutional alloys. Acta Metall. **20**, 351 (1972)

7. A.H. Cottrell, B.A. Bilby, Dislocation theory of yielding and strain ageing of iron. *Proc. Phys. Soc. A*, **52**, 49–62 (1949)
8. A. Beukel, Theory of the effect of dynamic strain aging on mechanical properties. *Phys. Status Solidi* **30**, 197–206 (2010)
9. G.Z. Voyiadjis, Y. Song, A physically based constitutive model for dynamic strain aging in Inconel 718 alloy at a wide range of temperatures and strain rates. *Acta Mech.* **231**, 19–34 (2020)
10. M.A. Soare, W.A. Curtin, Single mechanism rate theory for dynamic strain aging in fcc metals. *Acta Mater.* **56**, 4091–4101 (2008)
11. M.A. Soare, W.A. Curtin, Solute strengthening of both mobile and forest dislocations: The origin of dynamic strain aging in FCC metals. *Acta Mater.* **56**, 4046–4061 (2008)
12. F. Zhang, A.F. Bower, W.A. Curtin, Finite element implementation of a kinetic model of dynamic strain aging in aluminum–magnesium alloys. *Acta Mater.* **60**, 43–50 (2012)
13. J. Cheng, S. Nemat-Nasser, A model for experimentally-observed high-strain-rate dynamic aging in titanium. *Acta Mater.* **48**, 3131–3144 (2000)
14. C. Fressengeas, A.J. Beaudoin, M. Lebyodkin, L.P. Kubin, Y. Estrin, Dynamic strain aging: A coupled dislocation - solute dynamic model. *Matl Sci. Eng. A* **400–401**, 226–230 (2005)
15. M. Koyama, T. Sawaguchi, K. Tsuzaki, Overview of dynamic strain aging and associated phenomena in Fe–Mn–C austenitic steels. *ISIJ Int.* **58**(8), 1383–1395 (2018)
16. P.S. Follansbee, Further analysis of dynamic strain aging in context of an internal state variable constitutive formalism. *Metal. Mater. Transact.* **51A**, 1275–1285 (2020)
17. P.G. Shewmon: *Diffusion in Solids*, McGraw-Hill Series in Materials Science and Engineering, NY, 1963
18. S. Nemat-Nasser, W. Guo, Flow stress of commercially pure niobium over a broad range of temperatures and strain rates. *Mater. Sci. Eng. A* **A284**, 202–210 (2000)
19. H. Hänninen, M. Ivanchenko, Y. Yagodzinskyy, V. Nevdacha, U. Ehrstén, P. Aaltonen, Dynamic strain aging of Ni-base alloys Inconel 600 and 690, in *Proceedings of the 12th International Conference on Environmental Degradation of Materials in Nuclear Power System – Water Reactors, TMS*, ed. by T. R. Allen, P. J. King, L. Nelson, (2005), pp. 1423–1430
20. M. Doner, H. Conrad, Deformation mechanisms in commercial Ti-50A (0.5a at. pct O_{eq}) at intermediate and high temperatures (0.3 – 0.6 T_m). *Metall. Trans. A*, **4**, 2809–2817 (1973)
21. M. Bobadilla, A. Tschiptschin, On the nitrogen diffusion in a duplex stainless steel. *Mater. Res.* **18**, 390–394 (2015)
22. L.H. deAlmeida, K.C.C. Pires, C.R. Grandini, O. Florencio, Measurement of oxygen atom diffusion in Nb and Ta by anelastic spectroscopy. *Mater. Res.* **8**, 239–243 (2005)
23. J.J. Lander, H.E. Kern, A.L. Beach, Solubility and diffusion coefficient of carbon in nickel: reaction rates of nickel-carbon alloys with barium oxide. *J. Appl. Phys.* **23**(12), 1305–1309 (1953)
24. C.A. Wert, Diffusion coefficient of C in α -iron. *Phys. Rev.* **79**, 601–605 (1950)
25. H.H. Wu, E.R. Trinkle, “Direct diffusion through interpenetrating networks: oxygen in titanium,” arXiv:1106.3610v1 [cond-mat.mtrl-sci] 18 Jun 2011
26. R.A. Mulford, U.F. Kocks, *Acta Metall.* **27**, 1125–1134 (1979)

Chapter 14

Application of MTS Model to the Strength of Heavily Deformed Metals



Introduction

The analysis of deformation in irradiation-damaged austenitic stainless steel was used in Sect. 11.6 to demonstrate application of an internal state variable constitutive model to a uniquely processed material. In this case, the deformation of non-irradiation-damaged austenitic stainless steel was described using three internal state variables, and introduction of irradiation damage was analyzed by deducing changes in the magnitudes of one state variable— $\hat{\sigma}_\epsilon$ —and comparing predictions of the model to temperature and strain-rate-dependent stress–strain curves measured on irradiated metal. The ability to match both the measured strain-hardening rate and strain-rate sensitivity offers a sensitive test of the proposed constitutive model.

In this chapter, another unique processing route is studied. The use of large deformations to reduce the grain size, change the grain boundary character, and dramatically increase the strength has been a topic of considerable interest. Often the interest is in producing grain sizes that are well below 1 μm —even approaching 10 nm. Recent reviews offer thorough summaries of the techniques to produce large deformations, the ensuing mechanical properties, microstructural observations, and models of constitutive behavior [1–3].

14.1 Complications Introduced at Large Deformations

In context of the mechanical threshold stress (MTS) model, there are three specific complications introduced when large deformations are imposed. Two of these have already been discussed. The first is the observation that the normalized activation energy g_{oe} is not constant, as is normally assumed. This was illustrated in copper in

Supplementary Information The online version contains supplementary material available at https://doi.org/10.1007/978-3-031-04556-1_14.

Fig. 8.5, which summarizes the values of g_{oe} from the extensive set of prestrain and reload measurements reported by Follansbee and Kocks [4]. These measurements indicate that g_{oe} decreases with increasing stress, which implies that the obstacle population characterized by the interaction of mobile dislocations with stored dislocation density becomes more strain rate and temperature sensitive with increasing stress. A simple phenomenological model for this is discussed in the next section.

The second complication was discussed in Box 8.1 “Stress-State Dependence of Hardening in Copper” presented in Sect. 8.3. This discussion emphasized that the stress–strain behavior of copper varies with the imposed stress state. Stresses measured in uniaxial compression or tension are uniformly higher than those measured in torsion, which is a consequence of differences in texture (collective grain orientations) that evolve as a function of stress state. The MTS model is presented here as an isotropic model in that the effects of texture evolution are not included in the constitutive equations presented in Chap. 6. Furthermore, an attempt has been made to minimize the effects of texture evolution through a focus on small strain (e.g., less than 50%) and material without a strong starting texture in demonstrating the application of the model to metals and alloys in Chaps. 8 through 12. However, the effects of texture evolution cannot be ignored when discussing large-strain processing in this chapter. Without specifically introducing models for texture evolution, measurements on material deformed to large strains will be evaluated in this chapter with regard to the possible effects of texture evolution.

The third complication relates to the potential significant evolution in the athermal stress resulting from grain refinement. In fact, the potential for grain size reduction due to deformation twinning was modeled using a grain size-dependent athermal stress in Sect. 10.3 (cadmium) and Sect. 10.7.1 (zirconium). With reduction of grain size by 1000x or more during large-strain processing, the evolution of the athermal stress with strain must be considered. This topic is discussed in more detail in Sect. 14.4.

14.2 Stress Dependence of the Normalized Activation Energy g_{oe}

In their analysis of measurements in silver single crystals and copper polycrystals, Mecking and Kocks [5] noted an increase of $s(\dot{\epsilon}, T)$ with increasing stress. They characterized this as deviation from the Cottrell-Stokes law (see Sect. 5.5) and proposed the following phenomenological model for the strain-rate sensitivity ($m \times \sigma$, as defined by Eq. 8.3)

$$\left. \frac{\partial \sigma}{\partial \ln \dot{\epsilon}} \right|_{T, \hat{\sigma}} = \frac{\sigma}{r_o} \left(1 + \frac{r_o}{n} F \frac{\theta_r}{\theta_h} \right) \quad (14.1)$$

where n and F are constants and θ_r and θ_h represent the “recovery” and “hardening” contributions to strain hardening. The variable r_o in Eq. 14.1 is related to the strain-rate sensitivity of $s(\dot{\epsilon}, T)$

$$r = \left. \frac{\partial \ln \dot{\epsilon}}{\partial \ln s} \right|_T \quad (14.2)$$

and r_o is the value of r at low stresses (where Cottrell-Stokes is obeyed). From the Voce law (Eq. 5.12)

$$\frac{d\hat{\sigma}_\epsilon}{d\epsilon} = \theta_{II} \left[1 - \frac{\hat{\sigma}_\epsilon}{\hat{\sigma}_{\epsilon s}(\dot{\epsilon}, T)} \right] = \theta_{II} - \frac{\theta_{II} \hat{\sigma}_\epsilon}{\hat{\sigma}_{\epsilon s}(\dot{\epsilon}, T)} = \theta_h - \theta_r \quad (14.3)$$

and the ratio of the recovery term to the hardening term becomes

$$\frac{\theta_r}{\theta_h} = \frac{\hat{\sigma}_\epsilon}{\hat{\sigma}_{\epsilon s}(\dot{\epsilon}, T)} \quad (14.4)$$

Equations 14.1 with 14.4 suggests that the strain-rate sensitivity rises as θ_r approaches θ_h —or equivalently as $\hat{\sigma}_\epsilon$ approaches $\hat{\sigma}_{\epsilon s}$. From

$$\sigma = \sigma_a + \left[1 - \frac{kT}{\mu b^3 g_{oe}} \ln \frac{\dot{\epsilon}_o}{\dot{\epsilon}} \right] \hat{\sigma}_\epsilon \quad (14.5)$$

(which is Eqs. 6.11 and 6.12 with $p = q = 1$ and without normalizing by the temperature-dependent shear modulus to simplify the analysis), it can be shown that

$$r_o = \frac{\partial \ln \dot{\epsilon}}{\partial \ln s} = \frac{\mu b^3 g_{oe_o}}{kT} - \ln \frac{\dot{\epsilon}_o}{\dot{\epsilon}} \quad (14.6)$$

where g_{oe_o} is the value of g_{oe} when the Cottrell-Stokes law is obeyed, and

$$\left. \frac{\partial \sigma}{\partial \ln \dot{\epsilon}} \right|_{T, \hat{\sigma}} = \frac{kT}{\mu b^3 g_{oe}} \hat{\sigma}_\epsilon \quad (14.7)$$

Combining Eqs. 14.1 and 14.7 and rearranging give

$$g_{oe} = \frac{kT}{\mu b^3} \frac{r_o}{\sigma} \left(\frac{1}{\frac{1}{\sigma_\epsilon} + \frac{r_o F}{n} \frac{1}{\sigma_\epsilon}} \right) \quad (14.8)$$

It is possible to fit Eq. 14.8 to the Follansbee and Kocks measurements in copper (Fig. 8.5). This equation, however, is not very robust—particularly at low strains in annealed material where $\hat{\sigma}_\epsilon$ is initially zero and σ can also be very low. Accordingly, the following, somewhat related, expression is adopted

$$g_{o\epsilon} = \frac{kT}{\mu b^3} r_o \left(\frac{1}{1 + F \frac{\hat{\sigma}_\epsilon}{\hat{\sigma}_{ES}}} \right) \tag{14.9}$$

This expression also uses r_o (Eq. 14.6) as an initial condition—even though this was not evaluated for a fully rigorous yield stress equation, e.g., Eq. 6.10. Combining Eqs. 14.6 with 14.9 gives

$$g_{o\epsilon} = \left(g_{o\epsilon_0} - \frac{kT}{\mu b^3} \ln \left(\frac{\dot{\epsilon}_o}{\dot{\epsilon}} \right) \right) \left(\frac{1}{1 + F \frac{\hat{\sigma}_\epsilon}{\hat{\sigma}_{ES}}} \right) \tag{14.10}$$

According to Eq. 14.10, $g_{o\epsilon}$ starts at the (high) initial value when $\hat{\sigma}_\epsilon$ is low but decreases with increasing $\hat{\sigma}_\epsilon$. Figure 14.9 gives the measured $g_{o\epsilon}$ versus the value predicted from Eq. 14.9. It should be noted that the strain rate used in calculation of the factor r_o (Eq. 14.6) is a typical reload strain rate rather than the prestrain strain rate used to differentiate data points in Fig. 14.1 (see Box 14.1). The dashed line is the fit to Eq. 14.10 (excluding the five data points at the lowest values of strain for each of the strain rates because they deviate from the linear behavior). The line has a slope of unity and intercepts at the origin. The factor F in Eq. 14.9 has a value $F = 3.16$ and $g_{o\epsilon_0} = 4.7$. Although considerable scatter is observed in Fig. 14.1 and there is a slight trend with prestrain strain rate shown, the trends follow the behavior modeled using Eq. 14.9.

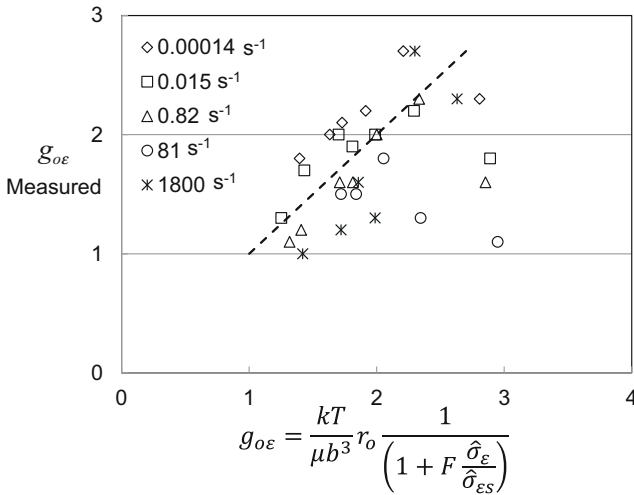


Fig. 14.1 The data of Follansbee and Kocks (see Fig. 8.5) showing variation of $g_{o\epsilon}$ with $\hat{\sigma}_\epsilon$ analyzed according to Eq. 14.9

Box 14.1 Data Analysis in the Presence of a Variable g_{oe}

Figure 8.1 showed reload yield stress measurements in copper prestrained to three conditions. The measured yield stresses were plotted on coordinates consistent with Eq. 6.9 (for a single-obstacle population). On these coordinates, the slope of the best fit line through the data points is related to g_o (or g_{oe}), and the intercept is related to $\hat{\sigma}$ (or $\hat{\sigma}_e$). A dependence of g_{oe} on reload test temperature and strain rate, as indicated in Eq. 14.10, calls into question these correlations, and it is appropriate to ask whether inclusion of Eq. 14.9 alters the recommended procedure for analyzing strain rate- and temperature-dependent yield stress measurements?

Typical reload test conditions use strain rates between 10^4 s^{-1} and 1 s^{-1} and temperatures between 76 K and 298 K. Over this range of conditions (in copper), the factor

$$\frac{kT}{\mu b^3} \ln \frac{\dot{\epsilon}_0}{\dot{\epsilon}}$$

from Eq. 14.10 varies from 0.02 to 0.15. (This is a dimensionless number.) This factor thus contributes $<3\%$ for $g_{oe_0} \approx 5$. The variation of g_{oe} with stress, on the other hand, is seen in Fig. 14.1 to be $>2X$. Thus, analysis of reload yield stress results may proceed as discussed in Chap. 6 through 8 to estimate values of g_{oe} and $\hat{\sigma}_e$. Equation 14.10 should be used when model predictions are sought at a particular strain rate or temperature.

Alberti [6] measured the strain-rate sensitivity in polycrystalline copper strained to very high strains in torsion. Figure 14.2 compares the Alberti measurements (after converting from shear stress to axial stress) and model predictions of m -value using Eqs. 14.7 with 14.9. Included in Fig. 14.2 are measurements of the strain-rate sensitivity reported by Dalla Torre et al. [7] in 0.9995 copper; these will be discussed in more detail in Sect. 14.5. It is interesting that the Dalla Torre et al. measurements converge with the Alberti measurements at stresses greater than ~ 200 MPa. The model predictions under-predict the amplitude of the m -values, but the variation with stress follows the measured trends.

The model predictions derive from Eq. 6.10, which is the more rigorous form of Eq. 14.5. Equation 14.9 gives the variation of g_{oe} with $\hat{\sigma}_e$, but solution of Eq. 14.5 also requires a large-strain hardening law. This is introduced in the next section.

Fig. 14.2 Measured (separate Dalla Torre et al. [7] and Alberti [6] experiments) and predicted variation of the strain-rate sensitivity m with stress in pure copper

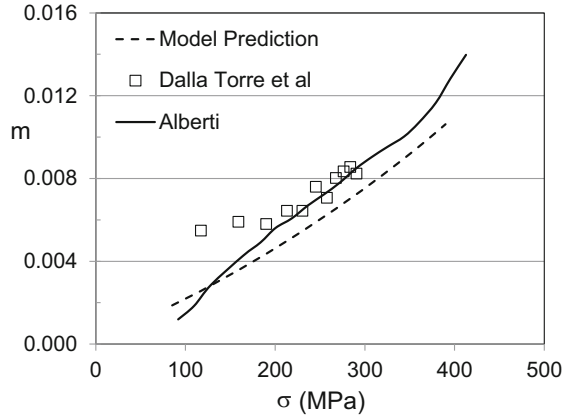
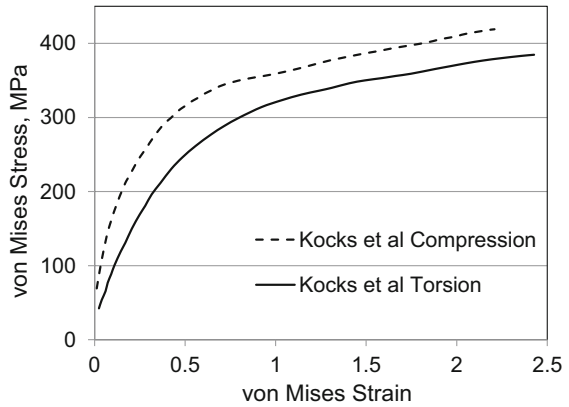


Fig. 14.3 Large-strain stress–strain curves in pure copper reported by Kocks et al. [8]



14.3 Addition of Stage IV Hardening to the Evolution Law

Figure 14.3 shows the large strain measurements of Kocks et al. [8] in copper at RT and a strain rate of 0.001 s^{-1} . Included are stress–strain curves (von Mises stress versus von Mises strain) measured in compression and torsion.¹ One notable observation in Fig. 14.3 is that the two curves do not coincide—even when plotted on von Mises coordinates that are designed to account for differences in stress state. The reason for this is that texture evolution differs in a uniaxial test from that in a torsion test. Another observation in Fig. 14.3 is that above a strain of ~ 1 , both the compression and torsion curves demonstrate an almost linear strain-hardening rate, deviating from the approach to a saturation stress modeled using the standard evolution law (Eq. 6.28). This behavior has been termed “Stage IV” hardening^(ix), which adds

¹Recall from the Box 1.2, entitled “Scaler Stress Representations,” in Sect. 1.11 that von Mises stress and strain are equivalent to uniaxial stress and strain in a tension or compression test.

another regime to the standard hardening behavior in single crystals illustrated in Fig. 3.11.

One simple way to include Stage IV hardening in the evolution law is to add a linear hardening term to Eq. 6.28

$$\frac{d\widehat{\sigma}_\varepsilon}{d\varepsilon} = \theta_{II}(\dot{\varepsilon}) \left(1 - \frac{\widehat{\sigma}_\varepsilon}{\widehat{\sigma}_{\varepsilon S}(\dot{\varepsilon}, T)} \right)^\kappa + \theta_{IV} \quad (14.11)$$

where θ_{IV} is a constant. Equation 14.11 is applicable when $\widehat{\sigma}_\varepsilon \leq \widehat{\sigma}_{\varepsilon S}$. When $\widehat{\sigma}_\varepsilon > \widehat{\sigma}_{\varepsilon S}$, the evolution law is simply

$$\frac{d\widehat{\sigma}_\varepsilon}{d\varepsilon} = \theta_{IV} \quad (14.12)$$

With the inclusion of Stage IV hardening behavior along with a stress-dependent $g_{o\varepsilon}$, the full model becomes Eqs. 6.11 with 6.12 and 14.9

$$\frac{\sigma}{\mu} = \frac{\sigma_a}{\mu} + \left[1 - \left(\frac{kT}{\mu b^3 g_{o\varepsilon}(\widehat{\sigma}_\varepsilon)} \ln \frac{\dot{\varepsilon}_o}{\dot{\varepsilon}} \right)^{1/q} \right]^{1/p} \frac{\widehat{\sigma}_\varepsilon}{\mu_o} \quad (14.13)$$

Note that the normalized activation-free energy term is written as $g_{o\varepsilon}(\widehat{\sigma}_\varepsilon)$, but per Eq. 14.9 it is also a function (albeit a very weak function) of temperature and strain rate (through r_o). Equation 14.13 is the governing equation which, when coupled with Eq. 14.10 for the stress dependence of $g_{o\varepsilon}$ and Eqs. 14.11 or 14.12 as the evolution law, comprises the constitutive model used to generate the m -value versus strain plot shown in Fig. 14.2.

Given a true stress versus true strain data set, such as the compression data in Fig. 14.3, and taking typical values for σ_a , p , q , and $\dot{\varepsilon}_o$ for copper (from Sect. 8.2), it is possible for every value of the stress to find a single value of $\widehat{\sigma}_\varepsilon$ that satisfies Eqs. 14.13 and 14.10. Equation 9.7 was introduced (for a BCC metal with a Peierls barrier and an impurity obstacle barrier) to compute $\widehat{\sigma}_\varepsilon$

$$\widehat{\sigma}_\varepsilon = \frac{\mu_o}{s_\varepsilon(\dot{\varepsilon}, T)} \left[\frac{\sigma}{\mu} - \frac{\sigma_a}{\mu} - s_p(\dot{\varepsilon}, T) \frac{\widehat{\sigma}_p}{\mu_o} - s_i(\dot{\varepsilon}, T) \frac{\widehat{\sigma}_i}{\mu_o} \right] \quad (9.7)$$

For the case of copper with a variable $g_{o\varepsilon}$, this equation becomes

$$\widehat{\sigma}_\varepsilon = \frac{\mu_o}{s_\varepsilon(g_{o\varepsilon}, \dot{\varepsilon}, T)} \left[\frac{\sigma - \sigma_a}{\mu} \right] \quad (14.14)$$

where s_ε is defined by Eq. 7.9 with the model variables given in Table 8.4 and in Table 14.1

$$s_\varepsilon(\dot{\varepsilon}, T) = \left\{ 1 - \left[\frac{kT}{\mu b^3 g_{o\varepsilon}} \ln \left(\frac{\dot{\varepsilon}_{o\varepsilon}}{\dot{\varepsilon}} \right) \right]^{1/q_\varepsilon} \right\}^{1/p_\varepsilon} \quad (7.9)$$

From Eq. 14.10, s_ε is now a function of $g_{o\varepsilon}$. Equation 14.10 includes the ratio $\widehat{\sigma}_\varepsilon/\widehat{\sigma}_{\varepsilon s}$, which includes the “unknown” $\widehat{\sigma}_\varepsilon$. A good initial assumption is to start with the previously established Eq. 6.26 for $(\widehat{\sigma}_{\varepsilon s})$ and Eq. 6.28 with the associated variables, compute the variation of $\widehat{\sigma}_\varepsilon$ with strain, establish a new set of variables for Eq. 6.28, and redo the calculation until a self-consistent solution is achieved.² Figure 14.4 gives the result for the Kocks et al. compression curve in Fig. 14.3. The solid line is the deduced values of $\widehat{\sigma}_\varepsilon$, whereas the dashed line gives Eq. 14.11 with the model parameters listed in Table 14.1. Model parameters for copper from Sect. 8.2 (Table 8.4) without a stress-dependent $g_{o\varepsilon}$ and without a Stage IV hardening term are included in Table 14.1. The only differences are the inclusion of θ_{IV} , a slight increase of $\widehat{\sigma}_{\varepsilon so}$ from 710 MPa in Table 8.4 to 725 MPa, and a decrease of A_o (Eq. 6.29 and 14.21) from 2390 MPa to 2307 MPa. These changes in model constants lead to a slightly improved fit to the experimental measurements, as shown in Fig. 14.4, but are insignificant; starting with the previously established model variables indeed produced a self-consistent solution.³

Table 14.1 Model parameters used for the large-strain copper stress–strain behavior (Fig. 14.4) compared to the model parameters presented in Sect. 8.2

Parameter	Figure 14.4		Section 8.2 (Table 8.4)	
	Equation	Value	Equation	Value
κ	14.11	2	6.28	2
$\widehat{\sigma}_{\varepsilon so}$ (MPa)	6.26	725	6.26	710
$g_{\varepsilon so}$		0.301		0.301
$\dot{\varepsilon}_{\varepsilon so}$ (s ⁻¹)		10 ⁸		10 ⁸
A_o (MPa) ^a	6.29	2307	6.29	2390
θ_{IV} (MPa)	14.11	75	–	–
σ_a (MPa)	14.13	40	6.11 ^b	40
p		0.667	7.9	0.667
q		1.0		1.0
$\dot{\varepsilon}_o$ (s ⁻¹)		10 ⁷		10 ⁷

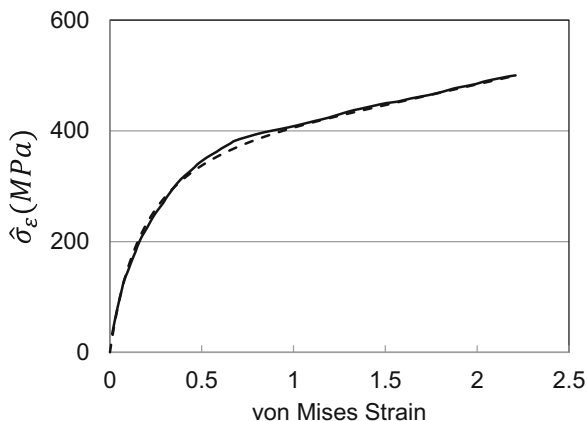
^aUsed to compute θ_{II} in Eq. 14.11

^bWith $\widehat{\sigma}$ equal $\widehat{\sigma}_\varepsilon$, i.e., the stored dislocation population

²Self-consistent here simply means that Eq. 14.14 with the adjusted Eq. 6.28 gives $\widehat{\sigma}_\varepsilon$ versus strain values consistent with Eq. 6.28.

³The analysis of large-strain deformation in nickel in Sect. 14.7 gives further evidence that the solution to Eq. 14.14 is insensitive to the parameters contributing to the ratio $\widehat{\sigma}_\varepsilon/\widehat{\sigma}_{\varepsilon s}$.

Fig. 14.4 Deduced variation of $\hat{\sigma}_\varepsilon$ with strain for the Kocks et al. large-strain compression curve. The dashed line is the fit to Eq. 14.11



14.4 Grain Refinement

A primary motivation of large-strain processing is the potential for significant grain refinement, which can influence [1] strength, ductility, fatigue and fracture, and corrosion properties [10]. Figure 14.5 shows grain size measurements on several metals that have been processed to large strains. These include measurements by Huang et al. in copper [11], Chang et al. in aluminum [12], Kim et al. in AZ61 magnesium [13], Foley et al. in a 9 Cr 1Mo ferritic-martensitic steel [14], Fukuda et al. in an 0.08% C steel [15], Gubicza et al. in aluminum⁴ [16], Gutierrez-Urrutia et al. in Al-0.5% Si [17], Terhune et al. in aluminum [18], Xu et al. in a Cu-Cr alloy [19], and Lewandowska et al. in an Al-Cu-Mg-Mn alloy [20].

A common processing method to achieve large strain is equal-channel angular pressing (ECAP), in which a work piece of circular or square cross section is forced through a die with a sharp bend as shown schematically in Fig. 14.6. Note that ideally the shape of the processed metal is the same as the shape before pressing. There are several possible die designs. The die in Fig. 14.6 shows right-angle bends, whereas some dies have radii rather than sharp angles at the outer corner (as shown with the long-dashed line in Fig. 14.6) or inner corner. Along with differences in die design, which includes variation in the angle φ in Fig. 14.6, the work piece can be rotated 90° or 180° between pressings. Deformation during a pressing is largely a shear process. The effective strain per pressing is given by

$$\varepsilon = \frac{2}{\sqrt{3}} \cot \varphi \quad (14.15)$$

⁴The measurements by Gubicza et al. [16] were of crystallite size determined using X-ray diffraction rather than actual grain size.

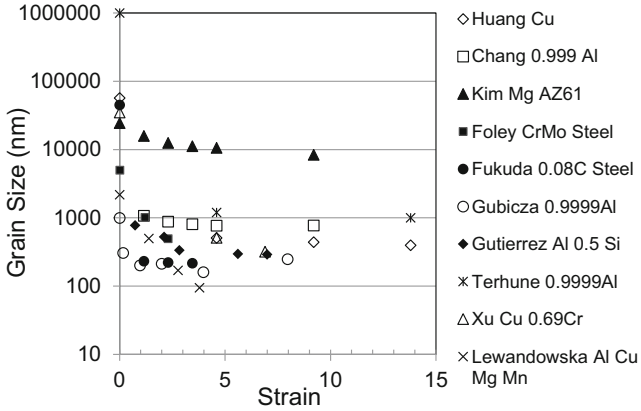
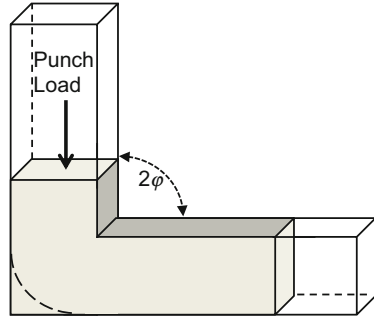


Fig. 14.5 Grain refinement (plotted on a logarithmic scale) as a function of strain in a variety of materials

Fig. 14.6 Schematic of equal-channel angular pressing (ECAP). The die design is shown for $\varphi = 45^\circ$ (referred to as 90° dies)



For 90° dies (where $\varphi = 45^\circ$) the equivalent strain is 1.15. The total equivalent strain for N pressings is simply

$$\varepsilon = \frac{2N}{\sqrt{3}} \cot \varphi \tag{14.16}$$

It is possible to achieve very large total strains, such as those plotted in Fig. 14.5, through use of multiple pressings.

Although most of the references in the measurements shown in Fig. 14.5 refer to “grain size,” there is no commonly accepted criterion that differentiates between subgrain boundaries, cell walls, or grain boundaries. Rollett addresses this point in his thesis work on the large strain hardening behavior of aluminum [21], where he documents significant microstructural refinement with increasing strain, but does not refer to these refined regions as “grains.” Many of the references included in Fig. 14.5 report the evolution of grain misorientation angle and aspect ratio along

with the grain size. The reason why the character of the boundaries is important is that it affects the strengthening contributed by the boundary.

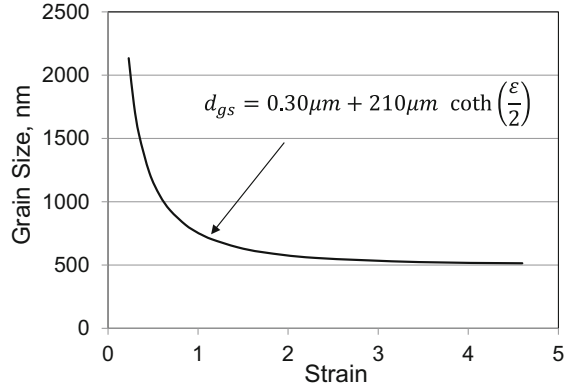
Indeed, one motivation for large-strain processing of metals is to generate high strength. One practice [22] has been to represent the strengthening from grain refinement using a Hall-Petch equation (Eq. 3.9). Measurements of the strengthening contribution of a decreasing grain size ideally involve a carefully prepared microstructure where the only microstructural variable is the grain size. This, for instance, could involve control of grain growth from the melt following a recrystallization heat treatment. Multiple ECAP presses lead to grain refinement as illustrated in Fig. 14.5, but they are likely to introduce a plethora of other microstructural changes that contribute to the strengthening. This leads to a higher k_d -value in Eq. 3.9 than observed in material at constant structure (e.g., well annealed) other than a variable grain size.

Note in Fig. 14.5 that the grain size is plotted on a logarithmic scale. The symbols at zero strain are the initial grain size (where reported). Evident in Fig. 14.5 is that the grain size rapidly decreases for all materials but then tends to level off or saturate. In some cases, the temperature of the work piece is high enough to promote recrystallization. In others the adiabatic temperature increase during processing may be high enough to promote recrystallization. It is apparent in the results shown in Fig. 14.5, however, that considerable grain size reduction occurs before a total strain of 2 is achieved. While most of the deformations in Fig. 14.5 were introduced by ECAP, similar levels of grain size refinement have been reported in material strained in high pressure torsion [23] and wire drawing [24].

In context of a constitutive model, the refined grain size is relevant because of its effect on the athermal stress σ_a . The constitutive model given by Eq. 14.13 along with Eqs. 14.10 and 14.11 assumes that the athermal stress does not change throughout the test. Given that the Kocks et al. compression test shown in Fig. 14.3 was taken to a strain of ~ 2.4 , it seems obvious that significant microstructural refinement occurred, which questions the assumption that σ_a remains single-valued.

It is worthwhile to estimate the increase in the grain size contribution to the total stress for the level of grain refinement illustrated in Fig. 14.5. To accomplish this, the strengthening due to grain refinement must be separated from that from other sources. The Huang et al. measurements in copper indicate that the grain size decreased from the starting grain size of 57 μm to 0.510 μm , 0.442 μm , 0.397 μm , and 0.389 μm after 4, 8, 12, and 16 presses, respectively, in 90° ECAP dies (which from Eq. 14.16 gives strains of 4.6, 9.2, 13.8, and 18.4, respectively). Unfortunately, this research group did not report on grain refinement after one or two presses, which makes it difficult to estimate the variation of grain size with strain between 0 strain and a strain of 4.6. The measurements in aluminum by Chang et al., however, do include grain sizes after one, two, and three presses. Assuming that grain refinement in copper is similar to that in aluminum, the shape (and normalizing the different stress levels in Al and Cu), the variation of grain size with strain roughly follows the

Fig. 14.7 Deduced variation of grain size with strain for copper from data in Fig. 14.5. The equation shown provides a useful correlation but has no fundamental significance



hyperbolic cotangent function $\coth(\epsilon/2)$.⁵ The curve is shown in Fig. 14.7. This correlation is derived only to assist in the estimate of strengthening due to grain refinement assuming that the strengthening follows that defined by the Hall-Petch relationship in copper. From the Feltham and Meakin [25] measurements, the k_{ϵ} -value in the Hall-Petch equation is $3500 \text{ MPa nm}^{1/2}$, and the equation describing the variation of the athermal stress with grain size becomes

$$\sigma_a = 22 \text{ MPa} + \frac{3500 \text{ MPa nm}^{1/2}}{d_{gs}^{1/2}} \quad (14.17)$$

which gives an athermal stress of 40 MPa with a $40 \mu\text{m}$ initial grain size.

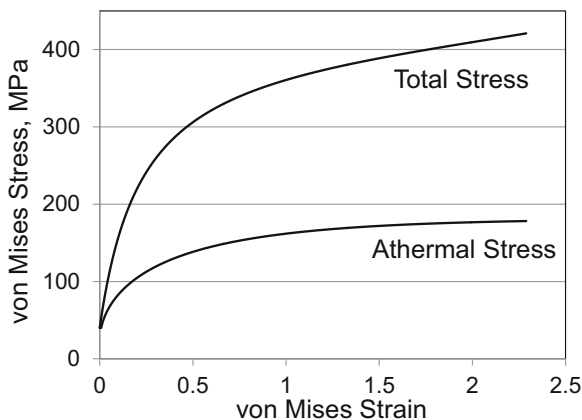
From Eq. 14.17 and the estimated variation of grain size with strain (Fig. 14.7), one can estimate the increase in the athermal stress from grain refinement in the Kocks et al. large-strain compression test. This estimate is shown in Fig. 14.8. Included is the total stress (Fig. 14.3).

Assuming that grain refinement follows the trends in Fig. 14.5 and estimated in Fig. 14.7 and furthermore that the strengthening due to this grain refinement follows the Hall-Petch behavior established for copper, the athermal stress increases from 40 MPa to almost 180 MPa for a test to a total strain of ~ 2.4 . This is a significant change from the model assumptions in the development of the constitutive model represented by Eq. 14.13. Incorporating the evolution of the athermal stress with evolving grain refinement would appear to call for major model revisions.

These model revisions, however, rely upon a microstructural-based model for the development of and strengthening contribution of cell boundaries and the evolution of the boundary character and their strengthening effect as cell boundaries transform to higher-angle grain boundaries. Such a model, though, is unnecessary, since the

⁵The hyperbolic cotangent of zero is infinity. In applying this correlation, the grain size is set at the initial value until the hyperbolic function gives a value less than this. With an initial grain size of $40 \mu\text{m}$, the grain size begins to reduce at $\sim 1\%$ strain.

Fig. 14.8 Estimated contribution of the grain size strengthening term (the athermal stress) compared to the total stress for large-strain deformation in pure copper

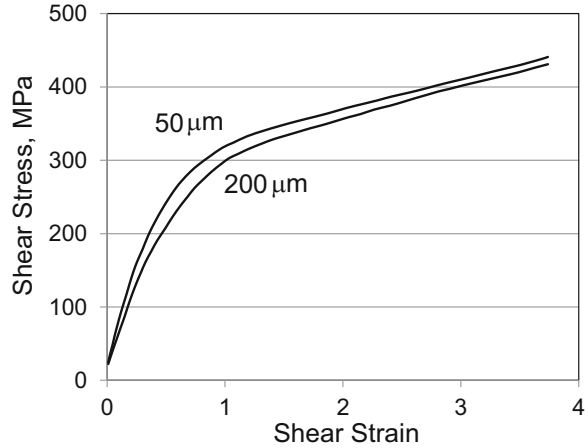


strengthening contribution from microstructural refinement is already included in the fit of the evolution law (Eq. 14.11 or equivalent) to measurements. Recall that the evolution law adopted in the MTS model (Eq. 6.28) is not based on first principles but is a phenomenological model in a convenient form capable of describing evolution as measured with prestrain plus reload experiments (as detailed for copper in Sect. 8.2) or as deduced from the analysis of stress–strain curves using Eq. 9.7 (or equivalent). Several of the data sets analyzed in Chap. 8 through 12 have included measurements to high enough strains that it is certain that a component of strain hardening derives from microstructural refinement. Many constitutive modelers have in fact treated strain hardening as an athermal strength contribution [26, 27]. Furthermore, the normalized activation energy of $g_{oe} = 1.6$ used in the MTS model (Table 8.4) to describe the kinetics of dislocation interactions with the stored dislocation density is in fact much larger than the normalized activation energy characterizing dislocation interactions with the Peierls barrier ($g_{op} \sim 0.1$) or dislocation interactions with solute atoms ($g_{oi} \sim 0.6$), reflecting an obstacle population that is only weakly thermally activated. While dislocation interactions with the stored dislocation density have been consistently treated as thermally activated and not athermal in the MTS model, the temperature and strain-rate dependence of these interactions are quite small. Accordingly, the assumption that the athermal stress is constant likely has a minimal effect on the model formulation or predictions.

The conclusion is that grain refinement is multifaceted and difficult to describe in a constitutive formulation. Large-strain processing introduces high stored dislocation densities which lead to complex dislocation substructures and boundaries that affect strength. These effects are assumed to be included in the phenomenological evolution law which implies that it is unnecessary to include grain refinement using a variable athermal stress.⁶ One final experimental result that supports these arguments

⁶Twinning in cadmium and zirconium was analyzed in Chap. 10 using an increasing athermal stress together with the same evolution law found for untwined material. This is appropriate and consistent with the arguments given in this section.

Fig. 14.9 Large strain stress–strain curves in pure Ni-30 Co at two starting grain sizes reported by Hughes [28]



is found in two large-strain stress–strain curves measured by Hughes [28] in Ni-30 Co of 50 μm and 200 μm initial grain sizes. These measurements, shown in Fig. 14.9, indicate that the curves retain an approximately constant stress differential. This stress differential arises from the difference in the initial grain size (athermal stress), but the resulting grain refinement during straining may be described using a single evolution law. It is appropriate to apply the constitutive law defined by Eq. 14.13 along with Eq. 14.9, which specifies how the normalized activation energy varies with stress, and Eq. 14.11, which is the evolution law revised to include Stage IV hardening behavior. The next sections will demonstrate application of this constitutive model to large-strain processed copper, nickel, stainless steel, and tungsten.

First, application of the assumed constitutive law to copper processed to large strains is demonstrated. Following the discussion in Sect. 14.3, the constitutive equation for large-strain deformation in pure copper, fit to the Kocks et al. measurement in compression, is (recall, $p_e = 2/3$ and $q_e = 1$)

$$\frac{\sigma}{\mu} = \frac{40 \text{ MPa}}{\mu} + \left\{ 1 - \frac{kT}{\mu b^3 g_{oe}(\hat{\sigma}_e)} \ln \frac{10^7 \text{ s}^{-1}}{\dot{\epsilon}} \right\}^{3/2} \frac{\hat{\sigma}_e}{\mu_o} \quad (14.18)$$

with

$$g_{oe} = \left(4.7 - \frac{kT}{\mu b^3} \ln \left(\frac{\dot{\epsilon}_o}{\dot{\epsilon}} \right) \right) \left(\frac{1}{1 + 3.16 \frac{\hat{\sigma}_e}{\sigma_{es}}} \right) \quad (14.19)$$

and

$$\frac{d\widehat{\sigma}_\varepsilon}{d\varepsilon} = \theta_{II}(\dot{\varepsilon}) \left(1 - \frac{\widehat{\sigma}_\varepsilon}{\widehat{\sigma}_{\varepsilon s}(\dot{\varepsilon}, T)} \right)^2 + 75 \text{ MPa} \quad (14.20)$$

The Stage II hardening rate comes from Eq. 6.29, which with the fitted model parameters is

$$\theta_{II} = 2307 \text{ MPa} + 12 \text{ MPa} \ln \dot{\varepsilon} + 1.70 \text{ MPa} s^{-1/2} \sqrt{\dot{\varepsilon}} \quad (14.21)$$

This is identical to the expression used for copper in Chap. 8, except for a slightly decreased value of the first coefficient. The equation for $\widehat{\sigma}_{\varepsilon s}$ (Eq. 6.26) also is the same as specified in Chap. 8, except for the slight difference in $\widehat{\sigma}_{\varepsilon s0}$ (see Table 14.1).

$$\ln \widehat{\sigma}_{\varepsilon s} = \ln (725 \text{ MPa}) + \frac{kT}{\mu b^3 (0.391)} \ln \frac{\dot{\varepsilon}}{10^8 s^{-1}} \quad (14.22)$$

It is worth noting that Eq. 14.19 contains several material-specific and test-specific parameters, including temperature, strain rate, Burgers vector (contained in the factor k / b^3), shear modulus, and $\widehat{\sigma}_{\varepsilon s}$. The generality of Eq. 14.20 across material systems is not demonstrated here but relies on validity of Eq. 14.10, with its relation to the Mecking and Kocks derivation of Eq. 14.1.

14.5 Application to Large-Strain ECAP Processing of Copper

Several extensive studies of mechanical properties and microstructural development following multiple ECAP pressings have been performed in pure copper and aluminum. Dalla Torre et al. [7] measured the reload stress–strain and strain-rate sensitivity behavior on 99.95% pure copper with a starting grain size of 21 μm deformed using 90° ECAP and 1, 2, 4, 8, 12, and 16 pressings. Equations 14.13, 14.19, and 14.20 may be used to predict the stress–strain behavior during deformation along with the stress–strain curve and strain-rate sensitivity upon reloading. For these calculations, the athermal stress is taken as 60 MPa to reflect the slightly smaller grain size in the Dalla Torre et al. material and an impurity obstacle ($\widehat{\sigma}_i$ in Eq. 8.5) of 46 MPa assumed to reflect the lower purity level than in, for instance, the copper used by Follansbee and Kocks.⁷ That is, Eq. 14.18 becomes

⁷Inclusion of a small impurity obstacle threshold stress for the Dalla Torre et al. material is consistent with the initially large m -value at low stresses in Fig. 14.2.

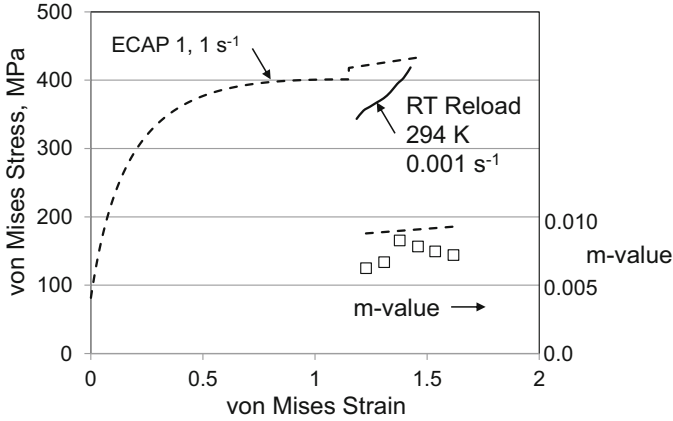


Fig. 14.10 Predicted (dashed-line) stress–strain curve for one ECAP pressing plus a RT reload in copper compared to the reload stress–strain curve measured by Dalla Torre et al. [7]. Included (right ordinate) are the measured and predicted m -values

$$\frac{\sigma}{\mu} = \frac{60 \text{ MPa}}{\mu} + \left\{ 1 - \frac{kT}{\mu b^3 g_{oe}(\hat{\sigma}_\epsilon)} \ln \frac{10^7 s^{-1}}{\dot{\epsilon}} \right\}^{3/2} \frac{\hat{\sigma}_\epsilon}{\mu_o} + s_i(\dot{\epsilon}, T) \frac{\hat{\sigma}_i}{\mu_o} \quad (14.23)$$

where s_i is as specified in Eq. 6.18 with $g_{oi} = 0.6$, which is a typical normalized activation energy for an impurity obstacle population, and $\hat{\sigma}_i = 46 \text{ MPa}$.

Figure 14.10 shows the predicted stress–strain curve (dashed line) during the first pressing and the measured (solid line) and predicted RT reload stress–strain curve at a strain rate of 0.001 s^{-1} . Included in this figure are the measured and predicted strain-rate sensitivities (right abscissa) at several values of strain during the reload operation. In these experiments the 20-mm-long work piece was fed at a velocity of 2 mm/s. If this were uniform loading, these variables would imply a strain rate of 0.1 s^{-1} . Given that deformation is localized in the region near the bend, the applicable strain rate is likely at least 1 s^{-1} , which has been assumed in making the model predictions. This strain rate is at the transition to an adiabatic condition, as noted in Sect. 6.6. This implies that the temperature rises during the pressing. For this test, the temperature is estimated to rise from the starting temperature of 294 K to a final temperature of 404 K at the final strain of 1.15, computed using Eq. 14.15. The measured reload yield stresses fall well below the predicted values, but the curves tend to converge with strain. The predicted stresses upon reload start at a stress slightly greater than the stress level achieved during ECAP processing because the temperature is assumed to return to room temperature. The model predictions show a uniform increase of m -value with strain; the measurements show similar values but more scatter.

14.5.1 Using the Torsion Curve Rather Than the Compression Curve

Figure 14.10 showed that the predicted stresses for the reload test fell well above the measured stresses. A contribution to this overprediction is the fact that the compression curve in Fig. 14.3 was used to predict the hardening rather than the torsion curve. Since the deformations in ECAP are predominantly shear, however, the torsion curve would be more representative of the stress state. To use the torsion curve, Eq. 14.14 is re-evaluated with σ representing the torsion stresses from Fig. 14.3. Figure 14.11 shows the results of the calculation using the same model parameters as listed in Table 14.1. Consistent with the difference in the stress–strain curves in Fig. 14.3, the dashed-line curve overpredicts the stresses. Interestingly, it is the early-strain predictions rather than the large-strain hardening behavior that is overpredicted. The early shape of the curve is mostly influenced by the values selected for θ_{II} —in particular the value of A_o in Eq. 6.29. Figure 14.12 shows a revised prediction with of A_o equal 1221 MPa, θ_{IV} decreased from 75 MPa to 60 MPa and $\hat{\sigma}_{eso}$ decreased slightly from the value of 725 listed in Table 14.1 to 719 MPa. The major change between the model parameters used in Fig. 14.4 is the decrease of A_o from 2307 MPa to 1221 MPa. With these changes, Eq. 14.20 becomes

$$\frac{d\hat{\sigma}_\epsilon}{d\epsilon} = \theta_{II}(\dot{\epsilon}) \left(1 - \frac{\hat{\sigma}_\epsilon}{\hat{\sigma}_{es}(\dot{\epsilon}, T)} \right)^2 + 60 \text{ MPa} \tag{14.24}$$

and Eq. 14.21 becomes

$$\theta_{II} = 1221 \text{ MPa} + 12 \text{ MPa} \ln \dot{\epsilon} + 1.70 \text{ MPa} s^{-1/2} \sqrt{\dot{\epsilon}} \tag{14.25}$$

Figure 14.13 shows the new prediction of the first ECAP procedure with the hardening parameters that reflect the torsion stress–strain curve. This figure should be compared to Fig. 14.10, which used the compression stress–strain curve. The

Fig. 14.11 Predicted (dashed-line) variation of $\hat{\sigma}_\epsilon$ with strain using model parameters in Table 14.1 established for the compression stress–strain curve shown in Fig. 14.3 compared to the torsion stress–strain curve

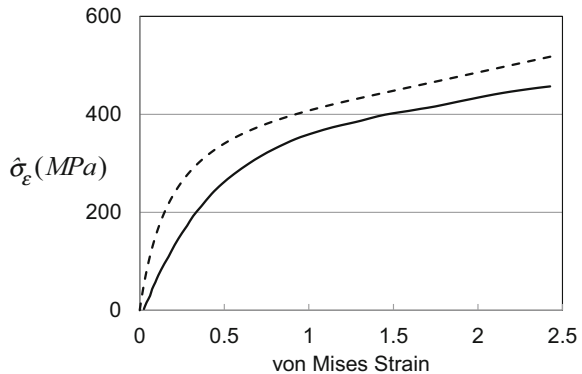


Fig. 14.12 Predicted (dashed-line) variation of $\hat{\sigma}_\epsilon$ with strain using modified model parameters ($\hat{\sigma}_{\epsilon_{SO}}$ and A_o) compared to the torsion stress-strain curve

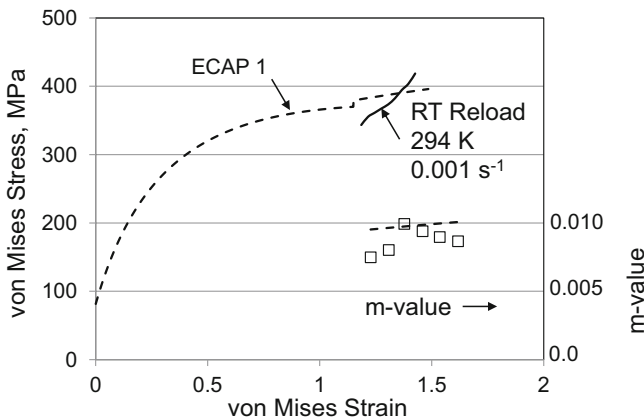
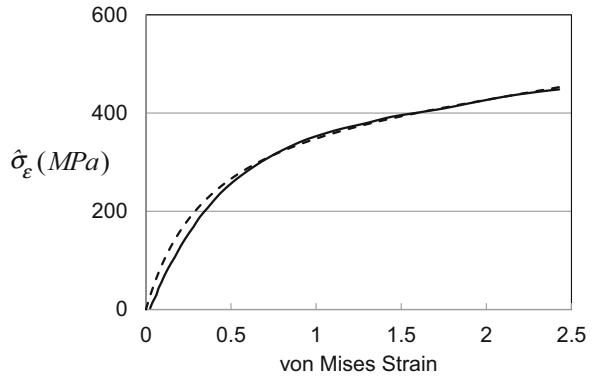


Fig. 14.13 Predicted (dashed-line) stress-strain curve for one ECAP pressing plus a RT reload in copper. This prediction differs from that in Fig. 14.10 in that in this case the hardening curve is derived from the torsion stress-strain curve. Included (right ordinate) are the measured and predicted m -values

predicted reload stresses are much closer to the measured stresses, although the measured hardening rate during the reload is well above that predicted. The predicted strain-rate sensitivities are also closer to the measured values than in Fig. 14.10.

Similar predictions can be performed for all of the processing cycles. For multiple pressings, it is assumed that the work piece cools to RT before subsequent pressing. Figures 14.14, 14.15, and 14.16 show the predicted loading and predicted and measured reloading stress strain curves and predicted and measured strain-rate sensitivities for two pressings, four pressings, and eight pressings. After two pressings, the reload yield stress is closely estimated, but the rate of strain hardening in the reload curve is higher than predicted. After four and eight pressings, the reload yield

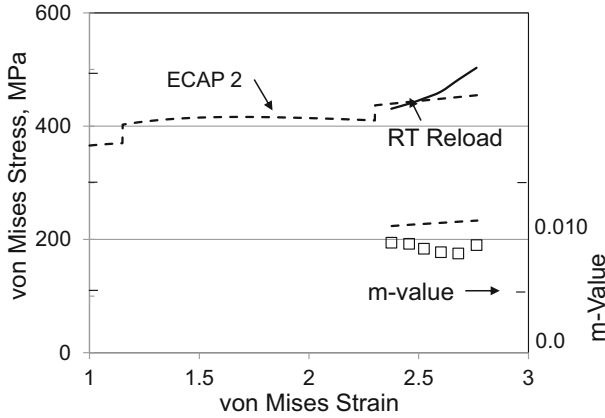


Fig. 14.14 Predicted (dashed-line) stress–strain curve for two ECAP pressings plus a RT reload in copper compared to the reload stress–strain curve measured by Dalla Torre et al. [7]. Included (right ordinate) are the measured and predicted m -values

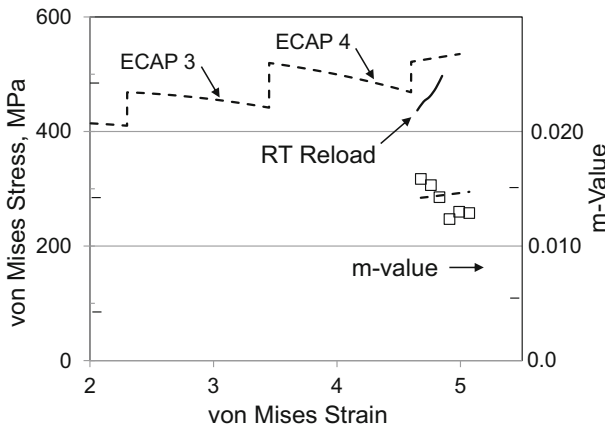


Fig. 14.15 Predicted (dashed line) stress–strain curve for four ECAP pressings plus a RT reload in copper compared to the reload stress–strain curve measured by Dalla Torre et al. [7]. Included (right ordinate) are the measured and predicted m -values

stress is increasingly overestimated. The agreement between the measured and predicted strain-rate sensitivities is fairly good.

The divergence between the measured and predicted yield stresses with increased pressings could result from the adiabatic temperature rise. From Eq. 6.32 the temperature increases as the stress level increases. The predicted maximum temperature at the end of the fourth pressing is 439 K, and the predicted maximum temperature rise at the end of the eight pressing is 478 K. For heavily cold worked copper, the recrystallization temperature is below 473 K even approaching 373 K [29]. It is quite possible that the microstructure is undergoing partial recrystallization

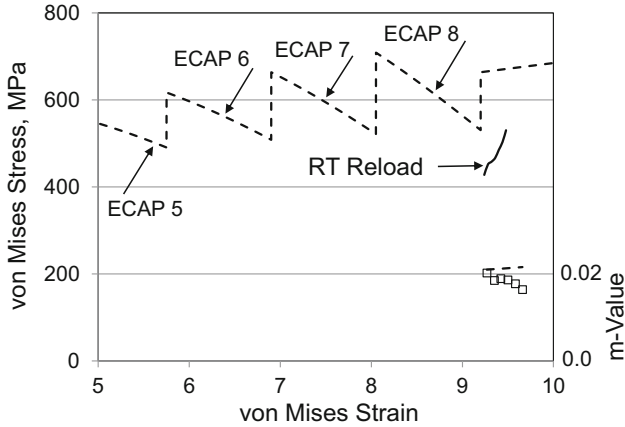


Fig. 14.16 Predicted (dashed-line) stress–strain curve for eight ECAP pressings plus a RT reload in copper compared to the reload stress–strain curve measured by Dalla Torre et al. [7]. Included (right ordinate) are the measured and predicted m -values

during these latter stage pressings, which acts to increase the difference between the predicted and measured stress levels.

Another observation in Figs. 14.13 through 14.16 is that the strain-rate sensitivity increases with pressings. This follows directly from the variation of g_{oe} with stress discussed in Sect. 14.2 and modeled using Eq. 14.10. The predictions generally track the measurements.

Gray et al. [30] studied the reload stress–strain behavior of 0.9998 Cu deformed by ECAP to large strains.⁸ Unique to these experiments is the use of variable reload temperature (including 77 K) and strain rate (to 4000 s^{-1}). Figure 14.17 compares the predicted ECAP 8P stress–strain curve and the predicted reload stress–strain curve in compression at 298 K and 0.001 s^{-1} with the stress–strain curve measured by Gray et al. For these model predictions, the athermal stress was taken as 40 MPa, and no $\hat{\sigma}_i$ was used in Eq. 14.23. Included in this figure is the Dalla Torre et al. reload curve in compression at 294 K and 0.001 s^{-1} for material subjected to eight pressings.

The reload stress levels in the two measurements are similar, but the rate of strain hardening in the Dalla Torre et al. measurement is higher than that in the Gray et al. measurement. Figure 14.18 shows the Gray et al. result at a reload temperature of 77 K and a strain rate of 0.001 s^{-1} . Whereas there was almost no strain hardening in the 298 K reload, the hardening in the 77 K reload is significant. The comparison for the reload at 298 K and 4000 s^{-1} is shown in Fig. 14.19. Once again, the reload yield stress is well under-predicted, but the rate of strain hardening is quite high. Note that this reload prediction assumes adiabatic deformation; accordingly, the stress level

⁸Communication with R. Valiev indicated these deformations involved at least eight pressings.

Fig. 14.17 Predicted (dashed-line) stress–strain curve for eight ECAP pressings plus a RT reload in copper compared to the reload stress–strain curve measured by Gray et al. [30]. Included (short-dashed line) is the measurement of Dalla Torre et al. for similarly processed copper

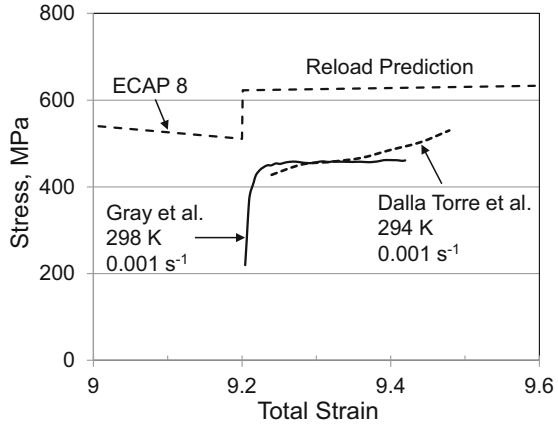
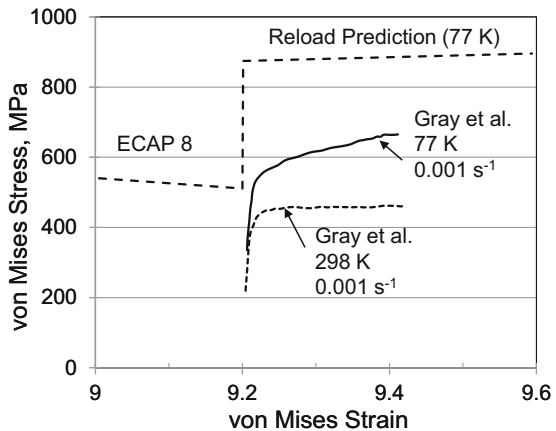


Fig. 14.18 Predicted (dashed-line) stress–strain curve for eight ECAP pressings plus a 77 K reload in copper compared to the reload stress–strain curve measured by Gray et al. [30]. Included (short-dashed line) is the RT reload stress–strain curve for comparison



decreases slightly as the specimen heats and the stress decrease associated with the temperature increase is larger than the rate of Stage IV hardening.

Gray et al. measured reload stress–strain curve at five combinations of temperature and strain rate. Three of these are indicated in Figs. 14.17 through 14.19. The remaining two loading conditions include 298 K and 0.10 s^{-1} and 77 K and 3750 s^{-1} . The measured and predicted yield stresses are plotted versus the standard temperature and strain rate function in Fig. 14.20. Clearly evident in this figure is the difference in stress level, which is the same as that seen in Figs. 14.17 through 14.19.

Several common observations may be drawn from these measurements in highly strained copper. The reload stress levels generally fall below those predicted with Eqs. 14.23, 14.24, 14.25, and the model constants listed in Table 14.1 (with the addition of a $\hat{\sigma}_i$ -term and a slightly larger athermal stress for the Dalla Torre et al. material). Secondly, except for the Gray et al. measurement at 298 K and 0.001 s^{-1} (as well as their measurement at 298 K and 0.1 s^{-1}), the rate of strain hardening is

Fig. 14.19 Predicted (dashed-line) stress–strain curve for eight ECAP pressings plus a RT, 4000 s^{-1} reload in copper compared to the reload stress–strain curve measured by Gray et al. [30]

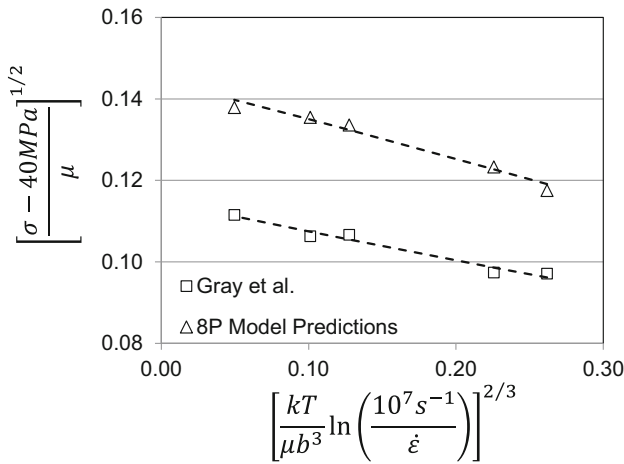
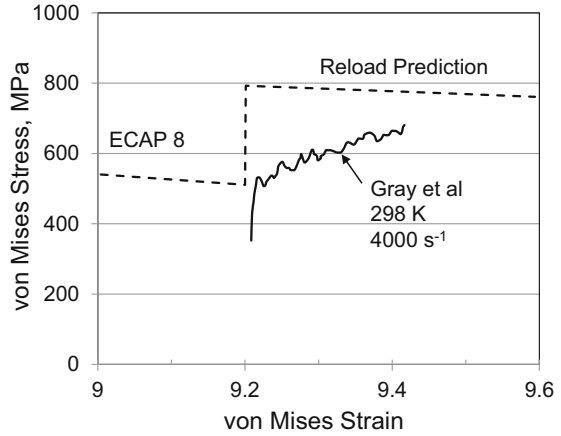


Fig. 14.20 Measured and predicted yield stress as a function of reload test temperature and strain rate after eight ECAP pressings

well above that predicted. Finally, predictions of temperature and strain-rate dependence on material deformed to these high strains are in line with the measured values. These comparisons generally improved with use of the torsion curve rather than the compression curve to establish the strain hardening rate.

14.6 Further Insight into the Strain Hardening at High Strains

The analysis of hardening induced by irradiation damage of Zircaloy-2 and austenitic stainless steel was analyzed in Sects. 10.8 and 11.6, respectively. In these cases the evolving stress–strain behavior during irradiation damage was not predicted. Instead, the availability of temperature-dependent reload stress–strain curves enabled an estimate of which mechanical threshold stress was evolving due to the damage and moreover to estimate how much the identified threshold stress increased. With the observation that hardening due to large-strain ECAP processing is less than predicted, it is possible to use a similar approach to analyze ECAP-induced strengthening.

The procedure entails starting with the measured yield stresses as a function of reload test temperature and strain rate and identifying a value of $\hat{\sigma}_\epsilon$ in Eq. 14.23 that provides the best fit to the reload yield stress. Note that in these computations, Eq. 14.19 (for g_{oe}) and Eq. 14.24 (for $d\hat{\sigma}_\epsilon/d\epsilon$) are used as straining progresses. Figure 14.21 shows the result for the reload after the first ECAP pass of the Del Torre et al. experiments. The dashed line is the prediction for $\hat{\sigma}_\epsilon = 325$ MPa. The computed value of $\hat{\sigma}_\epsilon$ after the first pass is 385 MPa, which is above the value of 325 MPa used in Fig. 14.21. This prediction should be compared to that shown in Fig. 14.13, where the reload yield stresses were overpredicted. Also shown in Fig. 14.21 are the predicted and measured m -values.

Figure 14.22 shows the prediction for the reload after the second pass. For these predictions, the initial value of $\hat{\sigma}_\epsilon$ was taken as 325 MPa, which was the value estimated at the end of the first pass. However, $\hat{\sigma}_\epsilon$ is allowed to evolve with

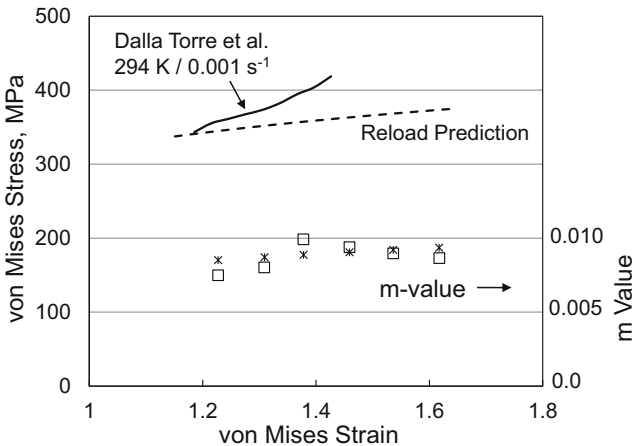


Fig. 14.21 Measured and predicted stress–strain curve and strain-rate sensitivity for the 294 K, 0.001 s^{-1} reload after the first ECAP cycle. For this prediction $\hat{\sigma}_\epsilon$ at the start of the reload was set to 325 MPa

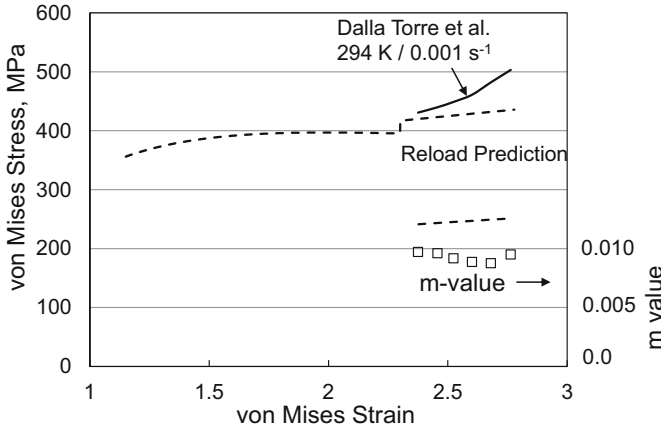
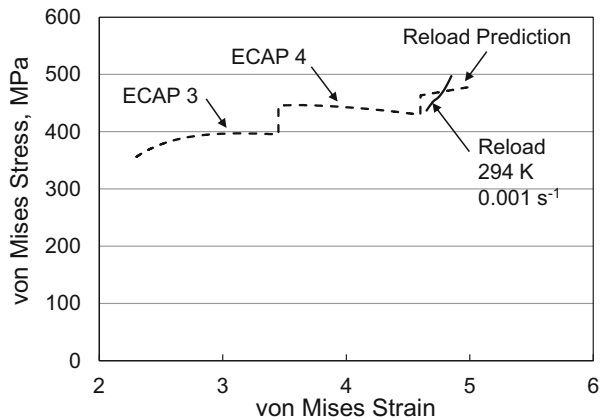


Fig. 14.22 Measured and predicted stress–strain curve and strain-rate sensitivity for the 294 K, 0.001 s^{-1} reload after the second ECAP cycle. For this prediction $\hat{\sigma}_\epsilon$ at the start of the reload was set to 325 MPa

Fig. 14.23 Measured and predicted stress–strain curve and strain-rate sensitivity for the 294 K, 0.001 s^{-1} reload after the fourth ECAP cycle. For this prediction $\hat{\sigma}_\epsilon$ at the start of the reload was set to 325 MPa



continued straining per Eq. 14.24. In this case, the reload stress after the second ECAP process is closely predicted. There is no need to further adjust $\hat{\sigma}_\epsilon$ for ECAP processes three and four.

Figure 14.23 shows the prediction for the third and fourth ECAP processing steps plus the 294 K, 0.001 s^{-1} reload. As stated above, the third processing step began with $\hat{\sigma}_\epsilon = 325 \text{ MPa}$, and $\hat{\sigma}_\epsilon$ was allowed to evolve. In fact, at the end of the fourth cycle, $\hat{\sigma}_\epsilon$ is predicted to rise to 512 MPa. In this case, however, the reload yield stress after the fourth cycle is overpredicted, which implies $\hat{\sigma}_\epsilon$ is not as high as 512 MPa. Figure 14.24 shows a prediction for the reload with $\hat{\sigma}_\epsilon$ at the start of the reload decreased to 462 MPa. Included in Fig. 14.24 are the predicted m -values. (In this case the von Mises strain accumulated during the reload step is plotted.) These predictions should be compared to those shown in Fig. 14.15, where $\hat{\sigma}_\epsilon$ was allowed to evolve without the adjustments.

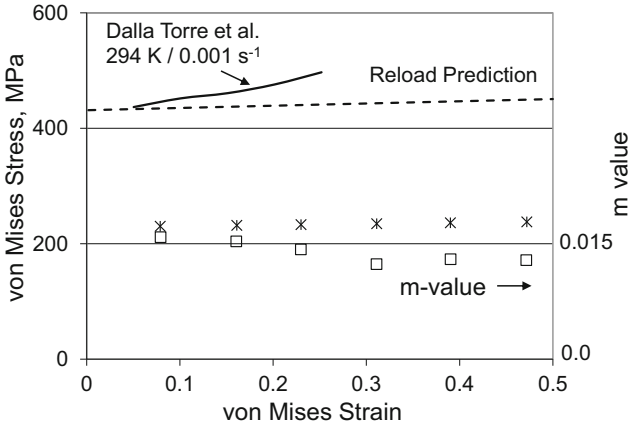
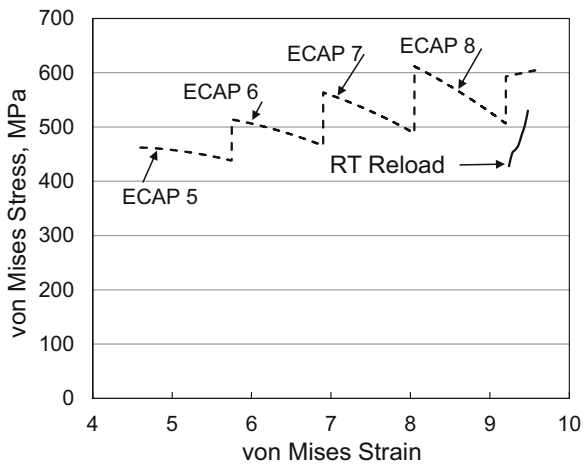


Fig. 14.24 Measured and predicted stress–strain curve and strain-rate sensitivity for the 294 K, 0.001 s^{-1} reload after the fourth ECAP cycle. For this prediction $\hat{\sigma}_\epsilon$ at the start of the reload was set to 462 MPa

Fig. 14.25 Measured and predicted stress–strain curve and strain-rate sensitivity for the fifth through eighth ECAP cycles along with the 294 K, 0.001 s^{-1} reload after the eighth ECAP cycle. For this prediction $\hat{\sigma}_\epsilon$ at the start of the fifth ECAP cycle reload was set to 462 MPa



For the fifth through eighth ECAP cycles, $\hat{\sigma}_\epsilon$ at the start of the fifth cycle is set to 462 MPa. Figure 14.25 shows the predicted behavior for these cycles, including the predicted 294 K, 0.001 s^{-1} reload, and the measured reload stress–strain curve. In this case, $\hat{\sigma}_\epsilon$ at the end of the eighth cycle is predicted to rise to 507 MPa. As shown, however, this leads to an overprediction of the reload yield stress. Figure 14.26 shows the predicted reload after the eighth ECAP cycle with $\hat{\sigma}_\epsilon$ at the start of the reload set back to 462 MPa, which is exactly the value set at the start of the fifth ECAP cycle. The implication is that there has been no additional strain hardening during the fifth through eighth ECAP cycles.

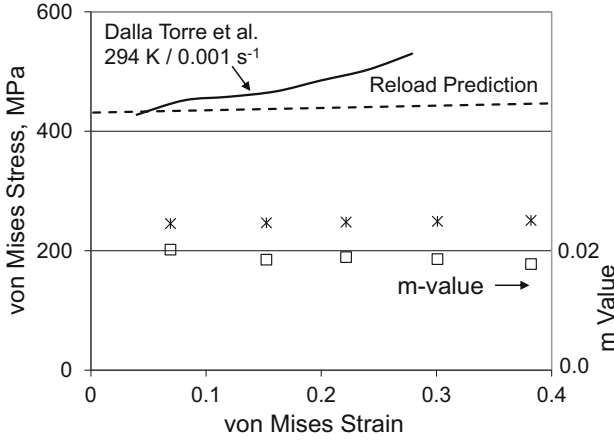
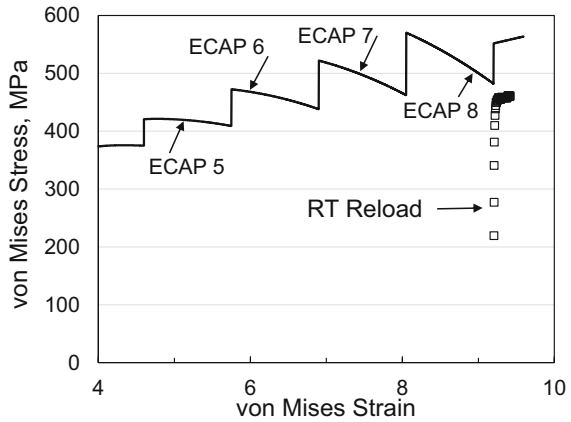


Fig. 14.26 Measured and predicted stress–strain curve and strain-rate sensitivity for the 294 K, 0.001 s^{-1} reload after the eighth ECAP cycle. For this prediction $\hat{\sigma}_\epsilon$ at the start of the reload was set to 462 MPa

Fig. 14.27 Measured and predicted stress–strain curve and strain-rate sensitivity for the fifth through eighth ECAP cycles of the Gray et al. experiments along with the 298 K, 0.001 s^{-1} reload after the eighth ECAP cycle. For this prediction $\hat{\sigma}_\epsilon$ at the start of the fifth ECAP cycle reload is set to 462 MPa



The same analysis is possible for the experiments of Gray et al. Recall a few of the model constants change slightly in these predictions. Figure 14.27 shows the predicted stress–strain curves for the fourth through eight ECAP cycles, the predicted 298 K, 0.001 s^{-1} reload, and the measured reload. For this prediction, the initial value of $\hat{\sigma}_\epsilon$ at the start of the fifth cycle was set at 462 MPa⁹ since this was the value deduced from the Del Torre et al. measurements described above. As in Fig. 14.25, with this starting value of $\hat{\sigma}_\epsilon$ the reload yield stresses are overpredicted, again suggesting that strain hardening is very much less than assumed.

⁹In order to have $\hat{\sigma}_\epsilon$ at the start of the fifth cycle equal to 462 MPa, the value of $\hat{\sigma}_\epsilon$ at the start of the fourth cycle was set to 368 MPa.

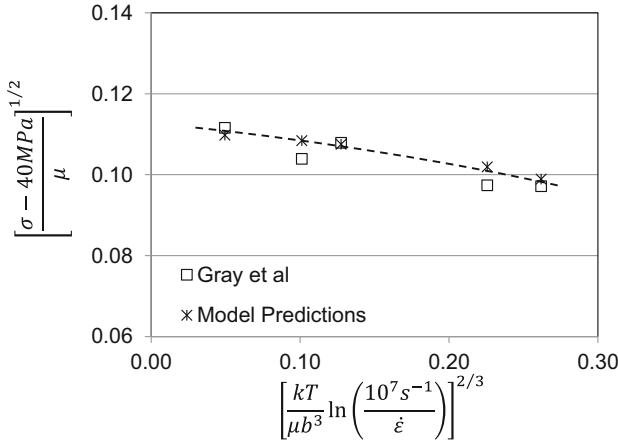


Fig. 14.28 Yield stress versus temperature and strain rate for the Gray et al. experiments. For these predictions, $\hat{\sigma}_\epsilon$ was set to 559 MPa

Fig. 14.29 Measured and predicted stress–strain curves for the reloads after the eighth ECAP cycle at three temperature and strain rate conditions. For these predictions $\hat{\sigma}_\epsilon$ at the start of the fifth ECAP cycle reload is set to 559 MPa

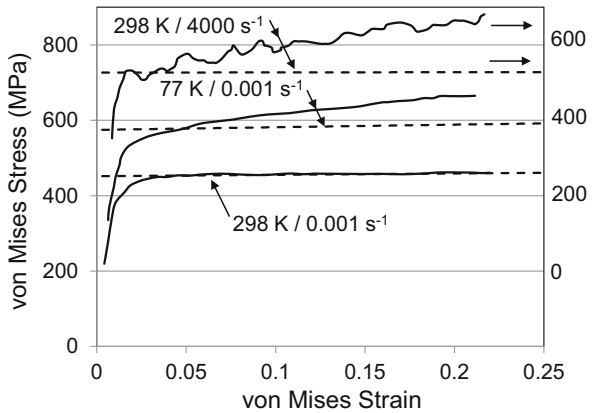
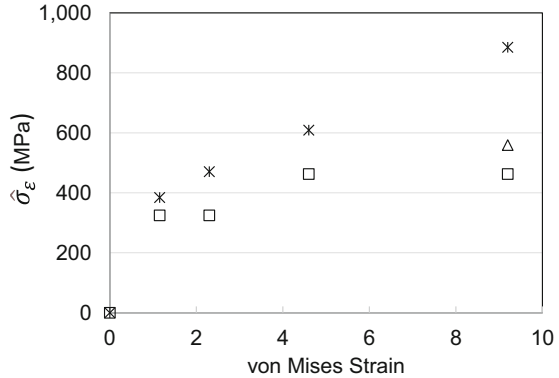


Figure 14.28 shows the predicted variation of yield stress with temperature and strain rate when $\hat{\sigma}_\epsilon$ is set at 559 MPa. The computed value of $\hat{\sigma}_\epsilon$ for eight passes is 886 MPa (without adjusting any $\hat{\sigma}_\epsilon$ values), which is well above the value of 559 MPa used in Fig. 14.28. Importantly, the lower value of $\hat{\sigma}_\epsilon$ enables a close fit with the stress levels—as well as the temperature and strain-rate dependence of the reload yield stress.

Figure 14.29 compares the measured reload stress–strain curves after the eighth cycle with the predicted behavior for three of the conditions used by Gray et al. Again, $\hat{\sigma}_\epsilon$ at the start of the reloads was set at 559 MPa. As in Fig. 14.28, good agreement is obtained for the reload yield stresses for these three tests. The rate of strain hardening between the predictions and measurements agrees for the 298 K, 0.001 s^{-1} test, but for the other tests, the measured rate of strain hardening is higher than predicted.

Fig. 14.30 Variation of $\hat{\sigma}_\epsilon$ with strain. The cross-hatched stars are the prediction based solely on Eq. 14.24. The open squares and the open diamond are the values selected to achieve agreement between the measured and predicted reload yield stresses from the Torre et al. and Gray et al. measurements



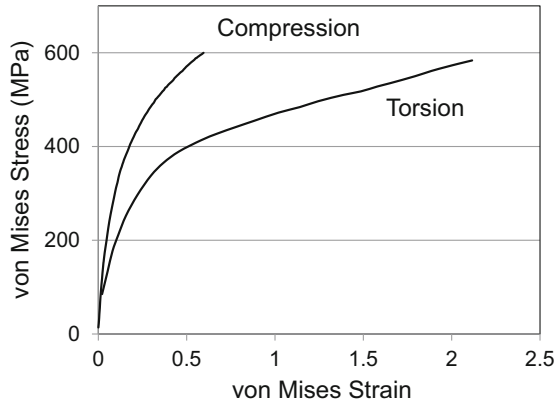
The value of $\hat{\sigma}_\epsilon$ selected for the reload after the eighth cycle in the Gray et al. measurements (559 MPa) is higher than that selected for the Del Torre et al. measurements (462 MPa). Nonetheless, these values are considerably below the values derived using Eq. 14.24. Figure 14.30, which shows the predicted and deduced increase of $\hat{\sigma}_\epsilon$ with von Mises strain, summarizes the results. After the first ECAP cycle at a strain of 1.15, $\hat{\sigma}_\epsilon$ falls only slightly below the value predicted using Eq. 14.24. This was shown graphically in Fig. 14.21 where the value of $\hat{\sigma}_\epsilon$ that led to good agreement with the measured yield stress was only 60 MPa below that predicted. After the second ECAP cycle at a strain of 2.30, this difference has increased to 151 MPa. The difference continues to rise with strain. The conclusion is that strain hardening is saturating at a lower stress level than predicted. The tendency to saturate is consistent with the contribution of dynamic recrystallization. However, this also might reflect that strain hardening does not proceed indefinitely according to Eq. 14.24.

In the next section, the analysis of the large-strain hardening of nickel will generally support the observations reached in copper. Sections 14.8 and 14.9 will consider the large-strain processing of nickel and austenitic stainless steels to assess whether the observations in copper apply to these material systems as well.

14.7 A Large-Strain Constitutive Description of Nickel

The large-deformation stress–strain behavior of pure nickel also has been extensively studied. Hughes [28] used torsion experiments in nickel and nickel-cobalt alloys. Figure 14.31 shows the RT stress–strain curve at a shear strain rate of 0.001 s^{-1} . The shear stresses have been converted to von Mises effective stresses. (See Box 1.2 entitled Scalar Stress Representations.) Included in Fig. 14.31 is a compression curve in Ni-270 presented in Sect. 8.6. In this case the difference between the compression and torsion curves is larger than observed in copper in Fig. 14.3. Even though curves in Fig. 14.31 are not in identical materials (purity

Fig. 14.31 Large strain stress–strain curves in pure nickel. The torsion curve is from Hughes [28]. The compression curve is the result for Ni270 from Sect. 8.6



levels and grain size), most of the difference between the torsion and compression curves arises from the development of deformation texture. Whereas in the previous section the large-strain compression curve was used to establish the hardening law, in this case the large-strain torsion curve will be used.

Except for use of the large-strain torsion curve to establish the hardening behavior, the analysis proceeds as in Sect. 14.5 for copper. Because a small impurity obstacle (presumed to be carbon) was included for Ni270, Eq. 14.18 is used (note that the small σ_i term used in the Ni270 analysis is omitted). Equations 14.19 through 14.22 must be adjusted to reflect deformation in nickel. Without data showing how $g_{o\epsilon}$ varies with σ_ϵ in nickel, it is assumed that the variation expressed by Eq. 14.19 is identical to that observed in copper. The coefficients in Eq. 14.18 are replaced with the coefficients for Ni 270 (see Table 8.7), and the physical constants for nickel also are inserted into these equations. The kinetics of evolution will be assumed to follow those established for Ni 270 in Sect. 8.6 and summarized in Table 8.9. The variation of $\hat{\sigma}_\epsilon$ with strain is computed (as in copper) from the true stress versus true strain torsion data set by finding for each value of von Mises stress the value of $\hat{\sigma}_\epsilon$ that satisfies Eqs. 14.14 with 14.10 in nickel. Starting with the constants in Table 8.9 (in particular, $A_o = 4600$ MPa and $\hat{\sigma}_{\epsilon so} = 1260$ MPa), Fig. 14.32 shows the calculated $\hat{\sigma}_\epsilon$ versus strain (dashed line) compared to the values deduced using Eq. 14.14 (with the model variables for nickel; see Eq. 14.28). For this calculation, the value of $\theta_{II} = 130$ MPa is chosen to match the high strain rate of strain hardening. It is evident in Fig. 14.32 that the stresses are well overpredicted. This can be remedied by adjusting values of A_o and $\hat{\sigma}_{\epsilon so}$ to give improved agreement. Figure 14.33 shows the same plot with $A_o = 2583$ MPa and $\hat{\sigma}_{\epsilon so} = 870$ MPa.

With the large changes to A_o and $\hat{\sigma}_{\epsilon so}$ going from the calculations in Fig. 14.32 to those in Fig. 14.33, the effect of these changes in evaluation of Eq. 14.14 due to the $g_{o\epsilon}$ calculation in Eq. 14.19 needs to be evaluated. Figure 14.34 shows the computed variation of s_ϵ with strain for both of these cases. As expected, s_ϵ decreases with increasing strain. The difference between the values for the two sets of model parameters is fairly insignificant. This likely relates to the fact that these parameters enter into Eq. 14.19 as the ratio $\hat{\sigma}_\epsilon/\hat{\sigma}_{\epsilon s}$.

Fig. 14.32 Deduced variation of $\hat{\sigma}_\epsilon$ with strain for the torsion curve in pure nickel reported by Hughes [28]. The dashed line is the fit to Eq. 14.28

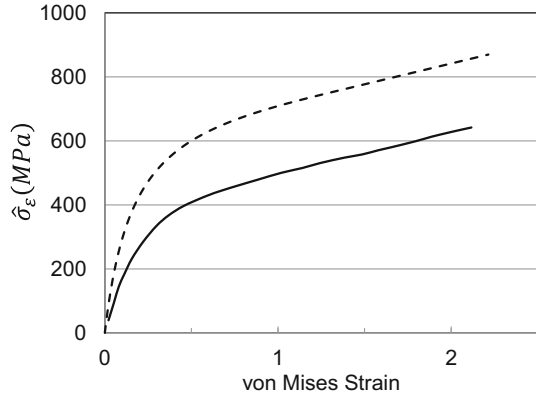


Fig. 14.33 Deduced variation of $\hat{\sigma}_\epsilon$ with strain for the torsion curve in pure nickel reported by Hughes [28] with A_o and $\hat{\sigma}_{\epsilon SO}$ adjusted to achieve agreement with the experimental curve. The dashed line is the fit to Eq. 14.28 with the new model constants

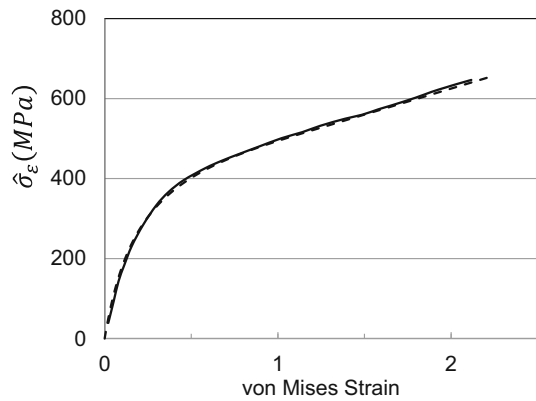
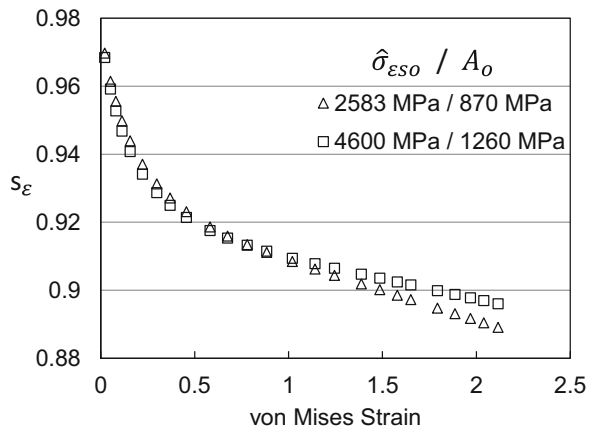


Fig. 14.34 Variation of s_ϵ (see Eq. 14.14) with strain illustrating that the changes in model constants (A_o and $\hat{\sigma}_{\epsilon SO}$) have a negligible effect on s_ϵ



The constitutive equation for large-strain deformation in pure nickel, fit to the Hughes measurement in torsion, becomes

$$\frac{\sigma}{\mu} = \frac{50 \text{ MPa}}{\mu} + \left\{ \left[1 - \frac{kT}{\mu b^3 g_{oe}(\hat{\sigma}_\varepsilon)} \ln \frac{10^7 s^{-1}}{\dot{\varepsilon}} \right] \right\}^{3/2} \frac{\hat{\sigma}_\varepsilon}{\mu_o} \quad (14.26)$$

with

$$g_{oe} = \left(4.7 - \frac{kT}{\mu b^3} \ln \left(\frac{\dot{\varepsilon}_o}{\dot{\varepsilon}} \right) \right) \left(\frac{1}{1 + 3.16 \frac{\hat{\sigma}_\varepsilon}{\hat{\sigma}_{es}}} \right) \quad (14.27)$$

and

$$\frac{d\hat{\sigma}_\varepsilon}{d\varepsilon} = \theta_{II}(\dot{\varepsilon}) \left(1 - \frac{\hat{\sigma}_\varepsilon}{\hat{\sigma}_{es}(\dot{\varepsilon}, T)} \right)^2 + 130 \text{ MPa} \quad (14.28)$$

The Stage II hardening rate comes from Eq. 6.29, which with the fitted model parameters is

$$\theta_{II} = 2583 \text{ MPa} + 13 \text{ MPa} \ln \dot{\varepsilon} + 2.0 \text{ MPa} s^{-1/2} \sqrt{\dot{\varepsilon}} \quad (14.29)$$

which is identical to the expression used for nickel in Sect. 8.5 except for the value of the first coefficient A_o .

The equation for the temperature and strain-rate dependence of the saturation threshold stress is

$$\ln \hat{\sigma}_{es} = \ln (870 \text{ MPa}) + \frac{kT}{\mu b^3 (0.168)} \ln \frac{\dot{\varepsilon}}{10^8 s^{-1}} \quad (14.30)$$

which is identical to the expression used for the nickel analyses in Sect. 8.5 except for the value of $\hat{\sigma}_{eso}$ (870 MPa).

Figure 14.35 compares the prediction of Eqs. 14.26 through 14.30 to the Hughes torsion measurement in nickel. The prediction is observed to closely match the experiment.

Except for the addition of Stage IV hardening (Eq. 14.28), a stress-dependent g_{oe} (Eq. 14.27), and the adjustment of two parameters (A_o and $\hat{\sigma}_{eso}$) to enable agreement with Hughes' large-strain torsion test, the constitutive model is the same as presented in Sect. 8.5. Predictions of these equations for ECAP processed metal are described in the next section.

Fig. 14.35 Predicted and measured large-strain stress–strain curve in pure nickel

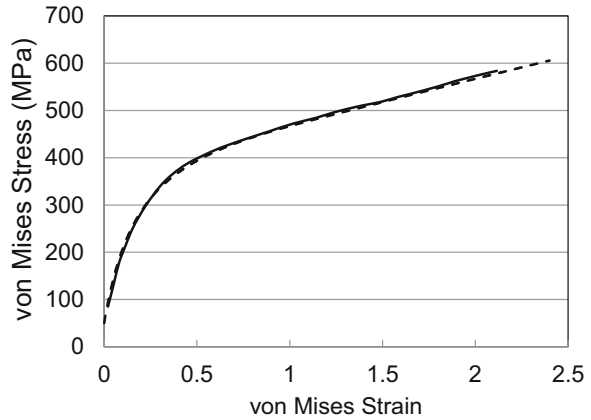
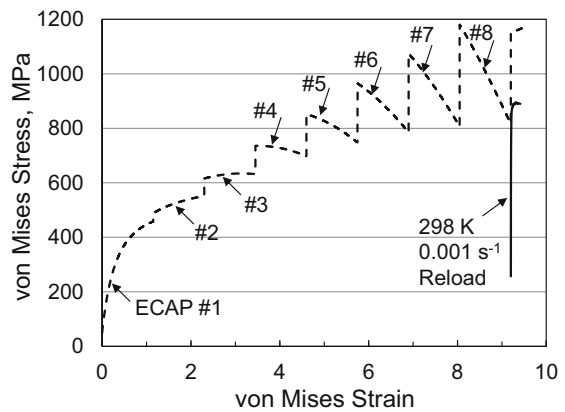


Fig. 14.36 Measured (solid line) and predicted (dashed-line) stress–strain curves for pure nickel subjected to eight ECAP pressings. The reload measurement is from Gray et al. [30]



14.8 Application to Large-Strain ECAP Processing of Nickel

Grey et al. [30] measured the reload stress–strain behavior of 99.99% nickel processed by ECAP (see footnote VI). As in the measurements of this research group in copper described in Sect. 14.5, the stress–strain response was measured at various temperatures and strain rates. Figure 14.36 shows the predicted stress–strain curve through eight ECAP cycles and the measured and predicted curve for the reload at 298 K and a strain rate of 0.001 s^{-1} . These predictions are calculated using Eqs. 14.26 through 14.30. The strain rate during each ECAP cycle is assumed to be 1 s^{-1} , and deformation is assumed to be adiabatic. As observed in copper in

Figs. 14.14, 14.15, and 14.16, the temperature rises during the ECAP cycle but falls back to room temperature for the next cycle; the stresses thus rise at the start of subsequent ECAP cycles.

At strains exceeding 1.59, which is reached in the second ECAP cycle, continued hardening only occurs through the Stage IV term in Eq. 14.28. As the stresses continue to rise, the temperature rise increases, and the delta between the beginning stress level and the ending stress level for each cycle increases. For the eighth cycle, the final temperature is estimated to be 547 K—a 253 K increase from the starting temperature. Figure 14.37 focuses on the reload behavior. The predicted reload yield stress is low by ~285 MPa. There is almost no strain hardening observed in the measurement. In fact, the predicted rate of strain hardening is also quite low. This is very similar to the Gray et al. measurement shown in copper in Fig. 14.17.

The measured and predicted stress–strain curves for the reload at 77 K and 0.001 s⁻¹ are shown in Fig. 14.38. Once again, the measured reload yield stress is much lower than the predicted value, but in this case the measured rate of strain hardening is significant and does not match the prediction. This, too, mirrors the

Fig. 14.37 Measured (solid line) and predicted (dashed-line) stress–strain curves showing the reload behavior for pure nickel subjected to eight ECAP pressings. The measurement is from Gray et al. [30]

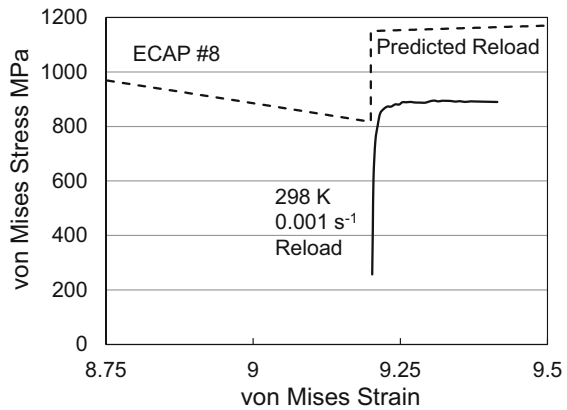


Fig. 14.38 Measured (solid line) and predicted (dashed-line) stress–strain curves showing the reload behavior for pure nickel subjected to eight ECAP pressings and reloaded at 77 K. The measurement is from Gray et al. [30]

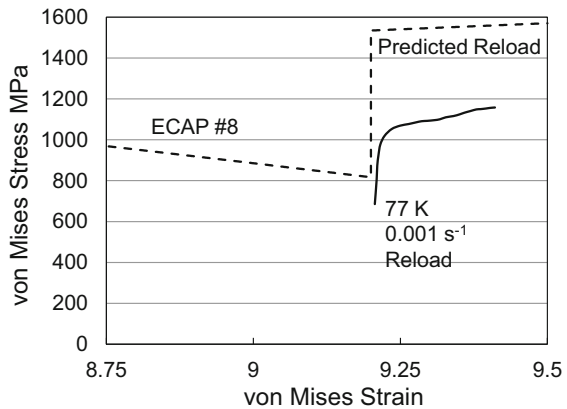


Fig. 14.39 Measured (solid line) and predicted (dashed-line) stress–strain curves showing the reload behavior for pure nickel subjected to eight ECAP pressings and reloaded at 298 K and a dynamic strain rate. The measurement is from Gray et al. [30]

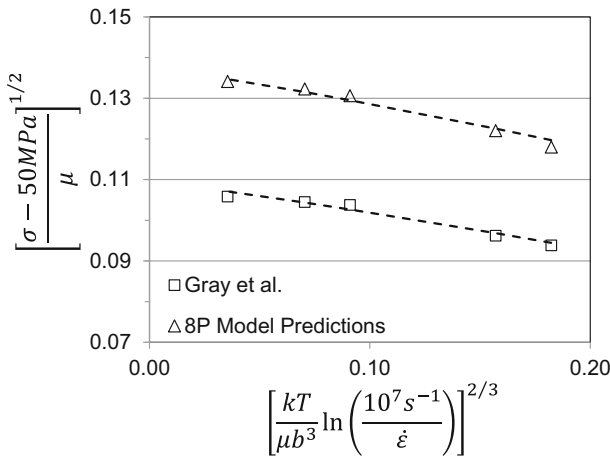
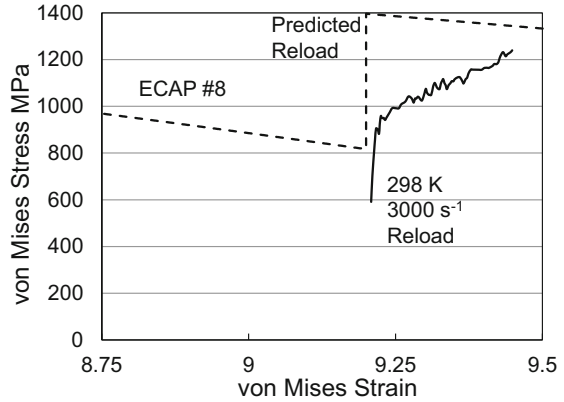


Fig. 14.40 Measured and predicted yield stress versus temperature and strain rate for reloads in pure nickel subjected to eight ECAP pressings

Gray et al. measurement in copper shown in Fig. 14.18. The prediction and measurement for the reload at 298 K and 3000 s^{-1} are shown in Fig. 14.39. In this case the reload is under adiabatic conditions so the stresses decrease with increasing temperature more than the stresses increase with increasing strain. Again, the measured rate of strain hardening in the 77 K reload in Fig. 14.38 and the dynamic reload in Fig. 14.39 is fairly high and differs from that predicted.

Figure 14.40 shows the measured and predicted reload yield stresses as a function of temperature and strain rate. As in the copper reload shown in Fig. 14.20, the measured stresses are lower than those predicted. The temperature and strain-rate dependence of yield, i.e., the slope of the dashed lines through the data points, exhibited by the measurements and predictions are similar.

Fig. 14.41 Measured (solid lines) and predicted (dashed-line) stress–strain curves for reload tests under three temperature and strain-rate conditions in pure nickel subjected to eight ECAP pressings for an assumed value of $\hat{\sigma}_\epsilon$ of 1040 MPa

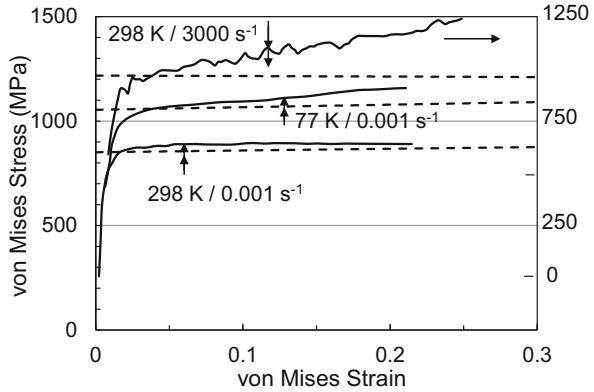
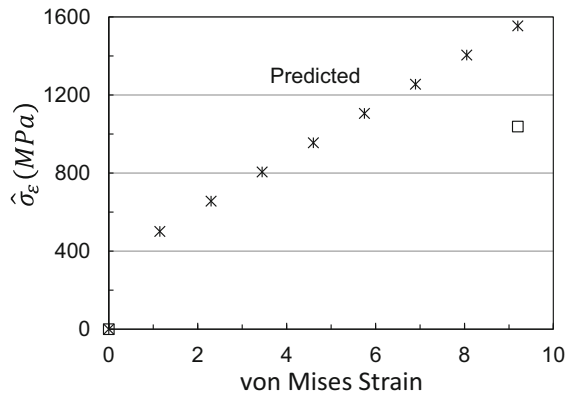


Fig. 14.42 Variation of $\hat{\sigma}_\epsilon$ with strain. The cross-hatched stars are the prediction based solely on Eq. 14.28. The open square is the value selected to achieve agreement between the measured and predicted reload yield stresses after the eighth ECAP cycle



As illustrated in Fig. 14.29, one can begin the reload cycles with an adjusted value of $\hat{\sigma}_\epsilon$ that forces agreement with the reload yield stresses. Figure 14.41 shows this comparison with three of the reload conditions tested by Gray et al. For this prediction, $\hat{\sigma}_\epsilon$ was decreased to 1038 MPa for the start of the reload. This compares to the value of 1554 MPa that is predicted purely with Eq. 14.28. The yield stresses for the three reload conditions compare favorably with the predictions. Figure 14.42 shows the predicted increase of $\hat{\sigma}_\epsilon$ with strain (starred symbols) versus the single value of $\hat{\sigma}_\epsilon$ that forces the yield stresses to agree. The trends are similar to those shown in Fig. 14.30 in copper. For copper, the deduced value of $\hat{\sigma}_\epsilon$ was 63% of the value determined solely with Eq. 14.24. For nickel deduced value of $\hat{\sigma}_\epsilon$ was 67% of the value determined using Eq. 14.28. It is clear that hardening at large strains does not proceed as strongly as specified using these equations.

14.9 Application to Large-Strain ECAP Processing of Austenitic Stainless Steel

Large-strain torsion tests in annealed 304 L stainless steel by Miller and McDowell [31] and reload measurements on ECAP processed 304 L stainless steel by Qu et al. [32] and Huang et al. [33] enable analysis of ECAP-induced hardening in this material in concert with the work presented in Chap. 11 on deformation in austenitic stainless steels. Figure 14.43 show the stress–strain curve measured by Miller and McDowell. The large-strain measurements were in torsion using the thin-walled specimen tube geometry developed by Lindholm et al. [34]. The shear stresses and shear strains have been converted to von Mises stresses and strains using Eq. 8.4. The 304 L stainless steel had an average grain size of 24 μm and nickel, chromium, carbon, and nitrogen compositions of 10.4%, 18.8%, 0.03%, and 0.05%.

Included in Fig. 14.43 is the compression stress–strain curve measured by Miller and McDowell. The von Mises strain rate for both the compression and torsion tests was 0.0004 s^{-1} . Also included is a tension stress–strain curve in 316 L SS measured by Albertini and Montagnani [35] (see Fig. 11.13). Even though the von Mises stresses and strains are plotted in Fig. 14.43, the difference between the strain hardening in torsion and that in tension and compression is notable. This presumably is due to the development of crystallographic texture.

The first step of the analysis is to select model parameters in Eq. 11.1. From the athermal stress term in Eq. 11.1 (with $k_d = 13.7 \text{ MPa mm}^{0.5}$; see Table 11.2), Eqs. 11.5a, and 11.5b, σ_a , $\hat{\sigma}_i$, and $\hat{\sigma}_N$ become 68.5 MPa, 508 MPa, and 182 MPa, respectively. Table 14.2 lists the values of these parameters. All other model parameters for these equations are identical to those listed in Table 11.3 (Fit 1) and in the paragraph following Eq. 11.3.

Fig. 14.43 Large strain torsion stress–strain curves measured in 304 L stainless steel by Miller and McDowell [31]. Included are the measurement in compression and a stress–strain curve measured by Albertini and Montagnani [35] in 316 L stainless steel

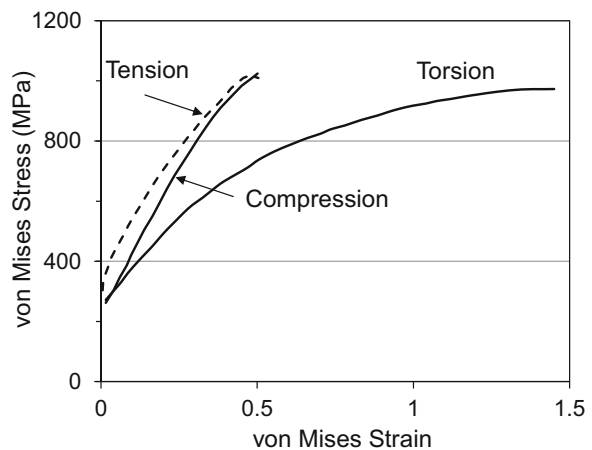


Table 14.2 Selected model parameters for the Miller and McDowell [31] stainless steels

Model parameter	Value		
	304 L SS	316 L	304 L SS
Miller and McDowell (torsion)		Albertini and Montagnani (tension) Tables 11.6 and 11.7	Qu et al. (tension)
$\hat{\sigma}_a$ (MPa)	68.5	50	50
$\hat{\sigma}_i$ (MPa)	508	572	286
$\hat{\sigma}_N$ (MPa)	182	243	79
$\hat{\sigma}_{eso}$ (MPa)	1500	2600	4000
A_0 (MPa)	2100	3120	2600

The next step in the analysis is to follow the approach introduced in Sect. 14.5.1 and implemented in Sect. 14.7 for nickel to establish the large-strain evolution behavior. That is, the model parameters $\hat{\sigma}_{eso}$ and θ_{II} listed in Table 11.6 will do well at representing the tension and compression curves in Fig. 14.43 but will overestimate the stress levels in torsion. As in nickel, the torsion curve is analyzed, and the values of $\hat{\sigma}_{eso}$ and θ_{II} are scaled from those listed in Table 11.6. The estimated values of these model parameters are included in Table 14.2. The operative constitutive law for room temperature deformation for the Miller and McDowell material is

$$\frac{\sigma}{\mu} = \frac{\sigma_a}{\mu} + s_i(\dot{\epsilon}, T) \frac{\hat{\sigma}_i}{\mu_o} + s_N(\dot{\epsilon}, T) \frac{\hat{\sigma}_N}{\mu_o} + s_\epsilon(g_{oe}, \dot{\epsilon}, T) \frac{\hat{\sigma}_\epsilon}{\mu_o} \quad (14.31)$$

For deformation at 294 K and a strain rate of 0.0004 s^{-1} , this equation becomes

$$\begin{aligned} \frac{\sigma}{\mu} = & \frac{50 \text{ MPa}}{\mu} + \frac{65.7 \text{ MPa}}{\mu_o} + \frac{125.2 \text{ MPa}}{\mu_o} \\ & + + \left\{ 1 - \frac{kT}{\mu b^3 g_{oe}(\hat{\sigma}_\epsilon)} \ln \frac{10^7 \text{ s}^{-1}}{\dot{\epsilon}} \right\}^{3/2} \frac{\hat{\sigma}_\epsilon}{\mu_o} \end{aligned} \quad (14.32)$$

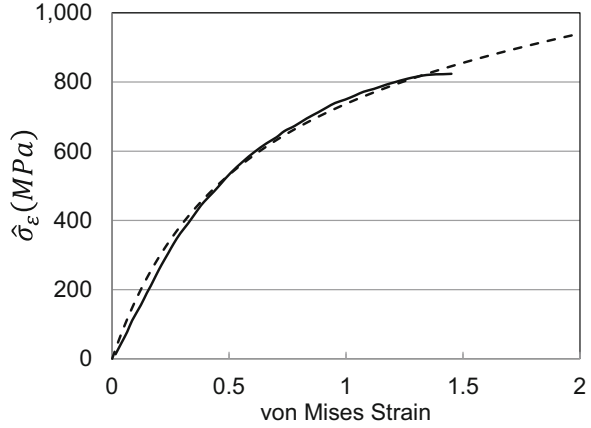
with (assuming the F-factor in Eq. 14.10 does not change)

$$g_{oe} = \left(4.7 - \frac{kT}{\mu b^3} \ln \left(\frac{\dot{\epsilon}_o}{\dot{\epsilon}} \right) \right) \left(\frac{1}{1 + 3.16 \frac{\hat{\sigma}_\epsilon}{\sigma_{es}}} \right) \quad (14.33)$$

and

$$\frac{d\hat{\sigma}_\epsilon}{d\epsilon} = \theta_{II}(\dot{\epsilon}) \left(1 - \frac{\hat{\sigma}_\epsilon}{\hat{\sigma}_{es}(\dot{\epsilon}, T)} \right)^\kappa + \theta_{IV} \quad (14.34)$$

Fig. 14.44 Deduced variation of $\hat{\sigma}_\varepsilon$ with strain for the torsion curve in 304 L stainless steel. The dashed line is the fit to Eq. 14.34



With large-strain stress–strain curves such as shown in Fig. 14.43, it is possible to find a self-consistent variation of $\hat{\sigma}_\varepsilon$ with strain and values of $\hat{\sigma}_{\varepsilon_{SO}}$ and θ_{IV} that satisfy Eqs. 14.31, 14.32, 14.33, and 14.29. Recall that $\hat{\sigma}_{\varepsilon_{SO}}$ and $\hat{\sigma}_\varepsilon$ are related through Eq. 6.26

$$\ln \hat{\sigma}_{\varepsilon S} = \ln (\hat{\sigma}_{\varepsilon_{SO}}) + \frac{kT}{\mu b^3 (g_{\varepsilon_{SO}})} \ln \frac{\dot{\varepsilon}}{\dot{\varepsilon}_{\varepsilon_{SO}}} \quad (6.26)$$

with the model parameters listed in Table 11.6. Figure 14.44 shows the resulting variation of $\hat{\sigma}_\varepsilon$ with strain calculated using the torsion stress–strain curve. The dashed line is the prediction according to Eq. 14.34. For this prediction, $\hat{\sigma}_{\varepsilon S} = 1050$ MPa, $\theta_{II} = 1850$ MPa, $\theta_{IV} = 130$ MPa, and $\kappa = 2$. From Eq. 6.26 with the model parameters in Table 11.6, this value of $\hat{\sigma}_{\varepsilon S}$ follows from $\hat{\sigma}_{\varepsilon_{SO}} = 1500$ MPa. From Eq. 6.29 with the model parameters in Table 11.6, this value of θ_{II} follows from $A_0 = 2100$ MPa.

Equations 14.31 through 14.34 with 6.26 comprise the large-strain constitutive law for 304 L SS that will be applied to ECAP-processed material below. The only missing equation is that expressing the adjusted value of θ_{II} becomes, with the values of the constants listed in Table 11.6,

$$\theta_{II} = 2100 \text{ MPa} + 32 \text{ MPa} \ln \dot{\varepsilon} + 0\sqrt{\dot{\varepsilon}} \quad (14.35)$$

Qu et al. [32] studied ECAP-processed 304 L stainless steel with a starting grain size of 52 μm using reload compression and tension tests and microstructural characterization after one, two, and four pressings. They used 90° dies and a processing temperature of 700 °C. Figure 14.45 shows the tension stress–strain curve in the starting material at room temperature and a strain rate of 0.001 s^{-1} . The lower dashed-line prediction is made using Eq. 14.31, with $\sigma_a = 50$ MPa, $\hat{\sigma}_i = 286$ MPa, and $\hat{\sigma}_N = 79$ MPa, Eq. 6.26 with $\hat{\sigma}_{\varepsilon_{SO}} = 4000$ MPa, and Eq. 14.35, with

Fig. 14.45 Tension stress-strain curve measured by Qu et al. [32] in 304 L stainless steel in the starting condition. The dashed line is the model fit

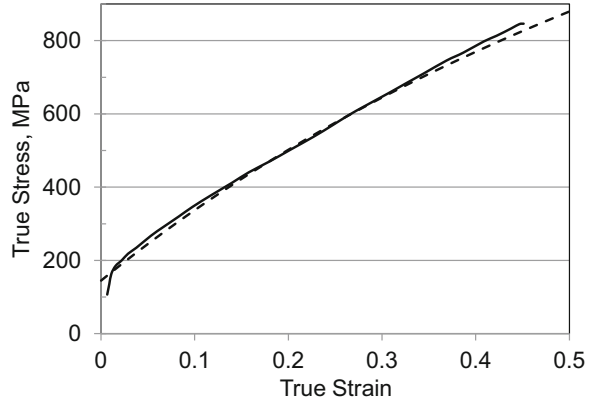
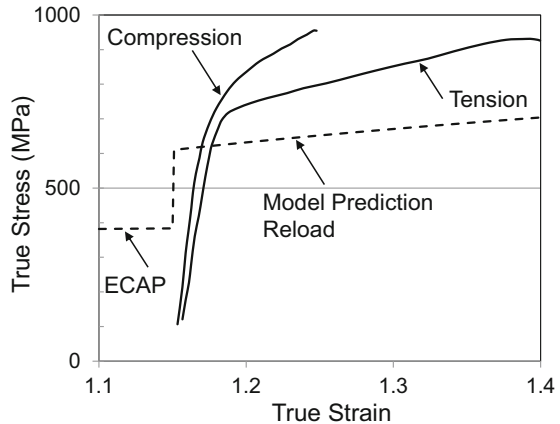


Fig. 14.46 RT, quasi-static reload stress-strain curves measured by Qu et al. [32] in tension and compression in 304 L stainless steel subjected to one ECAP pressing. The short-dashed line is the model prediction

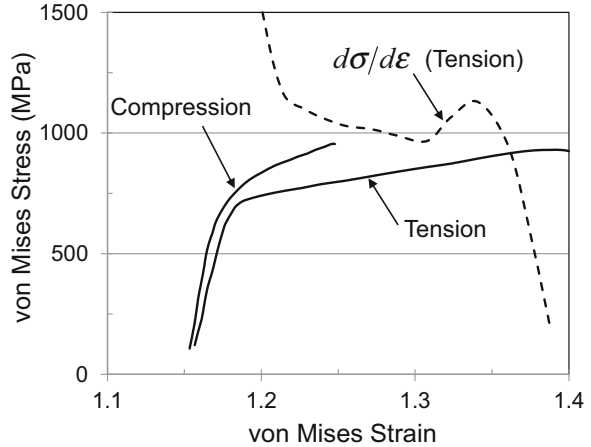


$A_0 = 2600$ MPa. These model constants are included in Table 14.2. All other constants (including κ and θ_{IV}) are as specified above. Several of the model parameters for the evolution equations for tension loading listed in Table 14.2 exceed those for torsion loading. Since ECAP is largely a shear-dominated process, use of the torsion curve to describe the hardening behavior is appropriate. The fit to Eq. 14.31 in Fig. 14.45 is largely to establish values of the threshold stresses ($\hat{\sigma}_i$ and $\hat{\sigma}_N$), which can vary with slight variations in chemistry.

The ECAP processing in the Qu et al. study was at 923°K which, from the related work in Sect. 11.5, is well within the dynamic strain aging regime. Accordingly, the processing stresses are likely to be greater than those predicted using Eqs. 14.31 through 14.35.

Figure 14.46 shows the reload stress-strain curves measured in tension and compression after one ECAP pressing. Qu et al. measured the reload compression curves in multiple orientations; the plotted curves are from an orientation parallel to the axis of the work piece. Included in Fig. 14.46 are the model prediction as using

Fig. 14.47 RT, quasi-static reload stress–strain curves measured by Qu et al. [32] in tension and compression in 304 L stainless steel along with the rate of strain hardening



Eqs. 14.31 through 14.35 with the model constants listed in Table 14.2. At low strains, both the compression and tension curves in Fig. 14.46 show an initial rate of hardening that is approximately linear but at a slope that is $\sim 20\%$ the elastic modulus. This may reflect local yielding. It is difficult to define the yield point because of this initial effect, but the estimated yield for both the tension and compression curves is near the model prediction. The rate of strain hardening at larger strains becomes higher than predicted. This high hardening rate is similar to that observed earlier in copper after one ECAP pressing (Fig. 14.13). The hardening rate in the tension test is less than that in the compression test. However, hardening in tension may be affected by the onset of a plastic instability (the Considère criterion; see Sect. 1.13) which implies local necking may be occurring. Figure 14.47 shows the tension stress–strain curve along with the rate of strain hardening. In the vicinity of a strain of 1.3, the rate of strain hardening is approaching the stress levels, which satisfies the conditions for the onset of a plastic instability.

The comparison after four ECAP pressings is shown in Fig. 14.48. At low strains the slope of the “elastic loading” is still lower than the elastic modulus—but only by a factor of $\sim 33\%$. The origin of differences in this near-yield region behavior between one pressing (Fig. 14.46) and four pressings (Fig. 14.48) is unclear. Given that the temperatures reached in the work piece are greater after four pressings than one pressing due to the higher stresses, one would expect more evidence of this (e.g., recrystallized grains) in the former than in the latter. Based on the model predictions (which do not take into account the stress amplification due to dynamic strain aging), the temperature increase during one pressing is 52 K, whereas the temperature increase during four pressings is 80 K. Given the high temperature of these ECAP processing cycles, these small adiabatic temperature rises may be sufficient to affect dynamic recrystallization. (In their microstructural characterization analysis, Qu et al. [32] noted evidence of more grain refinement in material subjected to four pressings than in material subjected to a single ECAP pressing, but they did not observe recrystallized grains.)

Fig. 14.48 RT, quasi-static reload stress–strain curves measured by Qu et al. [32] in tension and compression in 304 L stainless steel subjected to four ECAP pressings

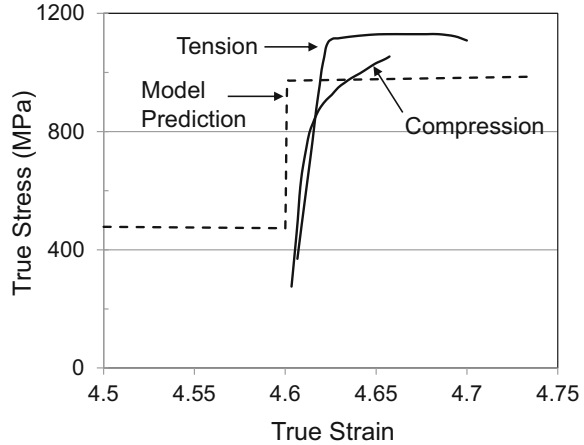
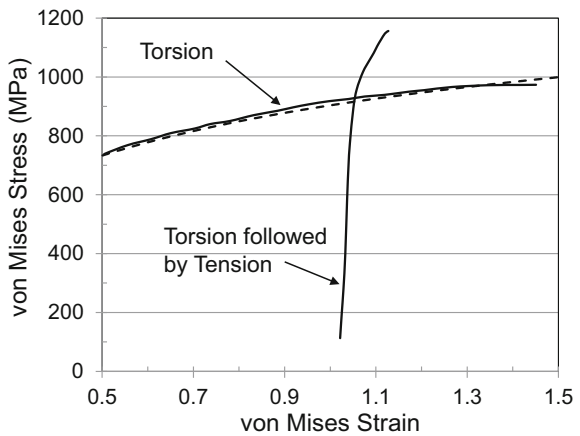


Fig. 14.49 Stress–strain curve for torsion followed by tension in 304 L stainless steel reported by Miller and McDowell [31]. The dashed line is the model fit to the torsion stress–strain curve



An interesting observation in Fig. 14.48 is that the apparent yield stress in compression is much less than that in tension, whereas these reload yield stresses were comparable after one pressing (Fig. 14.46). The rate of strain hardening is again quite different—with the tension curve demonstrating essentially no strain hardening beyond yield—but this may again reflect a tensile instability.

A comparison of the results in 304 L stainless steel with those presented earlier in copper and nickel leads to several common findings, some differences, and some inconsistencies. One common observation is that the rate of strain hardening following ECAP processing is generally higher than predicted using a large-strain constitutive model that has been fit to a large-strain stress–strain curve under known stress state—either compression or torsion. This is true in all cases examined except for the RT, quasi-static reloads of Gray et al. in copper (Fig. 14.29) and nickel

(Fig. 14.37) after eight ECAP pressings and in the tension reload of 304 L stainless steel after four ECAP pressings (Fig. 14.48). Given the very low rate of (Stage IV) strain hardening observed at strains as low as unity, it seems unlikely this is a model-dependent conclusion.

The reload yield stresses in copper and nickel were uniformly lower than the predicted yield stresses. In copper, the difference increased with increasing number of pressings (total strain) as illustrated in Fig. 14.16, when compared to Fig. 14.13. The reload yield stresses in 304 L stainless steel after one and four ECAP pressings, however, were comparable to the model predictions. Given the uncertainty in the actual large-strain stress–strain curve—particularly when extrapolating at high ECAP pressings beyond strains achieved in the mechanical test used to fit the hardening law—this may be a model-dependent conclusion.

Insight into the potential influence of the stress path change in transitioning from a predominantly shear stress state during ECAP processing to a uniaxial stress state during tension or compression reload testing is gained from measurements by Miller and McDowell [31]. In addition to measuring stress–strain curves in 304 L stainless steel using pure torsion and pure compression stress states, they studied the response of tubes strained in torsion to effective (or von Mises) strain levels of 0.5 and 1.0 followed by tension.¹⁰ Figure 14.49 shows the result for a prestrain of 1.0 at a strain rate of 0.0004 s^{-1} followed by tension at the same strain rate. The dashed line is the model fit to the torsion stress–strain curve, defined by Eqs. 14.31 through 14.35.

In this case the reload tension test shows yield at nearly the same von Mises stress level as observed in the torsion test, but the rate of strain hardening is very high. This behavior is reminiscent of the compression reload results shown in copper in Figs. 14.13 and 14.14 (and several other associated figures) and Figs. 14.38 and 14.39 for the reloads in nickel. It is suggested that high reload strain-hardening rate is a texture effect and that the softer texture formed during shear transforms upon reloading to a texture consistent with a uniaxial stress state, which is a stronger configuration. Since ECAP is a predominantly shear deformation process, the expectation is that high strain hardening in a uniaxial reload test should be commonly observed. When it is not observed, e.g., in the Gray et al. tests in copper (Fig. 14.17) and nickel (Fig. 14.37) and the Qu et al. tensile tests in 304 L stainless steel (Fig. 14.48), it is possible that a plastic instability has precluded the expected behavior.

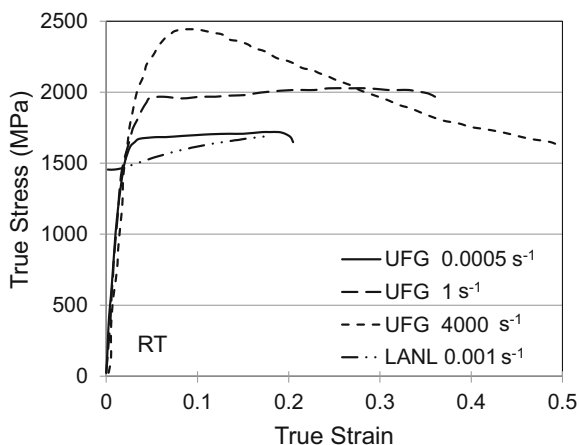
¹⁰Miller and McDowell report that torsion followed by compression was not possible due to plastic instability in the compression specimen.

14.10 Analysis of Fine-Grained Processed Tungsten

Tungsten is not normally a material that is expected to accommodate large deformations.¹¹ At high enough working temperatures, however, the material can be ECAP processed. Wei et al. [36] measured the reload stress–strain curves on commercial purity, polycrystalline tungsten ($\sim 40\ \mu\text{m}$ initial grain size) processed by ECAP at a starting temperature of $1000\ ^\circ\text{C}$ in 120° dies and by a combination of ECAP plus rolling at $800\ ^\circ\text{C}$. The ECAP processing alone yields from Eq. 14.15 an equivalent strain of 0.667 per pass. Wei et al. report that the rolling step added an equivalent strain of ~ 1.8 , and this material is referred to as ultra-fine grained (UFG) tungsten with a grain size reduced to $\sim 500\ \text{nm}$. Figure 14.50 shows the stress–strain curves measured by Wei et al. on the UFG material. Included are measurements at RT and reload strain rates of $0.0005\ \text{s}^{-1}$, $1\ \text{s}^{-1}$, and $4000\ \text{s}^{-1}$. Also included in this figure is a stress–strain curve at RT and a strain rate of $0.001\ \text{s}^{-1}$ in polycrystalline tungsten measured by Chen and Gray [37]. The Chen and Gray measurements used different material than did the Wei et al., but the yield stresses in the former are typical of those found in pure tungsten [38] and, thus, offer a possible baseline for non-UFG processed material.

The high temperatures and large deformations imposed on this material in the Wei et al. measurements, the lack of large strain stress–strain data at the processing temperatures of interest, and the added complication of a stress path (and processing temperature) change complicate prediction of the processing plus reload behavior as was demonstrated for copper, nickel, and stainless steel in previous sections of this chapter. Instead, the analysis methodology introduced in Sect. 14.6 is applied [39].

Fig. 14.50 Reload stress–strain curves measured at RT and three strain rates by Wei et al. [36] in ultra-fine-grained processed tungsten. Included for comparison is a RT measurement in pure tungsten by Chen and Gray [37]



¹¹ Much of the analysis in this section was performed by Frank McGrogan as part of an undergraduate research project at Saint Vincent College, Latrobe, PA.

Fig. 14.51 Yield stress versus test temperature for pure tungsten. The Chen and Gray measurements are for material in an annealed condition. The Wei et al. measurements are for material subjected to ultra-fine-grained processing. For the latter prediction, it was assumed that the starting $\hat{\sigma}_\epsilon$ equaled 245 MPa

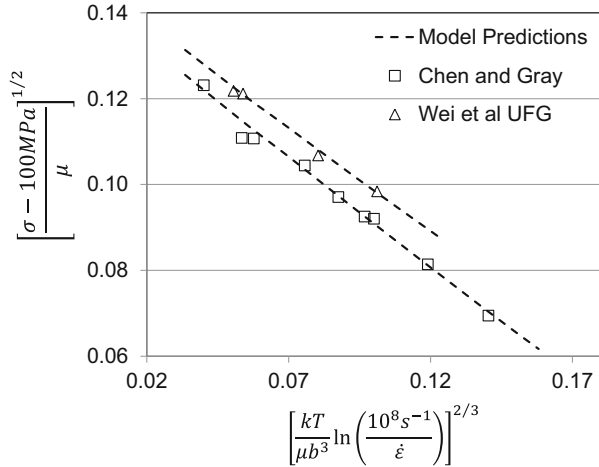


Table 14.3 Selected model parameters for Eq. 9.6 for tungsten

Parameter	Obstacle population			Athermal stress σ_a (MPa)
	Peierls “p”	Impurity “i”	Stored dislocation density, $\hat{\sigma}_\epsilon$ Chen and Gray Wei et al. UFG	
p	0.5	0.5	0.667	
q	1.5	1.5	1	
$\dot{\epsilon}_o$ (s ⁻¹)	10 ⁸	10 ¹⁰	10 ⁷	
g_o	0.125	0.52	1.6	
$\hat{\sigma}_\epsilon$ (MPa)	2936	424	0 245	100

^aFor the UFG material tested by Wei et al., only the value of $\hat{\sigma}_\epsilon$ was changed to reflect the stored dislocation density introduced through processing

Figure 14.51 shows the variation of the yield stress with temperature and strain rate in the Chen and Gray material and in the Wei et al. UFG material. The dashed-line model predictions were made using Eq. 9.6.

$$\frac{\sigma}{\mu} = \frac{\sigma_a}{\mu} + s_p(\dot{\epsilon}, T) \frac{\hat{\sigma}_p}{\mu_o} + s_i(\dot{\epsilon}, T) \frac{\hat{\sigma}_i}{\mu_o} + s_\epsilon(\dot{\epsilon}, T) \frac{\hat{\sigma}_\epsilon}{\mu_o} \tag{9.6}$$

Table 14.3 lists the model parameters. The model parameters for the Peierls and impurity obstacle populations are the same as those listed in Table 9.1. In this analysis the dependence of g_{oe} on $\hat{\sigma}_\epsilon$ modeled using Eq. 14.9 is not included. Rather the average value of $g_{oe} = 1.6$ is used. Note that the hardening introduced by fine-grained processing is represented by introducing $\hat{\sigma}_\epsilon = 245$ MPa.

The prediction of reload stress–strain curves requires an evolution equation. Equation 6.28 is used rather than Eq. 14.11 since there is no large-strain RT stress–strain curve to establish the Stage IV hardening parameter. The model parameters for Eqs. 6.28, 6.26 for $\hat{\sigma}_{es}(\dot{\epsilon}, T)$, and Eq. 6.29 for $\theta_{II}(\dot{\epsilon})$ are derived from the Chen and Gray measurements and listed in Table 14.4.

Table 14.4 Evolution parameters selected for tungsten

Parameter	Equation	Value	Unit
k	6.28	2	
$\hat{\sigma}_{eso}$	6.26	735	MPa
g_{eso}		0.0775	
$\dot{\epsilon}_{eso}$		10^8	s^{-1}
A_o	6.29	3300	MPa
A_1		30	MPa (when $\dot{\epsilon}$ in s^{-1})
A_2		5	$s^{-1/2}$

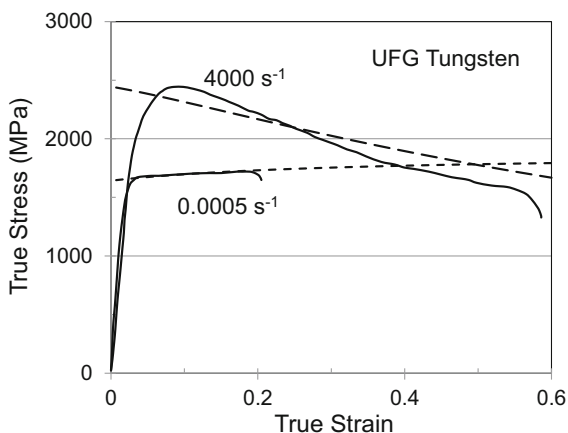
Fig. 14.52 Measured and predicted reload stress–strain curves at RT for two strain rates in UFG processed tungsten

Figure 14.52 compares predicted stress–strain curves with those measured by Wei et al. on UFG tungsten. The predicted rate of strain hardening at the lower strain rate agrees closely with the measurement. At the higher strain rate, the test is under adiabatic conditions. The measured curve falls off more rapidly with increasing strain than does the model prediction. Wei et al. [36] noted the presence of both cracks in shear bands in dynamically reloaded ECAP and UFG processed material, which could contribute to the observed rapid decrease in stress.

Of interest in Fig. 14.52 is that the reload stress–strain curve at the low strain rate does not show a higher rate of strain hardening than predicted, which was the typical observation in ECAP processed copper, nickel, and austenitic stainless steel. Recall that the UFG material saw initial ECAP processing coupled with a subsequent, large rolling reduction. In ECAP processed material, the earlier hypothesis was that the predominantly shear deformation imposed by ECAP created a softer texture and that the high rate of strain hardening reflected evolution of the texture upon reloading in tension or compression (see Fig. 14.49). The imposed rolling deformation in UFG tungsten replaces the shear texture with a rolling texture. The net effect appears to be that the rate of strain hardening in a specimen (with its axis parallel to the rolling direction) reloaded in compression is similar to that observed in a uniaxial compression test and modeled using Eq. 6.28.

The observation that grew out of the analysis of reload stress–strain curves in ECAP processed copper, nickel, and austenitic stainless steel was that with multiple pressings the rate of structure evolution fell below the prediction. (See Figs. 14.30 and 14.42.) Analysis of the reload stress–strain behavior in tungsten cannot be used to validate this observation because of the lack of information on the large-strain stress–strain behavior in this material at the processing temperatures of interest.

14.11 Summary

The objective of this chapter has been to demonstrate how to apply the internal state variable formalism to analyze deformation mechanisms in uniquely processed—heavily deformed, in this case—material. To accomplish this, three potentially complicating factors had to be addressed. This included (i) the assumption that the activation free energy characterizing interactions of mobile dislocations with stored dislocations— g_{oe} —was constant, (ii) the effect of a continuously refining grain size on the athermal stress, and (iii) the effect of texture evolution on the evolution law. A fourth consideration was the observation that at large strains a region of constant strain hardening termed Stage IV alters the evolution law.

A simple analysis of grain refinement in ECAP processed copper in Sect. 14.4 yielded an estimate of the variation with strain of the grain size strengthening term (the athermal stress). It was argued that this contribution is already included in the empirical evolution law and that, barring the availability of a better model, there was no need to revise the governing equations (e.g., Eq. 9.6 or equivalent).

Stage IV hardening was included through a simple revision of Eq. 6.28 given in Eq. 14.11. Large-strain stress–strain measurements are required to implement this revised evolution law.

Analysis of the variation of g_{oe} with strain was treated from the starting point of a model developed by Mecking and Kocks described in Sect. 14.2. Consistent with the internal state variable formalism, a model for $g_{oe}(\hat{\sigma}_e, T)$ rather than $g_{oe}(\epsilon)$ was adopted as described in Eq. 14.9. This model led to reasonable agreement between measured and predicted strain-rate dependencies in copper although further development of the model is required. Application of Eq. 14.9, developed for copper, to nickel and austenitic stainless steel required the assumption that the parameter F in Eq. 14.9, which was specified as $F = 3.16$ in Eq. 14.19, does not change. Further work to establish F for different material systems should be undertaken.

Texture evolution was not explicitly introduced, but the observed high initial rate of strain hardening in uniaxial test specimens machined from ECAP processed metal was argued to arise from the evolution of the softer texture produced by the predominantly shear deformation during ECAP to the harder texture typical of uniaxial deformation. Use of the torsion stress–strain curve rather than the compression stress–strain curve to establish the hardening law lessened the difference between measurements and predictions. This was possible in copper, nickel, and the austenitic stainless steel, but not in tungsten.

One common observation when reload stress–strain curves are compared to model predictions was that the rate of strain hardening in the measurements exceeded the predicted rate of strain hardening. A couple of the reload (e.g., the RT, quasi-static reload stress–strain curves in copper and nickel reported by Gray et al.) did not show a high rate of initial strain hardening. It was suggested that in these cases, a plastic instability may have affected the rate of strain hardening. One possible explanation for the high rate of strain hardening in tension or compression tests following predominantly shear loading was that this resulted from the transition from the crystallographic textures developed during shear to that developed during uniaxial loading. The measurement by Miller and McDowell shown in Fig. 14.49 presented a good example of the effect of this path change on the stress–strain curve in austenitic stainless steel.

Another common observation in the ECAP experiments in copper and nickel was that strain hardening did not proceed indefinitely according to Eq. 14.11 but that it seemed to saturate at a value of $\hat{\sigma}_e$ that was ~65% the value predicted solely using Eq. 14.11. It is not known whether this tendency toward saturation is due to the inability to extrapolate Eq. 14.11 well beyond the behavior observed at lower strains or the tendency toward dynamic recrystallization due to the adiabatic conditions during ECAP processing.

While the analyses in this chapter involved, often extensive, extrapolations of known behavior, these analyses demonstrate that it is possible to gain insight on a uniquely processed metal using the foundation of an internal state variable constitutive model coupled with the understanding of kinetics of deformation of that metal, e.g., under “normal” processing conditions. Fundamental to this is the correlation between a material’s structure, as represented by internal state variables, and its mechanical properties.

Exercises

- 14.1 Table 14.E1 lists the stress–strain data measured by Yapici et al. in Ti-6Al-4 V [40]. This material was powder processed with a large (70 μm) α colony size, and these measurements were in the as-received, heat-treated condition at RT and a strain rate of 10^{-3} s^{-1} . Compare these measurements with model predictions from Sect. 10.10. Use the model parameters listed in Table 10.19 and the values of $\hat{\sigma}_1$ and $\hat{\sigma}_2$ specified in Sect. 10.10 ($\hat{\sigma}_1 = 882 \text{ MPa}$ and $\hat{\sigma}_2 = 1103 \text{ MPa}$). Because this material has a much larger grain size (α colony size) than did the material studied by Follansbee and Gray, use Eq. 10.6 to estimate σ_a .
- 14.2 Yapici et al. processed the material described in Exercise 14.1 using ECAP with 90° dies. The material was processed with either one or two passes at 823 K or 1073 K. Table 14.E2 lists reload stress–strain data. The processing conditions are specified. Assuming a strain rate of 1.0 s^{-1} (but isothermal conditions), compare the measured and predicted reload stress–strain curves for each condition.

Table 14.E1 Stress versus strain measurements reported by Yapici et al. in powder processed Ti-6Al-4V (Exercise 14.1)

As received condition, RT, 0.001 s ⁻¹			
Strain	Stress (MPa)	Strain	Stress (MPa)
0.0009	867	0.078	1096
0.0017	900	0.086	1105
0.0026	922	0.094	1111
0.0050	944	0.099	1115
0.0095	967	0.105	1123
0.014	984	0.112	1129
0.019	1000	0.119	1134
0.024	1011	0.128	1140
0.029	1020	0.137	1147
0.036	1035	0.145	1151
0.041	1042	0.153	1156
0.047	1056	0.159	1162
0.054	1067	0.166	1167
0.060	1076	0.171	1170
0.069	1087	0.176	1173
0.073	1091	0.181	1178

Table 14.E2 Stress versus strain measurements reported on the Ti-6Al-4V material described in Exercise 14.1 that was subjected to one or two ECAP pressings (Exercise 14.2)

ECAP processed, RT, 0.001 s ⁻¹					
1 pass, 1073 K		2 passes, 1073 K		1 pass, 823 K	
Strain	Stress (MPa)	Strain	Stress (MPa)	Strain	Stress (MPa)
0.0009	900	0.0000	911	0.0000	967
0.0017	933	0.0005	978	0.0009	1000
0.003	963	0.003	1044	0.002	1044
0.006	990	0.005	1078	0.003	1078
0.009	1009	0.008	1092	0.003	1111
0.012	1022	0.012	1114	0.005	1142
0.014	1035	0.016	1134	0.007	1155
0.017	1048	0.021	1151	0.009	1167
0.020	1060	0.025	1164	0.011	1178
0.024	1078	0.029	1176	0.014	1181
0.028	1093	0.034	1189	0.016	1189
0.033	1104	0.039	1196	0.021	1195
0.036	1111	0.044	1207	0.026	1205
0.040	1119	0.049	1217	0.028	1211
0.044	1126	0.054	1228	0.031	1217
0.047	1130	0.061	1238		
0.052	1132	0.067	1241		
0.054	1133	0.072	1242		
		0.082	1243		
		0.085	1243		
		0.089	1233		

Table 14.E4 Hypothetical reload yield stress versus temperature measurements in ECAP processed Mg AZ31B (Exercise 14.4)

Temp (K)	Strain rate (s ⁻¹)	Stress (MPa)
295	0.001	412
295	1	591
100	0.001	1066
400	0.001	231
500	0.001	147

Table 14.E5 Reload stress versus strain measurements for the material and processing described in Exercise 14.4 (Exercise 14.5)

295 K and 1.0 s ⁻¹			
Strain	Stress (MPa)	Strain	Stress (MPa)
0.002	590	0.04	605
0.004	581	0.045	603
0.006	584	0.05	606
0.008	589	0.055	610
0.01	583	0.06	605
0.012	589	0.065	617
0.014	590	0.07	611
0.016	586	0.075	613
0.018	592	0.08	619
0.02	597	0.085	614
0.022	599	0.09	617
0.025	598	0.095	627
0.03	600	0.1	619
0.035	596		

- 14.3 How do the measured and predicted curves in Exercise 14.2 compare with the examples in Sect. 14.5, 14.8, and 14.9?
- 14.4 Consider hypothetical measurements on Mg AZ31B (Sect. 10.5). Model parameters for the alloy are listed in Table 10.8 and Table 10.10. The material is processed using 90° ECAP dies at 400 K and a strain rate of 1.0 s⁻¹ (assume isothermal conditions). Table 14.E4 lists reload yield stress measurements on material processed using a single pass. (a) Compare the measured yield stresses with predicted yield stresses for the conditions imposed. (b) What is the value of $\hat{\sigma}_\epsilon$ that gives good agreement between the model predictions and measurements?
- 14.5 Table 14.E5 lists stress–strain data measured at 295 K and a strain rate of 1 s⁻¹ on samples machined from the ECAP-processed material described in Exercise 14.4. (a) Plot the predicted stress–strain curve for the prediction made in part (a) of Exercise 14.4 and the predicted stress–strain curve for the prediction made in part (b) of Exercise 14.4 along with the measurements. Assume the deformation is isothermal. Include a prediction made by simply adjusting the athermal stress (and setting $\hat{\sigma}_\epsilon = 0$). How do the curves compare?

References

1. M. A. Meyers, A. Mishra, and D. J. Benson, "Mechanical properties of nanocrystalline materials," *Prog. Mater. Sci.*, Vol. 51, No. 4, May, 2006, pp.427-556.
2. K.S. Kumar, H. Van Swygenhoven, S. Suresh, Mechanical behavior of nanocrystalline metals and alloys. *Acta Mater.* **51**, 5743–5774 (2003)
3. Q. Wei, Strain rate effects in the ultrafine grain and nanocrystalline regimes – influence on some constitutive responses. *J. Mater. Sci.* **42**, 1709–1727 (2007)
4. P.S. Follansbee, U.F. Kocks, A constitutive description of the deformation of copper based on the use of the mechanical threshold stress as an internal state variable. *Acta Metall.* **36**, 81–93 (1988)
5. H. Mecking, U.F. Kocks, Kinetics of flow and strain-hardening. *Acta Metall.* **29**, 1865–1875 (1981)
6. J.M.G. Alberti, Large plastic deformations in polycrystalline Cu and Al at low temperatures. PhD Thesis (University Navarra, Spain, 1984)
7. F.H. Dalla Torre, E.V. Pereloma, C.H.J. Davies, Strain hardening behaviour and deformation kinetics of Cu deformed by equal channel angular extrusion from 1 to 16 passes. *Acta Mater.* **54**, 1135–1146 (2006)
8. U.F. Kocks, M.G. Stout, A.D. Rollett, Influence of texture on strain hardening, in *9th International Conference on the Strength of Metals and Alloys (ICSMA)*, ed. by P. O. Kettunen, T. K. Lepistö, M. E. Lehtonen, (Pergamon Press, Oxford, 1988), pp. 25–34
9. D. Rollett, U.F. Kocks, A review of the stages of work hardening. *Solid State Phenom.* **35-36**, 1–18 (1993)
10. V.S. Saji, J. Thomas, Nanomaterials for corrosion control. *Curr. Sci.* **92**, 51–55 (2007)
11. C.X. Huang, H.J. Yang, S.D. Wu, Z.F. Zhang, Microstructural characterizations of Cu processed by ECAP from 4 to 24 passes. *Mater. Sci. Forum* **584-586**, 333–337 (2008)
12. J.-Y. Chang, J.-S. Yoon, G.-H. Kim, Development of submicron sized grain during cyclic equal channel angular pressing. *Scr. Mater.* **45**, 347–354 (2001)
13. W.J. Kim, S.I. Hong, Y.S. Kim, S.H. Min, H.T. Jeong, J.D. Lee, Texture development and its effect on mechanical properties of an AZ61 magnesium alloy fabricated by equal channel angular processing. *Acta Mater.* **51**, 3293–3307 (2003)
14. D.C. Foley, K.T. Hartwig, S.A. Maloy, P. Hosemann, X. Zhang, Grain refinement of T91 alloy by equal channel angular pressing. *J. Nucl. Mater.* **389**, 221–224 (2009)
15. Y. Fukuda, K. Oh-ishi, Z. Horita, T.G. Langdon, Processing of a low-carb on steel by equal-channel angular pressing. *Acta Mater.* **50**, 1359–1368 (2002)
16. J. Gubicza, N.Q. Ching, T.G. Langdon, T. Ungar, Microstructure and strength of metals processed by severe plastic deformation, in *Ultrafine Grained Materials IV*, ed. by Y. T. Zhu, T. G. Langdon, Z. Horita, M. J. Zehetbauer, S. L. Semiatin, T. C. Lowe, (TMS (The Minerals, Metals, and Materials Society), Warrendale, 2006), pp. 231–236
17. M.M. Gutierrez-Urrutia, Munoz-Moris, D.G. Morris, Contributions of microstructural parameters to strengthening in an ultrafine-grained Al-7%Si alloy processed by severe deformation. *Acta Mater.* **55**, 1319–1330 (2007)
18. S.D. Terhune, D.L. Swisher, K. Oh-Ishi, Z. Horita, T.G. Langdon, T.R. McNelley, An investigation of microstructure and grain-boundary evolution during ECA pressing of pure aluminum. *Metall. Mater. Trans. A* **33A**, 2173–2184 (2002)
19. C.Z. Xu, Q.J. Wang, M.S. Zheng, J.W. Zhu, J.D. Li, M.Q. Huang, Q.M. Jia, Z.Z. Du, Microstructure and properties of ultra-fine grain Cu-Cr alloy prepared by equal-channel angular pressing. *Mater. Sci. Eng. A* **459**, 303–308 (2007)
20. M. Lewandowska, H. Garbacz, W. Pachla, A. Mazur, K. Kurzydowski, Grain refinement in aluminum and the aluminum Al-Cu-Mg-Mn alloy by hydrostatic extrusion. *Mater. Sci.-Pol.* **23**, 279–286 (2005)

21. D. Rollett, Strain hardening at large strains in aluminum alloys. Los Alamos National Laboratory, LA-11202-T Thesis, available from National Technology Information Service, OSTI ID: 5289489; Legacy ID: DE88007415, 1988, p. 59.
22. R.A. Masumura, P.M. Hazzledine, C.S. Pande, Yield stress of fine grained materials. *Acta Mater.* **46**, 4527–4534 (1998)
23. P. Zhilyaev, G.V. Nurislamova, B.-K. Kim, M.D. Baro, J.A. Szpunar, T.G. Langdon, Experimental parameters influencing grain refinement and microstructural evolution during high pressure torsion. *Acta Mater.* **51**, 753–765 (2003)
24. G. Langford, M. Cohen, Strain hardening of iron by severe plastic deformation. *Trans. ASM* **62**, 623 (1969)
25. P. Feltham, J.D. Meakin, On the mechanism of work hardening in face-centered cubic metals, with special reference to polycrystalline copper. *Philos. Mag.* **2**, 105–112 (1957)
26. S. Nemat-Nasser, W. Guo, Flow stress of commercially pure niobium over a broad range of temperatures and strain rates. *Mater. Sci. Eng.* **284**, 202–210 (2000)
27. H. Conrad, M. Doner, B. de Meester, Investigations to understand the plastic deformation and strengthening mechanisms of solid solution phases of titanium. Air Force Technical Report AFML-TR-84, 1972. Available through National Technical Information Service, <http://www.dtic.mil/cgi-bin/GetTRDoc?AD=AD0744711>.
28. D.A. Hughes, Strain hardening of f.c.c. metals and alloys at large strains. Ph.D Thesis (Stanford University, Palo Alto, 1986)
29. H.E. Boyer, T.L. Gall, Eds., *Metals Handbook Desk Edition*, ASM International, Materials Park, 1985, p. 28-70. (Data from G. Sachs and K. R. Van Horn, *Practical Metallurgy*, ASM, Metals Park, OH, 1951.)
30. G.T. Gray III, T.C. Lowe, C.M. Cady, R.Z. Valiev, I.V. Aleksandrov, Influence of strain rate & temperature on the mechanical response of ultrafine-grained Cu, Ni, and Al-4Cu-0.5Zr. *Nanostruct. Mater.* **9**, 477–480 (1997)
31. M.P. Miller, D.L. McDowell, The effect of stress-state on the large strain inelastic deformation behavior of 304L stainless steel. *ASME J. Eng. Mater. Technol.* **118**, 28–36 (1993)
32. S. Qu, C.X. Huang, Y.L. Gao, G. Yang, S.D. Wu, Q.S. Zang, Z.F. Zhang, Tensile and compressive properties of AISI 304L stainless steel subjected to equal channel angular pressing. *Mater. Sci. Eng. A* **47**, 207–216 (2008)
33. C.X. Huang, G. Yang, Y.L. Gao, S.D. Wu, Z.F. Zhang, Influence of processing temperature on the microstructures and tensile properties of 304L stainless steel by ECAP. *Mater. Sci. Eng. A* **485**, 643–650 (2008)
34. U.S. Lindholm, A. Nagy, G.R. Johnson, J.M. Hoegfeldt, Large strain high strain rate testing of copper. *ASME J. Eng. Mater. Technol.* **102**, 376–381 (1980)
35. C. Albertini and M. Montagnani, M., “Dynamic uniaxial and biaxial stress–strain relationships for austenitic stainless steels,” *Nucl. Eng. Des.*, Vol. 57, 1980, pp. 107-123.
36. Q. Wei, T. Jiao, K.T. Ramesh, E. Ma, L.J. Kecskes, L. Magness, R. Dowding, V.U. Kazykhanov, R.Z. Valiev, Mechanical behavior and dynamic failure of high-strength ultrafine grained tungsten under uniaxial compression. *Acta Mater.* **54**, 77–87 (2006)
37. S.-R. Chen, G.T. Gray III, Constitutive behavior of tungsten and tantalum experiments and modeling, in *2nd International Conference on Tungsten and Refractory Metals, Metal Powder Industries Federation*, ed. by A. Bose, R. J. Dowding, (Metal Powder Industries Federation, Princeton, 1995), pp. 489–498
38. D. Brunner, V. Glebovsky, *Mater. Lett.* **44**, 144–152 (2000)
39. F. McGrogan, Analysis of the Kinetics of Strengthening in Nanocrystalline and Fine-Grain Processed Materials Using an Internal State Variable Model. Proceedings of the National Conference On Undergraduate Research (NCUR) 2011, Ithaca College, New York, March 31 – April 2, 2011.
40. G.G. Yapici, I. Karaman, Z.P. Luo, H. Rack, Microstructure and mechanical properties of severely deformed powder processed Ti-6Al-4V using equal channel angular extrusion. *Scr. Mater.* **49**, 1021–1027 (2003)

Chapter 15

Summary and Status of Model Development



Introduction

The objective of this monograph has been to describe the basis for the mechanical threshold stress internal state variable constitutive model and to illustrate through numerous examples how model parameters are derived from experimental data and how the model can be applied to add insight into often complex behavior. It has been argued throughout that defining internal state variables as parameters representing the interactions of dislocations with unique obstacle populations enables a constitutive model that is able to predict the stresses upon path changes. This formulation offers an advantage over constitutive models that treat strain as a state variable.

An underlying principle throughout this monograph is that the deformation model builds from an understanding of crystal structure, defects, and dislocation motion. The basic equation describing stress-dependent, thermally assisted jerky glide (Eq. 4.3) was derived from the Orowan equation (Eq. 2.14), the Boltzmann Equation, and the geometry of a dislocation overcoming an obstacle, as illustrated in Fig. 4.5. Chapter 3 introduced concepts relating strength to grain size, impurity content, the stored dislocation density, and precipitate spacing. The analysis of experimental data in numerous pure metals and alloys in Chaps. 8, 9, 10, 11, and 12 validated these simple concepts and added information regarding similarities and differences in the activation volume for these strengthening contributions. This was important because it defined the temperature and strain-rate dependence of the distinct dislocation—obstacle interactions.

Slip systems for the most common crystal structures (BCC, FCC, and HCP) were described in Sect. 2.3 to emphasize important differences between deformation in these common crystal structures. The availability of the $\{111\}$ close-packed plane in FCC metals and the absence of the Peierls barrier contributes to their relative low strength when compared to their BCC counterparts. The HCP systems are complicated by the lower availability of this close-packed plane, which implies that other, less closely-packed planes must participate.

Chapters 2, 3, and 4 contained brief overviews of these fundamentals because they provide the foundation for the internal state variable constitutive model presented here. Much more detailed treatments of these topics are widely available, which justifies the brevity in this monograph.

This chapter will provide a current assessment of the status of the model development. The intent is to identify elements of the model that are on solid footing as well as elements of the model that are not as certain. The hope is that further research can be supported to address the latter.

15.1 Analyzing the Temperature-Dependent Yield Stress

Of interest here is the temperature and strain-rate dependence—the deformation kinetics—for a metal in a given state. Yield stress does not simply imply the transition from elasticity to plasticity in a well-annealed material. Rather, it can represent this transition in a material—such as an aluminum alloy—that is heat treated or mechanically worked to achieve a certain structure and set of properties. The common definition is that the yield stress reflects the transition from elasticity to plasticity in a material in a prescribed structural state. For this, Eq. 6.17 specified the governing equation

$$\frac{\sigma}{\mu} = \frac{\sigma_a}{\mu} + \sum_i^n s_i(\dot{\epsilon}, T) \frac{\widehat{\sigma}_i}{\mu_o} \quad (6.17)$$

where μ is the shear modulus at the temperature of interest, μ_o is the shear modulus at 0 K, and $\widehat{\sigma}_i$ is the internal state variable representing “ n ” obstacle populations. The s_i terms in Eq. 6.17 follow the form

$$s_i(\dot{\epsilon}, T) = \left\{ 1 - \left[\frac{kT}{g_{oi}\mu b^3} \ln \left(\frac{\dot{\epsilon}_{oi}}{\dot{\epsilon}} \right) \right]^{1/q_i} \right\}^{1/p_i} \quad (6.18)$$

In pure copper, n of Eq. 6.17 equaled unity, and the stored dislocation density was considered to be the only obstacle population. In simple FCC alloys (Ni – C and Cu – Al), n equaled two, and an obstacle population representing the interaction of dislocations with “impurity elements” (whether or not intentionally added) was introduced along with the stored dislocation density. In the austenitic stainless steels, n equaled three as evidence of distinct obstacle populations related to chemistry—particularly nitrogen content—was presented. Similarly, in BCC systems, n equaled three as the Peierls barrier presented a unique, highly strain-rate- and temperature-dependent obstacle population.

Equation 6.17 assumes that contributions from distinct obstacle populations add linearly. This assumption was assessed—at least to first order—in the analysis of measurements in the Ni-C alloys in Sect. 8.8. Moreover, application of this

assumption in analyses of data in numerous FCC systems (Chap. 8), BCC systems (Chap. 9), HCP systems (Chap. 10), austenitic stainless steels (Chap. 11), and nickel-based superalloys (Chap. 12) led in each case to sensible results with no suggestion that the governing equation was in error. Nonetheless, this represents a model assumption.

In application of Eq. 6.17, measurements of yield stress as a function of temperature and strain rate are readily available in metals in a “starting condition” whether this is well annealed, heat treated, or worked. Measurements of yield stress as a function of temperature and strain rate in these metals after straining according to a specified strain rate and temperature to a specified strain are less readily available. The intent of the extensive measurements by Follansbee and Kocks [1] and Follansbee et al. [2] was to produce a few such data sets in model materials. An important result of this is the definition of s_ϵ —where this is the s_i -value characterizing the interactions of dislocations with the stored dislocation density—as

$$s_\epsilon(\dot{\epsilon}, T) = \left\{ 1 - \left[\frac{kT}{1.6\mu b^3} \ln \left(\frac{10^7 s^{-1}}{\dot{\epsilon}} \right) \right]^{3/2} \right\} \quad (15.1)$$

These model constants have been held constant for all of the analyses undertaken in this monograph. It would be useful to have more validation that this is a good assumption across all metal systems, but support for this assumption is found in the model fits presented in this monograph which presented no evidence to the contrary. That is, the ability to replicate temperature and strain-rate sensitivities and strain-hardening rates (e.g., Fig. 8.35 in shock loaded nickel and Fig. 10.55 in irradiated Zircaloy-2) without additional changes to model parameters adds credence to the model assumptions.

The use of n -values in Eq. 6.17 of two and, certainly, three is open to the argument that this is simply a convenient means of representing curvature in the plot of normalized yield stress versus normalized temperature and strain rate. These n -values were adopted, however, when the active deformation mechanisms supported this assumption. The high temperature and strain-rate sensitivity in BCC metals at high strain rates and low temperatures (the left side of the abscissa in the normalized stress versus normalized temperature and strain rate plot, see Fig. 9.8, included here as Fig. 15.1) follow directly from the contribution to the stress from the Peierls barrier. At high temperatures and low strain rates, this barrier loses effectiveness, yet these materials retain a measure of temperature and strain rate sensitivity. It is apparent that the contribution to stress from “impurity” elements defines the deformation kinetics under these conditions.

Furthermore, in the lower-temperature and higher strain-rate regime, it is the combined contribution of both the Peierls barrier and the impurity elements that defines deformation kinetics. The evidence presented linking the magnitude of the threshold stress characterizing the interactions of dislocations with impurity additions with chemical content (e.g. Fig. 9.11, included here as Fig. 15.2, in iron; Fig. 10.77 in titanium; and Fig. 11.8 in austenitic stainless steel) offers strong

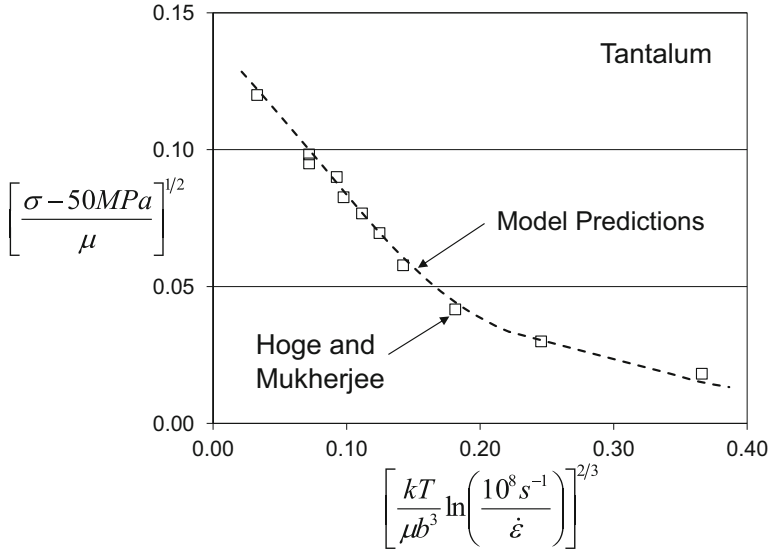
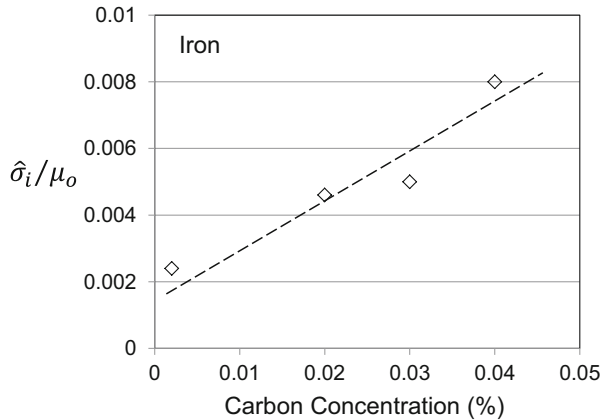


Fig. 15.1 Normalized yield stress versus normalized temperature and strain rate in tantalum illustrating the ability of a two-obstacle model to match the measurements

Fig. 15.2 Variation of the mechanical threshold stress characterizing interactions of dislocation with impurity elements with carbon concentration in pure iron



justification for definition and use of an internal state variable related to chemical content.

Certainly, a more thorough analysis of the individual (rather than the collective) contributions of impurity additions is warranted. It may well be the case in engineering alloys that n in Eq. 6.17 should be much larger than three. The experimental program to shed light on this would be a significant effort, however. A theoretical or atomistic approach, e.g., see Gröger and Vitek [3, 4], may offer another route to the derivation of activation volume correlations. In general, the myriad sets of data analyzed here suggest that Eq. 6.17 with Eq. 6.18 offers a good foundation for

specification of yield kinetics. It is suggested that the models that describe the temperature and strain-rate sensitivities as a constant structural state are fundamentally based and offer good predictive capability.

15.2 Stress Dependence of the Normalized Activation Energy $g_{o\epsilon}$

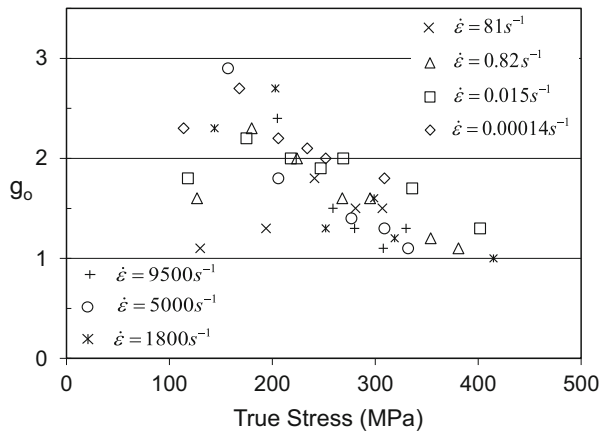
Equation 15.1 specifies a constant value of $g_{o\epsilon}$, but, as discussed in Sects. 8.2 and 14.2, $g_{o\epsilon}$ actually exhibits slight stress dependence. This was illustrated in Fig. 8.5, included here as Fig. 15.3, and is the source of the variation of m -value with stress noted in Fig. 14.2. A simple model, derived from a phenomenological model introduced by Mecking and Kocks [5], was specified using Eq. 14.9. A comparison of model predictions with Eq. 14.9 and m -values measured in large-strain experiments, e.g., Fig. 14.2, demonstrates that the essence of the trends can be modeled. In general, the range of strains to be modeled using a constitutive formulation are too low to require this modification. Further analysis of the source of this stress dependence would be worthwhile.

15.3 Evolution

Evolution was represented by an equation of the form

$$\frac{d\widehat{\sigma}_\epsilon}{d\epsilon} = f(\widehat{\sigma}_\epsilon, T, \dot{\epsilon}) \tag{15.2}$$

Fig. 15.3 Analyzed value of the normalized activation energy characterizing dislocation interactions with the stored dislocation density in copper showing stress dependence



Importantly, the evolving obstacle population was the stored dislocation density represented by the subscript ε . The model assumes that no other obstacle population is changing. Secondly, evolution of the internal state variable $\hat{\sigma}_\varepsilon$ is treated—rather than the differential change, for instance, of the stress. Finally, strain is included only through the differential change of $\hat{\sigma}_\varepsilon$; it is this formulation that enables path changes to be assessed.

The Voce law provided a simple expression for the differential rate of evolution

$$\frac{d\hat{\sigma}_\varepsilon}{d\varepsilon} = \theta_{II} \left[1 - \frac{\hat{\sigma}_\varepsilon}{\hat{\sigma}_{\varepsilon s}(T, \dot{\varepsilon})} \right] \quad (6.25)$$

where θ_{II} is the stage-two hardening rate and $\hat{\sigma}_{\varepsilon s}$ is a saturation stress. Clearly if $\hat{\sigma}_\varepsilon$ starts as zero, the initial hardening rate is θ_{II} , which is on the order of $\mu / 20$, and as $\hat{\sigma}_\varepsilon$ approaches $\hat{\sigma}_{\varepsilon s}$, the hardening rate approaches zero. Several previous investigators (e.g., Estrin [6]) have demonstrated how the Voce law derives from a balance between dislocation generation and recovery.

Two complications to this simple model have arisen. First, analysis of the measurements—particularly in copper over a very wide range of strain rates by Follansbee and Kocks—led to the conclusion that θ_{II} is not a constant but is in fact a function of strain rate and that as strain rates exceed 10^3 s^{-1} , the strain-rate dependence appears to increase. Although few of the data sets in Chaps. 9 and 10 covered as wide a range of strain rates with as rigorous an approach as applied to copper, a consistent trend in the analyses of these data sets has been a strain-rate dependence of θ_{II} . Equation 6.29 offers a purely empirical expression that is consistent with these measurements. A theoretical model able to predict this strain-rate dependence of dislocation storage has not been established and offers a topic for further research. Furthermore, it is possible that θ_{II} has a temperature dependence not included in Eq. 6.29. While evaluation of evolution using prestrain and reload experiments (as in copper, nickel, and the nickel-carbon alloys in Chap. 8) did not include prestrain temperatures other than room temperature, many of the analyses of BCC and HCP metals in Chaps. 9 and 10 using Eq. 9.7 (or equivalent) were based on stress–strain curves over a wide temperature range. The fact that an apparent temperature dependence to θ_{II} did not emerge in these analyses suggests that the temperature dependence—if any—is weak. Nonetheless, it would be useful to validate this with further experimentation. A temperature dependence of θ_{II} was suggested when dynamic strain aging was active. This, however, was argued in Appendix 13.A2 (see also Exercise 13.E7) to be an artifact of the analysis of $\hat{\sigma}_\varepsilon$ in Eq. 9.7 because of the contribution of σ_{DSA} to $\hat{\sigma}_\varepsilon$.

Another issue with application of Eq. 6.25 was that it does not always adequately model the shape of the evolution curve. To remedy this, the following purely mathematical alteration has been proposed

$$\frac{d\hat{\sigma}_\varepsilon}{d\varepsilon} = \theta_{II} \left[1 - \frac{\hat{\sigma}_\varepsilon}{\hat{\sigma}_{\varepsilon s}(T, \dot{\varepsilon})} \right]^\kappa \quad (6.28)$$

where κ can rise above $\kappa = 1$. Table 10.22 listed κ -values for several of the systems analyzed in this monograph. These values range from $\kappa = 1$ (in the HCP systems) to $\kappa = 2$ (in nickel, copper, niobium, 1018 steel, and austenitic stainless steel) and even $\kappa = 2$ in vanadium. The purely empirical nature of Eq. 6.28 points to the need for further research related to dislocation storage mechanisms.

Section 14.4 discussed grain refinement and argued that grain refinement would lead to an increasing athermal stress which, when σ_a is assumed to remain constant, would add to the estimated mechanical threshold stress characterizing the interaction of dislocations with the stored dislocation density $\hat{\sigma}_\varepsilon$. Very rough estimates in this Sect. 14.4 suggested that this contribution could be as large as 40%. It would be beneficial—particularly when analyzing strengthening in systems processed to achieve significant grain refinement—to have a clearer understanding of this contribution. A possible experimental approach would be to compare the yield stress versus temperature curves for elevated temperature reloads in material that has been processed to low strain (e.g., $\varepsilon = 0.10$) with material processed to very high strain (e.g., $\varepsilon = 2.0$).

15.4 Temperature and Strain-Rate Dependence of Evolution (Strain Hardening)

The first step in each of the deformation analyses presented in this monograph was to establish the deformation kinetics at yield (in this case, implying yield in an annealed, dislocation-free, condition). The plot of normalized yield stress versus normalized temperature and strain rate is used extensively (see, for instance, Figs. 15.1, 6.2, and 6.3). The next step was to establish the variation of $\hat{\sigma}_\varepsilon$ with strain for several specified temperature and strain rate loading paths. In copper (Sect. 8.2), nickel (Sect. 8.5), nickel-carbon alloys (Sect. 8.8), and Ti-6Al-4V (Sect. 10.10), a collection of prestrain and reload tests were used—as demonstrated in the fictitious FoLLyalloy in Sect. 7.6. For the other materials analyzed, Eq. 9.7 (or equivalent when written with the operating mechanical threshold stress terms) was used.

$$\hat{\sigma}_\varepsilon = \frac{\mu_o}{s_\varepsilon(\dot{\varepsilon}, T)} \left[\frac{\sigma}{\mu} - \frac{\sigma_a}{\mu} - s_p(\dot{\varepsilon}, T) \frac{\sigma_p}{\mu_o} - s_i(\dot{\varepsilon}, T) \frac{\sigma_i}{\mu_o} \right] \quad (9.7)$$

Accurate prediction of $\hat{\sigma}_\varepsilon$ relies on the accurate estimate of the mechanical threshold stress terms as well as an accurate estimate of the g_o -values comprising the various s -terms. In some cases (particularly in the BCC systems), large stresses are subtracted from the stress σ in estimating $\hat{\sigma}_\varepsilon$. Fortunately, as mentioned at the end of Sect. 15.1, a high level of confidence exists in these various terms—particularly

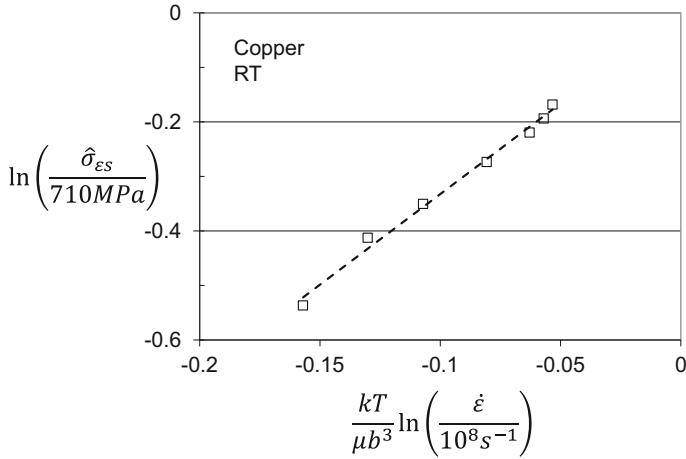


Fig. 15.4 Normalized variation of the saturation threshold stress (characterizing interaction of dislocations with the stored dislocation density) versus normalized temperature and strain rate in copper. The dashed line is the fit according to Eq. 6.26

when their analysis is based on the availability of a data set covering a wide range of temperatures and strain rates.

The third step in the analysis was to fit Eq. 6.28 to the $\hat{\sigma}_e$ versus strain curve to establish $\theta_{II}(\dot{\epsilon})$ and $\hat{\sigma}_{es}(\dot{\epsilon}, T)$. The latter was analyzed using Eq. 6.26, and plots of the logarithm of $\hat{\sigma}_{es}(\dot{\epsilon}, T)$ divided by an estimated 0 K value of this parameter versus a normalized temperature and strain rate term are found throughout the monograph (see Fig. 15.4). The quality of the fits in these plots varied significantly. The correlation for copper in Fig. 8.3, included here as Fig. 15.4, is similar to that developed for the fictitious FoLLyally in Fig. 7.23. Several of the other correlations are also quite good, e, g., zinc (Fig. 10.6) and zirconium (Fig. 10.40). However, the plots developed for AISI 1018 steel (Fig. 9.32, included here as Fig. 15.5), vanadium (Fig. 9.44), niobium (Figs. 9.56 and 9.57), cadmium (Fig. 10.16), magnesium alloy AZ31B (Fig. 10.29), and titanium (Fig. 10.68) show general agreement with the expected trend but either significant scatter or trends that deviate from expected behavior. Some of these deviations are thought to derive from the contributions of dynamic strain aging or deformation twinning. These are discussed below.

In several of the systems analyzed in this monograph, the $\hat{\sigma}_{es}(\dot{\epsilon}, T)$ correlation for an alloy was found to fall in line with the correlation for the pure metal. This was the case in pure magnesium and the magnesium alloy AZ31B (see Fig. 10.31, included here as Fig. 15.6 where the Suzuki data points were from pure magnesium while the other data were from the alloy), in pure zirconium and the alloy Zircaloy-2,¹ and in pure titanium and Ti-6Al-4V (Fig. 10.83). However, alloying does affect the

¹Evidence for this comes from the ability to predict stress–strain curves in Zircaloy-2 using the $\hat{\sigma}_{es}(\dot{\epsilon}, T)$ correlation that was developed for the pure metal.

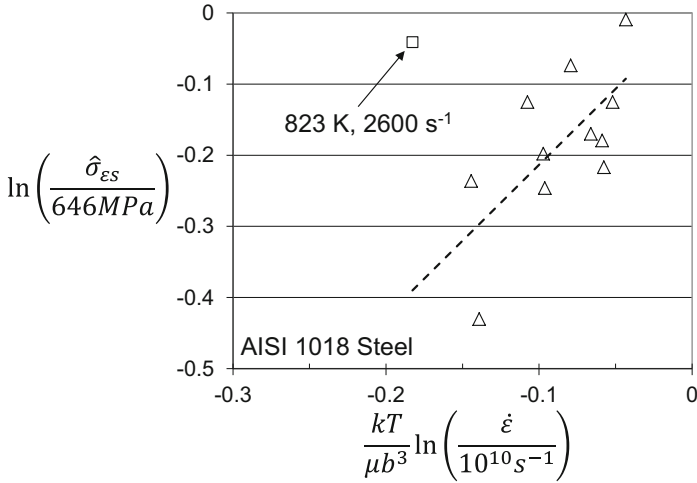


Fig. 15.5 Normalized variation of the saturation threshold stress (characterizing interaction of dislocations with the stored dislocation density) versus normalized temperature and strain rate in AISI 1018 steel. The dashed line is the fit according to Eq. 6.26

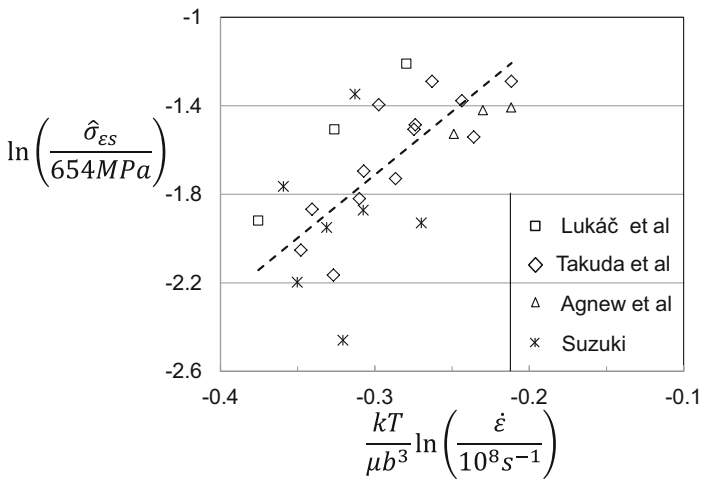


Fig. 15.6 Normalized variation of the saturation threshold stress (characterizing interaction of dislocations with the stored dislocation density) versus normalized temperature and strain rate in magnesium alloy AZ31B. Included are data points in pure magnesium from Suzuki. The dashed line is the fit according to Eq. 6.26

$\hat{\sigma}_{\epsilon s}(\dot{\epsilon}, T)$ correlation in the Ni-C alloys (with increasing deviations from nickel behavior with increasing carbon content; see Fig. 8.38, included here as Fig. 15.7) and in the Cu-Al alloys (see Figs. 8.44 and 8.45). Why this is observed in some systems but not in others should be a topic of further research.

Fig. 15.7 Variation with strain of the saturation threshold stress characterizing dislocation interactions with the stored dislocation density for Ni 270 and Ni 1900 ppm C. In this case, the rate of dislocation storage (the hardening rate) is influenced by the chemistry

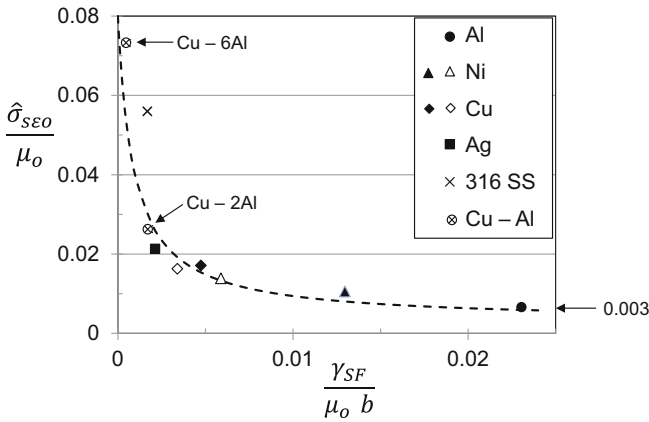
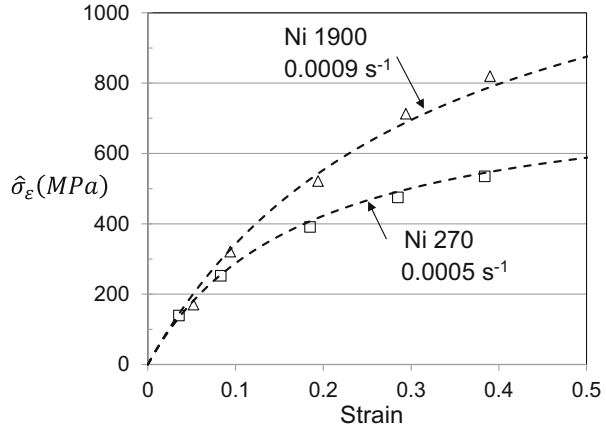


Fig. 15.8 Normalized 0 K saturation threshold stress versus stacking fault energy (also normalized to make this parameter dimensionless) showing a possible trend. Some of these data points are from Kocks and Mecking [7]

In general, Eq. 6.26 provides a descriptive phenomenological correlation relating the saturation threshold stress to temperature and strain rate. It serves to separate the kinetics of evolution from the kinetics of yield, described using Eq. 6.17. The separate treatment of these kinetic processes is a key element of the mechanical threshold stress model that enables the treatment of path dependence. The large scatter observed in some systems may suggest that Eq. 9.7 has not been optimally applied, which in turn may result from errors in the application of Eq. 6.17 or in assessing the constants (particularly g_{oi}) in Eq. 6.18. This observation emphasizes the need for robust data sets encompassing a wide range of temperatures, strain rates, and strains.

Figure 8.46, included here as Fig. 15.8, demonstrated that—at least in FCC systems—there may be a correlation between stacking fault energy and the 0 K

saturation threshold stress. (This plot was derived from a similar plot published by Kocks and Mecking [7].) In fact, the results for several of the HCP systems evaluated in Chap. 10 (Zr, Zn, and Cd—but not Mg) follow the trend observed in this plot (see Exercise 10.7). Another possible correlation was observed in Fig. 10.85 which suggests a dependence of g_{ESO} on $T_m/(c/a)$. However, consistent trends between material systems and σ_{ESO} and g_{ESO} are not evident in the results tabulated in Table 10.22. Perhaps the use of different κ -values and, to a lesser extent, different $\dot{\epsilon}_{\text{ESO}}$ values has confounded these correlations. Further research might help to unravel these inter-relations.

It is worth reiterating that evolution has been based on $d\hat{\sigma}_\epsilon/d\epsilon$ but the total stress is a combination of several terms. For instance, when total stresses are computed using

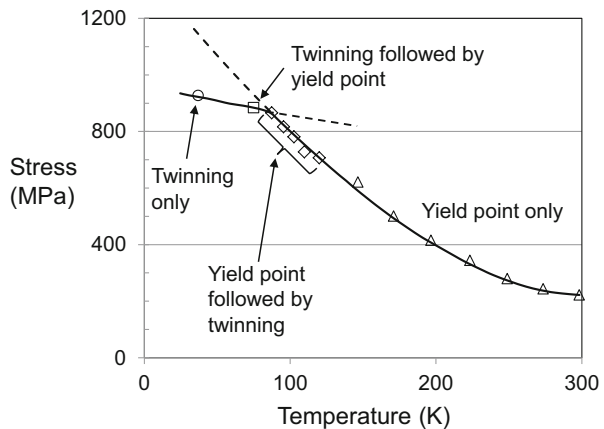
$$\sigma = \sigma_a + \sigma_p + \sigma_i + \sigma_e \quad (15.3)$$

the scatter associated with the $\hat{\sigma}_{\text{ES}}$ correlation is somewhat dampened. Most of the comparisons between measured and predicted stress–strain curves in Chaps. 8, 9, 10, 11, and 12 show good agreement. This was not the case, however, when deformation twinning and/or dynamic strain aging was active.

15.5 The Effects of Deformation Twinning

Deformation twinning was shown to influence both the yield stress kinetics and the rate of dislocation storage and strain hardening. The former was illustrated using measurements in low carbon steel accompanied by metallographic characterization by Erickson and Low [8] shown in Fig. 5.15, and included here as Fig. 15.9, where at low temperatures the yield stress deviates from its higher temperature. Data that followed this trend was presented in Fig. 5.14 and Fig. 10.37 (zirconium), Fig. 9.10

Fig. 15.9 Yield stress measurements combined with microstructural characterization of twinning in a low carbon steel from Erickson and Low [8]. The trend of yield stress versus temperature changes abruptly with the onset of deformation twinning



(iron), Fig. 10.12 (cadmium), and Fig. 10.23 (magnesium alloy AZ31B). A model that reduces s_i (and, therefore, $\hat{\sigma}_i$) at some value of $T \ln(\dot{\epsilon}_o/\dot{\epsilon})$ could not correlate with these deviations. While this could be a simple modification, evidence was not presented at enough temperature and strain-rate combinations to justify this transition value of $T \ln(\dot{\epsilon}_o/\dot{\epsilon})$. More research is warranted before a model modification to account for the effect of deformation twinning on yield kinetics can be introduced. However, the errors introduced by this omission can be large. This was illustrated in the measurements in zirconium at RT and a strain rate of 2800 s^{-1} (Fig. 10.42) where the predicted yield stress exceeded the measured yield stress by 350 MPa.

Deformation twinning was also observed to affect the shape of the stress–strain curve in two ways. Several stress–strain curves showed evidence of a low rate of strain hardening, suggesting that some strain was being accommodated by deformation twinning leading to a lower rate of dislocation storage. This appeared to be the case in vanadium tested at a strain rate of 0.001 s^{-1} and a temperature of 190 K (Fig. 9.41, included here as Fig. 15.10) where the hardening initially follows the expected trends but then essentially “turns off” at a strain of ~ 0.35 . This was also observed in zirconium (Fig. 10.44). In this case the rate of strain hardening decreases abruptly at a strain of ~ 0.08 for the test at the low strain rate but starts low and remains low during the entire test at the dynamic strain rate. Other systems showed evidence of a low initial rate of dislocation storage. This was observed in zinc (Fig. 10.5, included here as Fig. 15.11). In this figure two possible curves were drawn according to Eq. 6.28. However, if hardening in the presence of deformation twinning does not originate from dislocation multiplication and storage, application of Eq. 6.28 and analysis of a “saturation stress” using Eq. 6.26 may not be warranted. Similar shaped hardening curves were also observed in cadmium (Figs. 10.14 and 10.15) and in magnesium alloy AZ31B (Fig. 10.26). The general observation in these cases is that the initial rates of evolution lag the expected behavior.

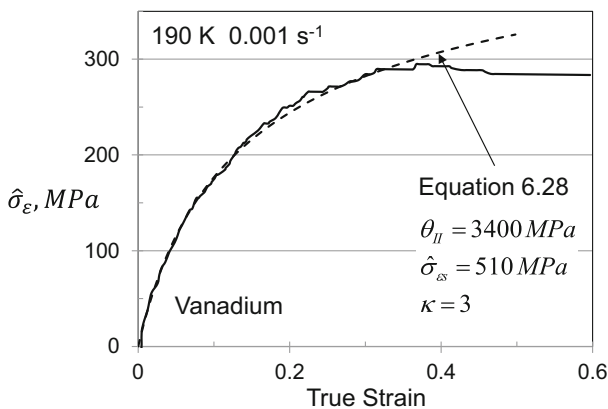


Fig. 15.10 Analyzed variation of σ_ε with strain for one test condition in pure vanadium illustrating that at strains greater than ~ 0.35 , the rate of dislocation storage decreases dramatically, presumably due to deformation twinning

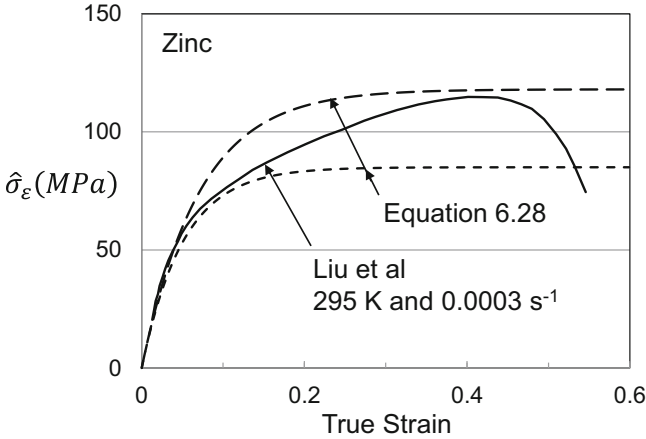
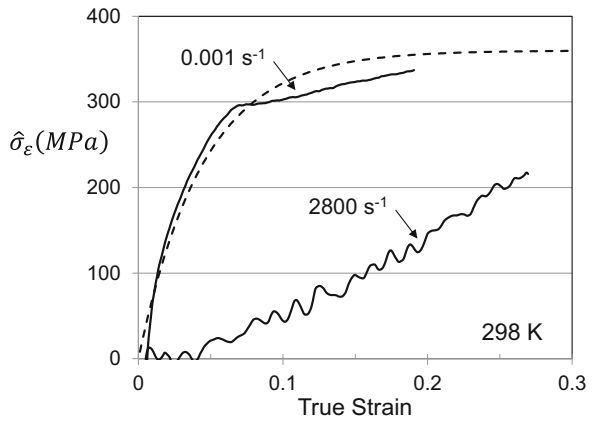


Fig. 15.11 Analyzed variation of σ_ϵ with strain for one test condition in pure zinc illustrating a low rate of initial dislocation storage, presumably due to deformation twinning

Fig. 15.12 Analyzed variation of σ_ϵ with strain for one test condition in pure zirconium illustrating a low rate of initial dislocation storage decreases followed by a high rate of hardening. The former is due presumably to strain accommodated by deformation twinning, whereas the latter is due to grain size refinement resulting from continued twinning



It is evident in the figures referenced in the previous paragraph that deformation twinning affects the shape of the stress–strain curve—the observed dependence of $\hat{\sigma}_\epsilon$ with strain. This is clearly observed in Fig. 10.44 (zirconium), included here as Fig. 15.12. When twinning activates, the increase in stress becomes almost linear with strain. In this case, it was proposed that grain refinement due to the action of twin boundaries is leading to an increased athermal stress. Analysis of the increased stress levels during straining led to an approximation of the grain refinement (see the discussion regarding Fig. 10.44 in Sect. 10.7.1). Once again, this process is difficult to include in a formal model, and no attempt was made to do so here.

While the mechanical threshold stress is not capable at this time of predicting actual stress levels and rate of hardening in the presence of deformation twinning, analysis of stress–strain curve in systems that were undergoing twinning using the

methodologies demonstrated in this monograph made it possible to gain insight on the effects of this alternate deformation mechanism.

15.6 The Signature of Dynamic Strain Aging

Dynamic strain aging (DSA) was observed in several of the systems analyzed in this monograph. The classic signature of DSA was shown in Fig. 5.13, included here as Fig. 15.13, from measurements in mild steel by Murty [9]. DSA leads to a high rate of hardening over a range of elevated temperatures. The effects of DSA were observed in vanadium (Sect. 9.7), niobium (Sect. 9.10), titanium (Sect. 10.9.1), austenitic stainless steel (Sect. 11.5), and Inconel 718 (Sect. 12.3.2).

The traditional understanding of DSA is that at these temperatures the mobility of one or more of the impurity species is sufficient to allow impurities to travel to dislocations and restrict their motion [10, 11]. When analyzing stress–strain curves in systems where DSA was active, several “signatures”—or patterns of deviation from typical behavior—were observed. One of these was evident in plots of the saturation threshold stress as a function of test temperature and strain rate. Fig. 9.44, included here as Fig. 15.14, shows the saturation threshold stress plot in vanadium where the $\hat{\sigma}_{es}$ —values are derived using Eq. 9.7. (See Fig. 9.56 for a similar analysis in niobium.) The three open triangles at values of the abscissa less than ~ -0.16 are at conditions where DSA is likely active. Here, the $\hat{\sigma}_{es}$ - values are very much larger than represented by the dashed-line fit according to Eq. 6.26.

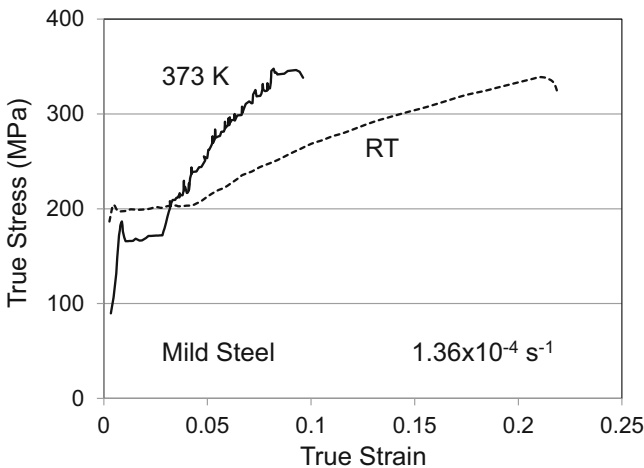


Fig. 15.13 Measurements by Murty [9] in mild steel. The measurement at the higher temperature shows a classic signature of dynamic strain aging with spikes in the stress and an abnormally high rate of hardening

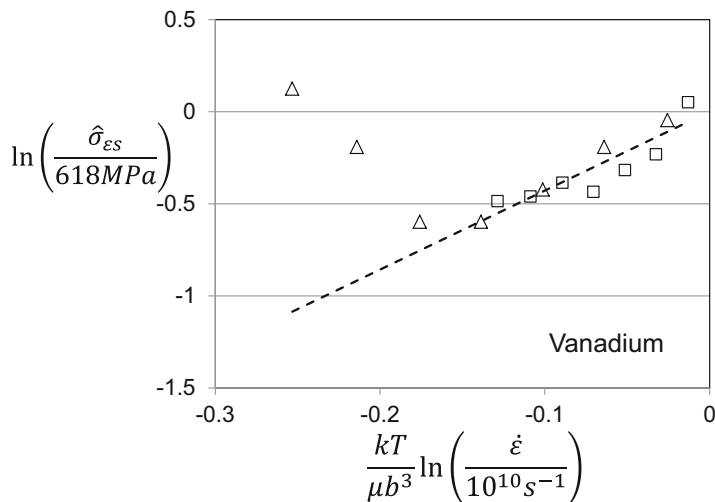


Fig. 15.14 Normalized value of the saturation threshold stress versus normalized temperature and strain rate in vanadium illustrating deviations from the dashed-line behavior (Eq. 6.26) at high temperatures

In Sect. 13.1 the assumption was made that DSA affects one of the s -values in Eq. 6.17. The analyses of stress–strain curves in the presence of DSA proceeded through use of Eq. 9.8

$$s_i = \frac{1}{\hat{\sigma}_i} \left[\frac{\mu_o}{\mu} (\sigma - \sigma_a) - s_p \hat{\sigma}_p - s_\varepsilon \hat{\sigma}_\varepsilon \right] \quad (9.8)$$

which is written for a BCC system (because of the inclusion of a Peierls term). Dislocation storage is assumed to proceed according to Eq. 6.28 with $\hat{\sigma}_{\varepsilon s}$ set by the fit to Eq. 6.26 (e.g., the dashed line in Fig. 15.14 for vanadium). An interesting observation—a second “signature”—in all of the systems analyzed was that the resulting plots of s_i versus σ_ε exhibited common trends. Figure 9.48, presented here as Fig. 15.15, shows the result for vanadium. In this case the values of s_i predicted by Eq. 6.18 with the model parameters from Table 9.13 are indicated by short horizontal dotted lines. At some value of $\sigma_{\varepsilon s}$, s_i is found to increase roughly linearly with σ_ε . Plots similar to Fig. 15.15 were generated for niobium (Fig. 9.62), titanium (Figs. 10.72 and 10.73), austenitic stainless steel (Fig. 11.17), and Inconel 718 (Fig. 12.20).

Although not analyzed in Sect. 9.6, Fig. 9.32 showed for AISI 1018 steel a data point at 823 K and a strain rate of 2600 s^{-1} in the plot of normalized saturation stress versus normalized temperature and strain rate that deviated from the trend established by the other data points in the same fashion as indicated for vanadium in Fig. 15.14. Applying Eq. 9.8 and the model parameters in Table 9.11, a plot of s_i versus σ_ε can be derived. The result is shown in Fig. 15.16.

Fig. 15.15 Analyzed value of s_i versus σ_ϵ for four test conditions (0.001 s^{-1}) in vanadium. The dotted lines are the values of s_i predicted from Eq. 6.18 and the model parameters in Table 9.13

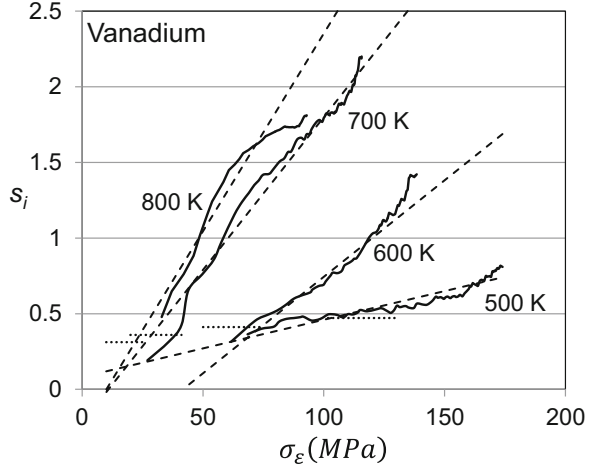
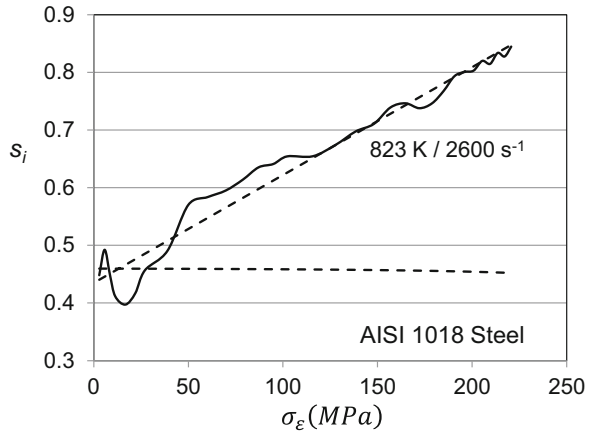


Fig. 15.16 Analyzed value of s_i versus σ_ϵ for the stress strain curve at 823 K and a strain rate of 2600 s^{-1} in AISI 1018 steel. The dotted lines are the values of s_i predicted from Eq. 6.18 and the model parameters in Table 9.11



As in the other analyses, the (almost) horizontal dashed line is the predicted s_i from Eq. 6.18 with the model parameters in Table 9.11 for obstacle “i.” The values decrease slightly with increasing σ_ϵ because this is an adiabatic test and the temperature is rising. In this material under these test conditions, s_i is seen to increase approximately linearly beginning near the yield point. The slope K_{DSA} is a little less than observed in vanadium (Fig. 9.48) but on the order of what was observed in stainless steel (discussed below and in Table 11.8).

A distinct increase of the slope of the plots of s_i versus σ_ϵ with increasing temperature was observed in vanadium (Fig. 13.6), titanium (Fig. 10.74), austenitic stainless steel (Fig. 11.18), and Inconel 718 (Fig. 12.22). The temperature dependence was analyzed using Eq. 9.9

$$K_{\text{DSA}}(T) = K_{\text{DSA}_0} \exp\left(-\frac{Q}{RT}\right) \quad (9.9)$$

but in each case the activation energies fell far from those known for diffusion of impurities in the host matrix.

In Sects. 13.3 and 13.4, the increased solution hardening due to DSA was computed from the dependence of solution strengthening on the square root of the solute concentration (the $k_c\sqrt{c}$ term in Eq. 3.10)

$$\sigma = \sigma_i + k_c\sqrt{c} \quad (3.10)$$

The actual form of the stress contribution due to DSA, σ_{DSA} , took the form

$$C'_i \cong 0.01 \left(\frac{\sigma_{\text{DSA}}}{s_i K \mu}\right)^2 \rho \quad (13.7)$$

where C'_i was the additional solute concentration (in g/cm^3) of the species contributing to DSA. From estimates of the flux of solute to the dislocation core, this analysis resulted in an equation relating the additional solute concentration to the diffusivity and other variables

$$C' \left(\frac{\text{g}}{\text{cm}^3}\right) = \frac{C_0}{100 - C_0} \times (2.446 \times 10^{-9}) \rho \left(\frac{D}{T}\right)^{2/3} \left(\frac{b}{\dot{\epsilon}}\right)^{2/3} \left(\frac{s_\epsilon M \alpha \mu b}{\sigma_\epsilon}\right)^{2/3} (\rho_m)^{5/3} \quad (13.15)$$

Analysis of stress versus strain measurements in a regime where DSA was active enabled a prediction of the correlation between the mobile dislocation density ρ_m and the stress contributed by the stored dislocation density σ_ϵ

$$\rho_m = K_{\rho_m} \sigma_\epsilon^2 \quad (13.17)$$

Figure 13.12 reproduced here as Fig. 15.17 shows the resulting plot for the analyses in Inconel 600, niobium, and 316 L stainless steel. Values of K_{ρ_m} were derived for the five materials analyzed (see Table 13.2), but it was emphasized this model variable showed no common trends across these materials.

The availability of strain-rate change tests in Inconel 600 in a regime where DSA was active offered an important validation of the proposed model. The comparison between predicted and measured m -values in Fig. 13.19 was notable. One important conclusion evident in Eq. 13.15 is that the temperature dependence is not well-described using Eq. 9.9. In addition, Eq. 13.15 includes a strain-rate dependence

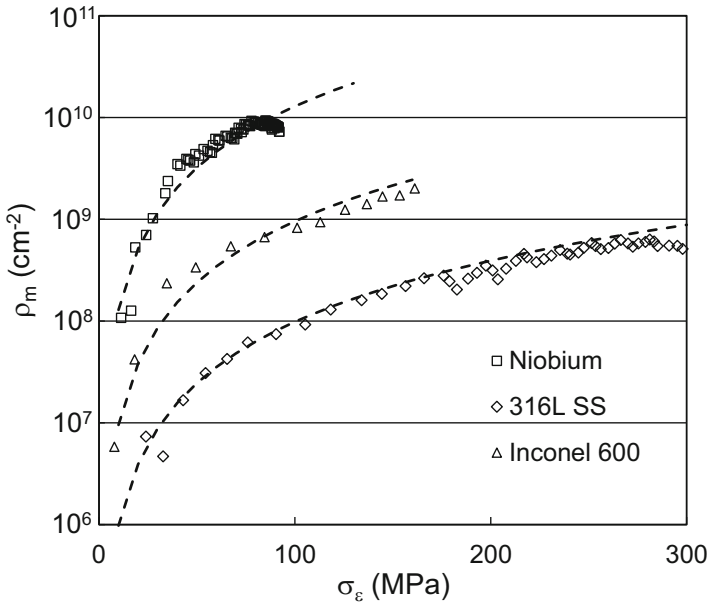


Fig. 15.17 Computed variation of the mobile dislocation density with stress according to Eq. 13.15. Estimates for niobium, Inconel 600, and 316L stainless steel are shown. The dashed lines are drawn according to Eq. 13.17

which was experimentally observed but not included in Eq. 9.9. A second conclusion was that the addition of σ_{DSA} to the stresses predicted without σ_{DSA} showed good agreement with the experimentally measured stresses. This was illustrated in Fig. 13.17. Finally, the prediction of $\hat{\sigma}_\epsilon$ using Eq. 9.7 when DSA is active—as illustrated in Fig. 15.14, for example—is inaccurate since Eq. 9.7 did not subtract the contribution due to DSA. This was discussed in Appendix 13.A2. The proposed DSA model gave considerable insight into DSA and the origin of the “signatures” (deviations from standard MTS model behavior) observed in several material systems.

An important question in understanding DSA is whether the increased stresses and high hardening rates reflect an increase in the stored dislocation density or whether they instead reflect a change in the kinetics influencing dislocation—obstacle interactions. None of the measurements included in this monograph provide a definitive answer to this question. To do so would necessitate a prestrain in a condition where DSA is prevalent followed by a campaign of reloads to establish $\hat{\sigma}_{\epsilon_s}$. However, the evidence in Chap. 13—particularly the analysis of DSA in Inconel 600 and AISI 316L stainless steel (Sect. 13.6)—leads to the conclusion that DSA contributes a large strengthening contribution from the interaction of mobile dislocations with solutes.

15.7 Adding Insight to Deformation in Nickel-Base Superalloys

Application of the MTS methodology to nickel-base superalloys was a significant challenge due to the confounding factors of the stress anomaly and DSA. In many of these systems, the availability of measurements in the “low-temperature” regime governed by Eq. 12.1 was limited. Experience with other FCC alloys, however, guided the use of this equation. Figure 12.2 illustrated this in comparing yield stress versus temperature measurements in Inconel 600 with those in Nickel +510 ppm C. Availability of yield stress versus temperature measurements in pure γ' also helped to deconvolute the affect of the stress anomaly at high temperatures. Dynamic strain aging also introduced strengthening at elevated temperatures. As described in Chap. 13, DSA in these systems exhibited the same “signatures” as observed in other systems. The collective experience with deformation modeling in the metals and alloys studied in this monograph, thus, helped to guide the modeling in the complex nickel-base superalloys. The value of this collective experience following a common, physically based phenomenology in a wide variety of metals and alloys was certainly demonstrated in Chap. 12.

15.8 Adding Insight to Complex Processing Routes

As detailed in this monograph, a major role of deformation models is to define constitutive laws capable of predicting the response of a metal to an arbitrary loading history. With this in hand for a particular metal, another function is to use the models to understand the effects of unique processing routes. Section 8.7 introduced this with shock-deformed nickel. In this case, measurement of the reload yield strength as a function of temperature led to an estimate of the extent of hardening (see Fig. 8.34) achieved by a planar shock wave. The shock loading and unloading step created a material with $\hat{\sigma}_\epsilon = 434$ MPa. Stress–strain curves on the shock-deformed material were predicted and observed to compare well with the measured curves (see Fig. 8.35). Impact events often are initiated by the transit of shock waves, and the ability to predict subsequent deformation behavior can be critical.²

Another application was introduced earlier in Box 5.1 (Sect. 5.1) entitled, “The Tapered Plate Experiment,” and further discussed in Box 6.3 in Sect. 6.3. In this case, the variation of hardening introduced from a rolling operation in an irregularly shaped geometry was measured across a work piece (labeled “along the gage length”). A plot from Box 6.3 is included here as Fig. 15.18. Knowing the distribution of $\hat{\sigma}_\epsilon$ led to the ability to predict a subsequent deformation step. This offered a

²Of course, one wouldn’t normally have the ability to measure the equivalent mechanical threshold stress after shock deformation and subsequent to deformation because these events occur sequentially. Models to predict the level of shock-induced hardening are required.

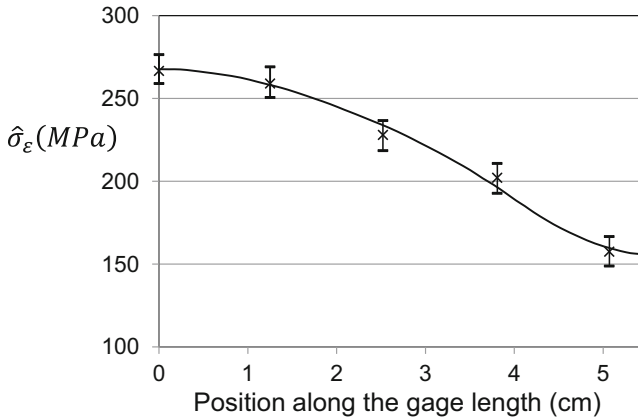


Fig. 15.18 Variation of $\hat{\sigma}_\varepsilon$ along a bar machined from an initially tapered plate rolled to uniform thickness. With this baseline starting distribution, a subsequent deformation step in this plate material can be modeled

realistic scenario in that it is common to use processing operations that do not produce an equivalent level of mechanical work throughout a work piece.

The analysis of the tapered plate and the analysis of the effects of a shock loading required an understanding of the model parameters in the base materials—copper and nickel, respectively. Furthermore, the assumption is made that the processing step does not alter these modeling parameters. In the two examples described above, the anticipation was that the inhomogeneous metal working and the shock deformation would affect a single parameter— $\hat{\sigma}_\varepsilon$. The approach was to estimate this parameter using reload experiments and, with this defining the starting condition, to compare the predicted and measured reload stress–strain curves.

Analysis of deformation in irradiation damaged metals in Sect. 10.8 (Zircaloy-2) and Sect. 11.6 (316 stainless steel) served as additional demonstrations of application of the internal state variable model to a unique processing step. In this case, it was not certain that another defect population (e.g., vacancies) introduced by irradiation in fact was the source of the observed strengthening. Furthermore, for Zircaloy-2 it was not certain that the model parameters assessed for pure zirconium would offer a valid starting point for the model parameters for the alloy. The availability of stress–strain curves at two different temperatures in unirradiated Zircaloy-2 allowed a good comparison with pure zirconium, and it was found that adjustment of a single model modification (the athermal stress) was necessary and that with this modification, the predicted and measured stress–strain curves in Zircaloy-2 agreed closely. (See Fig. 10.52.)

The next step in the analysis was to analyze reload stress–strain curves on irradiated material and to discover which model parameters—if any—appeared to be affected by irradiation. This is not as arbitrary as it might appear since in the Zircaloy-2 study reload measurements at two temperatures were reported. A valid model prediction must match both the stress levels and the rate of strain hardening

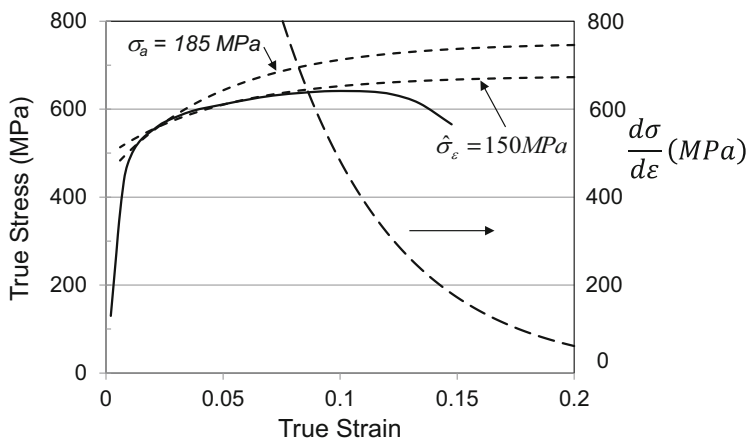


Fig. 15.19 A reload stress–strain curve in irradiated Zircaloy-2 compared with two model predictions illustrating the sensitivity of the model predictions to the model parameters

for these reload test conditions. Figure 10.53, presented here as Fig. 15.19, showed the sensitivity of the comparison to the choice of model parameters for one of the irradiation conditions ($3.6 \times 10^{19} \text{ n/cm}^2$). In Fig. 15.19 the prediction made by adjusting the athermal stress to 185 MPa matches the reload yield stress but overpredicts the rate of strain hardening, whereas the prediction made by increasing $\hat{\sigma}_\epsilon$ to 150 MPa shows excellent agreement with the yield stress and the rate of strain hardening. The latter also is reflected by a good agreement between the measured and predicted point of tensile instability.

Figure 10.54, included here as Fig. 15.20, compares the model predictions at two reload test temperatures for material irradiated at $2.7 \times 10^{20} \text{ n/cm}^2$. Again, these predictions were made with the adjustment of a single model parameter $\hat{\sigma}_\epsilon$ to 238 MPa. The conclusion of this analysis was that there was no need to introduce an additional mechanical threshold stress and that irradiation damage exhibited similarities to dislocation storage. This conclusion was consistent with that reached by previous investigators [12]. Similar results were reached in the analysis of AISI 316LN stainless steel in Sect. 11.6.

Application of the model to materials processed to large strains in Chap. 14 represented a substantial extrapolation. Two approaches were investigated. The first involved the prediction of the actual stress–strain curve during large strain processing, which in turn enabled a prediction of the reload stress–strain curve or, in some cases, the reload stress–strain curves when multiple reload test conditions were used. Section 14.1 highlighted the complications with this approach. These included (i) ability to predict the large strain stress–strain curve using Eq. 6.25 (or Eq. 6.28) and the modeling parameters established for Eq. 6.26 from measurements limited to lower strains, (ii) the stress dependence of g_{oe} , and (iii) the effects of stress state on strain hardening (and texture evolution). Availability of stress–strain curves taken to strains as high as 2.0 helped with the first complication. Furthermore,

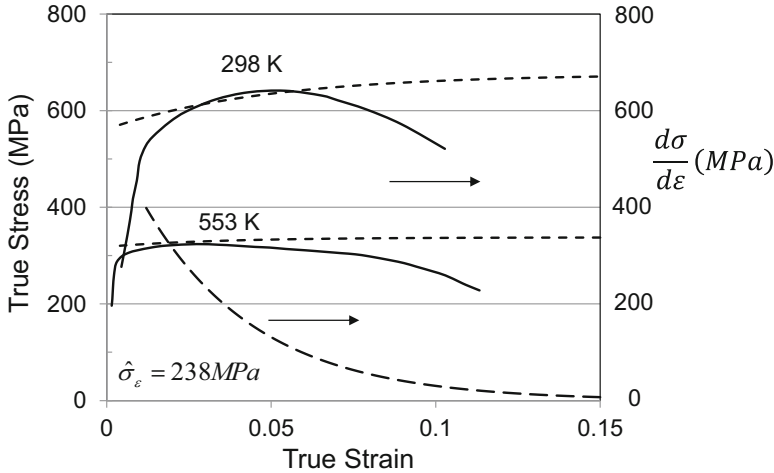


Fig. 15.20 Measured and predicted reload stress–strain curves at two reload test temperatures in irradiated Zircaloy-2 illustrating the agreement with stress level, rate of strain hardening, and temperature dependence

a Stage IV hardening term was added to Eq. 6.28 to improve the predictions (see Eq. 14.11). A proposed model for $g_{o\varepsilon}(\hat{\sigma}_\varepsilon)$ (see Eq. 14.9) helped with the second complication. Unfortunately, the confidence in the understanding of large strain stress–strain curve and $g_{o\varepsilon}(\hat{\sigma}_\varepsilon)$ decreases with increasing strain. Yet, many of the studies of large-strain grain refinement involved total strains of eight or more. Finally, effects of stress-state-dependent hardening were assessed by comparing model predictions and measurements with an eye toward known variations of stress–strain behavior with stress state (e.g., Fig. 14.3).

Dalla Torre et al. [13] published reload stress–strain curves and strain-rate sensitivity measurements in copper processed by equal-channel angular processing (ECAP) with 1, 2, 4, 8, 12, and 16 pressings. (As discussed in Sect. 14.4, a single ECAP pressing using 90° dies imposes an equivalent strain of 1.15.) Figure 14.10, included here as Fig. 15.21, compares the predicted stress–strain curve through the first ECAP pressing and with the measured reload curve and the measured strain-rate sensitivity. Several other comparisons are included in Sect. 14.5, but Fig. 15.21 is shown here because (i) it is at a condition where there is highest confidence in the model predictions and (ii) it illustrates several common trends that were observed in many of the ECAP comparisons shown in Chap. 14. For the latter, note that the reload yield stress is well over predicted and that the reload strain-hardening rate is well under predicted. It was argued in Sect. 14.5.1 that the predominantly shear stress state during ECAP would produce stress levels lower than predicted by a large-strain compression curve. In fact, predicted stress–strain curves were closer to measured stress–strain curves when the large-strain torsion stress–strain curve was used rather than the compression stress–strain curve. The high rate of strain hardening observed in tensile reloads following ECAP processing is consistent with the

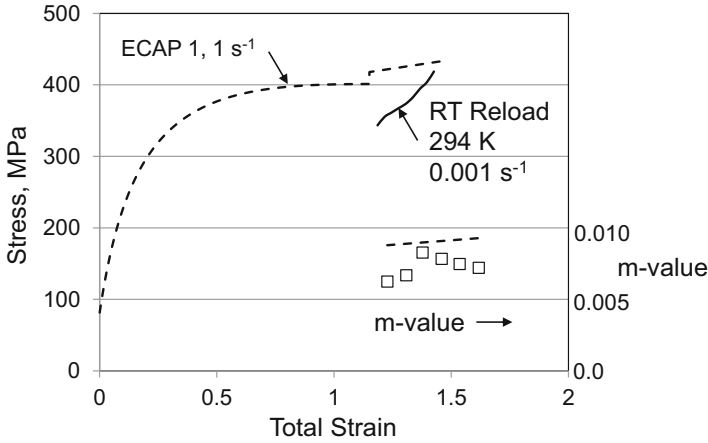
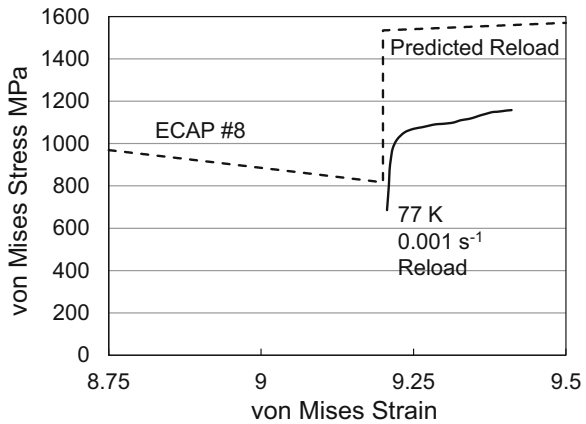


Fig. 15.21 Predicted stress–strain curve during a one-pass ECAP step followed by a reload test in copper compared to the measured reload stress–strain curve and strain-rate sensitivity

Fig. 15.22 Predicted stress–strain curve for eight ECAP pressings in nickel (only the end of step 8 is shown) followed by the predicted reload curve at 77 K and a strain rate of 0.001 s^{-1} compared to the measured curve



expected response with a uniaxial reload after shear prestrain. A stress–strain curve measured by Miller and McDowell [14] in 304L stainless steel for torsion prestrain to a strain of ~ 1 with a stress state change to uniaxial tension (see Fig. 14.49) was used in Sect. 14.9 to support this supposition.

In nickel, a large-strain torsion stress–strain curve was used to establish the hardening behavior, but the available reloads were on material processed with an estimated eight ECAP pressings, which complicated the analysis. Figure 14.38, included here as Fig. 15.22, compares the predicted stress–strain curves in the vicinity of the end of ECAP processing with the reload measurement at 77 K and a strain rate of 0.001 s^{-1} . Once again, the reload stress level is over predicted, and the rate of strain hardening is under predicted.

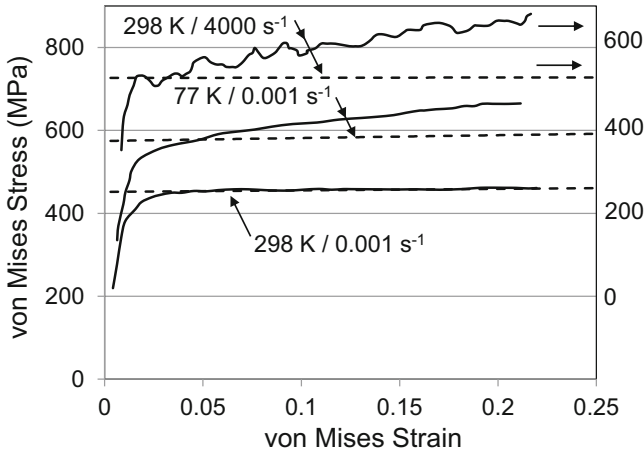


Fig. 15.23 Comparison of measured and predicted reload stress–strain curves at three reload test conditions in eight-pass ECAP copper with the initial value of $\hat{\sigma}_\epsilon$ set at 540 MPa

The general observation in ECAP-processed metals was that the level of hardening resulting from the ECAP steps was less than predicted. This difference warranted application of a second analysis methodology, discussed in Sect. 14.6. This approach was similar to that applied to the “tapered plate” material, the shock-wave strengthened material, and the irradiated material discussed above in that it relied on reload yield stress as a function of reload test conditions. Following the practice demonstrated for irradiation-damaged material, $\hat{\sigma}_\epsilon$ after ECAP (eight cycles) processing in copper was set at $\hat{\sigma}_\epsilon = 559$ MPa, which is less than the value $\hat{\sigma}_\epsilon = 886$ MPa predicted. Figure 14.29, included here as Fig. 15.23, showed the comparison for three reload test conditions. It was argued in Sect. 14.6 that the good agreement at 298 K and 0.001 s^{-1} may well be fortuitous, perhaps indicating presence of a shear instability,³ and the general trend is for the measured rate of hardening to exceed the predicted rate—perhaps due to the transition from predominantly shear loading during ECAP to uniaxial loading for the reload tests.

Availability of a physically based deformation model has enabled analysis of complex deformation histories in materials where a baseline understanding of deformation in the metal exists. Agreement between measured and predicted stress levels, rate of strain hardening, and temperature and strain-rate sensitivities with minor model variations (usually a single model parameter) supports the value of the internal state variable models introduced in this monograph.

³Evidence for this is the difference between the rates of strain hardening in the three measurements in Fig. 15.23.

15.9 Temperature Limits

A historic debate in the constitutive modeling literature has been the range of temperature validity of specific modeling approaches. Often, the focus of the debate is at what temperature do creep mechanisms exhibiting time dependence dominate the deformation map. As discussed by Weertman [15], the debate can hinge on the ratio of the time-dependent to time-independent strain. A test specimen held at a constant stress exhibits time-dependent strain when measurable strains occur as a function of time even at this constant stress. (At low temperatures, this is often referred to as logarithmic creep.) The models advocated in this monograph do not account for time-dependent strain. A popular rule of thumb when the time-dependent strain relies upon diffusion (e.g., for dislocation climb) is that temperatures must be greater than one-half of the melting temperature to promote dislocation climb [16]. However, time-dependent strain is possible at much lower temperatures, and there have been numerous experimental studies that have documented time-dependent strain, e.g., in copper and aluminum, at very low temperatures—well below one-half the melting point.

Table 15.1 lists for many of the experimental data sets analyzed in Chap. 8 through Chap. 12 the maximum temperature reached and the associated homologous temperature. The last column includes a comment related to the applicable strain rate or whether the highest temperature measurements are in line with model predictions. This latter observation is important. Good agreement between the model predictions using a “low” temperature model and the measurements at the highest temperatures adds credibility to the overall modeling methodology. The melting temperature of the alloys is generally taken as the melting temperature of the host element, unless actual melting temperatures are available (as in the austenitic stainless steels and Ti-6Al-4V).

The third column in this table shows that indeed most of the measurements do not exceed a homologous temperature of 0.5. Even though several of the measurements in the HCP systems are at quite a high temperature, many of these were at a high strain rate. For instance, the Suzuki et al. measurements at the strain rate of 10 s^{-1} went to a homologous temperature of 0.84. Assuming the model constants in Table 10.5 in conjunction with Eq. 6.17 (with $i = 2$) and Eq. 6.18, the equivalent temperature to achieve the same stress level at a strain rate of 0.001 s^{-1} brings the maximum homologous temperature to 0.64 (see Fig. 15.24).

Measurements in the BCC systems are at comparatively lower temperatures than those in the HCP and FCC systems. This likely reflects the melting point of metals such as W, Mo, Nb, and Ta and the difficulty in performing measurements at such high temperatures.

Some of the measurements in the austenitic stainless steels were at temperatures slightly above a homologous temperature of 0.50, but note that DSA was uniformly observed at the higher temperatures.

While quite a few of the measurements listed in Table 15.1 were at temperatures nearing a homologous temperature of 0.50 and, unless otherwise indicated, the

Table 15.1 Experimental conditions for the myriad materials analyzed in this monograph showing the maximum ratio of T/T_m . References can be found in the Chap. 8 through Chap. 12

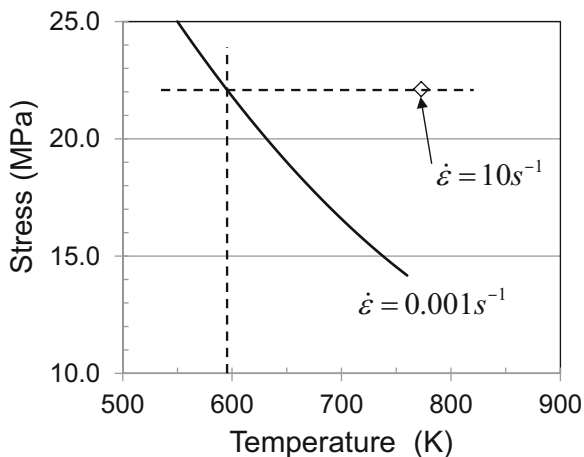
Metal	Reference	Maximum T/T_m	Comment
Zinc	Risebrough	0.52	
	Liu et al.	0.43	
Cadmium	Risebrough	0.58	Data point at this T falls below prediction; 0.50 okay
	Mannan and Rodriguez	0.50	
Magnesium	Suzuki et al.	0.62	At 0.1 s^{-1}
		0.73	At 2.5 s^{-1}
		0.84	At 10 s^{-1}
Mg AZ31B	Lukáč and Trojanová	0.62	
	Agnew et al.	0.57	
	Takuda et al.	0.62	
Zirconium	Akhtar and Duygulu	0.30	Yield stress measurements only
	Soo and Higgins	0.22	Yield stress measurements only
	Chen and Gray	0.30	
	Buch	0.41	Yield stress measurements only
Titanium	Conrad et al.	0.52	At 0.033 s^{-1} ; DSA observed
	Nemat Nasser et al.	0.40	At 0.001 s^{-1}
		0.51	At 2000 s^{-1}
Ti-6Al-4 V	Follansbee and Gray	0.26	
Molybdenum	Campbell and Briggs	0.17	Yield stress measurements only
Niobium	Campbell and Briggs	0.18	Yield stress measurements only
Tungsten	Brunner and Glebovsky	0.21	Yield stress measurements only
Tantalum	Hoge and Mukherjee	0.24	Yield stress measurements only
Iron	Nojima	0.16	Yield stress measurements only
	Pugh and Davidson	0.26	Yield stress measurements only
Low carbon steel	Campbell and Ferguson	0.39	Yield stress measurements only
Chromium	Wain et al.	0.12	Yield stress measurements only
AISI 1018 steel	Gray & Chen	0.31	At 0.001 s^{-1}
		0.45	At 2600 s^{-1}
Vanadium	Nemat-Nasser and Guo	0.32	At 0.001 s^{-1} and 1000 s^{-1}

(continued)

Table 15.1 (continued)

Metal	Reference	Maximum T/T_m	Comment
Niobium	Gray and Chen	0.24	At 4500 s^{-1}
	Nemat-Nasser and Guo	0.29	At 3300 s^{-1}
Copper	Follansbee and Kocks	0.35	At 5000 s^{-1}
		0.22	At 0.0001 s^{-1}
	Carreker and Hibbard	0.35	At 0.0007 s^{-1}
		0.5	At 0.0007 s^{-1} ; stresses over predicted; also, see Fig. 8.15.
Eleiche and Campbell	0.5	At 0.0017 s^{-1} and at 520 s^{-1} ; predictions okay but borderline	
Nickel	Gray and Chen	0.33	At 3200 s^{-1}
	Follansbee et al.	0.17	At 0.0005 s^{-1}
	Mueller	0.45	At 1750 s^{-1}
Inconel 718	Nalawade et al.	0.54	At $6.5 \times 10^{-5} \text{ s}^{-1}$; stress anomaly and DSA confound predictions
316L stainless steel	Norström	0.52	At 0.001 s^{-1} ; yield stress measurements only
304 stainless steel	Steichen	0.57	DSA observed
304 and 316 stainless steel	Conway et al.	0.49	DSA observed
Austenitic stainless steels	Byun and Farrell	0.43	DSA observed
Austenitic stainless steel	Brynes et al.	0.52	Yield stress measurements only

Fig. 15.24 Predicted variation of yield stress with temperature at a strain rate of 0.001 s^{-1} in pure magnesium. A temperature slightly below 600 K yields the same yield stress as observed at a temperature of 773 K and a strain rate of 10 s^{-1}



mechanical threshold stress model was able to describe yield and hardening kinetics in these systems, it is likely in most of these systems at the highest temperatures that measurable time-dependent strain would have been noted if, after loading to some stress level, the stress level were held constant and strain were continuously monitored with a sensitive strain-measuring device. Some of this strain is due to stress-enhanced rearrangements of dislocation structures [15]. The mechanical threshold stress includes a dynamic recovery model represented by Eq. 6.26. This offers a sound, albeit phenomenological, relation between saturation stress, strain rate, and temperature. Time is not a model parameter, but it is sensible to conclude that it could, or at the highest temperature, even should be. If the transients associated with these time-dependent deformations are considered to be critical for a specific application, then another deformation model should be implemented.

As Weertman writes [15], the transition between traditional low temperature and high temperature mechanisms may be the ratio of time-independent to time-dependent strains. Evidence presented in this monograph indicates that the mechanical threshold stress model is applicable at temperatures approaching a homologous temperature of 0.50 and that accurate predictions of yield and hardening are possible at these temperatures. The work presented here supports the 0.50 T_H rule of thumb for the onset of diffusional (dislocation climb) mechanisms that are better modeled using one of many available high-temperature creep formulations.

15.10 Summary

When first introduced in 1988 [1], the mechanical threshold stress model offered an explanation for a puzzling experimental observation, which was that at high strain rates, the stress at a constant strain exhibited a linear dependence on strain rate. A popular theory, even promoted by the author of this monograph in 1982 [17] and 1984 [18] publications, was that this linear strain rate dependence was consistent with a transition to a phonon drag controlled deformation mechanism. The inconsistency, of course, was that the stresses at a constant strain were being compared and that this was not a comparison at a constant structure. When stress at a constant structure was evaluated, as in [1], no dramatic upturn with increasing strain rate was observed. The implications of this result were significant with regard to predictive capability, even for strain rates only slightly beyond the regime where experimental measurements of stress were feasible.

Two problems with the mechanical threshold stress model, however, immediately emerged. The first was that the extensive experimental campaign required to establish the model parameters described in [1] for copper and in the subsequent Ni-C paper [2] appeared to present a significant obstacle to model implementation. The second problem was that the model was not easily introduced into engineering codes that were configured to use strain as a state variable. The second problem gradually subsided as the benefits of the internal state variable modeling approach encouraged code developers to allow the tracking of the state variables and to allow for the

update of strain according to Eq. 6.25. Experience with multiple materials systems—much arising out of decades of work by Gray, Chen, and coworkers at Los Alamos National Laboratory [19] and S. Nemat-Nasser and coworkers at the University of California at San Diego [20–22]—has begun to ease the requirements for extensive experimental campaigns.

This chapter has provided a review of the status of the mechanical threshold stress model. It was argued in Sect. 15.1 that the models for the temperature and strain-rate dependence of the yield stress (whether this was the yield stress of well-annealed material or of material in a hardened state) were on solid footing. One contribution of this monograph has been the use of as many as three internal state variables when justified by an understanding of the operative deformation mechanisms (and of obstacle populations opposing dislocation motion). Several examples of correlations between chemical content and the value of a state variable were presented. Evolution of the threshold stress characterizing the stored dislocation density was described in Sect. 15.3 as relying on a phenomenological relation (Eq. 6.28) with less physical basis. In Sect. 14.4 it was suggested that a portion of the hardening included in Eq. 6.28, when fit to large strain stress–strain curves, may well be an evolving athermal stress term. A physically based hardening law remains a grand challenge.

Even in light of these shortcomings, a key feature of the mechanical threshold stress model, which hopefully has emerged in this monograph, is its simplicity. The governing equation represented by Eq. 6.17 is sensible in that the stress is related to the contributions of dislocation interacting with populations of defects, but it is also mathematically simple. The s -values represented by Eq. 6.18 are easily analyzed. The inclusion of p_i , q_i , and $\dot{\epsilon}_{oi}$ may argue against this, but as has been emphasized, model predictions are relatively insensitive to the selected values of these parameters. As evident in Tables 10.21 and 10.22, these model parameters have not been used as fitting parameters, and for many metals these parameters are identical or nearly identical. The evolution equation, represented by Eq. 6.28, is simple to evaluate, yet it enables a surprisingly good fit to much of the experimental stress–strain curves evaluated in this manuscript.

A contribution to the model’s simplicity—or at least to the simplicity of model application—has been the growing comfort with deriving $\hat{\sigma}_\epsilon(\epsilon)$ from stress–strain curves using Eq. 9.7 (or equivalent). It now appears practical to develop a set of model parameters in a metal with a low initial dislocation density with only (i) a robust data set documenting the variation of yield stress with temperature and strain rate and (ii) a selection of stress–strain curves as a function of temperature and strain rate. If it is desired to develop a set of model parameters in a metal in a worked condition, it would be necessary to anneal this metal to gather the data set required by (i) and then to estimate $\hat{\sigma}_\epsilon$ in the worked condition (as illustrated in Fig. 15.23). Stress–strain curves measured on material beginning in a worked condition could still be analyzed, but revision of Eq. 9.7 is necessary to include the initial $s_\epsilon \hat{\sigma}_\epsilon$ term, and the limits of integration of Eq. 6.28 fit to $\hat{\sigma}_\epsilon(\epsilon)$ would need to be carefully specified.

Part of the simplicity arises from limiting the treatment to deformation by dislocation glide. Even the contribution of deformation twinning was shown in

several systems to lead to constitutive behavior that was not easily modeled. A benefit of the mechanical threshold stress model, however, was that deviations from typical behavior were easily identified, and the sign of the deviation (i.e., whether stress levels were greater than or less than predicted levels) seemed consistent with expectations. Dynamic strain aging introduced another deviation from typical behavior, but once again the deviations were easily identified. In this case a consistent trend—a signature—was observed in several metals and alloys.

None of the metal studied underwent stress-induced phase transformations that affect the results, and the model in its current form is not capable of tracking the effects of such transformations on strength. Remaining below a homologous temperature of 0.5 implied that dynamic recrystallization did not occur; this too would have been beyond the current model capabilities.

As evidenced by the variety of metals considered in Chap. 8 through Chap. 12, the applicability of the mechanical threshold stress model is pervasive. With additional research on topics identified in this chapter, the capabilities of the model will continue to increase, as will the number of metals and alloys included in the model data base.

References

1. P.S. Follansbee, U.F. Kocks, A constitutive description of the deformation of copper based on the use of the mechanical threshold stress as an internal state variable. *Acta Metall.* **36**(1), 81–93 (1988)
2. P.S. Follansbee, J.C. Huang, G.T. Gray, Low-temperature and high-strain-rate deformation of nickel and nickel-carbon alloys and analysis of the constitutive behavior according to an internal state variable model. *Acta Metall. Mater.* **38**(7), 1241–1254 (1990)
3. R. Gröger, A.G. Vailey, V. Vitek, Plastic deformation of molybdenum and tungsten: I. Atomistic studies of the core structure and glide of $\frac{1}{2}\langle 111 \rangle$ screw dislocation at 0K. *Acta Mater.* **56**, 5401–5411 (2008)
4. R. Gröger, V. Vitek, Plastic deformation of molybdenum and tungsten: III. Incorporation of the effects of temperature and strain rate. *Acta Mater.* **56**, 5426–5439 (2008)
5. H. Mecking, U.F. Kocks, Kinetics of flow and strain-hardening. *Acta Metall.* **29**, 2865–1875 (1981)
6. Y. Estrin, Dislocation-density-related constitutive modeling, in *Unified Constitutive Laws of Plastic Deformation*, ed. by A. S. Krausz, K. Krausz, vol. 48, (Academic Press, 2003), pp. 171–273
7. U.F. Kocks, H. Mecking, Physics and phenomenology of strain hardening: The FCC case. *Prog. Mater. Sci.* **48**, 171–273 (2003)
8. J.S. Erickson, J.R. Low Jr., The yield-stress temperature relations for iron at low temperatures. *Acta Metall.* **5**, 405–406 (1957)
9. K.L. Murty, Is neutron damage exposure always detrimental to metals (steels)? *Lett. Nat.* **308**, 51–52 (1984)
10. L.P. Kubin, Y. Estrin, Dynamic strain ageing and the mechanical response of alloys. *J. Phys. III* **1**, 929–943 (1991)
11. P.G. McCormick, Model for Portevin-Le Chatelier effect in substitutional alloys. *Acta Metall.* **20**, 351 (1972)

12. T.S. Byun, K. Farrell, N. Hashimoto, Plastic instability behavior of bcc and hcp metals after low temperature neutron irradiation. *J. Nucl. Mater.* **329-333**, 998–1002 (2004)
13. F.H. Dalla Torre, E.V. Pereloma, C.H.J. Davies, Strain hardening behaviour and deformation kinetics of Cu deformed by equal channel angular extrusion from 1 to 16 passes. *Acta Mater.* **54**, 1135–1146 (2006)
14. M.P. Miller, D.L. McDowell, The effect of stress-state on the large strain inelastic deformation behavior of 304L stainless steel. *ASME J. Eng. Mater. Technol.* **118**, 28–36 (1993)
15. J. Weertman, Microstructural mechanisms in creep, in *Mechanics and Materials, Fundamentals and Linkages*, ed. by M. A. Meyers, R. W. Armstrong, H. O. K. Kirchner, (John Wiley & Sons, Inc., New York, 1999), pp. 451–488
16. R.W.K. Honeycombe, *The Plastic Deformation of Metals*, 2nd edn. (Edward Arnold Publishers, Ltd., London, 1984), p. 393
17. P.S. Follansbee, J. Weertman, On the question of flow stress at high strain rates controlled by dislocation viscous flow. *Mech. Mater.* **1**, 345 (1982)
18. P.S. Follansbee, G. Regazzoni, U.F. Kocks, “The transition to drag controlled deformation in copper at high strain rates”, in Proceedings of the Third International Conference on Mechanical Properties of Materials at High Rates of Strain, J. Harding, ed., (1984), p. 71–80
19. G.T. Gray III, S.R. Chen, “MST-8 constitutive properties & constitutive modeling,” Los Alamos National Laboratory, LA-CP-07-1590. (Contact authors for further information.) (2007)
20. S. Nemat-Nasser, W. Guo, High strain-rate response of commercially pure vanadium. *Mech. Mater.* **32**, 243–260 (2000)
21. S. Nemat-Nasser, W. Guo, Flow stress of commercially pure niobium over a broad range of temperatures and strain rates. *Mater. Sci. Eng.* **A284**, 202–210 (2000)
22. S. Nemat-Nasser, W.G. Guo, Y.Y. Cheng, Mechanical properties and deformation mechanisms of a commercially pure titanium. *Acta Mater.* **47**, 3705–3720 (1999)

Index

A

Absolute zero, 80, 90
Activation energy
 normalized, 120, 126, 145, 146, 167, 172,
 215, 216, 289, 301, 302, 371, 380, 401,
 435–439, 441, 447, 448, 450, 491
Activation volume, 123, 124, 132, 133, 139,
 141, 223–226, 337, 357, 358, 370,
 487, 490
Adiabatic deformation, 135, 136, 138, 143,
 190, 209, 454
Al₂O₃, 8, 29, 45
Aluminum alloy, 8, 72, 111, 295, 488
Anomalous hardening, 377, 378, 393, 401, 403,
 404, 430
Areal density, 60
Athermal stress, 106, 108, 120, 139–141, 144,
 147, 178, 179, 186, 187, 198, 199, 201,
 208, 215, 234, 235, 243, 244, 255, 256,
 267, 268, 273, 274, 290, 291, 301, 309,
 311, 312, 314, 318, 319, 330, 336, 348,
 352, 367, 368, 370, 380, 393, 436,
 445–447, 449, 454, 455, 470, 478, 480,
 483, 493, 499, 506, 507, 515
Attempt frequency, 82
Attractive force, 35, 51
Austenite, 345, 349, 398
Austenitic stainless steel
 18-8, 363
 AISI 304, 346–348, 358, 360
 AISI 304L, 346–348, 360
 AISI 316, 346–348, 358, 360, 363
 AISI 316L, 346–348, 350, 360

AISI 316LN, 360
M₂₃C₆, 349
nitrogen strengthening in, 352

B

Basal plane, 42, 271
Beryllium, 8, 111
Body-centered cubic (BCC)
 metals, 60, 62, 63, 133, 146, 168, 186, 196,
 211–264, 271–273, 276, 278, 289, 305,
 322, 337, 338, 366, 370, 441, 489
Boltzmann equation
 Boltzmann's constant, 79, 105, 107, 121,
 417, 419
Bond energy, 37–39
Bonding, 35–50
Brass, 67, 336
Brittle metals, 60
Burger's vectors, 77, 78, 90, 227, 449

C

Cadmium, 272, 273, 275, 277–284, 288, 291,
 298, 307, 335–339, 398, 436, 447, 494,
 498, 512
Cam plastometer, 284
Carbide precipitation
 M₂₃C₆, 349, 392
Carbon, 45, 68, 87, 110, 111, 113, 138,
 184–188, 194–198, 200, 201, 203, 204,
 207, 211, 212, 217, 219, 295, 315, 322,
 359, 463, 470, 490, 495, 497, 512

- Ceramic particles, 72
 Ceramics, 7, 10, 60
 Chlorine, 35
 Chromium, 111, 212, 225, 226, 345, 350, 351, 394, 470, 512
 Close-packed, 40, 42, 51, 60, 62, 65, 66, 202, 271, 272
 Close-packed direction, 40, 46, 56, 60, 62, 63, 65, 66, 202, 271
 Close-packed plane, 42, 43, 56, 62, 63, 68, 487
 Cold worked material, 309–311, 314
 Compressibility
 incompressible, 10, 17
 Compression
 compression test, 3, 11–19, 29, 32, 84, 102, 112, 136, 169, 173, 175, 180, 185, 198, 285, 328, 336, 440, 445, 446, 474, 479, 481
 Computer modeling, 100
 Computer simulation, 96, 97, 99
 Condensed matter, 38, 79
 Considère criterion, 26, 474
 Constitutive behavior, 35, 97, 113, 185, 193, 194, 207, 227–247, 261, 435, 516
 Constitutive law, 95–107, 156, 158, 162, 163, 168, 169, 174, 190, 208, 245, 368, 379, 448, 471, 472, 505
 Copper
 Cu-Al alloys, 201, 203–206, 208, 495
 Cu-Nb, 44, 45
 oxygen-free electronic (OFE), 168, 169
 oxygen-free high conductivity (OFHC), 168, 179
 Cottrell-Stokes ratio, 115
 Critical resolved shear stress, 58, 59, 69, 73, 80, 90, 250, 378
 Cross head velocity, 346
 Cross-sectional area, 5–7, 11, 16
 Cross slip, 90, 197, 202, 336
 Crystal lattice
 planes and directions, 57–59, 63, 65
 Crystal plasticity, 19, 177, 398
 Current state, 119
- D**
- Defect, 25, 35, 45, 47, 50, 72, 73, 89, 90, 111, 134, 136, 201, 202, 368, 369, 371, 487, 506, 515
 Deflection measurement device, 1, 3, 22
 Deformation kinetics, 73, 83, 89, 115, 211, 225, 271, 305, 308, 314, 338, 348, 357, 377, 488, 489, 493
 Deformation twinning, 112, 113, 196, 206, 218, 247, 248, 250, 256, 271–274, 279, 281–285, 288, 290, 293, 305–307, 319, 320, 334–336, 339, 340, 398, 436, 494, 497–500, 515
 Diametrical strain, 9
 Die design, 96, 443, 444
 Diffusion
 activation energy, 252, 329, 366, 413, 419, 427, 503
 diffusion equation, 420
 stress assisted, 417
 Dislocation, 35, 60, 77, 106, 119, 144, 168, 211, 271, 345, 378, 409, 436, 487
 Dislocation core, 409, 414, 416, 417, 419, 427–429, 503
 Dislocation density
 mobile dislocation density, 417–419, 421–424, 427, 428, 503, 504
 Dislocation generation, 49, 71, 90, 134, 192, 412, 492
 Dislocation line, 45, 47, 48, 72, 80, 81
 Dislocation mobility, 206
 Displacements per atom (dpa), 367–369, 373
 Ductile metals, 60
 Ductile-to-brittle transition, 272
 Dynamic recovery, 90, 197, 336, 514
 Dynamic recrystallization, 113, 286, 291, 296, 335, 462, 474, 481, 516
 Dynamic strain aging (DSA)
 signatures, 250–252, 335, 336, 379, 399, 400, 402, 409–413, 422, 427, 428, 500–505
- E**
- Easy glide, 70
 Elastic, 5, 6, 10, 13–18, 22–24, 29, 35, 38, 39, 42, 43, 55, 70, 95, 122, 127, 139, 150, 233, 474
 Elastic modulus, 7, 8, 15, 22, 23, 29, 32, 38, 39, 43, 44, 50, 51, 53, 101, 122, 474
 Elastic strain, 10, 11, 16, 24, 32, 39
 Electromechanical, 1
 Electronic charge, 36
 Electron microscope, 45, 48
 Electron volts (ev), 51
 Energy-separation distance diagram, 38
 Energy storage during deformation, 136
 Engineering strain, 6, 16, 17, 24, 27, 28, 31, 32, 175
 Engineering stress, 5, 17, 24, 32
 Engineering stress-strain curve, 16, 17, 30, 32

- Equal channel angular pressing (ECAP), 22, 410, 443–445, 449–462, 465–477, 479–483, 508–510
- Equilibrium separation distance, 37
- Erickson and low, 112, 113, 497
- Evolution, 104, 108, 114, 116, 119, 134, 135, 143, 156, 160, 163, 172, 177, 188, 189, 193, 197, 201, 204, 206–208, 211, 223, 226, 250, 255, 256, 262, 264, 272, 275, 280, 281, 283, 284, 290, 292, 294–296, 300, 302–308, 314, 322, 323, 332, 334, 338, 360, 369, 371, 377, 383, 428, 436, 440–442, 444, 446–448, 463, 471, 479, 480, 492, 493, 496–498, 507, 515
- Evolution equation, 107, 131, 134, 152, 160, 161, 193, 228, 229, 236, 237, 243, 245, 276, 300, 301, 337, 393, 473, 478, 515
- Experimental scatter, 128, 139, 150, 226, 230, 238, 354, 421
- Explosively formed penetrator (EFP), 98, 99
- Extensometer
 - laser interferometry, 22
 - linear-variable-displacement transducer (LVDT), 22
 - non-contact strain measurement, 22
- F**
- Face-centered cubic (FCC)
 - metals, 60, 62, 63, 75, 167, 168, 194, 201, 202, 206, 208, 211, 212, 215, 222, 224, 227, 237, 247, 261, 262, 271, 337, 338, 342, 346, 487
- Failure, 10, 96, 97
- Fleischer, R.L., 68
- FoLLy alloy, 143, 147–154, 156, 162, 163, 165, 262, 264, 265, 493, 494
- Force, 1, 3–8, 11–13, 17, 22, 23, 26, 29–32, 35, 37–39, 42, 50, 58, 69, 78, 83, 90, 306, 403, 416, 469
- G**
- Gamma double prime (γ'')
 - Ni_3Nb , 382
- Gamma prime (γ')
 - lattice mismatch, 378
 - Ni_3Al , 378
 - volume fraction, 378, 381
- Gold, 8, 86, 139
- Grain
 - misorientation angle, 445
 - refinement, 283, 336, 436, 443–449, 474, 480, 493, 499, 508
 - size, 67, 75, 106, 112, 143, 144, 147, 168, 175, 176, 179, 186, 190, 197–199, 201, 207, 208, 227, 272, 273, 277, 279, 282–284, 290, 298, 307, 316, 318, 319, 330, 336, 340, 350–355, 359, 370, 371, 393, 435, 436, 443–449, 463, 470, 472, 477, 480, 481, 487, 499
- Grain size, 67, 75, 106, 112, 168, 175, 176, 179, 186, 190, 197–199, 201, 207, 208, 227, 288, 298, 350–355, 359, 370, 371, 435, 436, 443–449, 463, 470, 472, 477, 480, 481, 487, 499
- Grips, 1, 2, 136, 138
- Guinier-Preston (G-P) zone, 72
- H**
- Hall-Petch equation, 67, 106, 198, 199, 283, 318, 445, 446
- Hardness, 53
- Heat capacity
 - temperature dependence of, 136
- Heat treatment, 98, 349, 350, 354, 358, 382, 387, 445
- Heavily deformed metals, 435–481
- Hexagonal close packed
 - HCP metals, 62, 64, 113, 271, 346, 366, 371, 383, 492
- High pressure torsion, 445
- Homogenize, 97
- Homologous temperature (T_H), 168, 178, 183–185, 271, 272, 299, 335, 349, 511, 514, 516
- Honeycombe, 63, 68
- Hot-working, 97, 98
- Hydrogen, 68
- I**
- Ideal c/a ratio, 63
- Ideal gas, 79, 103
- Ideal gas equation, 103
- Impact events, 96, 97, 505
- Impurity atoms, 47, 67–69, 72, 80, 88, 89, 111, 185, 219, 223, 224, 370, 379
- Impurity element, 67, 149, 213, 215, 250, 279, 488–490
- Inconel 600, 378, 380, 381, 383–386, 388, 389, 393, 395, 396, 398, 399, 401, 403, 409, 420, 422–430, 503–505

Inconel 718, 64, 378, 381, 382, 384, 387,
389–395, 397, 399, 401–403, 409, 410,
412–414
Ingot, 97, 143, 185
Instability, 26, 27, 29, 32, 281, 313–315, 398,
474–476, 481, 507, 510
Interatomic forces, 7, 22, 35, 50
Intermetallic compounds, 309, 314
Internal state variable, 95, 98, 102, 108, 114,
119, 131, 132, 134, 155, 168, 183, 222,
223, 308, 370, 371, 377, 382, 435, 480,
481, 487, 488, 490, 492, 506, 510,
514, 515
Interplanar spacing, 60
Interstitials, 68
Interstitial, 68, 90, 111, 186, 194, 201, 213,
321, 326, 345, 349–352, 357, 370,
379, 381
Ion, 35–39, 50, 51
Ionic bonding, 35, 37, 38
Iron
 effect of carbon concentration, 490
Irradiation damage, 110, 132, 308, 312, 314,
367–369, 371, 435, 457, 506, 507, 510
Isotropic, 122, 143, 144, 185, 271, 436

J

Jerky glide, 81, 82, 487
Johnson-Cook model, 101

K

Kear-Wilsdorf, 378, 393
Kinetic factor, 90, 329, 379, 419
Kinetics, 73, 78, 82–84, 89, 91, 105, 111, 113,
115, 138, 147, 149, 150, 184, 211, 215,
222, 223, 225, 231, 235, 236, 250, 252,
271, 273, 277–279, 305, 308, 314, 315,
337, 338, 348, 357, 377, 379–383, 391,
393–396, 398, 401, 409, 412, 414, 416,
427, 447, 463, 481, 488, 489, 491, 493,
496–498, 504, 514
Kinetics of Hardening, 89, 90

L

Linear defects, 47
Linear strain hardening, 386
Load cell, 1
Lower yield point, 111, 232
Lüders bands, 111
Ludwik equation, 100

M

Machine modulus, 24
Magnesium
 magnesium alloy AZ31, 284, 287–290,
292–296, 298, 340, 494, 498
Martensitic transformation, 350
Material strength, definition, 14
Mechanical equation of state, 105
Mechanical threshold stress (MTS), 80, 83, 90,
99, 104–107, 114, 119, 125, 132, 134,
143, 170, 171, 186, 194, 207, 211, 215,
306, 356, 360, 370, 371, 379, 415, 417,
418, 435, 457, 487, 490, 493, 496, 499,
505, 507, 511, 514–516
Melting temperature, 39, 51, 53, 101, 168, 185,
272, 315, 337, 511
Metallic bonding, 38
Metal matrix composite (MMC), 72
Miller-Bravais, 271
Miller indices, 62
Mobile dislocation, 68, 132, 168, 194, 211, 212,
219, 417–419, 421–424, 427, 428, 436,
480, 503, 504
Model applicability at high temperature, 178
Model material, 107, 168, 489
Modified evolution law, 134
Molybdenum, 8, 59, 60, 73, 74, 80, 139–141,
212–215, 220, 394, 512
Monotonic, 109, 163, 178
MTS model, 114, 119–141, 168, 179, 181, 190,
192, 193, 208, 211, 221, 307, 315, 329,
335, 370, 390, 412, 425, 428, 435, 436,
447, 504
MTS model constant, 164, 420, 422, 423, 433
MTS model parameters, 190, 193, 207
Multiple obstacles, 88, 89, 124, 125, 127, 129,
131–133, 289, 349
Multiple strengthening mechanisms, 125, 329

N

NaCl, 51
Nano-laminate, 44
Neck (tensile test), 11, 25
Newton (unit of force), 5
Nickel
 Monel 400, 197–201, 204, 208, 338, 381
 Ni-C alloys, 186, 261, 488, 494
 nickel-base alloy C-22, 27
 Ni-30 Co, 447, 448
Nickel base superalloys
 Alloy C-22, 28, 394, 396
 Alloy C-276, 385, 391, 395, 398

HypoSuperalloy, 402–405, 430
 Inconel 600, 395, 398
 Inconel 718, 378, 395
 Rene N4, 401
 Niobium, 68, 69, 84, 85, 91, 95, 110, 111, 125, 127, 129, 130, 132, 139, 154, 212, 215, 216, 220, 236, 253–264, 322, 329, 336–338, 361, 364–366, 371, 386, 402, 409, 410, 412, 420, 422, 423, 427, 428, 493, 494, 500, 501, 503, 504, 512, 513
 Non-uniform strains, 98
 Normal stress, 12, 42, 124, 302
 Nucleation and growth, 65
 Nuclei, 65

O

Obstacle, 66, 77, 104, 119, 143, 167, 185, 194, 195, 200–202, 206–208, 213, 285, 346, 380, 412, 436, 487
 Obstacle population, 125, 126, 128, 133, 143, 146, 149, 150, 152, 154–156, 159, 223, 224, 235, 289, 301, 302, 314, 315, 318, 321, 326, 327, 337, 339, 358, 364, 371, 373, 380, 381, 383, 388, 396, 401, 414, 436, 447, 450, 478, 487, 488, 492, 515
 Obstacle profile, 77, 78, 88, 89, 104, 123, 126
 Obstacle strength, 104
 Octahedron, 62
 0.002 offset strain, 18, 19, 31, 308
 Omega term, 428
 Ordered intermetallic, 377, 396, 401
 Orowan equation, 48, 82, 418, 487
 Oxygen interstitial, 213

P

Packing density, 51
 Path change, 104, 108, 109, 114, 116, 476, 481, 487, 492
 Path dependence, 103, 104, 114, 152, 159, 496
 Peierls stress, 60, 63, 212, 225, 271
 Periodic table, 39, 53
 Permittivity of vacuum, 51
 Physical properties, 50, 144
 Plastic deformation, 17, 29, 35, 41–45, 48, 95
 Plastic strain, 16, 77, 86, 169, 192, 336
 Platens, 11, 12
 Poisson's ratio, 9, 10, 29, 122
 Polycrystal, 64–66, 70, 71, 90, 106, 177, 272, 298, 301, 302, 436
 Polymers, 10
 Portevin-Le Chatelier effect, 111

Powder materials, 481
 Power law hardening, 100
 Precipitate, 72, 75, 90, 309, 345, 349, 377, 379, 381, 382, 385, 393, 394, 399, 401, 403, 487
 Precipitate strengthening, 72, 73, 75, 90, 385, 401, 487
 Prestrain, 87, 101, 108, 152–156, 158–161, 164, 167, 169, 170, 172, 174, 175, 184, 185, 187, 188, 190, 192, 193, 195, 196, 201, 204, 207, 209, 211, 226, 227, 262, 265, 290, 316, 329, 332–334, 350, 410, 436, 438, 447, 476, 492, 493, 504, 509
 Prismatic plane, 63, 271
 Proportional limit, 18, 19, 30, 31, 74
 Pyramidal plane, 271

R

Rate-dependent, 169, 188, 192, 195
 Rate insensitive, 168, 222
 Rate of strain-hardening, 91, 108, 152, 182, 197, 198, 202, 208, 249, 281, 282, 313–315, 336, 384, 396, 398, 401, 452, 454, 455, 461, 463, 467, 474–476, 479–481, 498, 506–510
 Recovery, 70, 71, 90, 91, 96, 134, 207, 437, 492
 Recrystallization, 96, 335, 349, 445, 453
 Reload, 15, 86, 101, 132, 152, 167, 211, 290, 350, 410, 436, 492
 Repulsive force, 36–38

S

Saturation stress, 71, 90, 93, 107, 121, 161, 162, 188, 189, 323, 325, 326, 335, 386, 387, 391, 396, 399, 401, 402, 405, 412, 422, 428, 429, 440, 492, 498, 501, 514
 Saturation threshold stress, 93, 116, 171, 201, 205, 208, 209, 257, 258, 276, 283, 294, 295, 304, 310, 323, 334, 335, 342, 386, 390, 410, 433, 465, 494–496, 500, 501
 Scalar stress (and strain) representations
 effective stress and strain, 21, 462
 octahedral stress and strain, 21
 von mises effective stress and strain, 21
 von mises stress and strain, 20, 21, 177, 180, 440, 463, 470, 476
 Schmidt factor, 58, 59, 66, 177
 Sea of electrons, 38, 39
 Separation distance, 35, 37, 50
 Serrations, 110, 111, 363, 378, 409

- Shear, 12, 20, 57, 122, 173, 179, 207, 220, 443, 451, 476, 481, 510
- Shear modulus
 temperature-dependent shear modulus, 125, 139–141, 143, 144, 225, 330, 418, 437
- Shear strain, 20, 43, 69, 74, 220, 221, 462, 470
- Shear stress, 12, 13, 21, 42, 43, 53, 58, 59, 69, 70, 73, 80, 90, 124, 179, 180, 220, 221, 250, 299, 378, 390, 439, 462, 470, 476, 508
- Shock deformed material
 shock-deformed copper, 49
 shock deformed nickel, 192–194, 505
- Sigma hat, 80
- Silver, 69, 86, 202, 436
- Simple cubic, 39, 40, 45, 47, 51, 65, 66
- Single crystal, 45, 55–60, 64–66, 69, 70, 72, 73, 80, 89, 122, 139, 298–302, 401, 436, 441
- Single crystal airfoils, 401
- Slip
 planar slip, 49
 wavy slip, 49
- Slip direction (SD), 56–59, 62, 63, 73, 74, 202
- Slip plane, 56, 58–60, 62, 63, 67, 68, 70, 71, 77, 78, 80, 81, 88, 89, 122, 124, 202, 271
- Sodium, 35, 37, 51
- Solute atom, 68, 90, 349, 381, 387, 409, 447
- Solute concentration, 416, 417, 419, 420, 429, 433, 503
- Solute transport, 417
- Solution hardening, 143, 147, 164, 201, 204, 340, 345, 351, 384, 503
- Split Hopkinson pressure bar (SHPB), 101, 190, 284, 382
- Spring constant, 4, 5, 23
- Stacking fault energy, 201, 202, 205, 206, 208, 342, 350, 496
- Stage II hardening
 strain-rate dependence, 162, 172, 189, 325, 493
 temperature dependence, 298, 386, 401
- Stage IV hardening, 440–442, 448, 455, 465, 478, 480, 508
- State, 103, 104, 131, 164, 169
- State variable, 103–105, 108, 109, 114, 119, 131, 132, 134, 139, 155, 158, 163, 168, 183, 278, 308, 312, 332, 370, 371, 377, 382, 435, 480, 481, 487, 488, 490, 492, 506, 510, 514, 515
- Steel
 0.012% C steel, 294
 1018 steel, 13, 14, 18, 19, 55, 59, 69, 85, 86, 91, 231–240, 254, 262, 338, 361, 366, 371, 412, 420–422, 431, 493–495, 501, 502, 512
 mild steel, 3, 44, 110, 111, 409, 410, 500
- Stiffness, 23, 38
- Stored dislocation, 50, 69–72, 90, 132, 152, 154–156, 159, 164, 168, 173, 185, 186, 194, 204, 207, 211, 231, 263, 340, 357, 360, 379, 417, 418, 442, 480
- Stored dislocation density, 86, 89, 134, 310–312, 314, 368, 369, 371, 409, 419, 436, 447, 478, 487–489, 491–494, 496, 503, 504, 515
- Strain, 6, 39, 55, 77, 95, 119, 143, 167, 211, 271, 346, 409, 435, 487
- Strain hardening, 27, 95, 101, 108, 152, 154, 168, 177, 181, 183, 194, 197, 198, 201, 202, 208, 223, 234, 240, 247–249, 255, 273, 276, 280–282, 284, 302, 306, 307, 310–315, 319, 336, 339, 340, 369, 379, 383–399, 409, 430, 432, 435, 437, 440, 444, 447, 452, 454, 455, 457–463, 467, 468, 470, 474–476, 479–481, 489, 493, 497, 498, 506–510
- Strain-induced martensite, 398
- Strain rate
 quasi-static (QS), 86, 151, 197, 205, 307, 346, 348
- Strain-rate-change tests, 182, 183, 378, 427, 503
- Strain-rate dependence, 48, 100, 134, 135, 154, 161, 169, 172, 175, 191, 211, 226, 227, 237, 244, 247, 252, 262–264, 271, 286, 288, 294, 295, 302, 306, 315, 325, 352, 399, 423, 447, 456, 461, 465, 468, 487, 488, 492, 503, 514, 515
- Strain-rate sensitivity (m-value), 178, 179, 183, 262, 263, 483
- Strengthening, 55, 67, 68, 72, 73, 206, 213, 246, 314, 339, 349, 350, 352, 370, 382, 384, 398, 401, 410, 445–447, 457, 480, 487, 493, 503–506
- Strengthening mechanism, 72, 75, 90, 125, 139, 147, 167, 185, 262, 279, 329, 349
- Stress, 5, 42, 55, 77, 95, 119, 143, 154, 167, 211, 271, 346, 377, 378, 409, 487
- Stress state, 12, 13, 19, 96, 176, 177, 182, 440, 451, 475, 476, 508, 509
- Stress-state dependence of hardening, 177, 436
- Stress strain curve, 11, 44, 55, 89, 95, 136, 150, 173, 175–179, 226, 272, 273, 349, 383, 409, 435, 492
- Structure, 35, 55, 86, 96, 143, 168, 212, 271, 345, 378, 418, 445, 487
- Substitutional, 68, 111, 201, 352

T

- Tangled dislocations, 49, 50
- Tantalum, 8, 31, 212, 215, 217, 220, 490, 512
- Tapered plate experiment, 99, 131, 194, 505
- Taylor factor, 124, 390, 418, 419
- Temperature dependence, 8, 100, 101, 107,
 - 110, 119–125, 139, 163, 175, 184, 191,
 - 201, 212, 215, 226, 230, 236, 252, 253,
 - 261, 264, 271, 288, 301, 306, 309, 314,
 - 315, 319, 324, 332, 346, 350, 357, 365,
 - 368, 378, 380, 386, 390, 398, 400, 401,
 - 413, 418, 419, 423, 430, 492, 502,
 - 503, 508
- Tensile axis, 20, 57, 59, 69, 122
- Tension
 - tensile test, 3, 4, 6, 8–11, 13, 18, 21, 25, 27,
 - 29–32, 42, 48, 64, 96, 111, 122, 178,
 - 186, 272, 367, 394, 398, 476
 - test specimen, 1–6, 8–11, 13, 16, 18, 22–25,
 - 27, 29, 48, 49, 86, 103, 135, 136, 138,
 - 144, 156, 169, 179, 185, 480, 511
- Tension test, 11, 12, 16–20, 35
- Texture evolution, 177, 271, 436, 440, 480, 507
- Theoretical shear stress, 45, 48, 60
- Theoretical strength, 44, 45, 53
- Thermal activation, 73, 78, 81, 83, 90, 106, 120,
- 122–125, 133, 213, 220, 223, 224, 295,
- 349, 357, 370, 412
- Thermal energy, 78–80, 82, 90
- Thermal expansion coefficient, 38, 39, 50
- Thermal softening, 335
- Thermo-mechanical processing
 - forging, 96
 - rolling mill, 86, 87, 96, 98
 - swaging, 97, 98
 - wire drawing, 177, 340, 445
- Titanium
 - commercially pure (CP), 319
 - El 60 grade, 316
 - oxygen equivalent (Oeq), 315
 - Ti-50A, 315–317, 321, 326, 328, 341
 - Ti-6Al-4V, 346, 493, 494, 511
 - Ti-Al, 330–332
- Torsion tests, 13, 20, 179, 180, 440, 465,
- 470, 476
- Transformation induced plasticity (TRIP), 398
- Transition metals, 39
- True strain, 16, 24–28, 31, 32, 87, 198, 227,
- 231, 244, 332, 336, 346, 403, 404, 412,
- 430, 441, 463
- True stress, 16, 17, 24, 26, 227, 231, 403–405,
- 412, 430, 441, 463
- True stress-strain curve, 16, 17, 31, 32

Tungsten

- ultra-fine-grained (UFG), 477
- Turbine disk, 96, 100
- Twinning-induced plasticity (TWIP), 398
- Twinning stress, 250, 305, 306, 319

U

- UfKonel, 227–232, 234, 236, 238, 239, 242,
- 254, 262, 265, 273, 280, 290, 322, 332,
- 334, 360
- Unit cells, 40, 41, 46, 51, 55–57, 63, 64
- Upper yield point, 111

V

- Vacancy, 47, 68, 299
- Vacuum arc remelting (VAR), 143
- Vanadium, 212, 215, 236, 241–252, 254, 259,
- 261, 262, 264, 281, 307, 322, 324, 326,
- 328, 329, 334–338, 361, 364–366, 371,
- 386, 399, 402, 409–414, 427, 431, 493,
- 494, 498, 500–502, 512
- Vibrational frequency, 82
- Viscoelasticity, 18
- Voce law, 71, 160, 161, 205, 206, 430, 432,
- 437, 492
- von Mises yield criterion, 19, 177, 221

W

- Well-annealed condition, 69, 75, 167, 186, 271,
- 445, 488, 489, 515

Y

- Yield phenomena
 - yield drop, 253, 412, 421
- Yield point elongation, 111
- Yield stress, 14, 44, 55, 80, 95, 120, 143, 167,
- 211, 273, 346, 377, 421, 438, 488
- Young's modulus, 7, 70, 122

Z

- Zener and Hollomon, 105, 106
- Zinc, 67, 272–276, 280, 281, 291, 293, 298,
- 334, 335, 337–339, 494, 498, 499, 512
- Zircaloy-2, 138, 298, 308–315, 346, 457, 489,
- 494, 506, 507
- Zirconium
 - effect of oxygen concentration, 299–302